



***COMBUSTION SCIENCE TO  
REDUCE PM EMISSIONS  
FOR MILITARY PLATFORMS***

***WP-1577***

***FINAL REPORT***

***January 2012***

***Dr. W. M. Roquemore  
(Principal Investigator)  
Air Force Research Laboratory***

***Prof. T. A. Litzinger  
(Co-Principal Investigator)  
Pennsylvania State University***

**Approved for Public Release  
Distribution Unlimited**



## PERFORMING ORGANIZATIONS AND RESEARCHERS

*Air Force Research Laboratory (AFRL)*  
(CFM Burner, WSR, Mass Spec., T-63)

W. M. Roquemore (Principal Investigator)  
W. S. Anderson  
V. Belovich  
J. R. Gord  
A. C. Lynch  
R. Pawlik  
J. Zelina

*Pennsylvania State University (PSU)*  
(HP Reactor, Turbulent/Premixed Flame)

T. A. Litzinger (Co-Principal Investigator)  
R. J. Santoro (Lead-HP Reactor)  
Suresh Iyer  
Arvind V. Menon

*United Technologies Research Center*  
(Kinetics, Modeling, Premixed Flame)

M. B. Colket (Lead)  
R. J. Hall  
S. Zeppieri

*Yale University*  
(Kinetics and Modeling)

M. D. Smooke (Lead - Kinetics/Model)  
B. A. V. Bennett  
B. C. Connelly  
J. A. Cooke  
S. B. Dworkin  
M. B. Long

*Army Research Laboratory (ARL)*  
(Opposed Jet Flame)

K. L. McNesby (Lead)  
V. Babushok  
R. Benjamin  
M. Biss  
J. Densmore  
B. Homan  
M. Kurman  
C.-B. Kweon  
B. McAndrew  
T. Nguyen  
Z. Pvine  
Z. Quine  
W. Tsang

*Innovative Scientific Solutions, Inc. (ISSI)*  
(Modeling and Laser Diagnostics)  
V. R. Katta (Lead - Modeling)  
A. Forlines (Diagnostics)

*University of Dayton Research Institute*  
(Shock Tube and Well Stirred Reactor)

S. S. Sidhu (Lead - Shock Tube)  
S. D. Stouffer (Lead - Centerbody Burner)  
M. Arstingstall  
G. Justinger  
M. S. Kahandawala  
S. Saxena

## Table of Contents

<b>1.0</b>	<b><u>Executive Summary</u></b>	<b>1</b>
1.1	<u>Background and Approach</u>	1
1.2	<u>Major Outcomes from the Project</u>	2
<b>2.0</b>	<b><u>Introduction</u></b>	<b>4</b>
2.1	<u>Motivation for Program</u>	4
2.2	<u>Program Objectives</u>	5
2.3	<u>Overall Research Approach</u>	5
<b>3.0</b>	<b><u>Modeling Approaches</u></b>	<b>8</b>
3.1	<u>Introduction</u>	8
3.2	<u>Kinetics Modeling Overview and Coordination</u>	8
3.2.1	<u>Ethylene Kinetics Model (SERDP C2H4)</u>	8
3.2.2	<u>Surrogate Fuel Selection</u>	12
	<i>JP-8 Surrogate</i>	12
	<i>Surrogate Fuel for F-T Fuel</i>	13
3.2.3	<u>Kinetics Model for JP-8 Surrogate Fuel (SERDP SUR v1 and v2)</u>	14
	<i>First Generation JP-8 Surrogate Model (SERDP SURR v1)</i>	14
	<i>Second Generation JP-8 Surrogate Model (SERDP SURR v2)</i>	21
3.2.4	<u>Soot Models</u>	29
	<i>Soot Inception</i>	30
	<i>Surface Growth</i>	31
	<i>Surface Oxidation</i>	32
	<i>Aerosol or Particle Dynamics</i>	32
	<i>Soot Ageing</i>	33
	<i>Scrubbing</i>	34
	<i>Radiation</i>	34
	<i>Particle Transport</i>	34
	<i>Modifications for High Pressure Simulations</i>	35
3.2.5	<u>Incorporation of Soot Models into Combustion Codes used in this Program</u>	36
3.3	<u>UNICORN</u>	38
3.3.1	<u>Chemical Kinetics Models Evaluation</u>	38
3.3.2	<u>Soot Particle Simulation</u>	39
3.3.3	<u>Soot Models</u>	41
	<i>Two-equation Model</i>	41
	<i>Method-of-Moments Model</i>	42
3.4	<u>CHEMKIN Software</u>	47
<b>4.0</b>	<b><u>Experimental Methods</u></b>	<b>48</b>
4.1	<u>Introduction</u>	48
4.2	<u>Shock Tubes</u>	48
4.2.1	<u>UDRI High-pressure (non-heated) Shock Tube</u>	48
	<i>Product Characterization</i>	50
4.2.2	<u>UDRI High-pressure Heated Shock Tube</u>	52



4.2.3	Diagnostic Procedures	53
4.2.4	Experimental Conditions	58
4.2.5	Kinetic Modeling of Shock Tube Results	60
	<i>Ethylene Combustion</i>	60
	<i>M-Xylene Combustion</i>	60
	<i>Modeling n-dodecane and n-dodecane/m-xylene Blend Combustion</i>	63
4.3	Co-flow Diffusion Flame	64
4.3.1	Experimental Set-up	64
4.3.2	Experimental Procedure	68
4.3.3	Diagnostic Methods	71
	<i>Laser-Induced Incandescence</i>	71
	<i>Laser-Induced Fluorescence</i>	72
	<i>Laser Extinction</i>	72
4.4	Opposed-jet Diffusion Flame	74
4.4.1	Experimental Set-up	74
4.4.2	Experimental Procedure	81
4.4.3	Diagnostic Methods	82
	<i>Planar Laser Induced Fluorescence/Light Scattering</i>	82
	<i>Tunable Diode Laser Absorption Spectroscopy</i>	82
	<i>Imaging Pyrometry</i>	87
4.5	Centerbody Flame	95
4.5.1	Experimental Set-up	95
4.5.2	Experimental Procedure	101
4.5.3	Diagnostic Methods	101
	<i>Sheet Lightning and Flame Photography</i>	101
	<i>Infrared Flame Imaging</i>	103
	<i>High Speed Imaging</i>	103
	<i>Laser Induced Incandescence (LII)</i>	104
<b>5.0</b>	<b>Results</b>	<b>106</b>
5.1	Shock Tube	106
5.1.1	Ethylene Combustion at Elevated Pressures	106
5.1.2	M-xylene Combustion	115
	<i>Modeling Results</i>	120
	<i>Sensitivity and Reaction Path Analysis</i>	122
5.1.3	N-dodecane and n-dodecane/m-xylene Surrogate Combustion	125
5.1.4	Product Characterization	130
	<i>Ethylene Combustion</i>	130
	<i>m-xylene Combustion</i>	132
	<i>n-dodecane and n-dodecane/m-xylene Surrogate Combustion</i>	132
5.2	Co-flow Diffusion Flame	154
5.2.1	Impact of Soot Radiation on Dynamics of Co-flow Flames	154
5.2.2	N <sub>2</sub> -Diluted Ethylene Flames at Pressure	163
	<i>Modeling Studies</i>	164
5.2.3	Effect of m-xylene Addition on PAH and Soot in N <sub>2</sub> -Diluted Ethylene Flames	171
	<i>Modeling Studies</i>	172

5.2.4	Effect of Surrogate and its Components on Soot in N <sub>2</sub> -Diluted Ethylene Flames	181
5.2.5	Effect of JP-8 on Soot in N <sub>2</sub> -Diluted Ethylene Flames	188
5.2.6	Simulation of Attached Co-Flow Flames	192
5.3	Opposed-jet Diffusion Flame	199
	<i>Modeling</i>	199
	<i>Planar Laser Induced Fluorescence/Light Scattering</i>	199
	<i>Tunable Diode Laser Absorption Spectroscopy</i>	200
	<i>Imaging Pyrometry</i>	200
	<i>High Pressure Flame Results</i>	201
5.4	Centerbody Flame	216
5.4.1	Predictions on Sooting Behavior of Recirculation-Zone-Supported Flames	217
5.4.2	Soot Studies of Laminar Diffusion Flames with Recirculation Zones	223
5.4.3	Stability of Lifted Flames in Centerbody Burner	230
5.4.4	Dynamics of the Lifted Flame Supported by a Recirculation Zone	235
5.4.5	Sooting Characteristics of Partially Premixed Flames in Centerbody Burner	245
5.4.6	Comparisons with Experiments	258
5.4.7	Autoignition Phenomenon	265
5.4.8	Liquid Fuels	274
5.5	Kinetic Model Evaluation Using UNICORN	287
5.5.1	Ethylene Models	287
5.5.2	Heptane Models	295
5.5.3	JP-8 Models	305
5.6	Simulations of Flames with Recirculation Zones using JP-8 Surrogates	318
5.6.1	Centerbody Burner	318
5.6.2	Swirl-Stabilized Turbulent Flames	325
5.7	Simulation of Partially Premixed Flames	339
5.8	SNETPSR Simulations of Combustion Particulate Emissions	348
6.0	Conclusions and Recommendations	355
7.0	References	356
	Appendix: List of Archival Publications and Conference Papers	376

## List of Tables

Table 3.1	<u>Surrogates, Their Components and Computed Properties</u>	<b>13</b>
Table 3.2	<u>Computed Iso-butyl Structures in Fuels</u>	<b>14</b>
Table 3.3	<u>Thermodynamics of Key Species in m-Xylene System</u>	<b>19</b>
Table 3.4	<u>PAH Forming Reactions for m-Xylene System</u>	<b>20</b>
Table 3.5	<u>Literature Data Sets Used To Benchmark SERDP Mechanism</u>	<b>23</b>
Table 4.1	<u>Experimental Matrix for Ethylene Study</u>	<b>58</b>
Table 4.2	<u>Experimental Matrix for M-xylene Study</u>	<b>59</b>
Table 4.3	<u>Experimental Matrix for N-dodecane and n-dodecane / m-xylene Blend Study</u>	<b>59</b>
Table 4.4	<u>Experimental Conditions for Effects of Fuels Added to Ethylene Flame</u>	<b>74</b>
Table 4.5	<u>Temperature Dependence of <math>\text{line strength}^a</math> of P(23) Absorption Line of <math>(\nu_4 + \nu_5)</math></u>	<b>89</b>
Table 4.6	<u>Mass Flow Rates Used in Experiments with Air/N<sub>2</sub>/Ethylene Flames</u>	<b>96</b>
Table 4.7	<u>Flow Rates for Partially Premixed Ethylene and Air Flames</u>	<b>96</b>
Table 4.8	<u>Mass Flow rates for Vaporized Liquid Fuel Flames</u>	<b>97</b>
Table 5.1	<u>Volatile and Semi Volatile Species Extracted in Combustion of n-Dodecane</u>	<b>141</b>
Table 5.2	<u>Volatile and Semi Volatile Species Extracted in Combustion of M-xylene (<math>\Phi=3</math>)</u>	<b>143</b>
Table 5.3	<u>Species extracted from soot surface in Ethylene combustion</u>	<b>145</b>
Table 5.4	<u>Species extracted from soot surface in m-xylene combustion</u>	<b>147</b>
Table 5.5	<u>Species extracted from soot surface from n-dodecane combustion</u>	<b>150</b>
Table 5.6	<u>Species extracted from soot surface in combustion of n-dodecane/ m-xylene blend</u>	<b>152</b>
Table 5.7	<u>Volumetric Flow Rates (Standard Liters/Minute, SLPM) of Studied Flames</u>	<b>227</b>
Table 5.8	<u>Surrogate Mixtures for JP-8 Fuel</u>	<b>310</b>

## List of Figures

Figure 2.1	<u>Hierarchy of experiments used in the program</u>	<b>7</b>
Figure 3.1	<u>Comparison modeling, experimental results fuel-rich oxidation ethylene single-pulse tube</u>	<b>9</b>
Figure 3.2	<u>Additional comparisons oxygen containing species</u>	<b>10</b>
Figure 3.3	<u>Comparison computed decay of m-xylene using original combined mechanism data</u>	<b>15</b>
Figure 3.4	<u>Results from sensitivity analysis for the m-xylene reaction system</u>	<b>16</b>
Figure 3.5	<u>Set of PAH-forming reactions from the toluene system (Colket and Seery)</u>	<b>17</b>
Figure 3.6	<u>Examples of PAH forming reactions</u>	<b>18</b>
Figure 3.7	<u>Structures and nomenclature for C16 species</u>	<b>18</b>
Figure 3.8	<u>Structures and nomenclature for C13-C15 species</u>	<b>19</b>
Figure 3.9	<u>Comparison of PAH formation with and without added reactions</u>	<b>21</b>
Figure 3.10	<u>Comparison of Experimental and Computational Ignition Delay Times</u>	<b>24</b>
Figure 3.11	<u>Comparison of Species Profiles during m-Xylene Oxidation in a Flow Reactor</u>	<b>25</b>
Figure 3.12	<u>Species Profiles Associated with APFR m-Xylene Oxidation System</u>	<b>25</b>
Figure 3.13	<u>Fuel, Oxygen, CO, CO<sub>2</sub> Mole Fractions vs Reactor Temp. JSR Test Conditions</u>	<b>26</b>
Figure 3.14	<u>Mole Fractions of Light Species vs. Reactor Temperature in JSR</u>	<b>27</b>
Figure 3.15	<u>Mole Fractions of Cyclic Species vs. Reactor Temperature in JSR</u>	<b>27</b>
Figure 3.16	<u>Comparison of Predicted and Computed Flame Speeds</u>	<b>28</b>
Figure 3.17	<u>Soot formation processes in premixed, laminar flame (courtesy of H. Wang)</u>	<b>29</b>
Figure 3.18	<u>Predicted Peak Soot Volume Fractions vs. Pressure in Counterflow Ethylene Flames</u>	<b>36</b>
Figure 3.19	<u>Predicted Peak Soot Volume Fractions vs. Pressure Showing Decreased Pressure</u>	<b>36</b>
Figure 3.20	<u>Prediction soot particles in recirculation zone associated a sooty flame</u>	<b>40</b>
Figure 3.21	<u>Prediction soot particles in recirculation zone associated with nearly non-sooting flame</u>	<b>41</b>
Figure 3.22	<u>Number density, square mean value diameter, standard deviation for coagulation</u>	<b>44</b>
Figure 3.23	<u>Number density, square mean value diameter, standard deviation mean value</u>	<b>44</b>
Figure 3.24	<u>Temperature distribution predicted using MOM soot model co-flowing jet diffusion flame</u>	<b>45</b>
Figure 3.25	<u>Comparison of temperature and CO<sub>2</sub> jet diffusion flame at 40 mm</u>	<b>45</b>
Figure 3.26	<u>Comparison of temperature and CO<sub>2</sub> jet diffusion flame at 70 mm</u>	<b>46</b>

Figure 3.27	<u>Centerbody flames simulated with (a) two-equation and (b) MOM soot models</u>	<b>46</b>
Figure 4.1	<u>General schematic of the shock tube</u>	<b>48</b>
Figure 4.2	<u>A photograph of UDRI high-pressure shock tube</u>	<b>49</b>
Figure 4.3	<u>Schematic of the test section (TS)</u>	<b>50</b>
Figure 4.4	<u>Schematic of the sample preparation unit (SPU)</u>	<b>50</b>
Figure 4.5	<u>A photograph of UDRI heated high-pressure shock tube</u>	<b>52</b>
Figure 4.6	<u>Example of oscilloscope traces ethylene combustion experiment showing profiles</u>	<b>54</b>
Figure 4.7	<u>End-wall pressure profiles for ethylene-oxygen mixtures with 93% dilution in argon</u>	<b>55</b>
Figure 4.8	<u>End-wall pressure profiles for ethylene-oxygen mixtures with 96 and 98% dilution in argon</u>	<b>56</b>
Figure 4.9	<u>An example of an oscilloscope trace from an experiment with the non-heated shock tube</u>	<b>57</b>
Figure 4.10	<u>Ignition delay combustion n-dodecane/ m-xylene blend</u>	<b>57</b>
Figure 4.11	<u>An example of ignition delay time modeling procedure using SHOCKIN program</u>	<b>62</b>
Figure 4.12	<u>An example of m-xylene ignition delay time modeled using the SHOCKIN program</u>	<b>63</b>
Figure 4.13	<u>The high pressure chamber and burner used in co-flowing flame studies</u>	<b>67</b>
Figure 4.14	<u>Layout of the fuel and air delivery system for co-flow diffusion flame</u>	<b>68</b>
Figure 4.15	<u>Calibration for the LII signal at 3 atm</u>	<b>70</b>
Figure 4.16	<u>Effect of nitrogen flowrate on luminosity (Ethylene flowrate)</u>	<b>70</b>
Figure 4.17	<u>A schematic of the opposed flow burner showing gas flow and flame location</u>	<b>76</b>
Figure 4.18	<u>Photograph ethylene/air opposed jet flame showing separation sooting combustion regions</u>	<b>77</b>
Figure 4.19	<u>A photograph of an ethylene/air flame within the burner chamber</u>	<b>77</b>
Figure 4.20	<u>A schematic of the experimental apparatus, including some optical diagnostics</u>	<b>78</b>
Figure 4.21	<u>The Collision-type atomizer</u>	<b>78</b>
Figure 4.22	<u>A diagram of the vaporizer apparatus integrated into the burner system</u>	<b>79</b>
Figure 4.23	<u>A photograph of the burner assembly, the syringe pump, and the fluidized bath</u>	<b>79</b>
Figure 4.24	<u>Elevated pressure burner assembly, in co flow mode, sapphire window port removed</u>	<b>80</b>
Figure 4.25	<u>Schematic of elevated pressure rig and high speed imaging system</u>	<b>81</b>
Figure 4.26	<u>An image of an ethylene/m-xylene (5%)/air opposed jet flame</u>	<b>90</b>
Figure 4.27	<u>A schematic of the experimental setup for acetylene measurement by QCL</u>	<b>90</b>

Figure 4.28	<u>Laser output vs time measured through interferometer evacuated gas absorption cell</u>	<b>91</b>
Figure 4.29	<u>Variation of initial lasing frequency with substrate temperature</u>	<b>91</b>
Figure 4.30	<u>Frequency down-chirp of QCL output function of amplitude of driving current pulse</u>	<b>92</b>
Figure 4.31	<u>Acetylene transmission spectra converted to spectral absorbance</u>	<b>92</b>
Figure 4.32	<u>Integrated absorbance plotted against acetylene concentration and partial pressure</u>	<b>93</b>
Figure 4.33	<u>Intensity spectrum of Tungsten-Halogen light source</u>	<b>93</b>
Figure 4.34	<u>Measured spectral response curves for Vision Research Camera used in these measurements</u>	<b>94</b>
Figure 4.35	<u>Calculated temperature of calibrated blackbody source from still images taken with camera</u>	<b>94</b>
Figure 4.36	<u>Experimental set-up showing flow controllers, test section, laser-sheet-lighting arrangement</u>	<b>95</b>
Figure 4.37	<u>Vaporizer Concept for Centerbody Flame Rig</u>	<b>98</b>
Figure 4.38	<u>Photograph of the Vaporizer Tubing and Tee</u>	<b>99</b>
Figure 4.39	<u>Centerbody Fuel Tube Heat Shield Design</u>	<b>100</b>
Figure 4.40	<u>Fuel Vaporization System for the Centerbody Burner</u>	<b>100</b>
Figure 4.41	<u>Centerbody Flame During the Mie Scattering Experiment</u>	<b>102</b>
Figure 4.42	<u>Photo of the Centerbody Stack and Windows</u>	<b>103</b>
Figure 5.1	<u>Ignition delay in combustion of ethylene: shock waves at <math>\Phi=3</math>, Ar=93% &amp; P~2 atm</u>	<b>110</b>
Figure 5.2	<u>Ignition delay in combustion of ethylene: shock waves at <math>\Phi=3</math>, Ar=93% &amp; P~10 atm</u>	<b>110</b>
Figure 5.3	<u>Ignition delay in combustion of ethylene: shock waves at <math>\Phi=3</math>, Ar=93% &amp; P~18 atm</u>	<b>111</b>
Figure 5.4	<u>Ignition delay in combustion of ethylene: Effect of pressure at <math>\Phi=3.0</math> &amp; Ar=93%</u>	<b>111</b>
Figure 5.5	<u>Ignition delay in combustion of ethylene: Effect of pressure at <math>\Phi=1.0</math> &amp; Ar=93%</u>	<b>111</b>
Figure 5.6	<u>Ignition delay in combustion of ethylene: Effect of equivalence ratio at Ar=93% P~2</u>	<b>111</b>
Figure 5.7	<u>Ignition delay in combustion of ethylene: Effect of equivalence ratio at Ar=93% P~10</u>	<b>112</b>
Figure 5.8	<u>Ignition delay in combustion of ethylene: Fuel mixture dilution was 98% in argon <math>\Phi=1.0</math></u>	<b>112</b>
Figure 5.9	<u>Ignition delay in combustion of ethylene: Fuel mixture dilution was 96% in argon <math>\Phi=1.0</math></u>	<b>112</b>
Figure 5.10	<u>Ignition delay in combustion of ethylene: Dilution for conditions at <math>\Phi=1.0</math> and P~2 atm</u>	<b>112</b>
Figure 5.11	<u>Ignition delay in combustion of ethylene: Dilution for conditions at <math>\Phi=1.0</math> and P~10atm</u>	<b>113</b>
Figure 5.12	<u>Ignition delay in combustion of ethylene: Dilution for conditions at <math>\Phi=1.0</math> and P~18 atm</u>	<b>113</b>
Figure 5.13	<u>Ignition delay combustion of ethylene: Literature data at <math>\Phi=1.0</math>, Ar=96% and low pressures</u>	<b>113</b>

Figure 5.14	<u>Ignition delay in combustion of ethylene: Literature data at <math>\Phi=1.0</math>, Ar=98% low pressures</u>	<b>114</b>
Figure 5.15	<u>Shock-tube ignition data of ethylene-oxygen-argon mixtures</u>	<b>114</b>
Figure 5.16	<u>Ignition delay in combustion of m-xylene. <math>\Phi= 3.0</math>, Ar=98% and P = 2 atm with modeling</u>	<b>115</b>
Figure 5.17	<u>Ignition delay in combustion of m-xylene. <math>\Phi= 3.0</math>, Ar=98% and P = 18 atm with modeling</u>	<b>115</b>
Figure 5.18	<u>Ignition delay in combustion of m-xylene. <math>\Phi= 1.0</math>, Ar=98% and P=2 atm with modeling</u>	<b>116</b>
Figure 5.19	<u>Ignition delay in combustion of m-xylene. <math>\Phi= 1.0</math>, Ar=98% and P= 18 atm with modeling</u>	<b>116</b>
Figure 5.20	<u>Ignition delay in combustion of m-xylene. <math>\Phi=0.5</math>, Ar=98% and P = 2 atm with modeling</u>	<b>116</b>
Figure 5.21	<u>Ignition delay in combustion of m-xylene. <math>\Phi=0.5</math>, Ar=98% and P = 18 atm with modeling</u>	<b>116</b>
Figure 5.22	<u>Ignition delay in combustion of m-xylene. <math>\Phi= 0.5</math>, Ar=93% and P=18 atm with modeling</u>	<b>117</b>
Figure 5.23	<u>Ignition delay in combustion of m-xylene. <math>\Phi= 1.0</math>, Ar=93% and P = 18 atm with modeling</u>	<b>117</b>
Figure 5.24	<u>Ignition delay in combustion of m-xylene. <math>\Phi= 3.0</math>, Ar=93% and P = 18 atm with modeling</u>	<b>117</b>
Figure 5.25	<u>Ignition delay in combustion of m-xylene. Argon concentration =98% and P = 2atm</u>	<b>118</b>
Figure 5.26	<u>Ignition delay in combustion of m-xylene. Argon concentration =98% and P = 18 atm</u>	<b>118</b>
Figure 5.27	<u>Ignition delay in combustion of m-xylene. Argon concentration =93% and P = 18 atm</u>	<b>118</b>
Figure 5.28	<u>Ignition delay in combustion of m-xylene. Effect of dilution at <math>\Phi=0.5</math> and P = 18 atm</u>	<b>119</b>
Figure 5.29	<u>Ignition delay in combustion of m-xylene. Effect of dilution at <math>\Phi=0.5</math> and P = 18 atm</u>	<b>119</b>
Figure 5.30	<u>Global ignition delay correlation. Shock-tube ignition data of m-xylene/O<sub>2</sub>/Ar mixtures</u>	<b>120</b>
Figure 5.31	<u>GASKIN validation using hydrogen combustion</u>	<b>121</b>
Figure 5.32	<u>Model reduction: <math>\Phi=0.5</math>, Ar=93%, P= 18 atm</u>	<b>121</b>
Figure 5.33	<u>Simulation pressure from shock tube experiment using 1-D, CFD GASKIN program</u>	<b>122</b>
Figure 5.34	<u>Simulation temperature from shock tube experiment using 1-D, CFD GASKIN program</u>	<b>122</b>
Figure 5.35	<u>The reactions involved in the oxidation of m-xylene at T=1600 K</u>	<b>123</b>
Figure 5.36	<u>OH radical production SERDP model. <math>\Phi= 0.5, 1 \text{ \&amp; } 3</math>, T=1600 K; P=2 atm (Ar=98%)</u>	<b>125</b>
Figure 5.37	<u>OH radical production SERDP model. <math>\Phi= 0.5, 1 \text{ and } 3</math>, T= 1600 K; P=18 atm (Ar=98%)</u>	<b>125</b>
Figure 5.38	<u>Ignition delay in combustion of n-dodecane at <math>\Phi = 0.5</math>, P= 18 atm, Ar = 93% modeling</u>	<b>128</b>
Figure 5.39	<u>Ignition delay in combustion of n-dodecane at <math>\Phi = 1.0</math>, P= 18 atm, Ar = 93% modeling</u>	<b>128</b>
Figure 5.40	<u>Ignition delay in combustion of n-dodecane at <math>\Phi = 3</math>, P= 18 atm, Ar = 93% modeling</u>	<b>128</b>
Figure 5.41	<u>Ignition delay n-dodecane /m-xylene blend <math>\Phi =0.5</math>, P=18 atm, Ar =93% modeling</u>	<b>128</b>

Figure 5.42	<u>Ignition delay n-dodecane /m-xylene blend at <math>\Phi = 1.0</math>, <math>P=18</math> atm <math>Ar = 93\%</math> modeling</u>	<b>128</b>
Figure 5.43	<u>Ignition n-dodecane /m-xylene blend at <math>\Phi = 3.0</math>, <math>P=18</math> atm, <math>Ar = 93\%</math> modeling</u>	<b>128</b>
Figure 5.44	<u>Effect equivalence ratio on ignition delay in combustion n-dodecane at 18 atm, <math>Ar=93\%</math></u>	<b>129</b>
Figure 5.45	<u>Effect equivalence ratio on ignition delay in combustion the blend at 18 atm, <math>Ar= 93\%</math></u>	<b>129</b>
Figure 5.46	<u>Sensitivity analysis targeting OH radical production in combustion of n-dodecane</u>	<b>129</b>
Figure 5.47	<u>Combustion Ethylene: Model Yields Carbon Monoxide <math>\Phi=3.0</math>, <math>Ar=93\%</math> <math>P\sim 18</math> atm</u>	<b>134</b>
Figure 5.48	<u>Combustion Ethylene: Model Yields of Carbon Dioxide at <math>\Phi=3.0</math>, <math>Ar=93\%</math> <math>P\sim 18</math> atm</u>	<b>134</b>
Figure 5.49	<u>Combustion of Ethylene: Model Yields of Methane at <math>\Phi=3.0</math>, <math>Ar=93\%</math> <math>P\sim 18</math> atm</u>	<b>134</b>
Figure 5.50	<u>Combustion of Ethylene: Model Yields of Acetylene at <math>\Phi=3.0</math>, <math>Ar=93\%</math> <math>P\sim 18</math> atm</u>	<b>134</b>
Figure 5.51	<u>Combustion of Ethylene: Model Yields of Ethylene at <math>\Phi=3.0</math>, <math>Ar=93\%</math> <math>P\sim 18</math> atm</u>	<b>134</b>
Figure 5.52	<u>Combustion of Ethylene: Model Yields of Benzene at <math>\Phi=3.0</math>, <math>Ar=93\%</math> <math>P\sim 18</math> atm</u>	<b>134</b>
Figure 5.53	<u>Combustion of Ethylene: Model Yields of Toluene at <math>\Phi=3.0</math>, <math>Ar=93\%</math>, <math>P\sim 2, 10</math> and 18 atm</u>	<b>135</b>
Figure 5.54	<u>Combustion of Ethylene: Model Yields of Styrene at <math>\Phi=3.0</math>, <math>Ar=93\%</math> <math>P\sim 2, 10</math> and 18 atm</u>	<b>135</b>
Figure 5.55	<u>Combustion of Ethylene: Model Yields Phenyl acetylene <math>\Phi=3.0</math>, <math>Ar=93\%</math>, <math>P\sim 2, 10; 18</math>atm</u>	<b>135</b>
Figure 5.56	<u>Combustion of Ethylene: Model Yields of Naphthalene <math>\Phi=3.0</math>, <math>Ar=93\%</math>, <math>P\sim 2, 10; 18</math> atm</u>	<b>135</b>
Figure 5.57	<u>Soot Yields from Combustion of Ethylene at <math>\Phi=3.0</math>, <math>Ar=93\%</math>, <math>P\sim 2, 10</math> &amp; 18 atm</u>	<b>135</b>
Figure 5.58	<u>Carbon balance combustion-generated species ethylene combustion <math>\Phi=3</math>, <math>Ar=93\%</math> at 18atm</u>	<b>135</b>
Figure 5.59	<u>Combustion m-Xylene: Model Yields of Carbon Monoxide at <math>\Phi=3.0</math>, <math>Ar=93\%</math> <math>P\sim 18</math> atm</u>	<b>136</b>
Figure 5.60	<u>Combustion of m-Xylene: Model Yields of Carbon Dioxide at <math>\Phi=3.0</math>, <math>Ar=93\%</math> <math>P\sim 18</math> atm</u>	<b>136</b>
Figure 5.61	<u>Combustion of m-Xylene: Model Yields of Methane at <math>\Phi=3.0</math>, <math>Ar=93\%</math> <math>P\sim 18</math> atm</u>	<b>136</b>
Figure 5.62	<u>Combustion of m-Xylene: Model Yields of Acetylene at <math>\Phi=3.0</math>, <math>Ar=93\%</math> <math>P\sim 18</math> atm</u>	<b>136</b>
Figure 5.63	<u>Combustion of m-Xylene: Model Yields of Ethylene at <math>\Phi=3.0</math>, <math>Ar=93\%</math> <math>P\sim 18</math> atm</u>	<b>136</b>
Figure 5.64	<u>Combustion of m-Xylene: Model Yields of Benzene at <math>\Phi=3.0</math>, <math>Ar=93\%</math> <math>P\sim 18</math> atm</u>	<b>136</b>
Figure 5.65	<u>Combustion of m-Xylene: Model Yields of Toluene at <math>\Phi=3.0</math>, <math>Ar=93\%</math> <math>P\sim 18</math> atm</u>	<b>137</b>
Figure 5.66	<u>Combustion of m-Xylene: Model Yields of m-Xylene at <math>\Phi=3.0</math>, <math>Ar=93\%</math> <math>P\sim 18</math> atm</u>	<b>137</b>
Figure 5.67	<u>Combustion of m-Xylene: Model Yields of Phenol at <math>\Phi=3.0</math>, <math>Ar=93\%</math> <math>P\sim 18</math> atm</u>	<b>137</b>
Figure 5.68	<u>Combustion of m-Xylene: Model Yields of Phenylethyne at <math>\Phi = 3.0</math>, <math>Ar=93\%</math> <math>P\sim 18</math> atm</u>	<b>137</b>
Figure 5.69	<u>Combustion of m-Xylene: Model Yields of Ethylbenzene at <math>\Phi = 3.0</math>, <math>Ar=93\%</math> <math>P\sim 18</math> atm</u>	<b>137</b>



Figure 5.70	<u>Combustion of m-Xylene: Model Yields of Styrene at <math>\Phi=3.0</math>, Ar=93% P~18 atm</u>	<b>137</b>
Figure 5.71	<u>Combustion of m-Xylene: Experimental Yields of Naphthalene <math>\Phi=3.0</math>, Ar=93% P~18 atm</u>	<b>138</b>
Figure 5.72	<u>Soot Yields from Combustion of M-xylene at <math>\Phi=3.0</math>, Ar=93% and 98%, and 18 atm</u>	<b>138</b>
Figure 5.73	<u>Carbon balance combustion-generated species in m-xylene combustion Ar=93%, P=18 atm</u>	<b>138</b>
Figure 5.74	<u>Combustion n-Dodecane/m-Xylene blend: Yields Benzene <math>\Phi=3.0</math>, Ar=93% P~18 atm</u>	<b>138</b>
Figure 5.75	<u>Combustion n-Dodecane/m-Xylene blend: Yields Toluene <math>\Phi=3.0</math>, Ar=93% P~18 atm</u>	<b>138</b>
Figure 5.76	<u>Combustion n-Dodecane/m-Xylene blend: Yields m-Xylene <math>\Phi=3.0</math>, Ar=93% P~18 atm</u>	<b>139</b>
Figure 5.77	<u>Combustion n-Dodecane/m-Xylene blend: Model n-Dodecane <math>\Phi=3.0</math>, Ar=93% P~18 atm</u>	<b>139</b>
Figure 5.78	<u>Combustion n-Dodecane/m-Xylene blend: Model Yields Phenol <math>\Phi=3.0</math>, Ar=93% P~18 atm</u>	<b>139</b>
Figure 5.79	<u>Combustion n-Dodecane/m-Xylene blend: Model Phenylethyne <math>\Phi=3.0</math>, Ar=93% P~18 atm</u>	<b>139</b>
Figure 5.80	<u>Combustion n-Dodecane/m-Xylene blend: Model Ethylbenzene <math>\Phi=3.0</math>, Ar=93% P~18 atm</u>	<b>139</b>
Figure 5.81	<u>Combustion n-Dodecane/m-Xylene blend: Model Yields Styrene <math>\Phi=3.0</math>, Ar=93% P~18 atm</u>	<b>139</b>
Figure 5.82	<u>Combustion n-Dodecane/m-Xylene blend: Yields Naphthalene <math>\Phi=3.0</math>, Ar=93% P~18 atm</u>	<b>140</b>
Figure 5.83	<u>Soot N-dodecane and n-dodecane/ M-xylene blend <math>\Phi=3.0</math>, Ar=93%; 98%; 18 atm</u>	<b>140</b>
Figure 5.84	<u>Combustion of n-Dodecane: Model Yields of Benzene at <math>\Phi=3.0</math>, Ar=93% P~18 atm</u>	<b>140</b>
Figure 5.85	<u>Combustion n-Dodecane: Model Yields of Toluene at <math>\Phi=3.0</math>, Ar=93% P~18 atm</u>	<b>140</b>
Figure 5.86	<u>Combustion n-Dodecane: Model Yields of n-Dodecane at <math>\Phi=3.0</math>, Ar=93% P~18 atm</u>	<b>140</b>
Figure 5.87	<u>Combustion n-Dodecane: Model Yields of Phenylethyne at <math>\Phi=3.0</math>, Ar=93% P~18 atm</u>	<b>140</b>
Figure 5.88	<u>Comparison of soot yields from combustion of different fuels tested during SERDP</u>	<b>141</b>
Figure 5.89	<u>Comparison of soot yields from combustion of JP-8 and n-dodecane/m-xylene blend</u>	<b>141</b>
Figure 5.90	<u>Comparison predicted and measured temperature and soot-volume-fraction</u>	<b>159</b>
Figure 5.91	<u>Maximum radius 1000-K surface airside different levels soot radiation CFD model</u>	<b>159</b>
Figure 5.92	<u>Comparisons predicted, measured flame oscillations and respective PSDs</u>	<b>160</b>
Figure 5.93	<u>Comparisons predicted, measured soot structures at different phases</u>	<b>160</b>
Figure 5.94	<u>Comparisons predicted, measured PSDs of oscillations</u>	<b>161</b>
Figure 5.95	<u>Decay flame oscillations captured calculations 15% of methane replaced with acetylene</u>	<b>161</b>
Figure 5.96	<u>Transition steady-state flame periodically oscillating</u>	<b>162</b>
Figure 5.97	<u>Effect of radiation from soot on dynamics of 15%-acetylene flame</u>	<b>162</b>

Figure 5.98	<u>Images of nitrogen-diluted flames at pressures up to 5 atm</u>	<b>166</b>
Figure 5.99	<u>LII nitrogen-diluted flames pressures up to 5 atm</u>	<b>166</b>
Figure 5.101	<u>Peak volume fraction profiles derived from LII images</u>	<b>167</b>
Figure 5.102	<u>Small and large PAH profiles for diluted nitrogen flames (derived from 2-D images)</u>	<b>168</b>
Figure 5.103	<u>Effect of pressure on steady flame</u>	<b>169</b>
Figure 5.104	<u>OH concentration in N<sub>2</sub>-diluted ethylene jet diffusion flame</u>	<b>169</b>
Figure 5.105	<u>Soot concentration in N<sub>2</sub>-diluted ethylene jet diffusion flame</u>	<b>169</b>
Figure 5.106	<u>Instantaneous temperature distributions jet diffusion flame at normal pressure</u>	<b>170</b>
Figure 5.107	<u>Instantaneous soot distributions of a jet diffusion flame at normal pressure</u>	<b>170</b>
Figure 5.108	<u>Digital photographs of the C<sub>2</sub>H<sub>4</sub>-N<sub>2</sub> diffusion flame doped with 5% <i>m</i>-xylene</u>	<b>173</b>
Figure 5.109	<u>LII images of the C<sub>2</sub>H<sub>4</sub>-N<sub>2</sub> diffusion flame doped with 5% <i>m</i>-xylene at pressures</u>	<b>174</b>
Figure 5.110	<u>Peak Soot as function of height above burner for 5% Carbon from <i>m</i>-xylene</u>	<b>174</b>
Figure 5.111	<u>PAH images for ethylene diffusion flame with N<sub>2</sub> dilution and addition of <i>m</i>-xylene</u>	<b>175</b>
Figure 5.112	<u>PAH fluorescence profiles for large and small PAH in 5% Carbon</u>	<b>176</b>
Figure 5.113	<u>Radial soot profiles for 3, 4, and 5 atm with 5% Carbon from <i>m</i>-xylene</u>	<b>177</b>
Figure 5.114	<u>Peak Soot as function of height above burner for 2.5% Carbon from <i>m</i>-xylene</u>	<b>178</b>
Figure 5.115	<u>PAH fluorescence profiles for large and small PAH in 5% Carbon</u>	<b>179</b>
Figure 5.116	<u>Distributions of soot in a 5% <i>m</i>-xylene</u>	<b>180</b>
Figure 5.117	<u>Distributions of <i>m</i>-xylene in a 5% <i>m</i>-xylene</u>	<b>180</b>
Figure 5.118	<u>Distributions of soot in 5% <i>m</i>-xylene, nitrogen diluted ethylene jet diffusion flame</u>	<b>180</b>
Figure 5.119	<u>Distribution of <i>m</i>-xylene in 5% added nitrogen diluted ethylene jet flame</u>	<b>181</b>
Figure 5.120	<u>Peak soot volume fractions as a function of height above the burner for base <i>m</i>-xylene</u>	<b>183</b>
Figure 5.121	<u>Peak soot volume fractions as a function of height above the burner for base <i>n</i>-dodecane</u>	<b>184</b>
Figure 5.122	<u>Peak soot volume fractions as a function of height above the burner for base surrogate fuel</u>	<b>185</b>
Figure 5.123	<u>Comparison of peak soot volume fractions for surrogate fuel</u>	<b>186</b>
Figure 5.124	<u>Effect of <i>n</i>-dodecane concentration on peak soot volume fraction</u>	<b>187</b>
Figure 5.125	<u>Peak soot volume fractions JP-8 addition as a function of height above the burner</u>	<b>189</b>
Figure 5.126	<u>Comparison of effect of JP-8 surrogate fuel on peak soot volume fraction</u>	<b>190</b>

Figure 5.127	<u>Axial variation in peak soot volume fraction</u>	<b>191</b>
Figure 5.128	<u>JP-8/air coaxial jet nonpremixed flame computed using Violi's mechanism</u>	<b>194</b>
Figure 5.129	<u>Ignition delay times computed at various temperatures</u>	<b>195</b>
Figure 5.130	<u>JP-8/air coaxial jet nonpremixed flame computed using CRECK-0810 mechanism</u>	<b>196</b>
Figure 5.131	<u>Comparison of flame-base structures obtained with Violi and CRECK-0810 mechanisms</u>	<b>196</b>
Figure 5.132	<u>Velocity profiles used in different calculations</u>	<b>197</b>
Figure 5.133	<u>Air-jet-velocity profile on flame base location computed with CRECK-0810 mechanism</u>	<b>197</b>
Figure 5.134	<u>Effect of air-jet-velocity profile on flame base location computed with Violi mechanism</u>	<b>198</b>
Figure 5.135	<u>Predicted velocity and temperature profiles for the opposed jet burner using</u>	<b>202</b>
Figure 5.136	<u>A comparison of calculated acetylene profiles in the opposed jet ethylene/air flame</u>	<b>203</b>
Figure 5.137	<u>Photographs of the opposed jet ethylene/air flame with increasing amounts of m-xylene</u>	<b>204</b>
Figure 5.138	<u>Images of planar laser induced fluorescence/light scattering for ethylene/air flames</u>	<b>205</b>
Figure 5.139	<u>A series of pixel values from images of planar laser induced fluorescence/light scattering</u>	<b>206</b>
Figure 5.140	<u>Peak values of fluorescence/light scattering versus fraction of m-xylene in fuel gas</u>	<b>207</b>
Figure 5.141	<u>Prediction of OH and soot addition m-xylene to fuel side ethylene/air opposed jet flames</u>	<b>207</b>
Figure 5.142	<u>Change in OH fluorescence along centerline of burner, ethylene/air opposed flow flames</u>	<b>208</b>
Figure 5.143	<u>Change in PAH fluorescence along centerline of burner, ethylene/air opposed flow flames</u>	<b>208</b>
Figure 5.144	<u>A reconstruction of the acetylene concentration measured in absorption</u>	<b>209</b>
Figure 5.145	<u>Measured acetylene absorption through the flame region</u>	<b>210</b>
Figure 5.146	<u>A photograph of the ethylene-air candle-like diffusion flame</u>	<b>210</b>
Figure 5.147	<u>Temperature maps using the imaging pyrometer technique for acetylene-air</u>	<b>211</b>
Figure 5.148	<u>The wavelength resolved emission from three ethylene air flames</u>	<b>211</b>
Figure 5.149	<u>The imaging pyrometer technique applied to an opposed jet ethylene/air flame</u>	<b>212</b>
Figure 5.150	<u>Raw images of elevated pressure opposed flow flames at constant molar flow</u>	<b>213</b>
Figure 5.151	<u>Raw images of elevated pressure opposed flow flames at constant strain rate</u>	<b>214</b>
Figure 5.152	<u>Peak centerline temperatures (K) for elevated pressure ethylene/air flames</u>	<b>215</b>
Figure 5.153	<u>Centerbody flame with pure fuel calculated using detailed chemical kinetics</u>	<b>220</b>
Figure 5.154	<u>Centerbody flame with diluted fuel</u>	<b>220</b>

Figure 5.155	<u>Effect of fuel dilution on flame and vortex structure; soot and particle distributions</u>	<b>221</b>
Figure 5.156	<u>The effects of radiation on flame structure and soot formation in pure-fuel</u>	<b>221</b>
Figure 5.157	<u>Centerbody flame with pure fuel calculated using NIST chemical-kinetics mechanism</u>	<b>222</b>
Figure 5.158	<u>Centerbody flame with diluted fuel calculated using NIST chemical-kinetics mechanism</u>	<b>222</b>
Figure 5.159	<u>Photograph of fully sooting flame</u>	<b>227</b>
Figure 5.160	<u>Photograph of donut-shaped flame</u>	<b>228</b>
Figure 5.161	<u>Photograph of ring-shaped flame</u>	<b>228</b>
Figure 5.162	<u>Photograph of fully sooting flame</u>	<b>229</b>
Figure 5.163	<u>Photograph of donut-shaped sooting flame</u>	<b>229</b>
Figure 5.164	<u>Fully sooting flame with mass-less particles</u>	<b>229</b>
Figure 5.165	<u>Photograph of lifted flame obtained in centerbody burner pure ethylene central fuel jet</u>	<b>232</b>
Figure 5.166	<u>Computed lifted flame of centerbody burner</u>	<b>233</b>
Figure 5.167	<u>Close-up view of lifted flame base</u>	<b>233</b>
Figure 5.168	<u>Structure of lifted flame base. Radial distributions of temperature and axial velocity</u>	<b>234</b>
Figure 5.169	<u>Lifted flame for higher coannular flow</u>	<b>234</b>
Figure 5.170	<u>Lifted flame simulated for lower coannular nitrogen-air flow</u>	<b>235</b>
Figure 5.171	<u>Changes in height and radius I of flame base location and recirculation zone center</u>	<b>235</b>
Figure 5.172	<u>Photograph lifted flame obtained centerbody burner with central fuel jet</u>	<b>239</b>
Figure 5.173	<u>Computed lifted flame of centerbody burner</u>	<b>239</b>
Figure 5.174	<u>Second mode of lifted flame obtained centerbody burner with central and coannular flows</u>	<b>240</b>
Figure 5.175	<u>High-speed images of flame shown in Figure 5.4.4.1 obtained with exposure time of 2 ms</u>	<b>240</b>
Figure 5.176	<u>Dynamic flame computed sinusoidally driving coannular flow 50 Hz amplitude of 5%</u>	<b>241</b>
Figure 5.177	<u>Dynamic flame computed sinusoidally driving coannular flow 50 Hz amplitude of 10%</u>	<b>241</b>
Figure 5.178	<u>Distributions of temperature and OH, H, CH<sub>3</sub> concentrations of the dynamic flame</u>	<b>242</b>
Figure 5.179	<u>Distributions of time-averaged temperature and OH, H, CH<sub>3</sub> concentrations dynamic flame</u>	<b>242</b>
Figure 5.180	<u>Radial distributions of temperature and soot volume fraction 40 mm</u>	<b>243</b>
Figure 5.181	<u>Radial distributions of temperature and soot volume fraction 140 mm</u>	<b>244</b>
Figure 5.182	<u>Temperature distributions computed partially premixed jet flames for equivalence ratios</u>	<b>249</b>

Figure 5.183	<u>Soot distributions computed for partially premixed jet flames for equivalence ratios</u>	<b>250</b>
Figure 5.184	<u>Computed temperature distributions along centerline various partially premixed jet flames</u>	<b>250</b>
Figure 5.185	<u>Computed soot distributions along the non-dimensional axial position</u>	<b>251</b>
Figure 5.186	<u>Measured soot along non-dimensional axial position various partially premixed jet flames</u>	<b>251</b>
Figure 5.187	<u>Computed iso contours of <math>C_2H_2</math>, CH, and OH superimposed on temperature distributions</u>	<b>252</b>
Figure 5.188	<u>Computed streamlines are superimposed on soot-radiation distributions</u>	<b>252</b>
Figure 5.189	<u>Computed particle are superimposed on soot distributions</u>	<b>253</b>
Figure 5.190	<u>Radial distributions temperature, soot recirculation zone 10 mm above the burner surface</u>	<b>253</b>
Figure 5.191	<u>Radial distributions temperature soot the trailing flame 70 mm above the burner surface</u>	<b>254</b>
Figure 5.192	<u>Computed iso contours of <math>C_2H_2</math>, CH, OH superimposed on temperature distributions</u>	<b>254</b>
Figure 5.193	<u>Computed streamlines are superimposed on soot-radiation distributions</u>	<b>255</b>
Figure 5.194	<u>Computed particle trajectories are superimposed on soot</u>	<b>255</b>
Figure 5.195	<u>Radial distributions temperature, soot in recirculation zone 10 mm above burner surface</u>	<b>256</b>
Figure 5.196	<u>Radial distributions of temperature, soot in lame 70 mm above the burner surface</u>	<b>256</b>
Figure 5.197	<u>Temperature, soot, and acetylene distributions for different equivalence ratios</u>	<b>257</b>
Figure 5.198	<u>Acetylene distributions for different equivalence ratios across the trailing flames</u>	<b>258</b>
Figure 5.199	<u>Acetylene distributions in the recirculation zones (<math>z = 20</math> mm) for flames</u>	<b>258</b>
Figure 5.200	<u>Measured, computed soot distributions pure diffusion flame (<math>f = \infty</math>)</u>	<b>261</b>
Figure 5.201	<u>Measured, computed soot distributions premixed flame with equivalence ratio of 46</u>	<b>262</b>
Figure 5.202	<u>Measured,computed soot in a partially premixed flame with equivalence ratio of 11</u>	<b>263</b>
Figure 5.203	<u>Measured, computed soot distributions premixed flame with equivalence ratio of 5</u>	<b>264</b>
Figure 5.204	<u>Computed instantaneous flame structure with infrared image of experimental flame</u>	<b>265</b>
Figure 5.205	<u>Close-up of flow structure near base of lifted flame</u>	<b>269</b>
Figure 5.206	<u>Autoignition-zone structure upstream of flame base (<math>z = 9</math> mm)</u>	<b>270</b>
Figure 5.207	<u>Flame structure at a location <math>z = 13.5</math> in base region</u>	<b>271</b>
Figure 5.208	<u>Axial velocity (U), radial velocity (V) and temperature (T) along stoichiometry</u>	<b>272</b>
Figure 5.209	<u>Flame structure downstream of base (<math>z = 40</math> mm)</u>	<b>273</b>
Figure 5.210	<u>Effect of radiation and soot on flame lift-off height</u>	<b>274</b>

Figure 5.211	<u>Heptane- Air Centerbody Flame</u>	<b>275</b>
Figure 5.212	<u>Nd-YAG Sheet Illuminated Heptane Air Flame</u>	<b>276</b>
Figure 5.213	<u>Nd-YAG Sheet Illuminated Heptane Air Flame with N<sub>2</sub> dilution</u>	<b>277</b>
Figure 5.214	<u>Direct photographs of the flames formed with JP-8 fuel</u>	<b>280</b>
Figure 5.215	<u>Direct photographs of the flames formed with n-dodecane fuel</u>	<b>280</b>
Figure 5.216	<u>Direct photographs of flames formed a mixture of 77% n-dodecane and 23% m-xylene</u>	<b>280</b>
Figure 5.217	<u>Direct photographs of the Nd-YAG-illuminated flames formed with JP-8 fuel</u>	<b>281</b>
Figure 5.218	<u>Direct photographs of the Nd-YAG-illuminated flames formed with n-dodecane</u>	<b>281</b>
Figure 5.219	<u>Direct photographs Nd-YAG-illuminated flames formed 77% n-dodecane; 23% m-xylene</u>	<b>281</b>
Figure 5.220	<u>Temperature distributions n-dodecane flames semi-detailed chemical kinetics mechanism</u>	<b>282</b>
Figure 5.221	<u>Temperature 77%-n-dodecane-23%-m-xylene semi-detailed chemical kinetics mechanism</u>	<b>282</b>
Figure 5.222	<u>Soot distributions n-dodecane flames computed semi-detailed chemical kinetics</u>	<b>283</b>
Figure 5.223	<u>Soot distributions 77%-n-dodecane-23%-m-xylene semi-detailed chemical kinetics</u>	<b>283</b>
Figure 5.224	<u>Laser Induced Incandescence (LII) Images LII images for J8</u>	<b>284</b>
Figure 5.225	<u>Laser Induced Incandescence (LII) Images LII images for Dodecane</u>	<b>284</b>
Figure 5.226	<u>Laser Induced Incandescence (LII) Images LII images 23% M-Xylene-77% Dodecane</u>	<b>285</b>
Figure 5.227	<u>Average Soot Volume Fraction for JP-8 Flame in Centerbody</u>	<b>285</b>
Figure 5.228	<u>Average Soot Volume Fraction for Dodecane Fuel in Centerbody</u>	<b>286</b>
Figure 5.229	<u>Average Soot Volume Fraction for Surrogate (77% Dodecane- 23% M-xylene)</u>	<b>286</b>
Figure 5.230	<u>Comparison radial distributions of temperature CO<sub>2</sub> mole fraction without soot sub-model</u>	<b>290</b>
Figure 5.231	<u>Comparison radial distributions of CO, C<sub>2</sub>H<sub>2</sub> mole fractions without soot sub-model</u>	<b>291</b>
Figure 5.232	<u>Comparison radial distributions temp., CO<sub>2</sub> mole fraction w/two-equation soot sub-model</u>	<b>292</b>
Figure 5.233	<u>Comparison radial dist.CO mole fraction soot volume w/two-equation soot sub-model</u>	<b>293</b>
Figure 5.234	<u>Flame structure simulated using San-Diego mechanism</u>	<b>294</b>
Figure 5.235	<u>Flame structure simulated using Wang-Frenklach mechanism</u>	<b>294</b>
Figure 5.236	<u>Opposing-jet non-premixed xviieptanes flame</u>	<b>299</b>
Figure 5.237	<u>Distributions of temperature and axial velocity plotted along the centerline</u>	<b>300</b>
Figure 5.238	<u>Distributions of fuel, oxygen, H<sub>2</sub>O, and CO<sub>2</sub> plotted along the centerline</u>	<b>300</b>

Figure 5.239	<u>Distributions intermediate fuel species <math>H_2</math>, <math>C_2H_2+C_2H_4</math>, and CO plotted along centerline</u>	<b>301</b>
Figure 5.240	<u>Distributions of intermediate species <math>CH_4</math>, <math>C_3H_6</math>, and <math>C_2H_6</math> plotted along the centerline</u>	<b>301</b>
Figure 5.241	<u>Near-extinction opposing-jet non-premixed xviii eptanes flame simulated SD mechanism</u>	<b>302</b>
Figure 5.242	<u>Maximum flame temperatures obtained at different strain rates</u>	<b>302</b>
Figure 5.243	<u>Temperature distribution between opposing jets premixed xviii eptanes-air fuel 1282-K air</u>	<b>302</b>
Figure 5.244	<u>Maximum temperatures and OH concentrations obtained for different air temperatures</u>	<b>303</b>
Figure 5.245	<u>Premixed flame calculated using SD mechanism</u>	<b>303</b>
Figure 5.246	<u>Premixed flame calculated using LLNL mechanism</u>	<b>303</b>
Figure 5.247	<u>Premixed flame calculated using NIST mechanism</u>	<b>304</b>
Figure 5.248	<u>Non-premixed flame calculated using SD mechanism</u>	<b>304</b>
Figure 5.249	<u>Non-premixed flame calculated using LLNL mechanism</u>	<b>304</b>
Figure 5.250	<u>Non-premixed flame calculated using NIST mechanism</u>	<b>305</b>
Figure 5.251	<u>Temp. dist. JP-8/air coaxial-jet flame 6-COMP SERDP surrogate representations JP-8 fuel</u>	<b>311</b>
Figure 5.252	<u>Dist. soot JP-8/air coaxial-jet flame using 6-COMP and SERDP surrogate JP-8 fuel</u>	<b>311</b>
Figure 5.253	<u>JP-8/Air opposing-jet flame using 6-COMP and SERDP surrogate mixtures</u>	<b>312</b>
Figure 5.254	<u>Comparison flame obtained w/6-COMP, SERDP surrogate mixtures different strain rates</u>	<b>312</b>
Figure 5.255	<u>Peak temperatures of JP-8/air opposing-jet flames at different strain rates</u>	<b>313</b>
Figure 5.256	<u>Sensitivity of flame temperature at different strain rates</u>	<b>313</b>
Figure 5.257	<u>Sensitivity of opposing-jet flame to the variations in parent species concentrations</u>	<b>314</b>
Figure 5.258	<u>Temp. fields coaxial-jet flame obtained modifying composition mixture JP-8 fuel</u>	<b>315</b>
Figure 5.259	<u>Dist. soot in coaxial-jet flame modifying composition of surrogate mixture for JP-8 fuel</u>	<b>316</b>
Figure 5.260	<u>Sensitivity of various parent components of 6-COMP surrogate</u>	<b>317</b>
Figure 5.261	<u>Distributions of temperature in centerbody flames simulated with pure components</u>	<b>317</b>
Figure 5.262	<u>Distributions of soot radiation (left) and soot (right) in centerbody flames</u>	<b>318</b>
Figure 5.263	<u>Predicted flames centerbody burner fueled with 6-COMP and SERDP mixtures of JP-8</u>	<b>320</b>
Figure 5.264	<u>Soot radiation, soot volume fraction centerbody burner fueled 6-COMP SERDP mixtures</u>	<b>321</b>
Figure 5.265	<u>Comparison of homogeneous ignition processes of 6-COMP;SERDP mixtures JP-8</u>	<b>321</b>
Figure 5.266	<u>Ignition delay times stoichiometric mixtures of air</u>	<b>322</b>

Figure 5.267	<u>Flames obtained centerbody burner with fuel</u>	<b>323</b>
Figure 5.268	<u>Soot radiation soot volume fraction centerbody burner obtained with fuels</u>	<b>324</b>
Figure 5.269	<u>JP-8 fueled, swirl-stabilized, model gas-turbine combustor</u>	<b>329</b>
Figure 5.270	<u>Comparison simulated flames experiment for <math>\phi = 0.85</math></u>	<b>330</b>
Figure 5.271	<u>Comparison simulations experiment for <math>\phi = 1.0</math></u>	<b>331</b>
Figure 5.272	<u>Comparison of simulated flames with experiment for fuel-rich condition of <math>\phi = 1.15</math></u>	<b>332</b>
Figure 5.273	<u>Comparison of simulated flames with experiment for different equivalence ratios</u>	<b>333</b>
Figure 5.274	<u>Axial distributions centerline temperature obtained with 6-COMP and SERDP surrogates</u>	<b>334</b>
Figure 5.275	<u>Radial distributions temperature axial distance 0 mm obtained with 6-COMP and SERDP</u>	<b>335</b>
Figure 5.276	<u>Distributions of benzene, soot, and acetylene obtained 6-COMP mixture</u>	<b>336</b>
Figure 5.277	<u>Distributions benzene, soot, and acetylene obtained SERDP mixture</u>	<b>336</b>
Figure 5.278	<u>Axial distributions centerline benzene concentration obtained 6-COMP; SERDP</u>	<b>337</b>
Figure 5.279	<u>Radial distributions soot volume fraction axial distance 50 mm obtained 6-COMP; SERDP</u>	<b>338</b>
Figure 5.280	<u>Actual and simulated opposing-jet partially premixed flames</u>	<b>342</b>
Figure 5.281	<u>Comparisons structures the weakly stretched weakly premixed flame</u>	<b>343</b>
Figure 5.282	<u>Ignition delay time homogeneous, stoichiometric mixture n-heptane vapor</u>	<b>344</b>
Figure 5.283	<u>Comparisons the structures the weakly stretched moderately premixed flame</u>	<b>345</b>
Figure 5.284	<u>Comparisons the structures moderately stretched moderately premixed flame</u>	<b>346</b>
Figure 5.285	<u>Comparisons the structures moderately stretched weakly premixed flame simulated</u>	<b>347</b>
Figure 5.286	<u>Averaged Fluid Dynamics in Combustor</u>	<b>348</b>
Figure 5.287	<u>Reactor Network for Combustor Simulations</u>	<b>348</b>
Figure 5.288	<u>Specific growth; oxidation rates SNETPSR for run at 811 K and 16</u>	<b>349</b>
Figure 5.289	<u>Predicted PSD in Fuel Spray Shear Layer atm</u>	<b>350</b>
Figure 5.290	<u>Predicted PSD Evolution through Quench Zone</u>	<b>350</b>
Figure 5.291	<u>Evolution of PSD through Burn-Out Zone</u>	<b>351</b>
Figure 5.292	<u>Predicted trends in particulate emissions with f/a ratio for two surrogate fuels</u>	<b>354</b>



## List of Acronyms

ABF	Abel, Bockhorn, Frenklach
AF	Air Force
aAFB	Air Force Base
AFRL	Air Force Research Lab
AIAA	American Institute of Aeronautics and Astronautics
APFR	Atmospheric pressure flow reactor
Ar	argon
AR	Anti-reflective
ARL	Army Research Laboratory
ASM	Aerospace Sciences Meeting
ASME	American Society of Mechanical Engineers
ASTM	American Society for Testing and Materials
C <sub>2</sub> H <sub>2</sub>	acetylene
C <sub>2</sub> H <sub>4</sub>	ethylene
C <sub>12</sub> H <sub>26</sub>	dodecane
CH/CH*	methylidyne (* denotes excited state)
CBB	Centerbody burner
CCD	Charge coupled device
CFD	computational fluid dynamic
CFM	Specific type of combustor
CHEMKIN	Combustion Modeling Program
CH <sub>4</sub>	methane
CH <sub>2</sub> O	formaldehyde
CIE	International Society on Illumination
CMOS	Complementary metal oxide semiconductor

CO	carbon monoxide
CO <sub>2</sub>	carbon dioxide
COMP	component
CPC	condensation particle counter
CRECK-0810	Name of kinetic mechanism developed by Ranzi et al. (1995)
CW	continuous wave (i.e. non-pulsed)
DDT	Deflagration to detonation transition
DoD	Department of Defense
DOE	Department of Energy
DRGEP	Directed relation graph with error propagation
DSLR	Digital single lens reflex camera
ESTCP	Environmental Security Technology Certification Program
EPA	Environmental Protection Agency
FFT	Fast Fourier transform
FT	Fischer-Tropsch
FTIR	fourier transform infrared
FWHM	Full width at half maximum
GASKIN	Chemical kinetic modeling code for shock tubes
GC	Gas chromatograph
GC-MS	Gas chromatograph-mass spectrometer
GRI	Gas Research Institute
GT	Gas Turbine
GTE	Gas Turbine Engines
H	atomic hydrogen
H <sub>2</sub>	molecular hydrogen
H <sub>2</sub> O	water

H/C	ratio of fuel hydrogen to carbon
HACA	hydrogen-abstraction-carbonaddition
HITRAN	Database of infra-red spectra
HP	High Pressure
HW	Harris and Weiner
ICCD	Intensified charge coupled device
ID	internal diameter
IR	Infra-red
ISSI	Innovative Scientific Solutions, Inc.
JP-8	jet propulsion 8 (U.S. military jet fuel)
JSR	Jet-stirred reactor
LIF	laser-induced fluorescence
LII	laser-induced incandescence
LLNL	Lawrence Livermore National Laboratory
LOS	Line-of-sight
MCH	Methyl cyclohexane
MJ	Mega-Joule
MOM	Method of Moments
MS	Mass spectrometer
MURI	Multi-University Research Initiative
MXYLYL	m-methylbenzyl radical
Nd	Neodymium
SD	San Diego
SP	Smoke point
N <sub>2</sub>	molecular nitrogen
NAAQS	National Ambient Air Quality Standards
NIST	NIST National Institute of Standards and Technology

NO	nitric oxide
NO <sub>2</sub>	nitrogen dioxide
NO <sub>x</sub>	N-O emissions including NO, NO <sub>2</sub> , and N <sub>2</sub> O
O	atomic oxygen
O <sub>2</sub>	molecular oxygen
OH/OH*	hydroxyl radical (* denotes excited state)
OPPDIF	Opposed-jet diffusion flame module in CHEMKIN
ORZ	Outer recirculation zone
PAH	polycyclic aromatic hydrocarbons
PC	Personal computer
PCA	Primary component analysis
PLIF	planar laser-induced fluorescence
PLII	planar laser-induced incandescence
PM	particulate matter
PM <sub>2.5</sub>	particulate matter with an aerodynamic diameter less than 2.5 micrometers
PREMIX	Premixed flame module within CHEMKIN
PrIMe	Process Informatics Model – system for sharing combustion data and simulations
PMMA	Polymethyl methacrylate
PMT	Photomultiplier tube
POSF	Symbol of the Fuels Branch in Propulsion Directorate
PRZ	Primary recirculation zone
PSD	Power spectral density or particle size distribution
PSR	perfectly stirred reactor
PSU	Penn State University
RMS	Root-mean square
RZ	Recirculation zone

QCL	Quantum cascade laser
SA	Surface area
SCFM	Standard cubic feet per minute
SERDP	Strategic Environmental Research and Development Program
SHOCKIN	Shock Tube Modeling option within CHEMKIN
SIP	State implementation plan
SLPM	Standard liters per minute
SNETPSR	Sooting NETwork of Perfectly-Stirred Reactors
SP	Smoke Point
SPIE	Society of Photo-optical Instrumentation Engineers
SPU	Sample preparation unit
SRZ	Secondary recirculation zone
ST	Shock Tube
TCD	Thermal conductivity detector
TDLAS	tunable diode laser absorption spectroscopy
TP	Triple point in centerbody burner flame
TPO	Temperature programmed oxidation
TSI	Threshold Soot Index
TTL	Transistor-transistor logic
UC	University of California
UDRI	University of Dayton Research Institute
UHP	Ultra-high purity
UIC	University of Illinois at Chicago
UNICORN	UNsteady, Ignition, and COmbustion with ReactionS
U.S.	United States
USC	University of Southern California

UTRC	United Technologies Research Center
UV	ultraviolet
WP	Weapon Systems and Platforms
WPSON	Weapons Systems and Platforms statement of need
WSR	Well-stirred Reactor
YAG	yttrium aluminum garnet

## **Acknowledgements**

The financial support of the Department of Defense Strategic Environmental Research and Development Program (SERDP) for this project is hereby acknowledged. The authors wish to thank Ms. Donelle Stout and Ms. Angel Wedding for the hard work they put in editing and correcting this report. Your assistance is greatly appreciated. The authors also wish to thank Chuck Frayne for taking care of all of the contract administrative and financial requirements that enabled this program to function efficiently.

## Abstract

**Background:** Gas turbine engines are a major source of PM<sub>2.5</sub> emissions produced by the Department of Defense (DoD). Most of the PM<sub>2.5</sub> emissions consist of soot particles. Although technology advancements have resulted in significant reductions in soot emissions from gas turbine engines, additional reductions will be needed to meet future PM<sub>2.5</sub> National Ambient Air Quality Standards (NAAQS). Computational fluid dynamic (CFD) models will play a key role in designing future engines for low soot emissions from JP-8 or alternate fuels. Unfortunately, current models for soot formation and oxidation are insufficient to allow accurate predictions of emissions in CFD simulations. SERDP funded five programs that worked in concert to establish a fundamental database for developing and validating soot models for use in designing low emissions gas turbine combustors. The collective effort is referred to as the SERDP Soot Science Program. This report describes research performed by the joint university, industry, Army, and Air Force team as one part of the SERDP Soot Science Program.

**Objective:** The primary objective of this research program is to aid the DoD in meeting current and future NAAQS PM<sub>2.5</sub> regulations by establishing the fundamental science base needed to develop and validate accurate soot models for realistic fuels. This program focuses on understanding the fundamental effects of fuel chemistry and pressure on soot production and burnout, and on evaluating soot models as well as combustion chemistry mechanisms needed for accurate soot predictions.

**Approach:** The approach involves strongly coupled, mutually supportive experimental and simulation efforts conducted in concert with other members of the SERDP Soot Science Team. The approach includes a series of well-controlled laboratory experiments that methodically progress in complexity in a way that supports a systematic analysis and interpretation of results. State-of-the-art soot models and detailed chemical mechanisms for hydrocarbon fuels have been integrated into a unique simulation code called UNICORN.

**Results:** The results and accomplishments include establishing a database for soot emissions in shock tube, co-flow diffusion flames, opposed jet flames, centerbody flames, and swirl stabilized flames. Fuels investigated included: ethylene, m-xylene, dodecane, and a surrogate JP-8, developed in collaboration with the SERDP Soot Science Team. Detailed chemical kinetics models for ethylene and the JP-8 surrogate fuels with PAH chemistry up to pyrene are also developed in conjunction with the SERDP Soot Science Team. UNICORN simulations are used to interpret experimental results and evaluate the detailed soot and combustion chemistry models in the different experiments. A Sooting NETwork of Perfectly Stirred Reactors (SNETPSR) model for estimating the emissions of actual combustors is further developed in this program. The model incorporates the detailed chemical model for the JP-8 surrogate, which can also simulate paraffinic alternative fuels. This model can be used as a design tool for developing low-sooting gas turbine combustors.

**Benefits:** This program advanced the ability to develop and evaluate models for predicting soot emissions from gas turbine combustors through the creation of a validation database for a surrogate JP-8 and alternative fuels, and through the creation and validation of chemical kinetic models for the surrogate fuels.





## **1.0 Executive Summary**

### **1.1 Background and Approach**

SERDP funded five different programs that worked in concert to establish a fundamental database for developing and validating soot models for use in designing low emissions gas turbine combustors. The collective program was referred to as the SERDP Soot Science Program. The participants were: (1) Stanford University Team (WP-1574), (2) University of Illinois Chicago Team (WP-1575), (3) University of Utah Team (WP-1576), (4) Air Force Team (WP-1577), and (5) the Sandia Team (WP-1578). The Air Force had responsibility for coordination of the combined efforts among the SERDP Soot Science Teams. The coordination effort led to many synergistic collaborations, some of which are highlighted in the next section. Each team provided a final report to SERDP describing the results of their research activities.

This Final Report describes research performed on the Air Force SERDP Soot Science Program WP-1577 titled “Combustion Science to Reduce Particulate Matter Emissions for Military Platforms”. For the sake of completeness, this report describes the work performed in some detail. This Executive Summary highlights major outcomes of the work.

The Air Force team involved six different groups, led by the Air Force Research Laboratory (AFRL) Propulsion Directorate at Wright Patterson AFB. The six groups were: (1) Air Force Research Laboratory, (2) Army Research Laboratory, (3) Penn State University, (4) University of Dayton Research Institute, (5) Innovative Scientific Solutions, Inc., and (6) United Technologies Research Laboratory. These groups worked in concert to expand the fundamental science base related to the formation of carbonaceous particulate matter emissions, commonly referred to as soot, and to improve the ability of soot models to make predictions for realistic fuels. The overarching research strategy for achieving the objective of this program involved strongly coupled mutually supportive experiments and simulations. A set of five laboratory devices, shock tube, co-flow diffusion flame, opposed jet flame, centerbody flame, and swirl stabilized flame were used that progress in complexity in a way that permits systematic analysis of all of the data; thus, leading to a more unified understanding of soot processes.

A unique simulation code, called UNICORN, was an essential part of the research strategy for obtaining validated “full” chemistry and soot models for JP-8 and an alternate fuel. UNICORN was used to make predictions, using “full” chemistry and state-of-the-art soot models to aid in the interpretation of experimental results. To accomplish the goals of delivering validated chemistry and soot models suitable for use with combustor design codes, a PM emission modeling method, using a network of perfectly stirred reactors (SNETPSR) was also used in this program. It can be applied in conjunction with full 3-D combustor design codes to estimate soot emissions for gas turbine combustors.

The initial phase of the work included studies with ethylene at atmospheric and elevated pressure. Limited testing was also done on methane co-flow flames to test predictions on the effects of soot on flame dynamics. The majority of the effort focused on testing a JP-8 surrogate and JP-8. The surrogate had two components, m-xylene and n-dodecane, which were also

studied individually. The pure n-dodecane was used as a surrogate for a purely paraffinic alternative fuel such as one that might be produced in a Fischer-Tropsch process.

## 1.2 Major Outcomes from the Project

- Design of a JP-8 surrogate fuel in collaboration with all SERDP Soot Science Teams.
- Development of a chemical kinetics model for ethylene with PAH chemistry up to pyrene. This development was conducted in collaboration with Professor Hai Wang of the Sandia-led team. Interactions between the Sandia-led team and the Air Force team to reconcile model predictions of shock tube ignition delays under fuel rich conditions led to improvements in both the experimental measurements and the kinetics model (SERDP\_C<sub>2</sub>H<sub>4</sub>).
- Development of a chemical kinetics model for the JP-8 surrogate fuel with PAH chemistry up to pyrene. This was jointly developed with the Sandia-led team and the UIC-team. Development of the n-dodecane model was coordinated by Prof. Wang of the Sandia-led team. The m-xylene model was developed by the UIC team. The UTRC group, as part of the Air Force-led team, combined these two models and integrated PAH chemistry to create the surrogate fuel model (SERDP\_SURR\_v2). A preliminary surrogate model was also developed by UTRC and was labeled (SERDP\_SURR\_v1)
- Validation data sets of shock tube ignition delay, species, and soot yields for ethylene, m-xylene, n-dodecane, and the JP-8 surrogate at pressures up to 18 atm and equivalence ratios up to 3.0 were obtained. These ignition delay species results were modeled using CHEMKIN and SHOCKIN. The modeling results compared well with the experiment ignition delays for ethylene and m-xylene. However, the model predictions of the ignition delay of n-dodecane results and the surrogate were not satisfactory under fuel rich conditions. Species predictions using SERDP v1.0 showed poor agreement for many key aromatic species, indicating that further model development is required.
- *A priori* predictions were made of the effects of soot on co-flow diffusion flame dynamics using UNICORN and experimental validation of those predictions in a methane co-flow diffusion flame. The archival publication based on this work received a distinguished outstanding paper award at the 32<sup>nd</sup> International Combustion Symposium.
- Validation data sets were obtained for 2-D soot fields in co-flow diffusion flames at pressures up to 5 atm, for N<sub>2</sub>-diluted ethylene flames and for the same flame in which a portion of the total carbon flow was replaced with JP-8, the JP-8 surrogate, m-xylene and n-dodecane. For the base flame and the base flame with m-xylene added, qualitative PAH fields were also measured for single ring and multi-ring PAH using laser-induced fluorescence.
- The base N<sub>2</sub>-diluted ethylene flame and the m-xylene flames were simulated in UNICORN using kinetic mechanism SERDP\_SURR\_v1. Results showed reasonable agreement with soot field over the range of pressures studied.

- Validation data sets of flame images and soot fields in the centerbody burner with ethylene, n-dodecane, the JP-8 surrogate and JP-8 were obtained. The data set included a wide range of conditions. All experiments involved interaction of recirculation zones with the processes of formation and oxidation of soot to simulate similar processes in the primary zone of a gas turbine combustor. UNICORN simulations were completed for all fuels, including the JP-8 surrogate. The simulations captured key changes in flame structure and soot field.
- Detailed simulation studies were performed of the structure of partially premixed centerbody flames and their soot fields predicted unexpected trends in soot volume fraction with the amount of premixing. The trends were ultimately verified by experiments.
- Detailed simulation studies of lifted centerbody flames and the mechanism by which they are stabilized resulted in new insights into the stabilization mechanisms of these flames including the existence of an auto ignition region. The dynamic characteristics of these flames were also successfully simulated.
- A method for estimating the emissions of actual combustors was further developed in this program to improve the soot modeling capabilities. This model, the Sooting NETwork of Perfectly Stirred Reactors (SNETPSR), incorporates the detailed chemical model for the JP-8 surrogate, which can also simulate paraffinic alternative surrogate fuels.
- The team has published 17 archival papers and 33 proceedings papers to date. It is expected that at least four additional archival papers will be written based on work done in the project including research with a single swirl cup combustor from a gas turbine engine.

## 2.0 Introduction

### 2.1 Motivation for Program

The EPA considers PM<sub>2.5</sub> (Particulate Matter with particle sizes of 2.5 microns or less) to be the most important air pollutant because these small particles can penetrate deep into the lungs and cause significant health problems. In 2005, the EPA proposed revisions to the National Ambient Air Quality Standards (NAAQS) that would reduce the PM<sub>2.5</sub> 24-hour standard from 65  $\mu\text{g}/\text{m}^3$  to 35  $\mu\text{g}/\text{m}^3$ . This could pose problems for DoD air bases. Essentially all of the solid particles, soot, produced in gas turbine engines are PM<sub>2.5</sub> emissions. Indeed, the major source of PM<sub>2.5</sub> emissions produced by the DoD is gas turbine engine powered aircraft. In 2004, DoD aircraft produced about  $4.2 \times 10^{10}$  kg of PM<sub>2.5</sub> emissions. This corresponds to the production of about  $2.1 \times 10^{23}$  soot particles.

Much of these emissions occur in local areas around active air bases. If an air base is in a region that is noncompliant with the PM<sub>2.5</sub>, then by law the base has to comply with the state implementation plan (SIP) to bring the region into compliance with the local air quality standards. Thus, the SIP can indirectly regulate PM<sub>2.5</sub> emissions from military aircraft leading to adverse effects on aircraft basing and military activities. DoD has experienced this type of problem in the past related to NO<sub>x</sub> emissions from military aircraft operating from bases in noncompliant regions. The EPA is currently identifying the PM<sub>2.5</sub> noncompliant regions, which could cause similar problems for military bases in noncompliant regions.

Quantitative modeling of particulate matter (PM) emissions from flames, often referred to as soot or smoke, is one of the greatest challenges to computational modeling of combustion. First, formation of PM itself is an incompletely understood process. However, models exist that provide quantitative predictions of laboratory flames burning pure fuels at atmospheric pressure, but generally they are accurate over very limited conditions. Second, oxidation of these particles is dependent on accurate knowledge of the active surface area of the particles that, in turn, is dependent on the formation process. Third, the total emissions of PM from a practical burner are the difference between two large terms, the formation and the oxidation. At full power, for example, PM emissions can be two to three orders of magnitude less than the levels in the primary zone. Finally, turbulent mixing and reacting flow complicate the simulations with time scales of soot formation and oxidation substantially differently from the time scales of heat release. Hence, it is not surprising that authors are willing to present modeling results that agree only to within one to two orders of magnitude from the experimental values (Tolpadi et al 1997, Brocklehurst et al 1997).

Emission of soot from gas turbine engines is the net result of soot inception, growth, and oxidation processes that are coupled strongly to spray and mixing processes due to the strong dependence of soot production and oxidation on local air-fuel ratio and temperature. Thus, the ability to accurately model soot emissions from gas turbine engines requires improved understanding of complex, strongly coupled chemical and physical processes related to inception, growth, oxidation of soot and its precursors as well as turbulent mixing and radiative loss of energy. Frequently, a single experiment is sensitive to only one or two of these processes. The ability to model all of these processes accurately in a single comprehensive model

is a major challenge. Although considerable research has been performed, few experiments elucidate all the relevant physics/chemistry. In some cases, experimental data for validation is nonexistent or insufficient. This is especially true when applied to practical fuels since few experiments, especially at pressure, have been performed. Thus, the development and evaluation of soot models are based on a partial understanding of the processes, inferred from experiments that often had incomplete boundary conditions or no measurement of important parameters.

## 2.2 Program Objectives

*The overall objectives of this program are to aid the DoD in meeting current and future NAAQS PM2.5 regulations by establishing the fundamental science base needed to develop and validate soot models for realistic fuels and aid in obtaining substantial reductions of PM2.5 emissions from current and future GTEs in military platforms.*

These overall objectives are linked to two specific goals:

1. In the near- and mid-term, JP-8 will remain the primary fuel for military GTEs. The first goal of this program is to provide the science base that will enable the development and validation of PM2.5 models that can be used in the design process to minimize soot emissions from existing or new combustors burning JP-8 fuel.
2. In the long-term, reformulated fuels and alternate fuels will replace JP-8. The second goal is to extend the science base so that it can be used to (1) develop and validate PM2.5 models for accurate prediction, (2) evaluate and select low sooting alternate fuels, (3) aid in writing new fuel specs, and (4) design combustors with low PM2.5 emissions-burning alternate fuels.

The fundamental processes that influence the formation of soot in a gas turbine combustor engine are fuel injection, fuel-air mixing, gas-phase kinetics, soot inception, soot growth, and soot oxidation. Two other factors that play a central role in determining the amount of soot formed are the fuel composition and the pressure of the combustion system. From research available in the literature, conflicting information is found for the effects of fuel composition; some studies identify aromatic content as being the key factor while others identify carbon hydrogen (C/H) ratio. Pressure dependence of soot formation has been found to be dependent on the type of flame in which it is studied.

## 2.3 Overall Research Approach

A major problem in extending the soot and fuel chemistry science-base, is that the published burner and reactor experiments cannot be collectively analyzed to construct a complete picture of soot processes in different combustion environments. This is due to the wide variations and uncertainties associated with published experiments and experimental conditions. This program sought to correct this problem by using a unique collective approach that was successfully demonstrated in the SERDP WP1179 program. A broad range of well-defined and mutually supportive experiments and simulations were performed and the data were analyzed collectively

to establish a database and a unified understanding of soot processes consistent with the objective of this program.

The overarching research strategy for achieving the objective of this program involved strongly coupled mutually supportive experiments and simulations. A series of well-controlled laboratory experiments were performed that methodically progress in complexity in a way that permits systematic analysis of all of the data; thus, leading to a more unified understanding of soot processes. Our approach involved biannual review and planning meetings that included researchers from other SERDP and DoD programs working in the field. These review/planning meetings were intended to assure that all of the experiments were conducted so that they aided in establishing a unified understanding of soot processes and have well defined boundary conditions.

Development of validated surrogate fuel models for soot prediction depended on the availability of detailed “full” kinetic models for JP-8 and alternate fuels. The chemistry mechanisms and soot models were created in collaboration with other SERDP teams and other on-going efforts in the combustion community such as the development of Real Transportation Fuels Database and the DoD Surrogate Fuels Working Group.

A unique simulation code called UNICORN was an essential part of the research strategy for obtaining validated “full” chemistry and soot models for JP-8 and alternate fuels. UNICORN was used to make predictions for most of the experiments, using “full” chemistry and soot models. UNICORN was also a critical tool in the interpretation of experimental results. The comparison of UNICORN results with experiments was used to identify deficiencies in the soot model and the chemical mechanisms.

To accomplish the goal of the program of delivering validated chemistry and soot models suitable for use with combustor design codes, the SNETPSR model will be further developed and validated on this program. It can be used in full 3-D combustor design codes for the purpose of minimizing soot during the design process.

To summarize, our approach has four critical elements that allowed us achieve our program goal of advancing the fundamental combustion science relevant to PM formation in military gas turbine engines; thus satisfying the SERDP Statement of Need WPSON-07-01. These elements are given below:

- (1) A suite of five fundamental burners that are methodically selected to increase in complexity in a way that enables physics and chemistry to be systematically investigated over a range of phenomena occurring in gas turbine combustors.
- (2) A set of experiments at atmospheric and high pressures with surrogate fuels for JP-8 and a paraffinic alternate fuel thus providing a broad, well-defined database capable of being used to develop and validate soot, fuel chemistry, and other combustion models.
- (3) A unique simulation code, UNICORN, to predict and evaluate “full” chemistry mechanisms for JP-8 and alternate fuel and state of the art soot models.

- (4) A collective management approach, involving collaborations with NIST and other organizations, for planning and analysis of experimental and computational results.

It is extremely challenging to make the detailed measurements required to understand the effects of fuel type on the production of soot within gas turbine combustors. Thus, laboratory flames and reactors must be used when a fundamental understanding is required. However, due to the complexity of the combustion process in a gas turbine combustor, no single laboratory flame or reactor will suffice for such studies.

In this program, soot processes were being studied methodically in a suite of five different burners illustrated in Figure 2.1. This suite of burners has been judiciously selected so that there is a methodical progression in complexity of the physical and chemical processes. Shock tube experiments allow the study of chemical processes without the complications of mixing. Premixed jet flame studies highlight the effects of chemistry and molecular diffusion. Non-premixed jet flame experiments involve the combined effects of chemistry, diffusion, and molecular mixing of fuel and air. Opposed jet flame experiments investigate the coupled effects of chemistry, diffusion, fuel and air mixing, and controlled flame stretch. Center-body flame studies include all of the previously mentioned effects and a recirculation zone that stabilizes the flame. The final configuration studied is the swirl-stabilized flame. The combustion processes in the swirl-stabilized flame are similar to those in a gas turbine combustor in that they involve all of the previously mentioned combustion processes as well as fuel spray injection and turbulent mixing. However, the burner is simple enough that it can be operated in a well-controlled and well-instrumented laboratory environment.

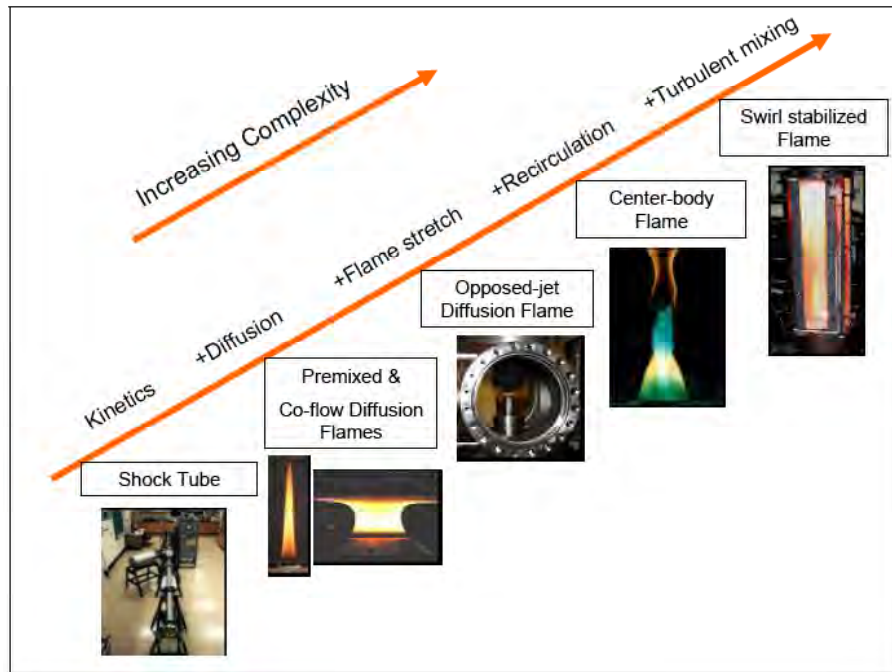


Figure 2.1 Hierarchy of experiments used in the program.



## 3.0 Modeling Approaches

### 3.1 Introduction

A central goal of this program is to create validated kinetic models for ethylene and for a surrogate fuel representing JP-8 jet fuel. The models needed for this study must include the formation of polycyclic hydrocarbons so that the computations of gas-phase species can be coupled to models that predict soot. This section begins with a discussion of the process of developing and evaluating models. It also includes discussion of the two models developed for this program: ethylene and the surrogate fuel, and the soot models that are being investigated. In addition, the UNICORN code and modifications that have been made in it as a result of this program are included.

### 3.2 Kinetics Modeling Overview and Coordination

In order to maintain coordination amongst the different SERDP contracts, a modeling team has been created. It consists of Med Colket and Steve Zeppieri (both of UTRC), Michael Frenklach (UC, Berkeley), Hai Wang (USC), Sukh Sidhu (Univ. Dayton), Ken Brezinsky (Univ. Illinois, Chicago), and Adel Sarofim (Univ. of Utah). In addition, Wing Tsang (NIST), who is not under contract by SERDP, was invited to participate. It was originally agreed that we would use the PrIME data base (<http://primekinetics.org/>) to communicate, and to share results and mechanisms, etc. A special user's site for the SERDP team within PrIME was created to facilitate information exchange. As part of the discussions within the coordination group, it was agreed early that a new baseline kinetics model would be created for ethylene and for a reaction subset of polycyclic aromatic hydrocarbons (PAHs). Following such development, a baseline kinetics model for a surrogate jet fuel would be created. In the subsequent sections, the development and analysis for both the ethylene kinetics model and for a surrogate kinetics mechanism are discussed. In the latter case, rationale for identifying the components of the surrogate fuel is also provided. Subsequently, the soot models utilized by the AF SERDP team are reviewed.

The utilization of PrIME was expanded to support exchange of information (beyond just the kinetics models) amongst the SERDP research teams. Overall objectives have been identified to enable file sharing of reports, papers and presentations. Based on these objectives, a revised file structure for the SERDP soot science folder in PrIME was created and this new file structure was communicated to all of the teams. Initially, the teams populated the folder with their reports and presentations, but sustaining this effort was challenging.

#### 3.2.1 Ethylene Kinetics Model (SERDP\_C<sub>2</sub>H<sub>4</sub>)

With primary assistance from Hai Wang, a baseline ethylene kinetics model has been selected. It is based on recent work by Wang and coworkers (2007). To this mechanism, we have added the PAH mechanisms (for species up to pyrene) of Babushok and Tsang (2004). The full reaction set and thermodynamics have been assembled and is operational using CHEMKIN tools. This ethylene mechanism is denoted SERDP\_C<sub>2</sub>H<sub>4</sub>.

An assessment of the detailed chemical kinetics model for ethylene combustion, with PAH chemistry, was completed and submitted to our AFRL-led team, to PrIME, and to the modeling contacts for each of the other four SERDP-funded teams. Comparison of the modeling results and unpublished fuel-rich oxidation of ethylene in a single-pulse shock tube (Colket, 1987) are shown in Figures 3.1 and 3.2a, b, c, and d. The data was obtained for 3.5% ethylene/ 0.52% O<sub>2</sub> with the remainder argon at approximately 10 atmospheres and for about 550 microseconds. A larger set of comparisons for validation were performed by H. Wang. These will be described below.

The mechanism has been used by (V. Katta, 2008) to model an ethylene co-flow flame and the results have been compared to simulations using an earlier kinetics model.

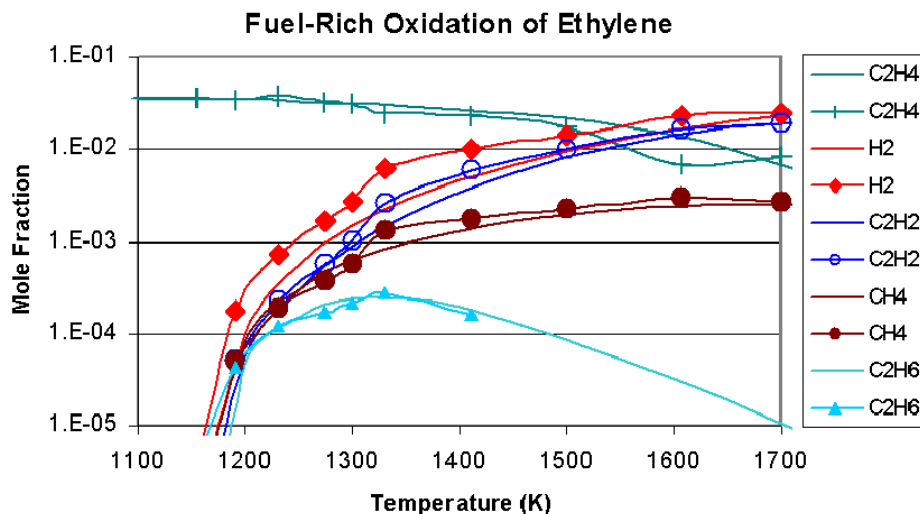


Figure 3.1 Comparison of modeling and experimental results for the fuel-rich oxidation of ethylene in a single-pulse shock tube. Selected light species are shown for approximate pressure and residence times of 10 atmospheres and 550 microseconds.

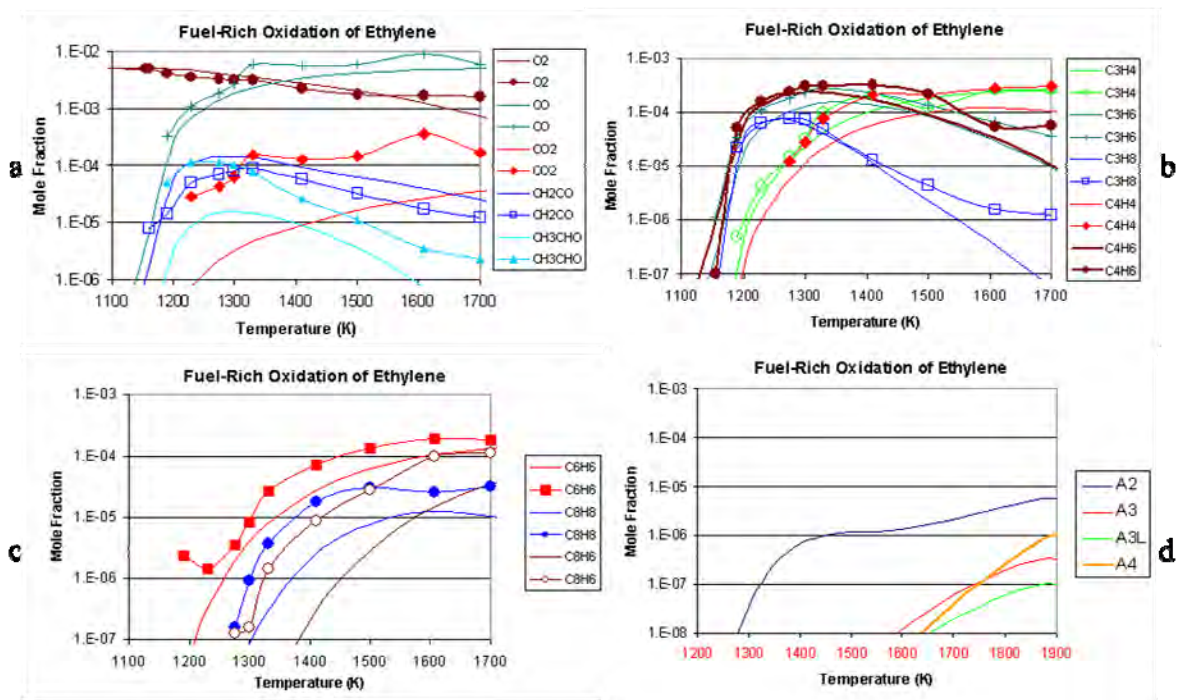


Figure 3.2a, b, c, d. Additional comparisons of (a) oxygen containing species, (b) light hydrocarbons, (c) aromatics and (d) large polycyclic aromatic hydrocarbons (PAH) following oxidative pyrolysis of ethylene in a single-pulse shock tube. No data was available for the species in (d) as their concentrations were below the detection limit.

The ethylene mechanism developed in this program was tested against other ethylene mechanism for their ability to simulate experimental results in a coflow jet diffusion flame. Similarities were observed in the model results, but significant differences also existed, particularly in the species key to soot formation processes, including acetylene and benzene. Note our new model also under predicts the data of benzene ( $C_6H_6$ ) and that of other light aromatics such as styrene ( $C_8H_8$ ) and phenyl acetylene ( $C_8H_6$ ) as shown in Figure 3.2c. These issues led to questions about which of the mechanisms tested were really the best. Hence, it was requested each of these mechanisms be evaluated against the test experimental data sets that had been used to ‘validate’ the recommended mechanism.

The four mechanisms evaluated for their ability to simulate ethylene reaction processes were:

1. Our recommended set, denoted SERDP\_ $C_2H_4$ . (M1)
2. The NIST reaction mechanism developed by Babushok and Tsang (2004) for Heptane. (M2)
3. A recent mechanism for ethylene developed by Zhang (2005) at the University of Utah. (M3)
4. The Wang and Frenklach (1997) mechanism that has been used extensively by many researchers in soot formation studies. (M4)

Simulations were compared to experimental data for flame speeds, ignition delay, product distribution in stirred reactors, flow reactors, burner-stabilized flat flames and a single pulse shock tube. Many of the simulations were performed by H. Wang at USC. Some of them were performed at UTRC. In addition, UTRC performed a detailed analysis of the pros and cons of each of the mechanisms. The comparisons indicate that the SERDP\_C2H4 mechanism is significantly superior to the other reaction sets.

Specifically, it was found that M2 under predicted ignition at temperatures below 1000K at atmospheric pressure, and also under predicted reaction rates by a factor of two in flow reactors for the same conditions. M2 under predicted ST ignition under lean conditions and over predicted aromatic production in fuel rich flames significantly. Overall, the M2 reaction mechanism does a good job on flame speeds.

M3 performed significantly worse in the flow reactor simulations with under prediction of overall reaction rates by a factor of three and more. Flame speeds were approximately 10% too high and the activation energies for ignition delays were too low.

M4 was generally the worst of the reaction sets examined. Ignition was too slow below 1000K, and once the reaction initiated, the reaction occurred very fast. Activation energies from shock tubes were too low, and flame speeds were 30% too high. Product distributions in flames were good however, which is the system where the mechanism has been predominately utilized.

Much better quantitative agreement in time scales and species concentrations were obtained using the M1 mechanism. Relatively minor differences were observed with M1 across all benchmark data sets. These differences are documented here in an effort to identify areas for future research. In particular, (1) reaction rates are slightly high in flow reactors, at 10 atmospheres, 850K, and fuel rich conditions; (2) selected species ( $\text{CO}_2$ ,  $\text{CH}_3\text{CHO}$ ,  $\text{C}_4\text{H}_4$ ,  $\text{C}_8\text{H}_6$ ,  $\text{C}_8\text{H}_8$ ) are low for 10 atmospheres, very fuel rich and 1500K in a single pulse shock tube; and (3)  $\text{C}_2\text{H}_2$  is over predicted for an atmospheric pressure flow reactor at stoichiometric and lean conditions near 1050K but slightly under predicts acetylene under fuel rich conditions. Finally, the profile shapes of predicted aromatics in fuel rich, premixed flames look a little odd. In short, no mechanism is perfect, especially given the extensive range of validation data to which the mechanisms have been compared, but the SERDP\_C2H4 model appears to perform significantly better than any of the others examined in this study. Hence, it is our recommended starting point for development of mechanisms for the oxidation of larger hydrocarbon fuels.

As a result of these additional studies, our recommendation of the preferred mechanism for ethylene stands as is. Furthermore, we used the differences amongst the kinetic performance of these four mechanisms to develop a qualitative explanation for the differences in results observed in the coflow simulations by Vish Katta.

### 3.2.2 Surrogate Fuel Selection

#### *JP-8 Surrogate*

In 2008, the team planned to initiate experiments and/or modeling efforts using a surrogate JP-8; hence it was necessary to define the make-up of this surrogate fuel for the full SERDP ‘soot science’ program. Thus, the spreadsheet tool that was developed to analyze fuels for the Jet Fuel Surrogate Working Group was extended to the SERDP program needs. In particular, an added computation of the Smoke Point was added to the tool. This computation is based upon the laboratory determined Threshold Sooting Index (TSI) for each fuel component which can be added together (Gill and Olson, 1984) to estimate the Smoke Point of the mixture (in mm). In particular, the relationship between the TSI and SP is given by:

$$TSI = a (MW/SP) + b$$

where a and b are constants determined empirically and MW is the mixture molecular weight (gm/mole). (We used  $a = 3.32$  and  $b = -1.47$  as determined by Gill and Olson.) The mixture TSIs can be estimated using Gill and Olson’s molar mixing rule:

$$TSI = \sum x_i TSI_i$$

where  $x_i$  is the mole fraction of the component,  $i$ , and  $TSI_i$  is the TSI of the  $i$ th component. (More recently, these empirical parameters have been updated and extended by other SERDP team members (Mensch, et al. 2010).) Initially, we explored the possibility of picking the components from the list suggested by the Princeton-led MURI on surrogate fuels (Dryer, 2008). However, the analyses indicated that it would be difficult to keep the H/C ratio to a value typical of jet fuels. Hence, after some discussion with the SERDP teams in a meeting in December 2008, along with some calculations of predicted performance of various options, it was decided to select a mixture composed of 77% dodecane and 23% m-xylene (liquid volume %). The computed characteristics, compared to specifications for JP-8 and computations for several other proposed surrogates are shown in Table 3.1. The colored red items represent computed properties that are outside the existing specifications for jet fuel and the yellowed cells indicate that a property that is outside the reasonable range of experience. This analysis has been recently reviewed by the jet fuels surrogate working group who has endorsed our suggested surrogate make-up. A similar mixture by (S. Hunter, 2007) has been tested and shown to exhibit combustion characteristics similar to those for jet fuel. However the mixture average MW for his proposed mixture appears fairly low and hence was not selected.

Table 3.1 Surrogates, Their Components and Computed Properties.

	Surrogate D	Surrogate C	Surrogate E	Aachen	Modified Aachen	S2	Utah Surrogate	S12	Violi 2	Seshadri	SERDP1	Jet Fuel Min	Jet Fuel max
n-decane	50		34	80		70		15	25				
n-dodecane		60			80		30	20	25	60	77		
n-tetradecane							20	15	20				
n-cetane								10					
iso-octane								5	5				
iso-cetane							10						
methylcyclohexane		20					20	5	5	20			
cyclo-octane								5					
n-butylcyclohexane	25		33										
toluene									20				
propyl benzene						30							
n-butylbenzene	25		33					5					
o-xylene (1,2)		20											
m-xylene (1,3)							15	5		20	23		
trimethylbenzene				20	20								
tetralin							5	5					
1-methylnaphthalene								5					
Density (g/cc)	0.780	0.779	0.796	0.757	0.772	0.770	0.785	0.796	0.769	0.776	0.775	0.775	0.84
Molecular Wt (g/mole)	139.46	132.90	138.65	136.55	155.77	134.01	140.76	146.92	134.22	133.04	147.48	167.31	
H/C atomic ratio	1.92	1.92	1.84	1.99	1.97	1.90	1.90	1.86	1.92	1.92	1.92	1.85	
Est boiling pt (K)	451.5	450.4	452.7	445.1	477.8	442.3	461.2	475.9	452.0	449.3	469.6	453.2	
Smoke Point* (mm)	21.8	22.9	17.8	21.5	21.5	19.1	21.9	16.4	24.1	23.8	22.7	19	

### Surrogate Fuel for F-T Fuel

Chris Shaddix of Sandia, a partner in this SERDP-funded project, requested ideas for identifying a surrogate for traditional F-T fuels that are being tested by the AF and other parties, see Colket, et al, 2008. These fuels generally are primarily fully hydrogenated alkanes (no or few aromatics, olefins, or cycloalkanes). Hence they have very high H/C ratios and are much less prone to forming soot particulates than for standard fuels. Typically, these alkanes are primarily weakly branched (isoalkanes) with only 10-15% normal alkanes. Unfortunately, a selection of species to represent the isoalkanes is challenging as the only economically available source are specific heavily branched isomers of iso-octane, iso-dodecane and iso-cetane. Chris had raised the question of whether the commercially available iso-dodecane (2,2,4,6,6-pentamethylheptane) could be used as a surrogate.

This request is reasonable considering the lack of availability of other options, however, the heavily branched isoalkane may behave differently than weakly branched isoalkanes, particularly in ignition characteristics. We propose that this surrogate might be used under the following assumptions: the key moiety affecting ignition are the isobutyl groups; hence, approximate the presence of the weakly branched alkanes with 2,2,4,6,6-pentamethylheptane, by equating the number of isobutyl groups. As an example, a calculation with a reasonable set of assumptions is shown in the table below, suggesting that a surrogate of 40% isododecane (2,2,4,6,6-pentamethylheptane) and 60% n-dodecane might provide a reasonable surrogate for an F-T fuel. (Note that F.L. Dryer and his team have subsequently adopted a similar procedure in the creation of surrogate fuels.

Table 3.2 Computed Iso-butyl Structures in Fuels.

	molar conc	ave no of isobutyl groups
<b>FT fuel</b>		
n-alkanes	15	0
isoalkanes	85	1.5
mixture ave		<b>1.275</b>
<b>Surrogate</b>		
n-dodecane	57.5	0
isododecane	42.5	3
mixture ave		<b>1.275</b>

### 3.2.3 Kinetic Model for JP-8 Surrogate Fuel

#### *First Generation JP-8 Surrogate Model (SERDP\_SURR v1)*

Sources of the kinetic mechanisms for the 77% n-dodecane / 23% m-xylene surrogate fuel have been considered. A draft mechanism was constructed out of existing dodecane and m-xylene mechanisms, although the latter is less well-established. At the time of this activity, at least four dodecane mechanisms existed (Dryer, 2008; Violi, et al., 2002; Wang, 2008; and Herbinet, et al., 2007). Generally, these reactions sets are reasonable, as they have been built upon those of lower MW alkanes. There were fewer m-xylene oxidation mechanisms (Violi, et al., 2002 and Battin-Leclerc, et al., 2006), and at least one (Violi, et al, 2002) will need to be extended, as it utilizes global reaction steps. These mechanisms were combined with the already developed SERDP mechanism for ethylene and PAHs (SERDP\_C<sub>2</sub>H<sub>4</sub>).

The n-dodecane model (JetSurf 0.2) developed by Wang (2008) was selected as it is compatible with the ethylene mechanism utilized for the first part of this study. Based on interactions with K. Brezinsky, the m-xylene model developed by Battin-Leclerc, et al. (2006) was selected for combination with the dodecane model. Hence, the ethylene mechanism (described previously) has been merged within the larger m-xylene mechanism of Battin-Leclerc et al. The ethylene mechanism is comprised of high-temperature reactions associated with hydrogen, carbon monoxide, and C1-C4 hydrocarbons. In addition, it includes aromatic (benzene, toluene, and associated radicals) species. The original m-xylene mechanism comprised 1243 reactions amongst 188 species, while the ethylene mechanism entailed 784 reactions of 111 different species. Since many of the species contained within either mechanism were also present in the other mechanism, the method for eliminating duplicate species was as follows: Compounds that contained the same numbers of the same atoms and had virtually equivalent heats of formation (based on their respective thermochemistry data) were considered to be the same compound and were given a common name. Once the species names were reconciled within the mechanisms, elimination of duplicate reactions between the two mechanisms was then performed. Reactions in the original ethylene mechanism were given preference over those contained within the xylene mechanism. Additionally, based on reasoning given above, all thermochemistry polynomial values for common species were taken from the ethylene mechanism. Ultimately, this merging

process created a mechanism that consisted of 1689 reactions and 216 species. This mechanism, based upon a merger of the Batten-LeClerc m-xylene chemistry, JetSurf 0.2 and an updated PAH-formation mechanism (see below) is denoted SERDP\_SURR v1.

Both the original mechanism and the new, updated mechanism were then compared against an atmospheric pressure flow reactor (APFR) dataset associated with m-xylene oxidation (Emdee, et al., 1991) via the Chemkin-II/Senkin codes. The comparison between the experimental data and both simulations for m-xylene decay is shown in the figure below. As can be seen, the updated mechanism produces a fuel decay rate that is slower than both the data and the original mechanism.

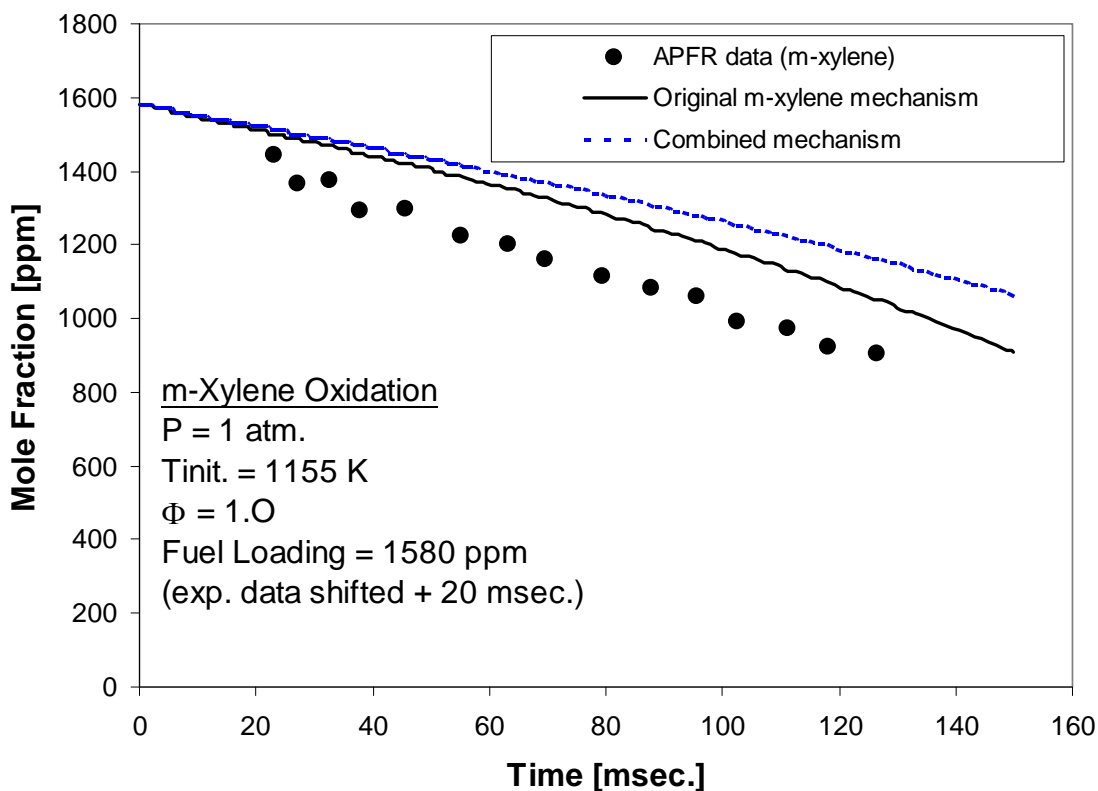


Figure 3.3 Comparison of computed decay of m-xylene using original and combined mechanism with experimental data.

To understand the differences between the mechanisms, we have performed a sensitivity analysis to identify the key reactions (and rates) that affect the decomposition rate. A plot of the most important reactions is given in the following figure:



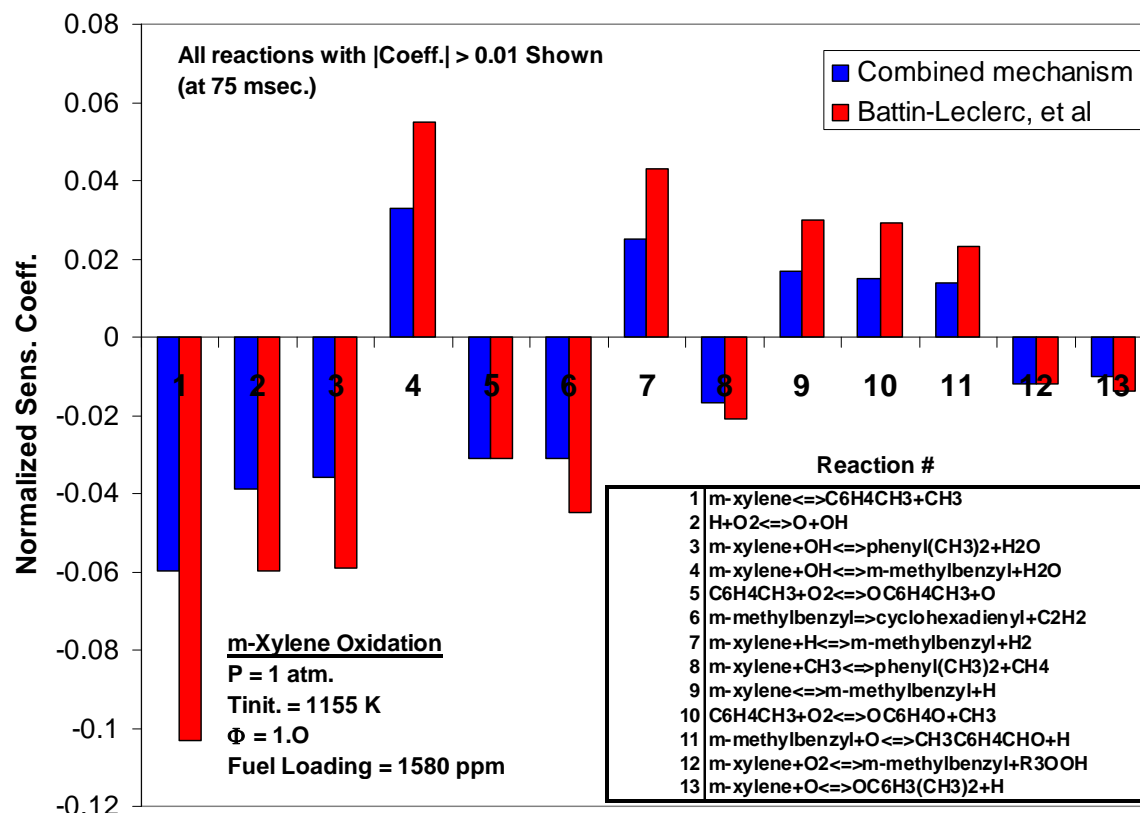


Figure 3.4 Results from sensitivity analysis for the m-xylene reaction system.

Not surprisingly, the reaction whose rate is most sensitive to the decomposition is the initiation step involving elimination of methyl radical from m-xylene. In review of this figure and the mechanism, it was recognized that a reaction, describing the unimolecular reaction of methylbenzyl radical was missing (based on an analogy to the toluene system). The reaction forming the products C<sub>2</sub>H<sub>2</sub> and cyclohexadienyl (R6 above) is included, but an alternate step to form cyclopentadienyl and methyl acetylene was not included. By simply adding this step, with a rate comparable to that of benzyl radical decomposition, the decomposition fits were enhanced. (Alternatively, by increasing the rate of Reaction 6 by a factor of 2-3, the decomposition profiles are also simulated better.) Nevertheless, we postponed recommending an alternate mechanism until a more careful review of product distributions has been performed.

At the SERDP/ESTCP meeting in December 2008, UTRC was assigned the task to extend the growth model for polycyclic aromatic hydrocarbons to the m-xylene system. We identified several steps, analogous to PAH growth steps identified in the toluene pyrolytic system (Colket and Seery, 1993). In particular, reactions analogous to both



and the reactions in Figure 3.5 needed to be identified and incorporated into the reaction set.

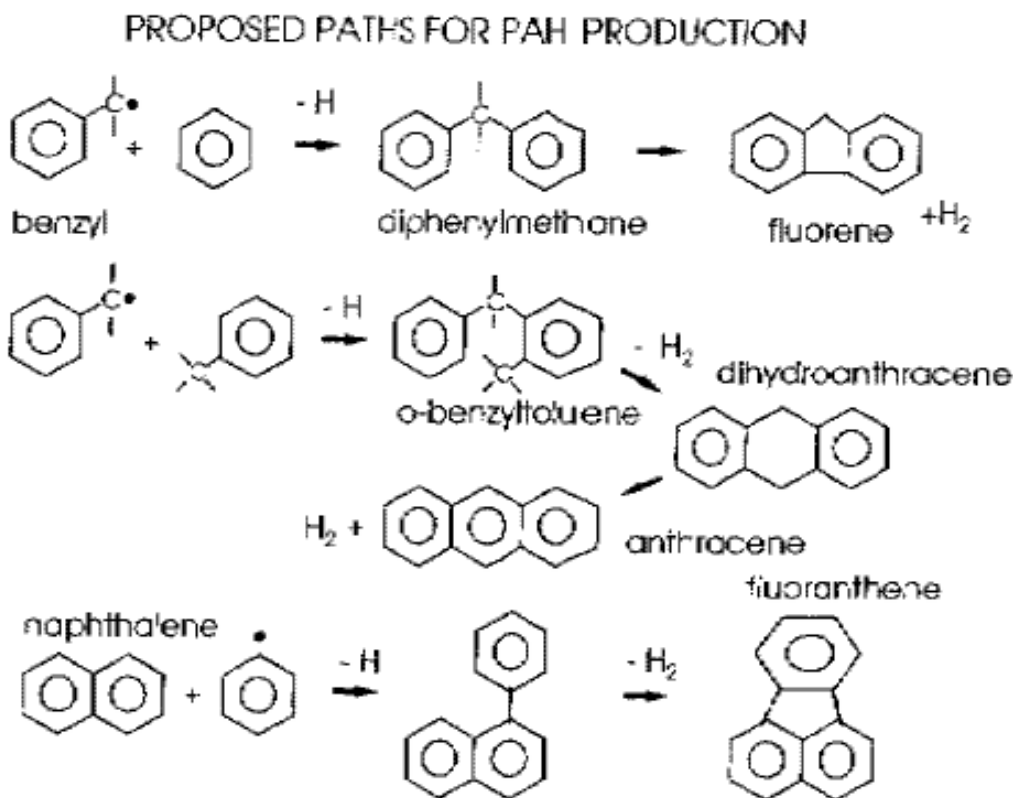


Figure 3.5 Set of PAH-forming reactions from the toluene system (Colket and Seery).

Two types of reactions were identified, specifically alkyl addition to benzylic groups and benzylic addition to aromatic rings. Examples of the former of these reactions for the toluene system are provided in Figure 3.6 (in grey) along with some examples of both types of reactions for the *m*-xylene system (blue background). What is of interest is that nearly all of these molecules have added methyl groups attached to the rings, which are residual from the additional methyl group attached to the ring in *m*-xylene. New species identified for inclusion into the *m*-xylene reaction system are shown in Figures 3.7 and 3.8. Also, a series of calculations were performed (based on group additivity) to estimate the thermodynamics of these species. The computed thermodynamics (heats of formation, entropy and heat capacities) at a reference temperature of 298K are provided in Table 3.3, along with a few other key species of interest.

Initially, rate coefficients were estimated based on the parameters determined empirically by Colket and Seery. Based on thermodynamic principles, reverse rates were then computed and as necessary forward rate coefficients were adjusted to ensure that reverse rates did not exceed collision theory. A full set of reactions added to the *m*-xylene system are provided in Table 3.4.

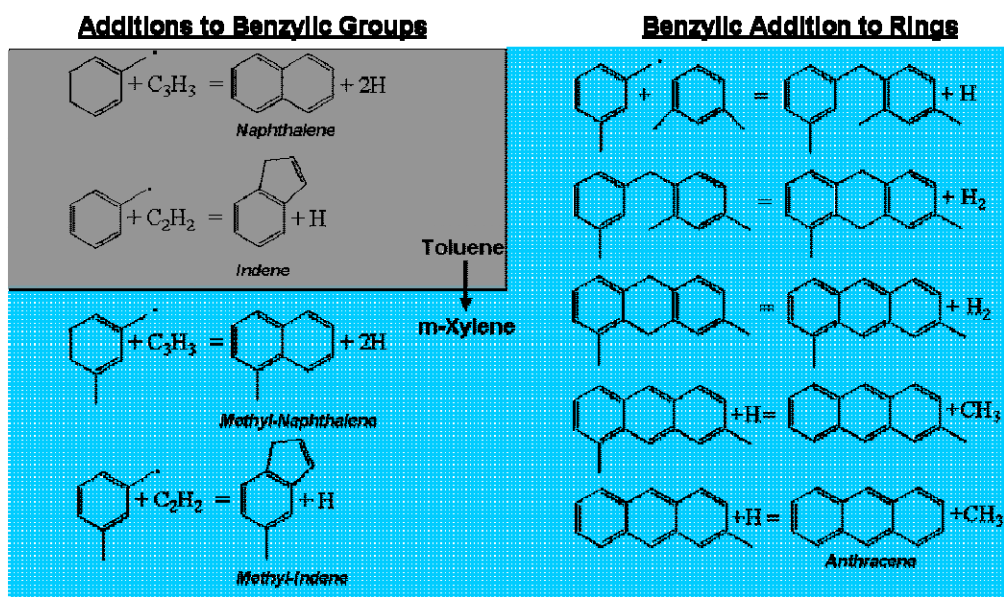


Figure 3.6 Examples of PAH forming reactions.

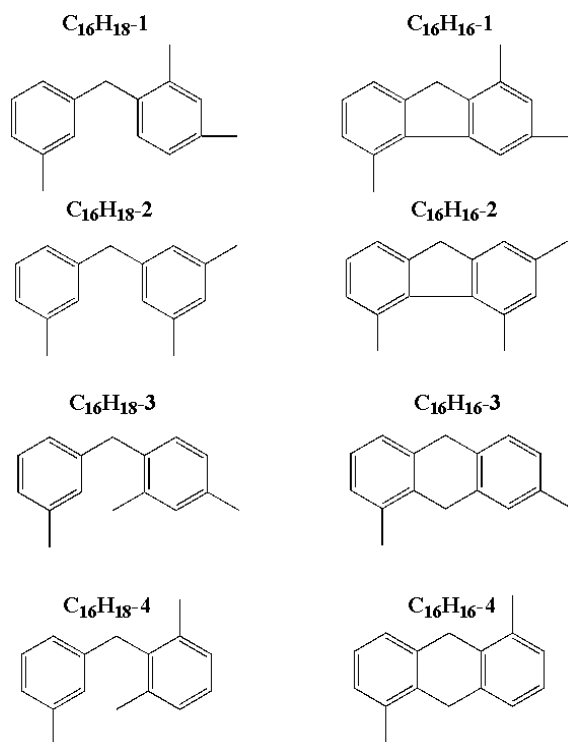


Figure 3.7 Structures and nomenclature for C16 species.

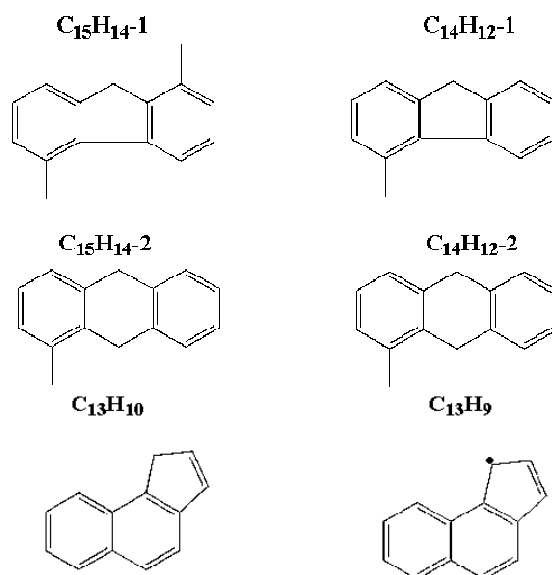


Figure 3.8 Structures and nomenclature for C13-C15 species.

Table 3.3 Thermodynamics of Key Species in m-Xylene System.

Species	$\Delta H$ [kcal/mole]	S [cal/K-mole]	Cp-298 K [kcal/mole]
m-xylene	4.06	85.30	30.43
m-methylbenzyl	41.53	86.77	29.50
H <sub>2</sub>	0.00	31.23	6.89
H	52.10	27.42	4.97
FLUORENE	47.86	94.24	39.51
CH <sub>3</sub> INDENE	34.29	90.48	33.04
CH <sub>3</sub>	35.11	46.37	9.18
C <sub>3</sub> H <sub>3</sub>	82.69	61.34	15.51
C <sub>2</sub> H <sub>2</sub>	54.54	48.02	10.52
C <sub>16</sub> H <sub>18</sub> -4	16.30	131.82	61.68
C <sub>16</sub> H <sub>18</sub> -3	15.70	134.81	61.08
C <sub>16</sub> H <sub>18</sub> -2	15.20	135.04	59.94
C <sub>16</sub> H <sub>18</sub> -1	15.70	134.81	61.08
C <sub>16</sub> H <sub>16</sub> -4	24.15	118.54	55.51
C <sub>16</sub> H <sub>16</sub> -3	24.15	118.54	55.51
C <sub>16</sub> H <sub>16</sub> -2	23.89	126.00	56.27
C <sub>16</sub> H <sub>16</sub> -1	23.89	126.00	56.27
C <sub>15</sub> H <sub>14</sub> -2	32.14	107.35	49.82
C <sub>15</sub> H <sub>14</sub> -1	31.88	115.26	50.73
C <sub>14</sub> H <sub>12</sub> -2	40.13	96.16	44.18
C <sub>14</sub> H <sub>12</sub> -1	39.87	104.07	45.10
C <sub>13</sub> H <sub>9</sub>	89.99	84.20	40.57
C <sub>13</sub> H <sub>10</sub>	56.49	88.01	42.12
A <sub>3</sub> L	52.20	92.55	46.84
A <sub>3</sub>	50.00	93.92	46.84
A <sub>2</sub> CH <sub>3</sub> -2	27.75	92.63	38.81
A <sub>2</sub> CH <sub>3</sub> -1	27.93	90.41	38.53
A <sub>2</sub> CH <sub>2</sub> -2	61.67	89.44	38.44
A <sub>2</sub> CH <sub>2</sub> -1	61.44	89.43	38.25

Table 3.4 PAH Forming Reactions for m-Xylene System.

<u>Reaction</u>	<u>A</u>	<u>n</u>	<u>Ea</u>
	$[(\text{cm}^3/\text{mol})/\text{sec}]$		$[\text{cal}/\text{mol}]$
m-xylene+m-methylbenzyl=C16H18-1+H	3.00E+12	0	28000
C16H18-1=C16H16-1+H2	1.00E+08	0	40000
m-xylene+m-methylbenzyl=C16H18-2+H	3.00E+12	0	28000
C16H18-2=C16H16-2+H2	1.00E+08	0	40000
m-xylene+m-methylbenzyl=C16H18-3+H	3.00E+12	0	28000
C16H18-3=C16H16-3+H2	1.00E+08	0	40000
m-xylene+m-methylbenzyl=C16H18-4+H	3.00E+12	0	28000
C16H18-4=C16H16-4+H2	1.00E+08	0	40000
C16H16-1+H=C15H14-1+CH3	1.20E+13	0	5120
C15H14-1+H=C14H12-1+CH3	1.20E+13	0	5120
C14H12-1+H=FLUORENE+CH3	1.20E+13	0	5120
C16H16-2+H=C15H14-1+CH3	1.20E+13	0	5120
C16H16-3+H=C15H14-2+CH3	1.20E+13	0	5120
C15H14-2+H=C14H12-2+CH3	1.20E+13	0	5120
C14H12-2=ANTHRACEN+H2	2.30E+12	0	43800
C16H16-4+H=C15H14-2+CH3	1.20E+13	0	5120
m-methylbenzyl+C3H3=A2CH3-1+H+H	6.00E+11	0	7913
m-methylbenzyl+C2H2=CH3INDENE+H	1.00E+12	0	5000
A2CH2-1+C3H3=A3+H+H	3.00E+12	0	0
A2CH2-2+C3H3=A3L+H+H	3.00E+12	0	0
A2CH2-2+C3H3=A3+H+H	3.00E+12	0	0
A2CH2-1+C2H2=C13H10+H	1.00E+12	0	5000
A2CH2-2+C2H2=C13H10+H	1.00E+12	0	5000
C13H10+H=C13H9+H2	5.40E+04	2.5	-1900
C13H9+CH3=A3+H+H	2.00E+12	0	0

To examine the relative impact of these reactions when added to the existing reaction mechanism on PAH formation, a series of computations were performed under simulated plug flow reactor conditions (constant pressure). Initial conditions were assumed to be 1500K, 1 atm, and an overall equivalence ratio of 2. The mixture was diluted in nitrogen with the initial concentration of m-xylene set to 1360 ppm. A comparison of results from the original mechanism and an updated reaction set that includes the steps in Table 3.4 are shown in Figure 3.9 Essentially, the added reactions dramatically increase the early production of PAH species while the parent molecule still survives (m-xylene concentration decays to zero within 1.5 milliseconds).

Separately, H. Wang and V. Katta have been exploring the combined (preliminary) reaction set. They identified numerical problems associated with several reactions in the base m-xylene mechanism that has been incorporated into our surrogate n-dodecane/m-xylene kinetics model. After some discussion with H. Wang and others, and recognizing an ongoing companion effort

underway by K. Brezinsky and colleagues for the enhancements to the m-xylene mechanism, we initiated a small effort to provide simple corrections to the existing model to enable simulations to proceed until the updated mechanism was available.

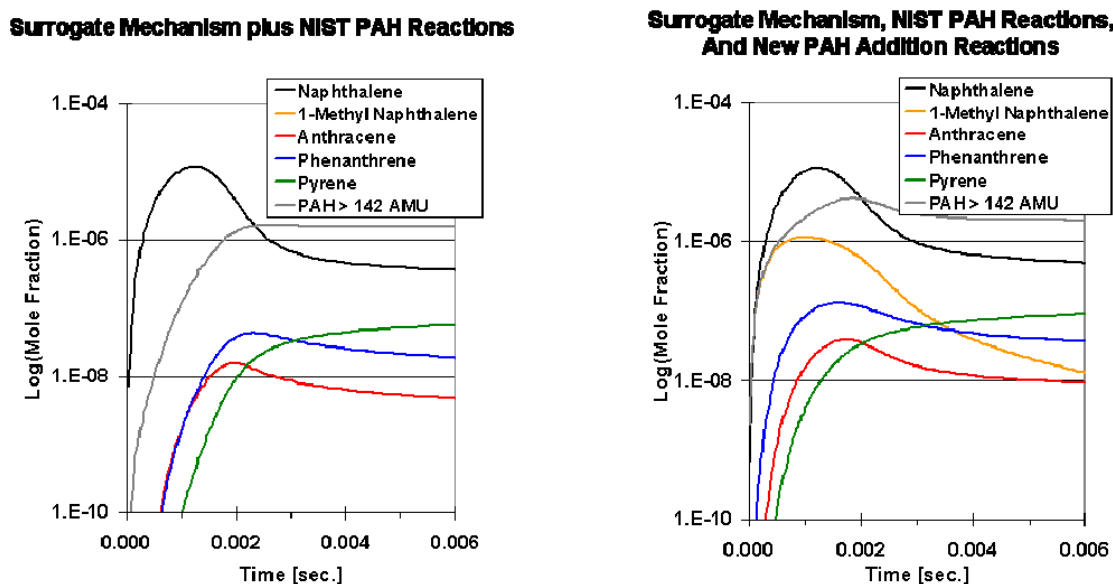


Figure 3.9 Comparison of PAH formation with and without added reactions.

The criteria and rationale for selection of the components of the surrogate fuel were discussed previously. Of note is that promising experimental results have been obtained in limited experimental investigations. In particular, the surrogate fuel consisting of 77% n-dodecane and 23% m-xylene was tested by partners in the SERDP ‘soot science’ program. The Sandia-led team has demonstrated that this surrogate closely matches ignition, flame structure and soot yields relative to those for JP-8 in studies of a diesel injection configuration (Shaddix, 2008). Furthermore, USC has directly measured the flame speed and extinction characteristics of this surrogate (Ji, et al., 2009). The results generally show that the surrogate fuel mimics the combustion characteristics of JP-8 fuel rather well. The laminar flame speeds of this surrogate were found to be only slightly faster than those of JP-8. However, flames of the 77%-23% surrogate fuel were determined also to exhibit higher extinction resistance compared to JP-8. It was suggested that improvements, if needed, might be made by adding an iso-paraffin and reducing the n-paraffin content in the proposed 77%-23% surrogate fuel as far as flame propagation is concerned.

#### *Second Generation JP-8 Surrogate Model (SERDP\_SURR v1)*

The latest SERDP n-dodecane/m-xylene two-fuel surrogate kinetic model was developed in collaboration with other SERDP-funded teams and followed the same methodology as previous versions of the SERDP two-component reaction models. Specifically, reactions associated with m-xylene oxidation and decomposition, as well as its decomposition products, were taken from the published mechanism of m-xylene oxidation of Gudiya et al. (2011) in work from the University of Illinois at Chicago, (UIC) in K. Brezinsky’s laboratory. Reactions associated with

n-dodecane, and its decomposition products, were taken from the “JetSurf, version 1.0” reaction set assembled by Sirjean et al. (2009) at the University of Southern California (USC). Lastly, the reaction set associated with small species chemistry (e.g., hydrogen, carbon monoxide, carbon dioxide, hydrocarbons with four or fewer carbon atoms) were those of the USC Mechanism, version 2.0.

To ensure consistency in nomenclature between the three mechanisms, tabulations of each species present in the three mechanisms, along with its atomic formula and thermochemical property data (heat of formation, entropy) were created. Entries with different names that had identical atomic populations and thermochemical values were considered to be equivalent species. For such cases, careful review of the conversion was required to ensure accuracy. Due to broader validation of the USC mechanism and thermodynamics, species, and thermochemical properties, associated with the USC mechanisms superseded the UIC-based compounds when duplication occurred.

After species name conflicts had been rectified, the reactions associated with each of the above mechanisms were assembled into one large reaction set. The next step was to eliminate redundant reactions that were created as a result of the combination of the three mechanisms. Due to the large number of reactions comprising the merged reaction set, the CHEMKIN-II kinetic mechanism interpreter code was used to identify any unintentionally duplicated reactions. As with species conflicts, for any reaction duplication issue, the USC-based reaction and rate data were maintained and the UIC-based reaction was removed from the larger kinetic mechanism. The final two-component model comprises 1682 reactions amongst 232 species.

One additional change was made to the m-xylene reaction set, as follows. Davis et al. (ref.) discussed the importance of fall-off formulations for aromatic unimolecular reactions at atmospheric pressure. Accordingly, the UIC-based Arrhenius rate data for the reaction of m-xylene undergoing a H-homolysis reaction to form the m-xylyl and hydrogen radicals was replaced with a Troe-style fall-off rate expression.

This new mechanism for surrogate jet fuel is denoted SERDP\_SURR v2.

Several published data sets were used to benchmark the performance of the assembled kinetic mechanism. The data sets and experimental conditions of each are shown below in Table 3.5. All data are for m-xylene studies.

Table 3.5 Literature Data Sets Used To Benchmark SERDP Mechanism.

Experiment	Temperature (K)	Pressure (atm.)	Equivalence Ratio	Diluent	Reference
Shock Tube	1700-1400	9.0	0.5,1.0,2.0	Argon (91.75-97.65%)	Battin-Leclerc et al.
Flow Reactor	1155	1.0	1.0	Nitrogen (98.18%)	Emdee et al.
Jet-Stirred Reactor	1100-1300	1.0	1.0	Nitrogen (98.85%)	Gail and Dagaut

Since these data sets all employed m-xylene as the fuel, the UIC m-xylene mechanism was also used to simulate these experiments, to ensure that the SERDP mechanism did not yield disparate results.

The comparison between the experimental ignition delay times and those generated by both mechanisms as functions of inverse temperature are shown below in Figure 3.10. For both sets of simulations, the ignition time was defined as the time at which the system temperature derivative was a maximum. No extrapolations to initial temperatures were made, although this is generally the procedure used in shock tube ignition measurements. Hence the computed values here can be expected to be longer than the experimental values. All simulation ignition delays are within an order of magnitude of the experimentally obtained values. Furthermore, the sensitivity of each mechanism's ignition delay time to the initial temperature is consistent with the experimental sensitivity, as indicated by the slopes of each data set. At the lean and stoichiometric mixtures, both mechanisms yield times that are within 10-30% agreement of each other. The rich mixture ignition times are within 50% agreement and the new (SERDP\_SURR v2) mechanism results in slightly longer delays. This agreement is consistent across the temperature range of the experiments and the differences may be at least partially due to the different manner by which ignition delays were determined.



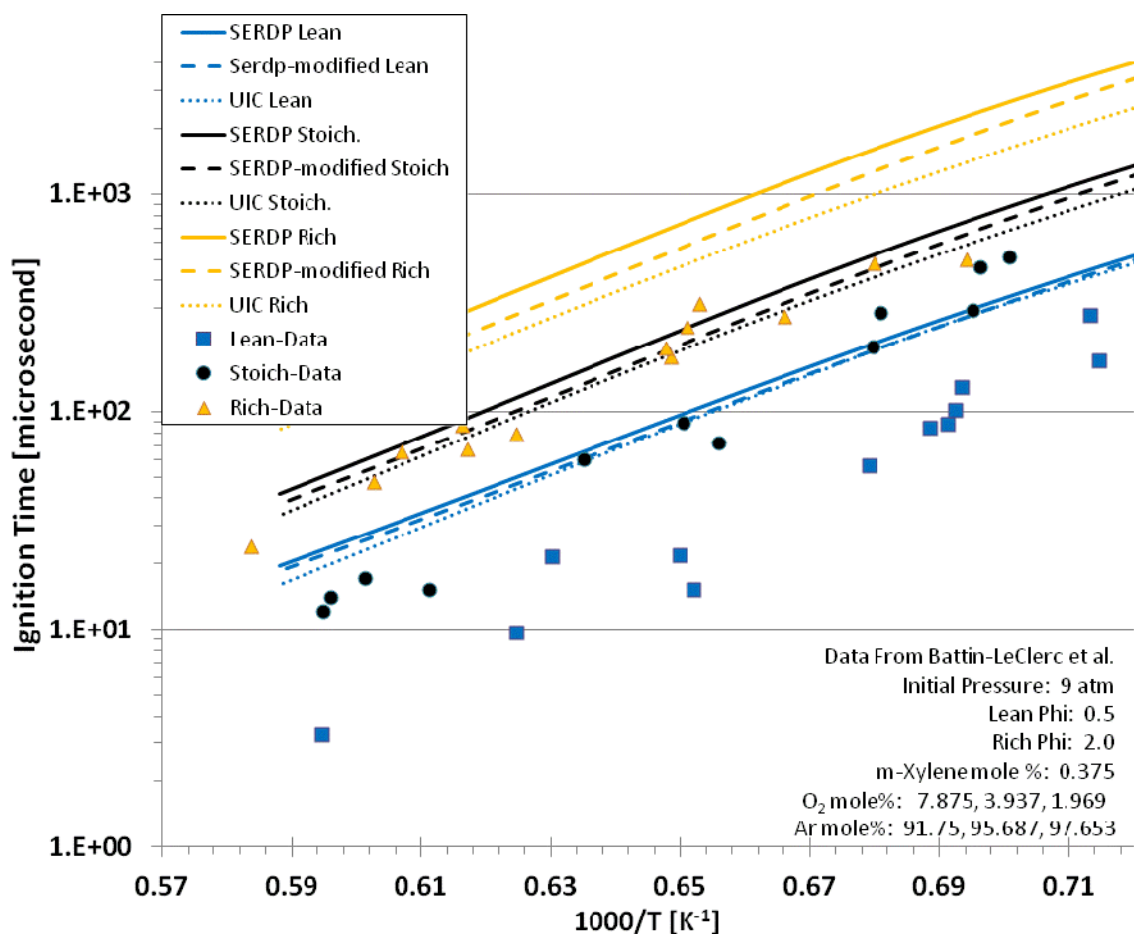


Figure 3.10 Comparison of Experimental and Computational Ignition Delay Times.

Comparison between the experimental and computational species profiles associated with an atmospheric m-xylene oxidation flow reactor study is shown below in Figures 3.11 and 3.12. In general, species profiles generated by both mechanisms are in reasonable agreement. Furthermore, agreement between the experimental and both computational decay rates for fuel and oxygen is good. The models under predict carbon monoxide production, as well as over predict methylbenzaldehyde formation.

Similarly, Figure 3.12 illustrates that while hydrogen, methane, and benzene formation are over predicted, toluene production is under predicted by the models.

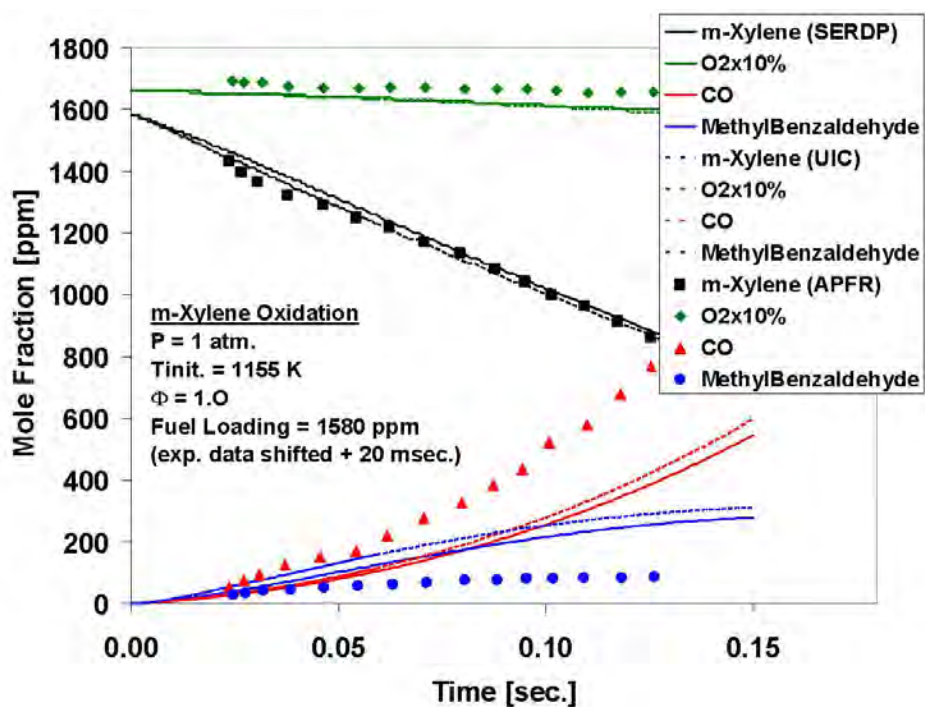


Figure 3.11 Comparison of Species Profiles during m-Xylene Oxidation in a Flow Reactor.

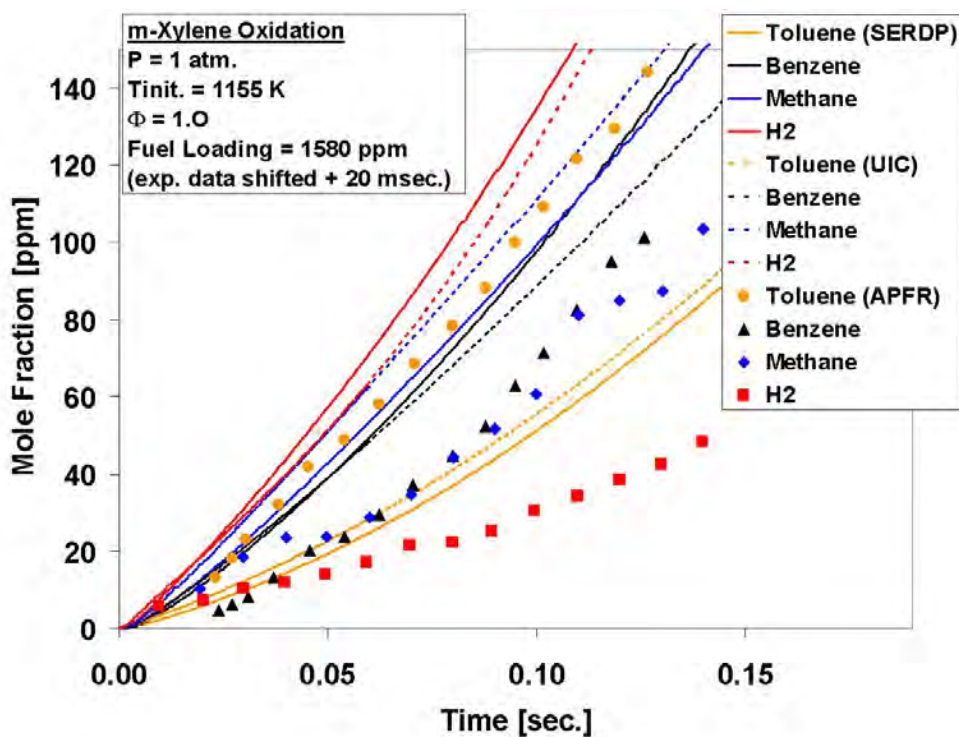


Figure 3.12 Species Profiles Associated with APFR m-Xylene Oxidation System.

Comparison between the experimental and computational species profiles generated in the JSR experiments are shown in Figures 3.13-3.15. As can be seen from Figure 3.12, both mechanisms over predict fuel conversion values at higher reactor temperatures. Specifically, the UIC mechanism exhibits a rise in reactor  $\text{CO}_2$  values near 1200 K and the SERDP mechanism exhibits a similar  $\text{CO}_2$  rise at 1250 K. At 1350 K, both mechanisms generate more than three times the  $\text{CO}_2$  values generated by the experiments. While the  $\text{CO}_2$  profiles are not well predicted, the SERDP generated CO profile matches the experimental CO values reasonably well over the temperature range of the studies. Due to the enhanced conversion reactions, the UIC mechanism exhibits a peak in the CO mole fraction profile at 1250 K and then drops as the CO values essentially relax to their equilibrium values at the higher temperatures. Comparison of the computational major product profiles to the experimental values also reveals the presence of maxima occurring at lower temperatures than experimentally observed. For instance, Figure 3.15 shows that the experimental benzene mole fraction value peaks at approximately 260 ppm near a reactor temperature of 1350 K. Both the SERDP and UIC models predict benzene peaks at lower reactor temperatures: 175 ppm at 1250 K and 75 ppm at 1200 K, respectively. These peak locations are consistent with the over prediction of m-xylene decomposition above 1250K, as shown in Figure 3.13.

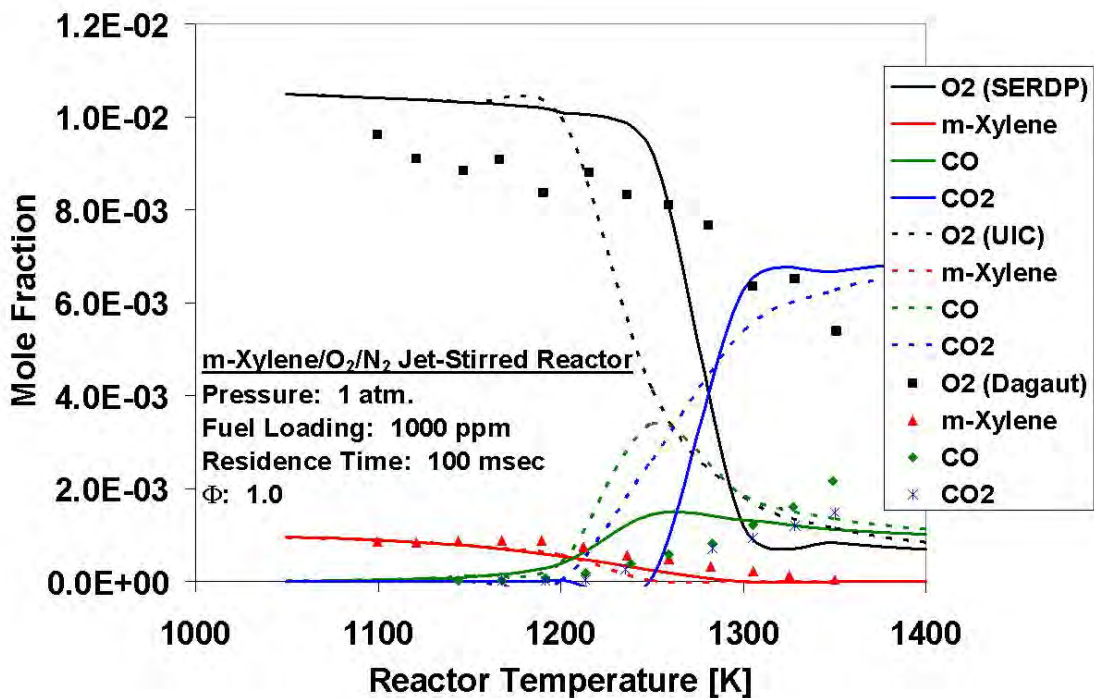


Figure 3.13 Fuel, Oxygen, CO, and  $\text{CO}_2$  Mole Fractions versus Reactor Temperature for JSR Test Conditions Shown.

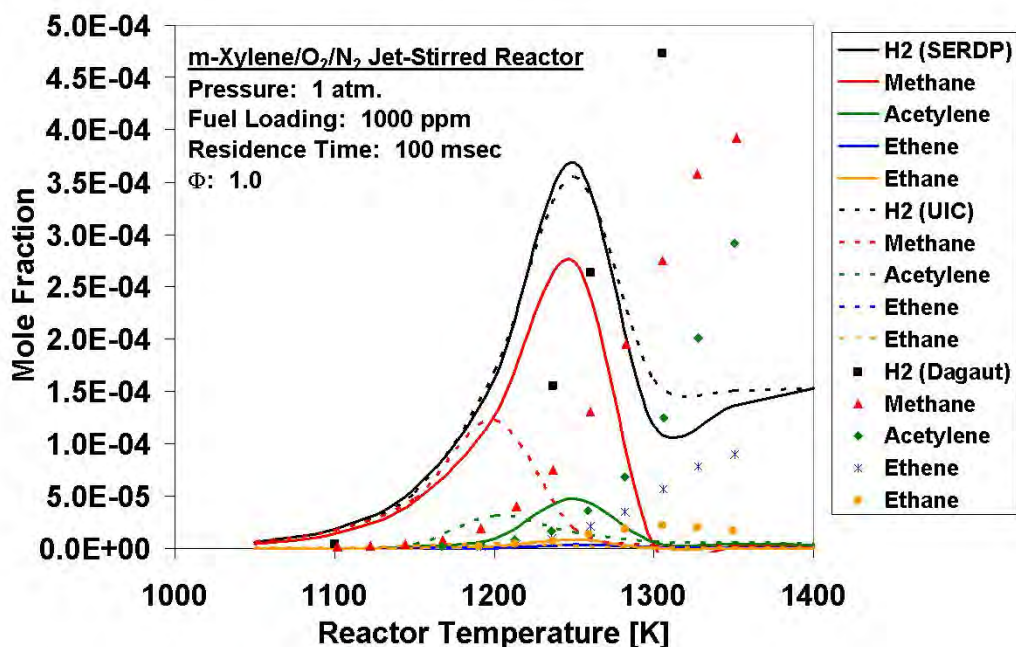


Figure 3.14 Mole Fractions of Light Species vs. Reactor Temperature in JSR.

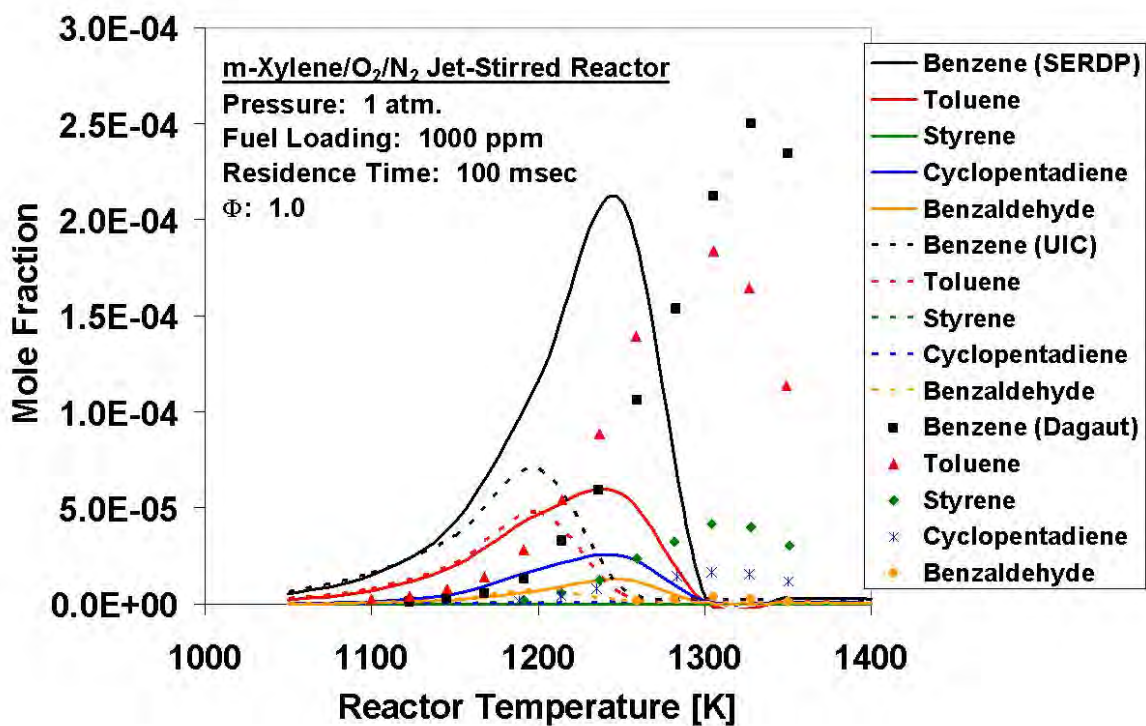


Figure 3.15 Mole Fractions of Cyclic Species vs. Reactor Temperature in JSR.



The SERDP two-fuel surrogate mechanism was also used to predict the adiabatic flame speed of a stoichiometric m-xylene/air mixture at initial conditions of 300 K and 1 atmosphere. The calculation was carried out using the PREMIX program of the CHEMKIN-II chemical kinetic software package with values of 0.15 for both the GRAD and CURV parameters to ensure convergence. Only a few experimental data sets are available for comparison. Johnston and Farrell (2005) reported a laminar flame speed of approximately 45 cm/sec for a stoichiometric m-xylene/air mixture at 450 K and 3 atmospheres. In our simulations, we predict 44.2 cm/sec in comparison to the Johnston and Farrell data. In addition, Ji, et al. (2009) reported flame speeds for several fuels as a function of equivalence ratio at 403K and 1 atmosphere. Our predictions of the m-xylene flame speeds are plotted in Figure 3.16 for the Ji, et al data sets, along with their data and our predictions for 100% n-dodecane and for our suggested Jet-A surrogate, 23% m-xylene and 77% n-dodecane (liquid volume percentages). It is apparent from these comparisons that the model is routinely under predicting the Ji, et al measurements of flame speeds for all of the fuels compared and the under prediction of m-xylene is the most severe.

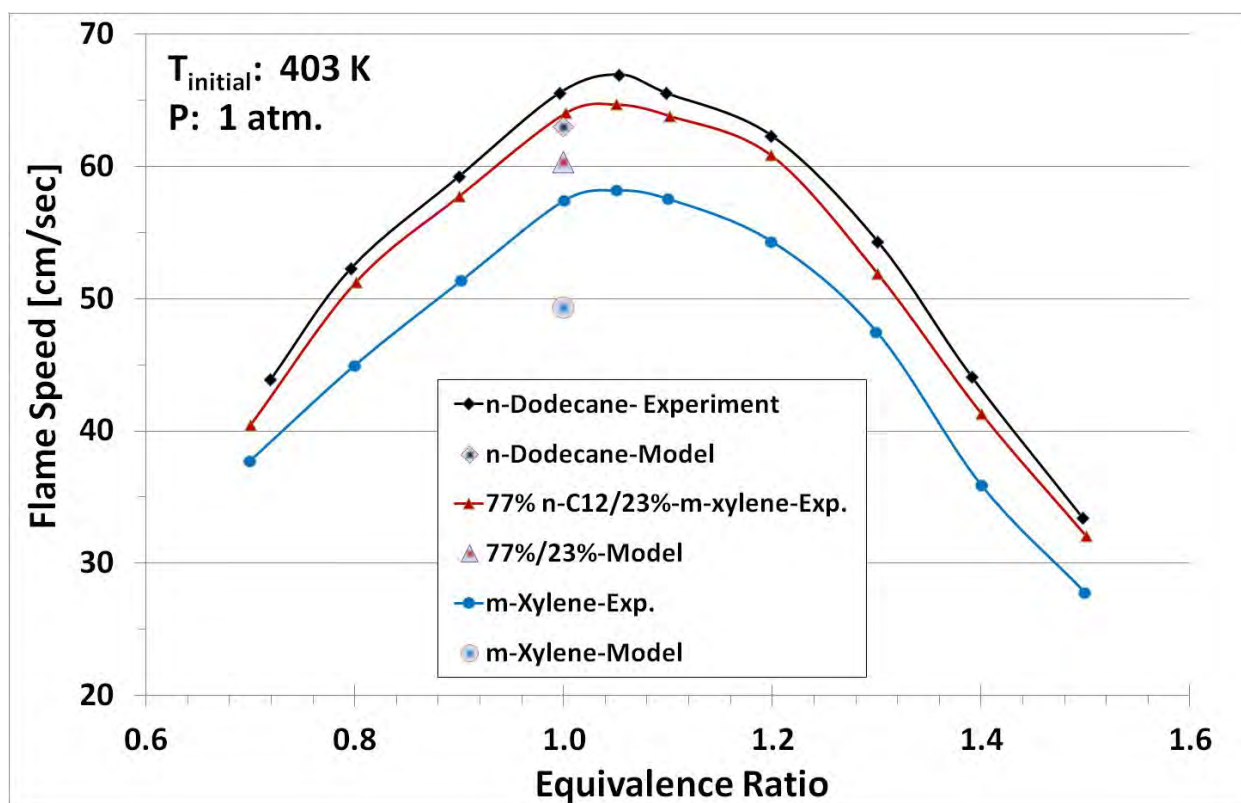


Figure 3.16 Comparison of Predicted and Computed Flame Speeds.

The under prediction of the Ji's m-xylene data vs. the nearly perfect agreement with the data by Johnston and Farrell, will likely be reconciled in the future with more data sets and more accurate experimental methods. This subject therefore remains a topic of interest for future research.

### 3.2.4 Soot Models

Quantitative modeling of particulate matter (PM), often referred to as soot or smoke, emissions from flames and burners is one of the greatest challenges to computational modeling of combustion. There exist models that provide quantitative predictions of soot production in laboratory flames burning pure fuels at atmospheric pressure, but generally they are accurate over very limited conditions. Oxidation of these soot particles is dependent on accurate knowledge of the active surface area of the particles which in turn is dependent on the formation process. The total emissions of PM from a practical burner are the difference between two large terms, the formation and the oxidation. At full power for example, PM emissions at the engine/combustor exhaust can be two to three orders of magnitude less than the levels in the primary zone. Finally, turbulent mixing and reacting flow complicate simulations with time scales of soot formation and oxidation substantially different from the time scales of heat release. Given the uncertainty in computing the growth and oxidation terms as well as turbulent and mixing impacts, the modeling challenge for this problem is readily recognized. Hence it is not surprising that authors are willing to present modeling results that agree only to within one to two orders of magnitude from the experimental values (Tolpadi, et al, 1997; Brocklehurst, et al, 1997).

In this section, a description of the modeling approaches utilized in this work for predicting soot evolution during combustion is presented. Prior to discussing models, however, a picture of soot formation during combustion is provided. Then, descriptions of each of the physical/chemical processes that must be treated in the modeling of soot formation in flames are briefly presented. The discussion includes particle inception, growth, agglomeration/coalescence, and oxidation.

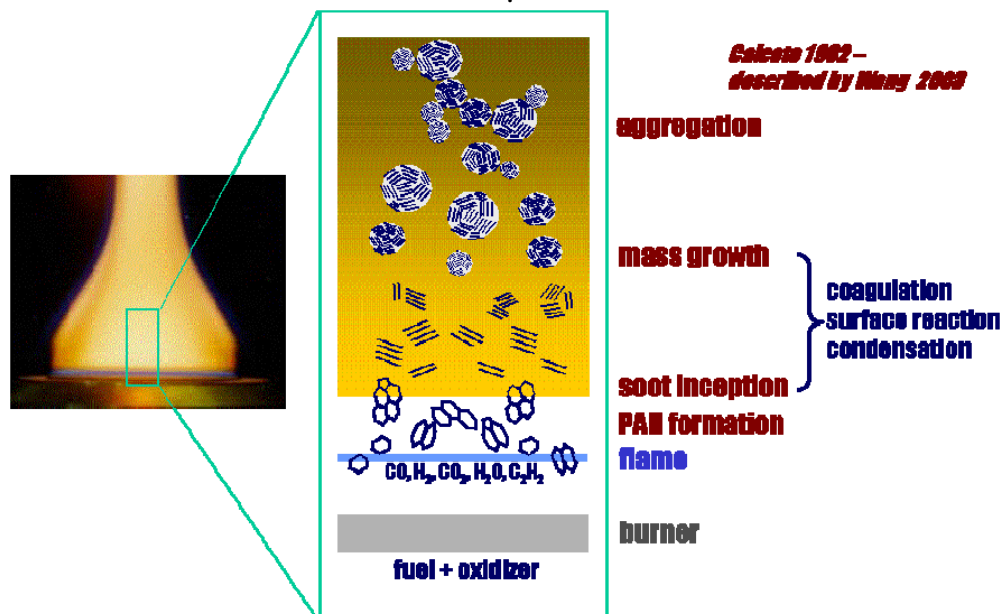


Figure 3.17 Soot formation processes in premixed, laminar flame (courtesy of H. Wang).

Processes related to soot formation in a laminar flame are depicted in Figure 3.17. A flame is stabilized over a porous plug burner, consuming the fuel-rich, premixed gases. Within the narrow flame front, reactive species lead to the formation of aromatic species (e.g., benzene, naphthalene, phenanthrene, pyrene, etc.) and acetylene. Polyaromatic hydrocarbon species are generally believed to lead to inception and can contribute to surface growth via condensation. Acetylene is recognized to be a key surface growth species. Inception generally occurs primarily within or just downstream of the flame front, while surface growth occurs primarily in the post flame zone. Temperature is a key primary variable: at low temperatures (e.g.,  $<1500\text{K}$ ), kinetics are not fast enough to support rapid ring formation, and at elevated temperatures ( $>1900\text{K}$ ), the ring structure is thermodynamically unstable and ring growth is slowed. The H/C atomic ratio of the fuel is important, as is the overall equivalence ratio, since these parameters affect both the carbon available for growth as well as the local temperature.

As depicted in Figure 3.17, above the flame front, models envisage aromatic structures dimerize (Appel, et al, 2000) to form co-planar structures, although there is some evidence that these incipient particles may in fact be better characterized as liquid droplets (for example, Dobbins, 1996). In the latter case, the droplets undergo carbonization (Dobbins, 1996) and related density changes. Particle size increases further downstream in the post-flame zone due to a combination of surface growth and coalescence. During coalescence, two particles merge into one and total surface area available for subsequent growth decreases. Alternatively, mature carbonized particles collide with each other and undergo agglomeration. In these cases, particles retain their individual structure and cluster into three dimensional fractal structures, typically with fractal numbers near to  $1.8 \pm 0.2$ . Hence aerosol dynamics is a critical process in defining total surface growth and hence the mass of PM present in the flame. Not shown in Figure 3.17 is the subsequent oxidation process that occurs downstream of the fuel-rich portion of a flame after additional air/oxidizer is added.

From this picture, it should be apparent that the characteristic time scale of the main combustion and heat release are much faster than the soot growth steps. The flame in fact creates the environment such that soot formation takes place in the post-flame region.

In the following sections, brief discussions of soot inception, soot growth, soot oxidation, soot ageing, aerosol dynamics (free molecular, transition and continuum), and radiation are presented.

A large range of soot modeling approaches exists. For each approach, there are multiple submodels included within the soot model, to account for physics such as inception, surface growth, oxidation, and aerosol dynamics.

### *Soot Inception*

The most ‘popular’ inception process utilizes the dimerization of pyrene (Appel, et al, 2000) to simulate the rate of soot inception. Yet use of this model requires the availability of a detailed (and ideally accurate) gas-phase model up to and including pyrene. It is presently acknowledged that this methodology is closer to reality than the use of acetylene (Fairweather, et al, 1992) to compute inception rates or equated naphthalene formation (Hall, et al, 1997) that were developed years ago. They are still used occasionally by authors to avoid the complexities and uncertainties

of computing gas-phase species leading to pyrene. Still there is no evidence that such a sequence adequately describes inception. Also, the sensitivity of the total soot formation to the initial inception rates are, in many cases, weak as agglomeration/coalescence processes of many small droplets buffer any dependence on the inception process.

The particle inception rate  $S_i$ , developed by Hall, et al (1997) is based on the formation rates of naphthalene ( $C_{10}H_7$ ) and phenanthrene ( $C_{14}H_{10}$ ) and is given by the expression

$$S_i = W_{C_{10}H_7} \frac{d[C_{10}H_7]}{dt} + W_{C_{14}H_{10}} \frac{d[C_{14}H_{10}]}{dt}, \quad (15)$$

where  $W_{C_{10}H_7}$  and  $W_{C_{14}H_{10}}$  are molecular weights. When  $C_{10}H_7$  and  $C_{14}H_{10}$  are not included in the chemical kinetic mechanism for a simulation, their formation rates cannot be obtained directly and must be estimated using simplified steady-state expressions. Via the steady-state expressions, inception depends on local acetylene ( $C_2H_2$ ), benzene ( $C_6H_6$ ), phenyl ( $C_6H_5$ ) and molecular hydrogen ( $H_2$ ) concentrations. Note that this model for inception effectively creates soot nuclei that are small PAHs. Hence, the model implicitly captures PAH addition to ‘soot’ particles via coalescence as well as surface growth, although it must be acknowledged that uncertainties remain in computation of these specific rates.

An alternate inception simulation of the inception process is utilized by Smooke, et al (2005) who utilized a series of steady-state assumptions on intermediate species to estimate the formation of a large polycyclic aromatic structure. The model is based on the sequence of growing naphthalenyl to pyrenyl through sequential acetylene addition, H-atom elimination, H-atom abstraction, and acetylene addition followed by ring closure. Overall, the reaction can be written  $C_{10}H_7 + 3C_2H_2 \rightleftharpoons C_{16}H_9 + 2H + H_2$ . This sequence is assumed to continue to form yet larger PAH structures with the overall balance of  $C_{10}H_7 + 3nC_2H_2 \rightleftharpoons C_{10+2n}H_{7+2n} + 2nH + nH_2$ . Quasi steady-state concentrations of intermediate polycyclic aromatic hydrocarbons are assumed, leading to steady-state expressions for the formation rates of these high molecular weight condensed polycyclic aromatic hydrocarbons (PAH). It is not recommended to use this model with  $n$  very high (e.g.,  $n$  should be limited to 1-3) since it does not capture the relaxation time to attain steady-state for all intermediate species and since the model implicitly will not capture the effect of PAH condensation (see Surface Growth section) for species smaller than the incepting species.

### *Surface Growth*

Surface growth is usually attributed to acetylene addition to the soot surface. However, there exists strong evidence that soot mass is increased through the surface condensation from PAH molecules. Selected models will implicitly include the effect of PAH condensation via particle-particle coalescence. A common surface growth model used in numerical simulations is based on the premixed flame data of Harris and Weiner (1984). Frequently, an activation energy of  $E = 31.8$  kcal/mole (Hura and Glassman, 1988) is utilized with this model. In this model, surface growth is first order in acetylene concentration in this model. The Lindstedt model (1994) also employs a similar approach. The HACA model is perhaps the most widely utilized model and was developed by Frenklach and Wang (1990). HACA refers to Hydrogen abstraction – acetylene (or Carbon) Addition; it employs a multi-step reaction model wherein H-atoms activate



a surface site, followed by acetylene addition and stabilization. The method includes an empirically-derived ageing parameter  $\alpha$ , to account for loss of reactive surface sites as a function of temperature. An alternate, 'MODFW' surface growth mechanism has been proposed by Colket and Hall (1994). It avoids the ageing issue by incorporating reverse reactions that allow for reverse decomposition of the acetylene-soot adduct at elevated temperatures. This model was shown to be successful in modeling soot growth in high temperature flames (Smooke, et al, 1999).

### *Surface Oxidation*

Oxidation of soot by  $O_2$  and OH is treated by including equations developed by Neoh, et al (1981) for OH and Nagle and Strickland-Constable (1962) for  $O_2$ . For examples, refer to Hall, et al (1997) or McEnally, et al (1998). In the assumed free-molecule regime, surface growth and oxidation rates are proportional to the particle surface area. No models exist that properly account for the oxidative break-up of soot aggregates, perhaps largely due to the lack of available data. Lighty and Sarofim (2011), under a companion SERDP soot science program, recently reported new data and interpretations of such phenomena. This information, as appropriate, will be incorporated into future modeling efforts.

### *Aerosol or Particle Dynamics*

Particles change size due to multiple processes. Aerosol dynamic models attempt to couple these separate processes to describe the evolution of particle size and soot mass during combustion. Surface growth due to acetylene addition or PAH condensation increase particle mass and size. Oxidation removes mass from particles and reduces particle size. Collision amongst two particles results a larger mass that it is the sum of the two individual particles. One can consider two contrasting results from such collisions: coalescence and agglomeration. Coalescence, which is the joining together of two (spherical) soot particles into a single spheroid, increases soot particle size, but decreases the surface area per particle mass. Agglomeration occurs when two spherical-like particles collide and stick together without merging into a new, single spherical particle. A particle with multiple particles stuck together is often referred to as an aggregate. Except for the contact regions between the two particles, no surface area available for growth (or oxidation) is lost during such collisions.

Early versions of soot models (Leung, et al, 1991) employed a single equation for particle number density, based on classical coagulation as a free-molecule aerosol dynamics problem. Such approaches resulted in computation only of an average particle size and particle number. A widely utilized alternate approach is the method of moments (Frenklach and Wang, 1994). This method allows for simulation of a particle size distribution, but unless many moments are utilized, the distributions may not be representative of actual phenomena for which much evidence exists for multi-modal size distributions. The growth of soot particles can also be modeled, using the well-known sectional particle size representation for spheres. This method is preferred as it provides much more detailed information on particle size distribution, as long as a sufficient number of sections are used. The application of the sectional approach to soot modeling was first described by Hall et al. (1997). The sectional procedure is based on the work of Gelbard, Seinfeld and coworker (1980). The contributions from the inception processes are

incorporated as a source term in the dynamical equation for the first sectional bin, whose lower mass boundary is set equal to the mass of the assumed inception species. In the Hall et al work, calculated results of total soot mass were found to be relatively insensitive to the number of sections assumed, although 20 sections or more are preferred. Later unpublished results by the present authors suggest that the number of sections ought to be at least 40 or more to ensure insensitivity to predictions of particle size distributions.

All of these models assume that soot particles can be approximated as carbon spheres and that they exist in the free molecular limit (*i.e.*, the mean free path of the gaseous mixture is much larger than the largest soot spheroid). The sectional approach specifies a minimum and maximum particle mass and divides the spheroid sizes logarithmically into  $N_{sec}$  bins or sections. A further assumption is that within a given section, spheroids of varying diameter do not exhibit vastly differing aerosol dynamical qualities. This assumption holds as long as  $N_{sec}$  is sufficiently large. The spherical particle sectional model nominally imposes no fundamental constraint on the final particle size as long as the peak particle size expected falls below the maximum size range for the sectional bins; yet even if this assumption is violated, soot mass will not be ‘lost’, but will build up in the largest bin available.

None of the described models account for aggregate formation. Coalescence destroys particle surface area, whereas aggregation, to the first order, does not. This is an important consideration because of the dependence of surface growth and oxidation on particle surface area. Adding equations for the number of primary spheroids within a section make it possible to model accurately the formation of soot aggregates. Alternatively, an approximate treatment of the aggregate formation effects on surface area can be employed. Such models, however, are not widely in use.

As part of this research program, the aerosol dynamic equations have been modified for simulations in high pressure environments. Under such conditions, collision and reaction rates need to be modified since the particles are no longer in the free molecule regime, *i.e.*, the particle size can be on the order of the mean free path. A derivation of the equations, which includes corrections to surface growth rates, etc. is attached as an appendix to this report.

### *Soot Ageing*

In practice, soot primary particles reach a maximum size due to active surface site deactivation (ageing). Dobbins (1997) has given a measured deactivation rate for the process, and some modeling of the effect has been carried out in premixed flames. Appel, et al. (2000) have fitted to various premixed flame data an empirical expression for the fraction of active sites that is a function of the average particle size and gas temperature, but not explicitly to individual particle age. Much remains uncertain about how to model this effect, particularly in a diffusion flame, however. Given this uncertainty, Smooke, et al (2005) have introduced a simple step function dependence of surface reactivity on particle size at which growth is shut off above a cut-off particle size (25 nm in their simulations). Modifications were also made to the coalescence model to account for aggregate formation.

### *Scrubbing*

In any solution methodology for modeling soot production, the source terms for conversion of gaseous species to soot must be accounted for by including the sink terms in the gas-phase equations. Here, ‘sink terms’ refer to the fact that gas-phase species can be consumed or formed during the formation or oxidation of soot particulates. In any fully coupled model, these sink terms must be added to the species conservation equations. Likewise, there is an enthalpy (sink) term that should be added to the gas-phase energy equation due to the formation of soot. The importance for inclusion of such terms should be readily recognized since it is not uncommon to convert 10-20% of the carbon to soot in the fuel-rich portion of the flame. The impact is that the local gas-phase equivalence ratio is significantly altered until the soot particulates are oxidized and re-introduced into the gas phase.

### *Radiation*

Flame radiation by both gaseous and soot particles can lead to significant temperature reduction and thus affect flame properties. As soot concentrations increase in a flame, radiation from soot becomes a dominating energy loss term and significantly drops flame temperatures which in turn reduce the reaction rates leading to soot production. Hence, soot formation itself is influenced by the presence of radiation. Most commonly, soot radiation is considered in the optically thin limit, with soot particles assumed to be Rayleigh range absorber-emitters (Hall, 1994). Gas band radiation from CO<sub>2</sub>, H<sub>2</sub>O, and CO is often significant. Studies of optical thickness effects in simple laboratory flames have shown that reabsorption effects can be relatively modest (40-50 K temperature variations) due to the small dimensions of the flames, so that the optically thin approximation should provide a good first approximation (Smooke, et al, 2004) especially considering the substantial added computational cost. In Smooke, et al (2004) in which steady-state ethylene/air coflow diffusion flames were modeled, predicted and measured soot volume fractions agreed to within 30% at high fuel (low dilution) levels and to within a factor of three at low fuel (high dilution) levels.

### *Particle Transport*

Models of soot formation in flames must consider two particle diffusion velocities: a particle thermophoretic velocity and a concentration-driven diffusive velocity. The thermophoretic velocity of gas-phase soot is the portion of the diffusion velocity that is driven by temperature gradients. Unlike gas-phase chemical species, for which temperature-gradient-driven diffusion can often be neglected, the thermophoretic velocity constitutes an important part of the soot diffusion velocity, as the soot molecules tend to be large compared to the other species present in the gaseous mixture (Gomez and Rosner, 1993). This velocity depends on gas properties, is independent of particle size in the free-molecular limit, and can be evaluated according to Gomez and Rosner. The concentration-driven diffusion velocity for soot can be taken from the Fickian form, as is done for gas-phase chemical species (see Hall, et al., 1997, for details).

### *Modifications for High Pressure Simulations*

At higher pressures of interest in practical combustion devices, simulations require corrections to the growth and transport coefficients to account for so-called continuum effects. The Knudsen Number

$$Kn = 2\lambda/d_p$$

where  $\lambda$  is the molecular gas mean free path, and  $d_p$  the particle diameter, is the key parameter governing these changes. At low pressure where  $\lambda$  and  $Kn$  are large, one is in the free molecule regime where the molecular velocity distribution in the vicinity of the particle is unaffected by the presence of the particle. Most soot-formation codes are based upon this assumption. At elevated pressures,  $\lambda$  decreases and the  $Kn$  number approaches one and will drop below one significantly for very high pressures and for the larger soot particles. Corrections to the model are required, at least to assess the effects.

Subroutines for treating soot formation at high pressure have been developed under this program for treating altered transport (diffusion and thermophoresis) and kinetics (agglomeration, growth, and oxidation).

These low Knudsen number equations modifying the soot aerosol dynamic equations have been added to equations describing soot formation in counterflow diffusion flames originally developed by Hall, et al. (1997). Predictions using both the old methodology (without pressure effects) and the corrected equations have been made. The approach follows that described by Sitarski and Seinfeld (1977). Predicted soot mass levels are slightly larger (~5%), as shown in Figure 3.18, and average sizes are slightly smaller with the low Knudsen number corrections. These results are encouraging in that simplifications can be made by avoiding such calculations. An effective pressure dependence (e.g., 'n' in  $f_v \sim P^n$ ) of the peak soot volume fractions can be estimated by looking at the slope of this curve in a semi-log plot. As shown in Figure 3.19, the pressure dependence, n, decreases with increasing pressure from about 2 near one atmosphere to about 0.5 at 20 atmospheres and above. This result of a decreasing dependence of peak soot concentrations on pressure is qualitatively consistent with data obtained by colleagues from (at PSU) that is described elsewhere in this report and many other studies including recent work in coflow diffusion flames by Joo and Gülder (2009).

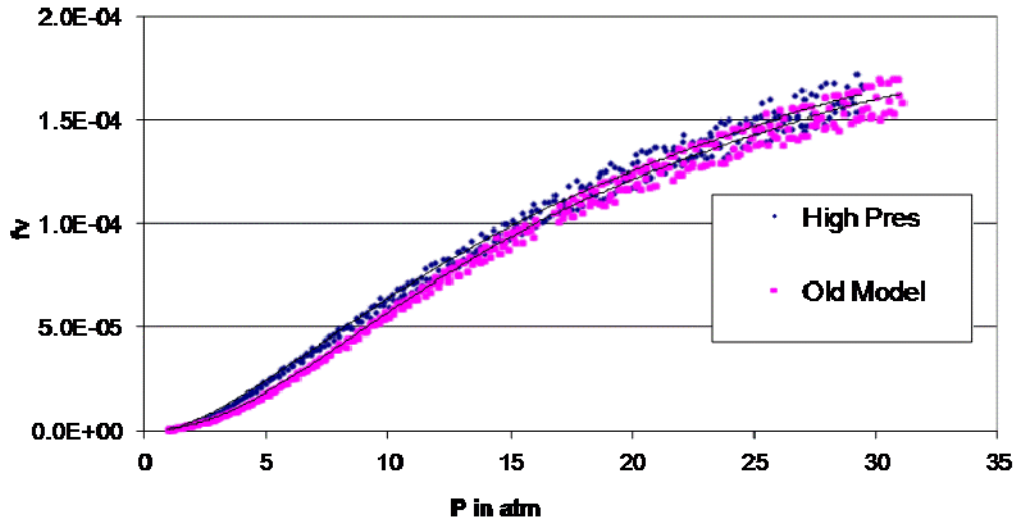


Figure 3.18 Predicted Peak Soot Volume Fractions vs. Pressure in Counterflow Ethylene Flames.

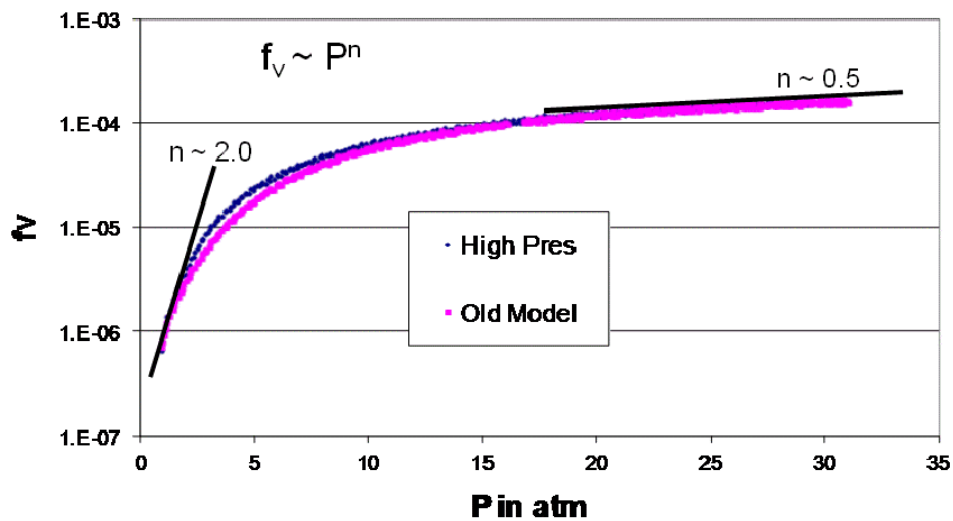


Figure 3.19 Log of Predicted Peak Soot Volume Fractions vs. Pressure Showing Decreased Pressure Dependence with Increasing Pressure.

### 3.2.5 Incorporation of Soot Models into Combustion Codes used in this Program

There are three main codes utilized in this work for predicting soot evolution in a combusting environment. These are (1) UNICORN developed by Vish Katta at AFRL, (2) SNETPSR (sooting network of perfectly stirred reactors) developed at UTRC and (3) a coflow flame transient code developed by a Yale-UTRC team. The first of these has broad range of capabilities and can be used to produce two-dimensional solutions for a range of laboratory (laminar) flames. Example flames for this program include the coflow flame studied at PSU, the opposed jet flame examined at ARL, and the centerbody flame investigated at AFRL. The SNETPSR code is being used to predict soot formation characteristics in a main combustor and is also used as a test bed

for the development of the high pressure modifications to the soot algorithms that have been developed under this program. Finally, the coflow transient code at Yale has been used to investigate dynamic sooting characteristics of a pulsating coflow ethylene flame (Dworkin, et al 2009).

UNICORN has two options for treating soot production. The first option derives from that proposed by Lindstedt (1994) and includes both inception and surface growth rates proportional to acetylene. The second option follows the proposal by Appel, et al (2000); inception is computed based on pyrene dimerization and surface growth is based on the HACA mechanism. Aerosol dynamics are treated using the moment method.

SNETPSR has the broadest range of options for simulating soot formation during combustion. Through simple keyword input, the user can select inception rates based on naphthenyl and phenanthrene (steady-state) production (Hall, et al, 1997), a steady-state computation of the production rate of a large polycyclic aromatic hydrocarbon (Smooke, et al (2005), or pyrene dimerization (Appel, et al, 2000). Surface growth models may be selected from Harris and Weiner (1984), the HACA mechanism used by Appel, et al (2000) or the modified HACA sequence suggested by Colket and Hall (1994). Aerosol dynamics are treated by the sectional model with 40 sections ranging from a minimum of a fraction of a nanometer to over 200 nm. Surface growth can be cut-off above a user-defined size to simulate loss of active surface sites. Particles may grow larger than this value due to collision of other particles. Such particles are assumed to be agglomerates.

### 3.3 UNICORN

#### 3.3.1 Chemical Kinetics Models Evaluation

Different chemical-kinetics mechanisms are available in the literature for the prediction of hydrocarbon flames. New mechanisms are also developed in the current SERDP program for improving PAH predictions in these flames. It is important to know how these mechanisms perform in predicting various types of flames and for selecting the best mechanism for our studies on soot. With this motivation, all these mechanisms are incorporated into UNICORN code and CFD studies for different flames are conducted. The mechanisms incorporated are

**Mechanism A:** Developed by Wang and Frenklach (1997) for the simulation of premixed acetylene and ethylene flames. It has 99 chemical species and 1066 elementary reaction steps. This mechanism contains polycyclic-aromatic-hydrocarbon (PAH) species up to pyrene.

**Mechanism B:** Developed by Wang and Colket (2008) for the simulation of ethylene flames. It has 171 chemical species and 2002 elementary reaction steps. This mechanism is basically a revised version of Mechanism A. The revision was made such that the largest PAH species is still pyrene but additional pathways for the formation of smaller PAH species were included. This mechanism is put together by Colket as a part of the current SERDP program.

**Mechanism C:** Developed by Babushok and Tsang (Tsang 2004) for NIST for the simulation of heptanes and lower hydrocarbon flames. It has 197 chemical species and 2926 elementary reaction steps. This mechanism doesn't include PAH species Phenanthrene (A3) and higher; however, it has a fairly detailed NO<sub>x</sub> chemistry mechanism.

**Mechanism D:** University of San Diego put together a semi-detailed mechanism, known as San Diego (SD) mechanism: (<http://www-mae.ucsd.edu/~combustion/cermech/Heptane-Reactions/>), for hydrocarbon fuels up to heptanes. It consists of 52 species and 544 elementary reactions.

**Mechanism E:** Charlie Westbrook has developed a detailed mechanism for heptanes fuel that has accurate sub mechanisms for smaller hydrocarbon species. For making it amenable to CFD calculations he also developed a smaller mechanism known as Lawrence Livermore National Laboratory (LLNL) mechanism ([http://www-cmls.llnl.gov/?url=science and technology-chemistry-combustion-nc7h16 reduced mechanism](http://www-cmls.llnl.gov/?url=science+and+technology-chemistry-combustion-nc7h16+reduced+mechanism)). It consists of 160 species and 1540 reactions.

**Mechanism F:** SERDP team member (Med Colket) formulated JP-8 fuel with a surrogate mixture of 77 % normal dodecane and 23 % meta-xylene. Both these components were used in the surrogate mixtures developed in the past by several investigators. However, the major difference between the existing surrogate mixtures and the one proposed by Colket is with the simplicity of the later two-component model. Both dodecane and m-xylene are in the University of Utah developed five-component surrogate mixture for which, Violi has developed a detailed chemical kinetics model (Violi et al. 2002). It has 161 species and 1538 reactions. Unlike the other detailed mechanisms several of the reactions described in Violi's mechanism are lumped,

which are global in nature. UNICORN code has been modified for considering lumped reactions. As a first step for evaluating the performance of the new SERDP surrogate mixture in various experimental rigs, Violi's chemical kinetics has been incorporated into UNICORN code. The experimental rigs simulated were 1) shock-tube at 1 atm pressure, 2) opposing-jet nonpremixed flame of Army Research Laboratory, 3) co-axial jet nonpremixed flame of Penn State University, and 4) the centerbody burner of Air Force Research Laboratory.

**Mechanism G:** SERDP team members (Med Colket and Hai Wang) formulated a mechanism (SERDP\_SURR V2) for JP-8 surrogate fuel. It consists of 285 species and 4758 reactions. This mechanism is incorporated into UNICORN code. Several test calculations have been performed for diffusion flames. It is found that some reactions in the mechanism are causing the simulations to diverge. Through switching off individual reactions and repeating the diffusion-flame simulations the reactions that are causing difficulties are identified. These are relatively less important reactions involving trace species. A more stable mechanism was obtained by turning off the problem-causing reactions.

**Mechanism H:** An improved model for the combustion of n-dodecane-m-xylene mixture is developed by SERDP team members (Med Colket, Hai Wang and Ken Brezinsky). It consists of 243 species and 3384 reaction steps. This is referred to as SERDP\_SURR\_v2 mechanism. UNICORN code has been updated through incorporating this mechanism.

**Mechanism I:** This is a semi-detailed chemical-kinetics model (CRECK-0810) developed by Ranzi et al (<http://creckmodeling.chem.polimi.it/kinetic.html>) for the combustion of JP-8 surrogates. It consists of 206 species and 5652 reactions. A vast number of these reactions (4993) are lumped (or global) reactions involving four or more product species. Note the computation of source terms in lumped reactions is significantly more cumbersome compared to that in elementary reactions. This mechanism is incorporated into UNICORN code.

### 3.3.2 Soot Particle Simulation

Current soot models treat soot particles either as a gaseous species or as groups of particles classified based on sizes or distribution functions. Various physical and chemical processes that soot particles undergo in flames are modeled and incorporated into these soot models. Reasonable predictions are made using these models for soot formation in different flames. On the other hand, none of the existing soot models have the ability to predict soot formation in recirculating flows. Centerbody burner considered in this SERDP program has the unique ability for giving insights into effects of recirculation zones on flame stabilization and on overall soot formation. Therefore, it is essential to develop a soot model that can predict soot formation in recirculating flows.

The major difficulty in modeling soot in recirculating flows is associated with the residence time. It is known that residence time in a steady recirculating flow becomes infinity and that in an evolving recirculating flow (moving vortex) it is much greater than the characteristic value obtained based on local velocity. Current soot models estimate residence time using local velocity and determine agglomeration, condensation, and burnout of soot particles based on such estimated residence time. Clearly this doesn't properly account for the physical and chemical



processes occur for soot particles in a recirculating flow. For example, experiments of centerbody burner suggested that soot particles in a stationary recirculating flow grow to a large-size particle and eventually falls off on to the burner plate due to gravity. Existing soot models cannot predict this behavior.

For understanding soot formation in recirculating flows a new soot model based on Lagrangian system is being developed. Nano-size soot precursors are released into the flowfield based on soot-inception theory. Evolution of these particles is tracked in Lagrangian coordinates while applying various physical and chemical processes to the individual particles. A preliminary model is developed by incorporating drag, thermophoresis and burnout process. Calculations are made with this new model based on soot-tracking approach for different centerbody flames. Results obtained for a sooty flame are shown in Figure 3.20 along with the experimental data. Predicted soot particles are superimposed on soot-radiation distribution (solid view) in Figure 3.20b. Distribution of CH concentration is also shown here in blue color. Photograph of the flame obtained with Nd-YAG laser turned on is shown in Figure 3.20a. Computations have reasonably predicted the soot spirals observed in the experiment. Note that the actual size of the recirculation zone is much larger than that depicted by the soot particles. Part of the recirculation zone located outside the high-temperature ( $> 1400$  K) region on the airside of the flame is not captured by the soot particles as they could not survive under those local conditions. Results obtained for a less sooty flame are shown in Figure 3.21. Calculations have correctly captured the shrinkage of soot spirals into almost a line. Note that the size of the actual recirculation zone is still the same as that of the flame in Figure 3.20a. However, soot particles survived only in a tiny region near the vortex center in the nearly non-sooty flame. Predictions shown in Figures 3.20 and 3.21b are quite encouraging for the development of soot model based on soot-tracking approach. Enhancements to this model by considering soot agglomeration and condensation are planned in the remaining part of the program.

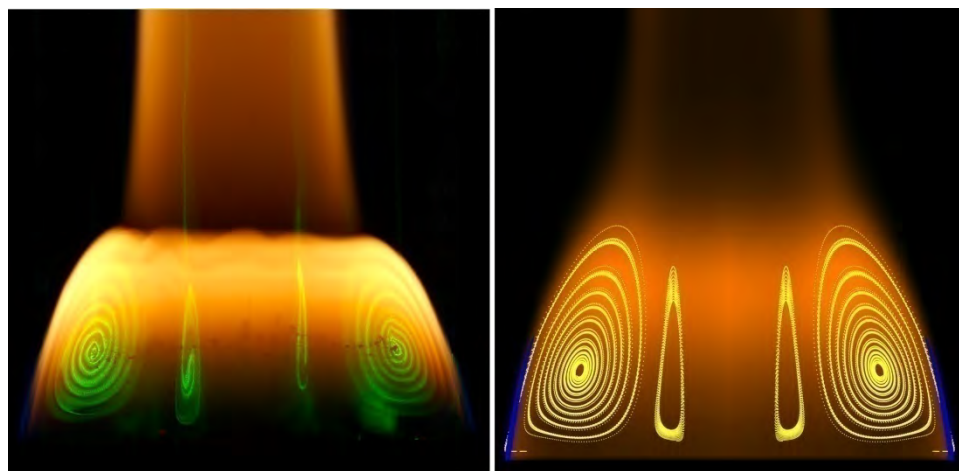


Figure 3.20 Prediction of soot particles in the recirculation zone associated with a sooty flame. (a) Visualization of soot particles in experiment using Nd-YAG laser. (b) Computed soot particles using new soot-tracking approach.

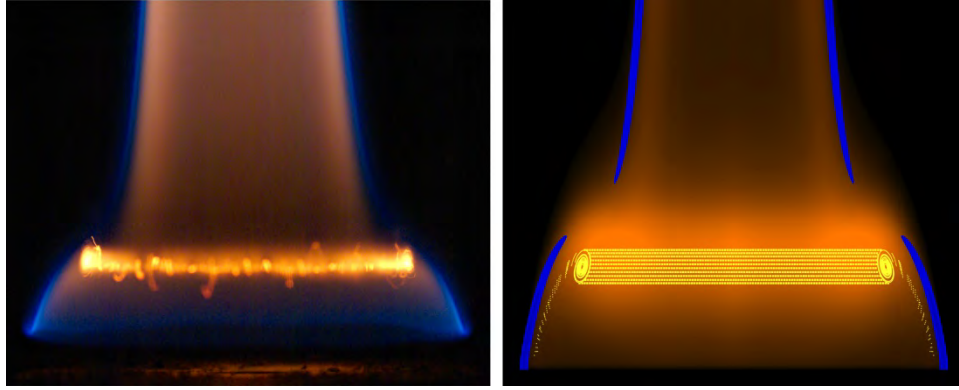


Figure 3.21 Prediction of soot particles in the recirculation zone associated with a nearly non-sooting flame. (a) Visualization of soot particles in experiment using Nd-YAG laser. (b) Computed soot particles using new soot-tracking approach.

### 3.3.3 Soot Models

Two different approaches have been used for predicting soot in the flames investigated during this research activity. The first approach is based on the assumption that soot consists of particles with mono-disperse size distribution. Soot formation, coupled directly to the fuel concentration, is then modeled by two equations: one for the particle volume fraction and the other for the particle number density. The second soot model used is somewhat detailed and has been calibrated against experimental data obtained in laminar, premixed or diffusion flames of simple configurations. This model developed by Frenklach and coworkers (Frenklach and Wang, 1991, Frenklach and Wang, 1994, Appel et al. 2000) consists of 1) gas-phase chemistry and 2) kinetics describing the particle growth and destruction processes. The gas-phase chemistry describes the formation of PAHs. The particle growth and destruction involve inception/ nucleation of particles resulting from coagulation of PAHs and are modeled via a set of surface reactions and particle coagulation is modeled based on the method of moments.

#### *Two-Equation Model*

Soot formation in flames is described using two transport equations, one for the particle number density,  $N_s$ , and the second one for the soot mass fraction,  $Y_s$ . These equations can be written for unsteady flow as

$$\frac{\partial N_s}{\partial t} + \nabla \cdot (\rho \mathbf{V} N_s) - \nabla \cdot (\rho D_{N_s} \nabla N_s) = \omega_{N_s} \quad (1)$$

$$\frac{\partial Y_s}{\partial t} + \nabla \cdot (\rho \mathbf{V} Y_s) - \nabla \cdot (\rho D_s \nabla Y_s) = \omega_s \quad (2)$$

where,  $\mathbf{V}$  is the velocity vector,  $\rho$  is density,  $D$  is the molecular diffusion coefficient, and  $Y$  is the production term from chemical reactions. The two source terms in Eqs. 1 and 2 are obtained

using Lindstedt's model (Lindstedt, 1994), which is based on the simplifying assumption that nucleation and growth are first-order functions of acetylene concentrations. Soot oxidation was considered primarily due to the presence of  $O_2$  and  $OH$ . Finally, soot agglomeration was treated as a source term in Eq. 2.

Various forms of this two-equation model have been implemented in UNICORN code. The original model of Lindstedt formulates soot inception from the acetylene produced in the flame. Since this model seemed inadequate for describing soot in flames formed with fuels such as JP-8 two alternative approaches have been attempted. In the first one soot inception was modeled from benzene and in the second one it is modeled from naphthalene.

#### *Method-of-Moments Model*

UNICORN code was initially developed with the two-equation soot model proposed by Lindstedt (1994) and described in the previous subsection. Lindstedt soot model is known for giving reasonable predictions for soot volume fraction in a variety of flames. However, this model is too simple for giving important details such as soot-particle-size distribution and is very restrictive for adding newly found physical and chemical mechanisms for soot growth and agglomeration. Considering these shortcomings and restrictions it was proposed to use higher-level soot models in UNICORN code. A literature search has been performed for identifying possible soot models that meet our program goals and that can be used with UNICORN code. After consulting with the other team members it has been decided to incorporate two soot models into UNICORN code. They are 1) Method-of-moments soot model and 2) Sectional soot model. During the first half of the program Method-of-Moments soot model has been incorporated into UNICORN code. Details of the implementation are as follow:

One of the salient features of UNICORN code is its high computational efficiency. This allowed the simulation of two-dimensional reacting flows using large chemical kinetics and grid points on a PC in a reasonable time. UNICORN offers stable solutions as it uses semi-implicit procedures for the integration of governing equations. Two approaches are considered for adding soot-prediction capabilities (based on method of moments) to UNICORN code. In the first approach, one could use the soot subroutines developed by Frenklach as they are and call them in UNICORN code whenever they are needed. This is an easy way to implement soot-calculation capabilities to an existing CFD code. However, the uniqueness of UNICORN code in computing reacting flows efficiently will be suffered since the soot calculations will be performed explicitly outside UNICORN. Method-of-moments approach for soot predictions is known for the problems associated with stiffness and demands small time steps. Special techniques must be adopted for overcoming such problems, which is not possible if one wants to use soot subroutines externally. The second approach is to build method-of-moments calculations for soot predictions in UNICORN code itself. This offers an efficient approach for developing a stable and reliable version of UNICORN code with enhanced soot capabilities. However, this requires significant time and efforts. In order to deliver an efficient product that can be used by several other researchers in the future, it was decided to go with the second approach.

The task of developing a new version of UNICORN code and verifying its accuracy is performed during the first year of SERDP program. Several efficient programming techniques are used for

speeding up the calculations. Several test cases were simulated and compared with those obtained with the soot subroutines of Frenklach. Results obtained for the test cases described by Frenklach in 1987 in the Journal of Colloid and Interface Science (Frenklach and Harris, 1987) are shown in Figures 3.22 and 3.23. These results closely followed the ones obtained by Frenklach using soot subroutines. The modified UNICORN code computed these cases stably with different time steps. Reproduction of these results gave confidence in the soot prediction capabilities of the modified UNICORN code.

Calculations for various diffusion and premixed flames have been performed using MOM approach for soot and some of the results are described here. Figure 3.24 shows time-dependent-UNICORN calculation for a laminar, ethylene jet diffusion flame at conditions previously studied by Santoro and co-workers (Santoro et al. 1983). Tube diameter was 11.1 mm. The fuel and annular-air jet velocities were 3.91 and 8.8 cm/s, respectively. Computed iso-temperature distribution is shown in Figure 3.24. Radial distributions of temperature, CO, CO<sub>2</sub>, and soot at 40 mm above the burner exit are shown in Figure 3.25 and those at 70 mm above the burner exit are shown in Figure 3.26. Here the data obtained with two-equation and MOM soot models are shown with solid and broken lines, respectively, while the corresponding experimental data (Santoro and Semerjian 1984, Anna et al. 2007) are shown with symbols. Measured soot volume fractions were obtained using laser-extinction technique. Temperatures were measured with thermocouples and corrected for radiation heat loss. In general, soot predicted with MOM model is less than that predicted with two-equation model. This higher soot resulted in lower temperatures in the flame predicted with MOM. Since two-equation model of Lindstedt (1994) was fine-tuned for ethylene flames it is natural to expect a better match between the predictions and experimental data. However, it is somewhat surprising to note that a more accurate model such as MOM is actually yielding soot concentrations much higher than those measured. Additional investigations will be performed in the future studies for understanding this discrepancy. It is also planned to develop and use sectional approach for soot modeling.

Calculations performed for centerbody flames using two-equation and MOM soot models are shown in Figure 3.27. Here, temperature and soot volume fraction distributions are shown on the left and right halves, respectively. Corresponding predicted velocity vectors and streamlines are superimposed on temperature and soot distributions, respectively. Both simulations have yielded nearly the same fluid flow. The heights and shapes of the fuel-side and air-side recirculation zones predicted by two-equation soot model (Figure 3.27a) and MOM soot model (Figure 3.27b) are close to each other. Interestingly, the amount of soot predicted by the latter model is lower than that predicted by the former. This is somewhat surprising since an opposite sooting behavior was observed in jet diffusion flame. This suggests that calibrated models such as two-equation soot model could give drastically different results under different flow situations. A thorough comparison will be performed once experimental data for the centerbody flames are obtained.

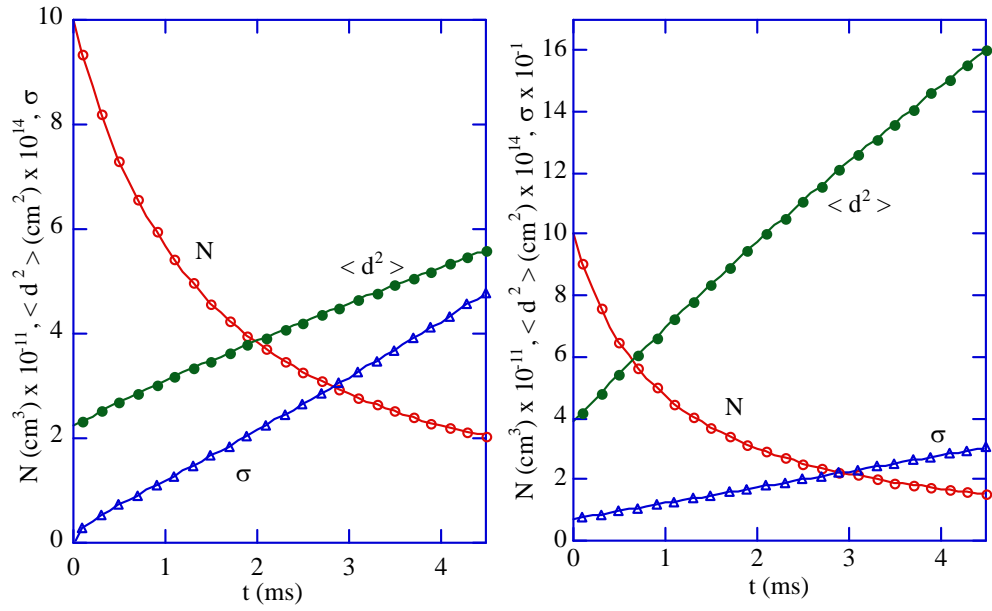


Figure 3.22 Number density, square of the mean value of the diameter, and standard deviation for the coagulation only cases of Frenklach.

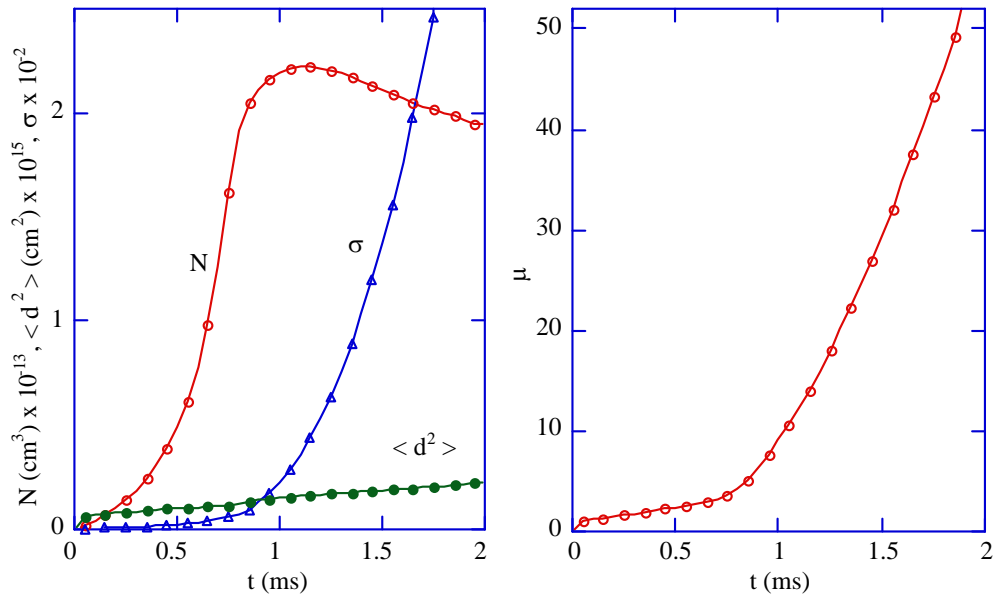


Figure 3.23 (a) Number density, square of the mean value of the diameter, and standard deviation and (b) mean value of  $i$  for the “soot case” of Frenklach.

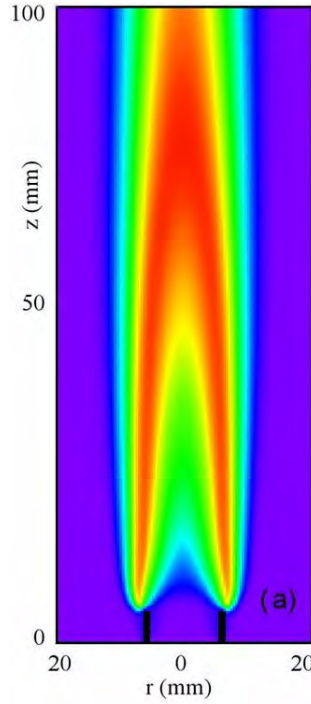


Figure 3.24 Temperature distribution predicted using MOM soot model for a co-flowing jet diffusion flame.

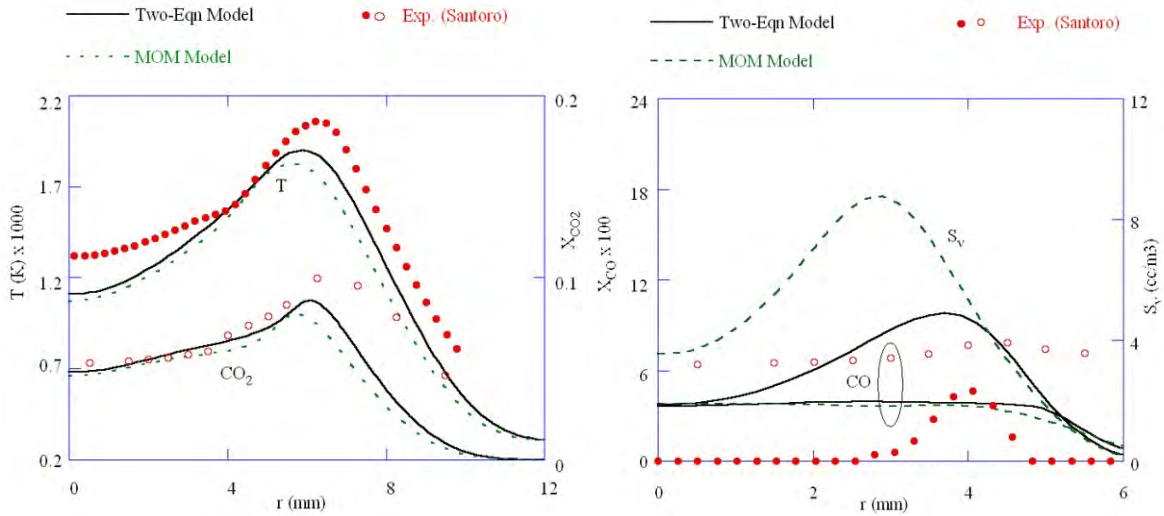


Figure 3.25 Comparison of temperature and CO<sub>2</sub> (a) and soot volume fraction and CO (b) predicted by the two soot models with measurements in co-flowing jet diffusion flame at 40 mm above the burner exit.

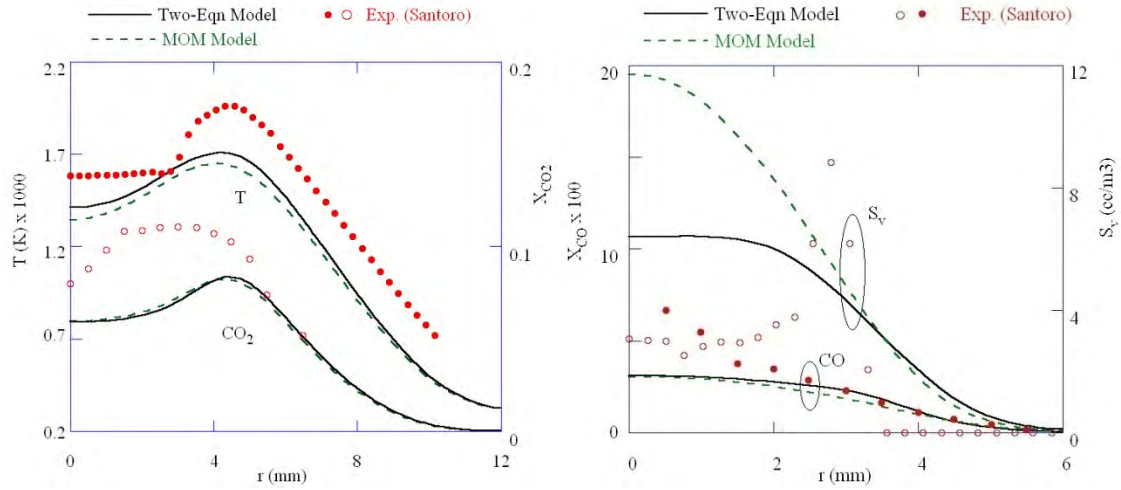


Figure 3.26 Comparison of temperature and  $\text{CO}_2$  (a) and soot volume fraction and CO (b) predicted by the two soot models with measurements in co-flowing jet diffusion flame at 70 mm above the burner exit.

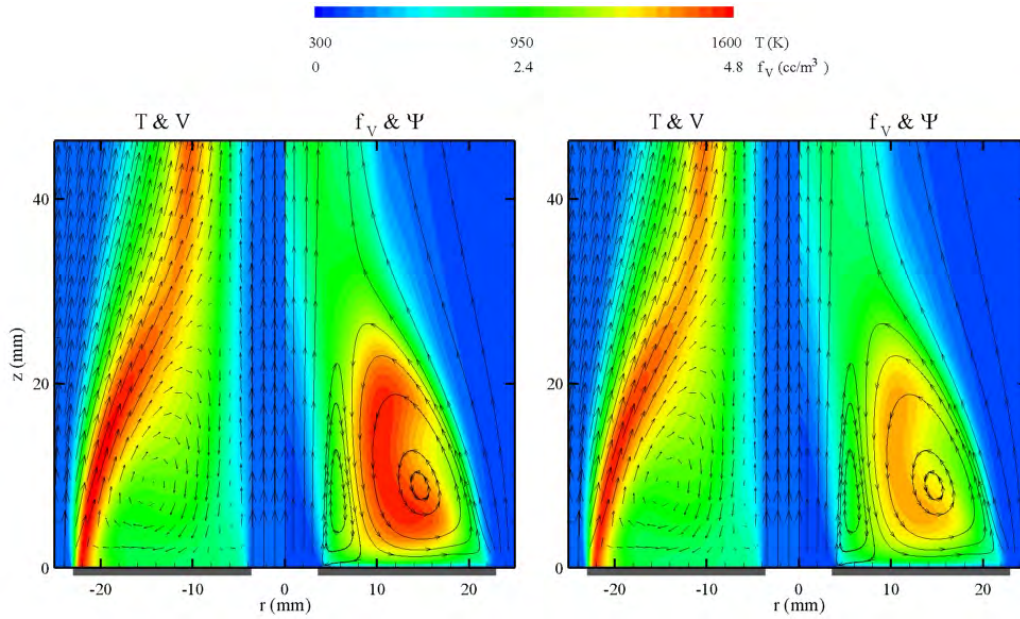


Figure 3.27 Centerbody flames simulated with (a) two-equation and (b) MOM soot models. Temperature and soot volume fractions are shown in the left and right halves, respectively.



### 3.4 CHEMKIN Software

CHEMKIN is a suite of software tools for simulation of reacting systems. It was initially developed at Sandia National Labs and has since evolved into a commercial product that is widely used to simulate combustion systems with complex kinetics. CHEMKIN flames models are limited to steady premixed and opposed-jet flames. In this project, it has been used to simulate the shock tube studies and the opposed-jet diffusion flame. UNICORN was also used to simulate the opposed-jet flames because it can more closely approximate the actual configuration of the flames including the use of a shroud gas.



## 4.0 Experimental Methods

### 4.1 Introduction

In this section of the report, the experimental set-up, procedures and diagnostic methods used in each of the four experiments are summarized. The conditions for individual experiments are included with the discussion of results in section 5.0 of the report.

### 4.2 Shock Tubes

Two single pulse shock tubes, one heated and one non-heated, were used to obtain the present set of ignition delay and product characterization data. The two shock tubes are described as below.

#### 4.2.1 UDRI High-pressure (non-heated) Shock Tube

The shock tube used in the present study was a single pulse reflected double diaphragm shock tube built from SS304 material with half-inch thick walls. As shown in Figure 4.1, the 6.71 m long high-pressure shock tube consists of four main sections. A driver section (7.62 cm I.D.; 274 cm L) that provides the energy to produce the supersonic shock wave, a driven section (5.08 cm I.D.; 274 cm L) that allows a planar shock front to develop, a breaker section (5.08 cm I.D.; 20.32 cm L) that initiates diaphragm rupture and connects the driver and the driven sections, and a test section (5.08 cm I.D.; 91.44 cm L) which houses the test mixture. A photograph of UDRI high-pressure shock tube is shown in Figure 4.2.

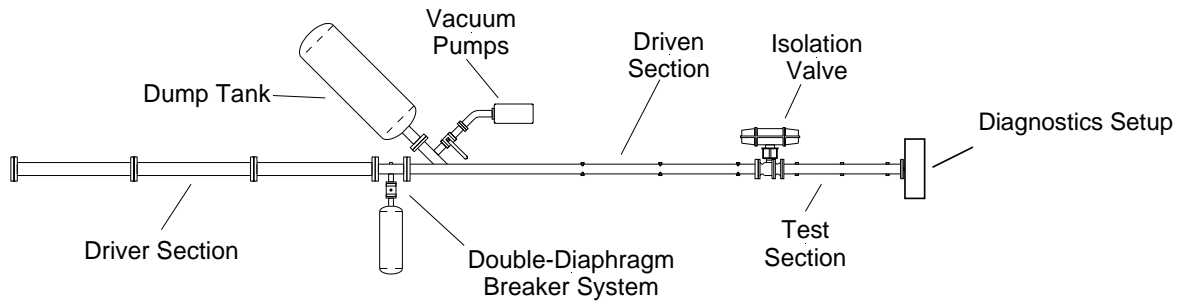


Figure 4.1 General schematic of the shock tube.



Figure 4.2 A photograph of UDRI high-pressure shock tube.

The test section is mated to the tube through a pneumatically operated ball valve, which is controlled by a dedicated digital fire control system. This shock tube system also has a dump tank with volume (ID=30.48 cm; L=101.6 cm). The dump tank assures a single pulse and prevents repetitive heating of the test gas from shock waves. The test section of the shock tube, as shown in Figure 4.3, is fitted with high-pressure transducers, a fuel injection port or delivery valve, a helium purge line, a diagnostic setup for ignition delay measurements, and an exhaust particle and gas sampling port.

The test section is filled with the fuel mixture containing the fuel and argon from a dedicated Sample Preparation Unit (SPU) through a delivery valve connecting the SPU with the test section. The oxidizer, oxygen, is filled from a separate oxygen tank connected to the SPU through the supply lines connected to the same delivery valve. The fuel mixture with oxygen is kept in this configuration for about 30 min to allow the fuel-argon mixture to mix thoroughly with the oxygen inside the test section via diffusion. The SPU is shown schematically in Figure 4.4. The gas leak rate was maintained below 0.0025 torr per minute across all sections and valves of the shock tube in the current study. The detailed operating procedure of the shock tube is provided elsewhere (Saxena et al., 2010).

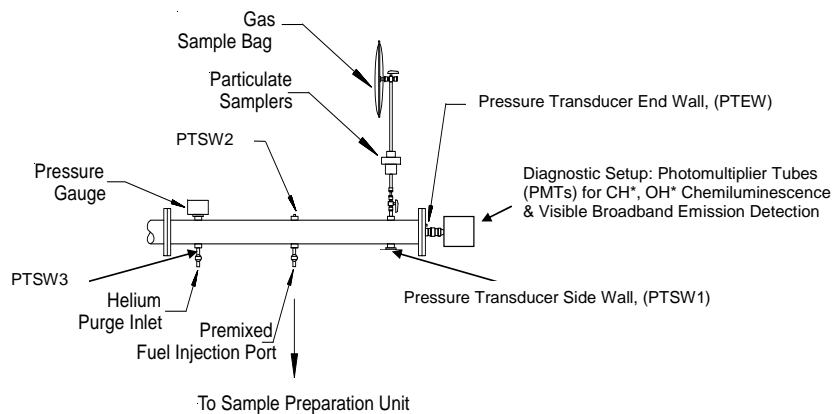


Figure 4.3 Schematic of the test section (TS).

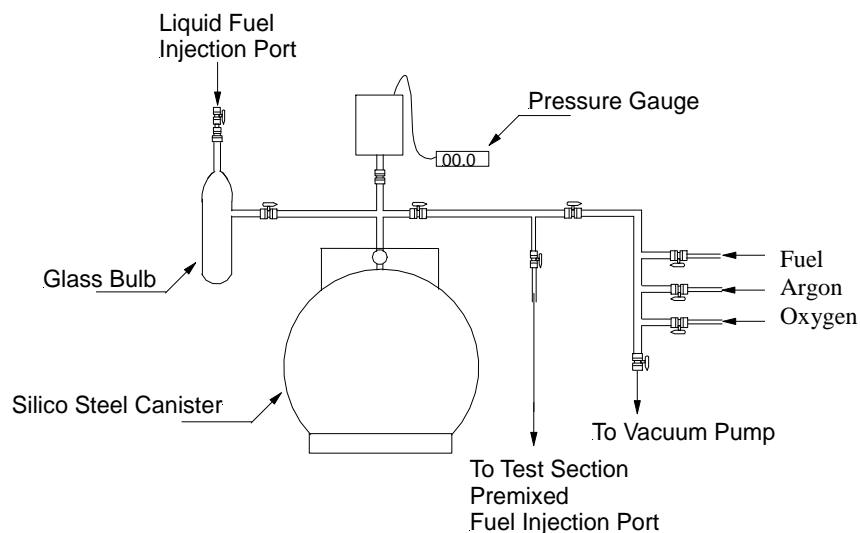


Figure 4.4 Schematic of the sample preparation unit (SPU).

In the present work, to generate quantifiable soot and PAH yields, the shock tube was operated at higher dwell times. The dwell time is determined by the interval from the moment the reflected shock departs the end plate of the test section to the moment the rarefaction wave arrives from the driver end of the shock tube, and quenches the shock heated gas back to low temperatures and pressures. In all experiments, dwell times were kept in the range of 7.55-7.85 ms. This was achieved by adding predetermined quantities of argon to the driver helium gas using the ‘tailored interface’ technique (Kahandawala et al., 2006).

### *Product Characterization*

Characterization of combustion-generated products was performed for a limited number of experiments under fuel-rich conditions only (at  $\Phi=3$  with argon=93%). Details of product sampling procedure are available elsewhere (Kahandawala, 2004). Here we briefly discuss several important features of the procedure. During each experiment, the fire control system closed the test section isolation valve approximately 0.5 s after the diaphragm burst, sealing the combustion products in the test section.

Samples of volatile gases were taken out directly from a port on the test section using a gas tight syringe immediately after the completion of the shock. Then, for each test, the exhaust valve to the sampler was opened and the test section purged with ~25 L (~10 change volumes) of dry helium (at P~70-100 psi). As the gas was swept from the system, the particulate fraction from the combustion products was captured on pre-cleaned quartz filters using a high volume particulate sampler, and the gas was captured in a 25 L Tedlar sample bag to identify and quantify the semi-volatile products. The filters used were pre-cleaned by baking them at 420°C

to remove any organics that could contribute to soot yields. A previous study by our group had shown that ~98% of the combustion products are captured in one sample bag using this sampling method (Kahandawla, 2004). The condensation of the heavier combustion products on the walls of the test section is practically eliminated by the high pressure purging with helium.

The collected gas sample was analyzed using a Gas Chromatograph (GC)-Thermal Conductivity Detector (TCD) system to quantify volatile components of the combustion-generated products. The TCD was connected to a Supelco Carboxen 1000 mega bore column.

Later, the gas sample bag was evacuated through a trap containing an XAD-2 polymeric sorbent trap to collect the semi-volatile compounds. After evacuating the sample bags, 10  $\mu$ l of a mixture of semi-volatile internal standards was injected into each sorbent trap and the traps were then extracted using 40 ml of methylene chloride (Pestisolv. grade). The semi-volatile internal standard mixture used contained (2000  $\mu$ g/ml of each compound) acenaphthene-d10, chrysene-d12, 1,4-dichlorobenzene-d4, naphthalene-d8, perylene-d12, phenanthrene-d10 in methylene chloride. The extracted sample was concentrated and then analyzed using a HP 6890 gas chromatograph (with a DB-5MS column) -5973 mass spectrometer for semi-volatile compounds. Where possible, standards were used to identify products. For other cases, products were identified based on the match quality with respect to the mass spectral library. A semi-quantitative approach was used to obtain the yields of the compounds from GC-MS analysis. Internal standards were used to determine the mass yields using a point calibration of structurally similar classes of compounds. The quantified yields were then normalized with respect to the carbon content of the fuel. The newly-developed, in-house modified Chemkin code, SHOCKIN was used to model product yields using the SERDP model.

The mass of the collected particulate matter (PM) or soot samples was determined via the temperature programmed oxidation (TPO) or carbon burnoff method using a LECO Model RC 412 Multiphase Carbon Determinator. In this method, the mass of the collected PM is determined by measuring the CO<sub>2</sub> generated during oxidation of the soot. The mass of the carbon from Leco analysis was normalized with respect to the carbon content of the fuel to obtain the carbon yields per unit mass of carbon in the fuel.

For a few selected experimental conditions, the soot filters were analyzed for compounds adsorbed on soot surface. The filter containing soot was spiked with the same internal standard mixture that was used for semi-volatile analyses. It was then extracted using 40 ml of toluene as solvent in a centrifuge tube. The centrifuge tube was capped and then placed in an ultrasonic bath for 60 minutes (no heat). After the sonication step, the solvent with the filter was centrifuged at 6000 rpm for 30 minutes. The resultant solvent mixture was then taken out and collected separately. The centrifuge tube with the soot filter was administered again with fresh 40 ml toluene. This cycle with toluene was followed by extraction using methylene chloride. After an appropriate number of sonication and centrifuge steps, the resultant liquid solvent mixture from all such cycles was concentrated and analyzed for the adsorbed heavy species with the GC-MS system using a high-temperature column (DB5HT). The extraction and quantification of organics adsorbed on soot surface is currently in progress. Species extracted from soot samples secured from a few selected experiments are reported in this report.

#### 4.2.2 UDRI High-pressure Heated Shock Tube

The heated shock tube is a modified single pulse reflected shock tube comprised of a 7.6 cm ID x 274 cm long driver section, a 5.08 cm ID x 275 cm long driven section, and a 5.08 cm ID x 90 cm long test section. It also includes a 30.5 cm ID x 61 cm long dump tank and an evacuation subsystem. For the homogeneous premixed combustion studies, the fuels were completely pre-vaporized and pre-mixed in a separate sample preparation unit (SPU) to ensure that a fully homogeneous gaseous mixture is introduced into the test section. The shock tube and the SPU were wrapped in a custom-designed heating jacket and the system could then be heated and maintained at temperatures up to 200°C. The heating jacket contains 2.5 cm thick insulation, heating elements, and control and measuring thermocouples. The control thermocouples are linked to a temperature control system that includes a thermal cutoff option. The heating system allows the shock tube to conduct experiments on very low vapor pressure fuels or to conduct premixed combustion experiments on multi-component real fuels like JP and alternate (F-T, Bio-derived) fuels. The operation and product sampling procedure for the heated shock tube are very similar to those for non-heated shock tubes. A photograph of heated shock tube is provided in Figure 4.5.



Figure 4.5 A photograph of UDRI heated high-pressure shock tube.

#### 4.2.3 Diagnostic Procedure

In the present study, all pressure and optical measurements were obtained using two four-channel digital oscilloscopes. The incident velocities were measured by dividing the distance over the last 81 cm of the test section between four piezoelectric pressure transducers mounted on the side and end walls of the test section by the arrival time of the shock wave past the transducers. The linear regression correlation ( $R^2 > 0.9999$ ) between the incident shock velocity and axial distance obtained was used to calculate an extrapolated incident shock velocity at the end wall of the test section. This extrapolated end wall incident velocity was then used to calculate exposure conditions of the fuel mixture in the test section by using the Shock-Solution Model of Chemkin 3.7 (Kee et al., 2002). Less than  $\pm 0.5\%$  uncertainty is expected in the reported incident shock velocities based on the uncertainty in incident shock time measurement ( $\pm 1 \mu\text{s}$ ), which can result in initial reflected shock temperature uncertainty of up to  $\pm 10 \text{ K}$ . The kinetic mechanism of combustion and thermodynamic data used in the present study was developed and compiled by the SERDP kinetic-modeling team. The calculated initial post-shock pressures obtained through this procedure agreed very well with the pressures obtained from oscilloscope records, thereby also verifying the accuracy of initial post-shock temperatures.

For the ethylene combustion study, most of the experiments were conducted with the visible light-detecting photodiode connected to a fiber optic cable placed at the end plate of the non-heated shock tube. Ignition delay was taken as “the time interval from the moment the incident shock arrives (and departs simultaneously) at the end plate to the moment, the onset of visible light signal is observed from the ignition event.” All measurements were relative to the pressure signal generated by the pressure transducer located at the end wall. A few additional experiments were conducted using a newly-developed diagnostic setup positioned at the end plate of the shock tube. This system is capable of simultaneous measurements of the ignition delay from visible broadband and chemiluminescence emissions of excited  $\text{CH}^*$  and  $\text{OH}^*$ . The photomultiplier tube (PMT) fitted with a 20 nm band pass interference filter centered at 430 nm was used to detect CH A-X chemiluminescence. A second PMT fitted with a 20 nm band pass interference filter centered at 307 nm was used to detect OH A-X chemiluminescence. The PMTs were of the same make, model PMT-Hamamatsu H5783-04, that includes the high voltage power supply. The photo detectors viewed emission through a fused quartz rod, flush mounted in the shock tube end plate. Two beam splitters were used for the  $\text{CH}^*$  and  $\text{OH}^*$  signal with the visible light passing through the beam splitters without being filtered. The rise time on PMT signals was about two microseconds (10 to 90%). The ignition delay time was defined as “the time difference between arrival of the shock at the end wall and onset of emission of  $\text{CH}^*$  or  $\text{OH}^*$ .” The reaction time was ascertained by subtracting ignition delay from the dwell time. Figure 4.6 shows a typical ignition-delay measurement profile from the ethylene study.

Ignition event was observed as a sharp peak in the pressure profile of the experiment in most conditions of the current study (see Figure 4.7 and 4.8 for the case of ethylene combustion). In some cases, a small gradual rise in post-reflected shock pressure (and thus temperature) can be observed. Some authors believe that this pressure rise is entirely due to pre-ignition energy release. However, this pressure rise could be due to the coupled effect of pre-ignition energy release and development of the boundary layer behind the incident shock wave (Petersen, 1998). The boundary layer causes the core pressure and temperature of the reflected shock to rise, as it

constricts the available cross-sectional area for its propagation. However, the effect of boundary layer formation is only appreciable for long ignition delay times ( $\tau > 1-2$  ms). From isentropic calculations, we estimated that the temperature at half of the ignition delay time increased by roughly 4-7 K over  $T_5$ . In this study, the overall estimated uncertainty in the computation of post-reflected shock temperature (up to  $\pm 10$  K) included the uncertainty from non-ideal pressure rise. At higher temperatures, the ignition delay times are short enough to offset any gas dynamical effect. We have proceeded by assuming the that the mixture behaves nearly ideally until 20 atm pressures and verified using 1-D CFD (Bileyu et al., 2009) that temperatures obtained by Chemkin Shock Module are very close to those obtained using 1-D CFD.

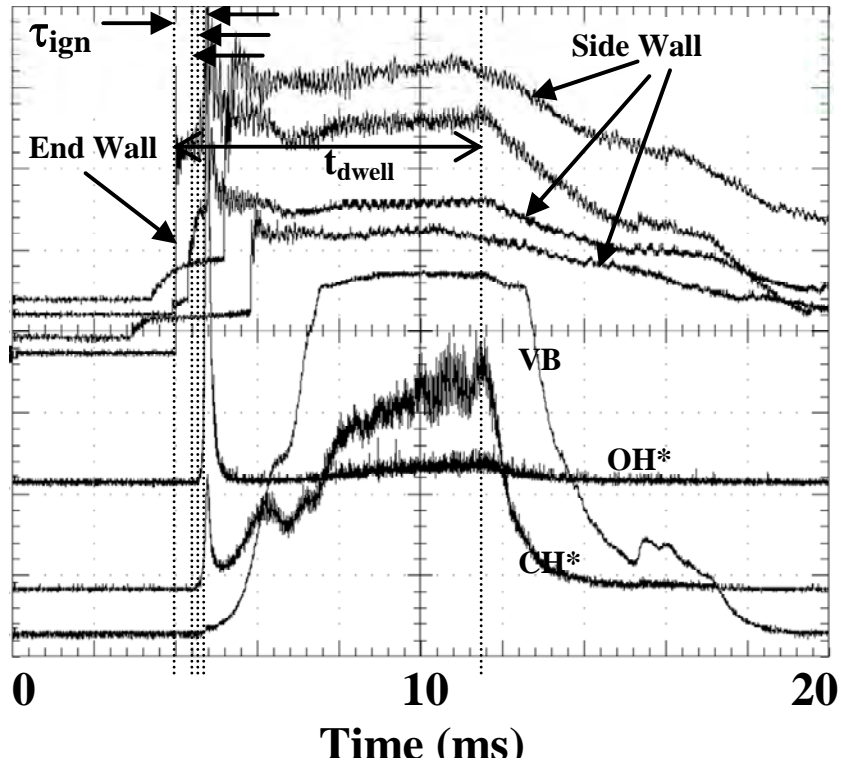


Figure 4.6 An example of oscilloscope traces from an ethylene combustion experiment showing profiles of the end plate, side wall pressure transducers,  $\text{CH}^*$  and  $\text{OH}^*$  chemiluminescence emissions. The mixture composition is 3.5%  $\text{C}_2\text{H}_4/3.5\text{O}_2/93\%\text{Ar}$ , ( $\Phi=3.0$ ) at post-shock conditions of,  $T_5=1194$  K,  $P_5=17.5$  atm. Temperature ( $T_5$ ) and pressure ( $P_5$ ) in the reflected shock region were determined using standard one-dimensional shock relations, as explained in the text. Strong ignition can be observed by looking at the sharp spikes in the pressure profile. The ignition delay times for this experiments were,  $\tau_{\text{CH}^*}=558\mu\text{s}$  and  $\tau_{\text{OH}^*}=570\mu\text{s}$ , measured as shown in the figure and explained in the text.

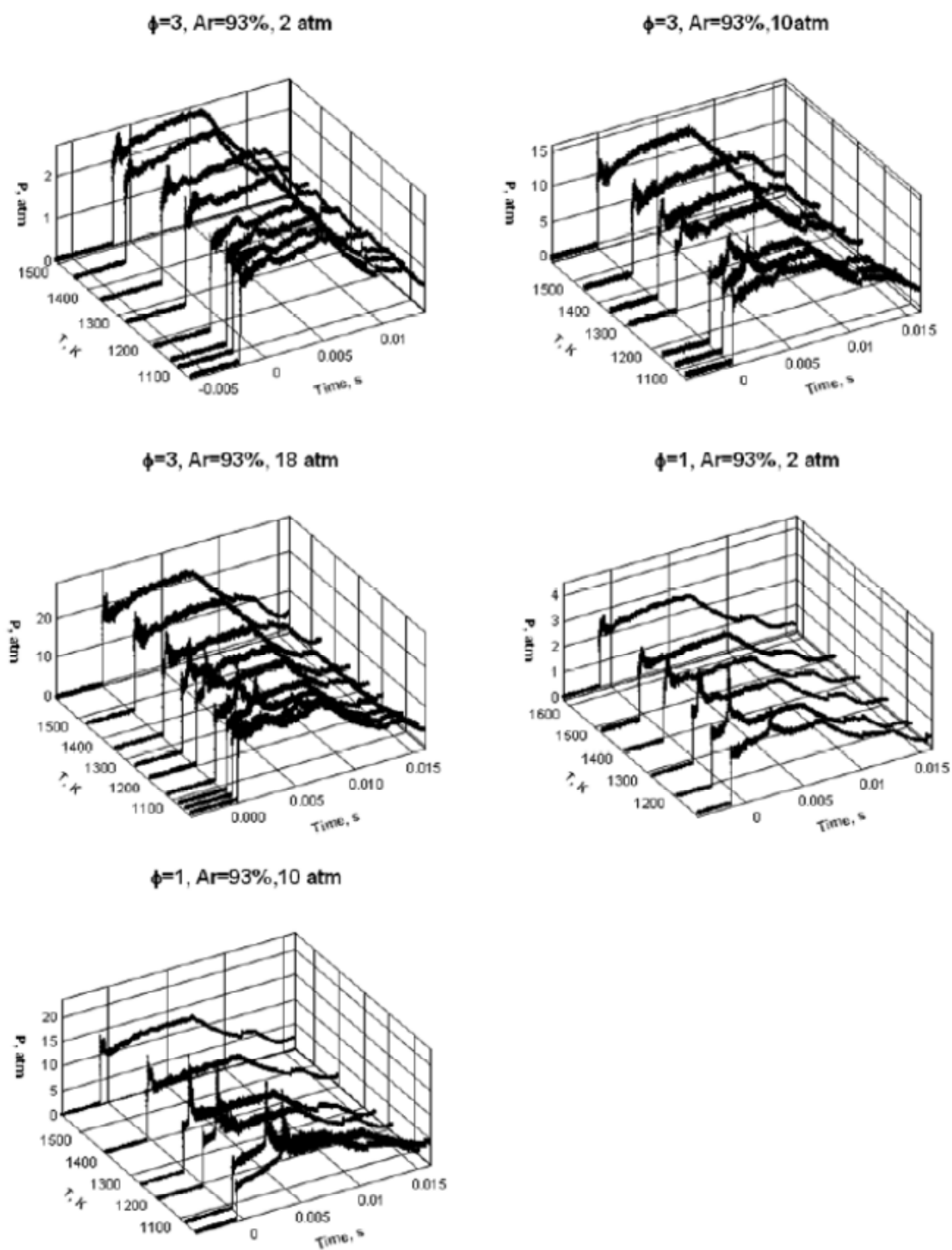


Figure 4.7 End-wall pressure profiles for ethylene-oxygen mixtures with 93% dilution in argon.



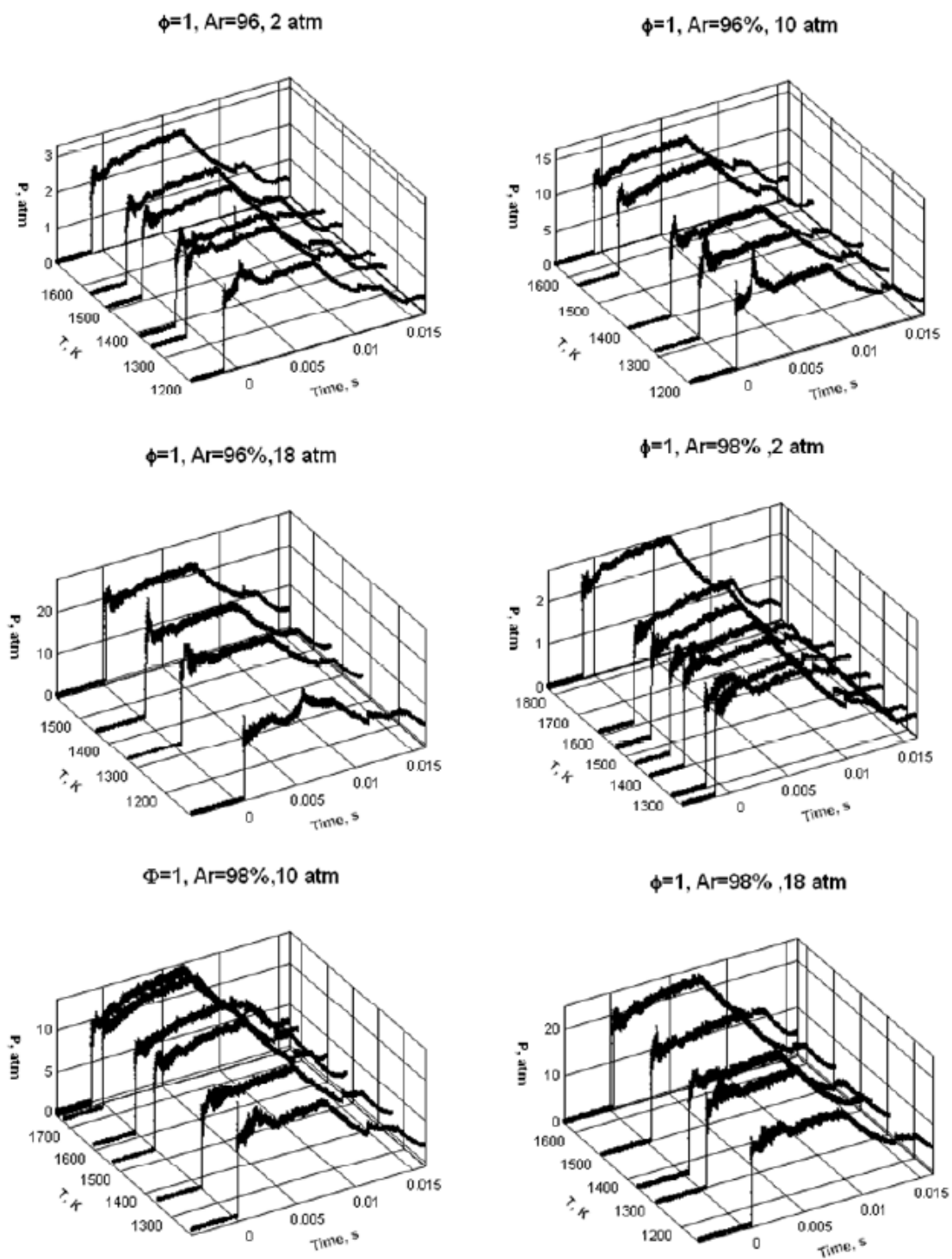


Figure 4.8 End-wall pressure profiles for ethylene-oxygen mixtures with 96 and 98% dilution in argon.

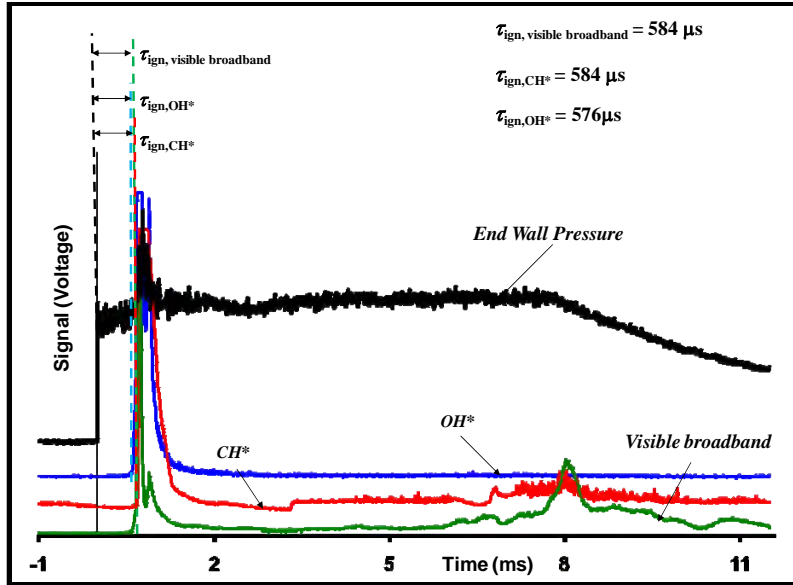


Figure 4.9 An example of an oscilloscope trace from an experiment with the non-heated shock tube. Ignition delay in combustion of m-xylene;  $\Phi = 0.5$ , Ar = 93%,  $P = 18 \text{ atm}$ ;  $T = 1379 \text{ K}$ . As is evident, all the three optical signals exponentially increase at the same time with a distinct spike in pressure pulse (signaling strong ignition with substantial energy release).

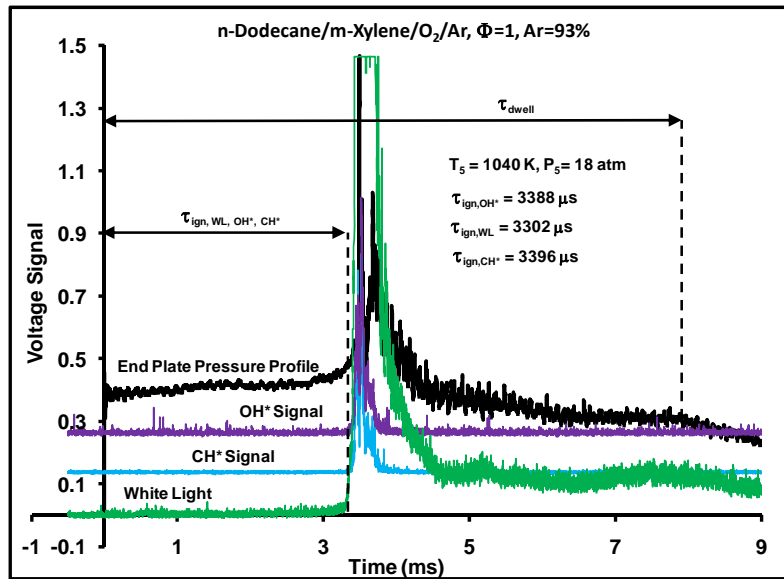


Figure 4.10 Ignition delay in combustion of n-dodecane/ m-xylene blend: Example of oscilloscope traces from an experiment. The sharp spike in pressure profile in this example characterizes a strong ignition. A small pre-strong ignition pressure rise, OH\* and CH\* emission was observed in low temperature experiments (mostly for temperatures below 1100 K) as a characteristic of energy release during mild ignition regime.

Careful observation of the gas dynamical effects in the pressure profiles of each experiment has also guided us in reaching a temperature of  $T_5 \sim 1100$  K, above which all estimations can be treated as very good. These real fuel run profiles were also compared with pure argon run profiles of matching conditions to ascertain the effect of pure gas dynamics only, with no reaction and heat release. The sample oscilloscope traces from ignition delay experiments of m-xylene and the blend combustion are provided in Figures 4.9 and 4.10, respectively.

#### 4.2.4 Experimental Conditions

The test gases were obtained from Air Gas: ethylene (UHP grade), argon (UHP grade), oxygen (research grade), helium (research grade) and air (research grade). M-xylene and n-dodecane (99+%, anhydrous) were obtained from Sigma Aldrich. The gases were metered based on calculated partial pressure using capacitance manometers (MKS Instruments, 660 series, non-heated shock tube) or pressure transducers (Omega PX 1004 series, heated shock tube) with a readout precision of 0.1 torr. Mixtures were filled to a precision of  $\pm 0.1$  torr. Uncertainty in test gas composition before shock heating was estimated to be less than 0.5%. A number of pure argon shock runs were conducted to ascertain conditions of desired pressure, temperature, and dwell time for the actual fuel runs. Two to four pure oxygen shocks were run after every four actual fuel runs to remove any impurities or soot residues left behind on test section walls. The test section of the shock tube was dry wiped and cleaned after each shock run for fuel-rich runs with solvent hexanes and purged by helium gas at 40 psi pressure for more than 2 min to remove any traces of the solvent left before using it for next shock run. The experimental matrices are provided in Tables 4.1 through 4.3.

Table 4.1 Experimental Matrix for Ethylene Study.

Equivalence ratio ( $\Phi$ )	Ethylene (%)	Oxygen (%)	Argon (%)	P (atm) (Variation $\pm 10$ %)	T (K) range
3	3.5	3.5	93	2, 10 and 18	1000-1590
1	1.75	5.25	93	2 and 10	1106-1645
1	1	3	96	2, 10 and 18	1109-1690
0.5	0.5	1.5	98	2, 10 and 18	1223-1828

Table 4.2 Experimental Matrix for M-xylene Study.

Equivalence Ratio ( $\Phi$ )	M-Xylene (%)	Oxygen (%)	Argon (%)	$P_5^{*,\#}$ (atm)	$T_5^{*}$ range (K)	Shock Tube
3.0	0.444	1.556	98	2, 18	1365 - 1948	Non heated
1.0	0.174	1.826	98	2, 18	1289 - 1824	Non heated
0.5	0.090	1.910	98	2, 18	1378 - 1924	Non heated
0.5	0.045	0.954	99	18	1397 - 1867	Non heated
0.5	0.318	6.681	93	18	1105 - 1622	Heated <sup>\$</sup>
1.0	0.609	6.391	93	18	1104 - 1557	Heated <sup>\$</sup>
3.0	1.556	5.444	93	18	1118 - 1574	Heated <sup>\$</sup>
* $P_5$ , $T_5$ are initial post reflected shock pressure and temperature respectively.						
# Variation in $P_5$ was up to $\pm 10\%$ of the reported value.						
<sup>\$</sup> Shock tube and sample preparation unit were heated to 140 °C.						

Table 4.3 Experimental Matrix for N-dodecane and n-dodecane / m-xylene Blend Study.

Equivalence Ratio ( $\Phi$ )	M-xylene (%)	N-dodecane (%)	Oxygen (%)	Argon (%)	T (K)
0.5	-	0.184	6.816	93	1010 - 1600
1.0	-	0.359	6.641	93	961 - 1482
3.0	-	0.977	6.023	93	930 - 1546
0.5	0.050	0.167	6.783	93	982 - 1607
1	0.096	0.324	6.580	93	1033 - 1515
3	0.259	0.867	5.874	93	935 - 1461
Variation in $P_5$ was up to $\pm 10\%$ of the reported value (18 atm). Shock tube and sample preparation unit were heated to 140 °C.					

#### 4.2.5 Kinetic Modeling of Shock Tube Results

##### *Ethylene Combustion*

The SERDP\_C2H4 model was used to compute post-shock conditions in the current ethylene study. This model, developed primarily by Wang and Colket, includes small hydrocarbon chemistry based on USC Mech II (Wang, 2007), aromatic /PAH reaction compilation by Babushok et al.(2004), and selected toluene related PAH chemistry from Colket et al.(1994) The CH\* chemistry added to SERDP\_C2H4 model was based on the work of Frenklach et al.(1992) The ignition delay times were modeled using the SERDP\_C2H4 model. The closed homogeneous batch reactor model of Chemkin-Pro was used for these simulations with the assumption of homogeneous adiabatic conditions and constant volume constraint. For fuel-rich conditions ( $\Phi=3$ ), an optimized USC Mech II model (Wang et al., 2009) was used in conjunction with an in-house modeling code developed by Wang et al. The optimization was based on quantification of the kinetic rate parameter uncertainty using spectral expansion techniques. In all conditions, the model ignition delay varied little with criteria based on CH\*, temperature inflection point or pressure rise, etc., which was later confirmed by experimental results. A temperature inflection point based criterion was chosen for computing model ignition delay times in stoichiometric conditions. For fuel-rich conditions ( $\Phi=3$ ), CH\* onset was chosen as the ignition delay criteria.

##### *M-xylene combustion*

The kinetic model used to simulate ignition delay times was the SERDP\_SURR\_v2.0 model for the two component surrogate. The m-xylene oxidation model includes analogous reactions of m-xylene based on the high-pressure toluene pyrolysis and oxidation model developed by Sivaramakrishnan et al. (2005, 2006). For the m-xylene mechanism, the thermochemistry is taken from Dagaut et al. (Gail, 2007) and Battin-Leclerc et al. (2006). The JetSurf 0.2 kinetic mechanism developed for the pyrolysis and oxidation kinetics of normal alkanes up to n-dodecane at high temperatures constitutes a part of this SERDP model (Wang et al. 2008). The JetSurf 0.2 mechanism, in turn, includes USC Mech II submechanism, which describes the oxidation of H<sub>2</sub> and CO and the high-temperature chemistry of C1-C4 hydrocarbons developed by Wang et al. (2007). Reactions pertaining to the kinetics of OH\* chemiluminescence were added to the SERDP model, based on the work of Hall and Petersen (2006). In total, the reaction model contains 1906 reactions of 289 species and is currently a work in progress.

The simulation of experimental ignition delay times using the SERDP model was attempted using three different modeling approaches. The closed homogeneous batch reactor model of Chemkin-Pro was used for ignition delay time simulations with the assumption of homogeneous adiabatic conditions and constant volume constraint (constant (U, V)) assumption. Conventionally, shock tube ignition delay experiments have been modeled using either a constant pressure (P) or a constant volume (V) assumption with an adiabatic constraint. However, under conditions where a strong ignition transitioning to detonation (for concentrated fuel mixtures when heat release from the combustion is significant) is possible, constant pressure assumption is no longer valid. The constant volume assumption holds until the start of strong ignition during an experiment. However, post-detonation, the assumption fails due to expansion

and equilibration of test gas in the test section. Additionally, previous studies have found that the constant (U, V) assumption is specifically insufficient for shock tube ignition delay modeling under lower temperature range (700-1200 K) (Saxena, 2011). At lower temperatures, accurate measurement of longer ignition delay times is susceptible to gas-dynamic non-idealities (condition dependent) and facility dependent effects (in specific cases only). Also, concerns have been raised over the effect of de-flagrative processes typical of mild ignition events, which serve to compress the test mixture prior to ignition, leading to reduced ignition delays. These de-flagrative processes could interfere with the true chemical kinetic start of the ignition process (Chaos, 2010). Therefore, a modeling approach that takes into account the gas-dynamic non-idealities and chemistry generated effects is needed to accurately simulate shock tube ignition delay times.

The modified Chemkin code SHOCKIN is currently being used as a new approach for ignition delay time simulation. SHOCKIN is an in-house code recently developed by our group that takes experimental pressure profile as an input to the program and accurately models the gas dynamics effects associated with the shock tube experiments. During each time step, for a control mass of gas-mixture, SHOCKIN uses Chemkin 2.0 (with constant volume (V) and internal energy (U) constraints) to model the combustion of the reacting system. In the next step, the system is isentropically brought to measured pressure at a frozen composition. Li et al. (2008) used a similar strategy in the development of the CHEMSHOCK shock tube modeling code. SHOCKIN was validated using a previously-validated “optimized USC Mech II” model in a shock tube combustion experiment on ethylene (shown in Figure 4.11). An example from current work on m-xylene ignition delay simulation using SHOCKIN code is shown in Figure 4.12.

Recently, Bilyeu et al. (2009) developed a 1-D CFD code (GASKIN) to simulate shock tube flows with finite-rate detailed chemistry. Here, the one-dimensional Euler equations for chemically reacting flow are employed to model the fluid flows and detailed finite-rate chemistry models are used to simulate chemical reactions. Application of this code could provide better insight in identifying the impact of de-flagration phenomenon at low temperatures on the measurement of a true kinetic ignition delay time. The code has been successfully used to model shock tube experiments with the GRI Mech 3.0 model for CH<sub>4</sub>/air reactions with 54 species and 325 reaction steps, and Hai Wang’s 1999 C<sub>2</sub>H<sub>4</sub>/O<sub>2</sub> mechanism with 76 species and 529 reactions. The 1-D CFD modeling of the ignition delay times obtained from this study using the GASKIN code is currently in progress. The number of species and reactions of the SEDRP model far exceed those of the models used thus far. Therefore, a mechanism reduction technique developed by Yu Shi et al. (2010) was used to reduce the present model to a reasonable size so that the model could be suitably run using the code. The approach is based on the directed relation graph with error propagation (DRGEP) and principal component analysis (PCA) methods. In the first stage, the DRGEP method is used to efficiently remove redundant species, followed by use of the PCA method to further remove insignificant reactions and species. During the entire process, the performance of the reduced mechanism is monitored to ensure that the generated mechanism satisfies user-specified error tolerances. The detailed analysis of the merits and accuracy of above-mentioned modeling approaches forms an important part of this study.

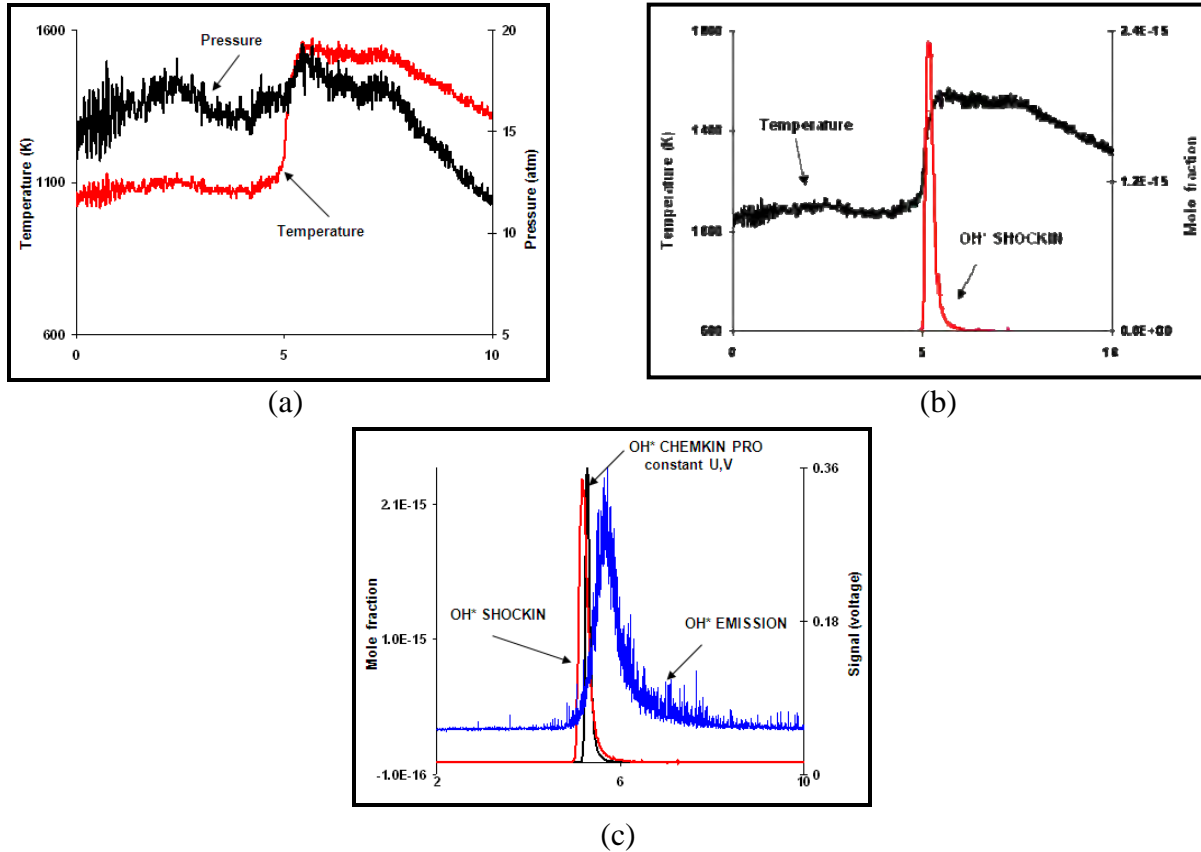


Figure 4.11. An example of ignition delay time modeling procedure using SHOCKIN program. Combustion of ethylene at  $\Phi=3.0$ ,  $T=1043$  K,  $P=18$  atm and 93% argon content. The Optimized USC Mech II model (Wang et al. 2008) was used here to simulate ignition delay times. The temperature profile obtained from SHOCKIN program follows the experimental end-wall pressure profile closely. The ignition delay time from the experimental pressure pulse rise is very close to the temperature inflection point on the SHOCKIN temperature profile (a). The time to OH\* emission rise and temperature inflection point are in close agreement (b). As observed, the OH\* profile using SHOCKIN and Const. (U,V) ChemkinPro approach are very close to the experimental OH\* profile(c). The small disagreement between simulated and experimental OH\* profile could be attributed to the level of accuracy of the kinetic model or OH\* kinetics in the model.

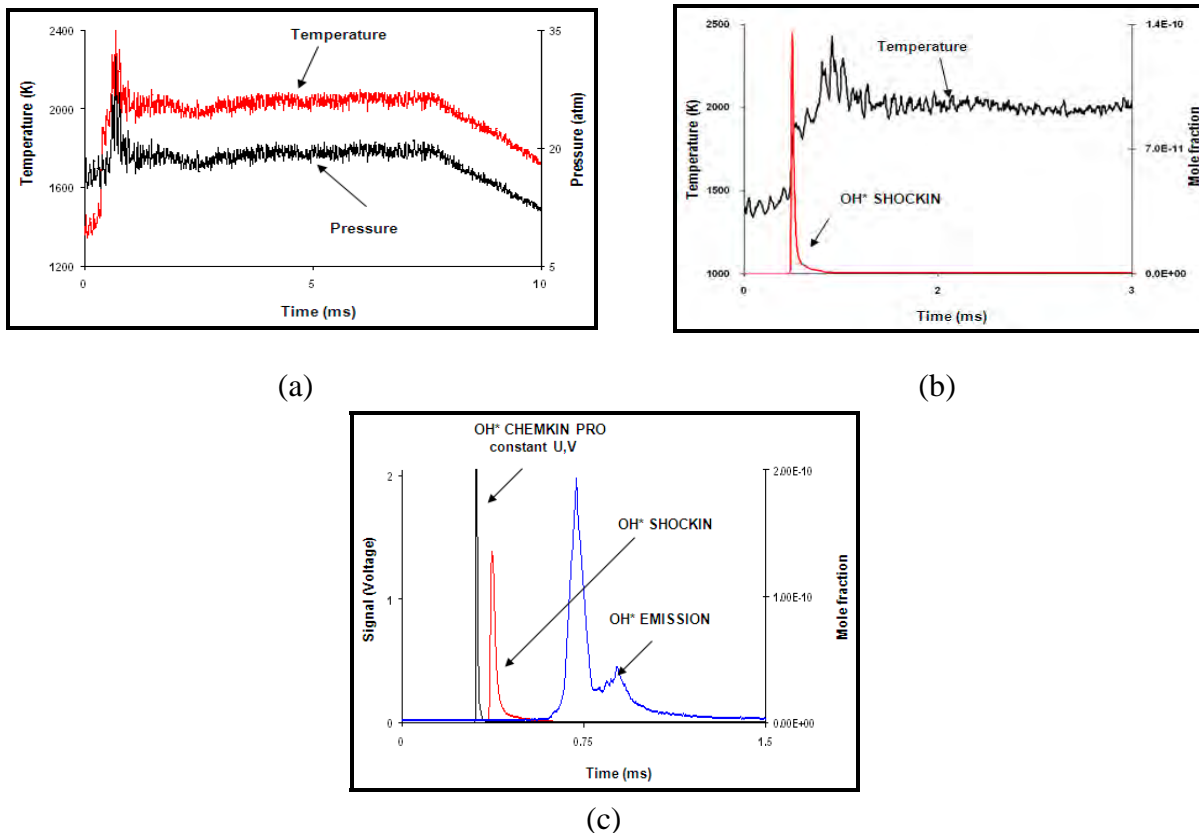


Figure 4.12 An example of m-xylene ignition delay time modeled using the SHOCKIN program. Combustion of m-xylene at  $\Phi = 0.5$ ,  $T = 1379$  K,  $P = 18$  atm and 93% argon content. The SERDP model was used here to simulate ignition delay times. The ignition delay time from experimental pressure pulse rise is slightly under-predicted by time to temperature inflection point on SHOCKIN temperature profile (a). However, time to OH\* rise and temperature inflection are in very good agreement (both SHOCKIN obtained, (b). As observed, OH\* profile using SHOCKIN and Const. (U,V) ChemkinPro approach predict shorter ignition delays than the experimental OH\* profile. However, the prediction of SHOCKIN appears slightly better (c). The disagreement between simulated and experimental OH\* profiles could be attributed to the level of accuracy of the SERDP kinetic model as well as from OH\* kinetics additionally included in the model.

#### *Modeling n-dodecane and n-dodecane / m-xylene blend combustion*

The ignition delay times were modeled using the kinetic model developed as a part of the SERDP. The latest SERDP model includes Jetsurf model version 1.0 for n-alkane oxidation. The model contains 241 species and 1641 reactions. The closed homogeneous batch reactor model of Chemkin-Pro was used for these simulations with the assumption of homogeneous adiabatic (U) conditions and constant volume (V) constraint. The temperature inflection point-based criterion was chosen for computing model ignition delay times under all conditions. It must be noted that at low temperatures (typically below 1100 K) and concentrated fuel mixtures



(e.g. 7% fuel-oxygen mixture used in present study), the Chemkin-based constant (U, V) assumption could be insufficient (Saxena, 2011 and Flora, 2011). Therefore, the nature of agreement between the model and experimental data at low temperature is being further investigated using SHOCKIN (a modified Chemkin code developed by our group and 1-D CFD). The results and discussion for the above-mentioned studies are provided in Section 5.1 of this report.

### 4.3 Co-flow Diffusion Flame

#### 4.3.1 Experimental Set-up

The high pressure flame reactor used in these studies was built from standard pipe sections. The chamber originally designed to accommodate the co-flow burner used in previous studies (Santoro et al. 1983), was built in two sections, Figure 4.13. The bottom section of the chamber, which housed the translation stage that provided the vertical motion of the burner, was made from a 8 inch i.d. Schedule 40 seamless carbon steel pipe, 24 inches in length. Both ends of the pipe were fitted with 15 inch o.d. companion flanges. The bottom section was also fitted with a burst disc (Fike) rated for 30 bar, via a 2 inch i.d. pipe welded to the pipe section, and was connected to a muffler to help absorb bursting of the disc. The top section of the chamber was constructed from a 6 inch i.d. Schedule 40 seamless carbon steel pipe section 30 inches in length, with a 15 inch o.d. flange at the bottom used to couple with the bottom chamber section, and a 12 inch o.d. flange at the other end. The two sections were coupled using a 1/8 inch thick fiber-reinforced gasket (Garlock). The top bottom ends of the coupled pressure chamber were capped with end flanges, which were used to locate the feed-throughs that delivered the reacting gases and also purged the exhaust gases. Feed-throughs (Conax Buffalo) were installed for delivery electrical lines, stepper motor control cables and thermocouple wires into the pressure vessel. The top end flange also housed the exhaust port of the system, which was connected to a pneumatically actuated three-way valve. One of the two ports the three-way valve was connected to a needle valve which was used to regulate the pressure inside the vessel. The shop-air delivery line to pneumatic actuator was connected to a solenoid valve that was controlled by an emergency button. This was implemented to facilitate a rapid purge of the chamber in case of an emergency.

Optical access to the flame was facilitated by way of four 2.5 in dia ports on the top section of the flame reactor, located at equal angles to each other. For the laser extinction and LII measurements, the ports were fitted with half-inch thick S1-UV fused silica windows 2.5 inches in diameter, coated with a broadband anti-reflective (AR) material optimized for the visible spectrum. For the LIF measurements, the AR coated windows were replaced with uncoated S1-UV fused silica windows, since the AR material absorbs UV radiation. The AR coating was necessary to prevent interference fringes formed as a result of the laser beam undergoing multiple reflections between diametrically opposite windows in the laser extinction measurements.

The burner had two degrees of freedom, one along the vertical direction and the other in the horizontal direction, perpendicular to the laser path. The vertical motion was achieved by using a stepper motor (Velmex PK266) coupled to a lead screw (0.065 in/turn pitch), which was in turn

attached to a linear bearing. The vertical translation system had an effective step resolution of  $2.5 \times 10^{-4}$  in or  $6.35 \times 10^{-3}$  mm. The horizontal translation was achieved by coupling a weight-actuated linear bearing to a commercially available translation stage (Velmex BiSlide), that had a step resolution of 5  $\mu$ m. The entire high pressure chamber assembly was mounted on the carriage of the linear bearing.

A schematic of the burner is shown in Figure 4.13(b). The burner consists of a stainless steel fuel tube with an inner diameter of 6 mm and a wall thickness of 0.5 mm. The co-annular air stream is provided using a 1 inch thick ceramic honeycomb (400 cells/in<sup>2</sup> cell density, Corning Environmental Technologies) that acted as a flow straightener. The tip of the fuel tube extends 5 mm above the top surface of the ceramic honeycomb.

The ceramic honeycomb and the fuel tube are concentric to a 101.6 mm I.D. brass tube 101.6 mm in length, with a wall thickness of 1.59 mm. The top surface of the flow straightener is flush with the top edge of the burner housing. The burner is sealed at the bottom using a 1.59 mm thick brass disc, 107.95 mm in diameter.

The fuel and the air flows are smoothened using solid glass bead matrices in the fuel tube and the air annulus. The air stream is smoothened by 3 mm diameter solid glass beads which completely fill the void between the brass disc and the lower surface of the ceramic flow straightener. The fuel stream is smoothened using 2 mm diameter solid glass beads filled to a height of approximately 30 mm below the tip of the fuel tube. A fine copper wire-mesh screen helped retain the glass beads. The glass beads were procured from Fisher Scientific.

The fuel and the air stream temperatures were monitored using K-type thermocouples (Omega). The fuel stream temperature was measured using a 0.020 inch diameter sheathed thermocouple which was positioned along the central axis of the fuel tube, measuring the fuel stream temperature at a distance of 25 mm from the tip of the fuel tube. The air stream temperature was also monitored by a similar K-type thermocouple.

Figure 4.14 shows the layout for the fuel and air delivery systems for the high pressure laminar flame experiments. The C<sub>2</sub>H<sub>4</sub> and N<sub>2</sub> flows were delivered using calibrated mass flow controllers (Brooks Instruments 5850 series) that are rated for operation at pressures of up to 100 atm with an accuracy of  $\pm 1\%$  of the set point. The ethylene gas used in these experiments was of chemical purity grade (99.9 %), whereas the nitrogen was industrial grade with a purity of 99.98%. Both gases were supplied by MG Industries in standard pressurized bottles. The two streams were mixed downstream of the mass flow controllers, the two lines were isolated with check valves.

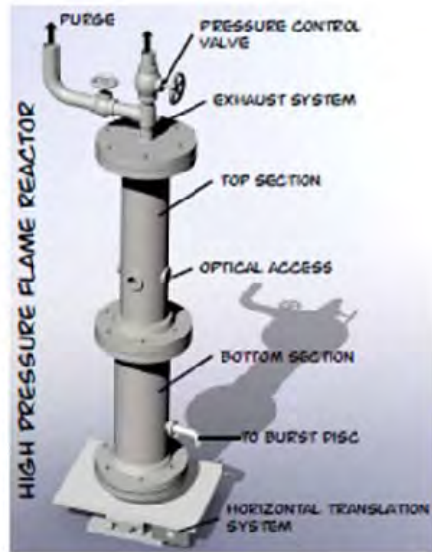
The co-flow air stream provided by the building compressor was filtered using a desiccant filter which removed any liquids in the stream. The air flow was controlled using a metering valve and was monitored using a laminar flow element (Teledyne Hasting LAFM-5). The pressure upstream of the metering valve was maintained at a constant 150 psig by a single-diaphragm pressure regulator. The air mass flow meter had a working range of 0 – 5 SCFM, with a working accuracy of  $\pm 1\%$  of full scale.

Initial experiments with *m*-xylene were conducted using a bubbler to add the *m*-xylene. The  $C_2H_4-N_2$  mixture was bubbled through *m*-xylene, which was held in a 200 cc stainless steel bubbler (Precision Fabricators Ltd.) immersed in a temperature regulated recirculating bath containing a 50–50 solution of ethylene glycol and distilled water. The recirculating bath had a temperature range of 5°C to 150°C above the ambient temperature of the recirculating fluid. To achieve the 5% *m*-xylene concentration level at 1 – 5 atm, the bubbler had to cooled to a minimum temperature of -2.6 °C, which could not be achieved with the default configuration. This was overcome by circulating the bath liquid of the above-mentioned bath (high temperature bath) through a copper coil heat exchanger immersed in another cooling bath (low temperature bath) that was maintained at -20 °C in a vacuum insulated dewar cooled by an immersion coil cooler (Haake 1000). The combination of the two baths yielded a working temperature range of 5°C up to 130 °C.

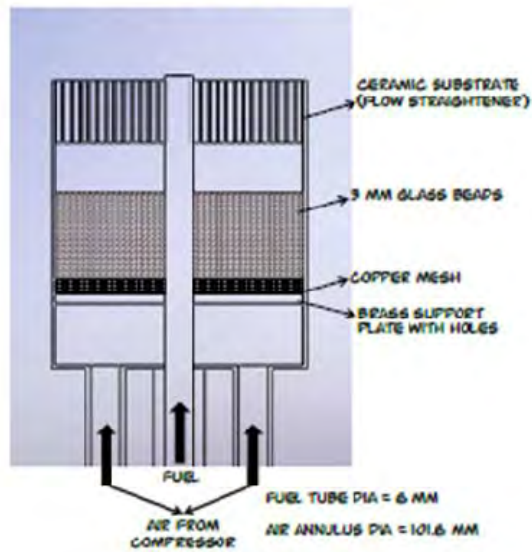
In order to complete experiments with dodecane, the surrogate fuel, and JP-8, it was necessary to implement a fuel vaporizer because the temperatures to achieve the required partial pressures of these fuels exceeded the capability of the bubbler system. The liquid fuel flow rate was controlled by a syringe pump (Chemyx inc. fusion 100 fitted with a gastight #1001 syringe from Hamilton). Energy for vaporization was delivered by an electrically heated, fluidized bed (Techne SBS-4) . The nitrogen/ $C_2H_4$  flowed into a stainless steel coil immersed in the fluidized bed. The liquid fuel was added to the stream in a T-fitting just before the fluidized bed. Heating tapes and a heated flexible line were used to maintain the temperature of the mixture above the dew point of the liquid fuel component. A heated flexible line (Atmoseal with temperature controller and maximum temperature of 250 °C) was used to connect the outlet of the vaporizer to the entrance of the high pressure chamber. Heated tapes were used around the fuel lines inside the high pressure chamber. In order to install the heating tapes, the flexible fuel lines inside the chamber were converted to standard stainless steel lines which means that the burner cannot be translated vertically anymore. This only affects the ability to perform absorption scans, not the LII or LIF measurements. Heating tapes with a maximum temperature of 230 °C were used in order to avoid hot spots that could lead to fuel decomposition. Thermocouples were placed between the fuel lines and the heating tapes to monitor the heating tape temperatures.

As a precaution against fuel condensation after the fuel stream entered the burner (Figure 4.13 b), the air flow was preheated to 100°C using an inline heater (Sylvania threaded in-line heater 4KW). Heating of the air decreased the stability of the flame. Several approaches were tried to stabilize the flame. Ultimately, insertion of a mesh screen and a conical chimney surrounded by honeycomb baffle about 65 mm above the flame led to acceptable flame stability. The effectiveness of the baffle/chimney combination indicates that recirculation within the pressure chamber caused the decreased stability.

All of the LII data with air heated to 100°C was collected using the vaporizer system. PAH data and light scattering data for *m*-xylene using unheated air were taken using the bubbler system.



(a) High pressure flame reactor



(b) Co-flow burner

Figure 4.13 The high pressure chamber and burner used in co-flowing flame studies.

Figure 4.14 Layout of the fuel and air delivery system for co-flow diffusion flame.

#### 4.3.2 Experimental Procedure

Although calibration curves for the fuel gases were provided by the manufacturer, the  $C_2H_4$  and  $N_2$  mass flow controllers were calibrated in the laboratory using a 'bubble meter'. The bubble meter is a graduated cylinder with an inlet port at the base of the cylinder and a rubber bulb containing some soap solution for making bubbles. A thin soap film is generated by bubbling the gas through the soap solution. The flow rate is obtained by measuring the time required for the soap film to travel between two graduations on the tube. For calibrating the flow meters used in these experiments, the graduated cylinder had a capacity of 100 cc with graduations every milliliter.

The air mass flow meter was calibrated using a calibrated turbine flow meter, where the air flow impinged on a turbine coupled via gears to a needle that rotated relative to a calibrated scale, one full revolution of which was equivalent to a volume of 1 liter. The volumetric flow rate of the air stream was obtained by measuring the time required for completing a fixed number of revolutions of the needle.

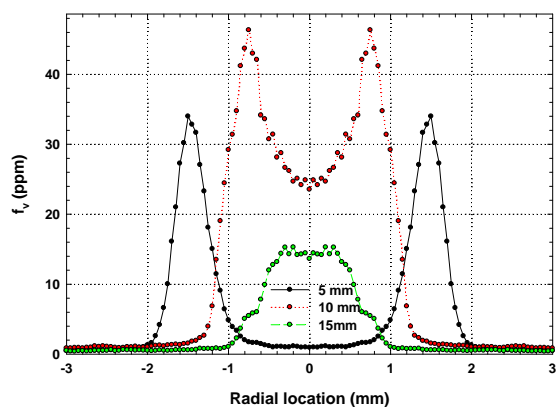
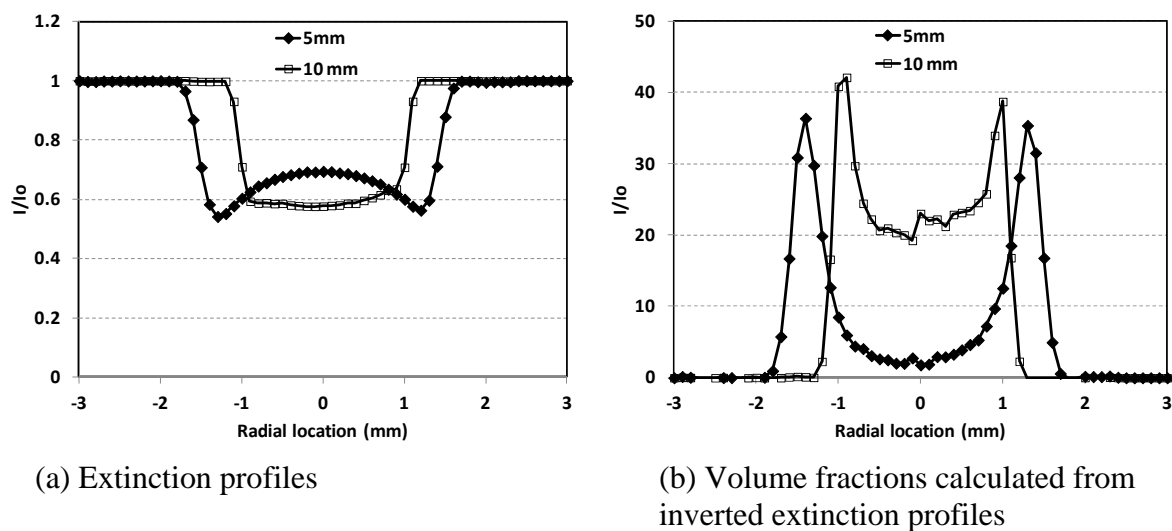
In addition, the mass flow rate of m-xylene was checked by condensing the m-xylene vapor after the outlet of the bubbler. The flow rates from the condensing the vapor matched the expected flow rates within 5 to 10% over three different tests. When the vaporizer system was implemented, the unheated m-xylene data was retaken with the vaporizer in order to compare with the data taken with the bubbler. The comparison showed that the systems were equivalent within experimental uncertainty. Several sets of measurements were made with different temperature settings in the fluidized bed and heated lines to ensure that the measurements did not vary when those settings were changed. During runs with the vaporizer system, all the thermocouples in the fuel path were maintained at least 30°C above the condensation temperature of the fuel/nitrogen mixture. The thermocouples used to monitor heating by the heating tape (placed between the line and heating tapes) were maintained above 150°C. The fluidized bed temperature was set between 300 and 400°C (depending on running pressure) and the heated line was set at 240°C.

For purposes of calibrating the LII, extinction measurements were made on an undiluted C<sub>2</sub>H<sub>4</sub> flame at 1, 3 and 5 atm at distances of 10 and 15 mm from the tip of the fuel tube. Measurements were made with a radial spatial resolution of 0.1 mm. The extinction measurements made at 3 atm at a distance of 10 mm from the tip of the fuel tube were used to calibrate the LII images. Hoffmann *et al.* (2003) determined that pressure had little effect on the calibration of LII. Any effect of pressure on the calibration will be maximum at the ends of the pressure range being investigated, i.e. 1 and 5 atm. Using the calibration at 3 atm will effectively average any pressure dependence behavior of the extinction measurements. The extinction measurement in terms of  $I/I_0$  for the C<sub>2</sub>H<sub>4</sub> flame at 3 atm are shown in Figure 4.15(a). The soot volume fractions shown in Figure 4.15(b) are calculated after tomographically inverting the profiles of  $I/I_0$ . The complex index of refraction  $\tilde{m}$  used for the calculation of  $f_v$  was  $1.57 - 0.56i$ . The peak soot volume fraction at a distance of 10 mm is then used as the reference value for the LII signal. A calibration factor of 38.77 ppm per 1401938 counts from the CCD was used for calibrating the LII images. The resulting soot volume fraction profiles are shown in Figure 4.15(c).

Initial experiments at elevated pressure were conducted on a C<sub>2</sub>H<sub>4</sub> diffusion flame without dilution. This served as a reference for comparison with the effects of N<sub>2</sub> dilution. The pure ethylene flame was stable at all pressures. It should be noted that previous studies of high pressure diffusion flames have shown that as pressure is increased, the flames begin to flicker at some constant frequency. Great care has been taken to avoid this unstable flame regime. At 1 atm the luminous flame height was 13 mm, with the luminous height increasing monotonically with pressure.

Nitrogen was added to the fuel in order to lower the soot volume fractions because of the high soot loadings as pressure increased. The addition of N<sub>2</sub> lowers the flame temperature and mass fraction of the fuel, thereby lowering the soot concentrations. The N<sub>2</sub> addition also increases the momentum of the fuel jet. During initial tests, the N<sub>2</sub> flow rate was increased in small increments (0.25 mg/s) and the flame luminosity and the lift-off distance was monitored visually by means of photographs from a digital camera. Figure 4.16 shows digital photographs of the N<sub>2</sub> —diluted C<sub>2</sub>H<sub>4</sub> flame at different dilution levels. The initial tests revealed that diluting the flame with N<sub>2</sub> successfully reduced the soot levels in the flame, while the flame remained stable. Lift-off was observed for N<sub>2</sub> flow rates greater than 6.0mg/s, and the flame blew off at a N<sub>2</sub> flow rate of

7.0mg/s. Based on these observations, a  $N_2$  flow rate of 5.5mg/s was selected for the baseline diluted  $C_2H_4$  flame.



(c) Volume fractions from LII data at 3 atm

Figure 4.15 Calibration for the LII signal at 3 atm.

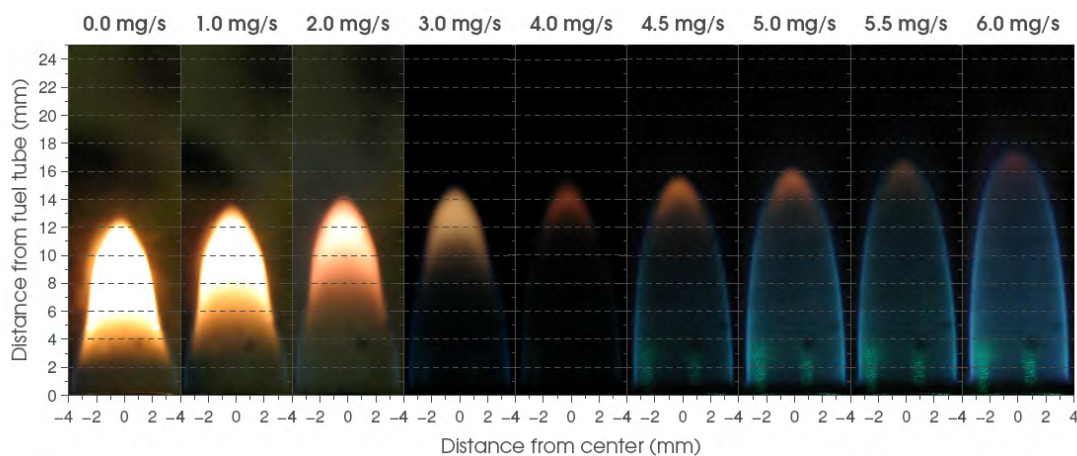


Figure 4.16 Effect of nitrogen flowrate on luminosity (Ethylene flowrate).

### 4.3.3 Diagnostic Methods

Three different laser-based diagnostic methods were applied to the flame – laser-induced incandescence, laser-induced fluorescence and laser extinction. This section describes the experimental configuration used for these techniques. Since the laser beams for the LII and laser extinction shared the same optical path, the experiments were not performed simultaneously. During the LII measurements, the integrating sphere was removed and a beam block installed in front of the 350 mm focusing lens for the extinction laser beam.

#### *Laser-Induced Incandescence*

The LII measurements were performed using a frequency-doubled Nd:YAG laser (Continuum Surelite III fitted with second harmonic generator SL3D2). The laser provided a 9 mm diameter Gaussian beam, with a pulse width of 7 ns at a flashlamp repetition rate of 10 Hz. The composite beam consisting of the fundamental beam (1064 nm) and the second harmonic (532 nm) were separated using a Pellin-Broca prism. The separated 1064 nm beam was then collected by a beam dump. The beam was then expanded into a vertical sheet using a fused silica cylindrical lens and focused at the center of the burner using a 500 mm focal length convex lens.

The LII signal was collected by an intensified CCD (Princeton Instruments ICCD) camera fitted with a 576 x 384 EEV chip. The LII radiation was focused on the CCD using an f2.8 105 mm UV lens (Nikon UV-Nikkor), fitted with a narrow band interference filter centered at 430 nm (Andover Optics, 10 nm FWHM). The gain on the intensifier was set to 8 for all experiments. The ICCD camera was controlled by a Princeton Instruments ST-138 controller and triggered by a Princeton Instruments PG-200 pulser.

The pulser, which provided at high-voltage gating pulse to the ICCD camera, was triggered by a TTL from the variable sync terminal of the laser controller, which corresponded to the opening of the Q-switch by the Pockels cell inside the Nd:YAG laser. The temporal location of the laser pulse and the camera gate was monitored using a 1GHz oscilloscope. A fast-response photodiode that was used to monitor the laser pulse provided a signal corresponding to the laser pulse. The temporal location of the leading edge of the gating pulse was then adjusted by changing the delay on the PG-200 pulser. For the LII measurements, the signal was collected using a “prompt” technique, where the intensifier was gated for the entire duration of the laser pulse, for a total length of 90 ns.

The images from the ICCD camera can be read in two ways, a) reading individual frames, each corresponding to a laser pulse, resulting in a large data file containing individual images, and, b) accumulate frames in an internal buffer and read out as a single image. All of the data collected for this experiment were acquired in the individual frame mode, and then accumulated post acquisition. This provided more flexibility with respect to looking at individual snapshots of the flame at different temporal locations. For the current series of experiments, 200 individual frames were acquired for each dataset.

The radiation collected by the camera contains both the LII signal as well as broadband emission from the soot particles. To obtain the actual LII signal, it is therefore required to subtract the



background flame luminosity from the LII image. For this purpose, the flame is imaged twice; the first image containing the LII signal from the soot particles excited by the laser sheet and the second image – the background – is acquired at the same settings after blocking the laser beam. The two images are accumulated using then the background image is subtracted from the LII image.

### *Laser-Induced Fluorescence*

Laser-induced fluorescence was used to probe the presence of polycyclic aromatic hydrocarbons (PAHs) in the high pressure diffusion flames. PAHs are widely believed to be the precursors of soot and their method of formation is of wide interest. It has been observed that PAH molecules exhibit broadband fluorescence over a wide range of excitation wavelengths (Prado et al. , 1985, Beretta et al., 1992). The spectral distribution of the fluorescence is dependent on the wavelength chosen for excitation. Among others, Beretta et al. (1992), Prado et al. (1985), and Miller et al. (1982), reported the spectral distribution of the fluorescence signal from molecules excited in the UV region.

Beretta et al. observed that different classes of PAH molecules fluoresce in different spectral regions, dependent on the size of the aromatic molecule. In general, they observed that the fluorescence smaller ring aromatic molecules tended to cluster around the 300 to 400 nm bandpass region, while heavier aromatics tended to fluoresce in the 400 to 500 nm bandpass. This observation is useful to monitor the bulk concentrations of the different classes of aromatic molecules. For this work two detection bandpasses were chosen, based on the recommendation of Beretta et al.. For the smaller aromatic molecules henceforth referred to as small PAH, a detection bandpass of 320–380 nm was used, which was achieved using a set of WG320 UV cutoff and UG11 bandpass filter. The large PAH were detected in the 420–80 nm spectral region, using a combination of GG420 and BG12 filters.

The fluorescence was excited using the same Nd:YAG laser, fitted with a fourth harmonic generator (SL3-F), which provided the 266 nm beam that was used to excite the broadband fluorescence. The same ICCD camera was used for imaging the flame, but was fitted with the bandpass filters for the different wavelength regions. The lifetime of the fluorescence signal is of the same order as the laser pulse, and the intensifier is gated a few nanoseconds before the onset of the laser pulse. The LIF signal was also acquired with an intensifier gate width of 90 ns and a gain of 8. The image acquisition process is identical to what was described in the previous section, but with a total of 500 frames being acquired for each dataset. This was to account for the lower signal levels for the fluorescence and improve the signal-to-noise ratio in the LIF images.

### *Laser Extinction*

The laser extinction measurements were conducted using the 514.5 nm line of a 2W Argon-Ion laser (Coherent Innova70). The laser beam was modulated at 1000 Hz using an optical chopper (Stanford Research SR560). A portion of the laser beam was guided on to a photo-diode which monitored the incident laser power using a beam splitter before it entered the flame region. After

passing through the flame region, the laser beam was collected by an integrating sphere (LabSphere) which was used to reduce the effects of “beam steering” at higher pressures.

Beam steering occurs as a result of the lensing effect generated due to the strong density gradients observed around co-flow diffusion flames at high pressure (Thomson et al., 2005). This results in the deflection of the beam from its original trajectory. While it is not possible to prevent beam steering in high pressure co-flow diffusion flames, it is possible to compensate for the beam steering in other ways. One method is to use a larger collection lens and focus the laser beam on a photo-diode. This method requires positioning the photo-diode at the exact focal point of the lens but carries the added risk of damaging the photo-diode with the focused laser beam. The second method is to use an integrating sphere, which is a large hollow sphere with a highly reflective, diffuse inner surface. The sphere has small ports to permit passage of the beam and collection of the signal. The laser beam hitting the inside wall of the integrating sphere undergoes multiple diffuse reflections and the energy of the beam is distributed evenly across the entire inner surface. The relatively large diameter of the inlet port (1 inch) is sufficient to compensate for any steering effects in the flame. The extinction signal is collected by focusing a collection lens on the wall of the integrating sphere through one of its outlet ports, on to a photo-diode.

The signals from the two photo-diodes are first converted to voltages using trans-impedance amplifiers and then fed to a lock-in amplifier. The lock-in amplifier, which is also fed the reference frequency from the optical chopper, extracts the signal corresponding to the reference frequency. The voltages from the lock-in amplifiers are recorded by a data acquisition system connected to a computer and saved to disk.

For a complete radial soot profile of the diffusion flame, extinction values were recorded every 100 $\mu\text{m}$ , by moving the high pressure chamber relative to the laser path using the horizontal translation stage. The measured beam waist for the argon-ion laser was approximately 90 $\mu\text{m}$ , so using a spatial resolution of 100 $\mu\text{m}$  was reasonable and avoided any spatial averaging of the extinction scans. The radial extinction profiles were tomographically inverted using Abel inversion (Dasch, 1992) for calculation of soot volume fractions.

The experimental conditions for the diluted ethylene flame experiments conducted with the vaporizer system are presented in Table 4.4.

Table 4.4 Experimental Conditions for Effects of Fuels added to Ethylene Flame.

Additive	% Carbon from Additive	Ethylene flow rate (mg/s)	Additive flow rate ( $\mu\text{l}/\text{min}$ )	Additive flow rate (mg/s)	N2 flow rate (mg/s)	Air flow rate (mg/s)
m-xylene	0%	1	0	0	5.5	2000
	2.5%	0.975	1.64	0.0236	5.5	2000
	5%	0.95	3.3	0.0473	5.5	2000
dodecane	0%	1	0	0	5.5	2000
	2.5%	0.975	2.02	0.0252	5.5	2000
	5%	0.95	4.05	0.0506	5.5	2000
surrogate	0%	1	0	0	5.5	2000
	2.5%	0.975	1.92	0.0248	5.5	2000
	5%	0.95	3.85	0.0497	5.5	2000
JP-8	0%	1	0	0	5.5	2000
	2.5%	0.975	1.88	0.0247	5.5	2000
	5%	0.95	3.77	0.0496	5.5	2000

#### 4.4 Opposed-Jet Diffusion Flame

Previous SERDP related studies using the ARL opposed jet diffusion flame burner have concentrated on soot formation in atmospheric pressure ethylene/air flames (McNesby, 2005). For the current program investigating soot formation, this burner has been modified to operate at fuel side temperatures up to 250 degrees centigrade, enabling the use of many fuels that are liquids at room temperature. The fuel vaporization methods applied to this atmospheric pressure burner are being extended to an elevated pressure (5 atmosphere total) opposed jet burner flame apparatus currently being constructed. The flames supported in these burners are probed using several types of optical diagnostics, including laser induced fluorescence (LIF), laser induced incandescence (LII), tunable diode laser absorption spectroscopy (TDLAS), and multicolor pyrometry.

##### 4.4.1 Experimental Set-up

An opposed jet burner consists of opposing, parallel gas ducts separated by a distance near to the duct diameter. Typically, the ducts are arranged vertically, with fuel gases flowing upwards from the lower duct, and oxidizer gases flowing downwards from the upper duct. After the gases exit the ducts, they travel a short distance in free space before colliding with each other. For gases of approximately equal densities, a stagnation plane occurs midway between the ducts where the axial velocities of the colliding gas streams approach zero. For the sooting opposed flow flames used in this program, peak soot concentration typically occurs near the stagnation plane, in fuel rich regions at temperatures slightly lower than peak combustion temperatures (Hwang and Chung, 2001). The gas flows, duct arrangements, and stagnation plane are conceptually shown in Figure 4.17. For these experiments, the stagnation plane location may be estimated by calculation and visualized using fluorescence techniques.

For opposed flow diffusion flames in which the stagnation plane is fuel rich (e.g., the flames reported here), the flame occurs at the location where fuel and oxidizer are close to stoichiometric combustion proportions. This occurs on the oxidizer side of the stagnation plane (see Figure 4.17), and the stoichiometric mixture is achieved by fuel gases diffusing upstream into the oxidizer flow. For the ethylene/air flames the overall chemical reaction (assuming air to be 20% oxygen) is:



Reaction R4.4.1 shows that for fuel ( $\text{C}_2\text{H}_4$ ) and oxidizer (air) flow rates that are approximately equal, in an opposed flow burner (our conditions), assuming gases with similar momenta (our conditions), the gas mixture at the stagnation plane will be fuel rich (Hwang and Chung, 2001). Because of this, regions of highest particulate and aromatic concentrations (sooting region) and the main combustion (flame radical production) region in opposed flow flames are physically separated (Hall, 1997). A photograph of an ethylene/air opposed jet flame showing the separation of sooting and combustion regions, is shown in Figure 4.18.

The opposed flow burner is constructed of 304 stainless steel, and is based upon the design of Lentati and Chelliah (1998). Fuel gas and oxidizer (air) ducts are 15 mm in diameter, and are separated by 7 mm. A photograph of an ethylene/air flame within the burner chamber is shown in Figure 4.19. Flow rates for the experiments reported here are typically 4.6 liters per minute fuel, and 6.2 liters per minute air. These values were chosen because they gave the most stable flame. When fuels are used that are liquids at room temperature, they are injected into heated fuel lines (see description in next section) using an injection pump (Isco). A shroud gas (nitrogen) surrounded both fuel and oxidizer ducts within the burner assembly to minimize entrainment of room air into the flame. The burner was enclosed in a chamber that was capable of being evacuated. However, for the atmospheric pressure experiments the access ports of the chamber were left open. A schematic of the experimental apparatus, including some optical diagnostics, is shown in Figure 4.20.

The liquid fuel vaporizer consists of a Collision-type atomizer using a preheated nitrogen gas stream as a carrier (see Figure 4.21). Fuel is introduced into the atomizer by an Isco syringe pump. Figure 4.22 shows a diagram of the vaporizer apparatus integrated into the burner system. The Collision-type atomizer is immersed in an  $\text{Al}_2\text{O}_3$  fluidized bath (Techne, Inc., Model SBS-4). Additionally, the fluidized bath is used to preheat all feed gases to the atomizer. Transfer lines from the fluidized bath to the burner are heated using thermostatically controlled heating tape (Omega). Figure 4.23 shows a photograph of the burner assembly, the syringe pump, and the fluidized bath.

A high pressure version of the opposed-jet flame burner was implemented for testing at higher pressures. The burner is shown in Figure 4.24. A schematic of the elevated pressure experimental apparatus, including some optical diagnostics, is shown in Figure 4.25.

The elevated pressure opposed flow burner is constructed of 304 stainless steel, and similar to the atmospheric pressure burner, is based upon the design of Lentati and Chelliah (Lentati, 1998). Fuel gas and oxidizer (air) ducts are 15 mm in diameter, and are separated by 6 mm.

This distance was used because it gave a stable flame. Originally, a separation distance of 7 mm was called for in design. However, pressure sealing problems after construction called for a slight modification in design, decreasing the duct separation by 1 mm. For the elevated pressure burner, the fuel and oxidizer ducts, and flame shroud ducting, are contained within an enclosure of 304 stainless steel initially designed for a strand burner. The enclosure is rated to withstand pressures to 130 bar (approx 2000 psi). The high pressure enclosure is equipped with two sapphire windows (25 mm diameter) for emission and transmission of probe radiation, and two PMMA (polymethyl methacrylate) windows (25 X 100 mm) for flame observation. Previous efforts by us using a high volume enclosure had problems with unburned fuel and air exploding and damaging windows. The current design minimizes chamber interior volume. A photograph of the elevated pressure burner, with one sapphire window port removed is shown in Figure 4.19. At the time of this report, the flow rates giving most stable flames at elevated pressure were approximately 5 liters per minute ethylene, and 4 liters per minute air. A shroud gas (nitrogen) surrounded both fuel and oxidizer ducts within the burner assembly to minimize flame formation away from the vicinity of the fuel and oxidizer ducts. It was necessary to bathe all windows in a nitrogen shroud to prevent condensation.

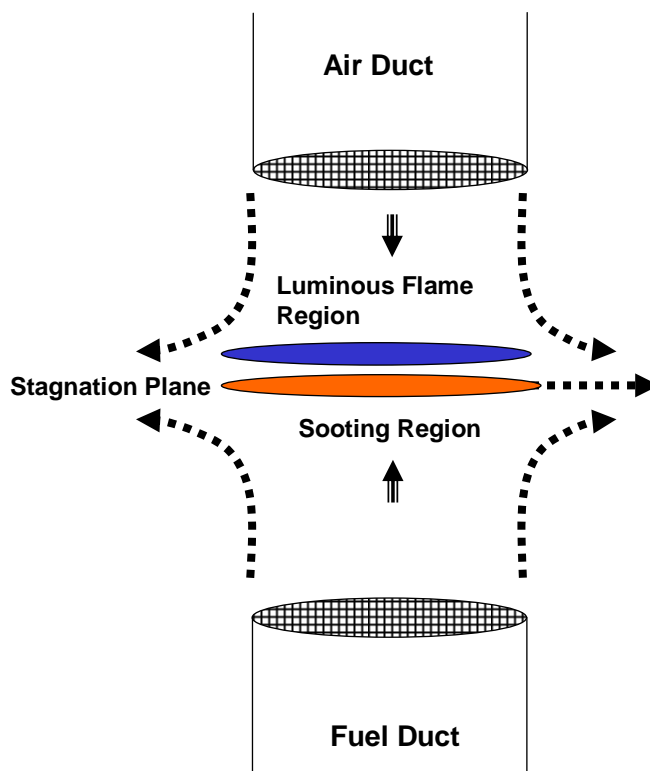


Figure 4.17 A schematic of the opposed flow burner showing gas flow and flame location.

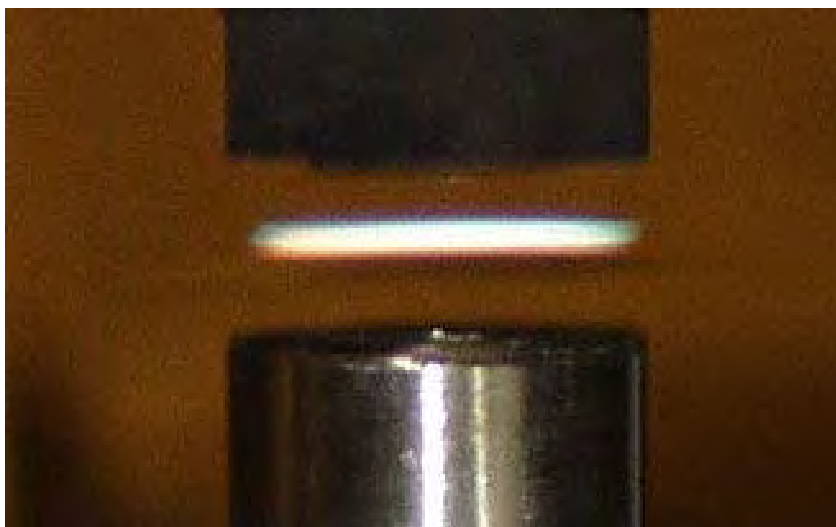


Figure 4.18 A photograph of an ethylene/air opposed jet flame showing the separation of sooting and combustion regions.

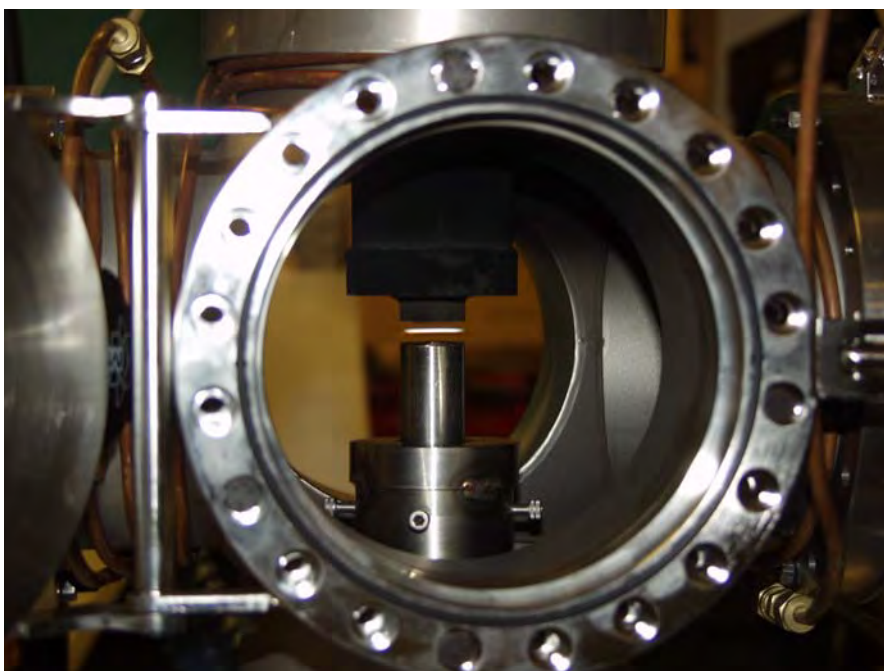


Figure 4.19 A photograph of an ethylene/air flame within the burner chamber.

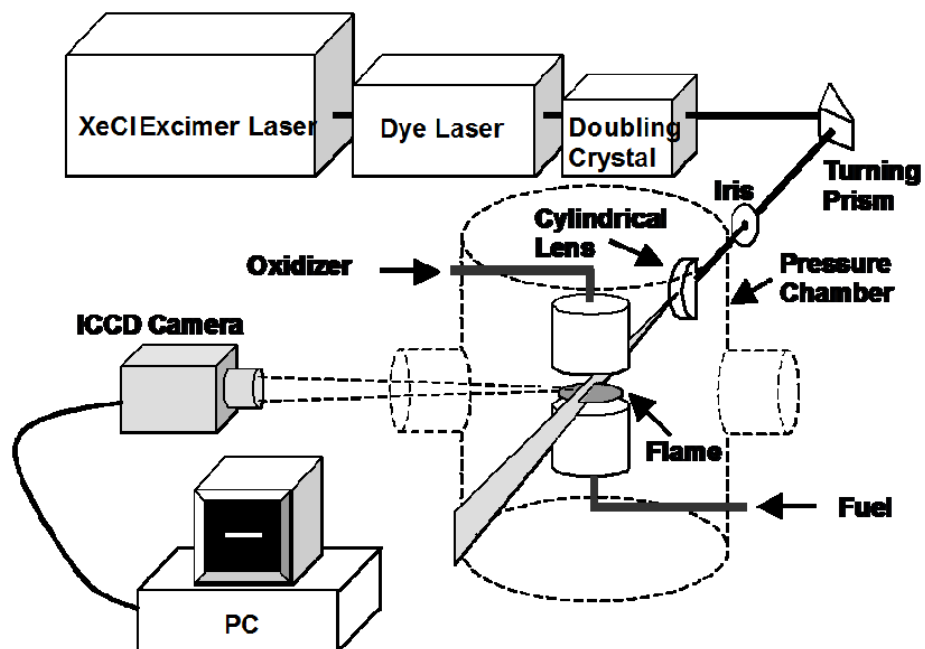


Figure 4.20 A schematic of the experimental apparatus, including some optical diagnostics.

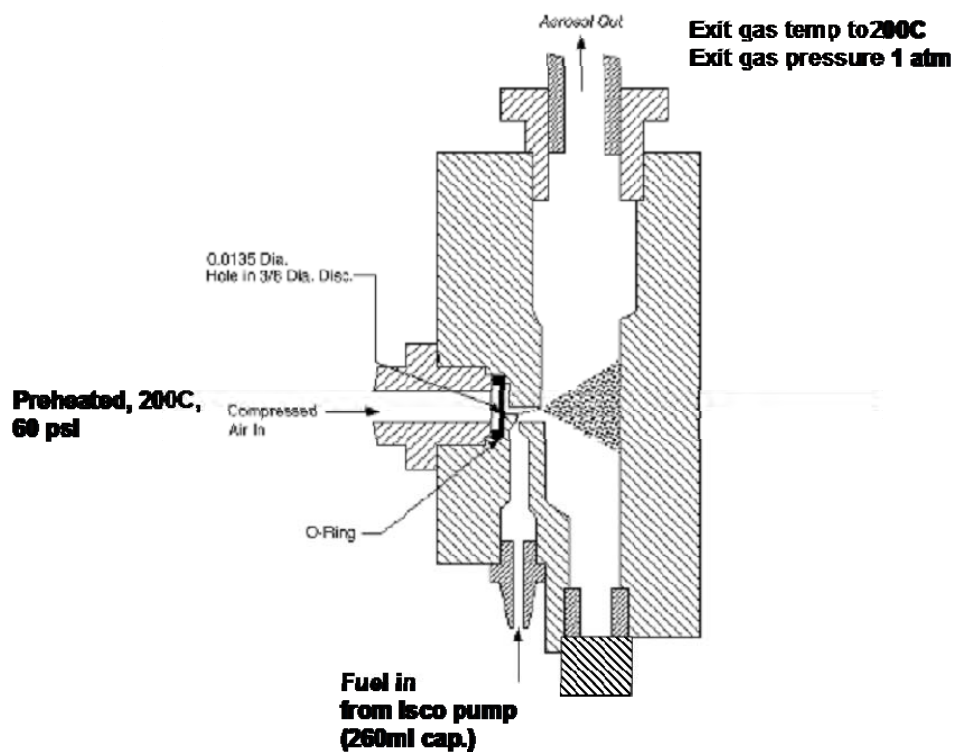


Figure 4.21 The Collision-type atomizer.

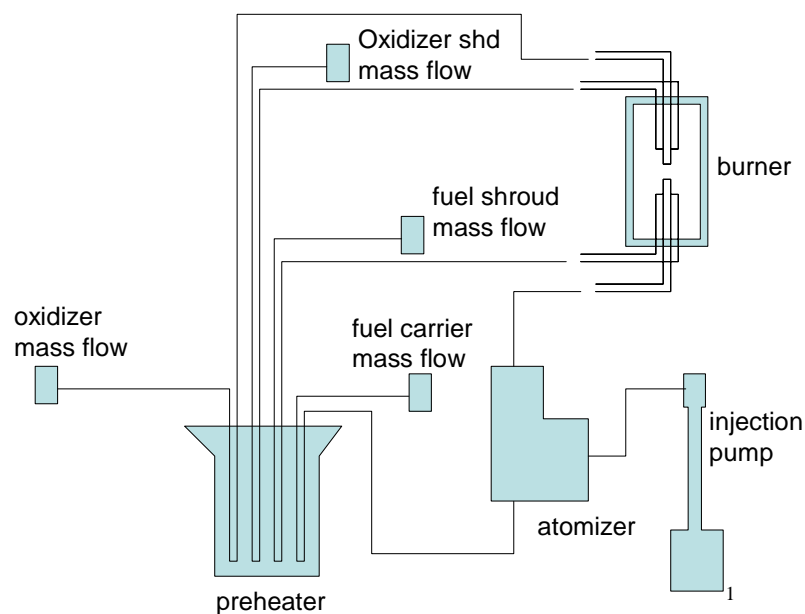


Figure 4.22 A diagram of the vaporizer apparatus integrated into the burner system.

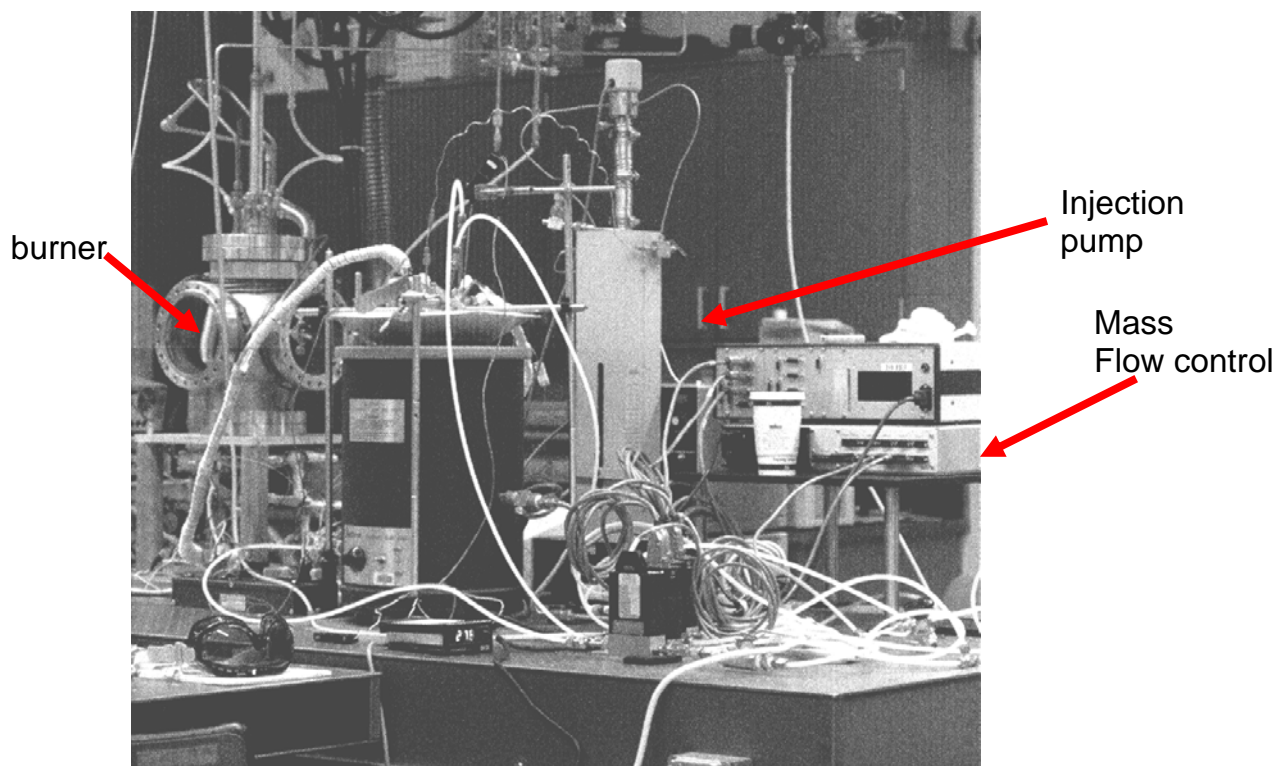


Figure 4.23 A photograph of the burner assembly, the syringe pump, and the fluidized bath.



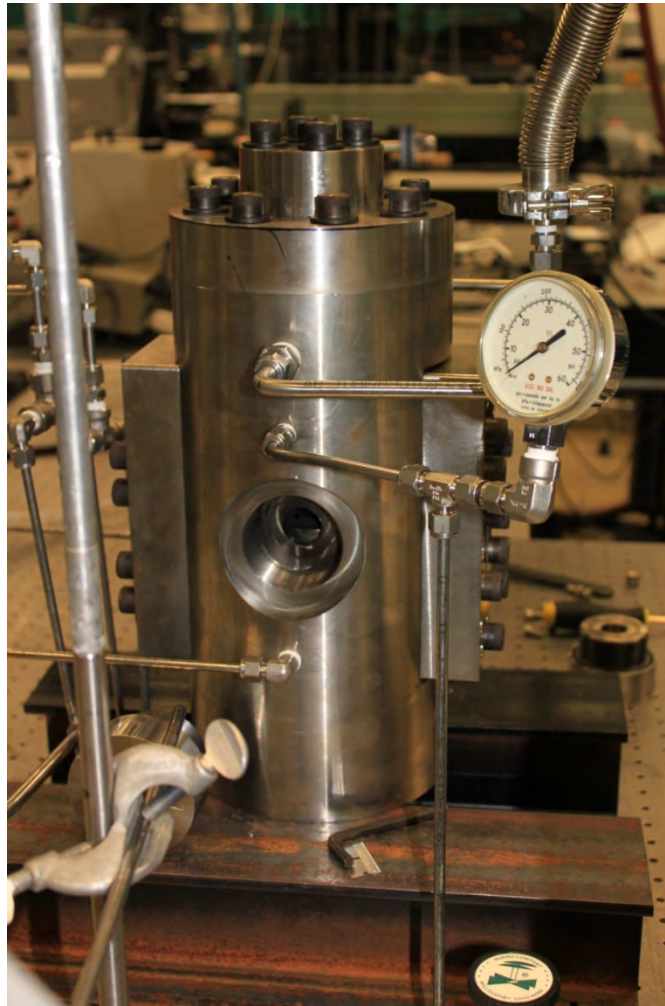


Figure 4.24 The elevated pressure burner assembly, on test bed, in co flow mode, with the sapphire window port removed. The fuel/air duct is visible within the chamber interior.

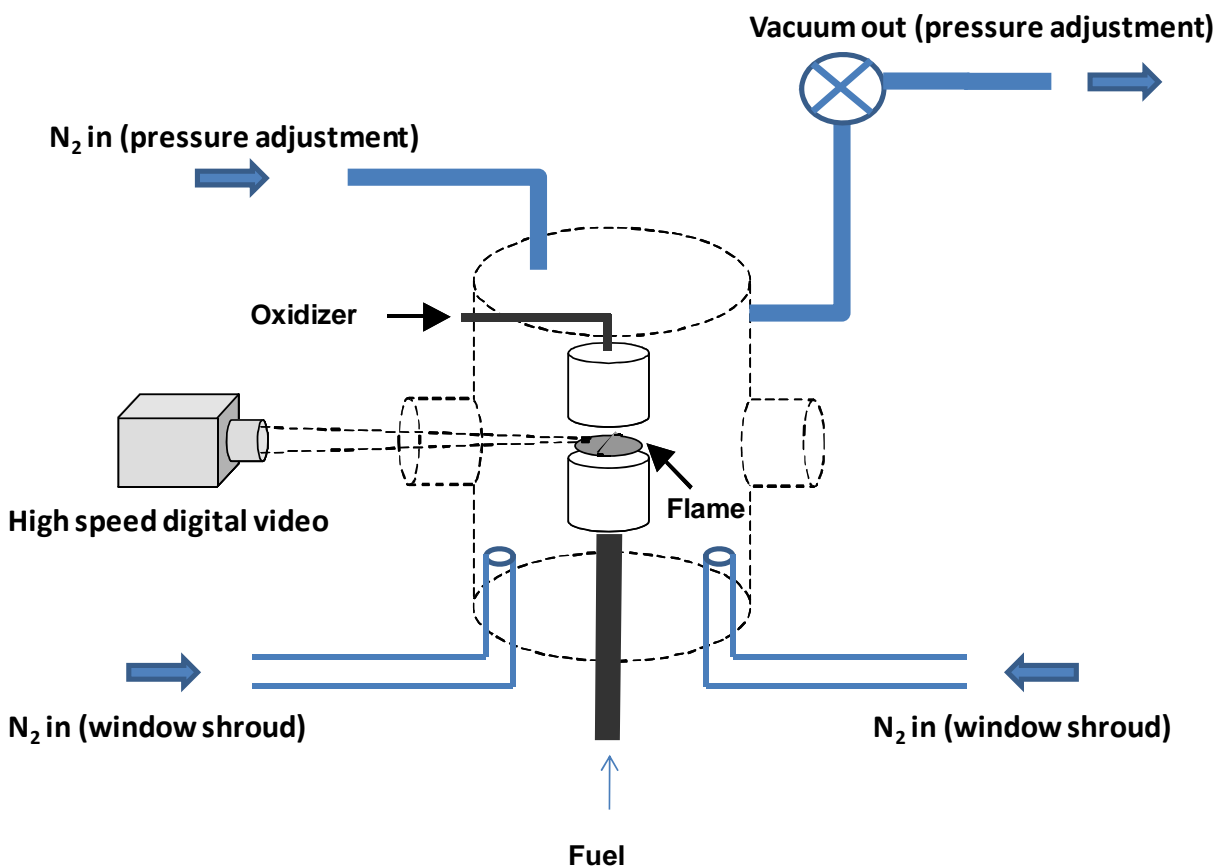


Figure 4.25 Schematic of elevated pressure rig and high speed imaging system.

#### 4.4.2 Experimental Procedure

For flames using a vaporized liquid as a fuel component the experimental procedure was as follows. The gas flow controllers (MKS) were turned on and allowed to warm up for approximately 1 hour. The nitrogen flow to the underside of the fluidized bed was initiated, and the fluidized bed heaters were turned on. Heaters and temperature controllers for all gas transfer lines, and burner heaters were turned on. The fuel carrier gas to the Collision atomizer (nitrogen) was turned on and the backpressure to the atomizer adjusted to approximately 15 psi. Shroud gas flow to the burner was turned on. The rig was allowed to warm to operating temperature (e.g., for fuel additive m-xylene, bath and lines were set to 200 degrees Centigrade) .

When the operating temperature was reached, a flame source was placed between the burner ducts and ethylene gas and air flow was commenced, with the opposed flow flame igniting immediately. The nitrogen shroud gas flow (5 liters/minute total) was initiated and the flame was allowed to stabilize for five minutes. For experiments using fuel additive, a valve on the injection pump was opened and flow of liquid fuel into the Collision atomizer was begun. After approximately one minute of flow of liquid fuel and a visual inspection of the flame to check for pulsation (an indication of incomplete vaporization).

#### 4.4.3 Diagnostic Methods

##### *Planar Laser Induced Fluorescence / Light Scattering*

A sheet of pulsed laser radiation (typically 0.5 MJ/pulse, approx. 20 nsec duration, formed using a double apertured, half cylindrical lens) near a wavelength of 281 nm (Lambda Physik Excimer/Scanmate system: Coumarin 153 dye: Fundamental @ 560 nm, 2x frequency to 281 nm; Pump  $A^2\Sigma^+ (v=1) \leftarrow X^2\Pi (v=0)$ , detect ((0,0), (1,1) around 310 nm) was passed through the flame region. A gated, unfiltered, intensified CCD camera (Roper Scientific, 256 X 1024 pixels), equipped with a Nikkor 1:4.5 UV lens, was used to measure laser scatter during and immediately following the laser pulse (camera gate width = 80 ns). The images produced by 100 laser pulses were averaged in the camera memory. An image obtained in this way for an ethylene/m-xylene (5%)/air flame is shown in Figure 4.26. From this average image, the maximum value at a given pixel location along the centerline between the fuel and oxygen ducts was selected in the sooting and combustion regions of the flame. A background value at that pixel location, measured prior to the flame initiation (also 100 averaged images), was subtracted from this value. This background corrected pixel value became the data point representing peak particle or OH concentration. Following data collection, the injection pump valve was closed, the pump flow parameters were reset, and the process repeated. Planar laser induced fluorescence and light scatter measurements at the beginning and end of each run series were performed to check that the flame returned to normal after the ethanol flow was stopped. Laser power was measured before and after each experimental run and typically varied by less than 2 percent. Other than subtraction of background, no corrections were made for changes in laser power or variations in spatial intensity, and no other specific dark field pixel corrections were made, although previous measurements of the CCD dark field (camera blocked) showed pixel to pixel output to vary by less than 2%. A schematic of this setup is shown in Figure 4.20.

##### *Tunable Diode Laser Absorption Spectroscopy*

Tunable diode laser spectroscopy was chosen to quantify acetylene formation in the opposed jet diffusion flames. Measuring the acetylene produced in the flame provides a metric for monitoring the soot production. Quantifying trace gas species concentration within a flame by laser absorption is a non-trivial measurement. The instrument must be sensitive and selective to distinguish weak signals from the target molecule from the myriad other species produced in a combustion reaction. The inherent difficulty of measuring absorption spectra at high temperature — where the population of initial states is spread over a much greater number of accessible states — is made even more difficult by measuring through turbulent flows of mixed gasses in excited states. To perform this measurement we have built and characterized a sensitive, selective infrared absorption spectrometer system capable of measuring, in real time, absolute acetylene concentration in low concentration samples at elevated temperature. This system is designed around a pulsed distributed feedback Quantum Cascade Laser (QCL). Recent work shows the QCL to be an extremely useful tool for Tunable Diode Laser Absorption Spectroscopy (TDLAS) (Kosterev, 2002). The QCL operates near room temperature and provides a powerful (~10 Mw), stable, single-mode, mid-infrared light source suitable for tunable laser spectroscopy. Nearly the entire IR spectrum is accessible to quantum cascade lasers, as the laser emission is determined by

the growth of the substrate interstitial layer spacing —not the composition, and a wide spectral range is accessible to a single QCL by temperature tuning the substrate. The quantum cascade laser used in this experiment is designed for pulsed, single longitudinal mode emission over a thermally tunable range of  $1279\text{ cm}^{-1}$ - $1273\text{ cm}^{-1}$ .

Working with pulsed diode lasers, a frequency down-chirp is inflicted on the laser output as a result of resistive heating as the current pulse deposits energy into the diode chip. There are two methods for working with this frequency chirp: inter-pulse spectroscopy and intra-pulse spectroscopy. Inter-pulse spectroscopy minimizes the effect of the chirp by driving the QCL with ultra-short pulses (3-5 ns) resulting in near Fourier-limited laser pulses which are scanned through the spectral range of interest by temperature tuning (Harris, 1983) or a subthreshold ramp (Kosterev, 2002). Typical resolution of  $\delta\nu < 0.01\text{ cm}^{-1}$  is attainable by this technique. Intra-pulse spectroscopy harnesses the near linearity of the frequency down-chirp to scan through a spectral region in a single long laser pulse (100 ns – several microseconds). The resolution of this technique is limited by the scan rate:  $\delta\nu = (C \cdot d\nu/dt)^{1/2}$  where C is a form factor dependent on the pulse shape — for long square pulses  $C = 0.883$  (Normand, 2001). Both techniques yield similar resolution. Inter-pulse spectroscopy can scan much longer spectral ranges (up to  $30\text{ cm}^{-1}$  has been reported (Kosterev, 2002)) but requires complex computer control of the driving current supply and long timescales for signal collection as the laser is scanned through the spectral range. The Intra-pulse technique is characteristically simple, yielding spectra similar to a cropped selection of a broadband absorption spectrum, however the maximum spectral range is limited to a few wavenumbers.

The real-time response of the Intra-pulse technique makes it attractive to studies of flame species concentration. The turbulent gas flow, steeply varying temperature/density of the flowing gasses, and onset of scattering soot particles all give rise to significant random fluctuations in the transmitted intensity. These variations yield line distortions and false peaks in the ratioed absorption spectrum if the time for scanning a spectral line is comparable to these environmental variations. Sub-threshold current tuning has millisecond scan times and temperature tuning of the substrate responds on the order of 1 minute; the microsecond response time of the QCL allows it to analyze a frozen flame. The typical maximum spectral range attainable in the Intra-pulse tuning method is just over  $2\text{ cm}^{-1}$ . This is only broad enough to scan a single acetylene absorption line because of the large rotational constant of acetylene, but even when the peak is broadened by high pressures the range is large enough to scan beyond the range and collect a background with each scan. To our knowledge this is the first measurement of absorption spectroscopy within flame made with this chirp based QCL technique.

The distributed feed-back quantum cascade laser used in this experiment (developed at Alpes Laser, Switzerland, supplied by Boston Electronics) is designed for pulsed, single longitudinal mode emission at 7.86 micrometers. The QCL substrate temperature and the driving pulse (current amplitude, pulse length, and frequency) are controlled via laptop running LabView control VI (Cascade Technologies). The QCL is mounted on a Peltier thermoelectric cooler, which can vary the substrate temperature from  $-30^{\circ}\text{C}$  to  $30^{\circ}\text{C}$  stabilized to  $0.01^{\circ}\text{C}$ . The output is collimated through ZnSe optics housed inside the sealed laser head and exits the case in a roughly collimated beam with waist  $\sim 1\text{ mm}$ . A schematic of the experimental setup is presented in Figure 4.27 For flame measurements, the laser beam is sent directly through a single pass 16

cm path length gas absorption cell with wedged BaF<sub>2</sub> windows and then through the flame. The gas cell is used to check absorption line position and is evacuated for quantitative flame measurements. The transmitted light is measured by a fast-rising, Peltier cooled (HgCdZn)Te detector (VIGO PVI-2TE-10) and recorded using a high speed signal processor from Boston Electronics. The detectivity of the photodetector is  $D^*=2 \times 10^9 \text{ cmHz}^{1/2}/\text{W}$  and the rise time is under 0.3 ns.

To characterize the laser output wavelength, the beam is sent through a fixed-mirror Michelson interferometer, built to dynamically measure the change in frequency of the laser output over the course of the pulse. The light exiting the interferometer is measured on the same (HgCdZn)Te detector. The wavelength range ( $\Delta\nu$ , expressed in wavenumbers,  $\text{cm}^{-1}$ ) between two maxima measured by the interferometer is a constant function of the geometry of the light path:  $\Delta\nu = (2\Delta L)^{-1}$  where  $\Delta L$  is the path length difference between the two legs of the interferometer.

A typical example of laser output versus time measured through the interferometer and the evacuated gas absorption cell is shown in Figure 4.28. Also shown in this figure is the time varying current pulse used to drive the laser. The sharp onset and constant amplitude of the ‘top-hat’ current pulse leads to abrupt lasing and nearly-linear frequency down-chirp. There are small reflections at the beginning of the pulse due to imperfect impedance matching in the cables delivering the driving signal to the laser head, these reflections are not atypical of this type of QCL system (Müller, 1999). The smaller modulation on the laser transmission is an interference effect caused by multiple reflections within the beamsplitter. This does not affect the absorption measurements, as it is a consistent feature of the background when it is observed. In Figure 4.28 the fringe spacing of the Michelson interferometer is  $0.1018(5) \text{ cm}^{-1}$  and the total useable spectral range of the pulse is about  $2.2 \text{ cm}^{-1}$ .

To exploit the frequency down-chirp of the QCL it is necessary to fully characterize the temporal and spectral evolution of the laser output. The output of this QCL is set by four controllable parameters: the bulk laser substrate temperature, the driving current pulse amplitude, the driving pulse time duration, and the driving pulse repetition rate. Each affect the chirp rate by controlling the heat dumped into the diode chip.

A high resolution Fourier Transform Infrared (FT-IR) spectrometer (ABB-Bomem, model DA-8) set to emission mode was used to calibrate the laser output wavelength as a function of substrate temperature (temperature tuning). Measurements were made at highest resolution and slowest scanning rate of the Bomem FT-IR spectrometer to ensure the instrument viewed a quasi-continuous light source from the pulsed QCL. The maximum resolution of this instrument is  $0.04 \text{ cm}^{-1}$  and the slowest scan speed is  $0.05 \text{ cm/s}$ . The bulk temperature of the Peltier-cooled QCL was varied over the full suggested range, from  $-30 \text{ }^\circ\text{C}$  to  $30 \text{ }^\circ\text{C}$ . Over this temperature range, the initial lasing frequency of the QCL varied nearly linearly over 4.4 wavenumbers (see Figure 4.29).

Measurements made using the FT-IR spectrometer showed a linear correlation between the spectral width of the DFB-QCL laser output and both the current pulse amplitude and duration. However, the FT-IR spectrometer as used here (asynchronous relationship between FT-IR spectrometer laser sampling fringe frequency and DFB-QCL repetition rate) does not provide

information about the change in laser output wavelength in time during the laser pulse. To observe the effect upon laser output wavelength and intensity of the driver pulse current amplitude and duration, calibration scans were measured on the fixed mirror Michelson interferometer as these parameters were varied over the full recommended operating ranges.

Plotting the calculated frequency spacing between Michelson interference fringes against the measured time between these points in the scan gives a direct measure of the change in frequency of the laser output over time. These fringes are measured in situ with each pulse of the QCL. Figure 4.30 shows the frequency down-chirp of the QCL output as a function of the amplitude of the driving current pulse. The voltage across the laser chip is set to control the current pulse amplitude. The laser was driven with 2000 ns pulses at a frequency of 5 KHz, keeping the duty cycle low (the recommended duty cycle is 3%). The chirp rate is not related to the pulse length at these duty cycles: shorter pulse lengths lie on the same calibration curve as shown in Figure 4.30. If the duty cycle exceeds 3% the chip does not fully cool between pulses and increasing the pulse length or pulse frequency will affect the chirp rate. The damage threshold for the laser quoted by the supplier was  $I \geq 4.0$  Amps. With the driving current amplitude of 3.48 A the thermoelectric cooler could not keep the substrate temperature at the set point and the laser output drifted in frequency over the course of minutes. To avoid damaging the chip our data was taken at lower current amplitudes of 1.80 A, which provided smooth, reproducible chirp behavior and no measured long term drift. As is evident in Figure 4.30, for pulses less than 400 ns the chirp-rate is essentially constant, and the frequency is linearly related to the scan time; however, for longer pulses the non-linear response of the lasing material must be taken into account for proper calibration.

Absorption spectra of acetylene vapor in a single pass absorption cell were measured to test the accuracy and sensitivity of the spectrometer by comparing the measured absorption against the well-characterized standard for the acetylene cross section as reported in the HITRAN database (Jacquemart, 2003).

The absorption band of the ( $\nu_4 + \nu_5$ ) compound bending vibration of acetylene is centered near  $1330 \text{ cm}^{-1}$ , the rotational constant of acetylene is  $1.125 \text{ cm}^{-1}$ . The higher J-value transitions of the P-band are relatively unobscured by absorption from atmospheric gases (e.g.,  $\text{H}_2\text{O}$ ,  $\text{CO}_2$ , etc.). The P(23) rotational line at  $1275.512 \text{ cm}^{-1}$  is measured in this experiment as it is near the peak of the P-branch at the elevated temperatures that is encountered when probing flames.

The transmitted laser intensity is recorded on the photodiode through varying partial pressures of acetylene gas diluted to one atmosphere total pressure in lab air. These transmission spectra are converted to spectral absorbance and plotted against a calibrated frequency scale in Figure 4.31. The central absorption feature in these spectra is the P(23) absorption line of the ( $\nu_4 + \nu_5$ ) compound bending vibration of  $\text{C}_2\text{H}_2$ , the smaller features in the spectrum are currently unidentified.

These absorbance spectra are analyzed in SigmaPlot to extract the linestrength from the data. The spectra are taken in the Beer-Lambert approximation, where the Absorbance is linearly related to the concentration of absorbers (X) and optical path-length L by the absorption cross-section  $\sigma(\nu)$ :

$$A(\nu) = -\ln\left(\frac{I(\nu)}{I_0(\nu)}\right) = \sigma(\nu) \times [X] \times L = S \times g(\nu) \times [X] \times L \quad (4.4.1)$$

In the final relation  $S \times g(\nu)$  is the linestrength of the absorption feature multiplied by a normalized peak function. The absorbance spectra are fit to the multi-Lorentzian function below (eq. 4.4.2):

$$F(\nu) = \sum_i f_i(\nu) = \sum_i \frac{A_i}{\pi} \times \left( \frac{\gamma_i}{\gamma_i^2 - (\nu - \nu_{oi})} \right) \quad (4.4.2)$$

where  $\nu$  is the frequency in  $\text{cm}^{-1}$ , the sum runs over five peaks centered at  $\nu_{oi}$ , and  $\gamma_i$  is the species-specific peak width. There is no constant background off-set as the absorption features fall to zero by the end of the laser pulse scan. The integrated absorbance of each peak,  $A_i$ , contains the linestrength ( $\text{cm}^{-1}/(\text{molecules cm}^{-2})$ ), the concentration ( $\text{molecules cm}^{-2}$ ), and the absorption length (cm):

$$A_{C_2H_2} = \int f_{C_2H_2}(\nu) d\nu = S_{C_2H_2} \times [X] \times L \quad (4.4.3)$$

The normalized Lorentzian peak function is chosen over the Voigt peak conventionally used in laser absorption spectroscopy because both return equivalent fits to the pressure broadened absorbance peaks, and there is evidence that the Voigt profile is not theoretically appropriate in fast frequency-chirped spectra (Duxbury, 2007)

Plotting the integrated absorbance in equation 4.4.3 against the product of the optical length and the acetylene concentration (converted from the partial pressure of gas in the cell) gives a measure of the linestrength parameter that can be compared to the value listed in HITRAN,  $S = 2.218 \times 10^{-20} \text{ cm}^{-1}/(\text{molecules cm}^{-2})$ . The integrated absorbance is plotted against acetylene concentration and pressure in Figure 4.32, showing a linear relationship in fairly good agreement with the predicted absorbance. The scatter about the predicted line is larger than explained by the quality of the fit or the standard deviation of repeated measurements of a sample. The most likely cause of this scatter is imprecise measuring of sample pressure, yielding incorrect predicted concentrations. The gas delivery system that was used to fill the absorption cell had leaks that could not be fully sealed in the course of the experiment, and assigned pressures of the samples could be off by as much as 10%. A linear, least-squares fit of the data, using the path length 16 cm, gives a linestrength  $S = 2.36 (\pm 0.18) \times 10^{-20} \text{ cm}^{-1}/(\text{molecules cm}^{-2})$ , in agreement with the accepted value. With the signal to noise level measured in the individual spectral scans, based on the RMS noise in the baseline of the spectrum, we can accurately measure absorption features with peak heights of  $1.5 \times 10^{-4}$  absorbance units, corresponding to an acetylene concentration\*length product of 2.4 ppM-m (parts per million meter).

The linestrength is dependent on the population difference between the two levels of the specified transition, and as the temperature increases so does the number of accessible initial states according to classical Boltzmann statistics. The population difference between the initial and final states in a transition at a temperature  $T$  is :

$$N'' - N' = \frac{N_{Total}}{Q(T)} \times \exp\left(-\frac{E_i'' hc}{kT}\right) \times \left[1 - \exp\left(-\frac{\nu_i hc}{kT}\right)\right] \quad (4.4.4)$$

where  $E''$  is the initial state energy and  $\nu_i = E' - E''$  is the energy of the transition,  $Q(T)$  is the temperature dependent partition function. Therefore the temperature dependence of the

absorption linestrength is the ratio of the linestrength at the measured temperature and some reference temperature (all HITRAN parameters are all listed at a reference temperature  $T_{ref} = 296$  K).

$$\frac{S_i(T)}{S_i(T_{ref})} = \frac{Q(T)}{Q(T_{ref})} \times \exp\left[\frac{-E_i''hc}{k}\left(\frac{1}{T_{ref}} - \frac{1}{T}\right)\right] \times \frac{\left[1 - \exp\left(\frac{\nu_i hc}{kT}\right)\right]}{\left[1 - \exp\left(\frac{\nu_i hc}{kT_{ref}}\right)\right]} \quad (4.4.5)$$

For the P(23) absorption line measured in this work the linestrength peaks at  $T = 500$  K. As shown in Table 4.5, the linestrength initially increases as temperature begins to rise and the band center shifts to higher J values, but at the peak flame temperature of an acetylene/air flame,  $T \sim 3000$  K, the line has fallen to less than 0.3 % of its initial strength.

### *Imaging Pyrometry*

Particle temperatures are often inferred from light emission using pyrometry. Typically the technique employs the ratio of two isolated spectral regions, and assumes the emitting species is a grey body, i.e., the emissivity is a function of temperature and is independent of wavelength. Separate detectors for each wave length region must be calibrated using a characterized source, and spatial alignment of the detectors must be maintained from calibration to measurement. With a spectrometer and either a calibrated light source or a calibrated detector of known spectral response, one can characterize any digital color camera for use as a calibrated temperature sensor. The output of a digital camera is related to the intensity and spectrum of the incoming light by the intensity response and spectral response:

$$Ci = \Psi_i * G * Dt / F^2 * \int (Si(w) * Iin(w))dw \quad (4.4.6)$$

where  $Iin(w)$  is the intensity spectrum of the incoming light per unit exposure time;  $Si(w)$  is the spectral response function of the  $i$ th channel of the system, which includes the response of the CCD pixel and of the focusing optics; and  $\Psi_i$  is a measure of the linearity of the intensity response.  $Dt$  is the exposure time,  $G$  is a geometrical term (describing the solid angle of light from the observed object captured by the imaging optics), and  $F$  is the aperture size. These last three parameters are equivalent for all channels of the CCD:  $i = R$  (red),  $G$  (green),  $B$  (blue) for standard color cameras.

When the object observed is a thermal emitter that is not reflecting environmental illumination, the intensity spectrum of the incoming light is dictated by the Planck blackbody emission spectrum and the emissivity of the object.

$$Iin(w) = \epsilon(\lambda, T) * I_{BB}(\lambda, T) = \epsilon(\lambda, T) * (2hc^2/\lambda^5 (\exp(hc/\lambda kT) - 1)^{-1}) \quad (4.4.7)$$

Once the spectral responses of the CCD pixels are measured and the linearity of the intensity response is confirmed, the camera intensity can be directly related to the temperature of the observed object. To calculate the temperature based on a single pixel measurement, detailed information about the collection geometry is needed to compute the absolute emitted intensity from the blackbody captured by the camera. However, because these factors are not dependent



on wavelength, by taking the ratio of two pixel intensities we come to a relationship that is only dependant on the temperature and emissivity of the observed object and the intensity response and spectral response of the CCD pyrometer.

$$R(T) = CG/CR \\ = \{ \Psi_{IR} \int (S_r(\lambda) * \epsilon(\lambda, T) * I_{BB}(\lambda, T) dt) \} / \{ \Psi_{IG} \int (S_g(\lambda) * \epsilon(\lambda, T) * I_{BB}(\lambda, T) dt) \} \quad (4.4.8)$$

The intensity response of the CCD must be measured first to confirm linear relation between the pixel output and the illumination. Commercial software additions such as brightness control or color balancing can alter the inherent linearity of the CCD chip response in order to extend the dynamic range of the camera system. These corrections are good for taking video that looks nice, but bad for recording accurate data. To check linearity, images are taken of a white sheet under constant illumination as the exposure time is increased from the minimum shutter time to pixel saturation. For the cameras used here (Vision Research) pixel intensity response is linear until saturation, however the zero exposure time intercept is not zero. This minimum camera black is taken into account when the pixel ratios are computed.

The spectral response of the three CCD channels (blue, green, red) was mapped to determine the color range of each pixel. A Princeton Instruments monochromator was used to measure the spectrum of a continuous light source over the visible wavelength range (380-710 nm) in 5 nm steps. This monochromator was designed to switch between an imaging spectrograph mode with a CCD as detector and a precision spectrometer mode with a PMT as a detector by inserting a turning mirror. The high speed camera being calibrated and a Hamamatsu R928 PMT (with known spectral response) were installed as detectors.

The reported intensity of CCD pixels is a product of input intensity spectrum and all the spectral response functions of the interceding instruments. The spectral response of the camera is measured by comparing the spectrum reported by an instrument of known spectral response to the spectrum reported by each pixel class (R,G, B) of the camera being characterized. Figure 4.33 shows the intensity spectrum of a Tungsten-Halogen light source after being affected by the instrument function of the spectrometer. This spectrum was measured on the PMT, and corrected based on that instrument's spectral response. The intensities of each pixel class are plotted in Figure 4.33 alongside the corrected PMT measurements. Spectra of multiple light sources — a calibrated Ocean Optics Tungsten Halogen source, a 'white' LED flashlight, and an incandescent light bulb — were measured with two 1200 g/mm blazed diffraction gratings — blaze angle 500 nm and 750 nm — to ensure that the spectral response of the camera was not affected by the instrument used to characterize it. The spectral response curves calculated from these measurements are presented in Figure 4.34.

The weaker response and misshapen distribution of the red pixel is an effect of the detector manufacturing process. The spectral ranges of the green and blue pixels are dictated by a filter laid over the CCD substrate. A filter is also used to limit the transmitted light to the red pixel on the blue end of the spectrum, but the deep-red to IR response of the pixel falls off with the decreasing quantum efficiency of the CCD substrate at these wavelengths. The combination of these two signatures produces the unique spectral response of the red pixel. The diminished

capability to measure light in the red to near-infra-red spectrum is unfortunate, as this limits the lowest temperature performance.

Using the measured spectral response curves for the three CCD channels, we calculate the intensity reported by the camera under illumination by a blackbody as a function of its temperature. Plugging the measured spectral response of the green and red pixels into equation 4.4.8, the ratio of green pixel intensity to red pixel intensity (G/R ratio) is calculated as a function of blackbody temperature. The G/R ratio is a smoothly varying function independent of collection geometry, focusing aperture, or (wavelength independent) absorption/scattering en route to the camera; the G/R ratio is solely dependent on the temperature of the blackbody emitter. We plot the temperature of the blackbody against the G/R ratio and fit the resulting curve with a 6<sup>th</sup> degree polynomial to yield a relation for temperature of an object based on measured intensities. A polynomial representation of the temperature as a function of pixel intensity is used instead of an analytical solution because it is easier for the computer during image analysis, where it must perform the calculation for every pixel in every frame of a video several hundred frames long.

This model was used to calculate the temperature of a calibrated blackbody source (Omega Engineering) from still images taken with the camera. The results of these measurements are presented in Figure 4.35. The blackbody had a maximum temperature of 1800 °F (1255 K), limiting the range of our calibration to the minimum temperatures measureable by this platform. The temperatures calculated from the images agree with the temperature set point of the blackbody source to within 5% at lower temperatures, and agree to within 1% above 1200 K.

Table 4.5 Temperature Dependence of the linestrength<sup>a</sup> of the  
P(23) Absorption Line of the ( $\nu_4 + \nu_5$ ) Compound Bending  
Vibration of C<sub>2</sub>H<sub>2</sub>.

Temperature	Linestrength(/10 <sup>-20</sup> )
(K)	(cm <sup>-1</sup> /molecule cm <sup>-2</sup> )
296	2.2180
400	2.9598
470	2.9624
600	2.4464
800	1.4687
1000	0.81326
2000	0.049290
3000	0.0069049

<sup>a</sup> as predicted in the HITRAN database.

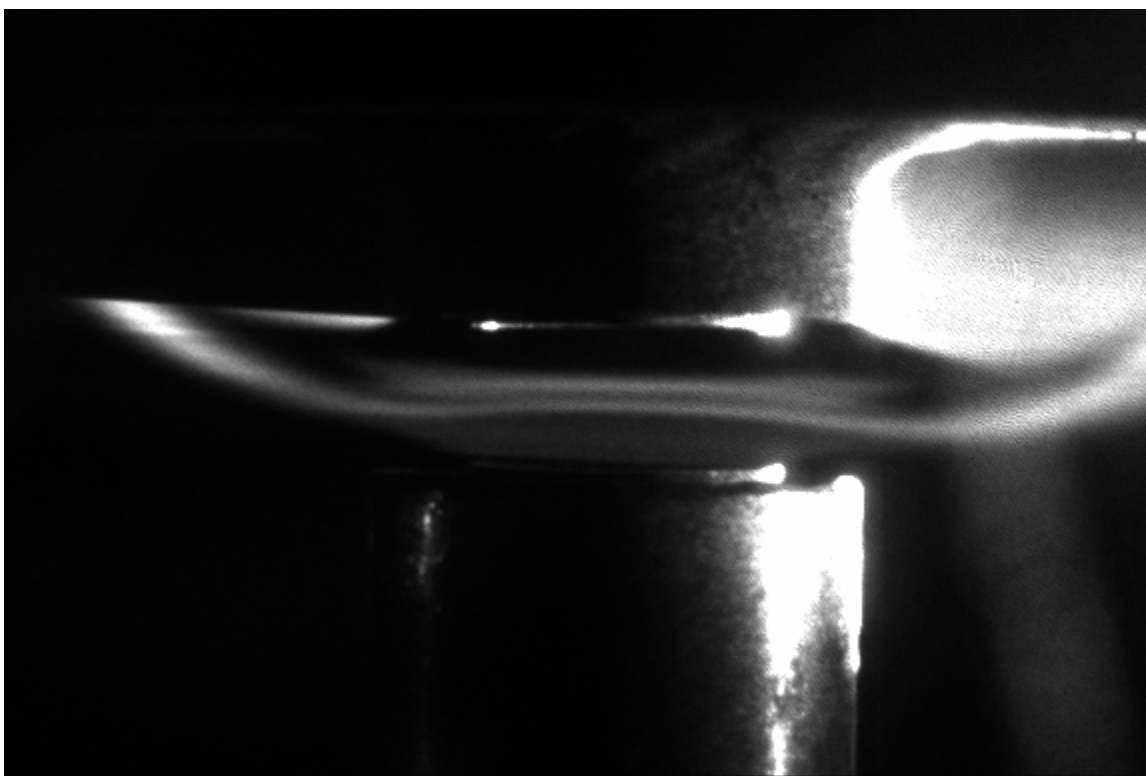


Figure 4.26 An image of an ethylene/m-xylene (5%)/air opposed jet flame.

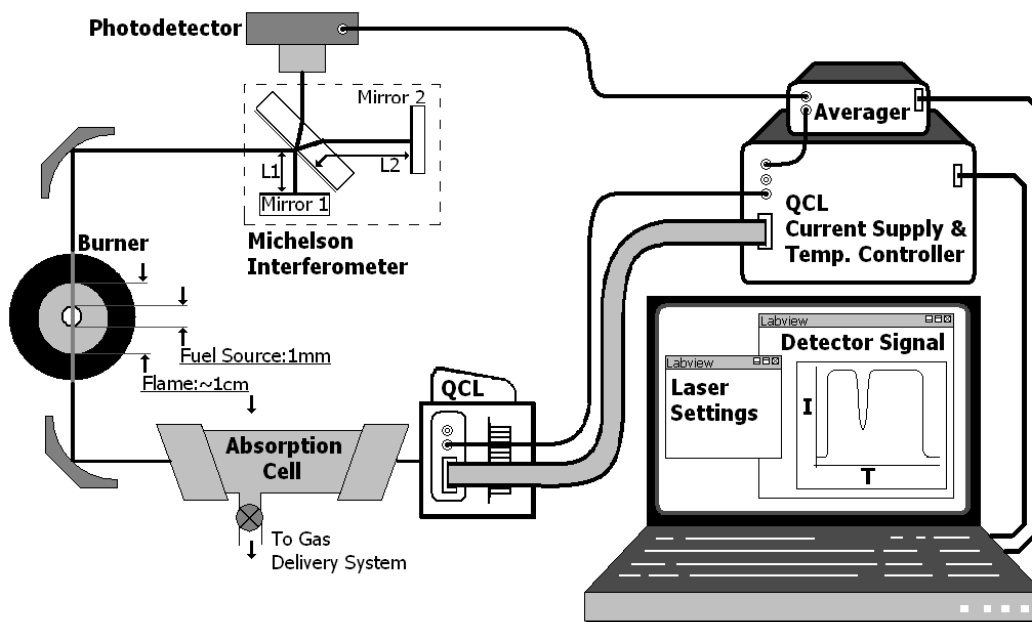


Figure 4.27 A schematic of the experimental setup for acetylene measurement by QCL.

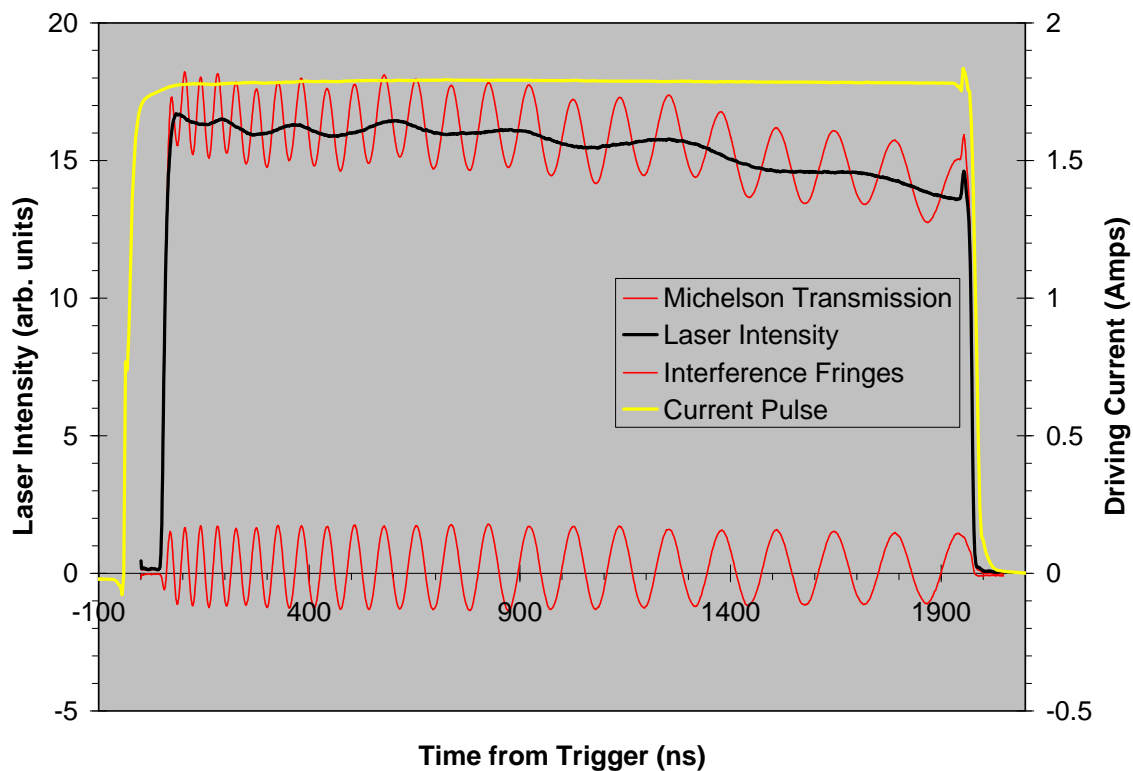


Figure 4.28 A typical example of laser output versus time measured through the interferometer and the evacuated gas absorption cell. Also shown is the time varying current pulse used to drive the laser.

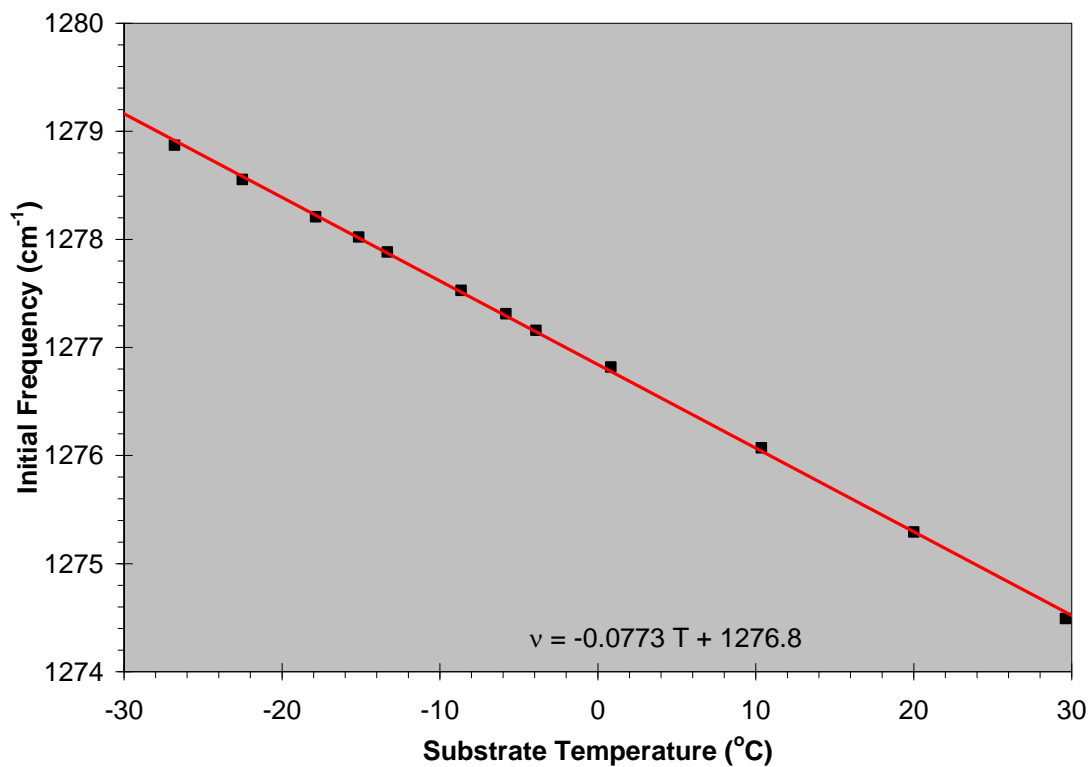


Figure 4.29 Variation of initial lasing frequency with substrate temperature.

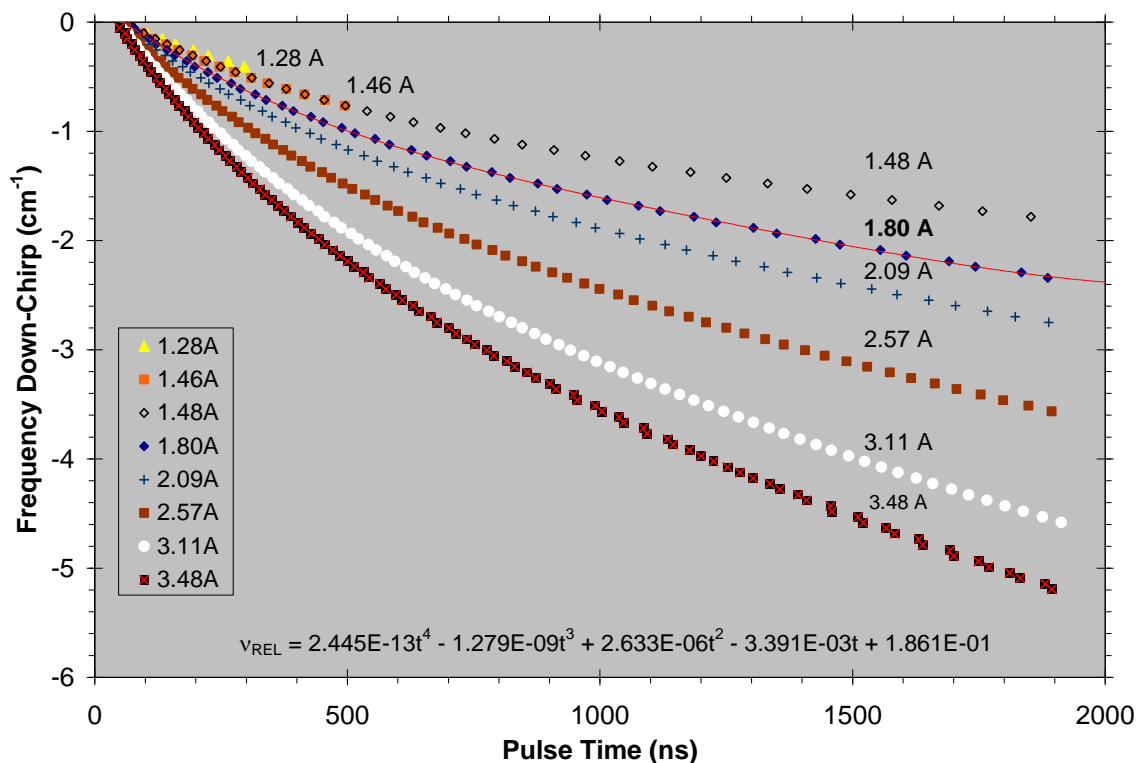


Figure 4.30 The frequency down-chirp of the QCL output as a function of the amplitude of the driving current pulse.

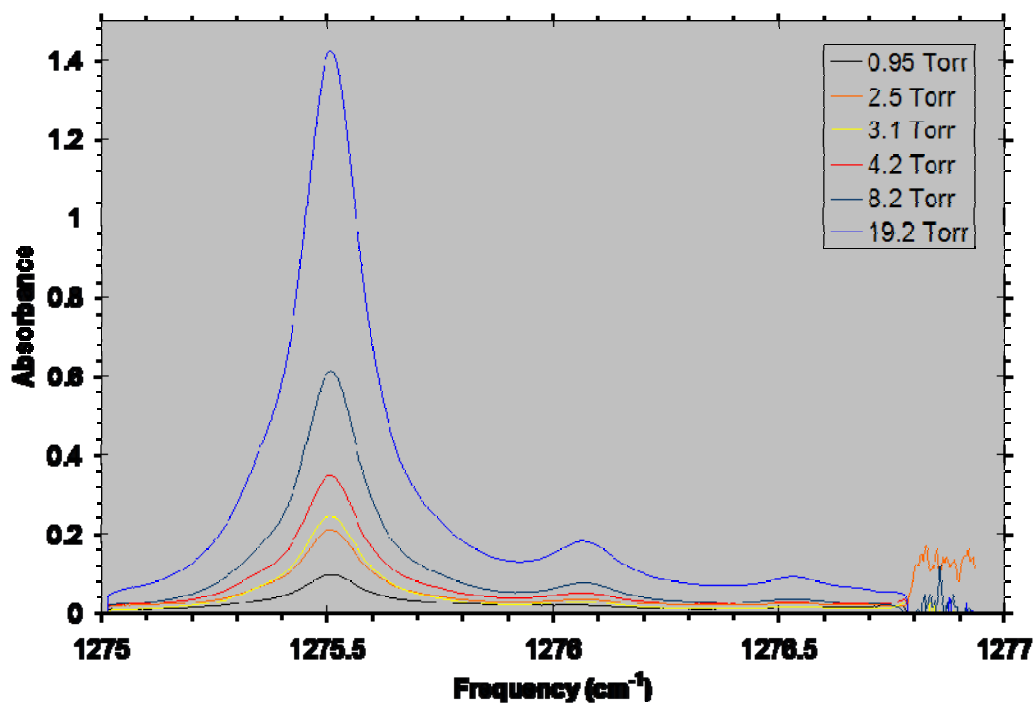


Figure 4.31 Acetylene transmission spectra converted to spectral absorbance and plotted against a calibrated frequency scale.

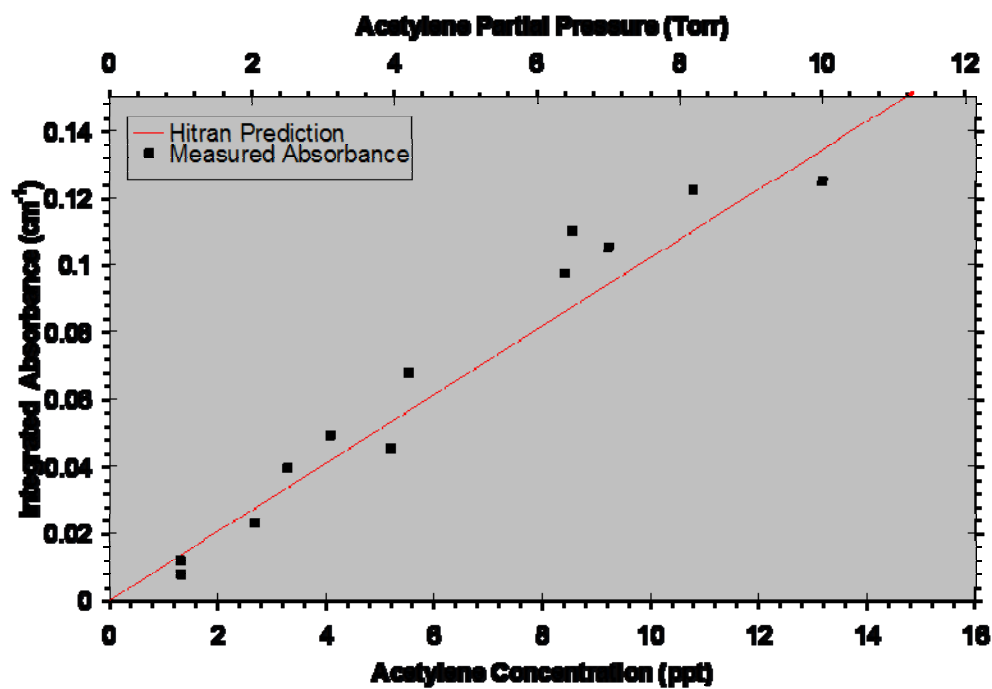


Figure 4.32 Integrated absorbance plotted against acetylene concentration and partial pressure.

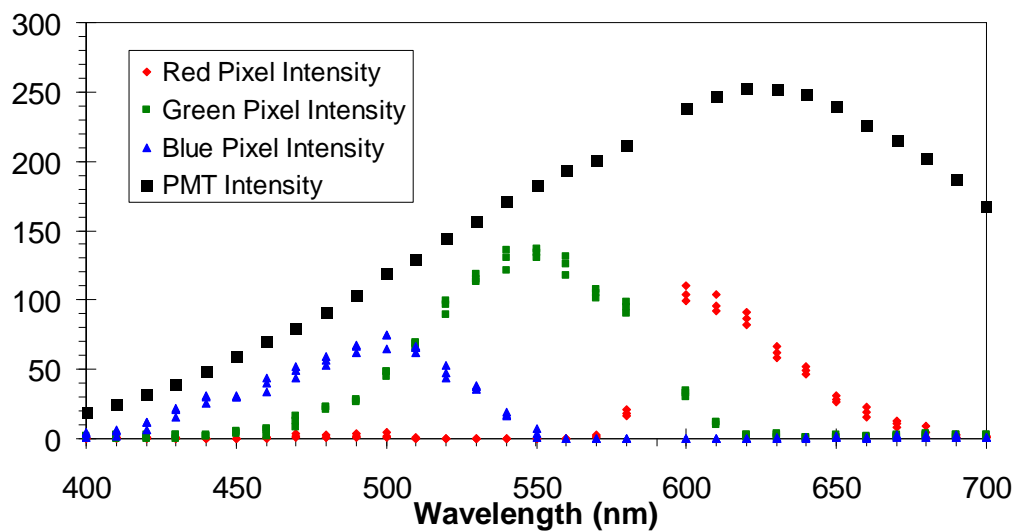


Figure 4.33 The intensity spectrum of a Tungsten-Halogen light source after being affected by the instrument function of the spectrometer.

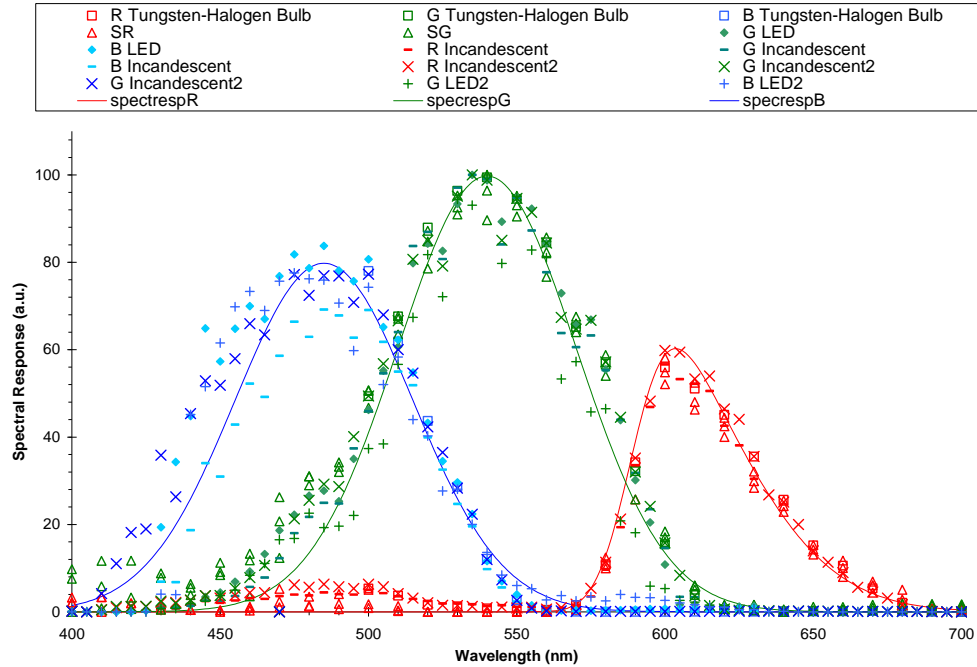


Figure 4.34 Measured spectral response curves for the Vision Research Camera used in these measurements.

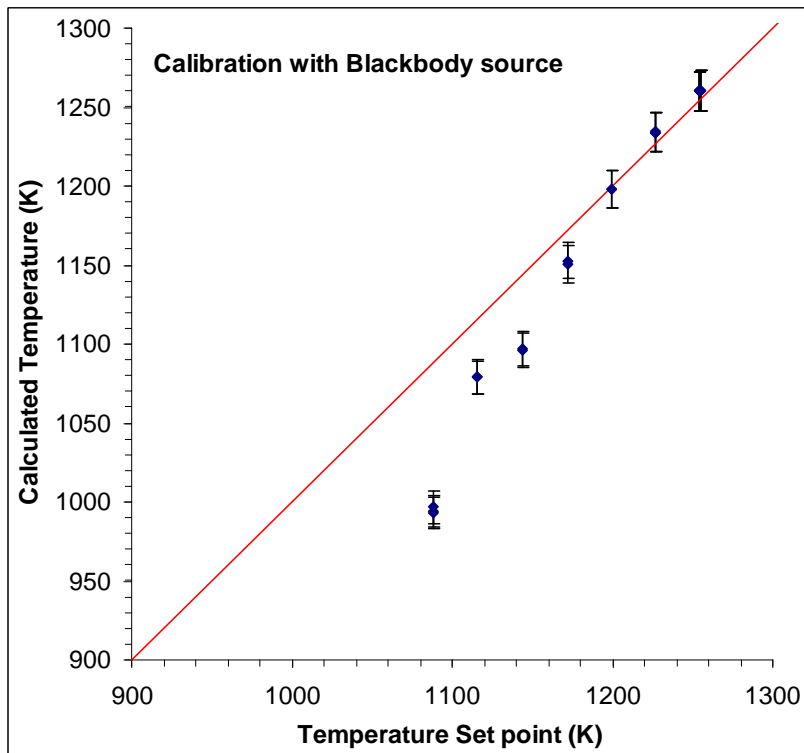


Figure 4.35 Calculated temperature of a calibrated blackbody source (Omega Engineering) from still images taken with the camera versus blackbody set point.

## 4.5 Centerbody Flame

### 4.5.1 Experimental Set-up

The centerbody burner set-up is shown in Figure 4.36 and is similar to that used for previous studies of dynamic flames by Roquemore et al.(1986). The centerbody can be thought of as an annular air stream and a central fuel jet separated by a bluff-body. The centerbody is contained in a vertical wind tunnel designed to provide a smooth flow into the test section. The centerbody is a contoured body with a 46-mm diameter bluff body attached to a 25 mm-diameter shaft with a 7.6-mm diameter gaseous fuel jet located at its center. The configuration is very flexible in that many different types of experiments can be conducted by flowing either gaseous fuel or mixtures of fuel with nitrogen or air from the central fuel jet and air /nitrogen mixtures from the annular jet.

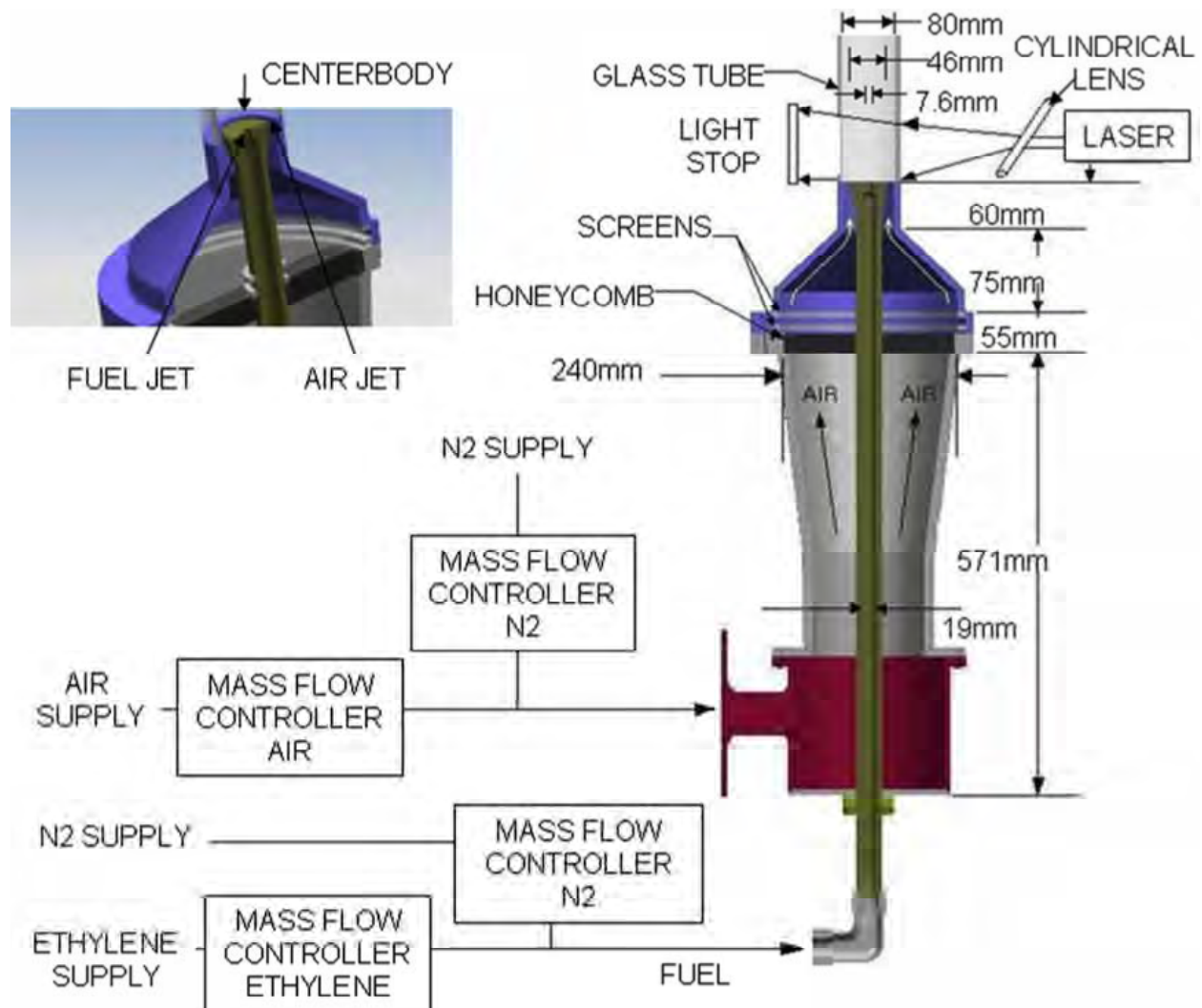


Figure 4.36 Experimental set-up showing flow controllers, test section, and laser-sheet-lighting arrangement. A digital camera (not shown) is mounted normal to the laser sheet and triggered by the laser.



At the start of the program the flow conditioning for the outer flow stream consisted of a diffuser to reduce the gas velocity, a honeycomb structured to further straighten the flow, a set of fine mesh screens to reduce the turbulence, and a flow contraction section that ends at the height of the centerbody face. For most of the program the flow conditioning was enhanced further by the addition of 18,000 4.8mm-diameter metal spheres in the diffuser section, and three perforated metal screens (0.51 mm holes on 1.1 mm centers) followed by a #200 mesh screen (29% open area, 0.06mm wire diameter). The flow conditioning resulted in a laminar flow entering the test section with a relatively flat velocity radial profile and a turbulence intensity of less than 1%. The fuel jet has a contraction nozzle that results in a flat velocity profile and turbulence intensity of about 2%. An 80 mm ID fused silica chimney is symmetrically mounted to the straight section of the wind tunnel so that the outer wall of the test section is smooth.

The annulus stream was always air or an air/nitrogen mixture and the flow rates were controlled using thermal mass flow controllers (Brooks 5853). The ethylene fuel flow rate was also controlled using thermal mass flow controllers (Brooks 5850). The liquid fuels were all measured in the liquid phase before vaporization using a set of syringe pumps (Isco 500D).

The experiments conducted with the centerbody burner can be grouped into three phases. For the first phase, non-premixed or diffusion flame experiments were conducted by flowing air and nitrogen through the outer stream and mixtures of ethylene and nitrogen flowed through the center body. Ethylene was selected as the fuel in these reported studies because a detailed chemistry mechanism exists (Wang, 1997), and because it has been widely used in soot studies (Smooke, et al. 2005). The second phase was a study of partially premixed ethylene and air through the centerbody and air flow through the outer stream. The third phase used vaporized liquid fuels with air flow through the outer stream. The range of the flow rates used in each phase of the experiments are listed in Tables 4.6 to 4.8. Further details of the experimental test conditions will be discussed in the Centerbody Flame Result (Section 5.5).

Table 4.6 Mass Flow Rates Used in Experiments with Air/N<sub>2</sub>/Ethylene Flames.

Stream	Compound	Flow (g/min)
Outer Stream	Air	160 to 300
	N <sub>2</sub>	0 to 140
Fuel Stream	C <sub>2</sub> H <sub>4</sub>	1.5 to 4.2
	N <sub>2</sub> Premix	0 to 2.2

Table 4.7 Flow Rates for Partially Premixed Ethylene and Air Flames.

Stream	Compound	Flow Rate(g/min)
Outer Stream	Air	300
Fuel Flow stream	Ethylene	0.59 to 4.0
	Premix Air in fuel	0 to 24

Table 4.8 Mass Flow rates for Vaporized Liquid Fuel Flames.

Stream	Compound	Flow Rate (g/min)
Outer flow	air	300
Fuel stream	Dodecane	0.75 to 1.5
	23%M-xylene- 77%Dodecane	.77 to 1.55
	JP-8	0.80 to 1.6
	Heptane	0.68 to 2.8

In order to study the combustion of liquid fuels, the gaseous fuel supply in Figure 4.36 was replaced by a liquid fuel vaporizer that was built for the experiments. The vaporization system design presented several design challenges to continuously supply completely vaporized liquid fuel without coking or thermally cracking the fuel. The approach used for vaporization was flashing of a supercritical fuel to a lower pressure, which allowed the instabilities associated with the two phase flow to be avoided. The fuel was first pumped to supercritical pressures, using a set of syringe pumps, before heating it to supercritical temperatures. The fuel then flowed through a small orifice where it was flashed at nearly constant enthalpy from supercritical pressure to the rig pressure, and was then transported as a vapor to the rig through heated tubing. Oxidative coking was avoided by sparging the fuel with  $N_2$  before the experiments to remove dissolved oxygen. Pyrolytic coking was avoided by restricting the temperature in the fluidized bed to less than 750 K.

With the low fuel flow rates used in the experiments there was little thermal capacity associated with the fuel flow. Therefore, excessively hot spots will tend to overheat the fuel while cold spots will tend to cool the vaporized fuel and cause condensation. To address these concerns, a commercially-available fluidized bed, using nitrogen as the carrier gas was used to heat the fuel before vaporization. The fluidized bed convectively heats objects placed in it to a near uniform temperature. A schematic of the vaporizer apparatus is shown in Figure 4.37. The fuel and the nitrogen are heated by flowing through small diameter tubing (fuel tube length = 3.7 m, ID = 0.56 mm) that is wound into a multi-loop coil and immersed in the fluidized bed. A photograph of the tubing is shown in Figure 4.38. The fluidized bed provides an almost uniform temperature control for the outside surface of the tubing containing fuel, preventing condensation at cold spots and pyrolysis of the fuel at hot spots. The temperature of the fuel before flashing was increased enough that it would remain a vapor after flashing to a lower pressure, yet not high enough that it decomposed before reaching the burner. The fuel was heated above the critical point ( $\sim 680$  K for JP-8) and maintained below temperatures that pose concern for pyrolytic coking reactions ( $\sim 750$  K for JP-8). To allow the fuel to be pressurized upstream of the vaporizer chamber, a small orifice (typically 40-100  $\mu\text{m}$ ) was laser-drilled into the end of a piece of tubing to act as a nozzle for the vaporizer. The ability to also flow  $N_2$  to the fuel steam was also incorporated in the design. For cases where nitrogen was added to the fuel, it was added immediately downstream of the fuel orifice in the vaporizer tee to efficiently mix the  $N_2$  with the fuel vapor.

After vaporization the neat fuel or fuel/N<sub>2</sub> mixture was maintained at a temperature above its dewpoint by heated lines. The overall fuel mass flow rate was typically between 0.7 and 3 grams/minute. Because of the low thermal mass of the fuel, insulation alone would not prevent enough heat loss to avoid condensation, so the lines were heated. To avoid overheating the lines with an electrically-heated approach, the lines and the centerbody were maintained at elevated temperatures by the use of heated gas (air or nitrogen) that flowed on the outside of the lines to act as a shield for heat loss. A sketch of the transfer line is also shown in Figure 4.37.

Figure 4.37 Vaporizer Concept for Centerbody Flame Rig.

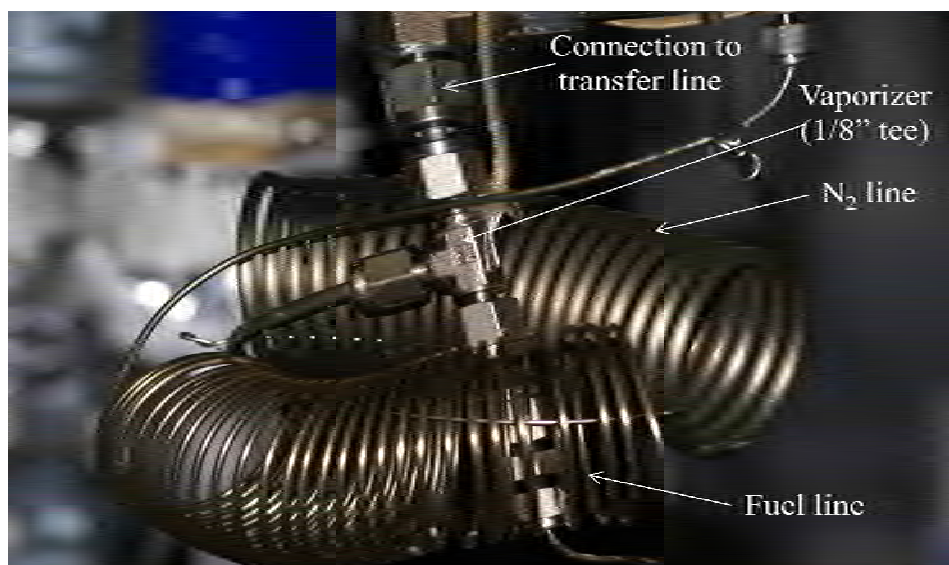


Figure 4.38 Photograph of the Vaporizer Tubing and Tee.

The vaporized fuel flowed through the transfer line (~2 m long) before reaching the bottom of the centerbody rig. The centerbody shaft is roughly 1 m long and also required shielding with a convective flow on the outer layer to maintain the temperature of the fuel above the dew point. Figure 4.39 shows the design of the internal flow for the centerbody. The internal nitrogen flow for the bluff body is a welded construction, which allows heating up to the tip of the body, while avoiding leakage. A co-annular flow of heated  $N_2$  was used to maintain the temperature of the fuel above the dew point. The spent shield  $N_2$  gas exited through the bottom of the rig where it did not interfere with the experiment. The temperature of the fuel at the centerbody nozzle was not directly measured, but was estimated from the temperature of the surrounding shield gas which was maintained at a temperature above the dew point temperature (~570 K) for JP-8. A photograph of the overall experimental setup is shown in Figure 4.40.

The vaporizer system was shown to reliably vaporize fuel for extended experiments (several hours duration). Coking was a concern in the design, but the critical 50  $\mu\text{m}$  orifice remained unblocked through the entire study. GC-MS analysis of the vaporized fuel jet at the burner showed little cracking of both JP-8 and dodecane fuel.

Figure 4.39 Centerbody Fuel Tube Heat Shield Design.

Figure 4.40 Fuel Vaporization System for the Centerbody Burner.

#### 4.5.2 Experimental Procedure

For experiments using gaseous fuels the flow controllers were allowed to warm up for an hour before starting the test. The flow rates of air/nitrogen for the outside stream was established and then the fuel flow was started. Ignition of the fuel was accomplished using a spark igniter. After ignition of the flame, the igniter was moved away from the flame and the quartz exhaust stack was placed on the top of the rig. Different flames were each established by adjusting the flow rates at the controllers. In the event of excessive soot accumulation on the bluff body the quartz stack was removed and the soot was gently scraped off. Usually the soot removal could be accomplished without shutting off the flame.

For experiments with liquid fuel flow, the fuel was first sparged with nitrogen to remove dissolved oxygen. The fuel was then loaded into the syringe pumps. Nitrogen flow was established through the fuel line before turning on the heated fluidized bed and transfer line heaters. Approximately 2 hours were required for the fluidized bed to reach operating temperature. After the fluidized bed reached operating temperature the liquid fuel flow to the rig was started using the syringe pumps and the nitrogen in the liquid fuel line was turned off. Ignition of the fuel was accomplished using a spark igniter in the same way it was for the gaseous fuels. Flow rates of liquid fuels and nitrogen and air flows were then adjusted to set the desired flame conditions. At the end of the experiments the fuel was turned off at the syringe pumps and nitrogen was used to continuously purge the residual fuel from the lines and nozzle as the fluidized bed cooled off.

#### 4.5.3 Diagnostic Methods

##### *Sheet Lighting and Flame Photography*

A YAG laser and cylindrical lens were used to form a laser sheet for visualizing the soot characteristics of the flames. Mie scattering images from soot particles were collected with a digital camera mounted normal to the laser sheet. Images, of a planar, gridded target located in the plane of the light-sheet, were collected before and after each experiment. The gridded target provided a way of locating the annular and fuel jets on the flame and Mie scattering images. Most of the flame images were obtained using a commercial grade DSLR camera (SONY Alpha 100) and synching off of the previous laser pulse with the aid of a delay generator. With this approach it was possible to use camera shutter speeds up to 1/500s while capturing the laser pulse. A photo of the rig during a Mie scattering experiment is shown in Figure 4.41

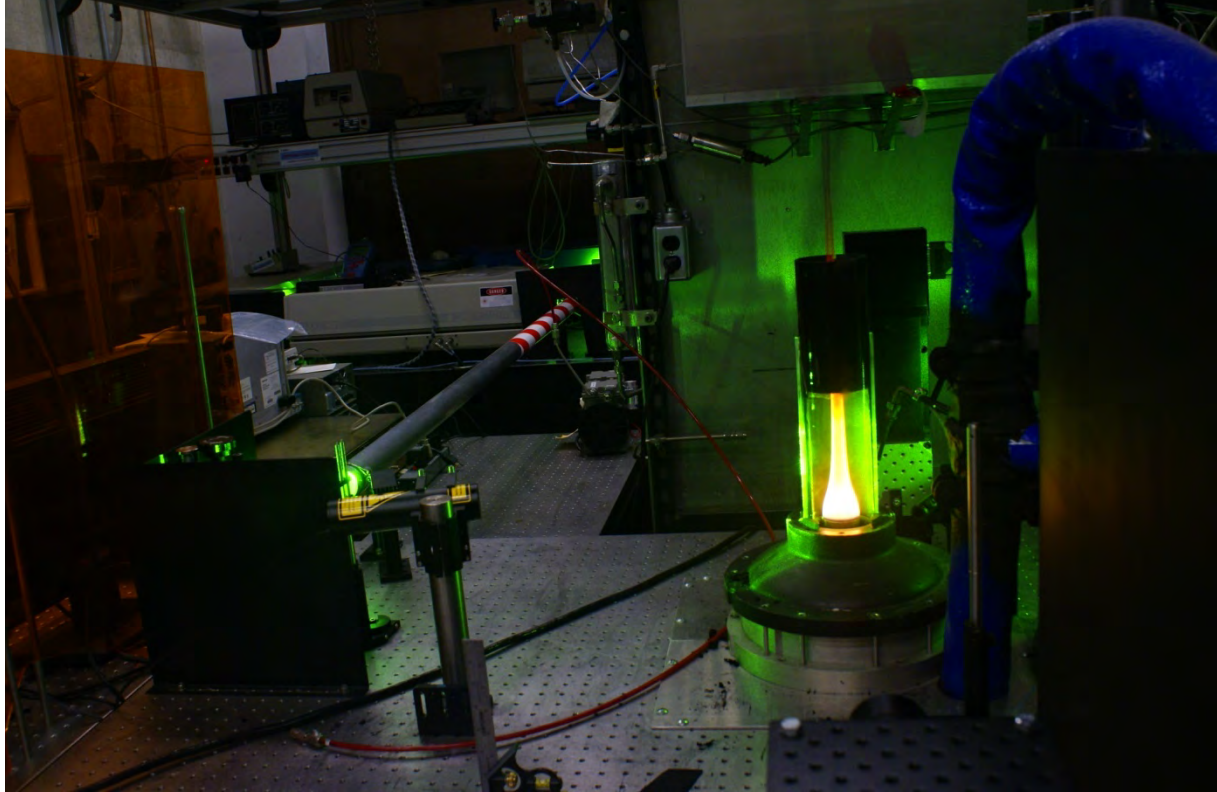


Figure 4.41 Centerbody Flame During the Mie Scattering Experiment.

The use of sheet lighting in a rig with cylindrical optical access presented several challenges. During early phases of the work the 80 mm-diameter glass stack was used but was found to cause problems with scattering. Attempts were made to operate the burner without the stack but the flames were not stable because of room air currents. Another approach attempted was to use a larger rectangular stack, but it was found that the corner effects altered the flame. Narrow slits were cut into the cylinder to allow the light sheet to freely pass through the cylinder without reflections at the walls, but air entrainment through the slots was shown to alter the flame shape. Finally, small windows were used to cover the slits and cut off secondary air flow into the stack. The windows provided a normal surface for the laser sheet to pass through while reducing reflections. A photograph of the stack showing the windows is shown in Figure 4.42 along with photographs showing the images made possible by the use of the of the slot windows.

Figure 4.42 (A) Photo of the Centerbody Stack and Windows. (B) Typical Photograph Showing Vertical Reflection Artifacts Using Plane Quartz Cylinder. (C) Reflection Artifacts eliminated with design shown in A.

### *Infrared Flame Imaging*

Planar radiation intensity measurements of the flames were acquired using an infrared camera (FLIR SC4000). The camera was mounted with a  $4.38 \pm 0.1 \mu\text{m}$  narrowband filter. The integration time and sampling frequency were 0.4 ms and 670 Hz respectively. The camera was aligned perpendicular to the flame axis and mounted ~56 cm from the burner center to the camera lens in the horizontal direction. The spatial resolution was  $0.54 \text{ mm}^2$  at the flame center for each pixel on the focal plane array. The center of the 25 mm lens was positioned ~80 mm above the burner surface in the vertical direction. This resulted in a nominal view angle of  $10^\circ$  (with respect to the horizontal) for a line of sight passing through the center of the burner surface. The computed infrared images neglected the effect caused by the small view angle. The infrared camera measures radiation intensity along line of sight paths through the flame.

### *High Speed Imaging*

High speed movies of the flames were also captured for several flames using a high-speed Phantom v7.1 camera. This CMOS camera is monochrome and is capable of capturing 4800 frames per second (fps) at a full resolution of 800x600 pixels. In the current experimental setup,



images were collected at 500-2500 fps, with a maximum resolution of 768 x 260 pixels that encompasses 361 mm x 132 mm.

### *Laser Induced Incandescence (LII)*

Laser induced incandescence (LII) imaging was utilized to monitor changes in the soot distribution with concomitant changes in the flame test conditions in an effort to test the validity of flame profiles derived from soot modeling. In this effort, a six inch tall, focused laser sheet with a width of 500  $\mu\text{m}$  was produced from the second harmonic (532nm) of a Q-switched Nd:YAG laser and directed exactly through the center of these approximately axis-symmetric flames whereby the soot within the volume of the laser sheet was heated to incandescence during the duration of the laser pulse. A CCD camera (1024x1024) with a gated image intensifier was positioned perpendicular to the propagation direction of the laser sheet and synchronized to collect the incandescence. A 55 mm focal length macro focus lens (f/2.8) was mounted to the camera to yield a field of view of 12.5 cm from the center body surface to the top of the flame. A 50 mm diameter, 455 nm short-pass filter was mounted to the front of the lens to prevent the undesirable contribution of laser induced fluorescence from the  $\text{C}_2$  Swan bands in conjunction with a 50 mm diameter notch filter (532 nm) to insure the camera was blind to scattering of the laser sheet that may not be completely eliminated by the short-pass filter. The LII signal is independent of the laser energy for fluence in excess of  $200\text{mJ}/\text{cm}^2$ , however excessive fluence will vaporize the soot, Schulz (2006). The fluence was maintained at  $220\text{mJ}/\text{cm}^2$  for the full height of the sheet.

Qualitatively, the processed LII images compare favorably with the images derived from the soot modeling, however it is of interest in the study of these flames to also determine the volume fraction of the soot for a range of heights from the center body surface by calibration with line-of-sight soot extinction. The extinction of a helium-neon (HeNe) laser beam (632 nm/1Mw) by the flame for each condition and height was measured by collecting the beam with an integrating sphere fitted with a photodiode. A narrow band pass filter (632 nm) was mounted to the entrance of the sphere to allow only extinction of the HeNe laser beam to be detected. The integrating sphere was employed to destroy the mode profile of the laser and compensate for beam deflection due to changes in refractive index in the flame that would otherwise lead to alignment challenges.

For soot particles that meet the Rayleigh size criterion, the soot extinction coefficient ( $\alpha$ ) can be determined from the Beer-Lambert-Bouguer law:

$$\frac{I}{I_o} = e^{-\alpha l}$$

Where  $l$  is the path length through the flame. The soot volume fraction ( $f_v$ ) is then determined from Santoro (2002):

$$f_v = \frac{\alpha \lambda}{6\pi E_{(m)}}$$

Where the dimensionless value of the soot absorption function ( $E_{(m)}$ ) from Schulz (2006) is 0.3 ( $\pm 0.06$ ) and  $\lambda$  is the laser wavelength (532 nm) in units of meters. The line-of-sight laser

extinction data collected for this flame study is currently under scrutiny to determine if the results can be utilized to yield absolute values of soot volume fraction.

## 5.0 Results

### 5.1 Shock Tube

#### 5.1.1 Ethylene Combustion at Elevated Pressures

Ignition delay times were measured in all experiments to facilitate the comparison between different sets of conditions. The end wall pressure profiles of some experiments covering a wide range of conditions of the current work are given in Figures 4.7 and 4.8.

The ignition delay times were modeled using the SERDP\_C<sub>2</sub>H<sub>4</sub> model. Closed homogeneous batch reactor model of Chemkin-Pro was used for these simulations with the assumption of homogeneous adiabatic conditions and constant volume constraint. For fuel-rich conditions ( $\Phi=3$ ), the optimized USC Mech II model (Wang, 2007) was used in conjunction with an in-house modeling code developed by Wang, et al. The optimization was based on quantification of the kinetic rate parameter uncertainty using spectral expansion techniques (Sheen et al., 2009). In all conditions, the model ignition delay varied little with criteria based on CH\*, temperature inflection point or pressure rise, etc., which was also later confirmed by experimental results. Temperature inflexion point based criterion was chosen for computing model ignition delay times in stoichiometric conditions. For fuel-rich conditions ( $\Phi=3$ ), CH\* onset was chosen as the ignition delay criteria.

Figures 5.1 through 5.4 represent fuel-rich conditions:  $\Phi=3.0$ , with a high concentration of ethylene/oxygen in diluent argon: 3.5% C<sub>2</sub>H<sub>4</sub> 3.5% O<sub>2</sub> 93% Ar, (vol), at pressures ~ 2, 10 and 18 atm. The pressure profiles (see Figure 4.7), shows strong oscillatory pressure peaks (at temperatures above 1100 K, spikes gradually becoming sharper with temperature rise), indicating strong ignition or a transition to detonation-like process (Oppenheim, 1972, 1985 and Fieweger, 1994). In the low pressure runs (see Figure 4.7 for 2 atm experiments), the sudden increase in pressure occurs less rapidly, but it is distinctly observable for moderate to high temperatures. Strong ignition with transition to detonation-like process occurs when large volumes of un-burnt gases are ignited homogeneously giving rise to shock waves in the test chamber. This differs from the mild, deflagrative self-ignition process, which commences due to hot spots developed from inhomogeneities arising from temperature, radical concentration, etc. in the test gas, leading to one or several flame kernels (Fieweger, 1994). Mild ignition gives rise to more or less smooth pressure profiles only. For highly concentrated mixtures like these (93% dilution with argon), strong ignition was expected due to the large heat release associated with such mixtures. No effect of detonation on ignition delay was considered, as it occurred after the onset of ignition (Brown, 1999). For low temperatures (roughly below 1400 K), the post-reflected shock pressures were found to be nearly constant. For higher temperatures, a gradual increase in post-reflected shock pressures was observed over the dwell time, which points to boundary layer buildup behind incident shock waves at higher temperatures, a common phenomenon noticed for relatively small internal diameter (ID) shock tubes at low pressures conditions (Petersen, 1998 and Davidson, 2004). The boundary layer causes the core pressure and temperature of the reflected shock to rise as it constricts the available cross-sectional area for its propagation. Due to very short ignition delay times (a few hundred to tens of microseconds

over a dwell time of  $\sim 8$  ms) at these temperatures it was assumed that the impact of boundary layer would be minimal on the ignition delay measurements. In a recent work on iso-octane oxidation, Oehlschlaeger et al. (2008) used a 5.7 cm ID shock tube and compared the results with a previous work by Oehlschlaeger et al. (2004) performed with a 14.1 cm ID shock tube. They found excellent agreement at 1 atm conditions, thereby validating the suitability of a relatively small ID shock tube for such work. In the current work using a 5.08 cm ID shock tube, we expect similar good results with no impact from boundary layer effects at our relatively high pressure conditions ( $P > 2$  atm in all cases).

The dwell times were kept in the 7.55 to 7.85 ms range for all the experiments by adding argon to the driver helium gas (Kahandawala, 2004). The amount of argon in the driver gas mixture typically varied from 14.6 to 17.6% between 1538 and 1094 K at 2 atm; 16.3 to 20.6% between 1580 and 1063 K at 10 atm; and 15.2 to 19.8% between 1650 and 1090 K at 18 atm conditions. Slight over- or under-tailoring was observed in some experiments, but reasonably flat pressure profiles were obtained in the majority of experiments. Heat transfer effects at the shock tube walls for longer test times ( $t_{\text{dwell}}$  up to 20 ms) were investigated by Frazier et al. (2007) and found to be negligible. Frazier et al. state that for most shock tubes, the heat losses to the wall should not be a problem, and that even with such long test times, the deviations from isothermal assumption are minimal at high pressures. In the current study, all such effects were considered inconsequential ( $t_{\text{dwell}} < 8$  ms in all cases of current work), though no separate calculations were attempted.

Ignition delay measurements with the new diagnostic setup ( $\text{CH}^*/\text{OH}^*$  based, in conditions  $P \sim 10$  & 18 atm,  $\Phi = 3$ ,  $\text{Ar} = 93\%$  only) agreed very well with the original data (visible light based). The difference between  $\text{OH}^*$  and  $\text{CH}^*$  measurements was found to be small (typically within  $\sim 10\%$  over most of the temperature range), with no definite pattern of one being greater or smaller than the other. Hall, Rickard, and Petersen. (2005) noticed a relatively shorter ignition delay from  $\text{OH}^*$  emission than  $\text{CH}^*$  especially at high temperatures, and concluded that the data could be deemed consistent if the agreement is within 20%, considering the inherent shock tube experimental data scatter. In another study, Yoshizawa et al. (1973) used total visible emission to quantify ignition delay in ethylene oxidation. They also obtained  $\text{OH}^*$  chemiluminescence data, but reported no difference between the two parameters. Prior to the strong ignition pressure rise,  $\text{OH}^*$  and  $\text{CH}^*$  emission was also observed in low temperature experiments (mostly at temperatures below 1200 K). This was also previously observed in several studies (Drummond, 1968 and Cadman, 2002) as a characteristic of energy release during mild ignition regime. A change in slope of the  $\log \tau$  versus  $1000/T$  (see Figures 5.7 through 5.9) plot indicates a decrease in global activation energy below approximately 1125 K. This indicates a change in controlling chemistry approximately at this temperature which was also observed in previous studies (Suzuki, 1973 and Cadman, 2002).

The simulated delay times computed using the optimized USC Mech II (Wang et al. 2008) model show a very good agreement at high pressures ( $P \sim 10$  and 18 atm) with the experiments. At low pressures ( $P \sim 2$  atm), the optimized model over-predicts the ignition delay times in low temperature ranges (less than 1250 K). The SERDP\_C2H4 model, which was based on an un-optimized USC Mech II model (Wang, 2007), shows good agreement at low pressures throughout the temperature range, but at high pressures ( $P > 8$  atm), the model under-predicts the

ignition delay times. As shown in Figure 5.4, the impact of pressure on ignition delay times was not discernible for this mixture composition. Slightly longer ignition delay times could be ascertained for 2 atm conditions, compared to those at 18 atm, if the scatter was ignored. For 18 atm, typical ignition delay (based on visible light emission) varied from approximately 4.4 ms at 1000 K to 14  $\mu$ s at 1590 K.

Figure 5.5 captures the ignition delay times at  $\Phi=1.0$ , (1.75%  $C_2H_4$  5.25%  $O_2$  93% Ar) at pressures of 2 and 10 atm. A sudden spike in the pressure pulse was observed in most of the experiments (see Figure 4.7), as in  $\Phi=3$  experiments with same amount of Ar dilution (93%), confirming the transition of mild ignition to detonation-like process. For the above mixture, the simulated ignition delay times calculated using the SERDP PAH 0.1 model were in good agreement in these conditions at low pressures ( $\sim 2$  atm, see Figure 5.6) but were shorter for high pressures ( $\sim 18$  atm, see Figure 5.4). Figure 5.4 shows that there is not a discernible difference between ignition delay times at the two pressures at this equivalence ratio ( $\Phi=1.0$ ). The effect of equivalence ratio ( $\Phi=1$  and 3) was found to be negligible at pressures of 2 and 10 atm, as shown in Figures 5.6 and 5.7, respectively.

The observed ignition delay times show little variance over the ranges of pressure and equivalence ratios tested using 93% argon dilution. These results prompted us to further investigate the effects of argon dilution on ignition delay times. Additional experiments were conducted with different argon dilution percentages covering a temperature range of 1100 to 1700 K, at pressures of  $\sim 2$ , 10, and 18 atmospheres and at an equivalence ratio of  $\Phi=1.0$ . The argon content of the fuel mixture was increased from 93 to 96% (vol) for first set of experiments and then to 98% (vol) for the second set of experiments. The ethylene and oxygen content of the test section was adjusted accordingly to give an equivalence ratio of 1. In the majority of these experiments, visible broadband emission was used to measure ignition delay; however, for a few mixtures,  $CH^*$  chemiluminescence emission-based measurements were also obtained. The pressure profiles (see Figure 4.8) show a reduced yet observable spike in pressure pulse in most runs at 96% argon dilution, especially at high pressures; however, the spike in pressure profile is largely unseen in all 98% argon runs. This suggests that of DDT (deflagration to detonation like process transition), phenomena exists even at the 96% argon dilution. Brown and Thomas (1999) and Kalitan et al. (2005) did not observe DDT at 96% argon dilution level. No trace of strong ignition was found in very dilute mixtures (Ar=98%). The heat released during ignition was not large enough to give rise to strong ignition and the mild ignition regime prevailed. Figures 5.8 and 5.9 show the effect of pressure on ignition delay for mixtures with 98% and 96% dilution with argon, respectively.

At 98% argon content and equivalence ratio of 1.0, the ignition delay times measured at low pressures were substantially longer than the ignition delay times observed at high pressures (see Figure 5.8). With increase in pressure (at pressures of 10 and 18 atm), the difference in ignition delay times became less pronounced. This difference due to pressure change was not clearly observable when argon content was 93 or 96% (Figures 5.4 and 5.9). A change in slope of the trend lines of ignition delay times at respective pressures, on a  $\log \tau$  versus  $1000/T$  plot confirms that global activation energy was lower at lower pressures (Figure 5.8). Figures 5.10 through 5.12 show the impact of dilution on ignition delay at 2, 10 and 18 atm pressures, respectively. Figure 5.10 shows that significant differences exist between delay times at different dilutions at 2

atm conditions, with the highest dilution leading to longest delay times. For 10 atm conditions, only at 98% dilution, the delay times look longer than those at 96 or 93% dilution, the latter two being very close in magnitude. At 18 atm (see Figure 5.12), the difference in ignition delay times that could be attributed to dilution completely goes away and the delay times are indistinguishable for different argon dilutions. The simulated ignition delay times from the model were found to be in reasonable agreement at low pressures at all dilution levels for  $\Phi=1.0$ . At high pressures, the model under-predicts the magnitude of ignition delay time toward the lower temperature range (at temperatures below 1350 K).

The results of this study are compared with literature data in Figures 5.3 through 5.5. The comparison shows that at higher dilutions (Ar=98 & 96%) and low pressures ( $P \sim 2$  atm), the delay times are very sensitive to even small changes in pressure (see Figures 5.3 and 5.4). The way ignition delay is defined also influences the ignition delay magnitude. For example, at  $\Phi=1.0$ , argon 96% (vol) (see Figure 5.13), Hidaka (CH\* onset, side wall measurement), Horning (CH\* peak, side wall measurement) is in very good agreement with data from our study (CH\* onset, end wall measurement). However, CH\* onset-based data is up to 30% shorter than visible emission onset data of our study at high temperatures. Horning et al. (2001) have measurements at two pressures, ( $P \sim 1$  & 2 atm). Their 1 atm data points are clearly higher on the plot than 2 atm values, which fall very close to our CH\* data. Since their side wall measurements of CH\* peak should be closer to CH\* onset end wall measurements, this agreement looks very good. Brown and Thomas (1999) (CH\*, onset at end wall) data shows shorter delay times at low temperatures though the agreement is good at moderate temperatures. The reason for the small disagreement may be due to systemic differences, as they have quite a lot of scatter under these conditions. The results of this study also agree well with Kalitan et al. (2005). The sensitivity of ignition delay times to small changes in pressure at low pressures clearly explains the variation observed in their data set at low pressures. Correlation of Baker and Skinner (1972) was used to obtain delay times in our conditions, and their actual data points at  $P \sim 3$  atm were also plotted. Agreement of ignition delay times obtained from Baker and Skinners' correlation with visible emission data (onset) of the present study is good at high temperatures, but at low temperatures, the correlation predicts longer delay times. This can be attributed to their definition of ignition delay employing OH\* maximum emission-based criterion. The actual data points of their work show a shorter ignition delay, which is understandable because those were obtained at a higher pressure of 3 atm. Correlation of Colket and Spadaccini (2001) is also plotted in the same figure, which predicts slightly longer delay times than Baker and Skinner's correlation, under conditions of the current study at higher temperatures. One reason could be that they have not considered dependencies of ethylene or argon in the correlation and their oxygen dependency is slightly higher (-1.2) than what has been reported in literature.

As shown in Figure 5.15, at  $\Phi=1.0$  with argon dilution 98% (vol), the results of this study (visible emission onset) are in agreement with the literature. According to Hidaka et al. (1982), the "heat release rate maximum" based definition of ignition delay appears to produce longer times, but the effect could well be due to the very low post-shock pressures ( $P < 0.3$  atm) of that study. Hidaka et al. (1999) ( $4.2 \mu\text{m}$  CO<sub>2</sub> emission onset) agree closely with the data from this study throughout the temperature range. Kalitan et al. (2005) data for OH\* onset under similar pressures, agrees very well with our results at high temperatures. Among correlations, Baker and Skinners' appears closer to our data than Colket and Spadaccinis', which produces longer delay

times. In Horning's work, the delay times for mixtures having argon 92 and 84% (vol) were progressively shorter with a decrease in argon dilution (not shown on the plot), confirming the trends observed in our study.

The effect of shock tube diameter is seemingly negligible as there is excellent agreement among different shock tube studies once the effect of diagnostics and pressure is identified and explained. This validates the use of a relatively smaller ID shock tube for reliable ignition delay studies. The location of diagnostics (side or end wall) appears to be insignificant for mixture compositions (96 and 98% argon) that may be regarded as reasonably dilute. A global correlation for the combustion of ethylene has been obtained based on the data from this study and literature, which is given below:

$$\tau(\mu s) = 10^{-29.5405} T^{6.7} e^{23840.1/T} [C_2H_4]^{0.7} [O_2]^{-0.91} [Ar]^{0.41},$$

where [X] are initial concentrations of reactants in mol/cc and all other symbols have their conventional meaning. This global correlation is valid for temperatures approximately ranging from 1000-2300 K, pressures from 0.2 to 20 atm, and equivalence ratios from 0.125 to 3. As shown in Figure 5.15, all the data from current study and some selected literature studies could be fit into this single correlation. The above correlation reconfirms the strong dependence of ignition on oxygen concentration (-0.92), which is consistent with the conclusion of earlier studies. The dependence on fuel concentration is very weak and the dependence on argon concentration is reasonably significant.

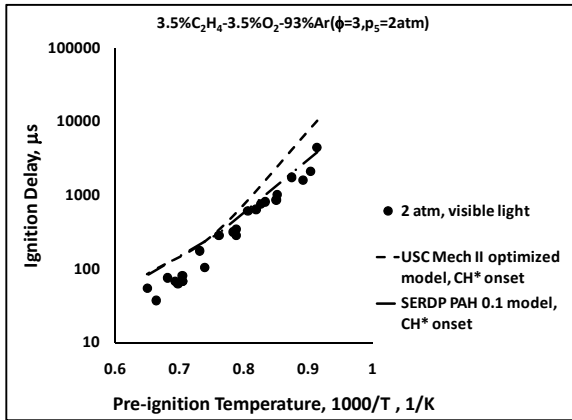


Figure 5.1 Ignition delay in combustion of ethylene: Comparison of experimental (symbols) and computed (lines) ignition delay times behind reflected shock waves at  $\Phi=3$ , Ar=93% & P~2 atm. The computational ignition delay was determined by the CH\* chemiluminescence onset based criterion, as explained in the text.

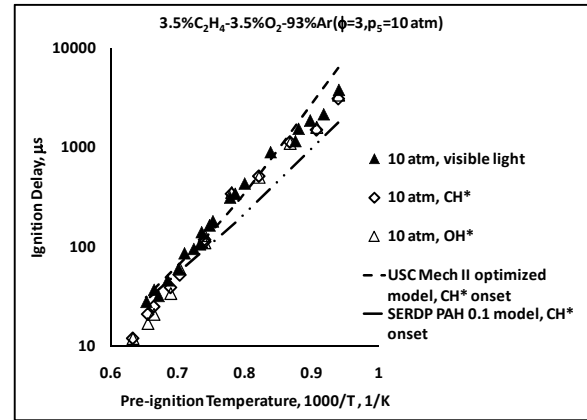


Figure 5.2 Ignition delay in combustion of ethylene: Comparison of experimental (symbols) and computed (lines) ignition delay times behind reflected shock waves at  $\Phi=3$ , Ar=93% & P~10 atm. The computational ignition delay was determined by the CH\* chemiluminescence onset based criterion.

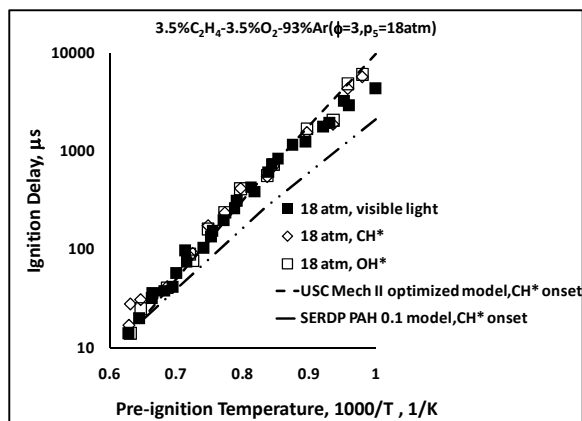


Figure 5.3 Ignition delay in combustion of ethylene: Comparison of experimental (symbols) and computed (lines) ignition delay times behind reflected shock waves at  $\Phi=3$ ,  $\text{Ar}=93\%$  &  $P\sim 18$  atm. The computational ignition delay was determined by the  $\text{CH}^*$  chemiluminescence onset based criterion.

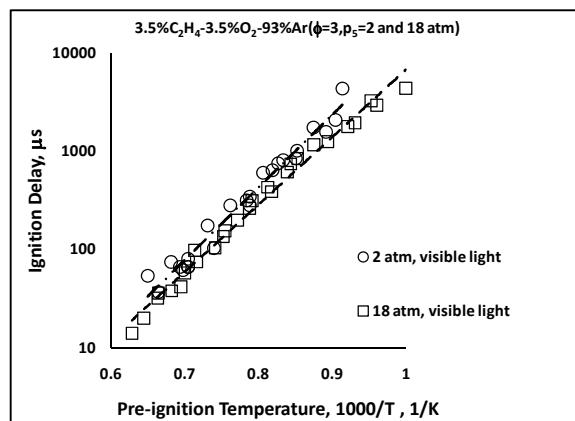


Figure 5.4 Ignition delay in combustion of ethylene: Effect of pressure at  $\Phi=3.0$  &  $\text{Ar}=93\%$ . Experimental data presented with respective trend lines.

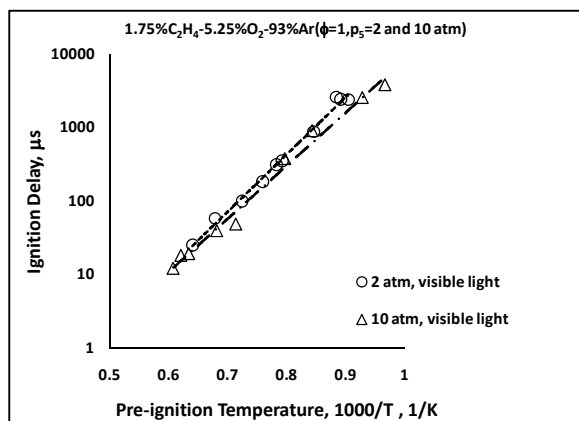


Figure 5.5 Ignition delay in combustion of ethylene: Effect of pressure at  $\Phi=1.0$  &  $\text{Ar}=93\%$ . Experimental data presented with respective trend lines.

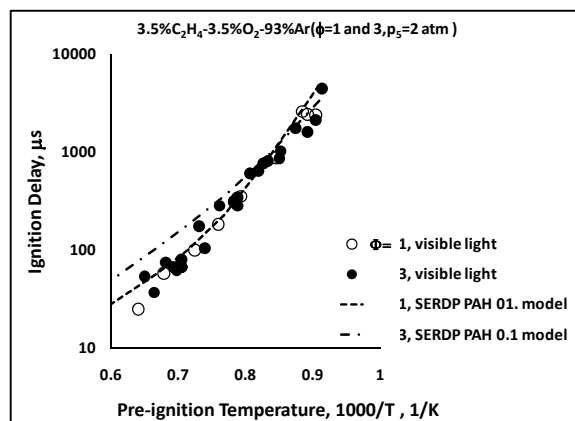


Figure 5.6 Ignition delay in combustion of ethylene: Effect of equivalence ratio at  $\text{Ar}=93\%$   $P\sim 2$ . The computational ignition delay was determined by the maximum temperature gradient based criterion.



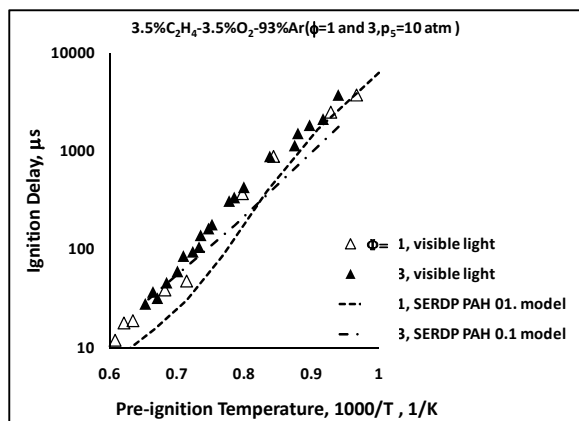


Figure 5.7 Ignition delay in combustion of ethylene: Effect of equivalence ratio at Ar=93% P~10. The computational ignition was determined by the maximum temperature gradient based criterion.

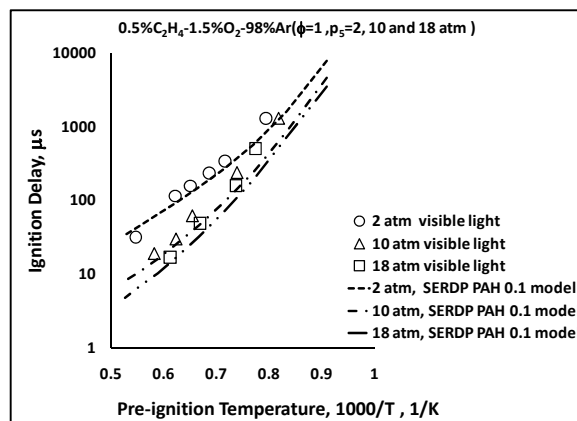


Figure 5.8 Ignition delay in combustion of ethylene: Effect of pressure for conditions where fuel mixture dilution was 98% in argon and  $\Phi=1.0$ . Comparison of experimental (symbols) and computed (lines) ignition delay times behind reflected shock waves. The computational ignition was determined by the maximum temperature gradient based criterion.

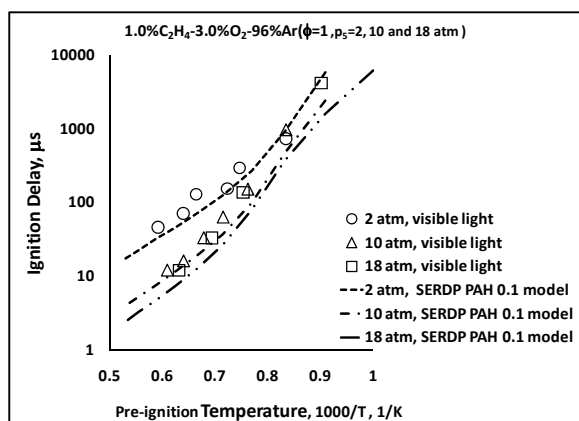


Figure 5.9 Ignition delay in combustion of ethylene: Effect of pressure for conditions where fuel mixture dilution was 96% in argon and  $\Phi=1.0$ . Comparison of experimental (symbols) and computed (lines) ignition delay times behind reflected shock waves. The computational ignition was determined by the maximum temperature gradient based criterion.

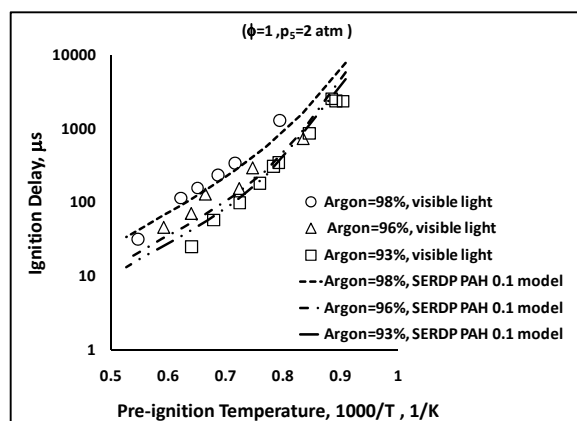


Figure 5.10 Ignition delay in combustion of ethylene: Effect of dilution for conditions at  $\Phi=1.0$  and P~2 atm. The computational ignition was determined by the maximum temperature gradient based criterion.

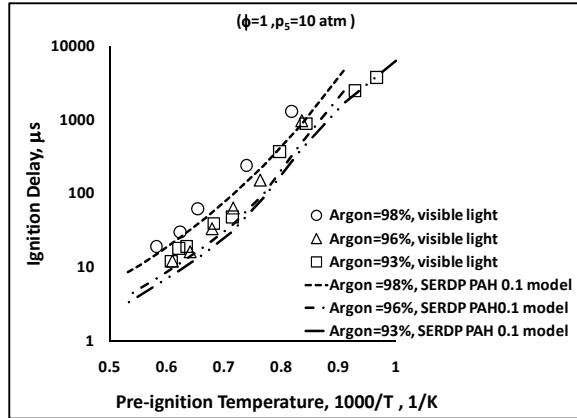


Figure 5.11 Ignition delay in combustion of ethylene: Effect of dilution for conditions at  $\Phi=1.0$  and  $P \sim 10$  atm. The computational ignition was determined by the maximum temperature gradient based criterion.

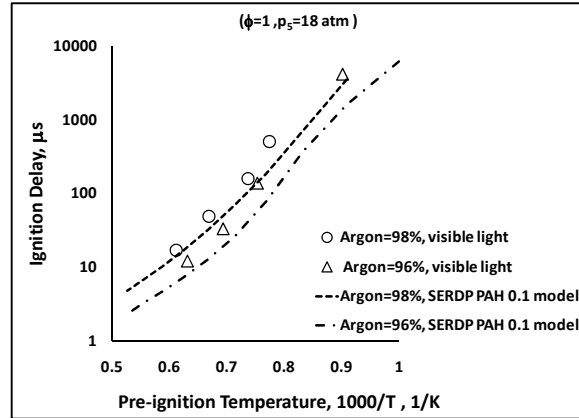


Figure 5.12 Ignition delay in combustion of ethylene: Effect of dilution for conditions at  $\Phi=1.0$  and  $P \sim 18$  atm. The computational ignition was determined by maximum temperature gradient based criterion.

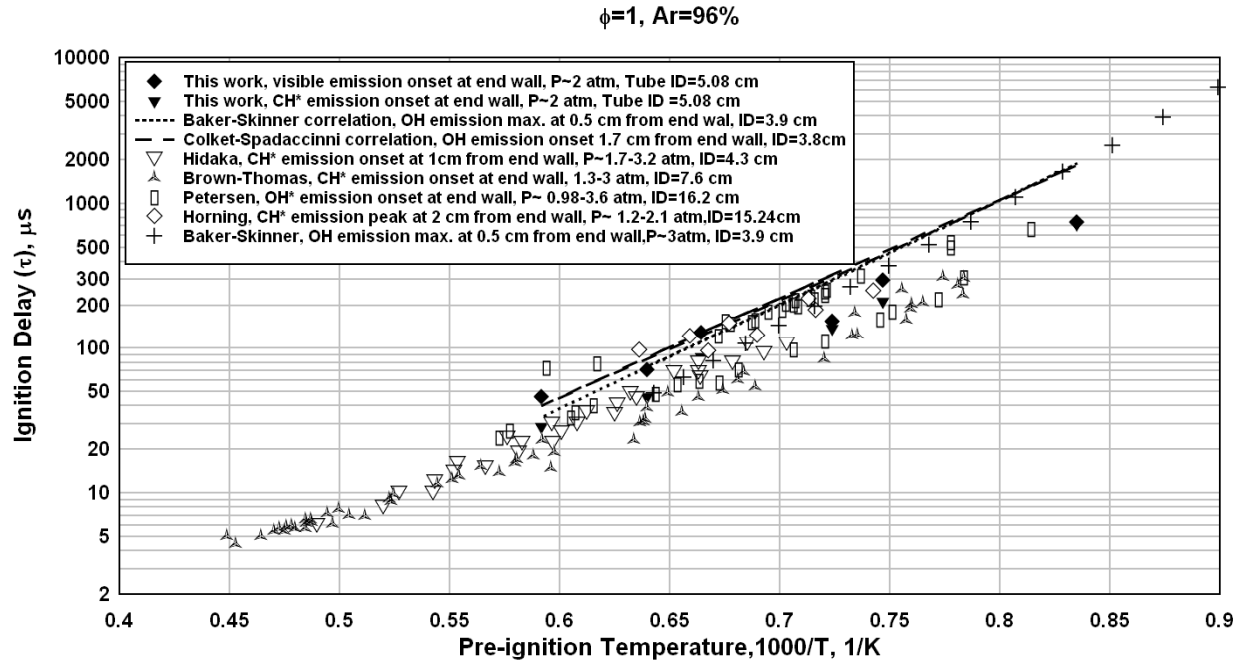


Figure 5.13 Ignition delay in combustion of ethylene: Comparison with literature data at  $\Phi=1.0$ ,  $Ar=96\%$  and low pressures. The correlations for ignition delay times were evaluated using experimental conditions from the present study specific to this plot.

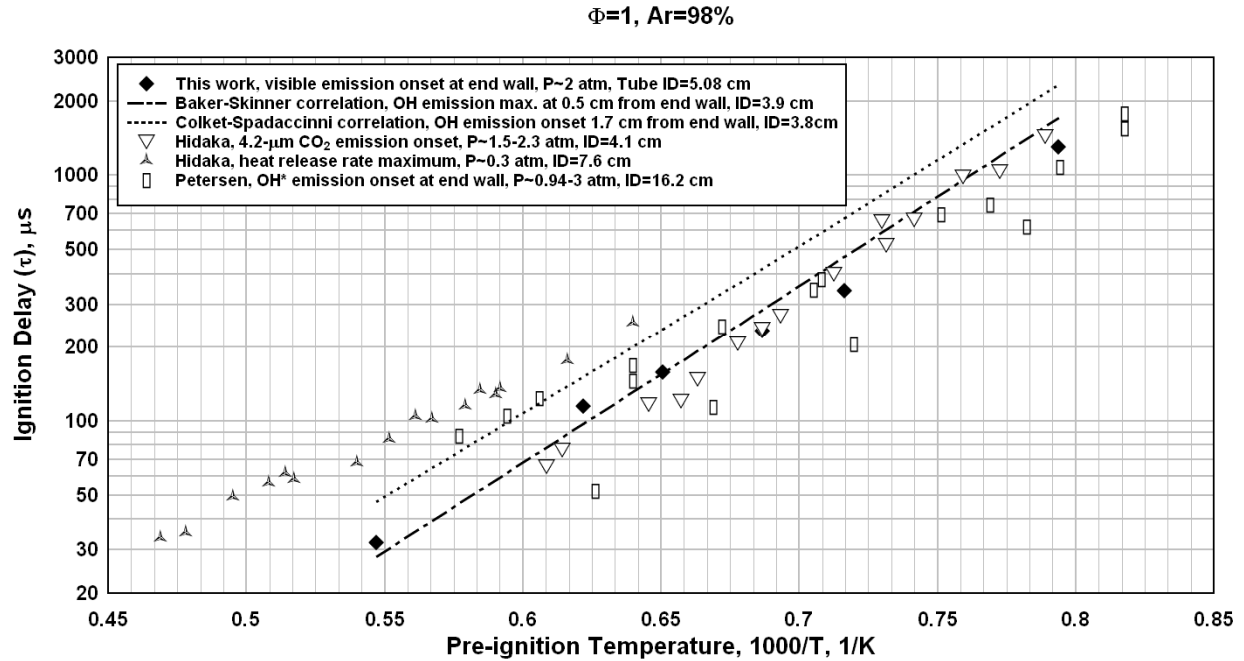


Figure 5.14 Ignition delay in combustion of ethylene: Comparison with literature data at  $\Phi=1.0$ ,  $\text{Ar}=98\%$  at low pressures. The correlations for ignition delay times were evaluated using experimental conditions from the present study specific to this plot.

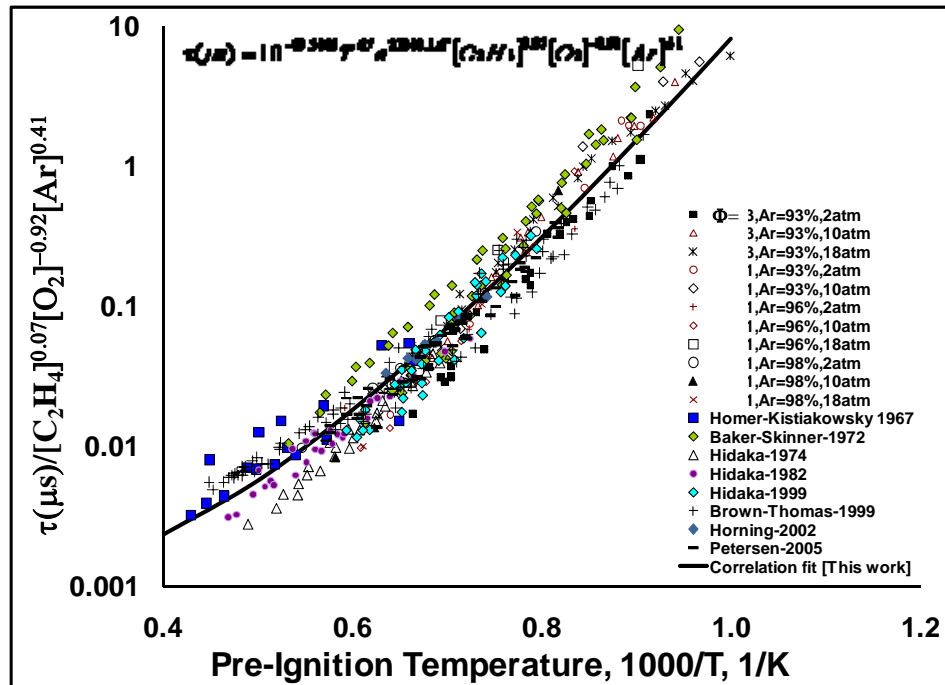


Figure 5.15 Shock-tube ignition data of ethylene-oxygen-argon mixtures from present work and literature studies. Symbols are experimental data, line is the correlation equation given in the panel. The global correlation is valid for temperatures approximately ranging from 1000-2300 K, pressures from 0.2 to 20 atm, and equivalence ratios from 0.125 to 3.

### 5.1.2 M-xylene Combustion

Ignition delay times were measured for all shock tubes to facilitate the comparison between different sets of conditions. The ignition delay data is presented in Figures 5.16 through 5.30. The experimental conditions covered a temperature range of 1100-1950 K, at pressures of 2 and 18 atm and equivalence ratios of 0.5, 1, and 3. The ignition delay times were modeled using the SERDP model. The SHOCKIN and closed homogeneous batch reactor model of Chemkin-Pro (with constant (U, V) assumption) were used for these simulations. As stated earlier, modeling of ignition delay times using 1-D CFD model (GASKIN) is currently in progress. In all conditions, the model ignition delay varied little with criteria based on OH\*, CH\* emission onset, pressure rise and temperature inflection point, which was later confirmed by experimental results. A temperature inflexion point-based criterion was chosen for computing model ignition delay time under all conditions using ChemkinPro or the SHOCKIN code.

Figures 5.16 and 5.17 represent fuel-rich conditions ( $\Phi=3.0$ , Ar= 98%) at pressures of 2 and 18 atm. The difference between ignition delay times using OH\* and CH\* measurements was found to be small (typically within ~25% over most of the temperature range). The data is usually deemed consistent if the agreement between optical diagnostics OH\* and CH\* is under 20%, considering the inherent shock tube experimental data scatter (Hall and Petersen 2005). The ignition delay times for different pressures are plotted individually with respective modeling predictions. The impact of pressure on ignition delay times is less discernible for this mixture composition (not shown). The simulated delay times computed using the SERDP model show very good agreement with experimentally measured delay times at high pressures (18 atm). At low pressures (2 atm), agreement is not very good given the scatter in the data. Modeled ignition delay times using SHOCKIN agree very well with constant (U, V) modeling (ChemkinPro) under the temperature range (1369-1948 K) and conditions considered here.

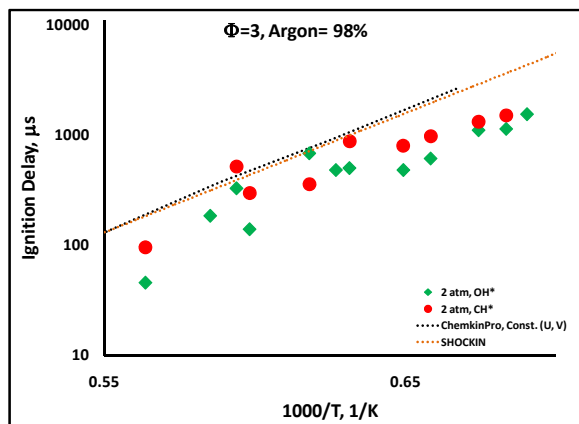


Figure 5.16 Ignition delay in combustion of m-xylene.  $\Phi= 3.0$ , Ar=98% and P = 2 atm with modeling.

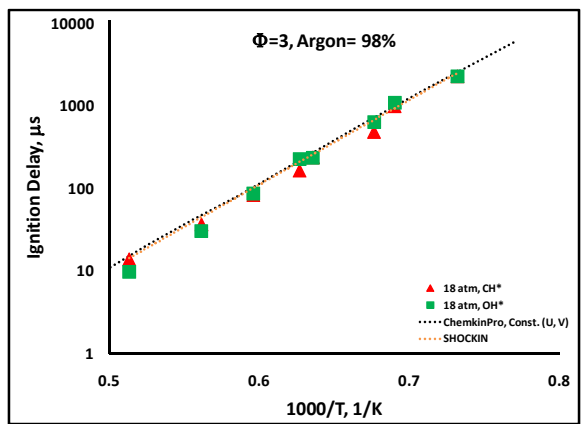


Figure 5.17 Ignition delay in combustion of m-xylene.  $\Phi= 3.0$ , Ar=98% and P = 18 atm with modeling.

Figures 5.18 and 5.19 show experimentally measured ignition delay times along with modeling under stoichiometric conditions at 98% argon dilution. Shorter ignition delay times were observed at high-pressure conditions throughout the temperature range tested. The difference in measurement among optical diagnostics of visible light, CH\*, and OH\* is very small in this case

(less than 5%). The agreement with the kinetic model is excellent under stoichiometric conditions at both low and high pressures.

Figures 5.20 and 5.21 show ignition delay times under fuel-lean conditions ( $\Phi=0.5$ ) with 98% argon dilution. The observed difference between ignition delay times at high and low pressures was small but noticeable. The impact of pressure was to enhance the ignition process, an effect that was also observed for fuel-rich and stoichiometric conditions, as discussed above. A small under-prediction of ignition delay times was observed with the model under these conditions. Again, modeled ignition delay times using SHOCKIN agree very well with ChemkinPro constant (U, V) modeling under the temperature range (1214-1987 K) considered for data shown in Figures 5.20 and 5.21.

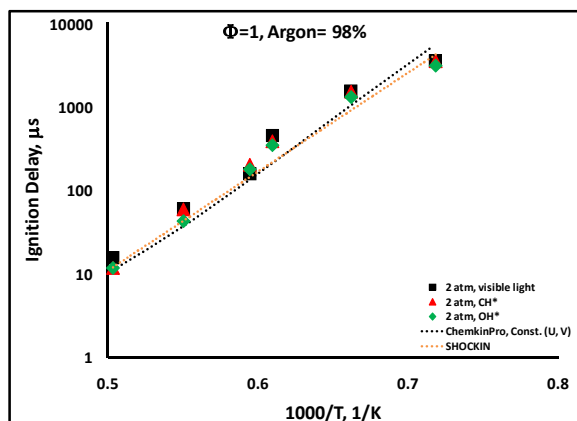


Figure 5.18 Ignition delay in combustion of m-xylene.  $\Phi=1.0$ , Ar=98% and  $P=2$  atm with modeling.

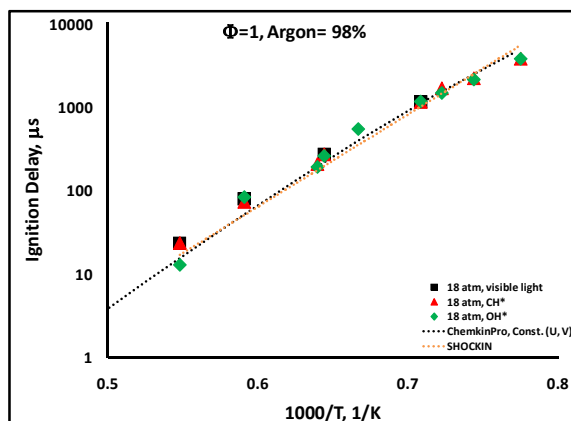


Figure 5.19 Ignition delay in combustion of m-xylene.  $\Phi=1.0$ , Ar=98% and  $P=18$  atm with modeling.

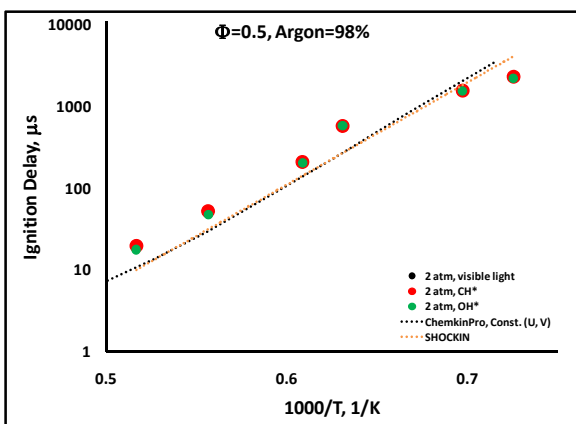


Figure 5.20 Ignition delay in combustion of m-xylene.  $\Phi=0.5$ , Ar=98% and  $P=2$  atm with modeling.

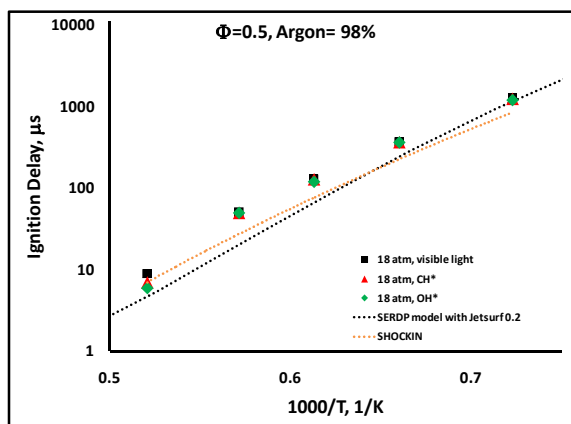


Figure 5.21 Ignition delay in combustion of m-xylene.  $\Phi=0.5$ , Ar=98% and  $P=18$  atm with modeling.

Figures 5.22 through 5.24 represent concentrated m-xylene / oxygen mixtures (Ar=93%). The data under these conditions was obtained using our heated shock tube facility. For  $\Phi=0.5$  (Ar=93%), ignition delay data was obtained using both heated and non-heated shock tubes (see Figure 5.24). The data showed excellent agreement, highlighting the reproducibility and mutual

consistency of the two shock tubes. The SERDP model, when used with SHOCKIN code, produced excellent agreement with the experimental ignition delay data at all equivalence ratios tested ( $\Phi=0.5, 1$  and  $3$ ). The ChemkinPro with constant (U, V) assumption based modeling over-predicted the ignition delay at  $\Phi=0.5$  and  $1$  by a small degree at the lower temperatures, whereas the model under-predicted the delay times at higher temperatures at  $\Phi=3$ . As is evident from the above discussion, the SHOCKIN code showed that the model had a better agreement with the experimental data than when modeled with ChemkinPro with constant (U, V) assumption under conditions with concentrated fuel-oxygen mixtures (Ar=93%). For leaner mixtures (Ar=98%) (see Figures 5.20 through 5.22 at all equivalence ratios tested in the study), the ChemkinPro with constant (U, V)-based approach produced the nearly same degree of accurate modeling as with SHOCKIN. The above results signify the fact that using the SHOCKIN program essentially incorporates any non-ideal gas-dynamic or heat release related effect in the modeling. Any disagreement between the model and the experimental results could then be attributed to the deficiencies of the kinetic model.

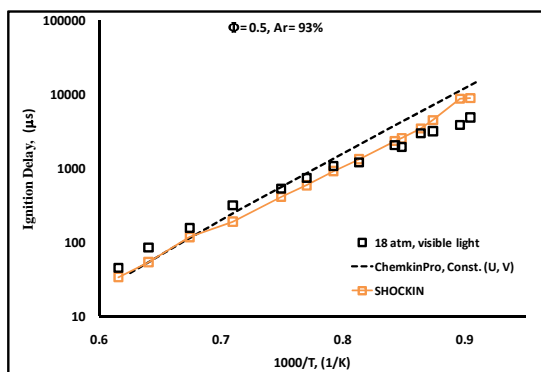


Figure 5.22 Ignition delay in combustion of m-xylene.  $\Phi = 0.5$ , Ar=93% and P=18 atm with modeling.

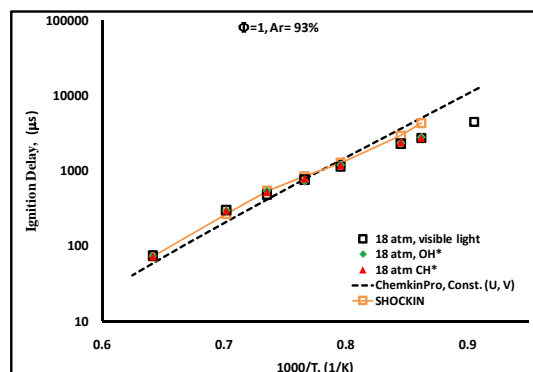


Figure 5.23 Ignition delay in combustion of m-xylene.  $\Phi = 1.0$ , Ar=93% and P = 18 atm with modeling.

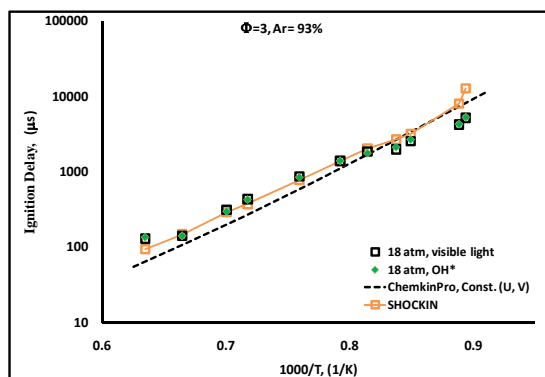


Figure 5.24 Ignition delay in combustion of m-xylene.  $\Phi = 3.0$ , Ar=93% and P = 18 atm with modeling.

The ignition delay times varied little when compared with the equivalence ratio ( $\Phi=0.5, 1$  and  $3$ ) at respective pressures (see Figures 5.25 -5.27). However, the model predicts faster ignition for stoichiometric and fuel-lean mixtures in the order of increasing leanness of the mixture. Figures 5.28 and 5.29 show the effect of argon dilution on experimentally observed ignition delay times. An increase in fuel oxidant concentration in the given mixture enhances the ignition process and produces shorter ignition delays. This effect is due to the increased exo-thermicity of the more concentrated mixture and has been observed previously in the literature.

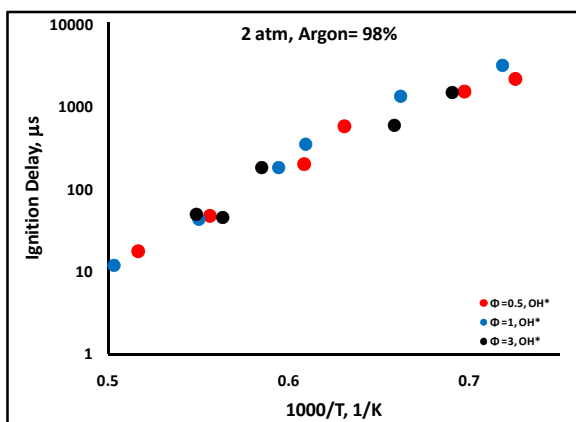


Figure 5.25 Ignition delay in combustion of m-xylene. Effect of equivalence ratio at argon concentration =98% and  $P = 2$  atm.

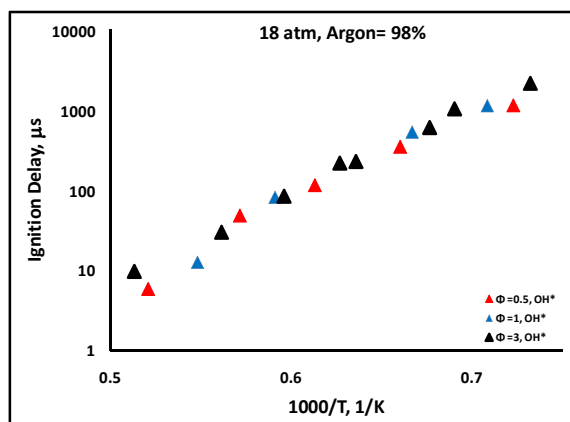


Figure 5.26 Ignition delay in combustion of m-xylene. Effect of equivalence ratio at argon concentration =98% and  $P = 18$  atm.

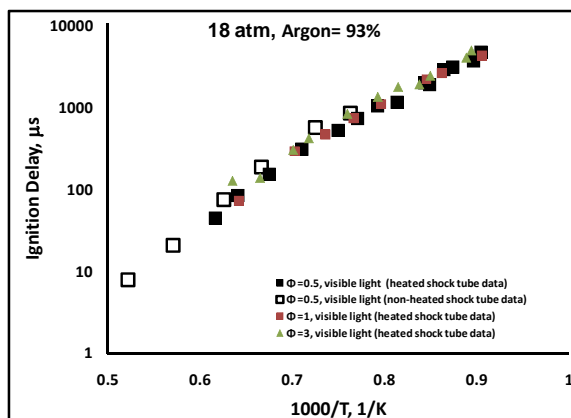


Figure 5.27 Ignition delay in combustion of m-xylene. Effect of equivalence ratio at argon concentration =93% and  $P = 18$  atm.

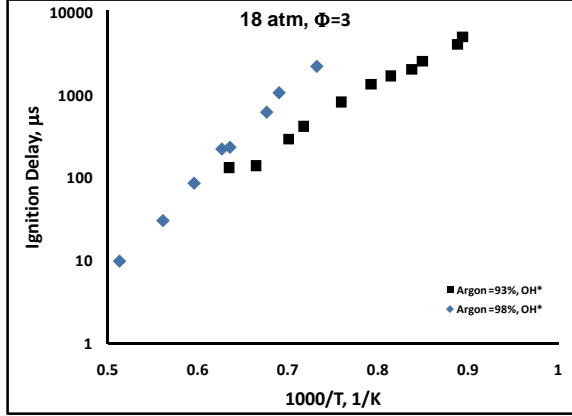


Figure 5.28 Ignition delay in combustion of m-xylene. Effect of dilution at  $\Phi=0.5$  and  $P = 18$  atm.

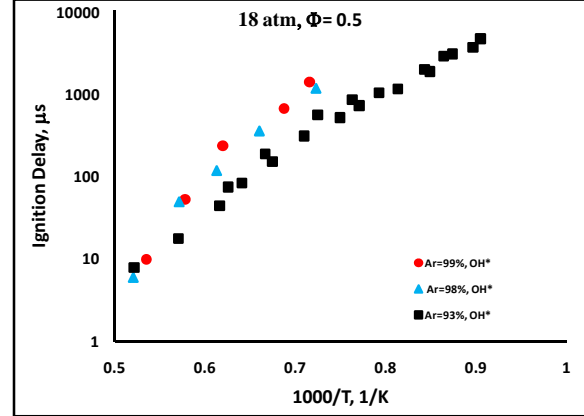


Figure 5.29 Ignition delay in combustion of m-xylene. Effect of dilution at  $\Phi=0.5$  and  $P = 18$  atm.

A global correlation for the combustion of m-xylene has been obtained based on the data from this study, which is given below:

$$\tau(\mu s) = 10^{112.2} T^{-32.7} \exp\left(-\frac{28390.8}{T}\right) [m-xylene]^{0.08} [O_2]^{-0.76} [Ar]^{0.28}$$

where  $[X]$  are initial concentrations of reactants in mol/cc and all other symbols have their conventional meaning. This global correlation is valid for temperatures approximately ranging from 1100 to 2000 K, pressures from 2 to 20 atm, and equivalence ratios from 0.5 to 3. As shown in Figure 5.30, all the data from current study could be fit into this single correlation. The above correlation suggests a strong dependence of ignition delay times on oxygen concentration (-0.76). The dependence on fuel concentration is very weak and the dependence on argon concentration is reasonably significant (0.28). The ignition delay data from a study by Battin-Leclerc, et al. (2006) is also plotted using the correlation developed in this study. The agreement is reasonable at high temperatures for concentrated fuel-mixtures, but under other conditions the agreement with our data deteriorates. Battin-Lecerc et al. mentioned having issues with fuel condensation during mixture preparation. M-xylene has very low vapor pressure; unless one is using a heated shock tube or extremely dilute mixtures, it is difficult to conduct reliable experiments. The scatter in the Battin-Leclerc et al. (2006) data also points toward this systemic difficulty.

We verified the ignition delay times for a few experiments using the 1-D CFD code, GASKIN. In the first stage of validation of the GASKIN code, we conducted a small number of hydrogen ignition delay experiments ( $\Phi=3$ , Ar=93%, for  $H_2/O_2/Ar$  mixtures). Figure 5.31 (a and b) show the experimental pressure profiles and the GASKIN modeling using a previously-validated hydrogen combustion model developed by Li et al. (2003). As is evident from the figure for low temperatures (1010 and 1097 K) and under fuel-rich conditions, the GASKIN code very accurately reproduces the experimental pressure profiles. The small perturbations appearing in the experimental pressure profile are due to less-than-perfect driver gas tailoring and are accurately captured by the CFD code. These perturbations cause further reflection or transmission of reflected shock wave from the contact interface, thereby causing a small increase or decrease in the pressure and temperature of the reaction zone. An important highlight of the



simulation is the accurate prediction of dwell time and quenching of reflected shock due to arrival of a rarefaction wave.

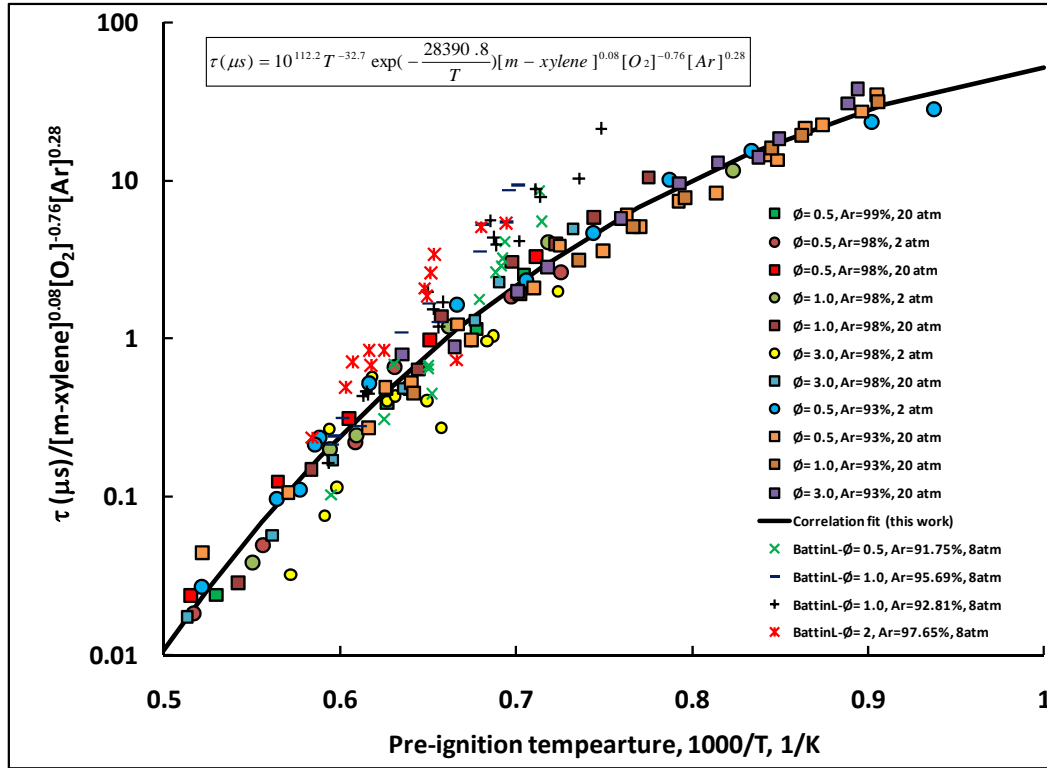


Figure 5.30 Global ignition delay correlation. Shock-tube ignition data of m-xylene/ $O_2$ /Ar mixtures from present work and a study by Battin Leclerc et al. (2006). Symbols are experimental data, line is the correlation equation given in the figure. The global correlation is valid for temperatures approximately ranging from 1100 to 2000 K, pressures from 2 to 20 atm, and equivalence ratios from 0.5 to 3.

### Modeling Results

We modeled a small number of m-xylene ignition delay experiments using the GASKIN code. A kinetic model reduction procedure was followed (as explained in Section 4.5.1), and the reduced model had 104 species and 646 reactions. As is evident in Figure 5.32, the ignition delay predictions by the reduced model and the full SERDP model agree very well under the selected experimental condition ( $\Phi = 0.5, Ar = 93\%$ ).

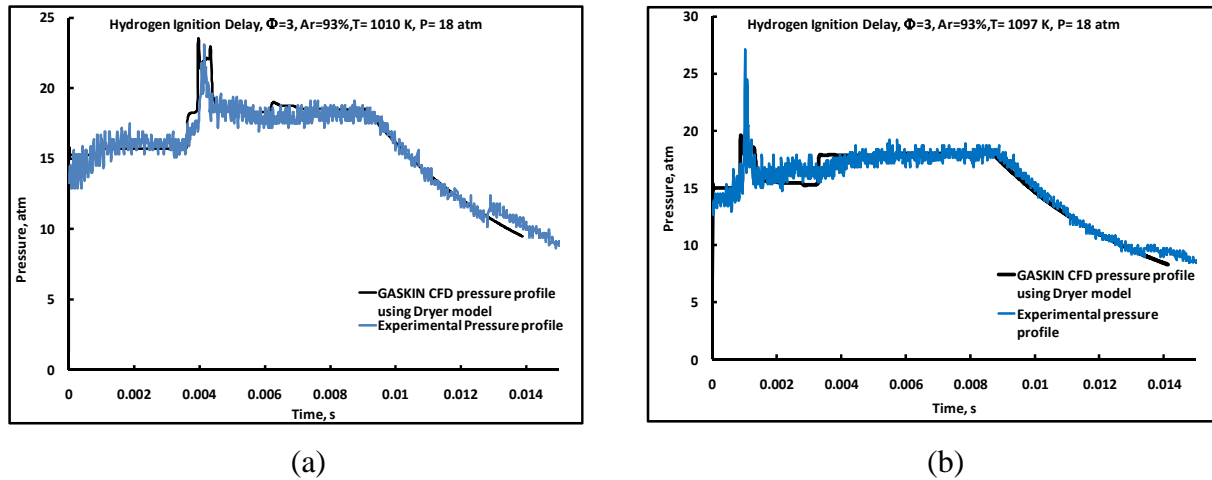


Figure 5.31 GASKIN validation using hydrogen combustion experiments at low temperatures and long test times (8 ms).

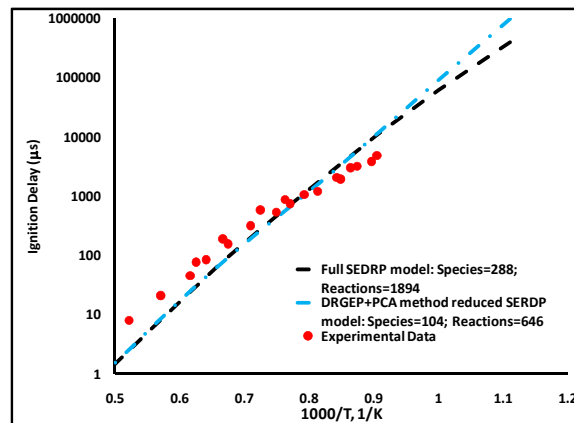


Figure 5.32 Model reduction:  $\Phi=0.5$ , Ar=93%, P= 18 atm: SERDP model reduction using Directed Relation Graph with Error Propagation (DRGEP) and Principal Component Analysis (PCA) techniques, used in that order.

Figure 5.33 shows an experimental pressure profile ( $\Phi=0.5$ , T=1379 K, P~18 atm) and simulated pressure profile by GASKIN (using the reduced and full SERDP models) that are in excellent agreement. Small perturbations due to imperfect driver gas tailoring were accurately predicted by the CFD code. Figure 5.34 shows a comparison of temperature profiles obtained using the SHOCKIN and GASKIN codes. Again, the agreement between the two modeling approaches appears excellent and mutually consistent. All the gas-dynamic and chemical kinetic changes appear to be accurately captured by the two modeling approaches. The GASKIN simulation times using reduced and full models were 1 and 11 days, respectively.

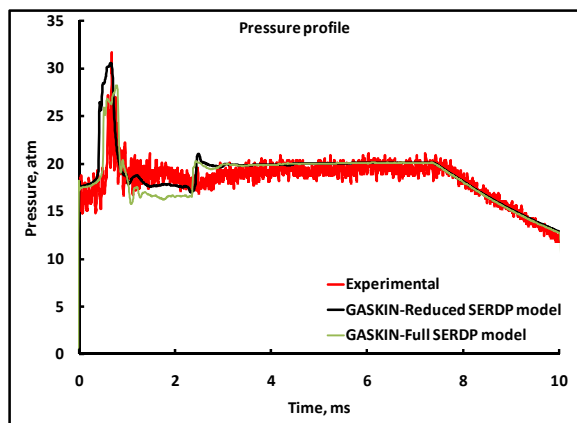


Figure 5.33 Simulation of pressure from a shock tube experiment using 1-D, CFD GASKIN program with SERDP model based detailed chemistry. M-xylene at  $\Phi = 0.5$ ,  $T = 1379$  K,  $P = 18$  atm and 93% argon content.

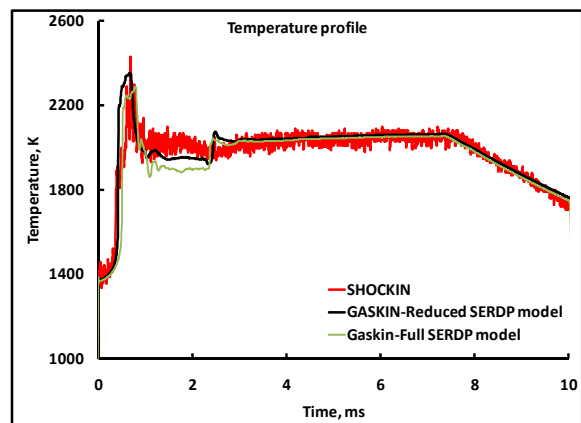
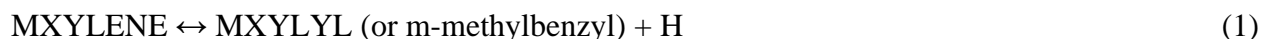


Figure 5.34 Simulation of temperature from a shock tube experiment using 1-D, CFD GASKIN program with SERDP model based detailed chemistry. M-xylene at  $\Phi = 0.5$ ,  $T = 1379$  K,  $P = 18$  atm and 93% argon content.

### *Sensitivity and Reaction Path Analysis*

Reaction path and sensitivity analyses were performed with the SERDP model using Chemkin-Pro software to identify key reactions important in m-xylene oxidation for the determination of ignition delay times. The accuracy of the conclusions drawn from such analyses totally depends upon the accuracy of the model used; specifically, accuracy of reaction channels proposed, thermo-chemistry, and available kinetic information limits the capabilities of a model. Here also, all the conclusions deduced from modeling should be viewed in the light of the proposed SERDP model only. The species nomenclature followed in the SERDP model is taken from the Gail and Dagaut model (2007).

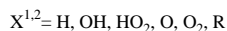
The decomposition channels of m-xylene are as given below:



According to the model, the dominant channel for decomposition of m-xylene leads to the formation of m-methylbenzyl radical and H atom (see reaction (1)). The question of branching ratio between uni-molecular initiation channels of xylenes (Battin-Leclerc, 2006; Gail, 2007; and Lange, 1994) and analogous reactions of toluene (Sivaramakrishnan et al., 2005; Gail, 2007; and Bounaceur, 2005) had been a subject of debate in recent literature. The model used in the present study uses a branching ratio (0.03 to 0.29 from 1100 to 1900 K between reactions 1 and 2) recommended by Lange, et al. (1994).

$$\text{MXYLENE} + \text{OH} \leftrightarrow \text{MXYLYL} + \text{H}_2\text{O} \quad (4)$$

(bimolecular initiation by molecular oxygen)

$$\text{C}_5\text{H}_5\text{-1CH}_2 + \text{O}_2 \leftrightarrow \text{C}_6\text{H}_6 + \text{HO}_2 \quad (8)$$


123

Reaction of m-methyl-phenyl radical with O<sub>2</sub> generates benzene and carbon monoxide via reactions:



Here, reaction (10) is shown as a global reaction that includes the following steps shown in reaction 11(a and b).



The oxidation of m-methylbenzyl radical generates m-tolualdehyde (MCPHHCO) and H atom:



Further reactions of m-tolualdehyde generate m-methyl benzoyl radicals (MCPHCO) (reaction 13), which can then either give way an H atom to form m-methyl phenoxy radicals or can decompose into methyl cyclo-pentadienyl radical and CO via reactions 14, 9, and 10:



The major reaction pathways involved in the oxidation of m-xylene at T=1600 K are presented in Figure 5.35. The sensitivity analysis was conducted using a technique elaborated by Saylam, et al. (2007). The OH radical is understood to be the main chain carrier in the oxidation and auto ignition chemistry of hydrocarbons at high temperatures. Therefore, OH radical was used as the target species for sensitivity analysis. The reactions that exhibited higher-local sensitivity with respect to OH radical were designated as the key reactions. The relative importance of these reactions for ignition delay chemistry was presumed accordingly.

According to the reaction path and rate of production analyses, the characteristic auto ignition chemistry was found to be very active approximately halfway prior to the start of the ignition. This was previously observed in several literature studies. The calculated sensitivity coefficients of corresponding reactions at half of the ignition delay time were used for the analysis. The analysis temperature was taken as 1600 K. At approximately 1600 K, the characteristic high-temperature hydrocarbon chemistry regime is known to prevail. Sensitivity analysis was also performed with m-xylene as target species. Rate of production analyses of m-xylene, m-methylbenzyl (MXYLYL) and m-methylphenyl radicals (identified as key components from m-xylene oxidation) were performed to recognize the primary pathways important for ignition and their relative importance.

The results of the sensitivity analyses targeting OH radical production are presented in Figures 5.35 - 5.37, comparing sensitivity coefficients for  $\Phi=0.5$ , 1, and 3 at pressures of 2 and 18 atm, respectively. The absolute values of sensitivity coefficients among the different equivalence ratios are not comparable as the analyses under given conditions were performed at different times. Only the relative rankings of the coefficients of identified reactions at a particular equivalence ratio are relevant here. In all cases, the most important reaction influencing the production of OH radical is  $\text{H} + \text{O}_2 \leftrightarrow \text{O} + \text{OH}$  (15). However, the relative sensitivity of

reaction (15) for  $\Phi=0.5$  is highest, followed by  $\Phi=1$  and 3, in that order. At high pressure (18 atm, see Figure 5.37) conditions, the most important reactions included reaction of m-xylene with molecular oxygen (6), oxidation of m-methylphenyl radical (9), decomposition of toluene, and abstraction of benzylic H from m-xylene by H-atom to form m-methylbenzyl (MXYLYL) radical and  $H_2$  (1). No significant difference was observed among the top reaction pathways for the three equivalence ratios (see top reactions in Figures 5.36 and 5.37). At low pressure conditions, the beta-scission of m-methylbenzyl (MXYLYL) radical leading to the formation of methyl-cyclopentadienyl radical and acetylene (7) was important according to the model.

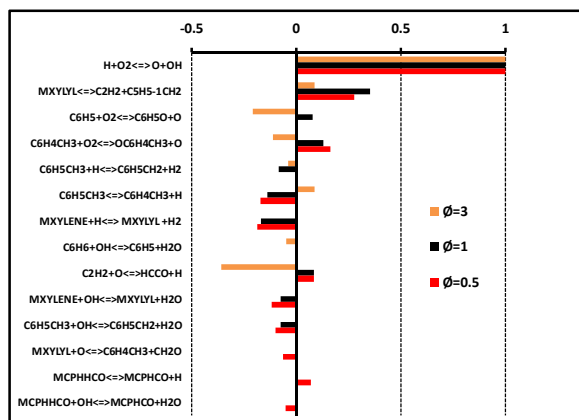


Figure 5.36 Sensitivity analysis targeting OH radical production using SERDP model.  $\Phi=0.5, 1$  &  $3$ ,  $T=1600$  K, and  $P=2$  atm ( $Ar=98\%$ ). The time of analysis,  $t=123, 185$ , and  $438$   $\mu s$  ( $\Phi=0.5, 1$  and  $3$  respectively), approximately equal to half of the ignition delay time under the given conditions. Absolute values of sensitivity coefficients not comparable as the analyses under given conditions were performed at different times. Only relative rankings of the coefficients of identified reactions at a particular equivalence ratio are relevant here.

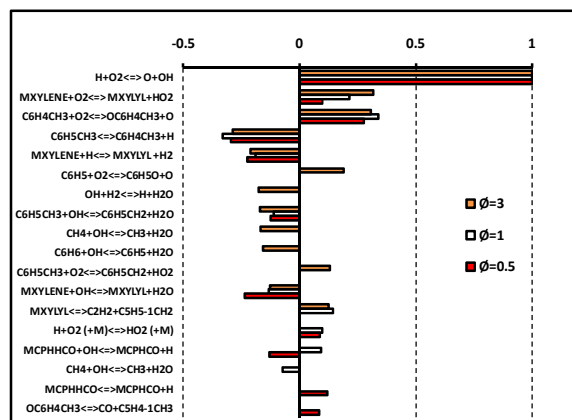


Figure 5.37 Sensitivity analysis targeting OH radical production using SERDP model.  $\Phi=0.5, 1$  and  $3$ ,  $T=1600$  K, and  $P=18$  atm ( $Ar=98\%$ ). The time of analysis,  $t=45, 70$ , and  $105$   $\mu s$  ( $\Phi=0.5, 1$  &  $3$  respectively), approximately equal to half of the ignition delay time under the given conditions. Absolute values of sensitivity coefficients not comparable as the analyses under given conditions were performed at different times. Only relative rankings of the coefficients of identified reactions at a particular equivalence ratio are relevant here.

### 5.1.3 N-dodecane and N-dodecane / M-xylene Surrogate Combustion

The ignition delay data from the present study for the combustion of n-dodecane and n-dodecane/ m-xylene blend are shown in Figures 5.38 through 5.45. In all conditions, the measured ignition delay varied little with criteria based on visible light,  $CH^*$ ,  $OH^*$ , or pressure rise, etc. (1-5% over the temperature range). As evident, the ignition delay times for both fuels at all three equivalence ratios appear to follow a non-mono-linear (a weak S-shaped) dependence on  $\log \tau_{ign}$  vs inverse temperature plot. The S-shaped dependence indicates a change in controlling chemistry over the temperature range tested.

The ignition delay times were modeled using the SERDP\_SURR\_v2 kinetic model developed as a part of the Strategic Environmental Research and Development Program (SERDP). The reaction model of a 2-component surrogate for jet fuel combustion and polycyclic aromatic hydrocarbons PAH formation was developed primarily by Gudiyella, Brezinsky, Zeppieri, Colket, Dames and Wang. The latest SERDP model includes Jetsurf model version 1.0 for n-alkane oxidation. The model contains 241 species and 1641 reactions.

The closed homogeneous batch reactor model of Chemkin-Pro was used for these simulations with the assumption of homogeneous adiabatic (U) conditions and constant volume (V) constraint. The temperature inflection point-based criterion was chosen for computing model ignition delay times under all conditions. Figures 5.38 and 5.41 show ignition delay data for n-dodecane and the blend at  $\Phi=0.5$ . The constant (U, V) assumption-based modeling using the SERDP model suggests good agreement with the experiments over the temperature range roughly from 1050-1250 K. The model predicts faster ignition at higher and slower at lower temperatures, but the overall agreement with the model appears reasonably good. At  $\Phi=1$  (see Figures 5.39 and 5.42), the agreement between the model and the experiments follow the trend recognized at  $\Phi=0.5$ . At  $\Phi=3$  (see Figures 5.40 and 5.43), the agreement between the model and the experiments is not very good for both the fuels. It must be noted that at low temperatures (typically below 1100 K) and concentrated fuel mixtures (e.g., 7% fuel-oxygen mixture used in present study), the Chemkin-based constant (U, V) assumption could be insufficient (Saxena, 2011 and Flora, 2011). Therefore, the nature of agreement between the model and experimental data at low temperature is being further investigated using SHOCKIN (a modified Chemkin code developed by our group (Saxena, 2011 and Flora, 2011))) and 1-D CFD (Bileyu, 2009).

Figure 5.44 shows the effect of equivalence ratio on ignition delay times of n-dodecane. At high temperatures ( $T > 1200$  K), the ignition delay times become progressively shorter under fuel-lean conditions ( $\Phi=0.5$ ), with increasing pre-ignition temperatures when compared to those at fuel-rich conditions ( $\Phi=3.0$ ). For stoichiometric conditions, the values for delay times are somewhere in the middle of corresponding fuel-rich and fuel-lean values. In the low temperature regime, the trend is reversed - the delay times under fuel-lean conditions become progressively longer with decreasing temperature when compared to their fuel-rich counterparts. It appears that in the small temperature range ( $\sim 1100$ -1200 K) the ignition delay times lose their sensitivity to equivalence ratio. The controlling chemistry in this temperature regime is changing. Such a trend in the variation of ignition delay times with equivalence ratios was previously described by Curran et al. (2002) in a modeling study on iso-octane oxidation to be due to the nature of the chain-branching process. At higher temperatures (above 1150 K), the reaction of a hydrogen atom with molecular oxygen to produce a hydroxyl radical and an oxygen atom is of central importance. At lower temperatures (below 1150 K), the production of carbonyl-hydroperoxide species, which leads to chain branching, is directly proportional to the fuel concentration. For the blend (see Figure 5.45), a similar but relatively weak dependence of ignition delay times on equivalence ratio was observed.

We compared the ignition delay times of n-dodecane and the blend at identical equivalence ratios (not shown here). Within experimental scatter, the ignition delay times were very similar. Effects related to the change in composition seem to have a small effect on the variability of high temperature ( $T$  over 1000 K) ignition delay times. This observation is consistent with earlier

studies by our group (Kahandawala, 2008; Flora, 2011; and Balagurunathan, 2011). We have discussed several important results in this regard (Flora, 2011 and Balagurunathan, 2011). Balagurunathan found that in a mixture where normal paraffins are present in significant quantities, the ignition delay is primarily controlled only by their ignition. Slower-igniting hydrocarbons of other structural classes like aromatics do not play an important role in this respect. Balagurunathan et al. investigated ignition delay times under fuel-lean conditions. In the current study, we observed no measurable difference between ignition delay of n-dodecane and the blend under stoichiometric and fuel-rich conditions. Therefore, it appears that n-alkane oxidation chemistry is also prevalent under stoichiometric and rich conditions.

Sensitivity analyses were performed with the SERDP model using Chemkin-Pro software, and results are provided in Figure 5.46 (a through f). The purpose of the analyses was to identify key reactions important in the oxidation of n-dodecane and the blend for the determination of ignition delay time according to the model. The sensitivity analyses were conducted using a technique elaborated by (Saylam, et al. 2007). OH radical was used as the target species for sensitivity analysis. Reactions that exhibited higher local sensitivity with respect to OH radical were designated as the key reactions. The relative importance of these reactions for the ignition delay chemistry was presumed accordingly. The calculated sensitivity coefficients of corresponding reactions at half of the ignition delay time were used for analyses conducted at 1100 and 1400 K.

As observed, the most important reactions determining OH radical production in the oxidation of n-dodecane and the blend are the same (see Figure 5.46). These reactions represent the oxidation of fragments of n-dodecane, mainly C<sub>1</sub>-C<sub>3</sub> chemistry. Wang et al. (2009) concluded that in the combustion of a large n-alkane, the kinetics of fuel cracking is fast and could be decoupled from oxidation kinetics of the fragments. The entire pre-ignition chemistry of a large n-alkane then reduces to the oxidation kinetics of C<sub>1</sub>-C<sub>4</sub> hydrocarbons, so it is not surprising to see that none of the decomposition steps in the combustion of n-dodecane or the blend figures into the top-most reactions. However, it is important to note that m-xylene reactions (pyrolytic or oxidation pathways) are not necessary when deciding the course of pre-ignition reactions of the blend. The sensitivity analysis of pure m-xylene under similar conditions (not shown) revealed that reactions involving m-xylene do form an important part of pre-ignition when no alkane is present (Saxena, 2011). Therefore, we arrive at the conclusion that even in the presence of an aromatic like m-xylene, the pre-ignition chemistry of the blend is essentially that of oxidation of n-dodecane fragmentation products. Detailed analysis of the performance of the kinetic model is currently in progress.



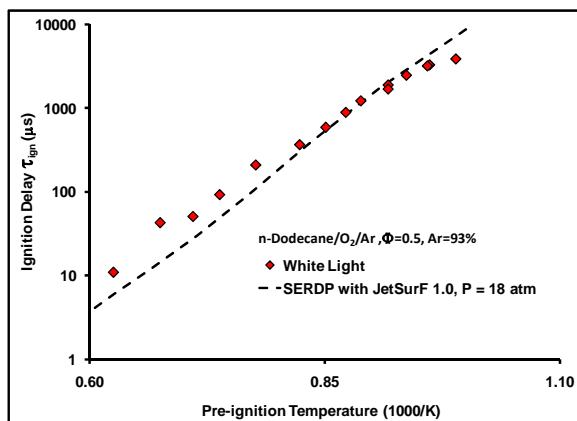


Figure 5.38 Ignition delay in combustion of n-dodecane at  $\Phi = 0.5$ ,  $P = 18$  atm,  $Ar = 93\%$  with modeling.

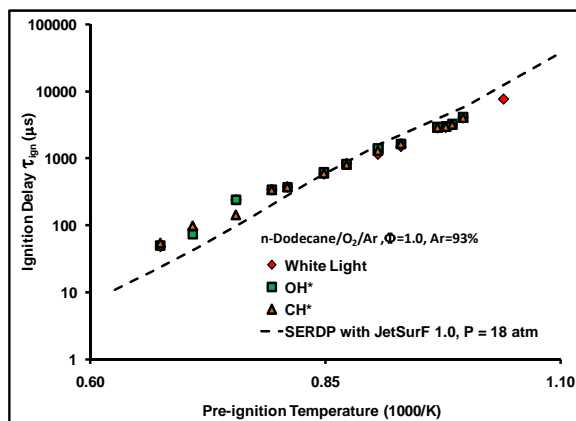


Figure 5.39 Ignition delay in combustion of n-dodecane at  $\Phi = 1.0$ ,  $P = 18$  atm,  $Ar = 93\%$  with modeling.

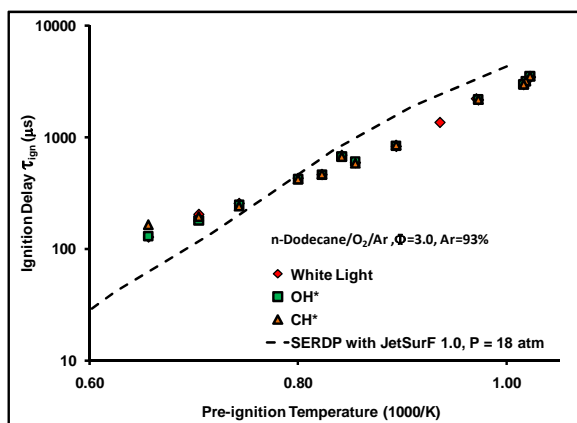


Figure 5.40 Ignition delay in combustion of n-dodecane at  $\Phi = 3$ ,  $P = 18$  atm,  $Ar = 93\%$  with modeling.

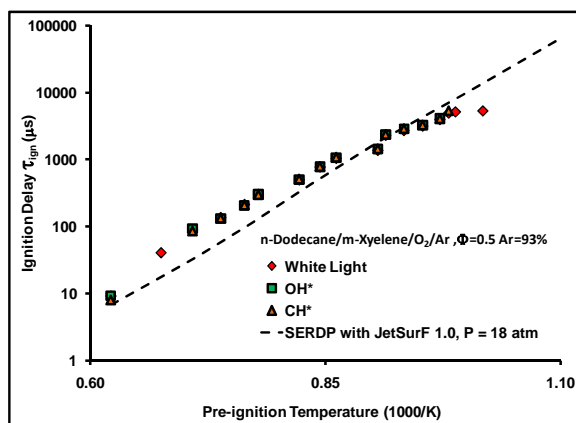


Figure 5.41 Ignition delay in combustion of n-dodecane / m-xylene blend at  $\Phi = 0.5$ ,  $P = 18$  atm,  $Ar = 93\%$  with modeling.

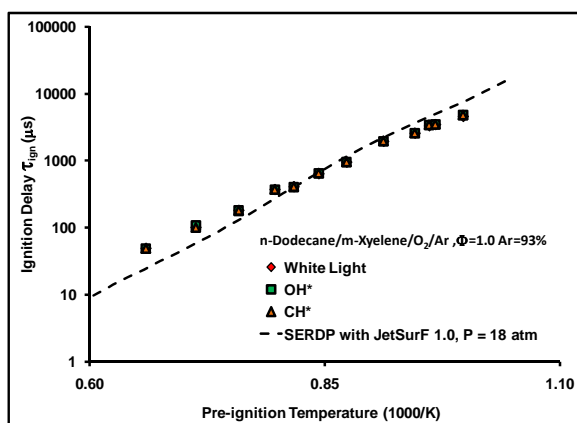


Figure 5.42 Ignition delay in combustion of n-dodecane / m-xylene blend at  $\Phi = 1.0$ ,  $P = 18$  atm,  $Ar = 93\%$  with modeling.

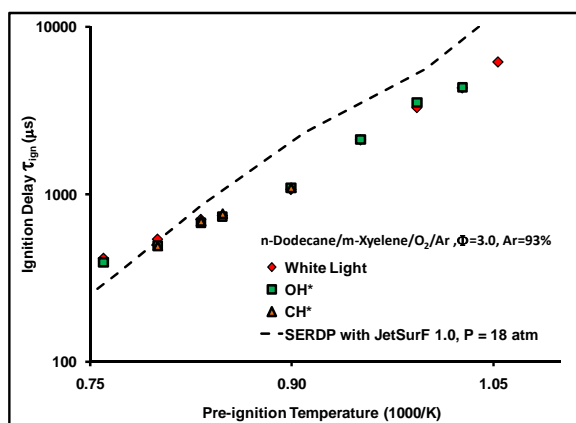


Figure 5.43 Ignition delay in combustion of n-dodecane / m-xylene blend at  $\Phi = 3.0$ ,  $P = 18$  atm,  $Ar = 93\%$  with modeling.

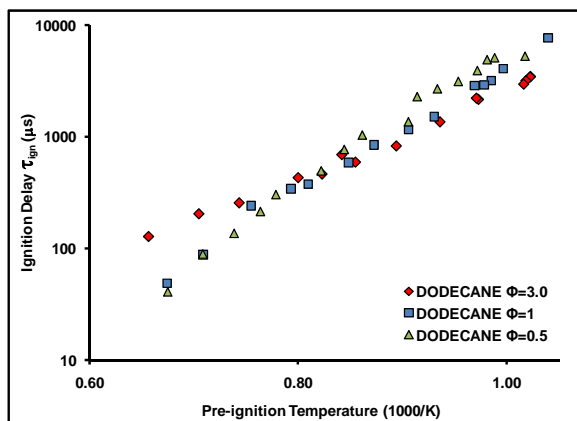


Figure 5.44 Effect of equivalence ratio on the ignition delay in combustion of n-dodecane at 18 atm, Ar=93%.

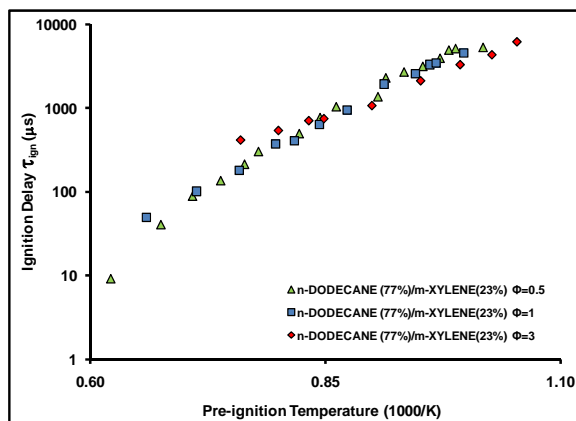
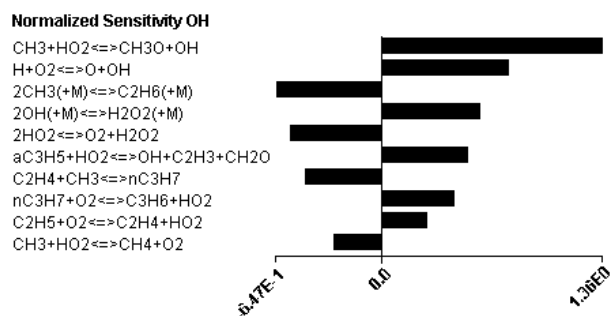
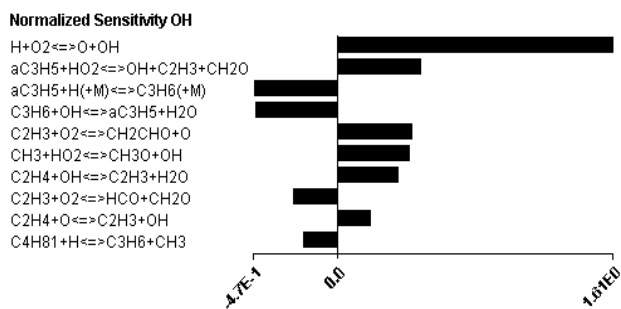


Figure 5.45 Effect of equivalence ratio on the ignition delay in combustion of the blend at 18 atm, Ar= 93%.

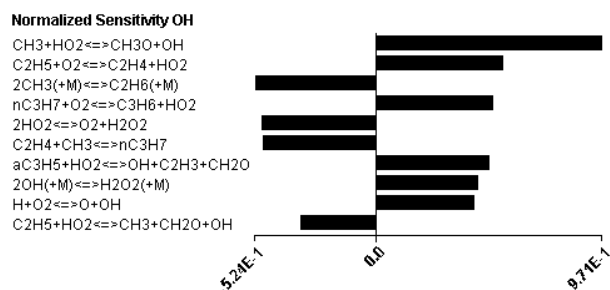
Figure 5.46 Sensitivity analysis targeting OH radical production in the combustion of n-dodecane using SERDP model at half of ignition delay times under respective conditions.



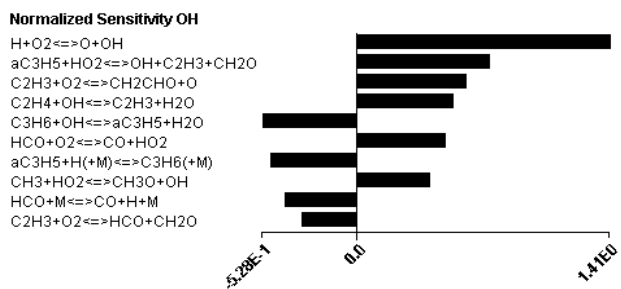
(a)  $\Phi = 0.5$ ,  $T = 1100$  K,  $P = 18$  atm.



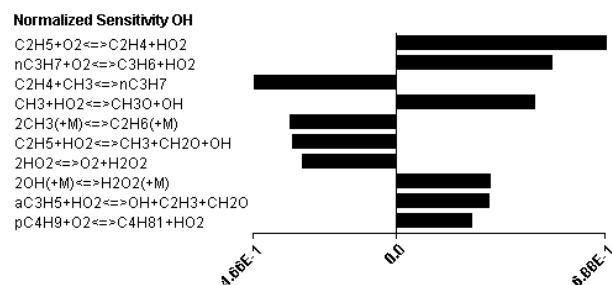
(b)  $\Phi = 0.5$ ,  $T = 1400$  K,  $P = 18$  atm.



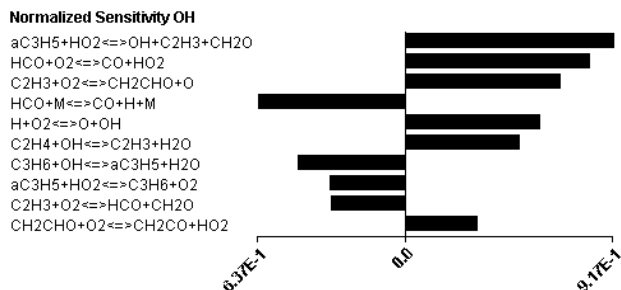
(c)  $\Phi = 1$ ,  $T = 1100$  K,  $P = 18$  atm.



(d)  $\Phi = 1$ ,  $T = 1400$  K,  $P = 18$  atm.



(e)  $\Phi = 3$ ,  $T=1100$  K,  $P=18$  atm.



(f)  $\Phi = 3$ ,  $T=1400$  K,  $P=18$  atm.

#### 5.1.4 Product characterization

In the present study, a wide range of combustion-generated products were characterized for rich and concentrated fuel-oxygen mixtures ( $\Phi=3$ ,  $Ar=93\%$ ). Figures 5.47 through 5.49 present experimental product characterization data for the fuels tested. Tables 5.1 through 5.6 present the semi-volatile (mainly) organics and species extracted from soot surface. The recovery of all the combustion-generated products is a very difficult analytical task under rich conditions due to the formation of soot and heavier condensable species. The reported yields of major combustion-generated species were estimated to be within 20% accuracy based on previous studies by our group (Kahandawala et al., 2004). The Chemkin-Pro Constant (U,V) model was used to simulate zero dimensional temporal evolution of species concentration profiles with the kinetic model SERDP 0.1 (with JetSurf 0.2). To compare model simulation profiles with experimental observations, the temporal species concentration values obtained from simulation were normalized with respect to the mass of the carbon in the fuel. In the case of m-xylene combustion, model yields were obtained using the SERDP model applied with SHOCKIN code (Flora et al., 2011 and Saxena et al., 2011). SHOCKIN accounts for the effects of changing pressure and temperature (both gas-dynamic and chemistry-related) through the use of the experimental pressure history over the entire time period of the experiment. It also accounts for the temperature and pressure changes during quenching by the arrival of rarefaction wave. Therefore, SHOCKIN was chosen over Constant (U, V) assumption to improve the prediction of product yields using the SERDP model. For the other fuels tested during SERDP (ethylene, n-dodecane, and n-dodecane/ m-xylene blend), modeling using SHOCKIN code is in progress.

#### Ethylene Combustion

The volatile components were analyzed using the GC-TCD technique. Among combustion generated volatile species, CO, CO<sub>2</sub>, C<sub>2</sub>H<sub>2</sub>, C<sub>2</sub>H<sub>4</sub>, CH<sub>4</sub>, and benzene were found in significant quantities. The experimental yields of volatile species from the combustion of ethylene are presented in Figures 5.47 through 5.52. The model (using Chemkin-Pro) over-predicts the yields of carbon monoxide within 20% throughout the temperature range. Model yields of CO<sub>2</sub>, C<sub>2</sub>H<sub>2</sub>, C<sub>2</sub>H<sub>4</sub>, and CH<sub>4</sub> are under-predicted. Faster depletion of benzene is predicted from the model with an increase in temperature (see Figure 5.52).

A good kinetic model that deals with the gas-phase chemistry of soot formation must be able to predict the correct order of magnitude levels of aromatics and PAH concentrations and order of PAH appearance. Thus, in an attempt to validate the SERDP 0.1 model, the model and

experimental yields of such species were compared. To model semi-volatile species from ethylene combustion the shock-solution model of Chemkin 3.7 was used to simulate zero dimensional temporal evolution of species concentration profiles for the SERDP\_C2H4. Constant post-reflected shock pressure model was used during simulations (only for ethylene semi-volatile species shown in Figure 5.53 through 5.1.4.10).

For ethylene combustion, the following compounds were identified and quantified using the internal standard Naphthalene-d8: toluene, styrene, phenylacetylene and naphthalene. The difference in magnitude of the two axes shown in figures (5.53 through 5.56) for experimental and model yields should be noted when comparing the trends.

For toluene (Figure 5.53), the model over-predicts the yields by approximately an order of magnitude. For styrene (Figure 5.53) and phenyl-acetylene (Figures 5.54 and 5.55), the model predicts the experimental trends reasonably well but over-predicts the yields by approximately one to two orders of magnitude. For naphthalene (a two ring aromatic, see Figure 5.56), the model predicts the pressure and temperature dependence well and over-predicts the magnitude of experimental yields within an order of magnitude. The over-prediction of yields by models has been observed in the past, and could be due to several reasons, such as inaccurate thermodynamic or kinetic data or the absence of some species from the reaction mechanism, which can alter the rate of production and consumption of several species involved in the reaction scheme.

Figure 5.57 shows soot yields in the combustion of ethylene obtained using Leco carbon analysis. The carbon yields obtained from the combustion of ethylene normalized with respect to the mass of the carbon in the fuel at 2, 10 and 18 atm under fuel-rich ( $\Phi = 3.0$ ) conditions are shown in the figure. The post-shock pre-ignition temperature range covered was approximately from 1050 to 1600 K. The experiments were conducted at close temperature intervals to cover the entire temperature range instead of repeating the same experiments so that a better experimental trend could be obtained. As shown in Figure 5.57, the low soot yields observed at the lower temperatures are due to the slower rate of particle formation. As the temperature increased, the particle formation accelerated and a maximum in the soot yields was observed. A further temperature increase caused the oxidation rate to dominate and lower the particle yield. This phenomenon has been described in many soot studies and results in a bell-shaped trend in soot yield vs. temperature plot. As can be observed, the decrease in pressure caused a significant reduction in soot yields throughout the temperature range considered. The maximum yields at 18 atm at ~1325 K dropped from 5.5% to approximately 2% at 2 atm at approximately 1300 K.

The species extracted from soot surface (mostly non-volatile compounds) and identified from the GC/MS analysis are reported in Table 5.3. These were identified based on the match quality with respect to the mass spectral (MS) library (NIST library). A qualitative understanding of the non-volatile species (including heavy PAHs) formed during the combustion could provide a better insight into the reaction pathways involved.

The carbon balance was estimated by summing the yields of quantified species for the experiments conducted. As shown in Figure 5.58, the carbon balance is close to 100% (typically within  $\pm 10\%$  analytical uncertainty) over the temperature range tested.

### *M-xylene Combustion*

The volatile organics observed and quantified during combustion of m-xylene are reported in Figures 5.59 through 5.70. As mentioned earlier, for m-xylene, model yields were obtained using the SERDP model applied with SHOCKIN code. Model yields of CO agree reasonably with those determined experimentally (Figure 5.58); however, the model under-predicts CO<sub>2</sub>, CH<sub>4</sub>, C<sub>2</sub>H<sub>4</sub> and benzene yields, and over-predicts yields of acetylene by a significant margin (up to 20%, see Figure 5.62).

The semi-volatile species identified from the GC/MS analysis (using NIST library search report) are reported in Table 5.2. We determined normalized yields of major species recovered from the semi-volatile analysis semi-quantitatively. The following compounds were identified and quantified using the internal standard Naphthalene-d<sub>8</sub>: toluene (C<sub>7</sub>H<sub>8</sub>), m-xylene (C<sub>8</sub>H<sub>10</sub>), styrene (C<sub>8</sub>H<sub>8</sub>), phenyl-ethyne (C<sub>8</sub>H<sub>6</sub>), ethyl-benzene (C<sub>8</sub>H<sub>10</sub>), phenol (C<sub>6</sub>H<sub>6</sub>O) and naphthalene (C<sub>10</sub>H<sub>8</sub>).

The model predicted faster removal of m-xylene from the system (see Figure 5.66). However, the experimental yields suggested that a significant amount of m-xylene was still present after the end of the combustion (typically 1%). Based on our previous studies (Kahandawala, 2004), it was estimated that about 4% of the fuel mixture trapped inside the crevices and dead volumes of the shock tube test section remains unreacted, but, computationally adjusting for this caused more disagreement with the model predictions. Similarly, for toluene, phenyl-ethyne, ethyl benzene, styrene, and phenol, the model predicted very fast decay in concentration with respect to the temperature rise. In the present version of the SERDP model, naphthalene reactions were blocked; therefore, naphthalene yields were reported without comparison with the model yields (see Figure 5.71).

Species adsorbed on soot surface (mostly non-volatile PAHs and heavy hydrocarbons) were extracted for a single experiment in m-xylene combustion (T= 1614 K, P = 19 atm  $\Phi=3$ ). The species identified from the GC/MS analysis are reported in Table 5.1. Up to seven ring PAHs (Coronene) were seen in this particular experiment.

The soot yields from m-xylene combustion ( $\Phi=3$ , Ar =93 and 98%) are presented in Figure 5.72. For the 93% argon fuel mixture, the maximum soot yields were ~13% at approximately 1275 K. However, for 98% argon fuel mixtures, the maximum of the soot bell-shaped curve shifted to higher temperatures (~1750 K) with a decrease in maximum yield (~6%).

As shown in Figure 5.73, the carbon balance is close to 100% (typically within  $\pm 10\%$  analytical uncertainty) over the temperature range tested.

### *N-dodecane and N-dodecane/ m-xylene Surrogate Combustion*

Volatile and semi-volatile organics from the combustion of n-dodecane / m-xylene blend (Figures 5.74 through 5.82) and n-dodecane (Figures 5.84 through 5.87) were quantified. For combustion of blend, yields of benzene, toluene, m-xylene, n-dodecane, phenol, phenylethyne, ethylbenzene, styrene and naphthalene were obtained (semi-quantitatively). For n-dodecane, combustion yields of benzene, toluene, n-dodecane and phenylethyne were obtained. The SERDP model did not produce good agreement with experimental ignition delay times in the case of n-dodecane and the blend (for Ar=93 %,  $\Phi=3$ , see Figures 5.40 and 5.43). Preliminary

modeling using Chemkin-Pro produced high degree of disagreement with the experimental results. Therefore, for n-dodecane and the blend, the experimental yields are reported without modeling predictions.

Some volatile and semi-volatile species identified from n-dodecane combustion are reported in Table 5.1. Species extracted from soot surface following the combustion of n-dodecane and the blend are reported in Tables 5.5 and 5.6, respectively. The soot yields from the combustion of n-dodecane and the blend are reported in Figure 5.83. In Figure 5.88 a comparison of soot yields from the combustion of the four fuels tested in present study is shown. M-xylene produced the highest soot yields, whereas n-dodecane produced the least. Yields of soot from JP-8 combustion (Kahandawala, 2008) were compared with those of the blend (a proposed JP-8 surrogate, see Figure 5.89). The yields of JP-8 and the blend were very similar, considering the experimental scatter.

Important conclusions:

- For ethylene and m-xylene, the ignition delay times for relatively concentrated mixtures (argon=93%) showed indiscernible difference over the range of pressures and equivalence ratios tested. However, for n-dodecane and n-dodecane/ m-xylene blend, the dependence of ignition delay times on equivalence ratio was observable.
- We developed SHOCKIN code to produce an improved shock tube modeling approach. In m-xylene combustion, the improved agreement over Chemkin-Pro based constant (U,V) modeling assumption signified the fact that shock tube modeling approach using SHOCKIN program essentially frees the data from any non-ideal gas-dynamic/ heat release related or any other effects.
- Preliminary modeling results of ignition delay times obtained from this study using the 1-D CFD code, GASKIN with detailed chemistry were very encouraging. GASKIN estimations of experimental pressure profile and dwell time were highly accurate in a given m-xylene combustion experiment using both reduced and full chemistry SERDP 0.1 model.
- The kinetic models developed during the SERDP (SERDP 0.1, with Jetsurf 0.2) predicted ignition delay times reasonably well over a range of experimental conditions in case of ethylene and m-xylene. For n-dodecane and the blend, the agreement between experimental data and modeling predictions under rich conditions was not satisfactory.
- The agreement between experimental and model yields of major species was not satisfactory when SERDP 0.1 was applied with Chemkin. Refinement of the kinetic-model, experimental procedure (e. g. improving analytical accuracy), and modeling approach (e.g using SHOCKIN code) could reduce this gap. This work is ongoing and will be reported in forthcoming publications.

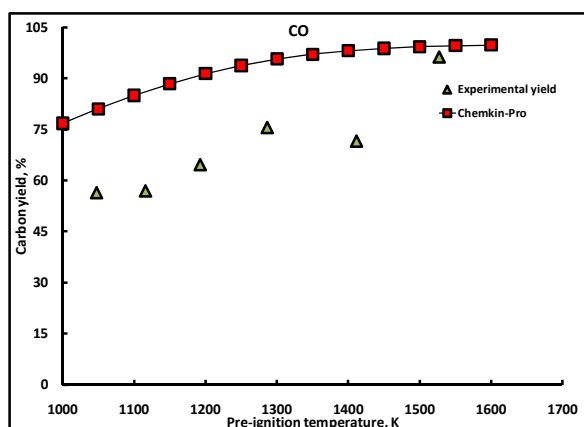


Figure 5.47 Combustion of Ethylene: Experimental and Model Yields of Carbon Monoxide at  $\Phi=3.0$ , Ar=93% P~18 atm.

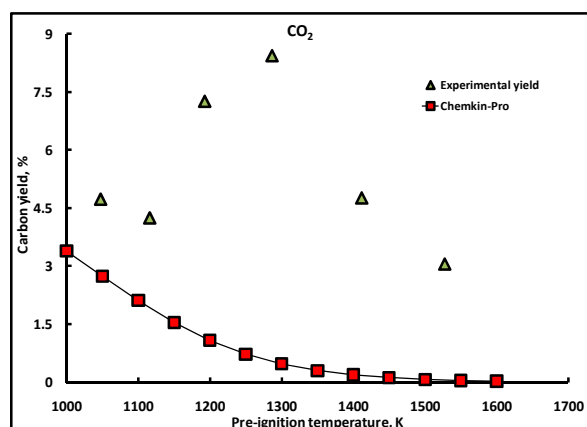


Figure 5.48 Combustion of Ethylene: Experimental and Model Yields of Carbon Dioxide at  $\Phi=3.0$ , Ar=93% P~18 atm.

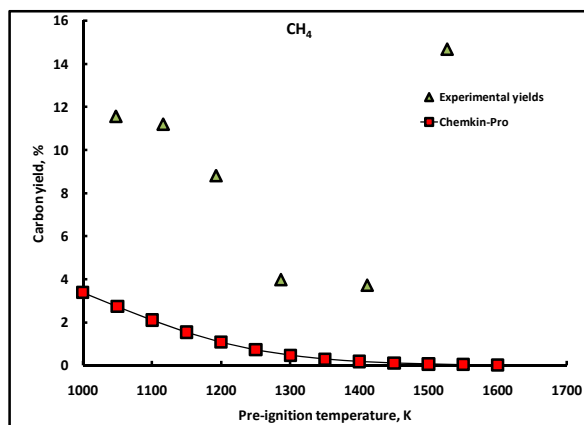


Figure 5.49 Combustion of Ethylene: Experimental and Model Yields of Methane at  $\Phi=3.0$ , Ar=93% P~18 atm.

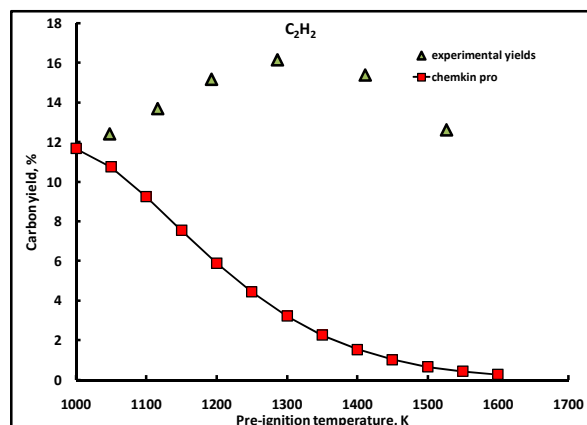


Figure 5.50 Combustion of Ethylene: Experimental and Model Yields of Acetylene at  $\Phi=3.0$ , Ar=93% P~18 atm.

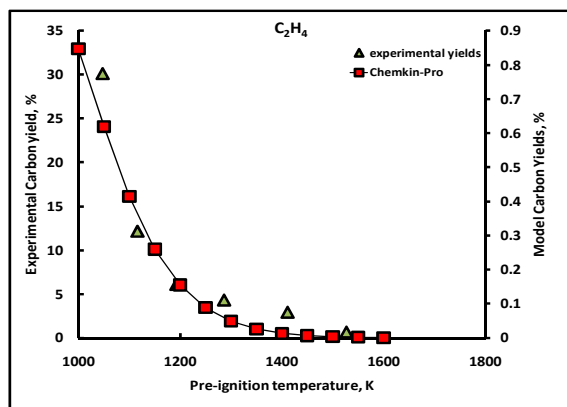


Figure 5.51 Combustion of Ethylene: Experimental and Model Yields of Ethylene at  $\Phi=3.0$ , Ar=93% P~18 atm.

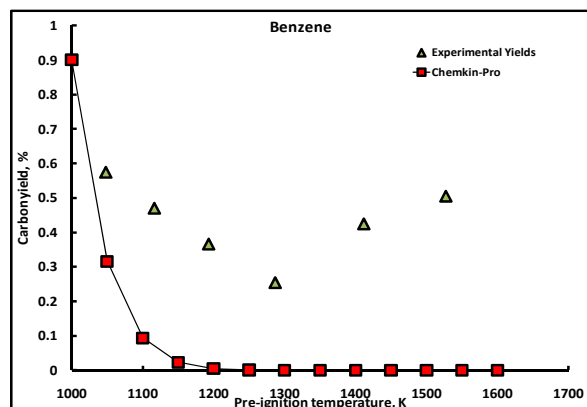


Figure 5.52 Combustion of Ethylene: Experimental and Model Yields of Benzene at  $\Phi=3.0$ , Ar=93% P~18 atm.

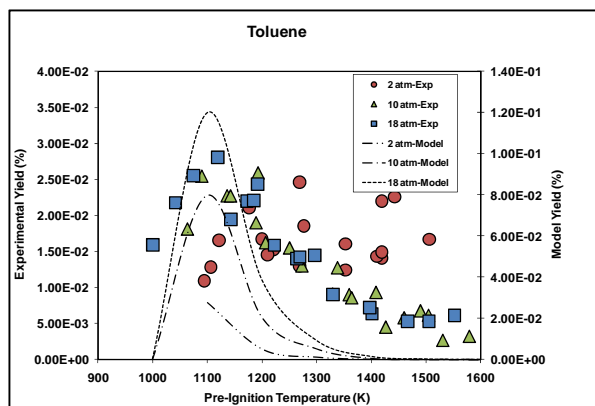


Figure 5.53 Combustion of Ethylene: Experimental and Model Yields of Toluene at  $\Phi=3.0$ , Ar=93%, P~2, 10 and 18 atm.

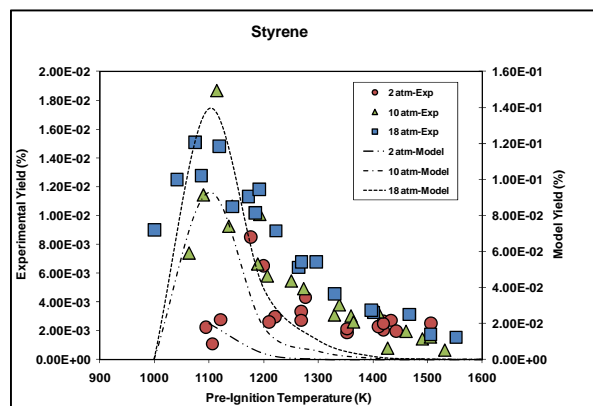


Figure 5.54 Combustion of Ethylene: Experimental and Model Yields of Styrene at  $\Phi=3.0$ , Ar=93% P~2, 10 and 18 atm.

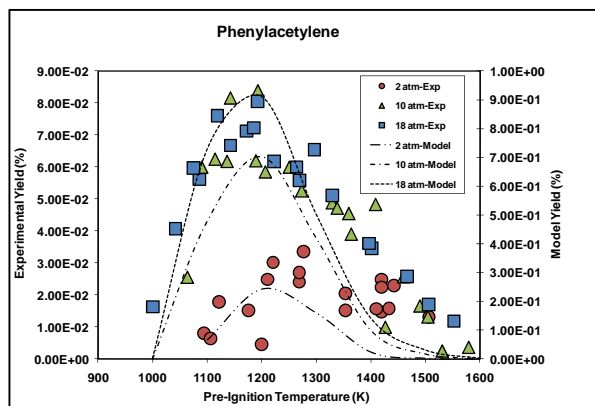


Figure 5.55 Combustion of Ethylene: Experimental and Model Yields of Phenyl acetylene at  $\Phi=3.0$ , Ar=93%, P~2, 10 and 18 atm.

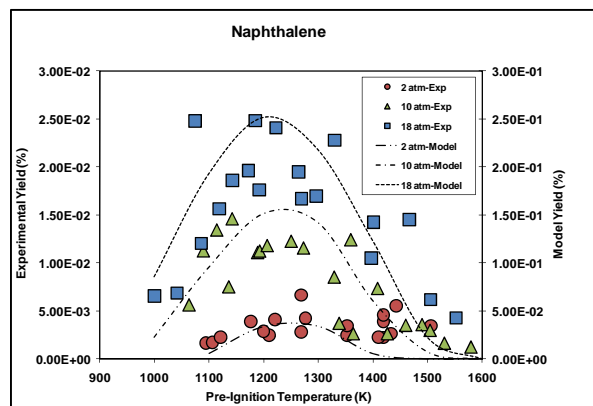


Figure 5.56 Combustion of Ethylene: Experimental and Model Yields of Naphthalene at  $\Phi=3.0$ , Ar=93%, P~2, 10 and 18 atm.

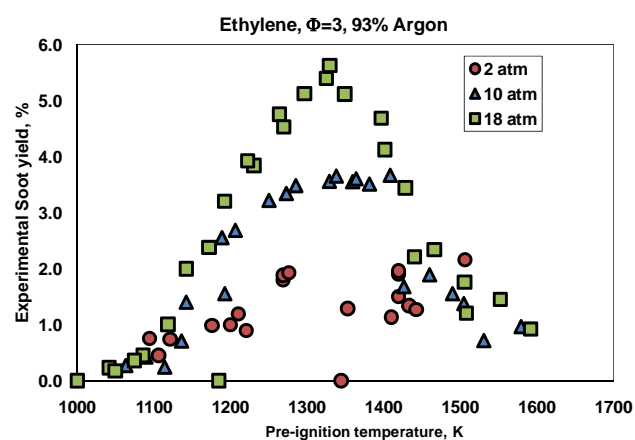


Figure 5.57 Soot Yields from Combustion of Ethylene at  $\Phi=3.0$ , Ar=93%, P~2, 10 & 18 atm.

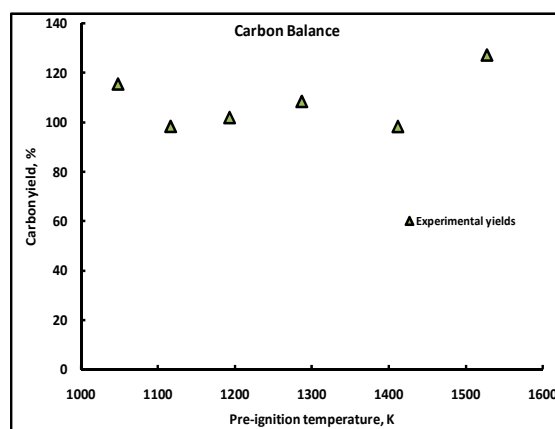


Figure 5.58 Carbon balance for the combustion-generated species quantified in ethylene combustion at  $\Phi=3$ , Ar=93% at 18 atm.



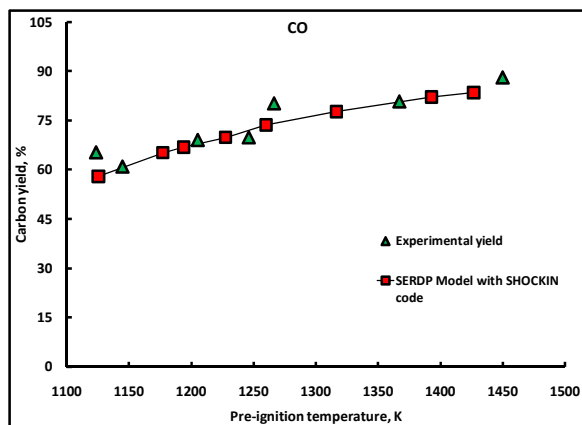


Figure 5.59 Combustion of m-Xylene: Experimental and Model Yields of Carbon Monoxide at  $\Phi=3.0$ , Ar=93% P~18 atm.

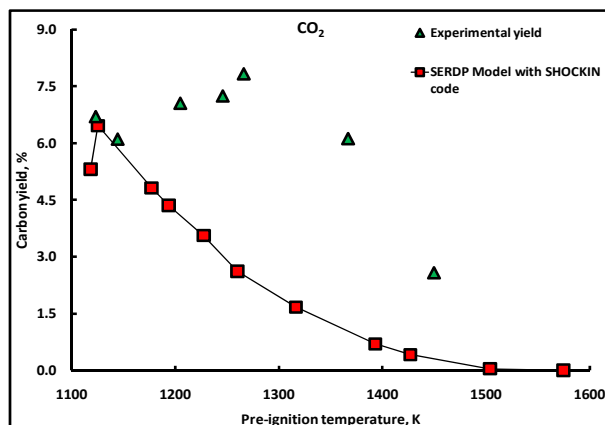


Figure 5.60 Combustion of m-Xylene: Experimental and Model Yields of Carbon Dioxide at  $\Phi=3.0$ , Ar=93% P~18 atm.

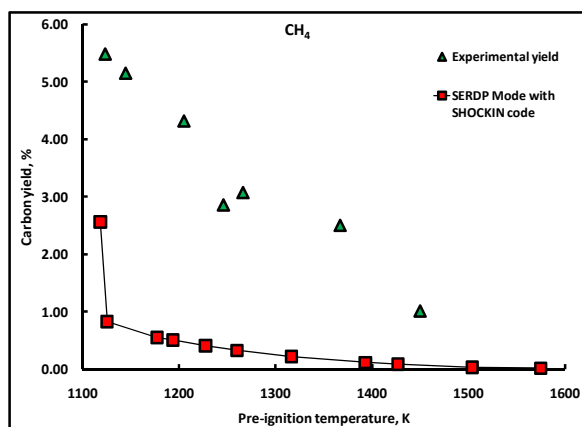


Figure 5.61 Combustion of m-Xylene: Experimental and Model Yields of Methane at  $\Phi=3.0$ , Ar=93% P~18 atm.

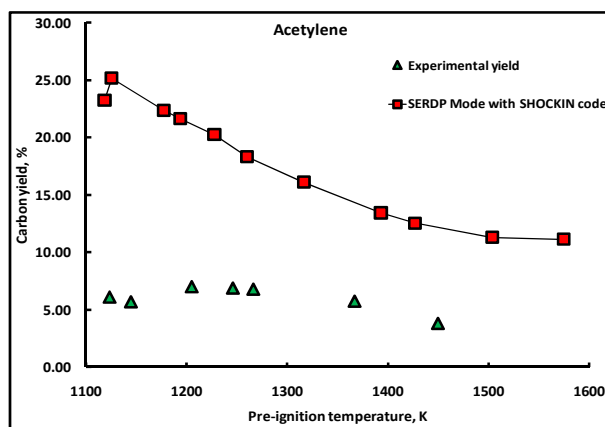


Figure 5.62 Combustion of m-Xylene: Experimental and Model Yields of Acetylene at  $\Phi=3.0$ , Ar=93% P~18 atm.

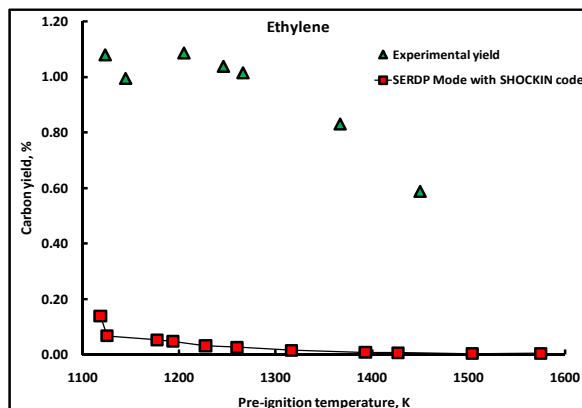


Figure 5.63 Combustion of m-Xylene: Experimental and Model Yields of Ethylene at  $\Phi=3.0$ , Ar=93% P~18 atm.

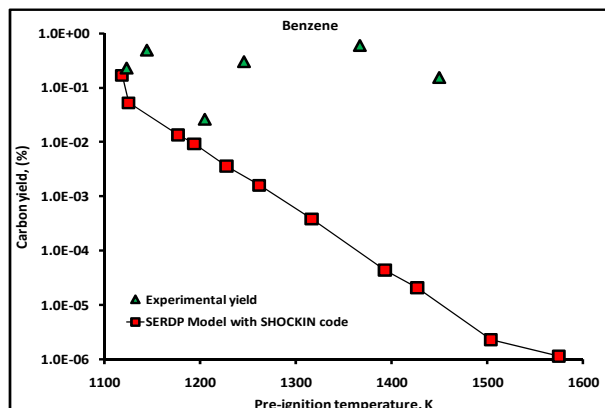


Figure 5.64 Combustion of m-Xylene: Experimental and Model Yields of Benzene at  $\Phi=3.0$ , Ar=93% P~18 atm.

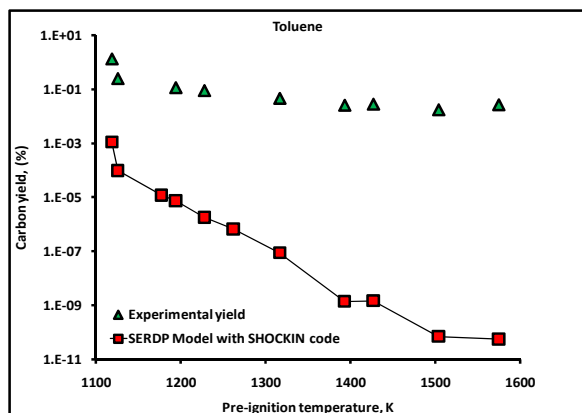


Figure 5.65 Combustion of m-Xylene: Experimental and Model Yields of Toluene at  $\Phi=3.0$ , Ar=93% P~18 atm.

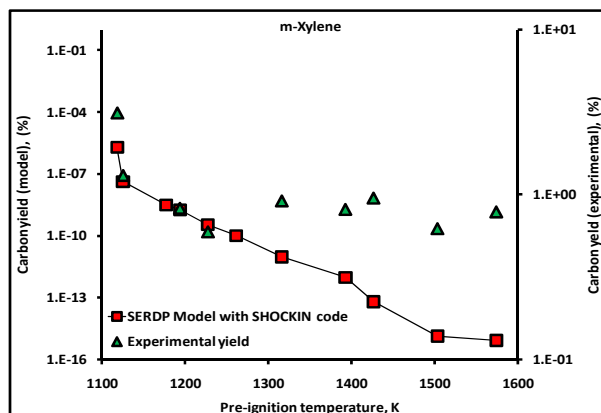


Figure 5.66 Combustion of m-Xylene: Experimental and Model Yields of m-Xylene at  $\Phi=3.0$ , Ar=93% P~18 atm.

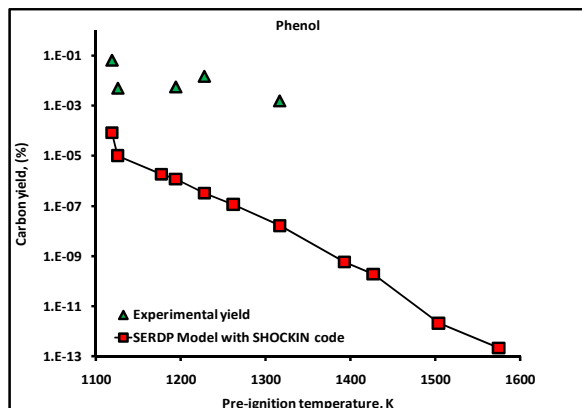


Figure 5.67 Combustion of m-Xylene: Experimental and Model Yields of Phenol at  $\Phi=3.0$ , Ar=93% P~18 atm.

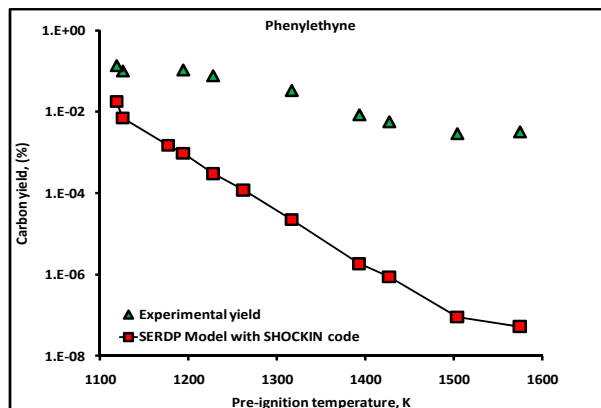


Figure 5.68 Combustion of m-Xylene: Experimental and Model Yields of Phenylethyne at  $\Phi=3.0$ , Ar=93% P~18 atm.

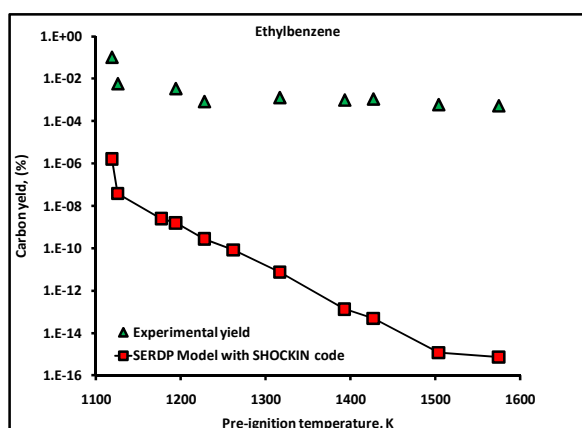


Figure 5.69 Combustion of m-Xylene: Experimental and Model Yields of Ethylbenzene at  $\Phi=3.0$ , Ar=93% P~18 atm.

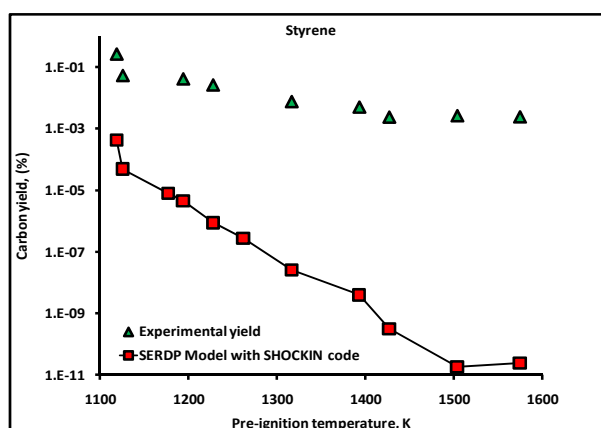


Figure 5.70 Combustion of m-Xylene: Experimental and Model Yields of Styrene at  $\Phi=3.0$ , Ar=93% P~18 atm.

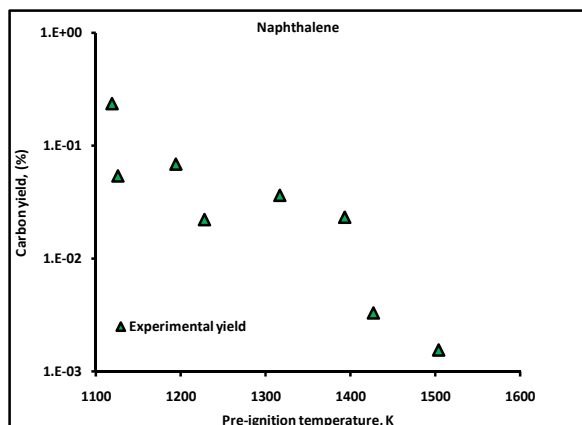


Figure 5.71 Combustion of m-Xylene: Experimental Yields of Naphthalene at  $\Phi=3.0$ , Ar=93% P~18 atm.

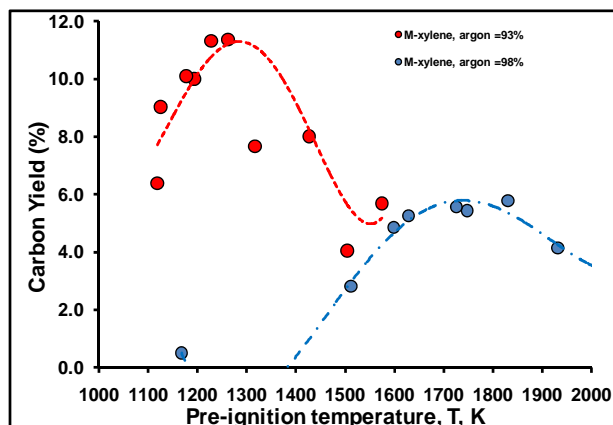


Figure 5.72 Soot Yields from Combustion of M-xylene at  $\Phi=3.0$ , Ar=93% and 98%, and 18 atm.

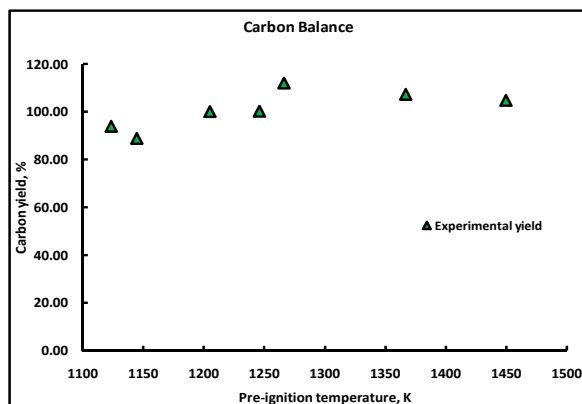


Figure 5.73 Carbon balance for the combustion-generated species quantified in the m-xylene combustion at Ar=93%, P=18 atm.

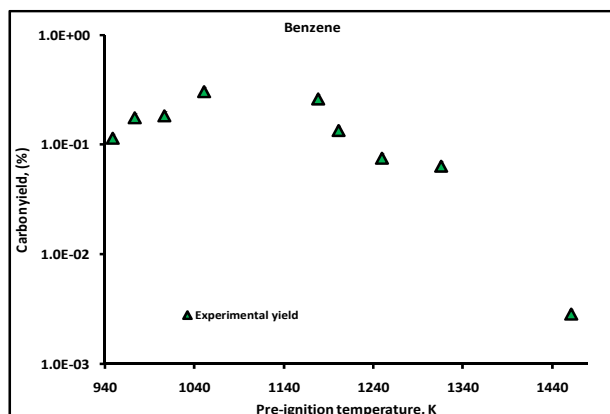


Figure 5.74 Combustion of n-Dodecane/m-Xylene blend: Experimental and Model Yields of Benzene at  $\Phi=3.0$ , Ar=93% P~18 atm.

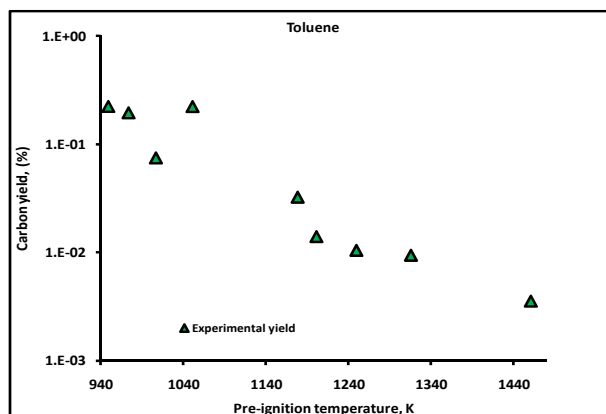


Figure 5.75 Combustion of n-Dodecane/m-Xylene blend: Experimental and Model Yields of Toluene at  $\Phi=3.0$ , Ar=93% P~18 atm.

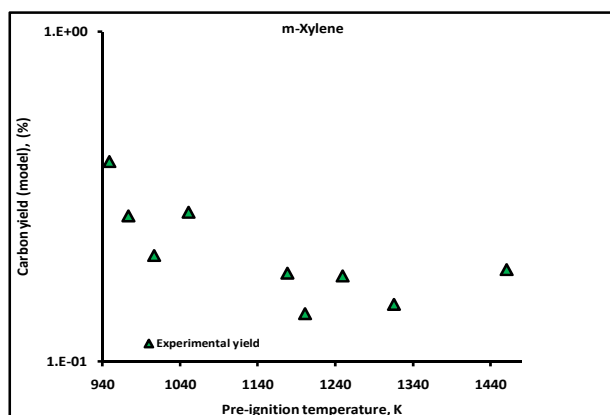


Figure 5.76 Combustion of n-Dodecane/m-Xylene blend: Experimental and Model Yields of m-Xylene at  $\Phi=3.0$ , Ar=93% P~18 atm.

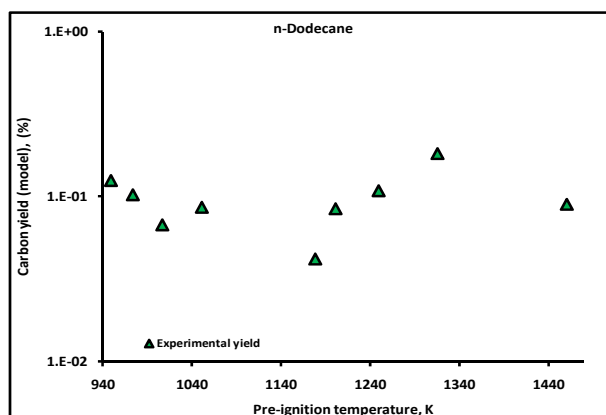


Figure 5.77 Combustion of n-Dodecane/m-Xylene blend: Experimental and Model Yields of n-Dodecane at  $\Phi=3.0$ , Ar=93% P~18 atm.

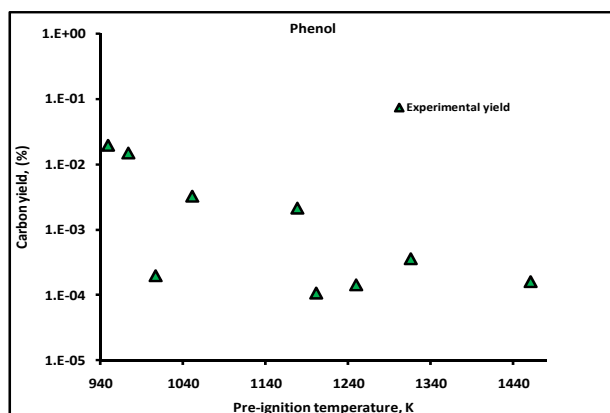


Figure 5.78 Combustion of n-Dodecane/m-Xylene blend: Experimental and Model Yields of Phenol at  $\Phi=3.0$ , Ar=93% P~18 atm.

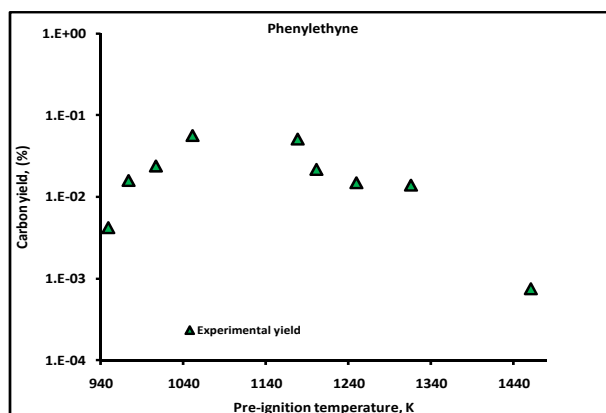


Figure 5.79 Combustion of n-Dodecane/m-Xylene blend: Experimental and Model Yields of Phenylethyne at  $\Phi=3.0$ , Ar=93% P~18 atm.

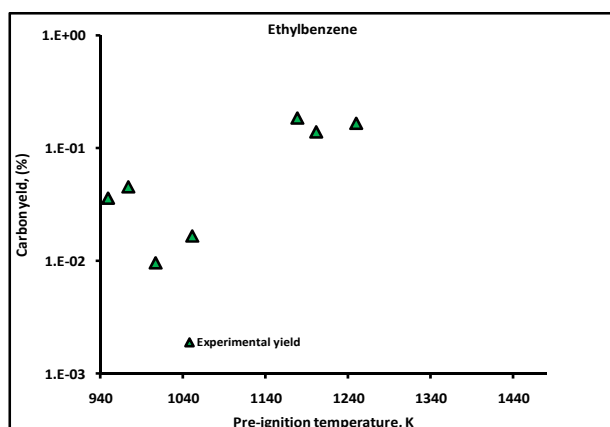


Figure 5.80 Combustion of n-Dodecane/m-Xylene blend: Experimental and Model Yields of Ethylbenzene at  $\Phi=3.0$ , Ar=93% P~18 atm.

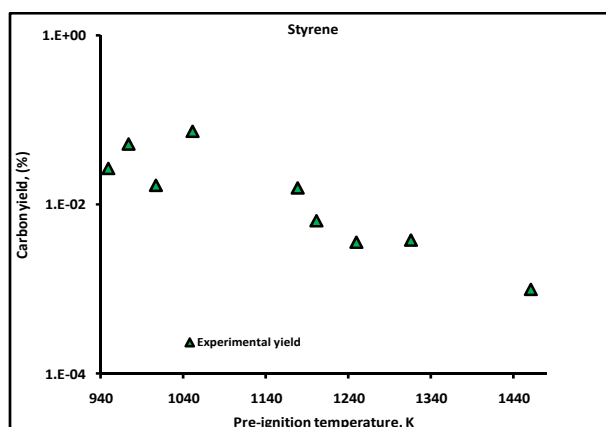


Figure 5.81 Combustion of n-Dodecane/m-Xylene blend: Experimental and Model Yields of Styrene at  $\Phi=3.0$ , Ar=93% P~18 atm.

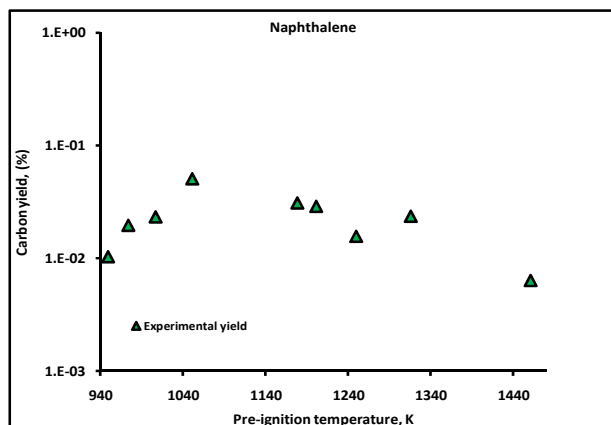


Figure 5.82 Combustion of n-Dodecane/m-Xylene blend: Experimental Yields of Naphthalene at  $\Phi=3.0$ , Ar=93% P~18 atm.

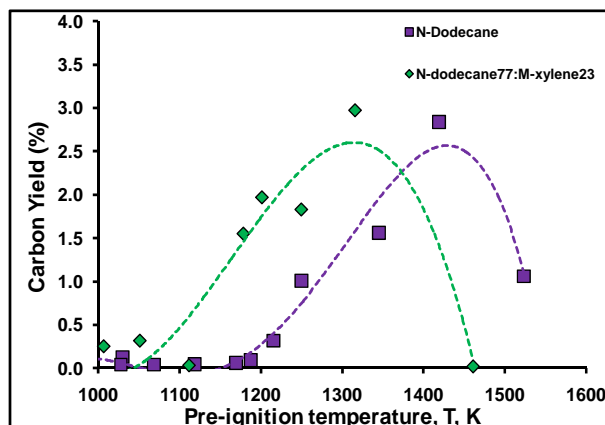


Figure 5.83 Soot Yields from Combustion of N-dodecane and n-dodecane/ M-xylene blend at  $\Phi=3.0$ , Ar=93% and 98%, and 18 atm.

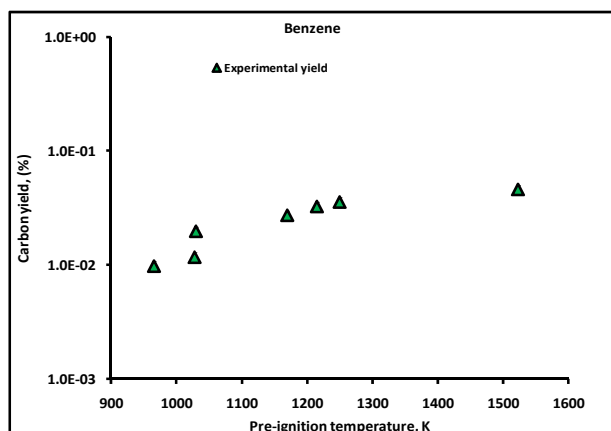


Figure 5.84 Combustion of n-Dodecane: Experimental and Model Yields of Benzene at  $\Phi=3.0$ , Ar=93% P~18 atm.

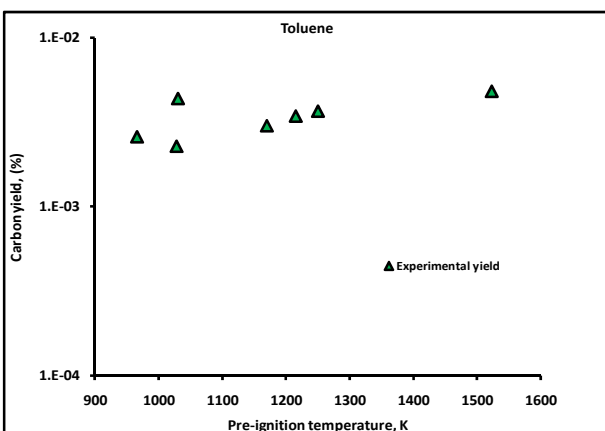


Figure 5.85 Combustion of n-Dodecane: Experimental and Model Yields of Toluene at  $\Phi=3.0$ , Ar=93% P~18 atm.

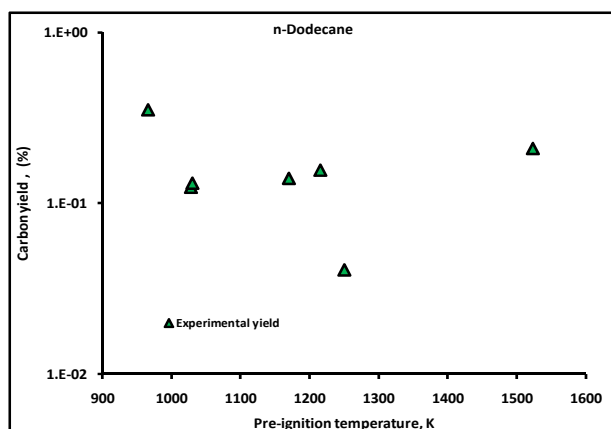


Figure 5.86 Combustion of n-Dodecane: Experimental and Model Yields of n-Dodecane at  $\Phi=3.0$ , Ar=93% P~18 atm.

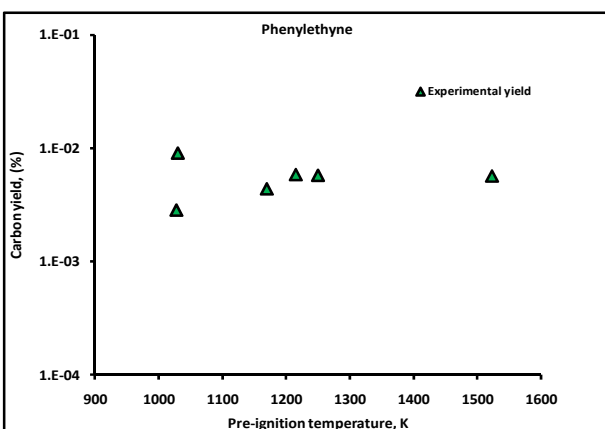


Figure 5.87 Combustion of n-Dodecane: Experimental and Model Yields of Phenylethyne at  $\Phi=3.0$ , Ar=93% P~18 atm.

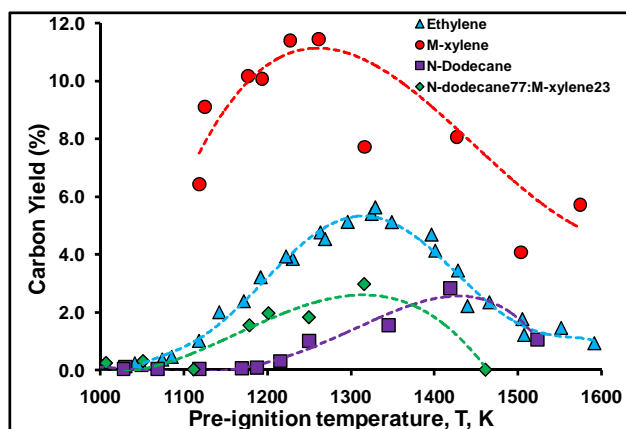


Figure 5.88 Comparison of soot yields from combustion of different fuels tested during SERDP.

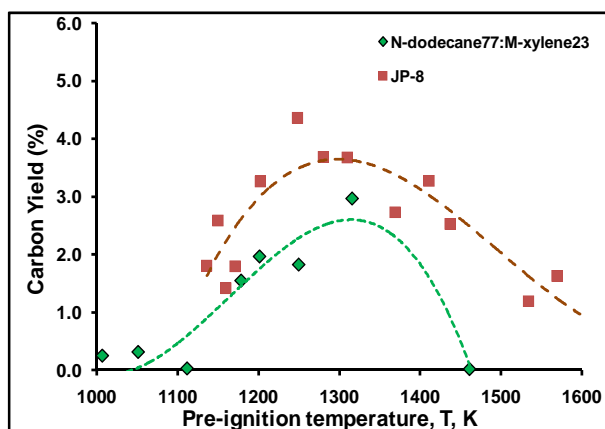


Figure 5.89 Comparison of soot yields from combustion of JP-8 and n-dodecane/m-xylene blend (surrogate JP-8).

Table 5.1 Volatile and Semi Volatile Species Extracted in Combustion of n-Dodecane ( $\Phi=3$ ).

Species	Formula	Structure
Butanal, 3-hydroxy-	$C_4H_8O_2$	
3-Buten-2-one, 3-methyl-	$C_5H_8O$	
3-Penten-2-one	$C_5H_8O$	
2-Butenal, 2-methyl-	$C_5H_8O$	
3-Penten-2-ol	$C_5H_{10}O$	
2-Butanone, 3-methyl-	$C_5H_{10}O$	
Benzene	$C_6H_6$	
Phenol	$C_6H_6O$	
3-Hexen-1-ol	$C_6H_{12}O$	
2H-Pyran-2-methanol, tetrahydro-	$C_6H_{12}O_2$	
1-Butanol, 2,3-dimethyl-	$C_6H_{14}O$	

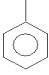
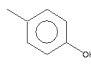
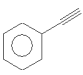
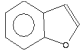
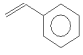
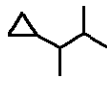
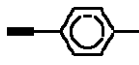
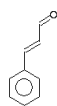

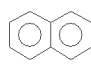
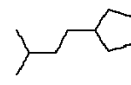
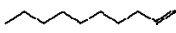
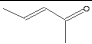
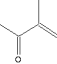
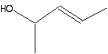
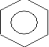
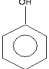
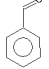
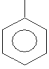
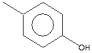
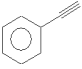
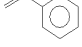

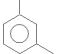
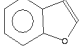
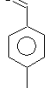
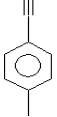
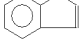
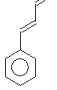
Toluene	$C_7H_8$	
Phenol, 4-methyl-	$C_7H_8O$	
Phenylethyne	$C_8H_6$	
Benzofuran	$C_8H_6O$	
Styrene	$C_8H_8$	
Cyclopropane, (1,2-dimethylpropyl)-	$C_8H_{16}$	
Benzene, 1-ethynyl-4-methyl-	$C_9H_8$	
2-Propenal, 3-phenyl-	$C_9H_8O$	
Nonene	$C_9H_{18}$	
Naphthalene	$C_{10}H_8$	
Cyclopentane, (3-methylbutyl)-	$C_{10}H_{20}$	
Decene	$C_{10}H_{20}$	

Table 5.2 Volatile and Semi Volatile Species Extracted in Combustion of M-xylene ( $\Phi=3$ ).

Species	Formula	Structure
3-Penten-2-one	$C_5H_8O$	
3-Buten-2-one, 3-methyl-	$C_5H_8O$	
3-Penten-2-ol	$C_5H_{10}O$	
Benzene	$C_6H_6$	
Phenol	$C_6H_6O$	
Benzaldehyde	$C_7H_6O$	
Toluene	$C_7H_8$	
Phenol, 4-methyl-	$C_7H_8O$	
Phenylethyne	$C_8H_6$	
Styrene	$C_8H_8$	
Ethylbenzene	$C_8H_{10}$	
m-xylene	$C_8H_{10}$	
Benzofuran	$C_8H_6O$	
Benzaldehyde, 4-methyl-	$C_8H_8O$	
Benzene, 1-ethynyl-4-methyl-	$C_9H_8$	
Indene	$C_9H_8$	
2-Propenal, 3-phenyl-	$C_9H_8O$	



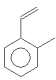
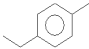
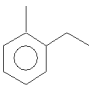
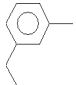
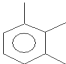

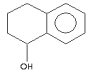
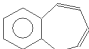
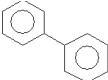

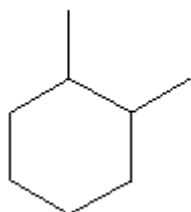
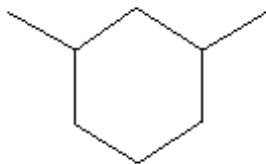
Benzene, 1-ethenyl-2-methyl-	$C_9H_{10}$	
Benzene, 1-ethyl-4-methyl-	$C_9H_{12}$	
Benzene, 1-ethyl-2-methyl-	$C_9H_{12}$	
Benzene, 1-ethyl-3-methyl-	$C_9H_{12}$	
Benzene, 1,2,3-trimethyl-	$C_9H_{12}$	
Naphthalene	$C_{10}H_8$	
1-Naphthalenol, 1,2,3,4-tetrahydro-	$C_{10}H_{12}O$	
Benzocycloheptatriene	$C_{11}H_{10}$	
Biphenyl	$C_{12}H_{10}$	
Acenaphthylene	$C_{12}H_8$	

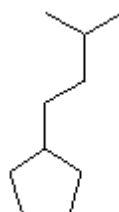
Table 5.3 Species extracted from soot surface in Ethylene combustion.



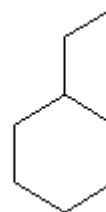
Cyclohexane, 1,2-dimethyl-



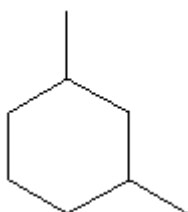
Cyclohexane, 1,3-dimethyl



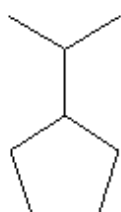
Cyclopentane, (3-methylbutyl)-



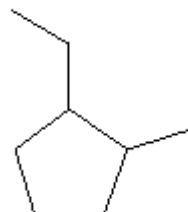
Cyclohexane, ethyl



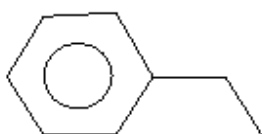
Cyclohexane, 1,3-dimethyl-



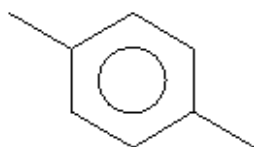
Cyclopentane, 1-methylethyl-



Cyclopentane, 1-ethyl, 2-methyl-



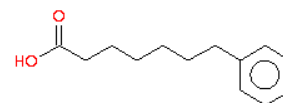
Ethylbenzene



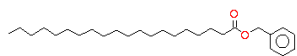
p-xylene



Nonane



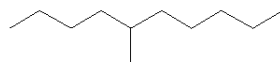
7-phenylheptanoic acid



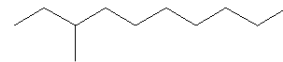
Eicosanoic acid,  
phenylmethyl ester



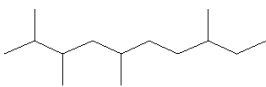
Decane



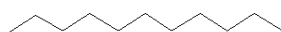
Decane, 5-methyl-



Decane, 3-methyl-



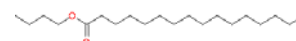
Decane, 2,3,5,8-  
tetramethyl



Undecane



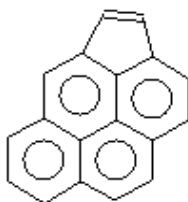
Octadecanoic acid,  
methyl ester



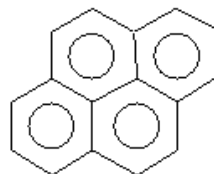
hexadecanoic acid, butyl  
ester



Octadecanoic acid, butyl  
ester

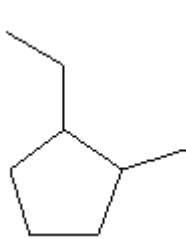
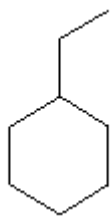
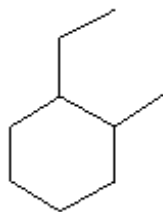
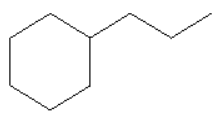
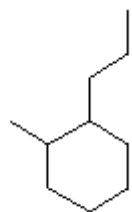
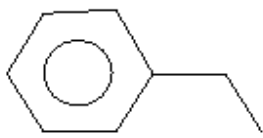
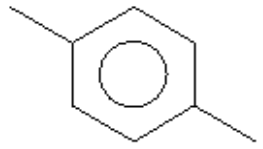
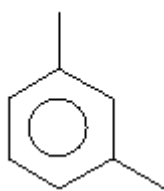
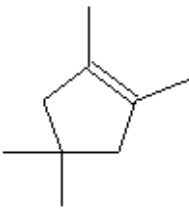
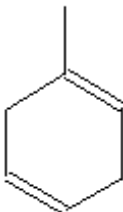
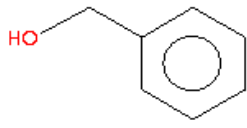
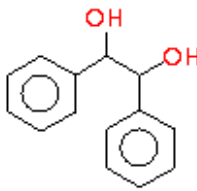

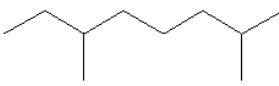
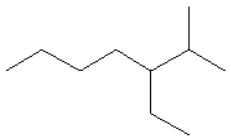
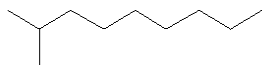
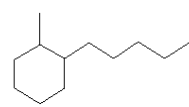

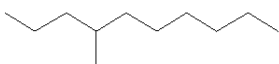
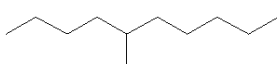


Cyclopenta(cd) pyrene

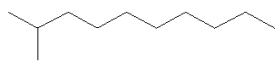


Pyrene

Table 5.4 Species extracted from soot surface in m-xylene combustion.

			
Cyclopentane, 1-ethyl, 2-methyl	Cyclohexane, ethyl-	Cyclohexane, 1-ethyl, 2-methyl	Cyclohexane, propyl-
			
Cyclohexane, 1-methyl, 2-propyl	Ethyl benzene	p-xylene	m-xylene
			
1,2,4,4-Tetra-methylcyclopentene	1,4-Cyclohexadiene, 1-methyl-	Benzyl alcohol	1,2-Ethanediol, 1,2 diphenyl
			
Nonane	Octane, 2,6 dimethyl	Heptane, 3-ethyl, 2-methyl	Nonane, 2-methyl
			
Cyclopentane, 1-methyl,	Decane	Decane, 4-methyl	Decane, 5-methyl

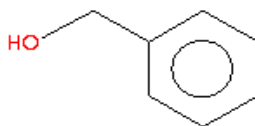
2-pentyl



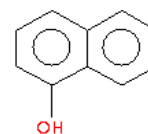
Decane, 2-methyl



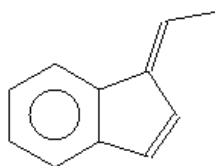
Dodecane



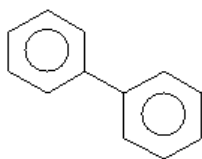
Benzyl alcohol



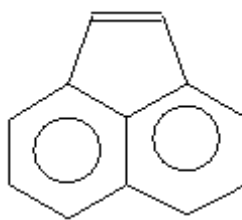
1-Naphthalenol



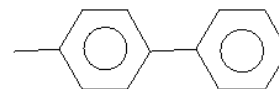
1-H indene, 1-ethylidene



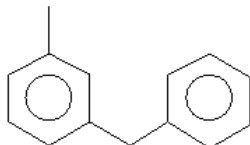
Biphenyl



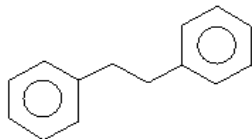
Acenaphthylene



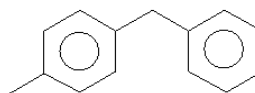
1,1' -Biphenyl, 4-methyl



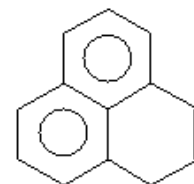
Benzene, 1-methyl-3-phenylmethyl-



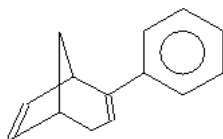
Bibenzyl



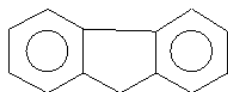
Benzene, 1-methyl-4-phenylmethyl-



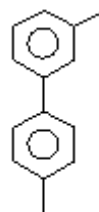
1-H-phenalene



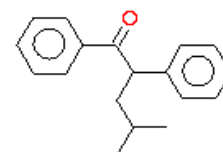
Bicyclo(3,2,1) Octa, 2,6-diene, 2-phenyl-



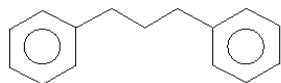
Fluorene



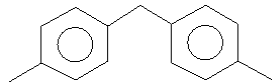
1,1' Biphenyl 3,4'-dimethyl



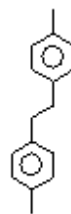
Valerophenone, 4-methyl, 2-phenyl



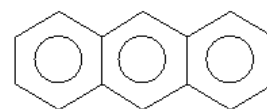
Benzene, 1,1'-(1,3  
propanediyl)bis-



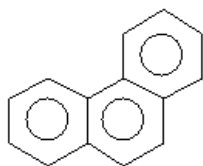
Benzene, 1,1'methylene  
bis(4-methyl)-



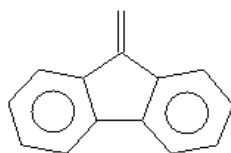
Benzene, 1,1'  
(1,2,ethanediyl) bis-  
(4methyl)



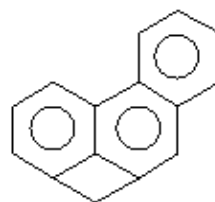
Anthracene



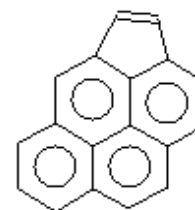
Phenanthrene



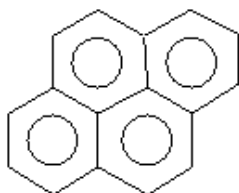
9-H- Fluorene, 9-  
methylene



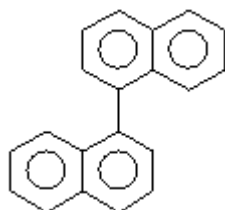
6H-cylcobuta(jk)  
phenanthrene



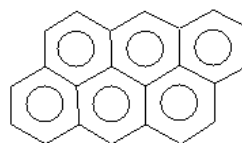
Cyclopenta-(cd) pyrene



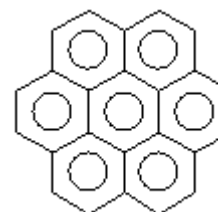
Pyrene



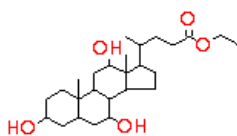
1,1'-Binaphthalene



Dibenzo-(def,mno)-  
chrysene



Coronene

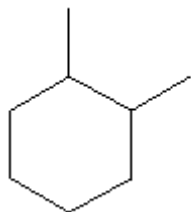


Ethyl-iso-allocholate

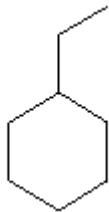


Octadecanoic acid, butyl  
ester

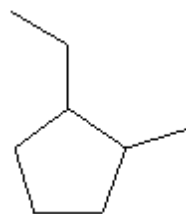
Table 5.5 Species extracted from soot surface from n-dodecane combustion.



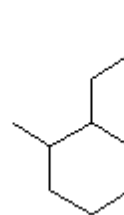
Cyclohexane, 1,2-dimethyl-



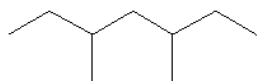
Cyclohexane, ethyl-



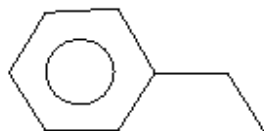
Cyclopentane, 1-ethyl, 2-methyl-



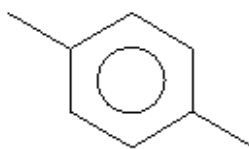
Cyclohexane, 1-methyl, 2-propyl-



Heptane, 3,5 -dimethyl-



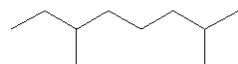
Ethylbenzene



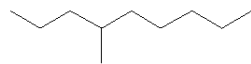
p-xylene



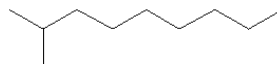
Nonane



Octane, 2,6-dimethyl-



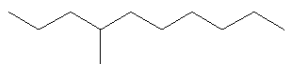
Nonane, 4-methyl-



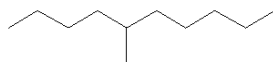
Nonane, 2-methyl-



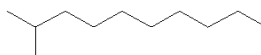
Decane



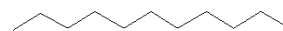
Decane, 4-methyl



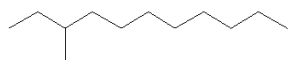
Decane, 5-methyl



Decane, 2-methyl-



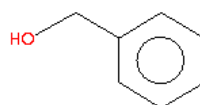
Undecane



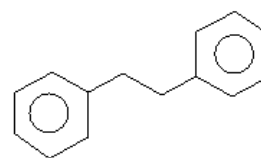
Undecane, 3-methyl



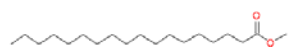
Dodecane



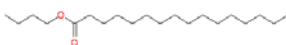
Benzyl alcohol



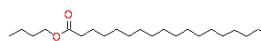
Bibenzyl



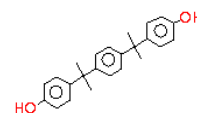
Octadecanoic acid,  
methyl ester



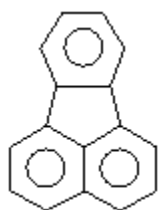
Hexadecanoic acid,  
butyl ester



Octadecanoic acid, butyl  
ester



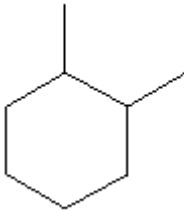
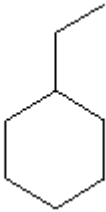
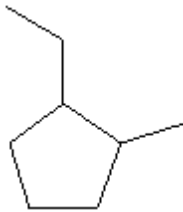
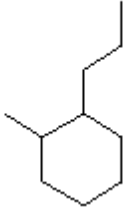
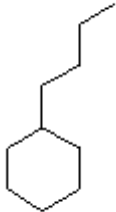
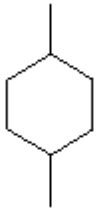
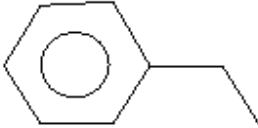
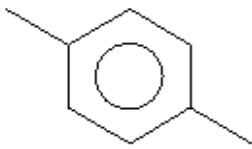
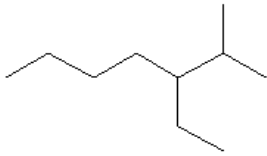
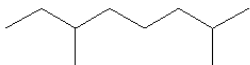

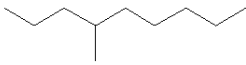
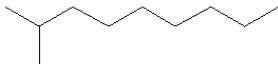

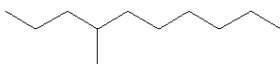
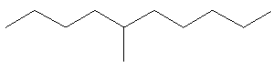
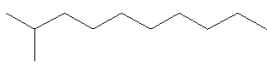
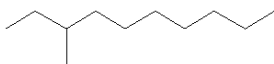


4,4'-((p-phenylene) di-  
isopropylidene)diphenol

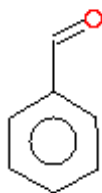


Fluoranthene

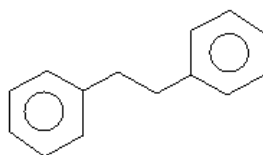


Table 5.6 Species extracted from soot surface in the combustion of n-dodecane/ m-xylene blend.

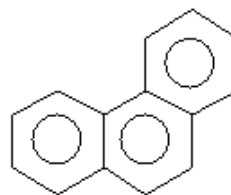
			
Cyclohexane, 1,2 dimethyl-	Cyclohexane, ethyl-	Cyclopentane, 1-ethyl, 2-methyl-	Cyclohexane, 1-methyl, 2-propyl-
			
Cyclohexane, butyl-	Cyclohexane, 1,4 dimethyl-	Ethylbenzene	p-xylene
			
Heptane, 3 ethyl, 2 methyl-	Octane, 2,6-dimethyl-	Nonane	Nonane, 4-methyl-
			
Nonane, 2-methyl-	Decane	Decane, 4-methyl	Decane, 5-methyl
			
Decane, 2-methyl-	Decane, 3-methyl-	Undecane	Dodecane



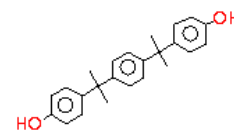
Benzaldehyde



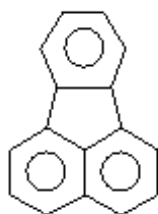
Bibenzyl



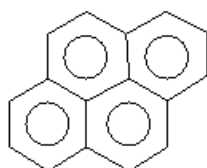
Phenanthrene



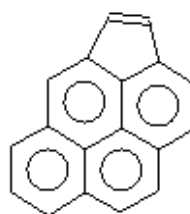
4,4'-((p-phenylene)  
diisopropylidene)  
diphenol



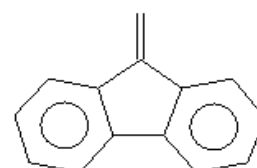
Fluoranthene



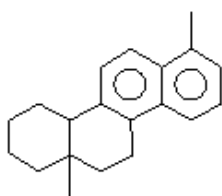
Pyrene



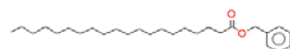
Cyclopenta(cd) pyrene



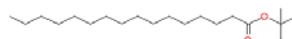
9H-Fluorene, 9-  
methylene



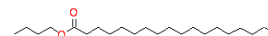
7,12a dimethyl-1,2,3,4-  
4a,11,12,12a  
Octahydrochrysene



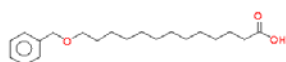
Eicosanoic acid,  
phenylmethyl ester



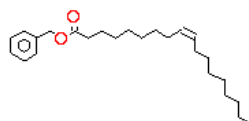
Hexadecanoic acid, 1,1-  
dimethylethyl ester



Octadecanoic acid, butyl  
ester



Benzyloxy tridecanoic  
acid



9-Octadecenoic acid (z),  
phenylmethyl ester

## 5.2 Co-flow Diffusion Flame

### 5.2.1 Impact of Soot Radiation on Dynamics of Co-flow Flames

The purpose of the present study was to investigate the impact of soot radiation on flame flicker—a low-frequency 12-Hz oscillation of the flame. The impetus for the study was the observation that a jet diffusion flame being used to study soot was steady, whereas similar vertical flames used in other studies exhibited flame flicker. Specifically, Santoro and co-workers conducted extensive experimental studies of soot-formation and —growth characteristics in a laminar, ethylene jet diffusion flame (Santoro and Semerjian, 1984). Kennedy et al. (1996) and D’Anna et al. (2007) used the same flame for modeling studies. This flame was experimentally determined to be steady. However, the jet diffusion flames studied by Davis et al. (1991), Ellzey et al. (1991), and Katta et al. (1993), at flow conditions similar to those used by Santoro and co-workers, exhibit a buoyancy-induced oscillation at a frequency of about 12 Hz. It is unclear why at similar conditions some flames are steady and others tend to oscillate.

The above discussion raises a question as to why the Santoro and co-workers flame is steady. While addressing this question, one of the marvelous events in research occurred. A prediction was made and later confirmed by experiments concerning a phenomenon that was new to the authors and perhaps to the combustion community. The prediction was that radiation from soot can influence flame flicker to such an extent that it becomes completely suppressed. As often is the case with a new insight, once it has been realized, it seems almost trivial. Indeed, it is hard to believe that it has been overlooked for many decades. One paper by Davis et al. (1990) that was found in the literature hinted that soot radiation might influence flame stability; but, to the authors’ knowledge, this subject has never been investigated.

Vertically mounted, laminar, ethylene-air jet diffusion flames are generated in the laboratory using a well-studied coannular burner operated at atmospheric pressure that consists of two concentric brass tubes of 11.1-mm and 101.6-mm inner diameters, with fuel flowing through the central tube and air through the annular passage. The larger air passage contains brass screens, glass beads, and a ceramic honeycomb at the exit to produce a uniform exit-velocity profile. The fuel tube, which extends 2.5 mm above the burner surface, is also partially filled with glass beads to facilitate flow conditioning. A 46-cm-long glass chimney is mounted on the outer brass cylinder to shield the flame from room-air disturbances. All reactant flows were controlled using mass flow meters ( $\pm 1.0\%$  at full scale). Two-dimensional images of the flame were obtained using an Intensified CCD (ICCD) camera. The ICCD camera was phase locked with the flame oscillation using the output voltage from a photomultiplier tube (PMT) as a reference signal to trigger a pulse generator (DG-535). The delay time between the trigger signal from the PMT and the output of the pulse generator was varied to change the phase location with respect to the oscillation. This procedure enabled imaging of the flickering flame at different phases of its oscillation.

Calculations for this flame are performed using UNICORN code. Chemical kinetics is modeled using Wang-Frenklach mechanism and soot is modeled using two-equation approach described earlier. Figure 5.98 shows time-dependent-UNICORN calculations and measurements in a

laminar, ethylene jet diffusion flame at conditions previously studied by Santoro and co-workers. The fuel and annular-air jet velocities were 3.91 and 8.8 cm/s, respectively. Radial distributions of temperature and soot at 70 mm above the burner exit are shown by solid lines, while the corresponding experimental data are shown with symbols. Soot volume fractions were obtained using a laser-extinction technique. Temperatures were measured with thermocouples and corrected for radiation heat loss. The calculated two-dimensional temperature field is shown in the inset. Comparisons between the predictions and the measurements for temperature and soot are reasonably good especially after considering the simple nature of the soot model and the uncertainties associated with the radiation corrections of the thermocouple data.

The most important result shown in Figure 5.98, is that the unsteady simulation yielded a steady flame, which is consistent with experimental observations. The question is raised as to why this flame is steady. As mentioned in the introduction, previous experiments and dynamic simulations have indicated that coannular jet flames, with inlet velocities in the range of the flame shown in Figure 5.98 are dynamic. It was initially thought that the burner geometry or inlet boundary conditions might be responsible for the flame steadiness. These possibilities were investigated using UNICORN. Computational experiments were performed in which geometrical and flow parameters were systematically changed. Calculations did not result in a flickering flame under any of the following conditions: (1) with flat or parabolic velocity profiles at the exits of the fuel and air tubes, 2) with and without the chimney surrounding the annular air flow, and 3) with and without the burner rim. Other numerical experiments were also performed using different grid systems and chemical kinetics. None of the numerical experiments resulted in a flickering flame. However, when the blackbody radiation from soot was turned off in the simulation, a periodically oscillating flame with a frequency of about 12 Hz was observed.

Although radiation was not expected to have an impact on flame oscillation, there was a hint in the literature that this might be the case. Davis et al. (1990), while investigating flame flicker at elevated pressures, found that the calculated onset of flame oscillations occurred at a significantly lower pressure than that observed in experiments. They concluded that the difference was probably due to the use of the flame-sheet approximation and the lack of radiation in the model. They suspected that the higher temperatures, resulting from the lack of a radiation model, rendered the computed flame less stable. However, they did not investigate the relationship between soot radiation and flame oscillation, and the questions that they raised have remained unanswered until the present study.

The inset in Figure 5.91 illustrates the process responsible for the low-frequency flame oscillation. The convection of high-temperature products along the flame surface results in the formation of a buoyancy-driven, large-scale, toroidal-type vortex structure. The vortex is formed on the air-side of the flame and rolls along the outer flame surface as it is convected downstream. During this process the rotational motion of the vortex velocity field interacts strongly with the flame, causing the flame surface to oscillate by expanding and contracting radially. The flame oscillation is very evident to an observer, but the large-scale structures responsible for the flame oscillation must be visualized using shadowgraph, schlieren, or particle-tracking-type techniques. Surprisingly, the frequency of the oscillation is relatively insensitive to fuel velocity, fuel type, and jet diameter. However, the magnitude of the flame flicker does depend on geometrical and

flow parameters. In this study the magnitude of the flame oscillation was found to be a function of the amount of soot radiation included in the calculations.

The plots in Figure 5.91 illustrate how the computed maximum amplitude of the flame oscillation is dependent on the level of soot radiation at two different flame heights. The maximum amplitude of the oscillation, at a given flame height, is defined as: the difference in the radius of the 1000-K temperature contour line at the peak of the radial oscillation minus the radial location of the 1000-K line for the steady flame with 100% radiation. It should be noted that the flame oscillation decreases with the soot radiation level. Also, the flame becomes steady when soot radiation is greater than 80% of that estimated by the radiation model. The calculations clearly show that radiation from the soot caused the ethylene flame studied by Santoro et al. (1983, 1984) to become steady. The question now is how can this be proven experimentally?

Several experimental approaches were considered for demonstrating that radiation from soot can impact flame flicker. The predictions in Figure 5.91 suggest that the steady flame in Figure 5.90 would oscillate if the soot generation in the flame were suppressed. To be definitive, the soot-suppression technique should not significantly change the flame structure or inlet velocities. Several soot-suppressing additives were investigated but were unable to reduce the soot level to the point where the flame would oscillate. The second approach involved the inverse idea. That is, start with an oscillating flame and then add a soot-producing compound until the flame becomes steady. This approach was very successful.

A methane flame with acetylene addition was selected for this study. The first experiment was conducted with a pure-methane jet diffusion flame, using the burner described in the experimental section. The fuel- and air-inlet jet velocities were 8.27 cm/s and 9.20 cm/s, respectively. Calculations for this flame were made using the UNICORN code on a variable-spacing grid system that has 201 and 91 points in the axial and radial directions, respectively. The calculated peak soot volume fraction of this lightly sooting flame was ~1.4 ppm. The calculated flicker frequency was 12.4 Hz, which was in close agreement with the measured frequency. In additional experiments, the soot concentration was increased by adding industrial-grade acetylene (may contain up to 20% acetone) to the methane flame while holding the volumetric flow rate of the total fuel mixture constant. With a 15% (by volume) addition of acetylene, a steady-state flame was obtained, which was also in agreement with the calculations. Details of the comparisons of simulations and experiments are given below.

The unsteady behavior of the experimental and computed flames is compared in Figures 5.92 and 5.93. The calculated time evolution of the temperature along the centerline at a height of 80 mm above the burner exit is shown by the solid line in Figure 5.92a. The time-evolving luminous soot intensity, which was measured with a PMT and converted into voltage, is shown by the dashed line. The Power-Spectral-Density (PSD) distributions, which were obtained by performing a Fast Fourier Transformation (FFT) of the signals in Figure 5.92a, are shown in Figure 5.92b. The PSDs are normalized with respect to the peak value of the corresponding fundamental frequency. Excellent agreement between computation and experiment was obtained for the periodic behavior of the flame. Differences in the shape of the signals (Figure 5.92a) were expected since the two signals represent different quantities (temperature at a point versus line-

of-sight soot radiation). The fundamental frequencies of the oscillations of the experimental and computed flames are 12.0 and 12.4 Hz, respectively. Calculations have also predicted the three harmonic frequencies of the oscillation reasonably well.

The dynamics of soot growth and pinch-off of a pocket of soot obtained in the experiment and from calculations are compared in Figure 5.93. Two-dimensional distributions of soot volume fraction in the experiment were obtained by locking the flame to a particular phase and then imaging the visible light from the flame. At phase 0 ms, the flame is growing in height, and peak soot concentration occurs at the flame tip. As the buoyancy-induced vortex (not shown in the figure) begins to form on the airside of the flame surface, it squeezes the flame in the radial direction and stretches it in the axial direction (41.0 ms). These vortices form as the flame becomes absolutely unstable in the presence of the upward buoyancy force that is established by the heat from the flame in an analogous way to the vortices that form along a helium (or heated) jet. Unlike other spatially unstable flows such as Kelvin-Helmholtz shear layers, neither the experiment nor the calculations required a continuous disturbance for the development of these vortices. Because of the absolute instability of the flowfield, periodic oscillations corresponding to the limit cycle were automatically established both in the experiments and in the calculations.

Flame flicker results as the tip separates from the main body of the flame. This can be observed in Figure 5.93 at a phase of 61.5 ms, where the sooting flame tip becomes separated from the main body and is transported downstream along with the exhaust products. Although this process is slightly delayed in the calculations, the agreement is still very good. This type of flame-separation phenomenon has also been observed and calculated by others (Chen et al., 1988, Ellzey et al., 1990).

Calculations and experiments were repeated for the flame in Figure 5.92 after replacement of 5%, 10%, or 15% by volume of methane with an equal amount of acetylene-not changing the fuel and air exit velocities. The industrial-grade acetylene used in the experiments contains acetone that will have little effect on soot. Since the presence of acetone is not taken into account in the calculations, an additional uncertainty is present in the computed soot concentration. However, the uncertainty in the predicted soot is estimated to be less than 5% of the total amount of soot produced in the flame.

The normalized PSDs of the experimental and computed flame oscillations are shown in Figures 5.94a and 5.94b for the 5% and 10% acetylene cases, respectively. The calculated PSD is for the centerline temperature (continuous red line) at a height of 80 mm from the nozzle. The experimental PSD (dashed black line) is for soot luminosity of the entire flame. The experimental and computed fundamentals and harmonics are in excellent agreement. Also, the frequencies are the same as that observed for the 100% methane flame shown in Figure 5.92b. Note that the flicker frequency does not change with the soot concentration and, thus, is independent of soot concentration. However, the magnitude of the oscillation is very dependent on soot concentration or, more specifically, on the intensity of the blackbody radiation of the soot; this is shown in Figure 5.95.

The transient behavior of the computed flame temperature is shown in Figure 5.95 for a height of 80 mm. The calculations began with a 10% acetylene flame; at  $t = 0$  the fuel was instantaneously

switched to 15% acetylene. As shown in Figure 5.95, the flame remains unsteady for a period of  $\sim 12$  s. This is somewhat surprising since the calculated temperature shows that the 15%-acetylene fuel completely replaced the 10%-acetylene fuel in less than 200 ms. During this time, the local temperature on the high side of the temperature fluctuation decreased from 1900 to 1820 K, while on the lower side, it decreased from 1590 to 1520 K. This decrease in temperature is thought to be the result of the radiation from the soot. Equilibrium calculations of the adiabatic flame actually showed an increase in temperature from 2268 to 2289 K when the 10%-acetylene fuel was replaced by the 15%-acetylene fuel. Thus, the drop in calculated local temperature is thought to result from the increased soot concentration and, thereby, its radiation. The peak soot volume fractions calculated for the 0-, 5-, 10-, and 15%-acetylene flames are 1.4, 2.3, 3.6, and 6.1 ppm, respectively.

In both the experiment and the calculation the dynamic behavior of the methane-acetylene jet diffusion flame is completely suppressed when the acetylene volume fraction reaches 15%. This is noted in the inset of Figure 5.95 by a flat experimentally determined PSD plot of flame luminosity along the x-axis (red line). The three computed PSD plots in blue are for 4-s segments of the centerline temperature at a height of 80 mm. The PSDs obtained from the calculations are normalized to the magnitude of the fundamental frequency in the first section (0-4 s). The PSD plots clearly show that the experimental and computed flames are steady after 12 s. Also, note that the calculations predict that the oscillation frequency will not change as the oscillation amplitude decreases.

To eliminate the possibility that the damped-flame oscillations in Figure 5.95 occur naturally over a period of time rather than because of the increased soot, calculations were repeated by removing acetylene from the steady flames that were formed with 15% acetylene. Figure 5.96 shows the result of acetylene being instantaneously removed from the fuel to form the original methane-air jet diffusion flame. The initial and final flames (temperatures and soot distributions) are shown in the insets. These insets also contain photographs of the experimentally observed steady and oscillating flames obtained with 15%-acetylene and pure-methane fuels, respectively. Note that the computed temperature increases from 1677 to 1728 K when the new fuel (pure methane) reaches the flame—the opposite of the temperature decrease observed in Figure 5.95. The temperature increase is thought to trigger an absolute instability in the flowfield and transform the initial disturbances (at  $t = 0$ ) into a limit-cycle oscillation at 12.4 Hz. The details of this absolute instability are not well understood, but the use of soot to control the oscillation may provide a new way to study this instability.

The predictions in Figure 5.91 suggest that the ethylene flame used by Santoro and co-workers, shown in Figure 5.90, was steady because soot radiation inhibited the instability that was responsible for the flame flicker. This was evident when the computed flame began to oscillate once the calculated blackbody radiation from the soot was turned off. The initial experiments failed to demonstrate this effect with the ethylene flame. However, the inverse effect was experimentally demonstrated, i.e., a flickering methane flame was made steady by adding 15% by volume of acetylene. The question is whether one can start with the steady 85%-methane/15%-acetylene flame and obtain a flickering flame by turning off the radiation in the simulation, as in the case of the steady ethylene flame. As noted in Figure 5.97, the answer to this question is yes. In each of the images in Figure 5.97, the temperature and soot are plotted on

the left and right halves of the jet centerline, respectively. Figure 5.97a, is the steady flame; and Figure 5.97b, with the outer vortex structure, shows one phase of the dynamic flame resulting from zero radiation from the soot.

In conclusion, a prediction was made of a phenomenon that was new to the authors and perhaps to the combustion community. That is, soot can influence flame flicker to such an extent that the oscillation is completely suppressed. The prediction was experimentally confirmed and computationally studied.

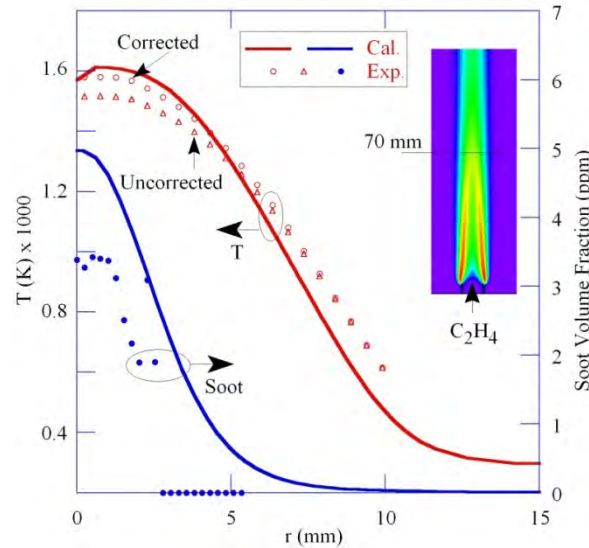


Figure 5.90 Comparison of predicted and measured temperature and soot-volume-fraction distributions across flame at 70 mm above burner exit. Two-dimensional structure of computed flame is shown in inset by plotting temperature field.

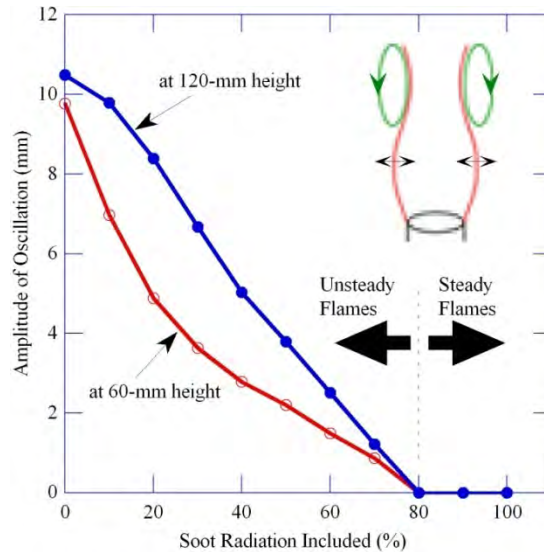


Figure 5.91 Maximum radius of 1000-K surface on airside for different levels of soot radiation considered in CFD model. Flame became steady as in Figure 5.96 inset when soot radiation considered was  $> 80\%$  of locally estimated value.



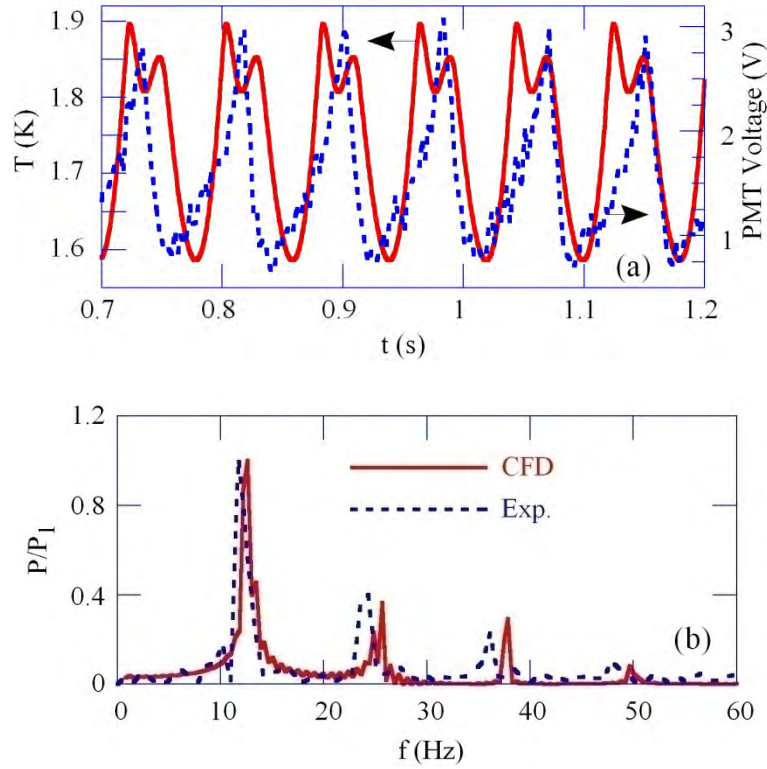


Figure 5.92 Comparisons of predicted and measured (a) flame oscillations and (b) respective PSDs for pure-methane jet diffusion flame.

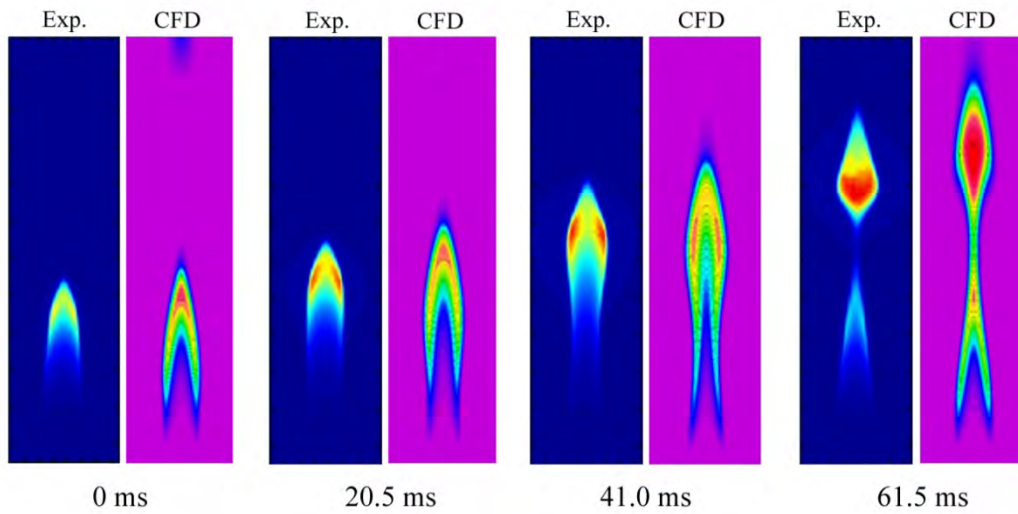


Figure 5.93 Comparisons of predicted and measured soot structures at different phases of periodically oscillating methane jet diffusion flame.

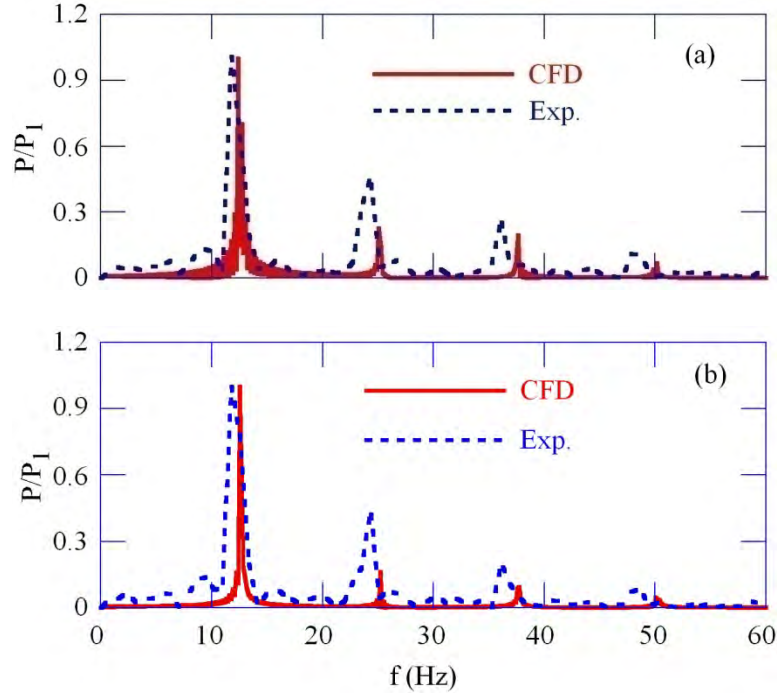


Figure 5.94 Comparisons of predicted and measured PSDs of oscillations when (a) 5% and (b) 10% of methane was replaced with acetylene.

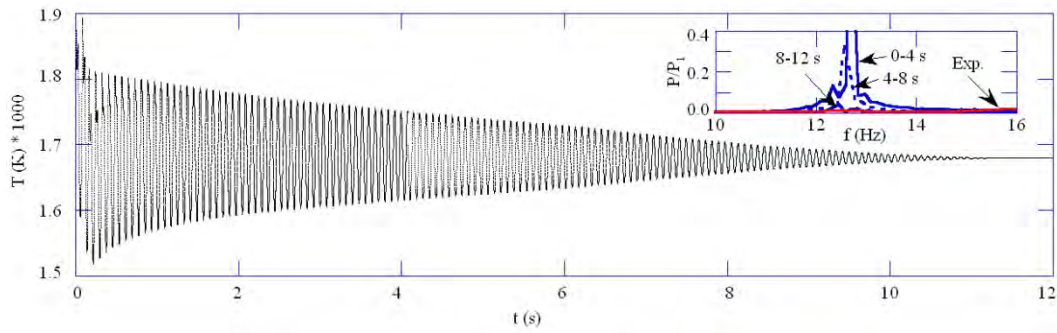


Figure 5.95 Decay of flame oscillations captured in calculations when 15% of methane was replaced with acetylene. Decay in PSDs of oscillations calculated from temperature signals obtained over different time periods is shown in the inset. Measured PSD is also shown in inset.

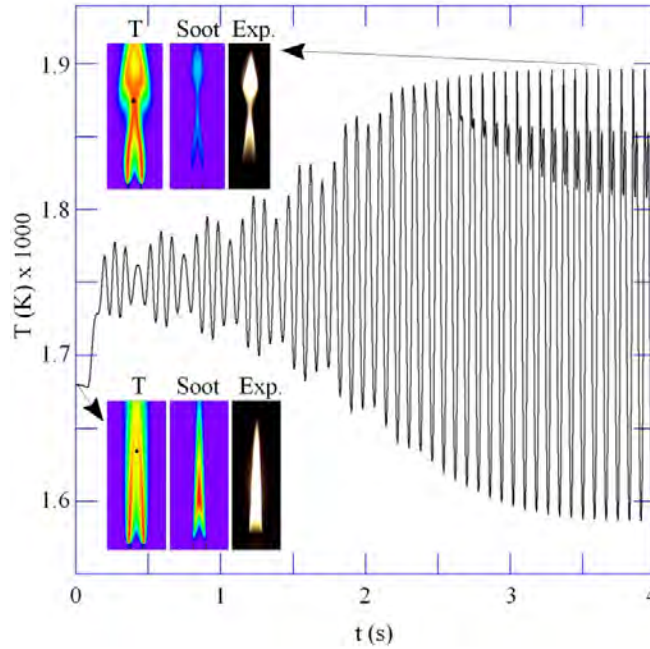


Figure 5.96 Transition of steady-state flame (lower inset) to periodically oscillating one (upper inset) when acetylene was removed from fuel jet. Fluctuations in temperature at fixed location are shown for entire calculation time.

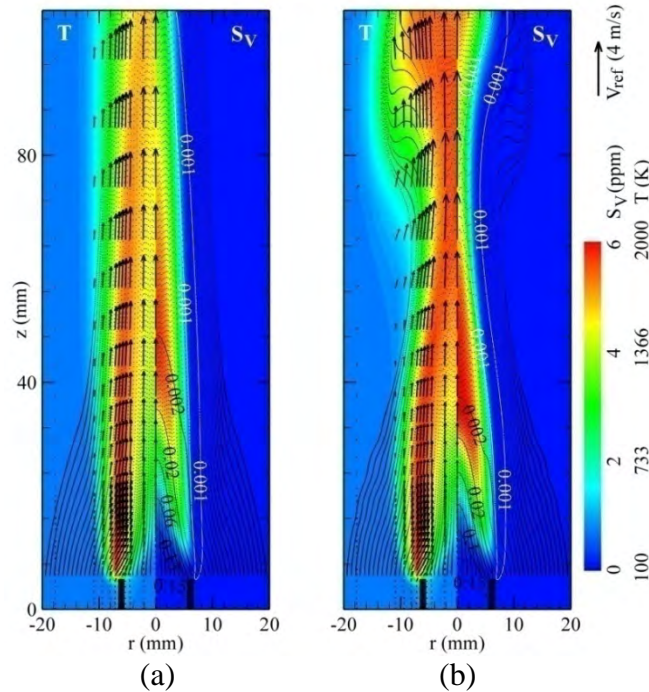


Figure 5.97 Effect of radiation from soot on dynamics of 15%-acetylene flame. (a) Steady-state flame computed when radiation from soot was considered, and (b) unsteady flame computed when radiation from soot was ignored. Velocity vectors are superimposed on temperature field on left halves of images, and iso-contours of acetylene (black) and OH (white) concentrations are superimposed on soot field on right halves. Instantaneous locations of particles are also superimposed to show streaklines.

### 5.2.2 N<sub>2</sub>-Diluted Ethylene Flames at Pressure

The data in this section were taken using room temperature air and served as the baseline for the m-xylene studies using the bubbler system, which were also conducted using room temperature air.

Figure 5.98 shows photographs of the N<sub>2</sub>-diluted flame with a nitrogen flow rate of 5.5mg/s. The dilution results in a flame with only a small luminous tip. The flame remains stable at all pressures up to 5 atm, with increasing soot concentrations. Although the flame was luminous at the higher pressures, there was no visible breakout of soot at any of the different operating conditions. The flames were approximately 18 mm in height on the basis of luminosity. The heights remained unchanged with increase in pressure. The invariance in the luminous flame height is in agreement with the results recently reported by Joo and Gülder (2009) on high pressure CH<sub>4</sub> flames at pressures of up to 60 bar.

Figure 5.99 shows the LII images for the N<sub>2</sub>-diluted C<sub>2</sub>H<sub>4</sub> diffusion flame at 1 to 5 atm. The images were normalized to the peak LII signal at 5 atm. The soot concentrations for the flames at 1 and 2 atm were below the detectability limit for the LII measurement system that was used for these experiments; the LII signal could not be distinguished from the background signal. LII signals were obtained for pressures of 3, 4 and 5 atm. Figure 5.101 shows the axial profiles of peak soot volume fraction for the N<sub>2</sub>-diluted flames.

The axial  $f_v$  profiles show the soot concentrations tapering off to zero at the same distance from the tip of the fuel tube. As can be seen from Figure 5.101, there is a slight shift in the location of peak soot concentration with pressure. This is possibly due to the increasing pressure causing the soot inception to occur earlier. This shift in peak location is similar to the observations made by Thomson *et al.* (2005) and Joo and Gülder (2009) on methane diffusion flames and Bento *et al.* (2006) in propane flames where the initial sooting regions in the flames continually moved closer to the tip of the fuel tube with increasing system pressure.

Estimated soot mass flow rates and the soot yields show the impact of the addition of N<sub>2</sub> on the soot production in the C<sub>2</sub>H<sub>4</sub> flames. The pure C<sub>2</sub>H<sub>4</sub> flame had a peak soot mass flow rate of 0.65mg/s; an effective soot yield of roughly 76%. The presence of nitrogen (5.5mg/s) in the fuel stream results in a drastic reduction in the soot formation rate; thus, lowering the soot mass flow rate to approximately 0.005mg/s and the effective soot yield of 0.6%. The rate of oxidation in the flame is greater than the rate soot formation and growth, thus preventing soot breakout from the tip of the flame. The 5 atm flame had the highest soot concentrations, with a peak soot volume fraction of approximately 1 ppm, with the concentrations peaking at approximately 15 mm above the tip of the fuel tube.

The low soot concentrations in the baseline flame make it an ideal candidate for the application of laser-based diagnostics to detect minor species such as PAH. Use of techniques such as LIF is made easier since the low optical thickness of the flames minimizes issues with self-absorption from soot particles in the flame. Figures 5.102(a) and (b) show the peak and centerline profiles of the fluorescence signal from the small and large PAH.

Assuming that the magnitude of the fluorescence signal is directly proportional to concentration, some initial observations can be made from the PAH fluorescence profiles, referring to the fluorescence signal collected in the 320-380 nm and 420-480 nm band passes as the small and large PAH concentrations respectively. As can be seen from Figure 5.102(a), the concentration of small PAH increases the distance from the tip of the fuel tube, reaches a maximum and decreases to zero after the tip of the flame. The large PAH concentrations show a similar behavior.

At 1 atm, the peak concentrations of the small PAH (1 and 2 ring aromatic compounds) outweigh the large PAH (greater than 2 aromatic rings) at all axial locations. The concentration of small PAH peaks at approximately 15mm above the tip of the fuel tube, with the peak large PAH concentrations occurring further downstream by about 2mm. This follows the expected behavior for the growth of aromatic hydrocarbons in a diffusion flame, with the initial breakdown of the fuel molecules leading to the formation of small aromatic compounds, which grow into larger aromatic hydrocarbons. The centerline profiles are very similar to the profiles of peak values. The behavior is replicated in the flame at 2 atm.

For both collection wavelength ranges, the peaks of the fluorescence signal profiles along the axis of the flame shift upstream with increasing pressure. This indicates the earlier formation of aromatic compounds with increasing pressure. At higher pressures, the reaction rates are enhanced. The higher pressures also lead to higher local concentrations of the small radicals formed from fuel pyrolysis. The combination of these two factors would lead to a faster formation of the aromatic compounds, causing them to appear earlier in the flame.

### *Modeling Studies*

For verifying the capabilities of UNICORN code in predicting pressure effects on jet diffusion flames, calculations are performed for the Hyun and Gulder flames (2008). It was experimentally observed that the height of a small jet flame remains unchanged with pressure. Initial calculations made with UNICORN code could not predict these characteristics of small flames under pressure. Calculated flames became taller with increase in pressure. Several attempts made with modifying boundary conditions, chemical-kinetics, and soot models could not yield the experimentally observed pressure-independent flame height. A step-by-step evaluation of the various parts of the code guaranteed that pressure phenomenon was correctly incorporated in the code. However, the chosen time-step for advancing the calculations was found to be too large for simulating the extremely slowly moving fuel in the burner tube. This inaccuracy lead to higher fuel velocity (and, hence, flow rate) at the burner exit and caused the flames to become taller. Typically, one would worry about the time-step in the regimes where velocities are large due to stability issues. Present calculations revealed that while calculating the extremely low velocity regimes one should also be cautious about the time-step from accuracy point of view. Using a small time step calculations for the Hyun and Gulder flames (2008) were repeated and obtained pressure independent flame height.

Calculations for an experimentally studied, steady jet diffusion flame are made using UNICORN code at different pressures. Fuel used was nitrogen-diluted ethylene. As the motivation for this study was to add small amounts of aromatic compounds to the fuel, SERDP JP-8 mechanism (Mechanism G) was initially considered for these calculations. However, due to convergence issues, calculations are performed using Violi's JP-8 mechanism (Mechanism F). The fuel-tube inner diameter was 6 mm. Fuel, a mixture of ethylene and nitrogen, was issued from this tube at a velocity of 0.184 m/s under normal pressure conditions. Annulus air flow velocity was 0.088 m/s. These velocities are proportionally decreased when the system pressure is increased.

Temperature distributions obtained for pressures between 1 and 5 atm are shown in Figure 5.103. Computed flame height initially decreased slightly when pressure was increased (2 and 3 atm) and then became nearly constant for higher pressures. On the other hand, it was noted in the experiment that the height of the flame doesn't change much with pressure. The discrepancy between the calculations and experiment with regard to flame height could be due to the visualization techniques used. The blue flame captured in the photographs represents the reaction zone, which may or may not closely follow the peak temperature contour. For a fair comparison between the computations and experiment, OH-concentration distributions of the computed flame are plotted in Figure 5.104. Indeed, the changes in flame height with pressure are less significant in these figures. Computed flame height has decreased by 4 mm when the pressure was increased to 2 atm and then decreased further by 2 mm when pressure was increased to 3 atm. Flame height remained nearly constant for further increases in pressure. The initial drop in flame height could be due to the flame quenching predicted near the base for 1- and 2-atm pressures. Violi's mechanism used in these calculations may not give accurate flame shapes for ethylene fuel as it was originally developed for the JP-8 fuel. The new SERDP mechanism should resolve this issue. Work is in progress for sorting out the numerical issues associated with this new SERDP mechanism.

Previous studies on the co-flow diffusion flame at atmospheric pressure (Section 5.2.1) suggested that the frequency of oscillations (flame flicker) decreases with soot formation. Further calculations for this flame are performed at elevated pressures. Results obtained at 2 atm and 5 atm are compared with those of normal pressure in Figures 5.105 - 5.107. Temperature distributions shown in Figure 5.105 suggest that 1) height of the dynamic flame gets shorter, 2) flame becomes narrower, and 3) frequency of vortex shedding increases with pressure. Last observation also corresponds to an increase in the frequency for flame flicker. Similar to that observed in steady flames, soot production has significantly increased with pressure in the dynamic flames (Figure 5.107). These results are consistent with the experimental findings and suggest that UNICORN code can be used for simulating steady and dynamic flames at elevated pressures.

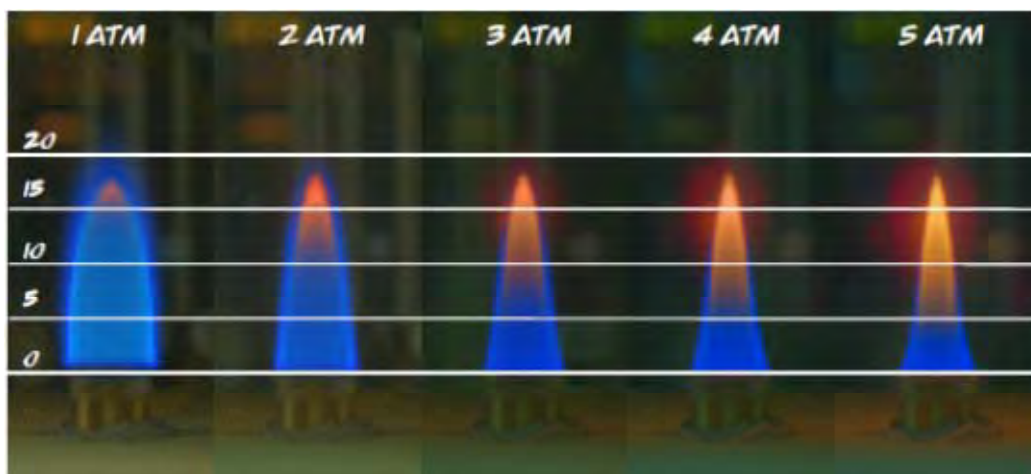


Figure 5.98 Images of nitrogen-diluted flames at pressures up to 5 atm (These are composite images made from multiple exposures of each flame to show blue regions of the flames.).

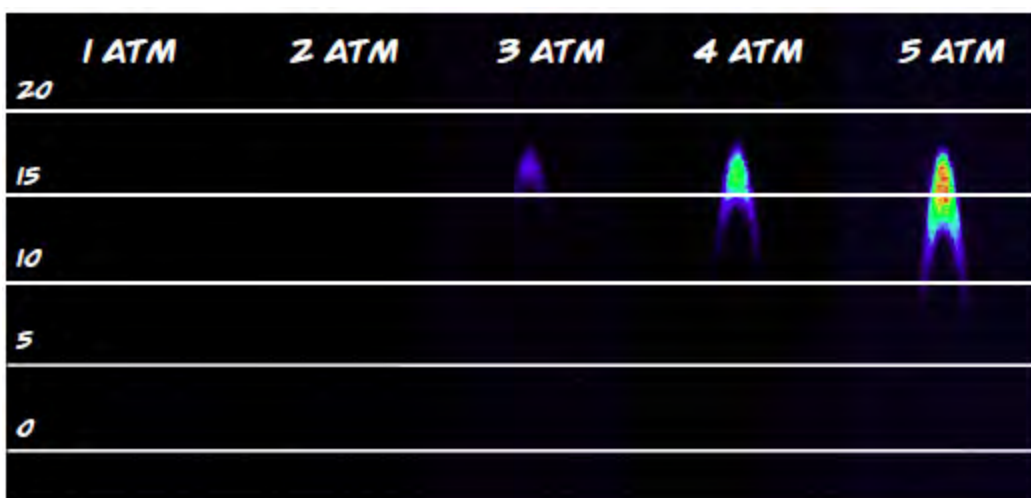


Figure 5.99 LII images from nitrogen-diluted flames at pressures up to 5 atm;  $\text{C}_2\text{H}_4$  mass flow rate = 1.0mg/s,  $\text{N}_2$  mass flow rate = 5.5mg/s.



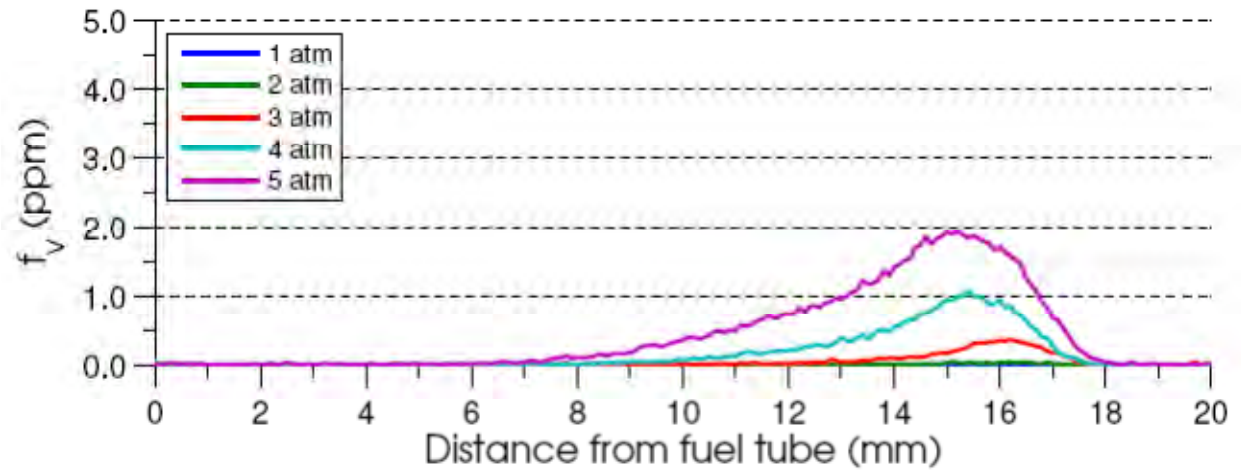
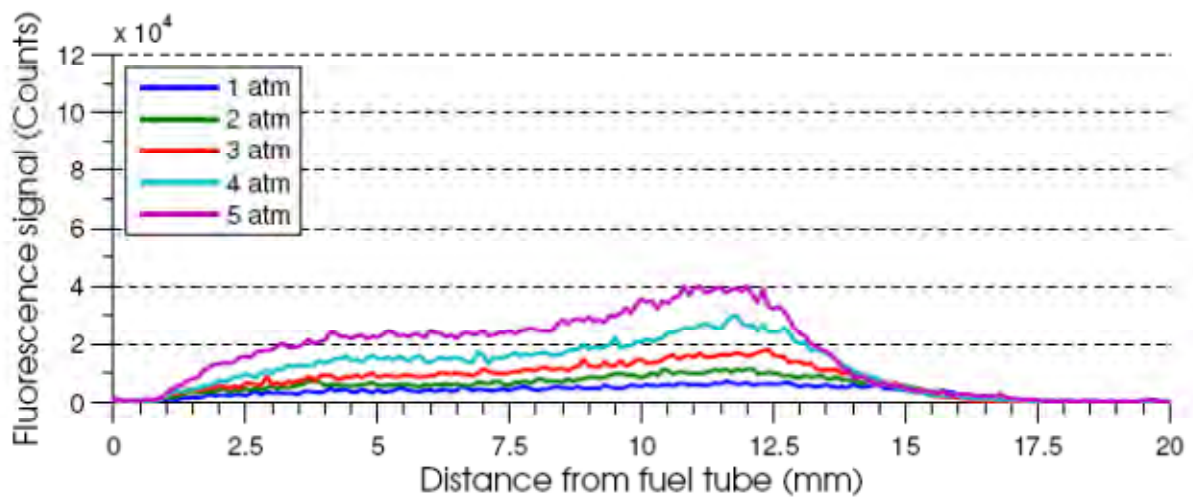
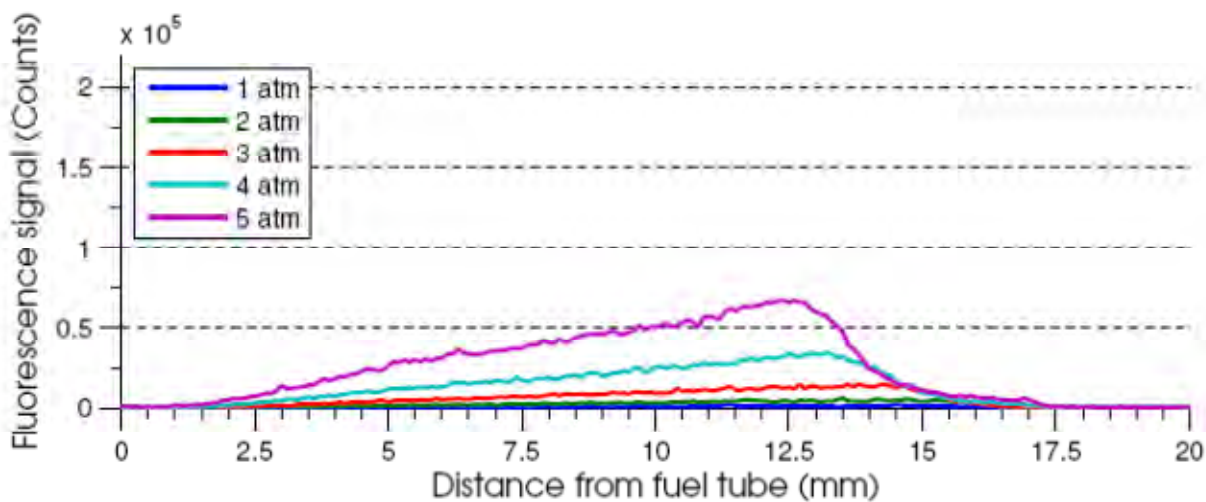


Figure 5.101 Peak volume fraction profiles derived from LII images.





(a) Small PAH



(b) Large PAH

Figure 5.102 Small and large PAH profiles for diluted nitrogen flames (derived from 2-D images)

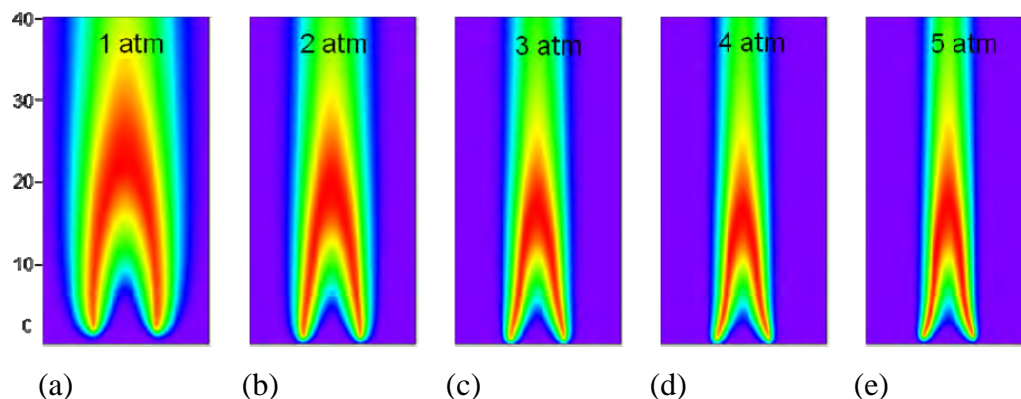


Figure 5.103 Effect of pressure on steady flame. Temperature distributions in a  $N_2$ -diluted ethylene jet diffusion flame at (a) 1 atm, (b) 2 atm, (c) 3 atm, (d) 4 atm, and (e) 5 atm.

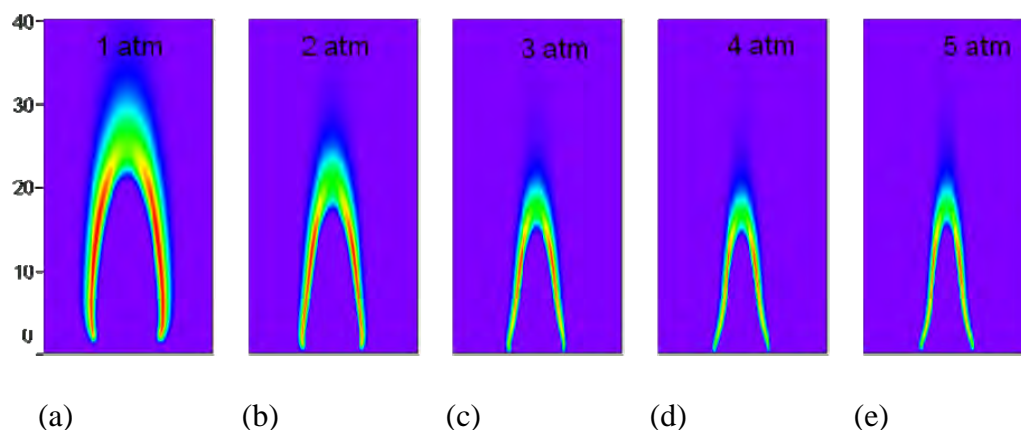


Figure 5.104 Distributions of OH concentration in a  $N_2$ -diluted ethylene jet diffusion flame at (a) 1 atm, (b) 2 atm, (c) 3 atm, (d) 4 atm, and (e) 5 atm.

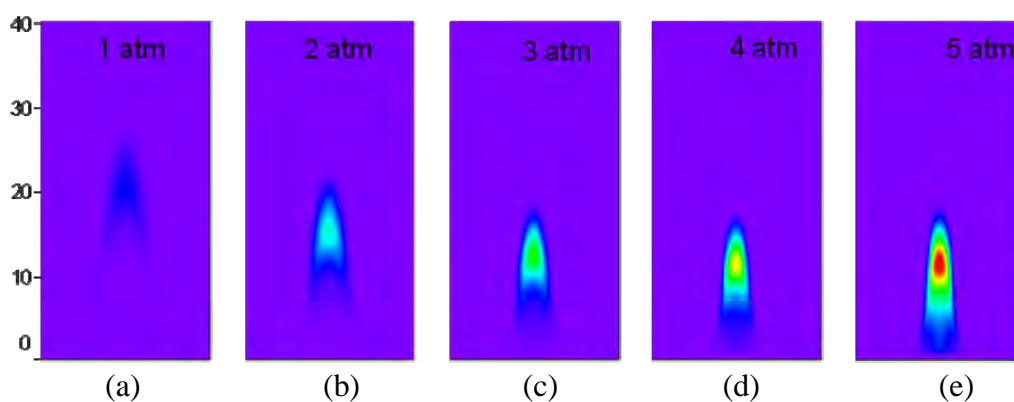


Figure 5.105 Distributions of soot concentration in a  $N_2$ -diluted ethylene jet diffusion flame at (a) 1 atm, (b) 2 atm, (c) 3 atm, (d) 4 atm, and (e) 5 atm.

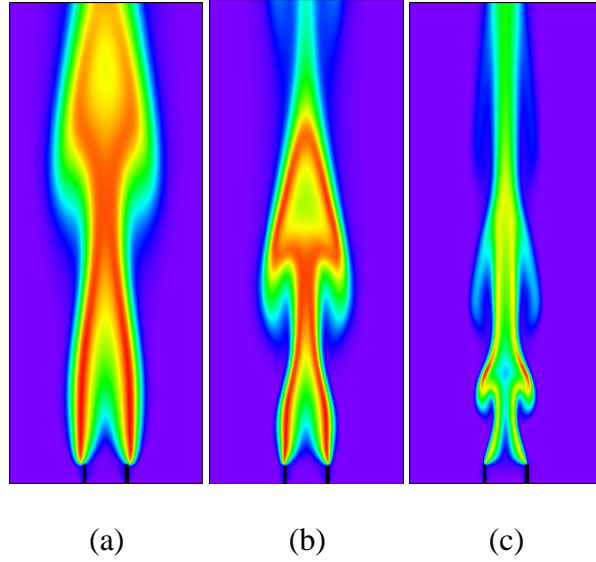


Figure 5.106 Effect of pressure on flame dynamics. Instantaneous temperature distributions of a jet diffusion flame at (a) normal pressure, (b) 2 atm, and (3) 5 atm.

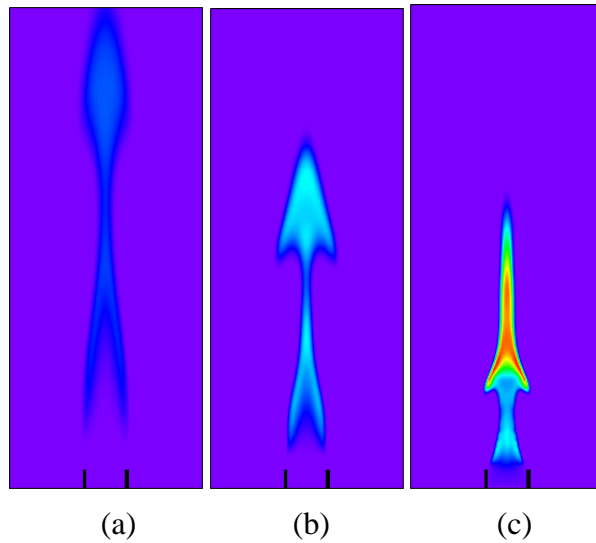


Figure 5.107 Instantaneous soot distributions of a jet diffusion flame at (a) normal pressure, (b) 2 atm, and (3) 5 atm.

### 5.2.3 Effect of *m*-xylene on PAH and Soot in N<sub>2</sub>-diluted Ethylene Flames

The data in this section were all collected using the bubbler for addition of the *m*-xylene to the fuel. The air was at ambient temperature. Two *m*-xylene concentrations were studied corresponding to 5% and 2.5% of the carbon from the *m*-xylene. (The next section of the report will present soot data for *m*-xylene in experiments conducted with heated air so that the data can be compared to that for dodecane, the surrogate mixture, and JP-8.)

Figure 5.108 shows photographs of the C<sub>2</sub>H<sub>4</sub> diffusion flame diluted with N<sub>2</sub> and doped with *m*-xylene at 5% of the total carbon flow rate. The luminous height of the flame was unchanged with the addition of *m*-xylene and was approximately 18 mm for pressures between 1 and 5 atm. As with the baseline N<sub>2</sub>-diluted flame, the flame height is unchanged with increase in pressure and there is no visible breakout of soot from the top of the flame. The flame with *m*-xylene added shares some other similarities with the N<sub>2</sub>-diluted C<sub>2</sub>H<sub>4</sub> flame. As with the baseline flame, the luminosity from soot particles is initially observed near the tip of the flame at 1 atm. Increasing the pressure results in the propagation of the soot field upstream, partly due the increased residence times available for soot growth and the higher pressures leading to faster reaction rates.

Figure 5.109 shows the LII images acquired for the N<sub>2</sub>-diluted C<sub>2</sub>H<sub>4</sub> flame doped with *m*-xylene at a carbon flow rate of 5%. The axial profiles of the peak soot volume fractions calculated from the LII images are shown in Figure 5.110. The peak axial profile of the *m*-xylene-doped flame show trends similar to the baseline N<sub>2</sub>-diluted flame. The addition of *m*-xylene results in greater soot production, with a peak soot volume fraction of approximately 4.5 ppm at 5 atm.

The structure of the soot field with the addition of *m*-xylene is observed to be similar to the baseline flame. In the baseline flame, the maximum value of the centerline soot volume fractions was 0.53 ppm at 5 atm, whereas the maximum soot concentration was 0.98 ppm, indicating that the peak soot concentrations occurred at the flame edges. The substitution of 5% of the carbon flow rate from *m*-xylene results in an increase in the peak soot concentrations approximately by a factor of 4.5. The peak soot concentrations are higher in the *m*-xylene flame at all locations along the axis of the flame.

The PAH fluorescence images for the C<sub>2</sub>H<sub>4</sub>-N<sub>2</sub> doped with *m*-xylene are shown in Figure 5.111. The most striking feature of the PLIF images is the prominent cone of fluorescence near the tip of the fuel tube for the small PAH. This strong fluorescence signal is a few orders of magnitude higher than the fluorescence signal from regions further downstream. It is reasonable to conclude that this signal is due to the presence of *m*-xylene from the fuel stream, which fluoresces strongly in the 320–380 nm bandpass (Beretta, *et al.*, 1992). As with the baseline flame, the dynamic ranges are identical for the PLIF images for the small and large PAH at the same pressure.

The PAH fluorescence profiles for the C<sub>2</sub>H<sub>4</sub>-N<sub>2</sub> flame doped with *m*-xylene to provide 5% of the total carbon flow are shown in Figure 5.112. Near the tip of the fuel tube, the small PAH fluorescence signal rises sharply, reaches a maximum and then decreases, as the *m*-xylene is consumed by diffusion into the flame zone. This sharp rise near the tip of the fuel tube is an artifact due to the laser beam being blocked close to the edge of the fuel tube. Initial experiments had revealed interference from the laser sheet hitting the stainless steel fuel tube in

both collection bandpasses. In an ideal situation, where the stainless steel in the fuel tube is not excited by the UV, the laser sheet could fill the entire area around the exit of the fuel tube and not cause any interference. In order to prevent signal interference, the laser bottom edge of the laser sheet was blocked such that the laser sheet just grazed the tip of the fuel tube. This causes the drop in the LIF signal close to the tip of the fuel tube.

The magnitude of the fluorescence signal from *m*-xylene near the tip of the fuel tube increases with pressure. This is to be expected, since the local concentration of the *m*-xylene is directly proportional to pressure for the same inlet mass flow rate. The LIF signal from the small PAH falls off quickly due to the consumption of the *m*-xylene, reaches a maximum in the regions where soot is observed and then decreases to zero downstream of the flame. The LIF images for the large bandpass show no contribution from the *m*-xylene thus validating the observations made by Beretta *et al.* (1992) that the fluorescence in the small bandpass is due to single and double ringed aromatic compounds.

Figure 5.113 shows radial profiles of soot for the 5% Carbon from *m*-xylene case for 3, 4 and 5 atm. The signal levels from LII at 1 and 2 atm were quite low so the profiles for these pressures are not presented. The profiles show similar shapes to those observed in pure ethylene flames at atmospheric pressure. At lower heights, the highest soot concentrations appear off the centerline. As height increases, the soot volume fraction on the centerline increases and the peak soot level in the 'wings' falls until the peak soot volume fraction occurs on the centerline.

Axial soot and PAH profiles for the 2.5% carbon from *m*-xylene are presented in Figures 5.114 and 5.115. The corresponding radial soot profiles are presented in Figure 5.115. Overall the trends at the lower *m*-xylene concentration behave as expected with lower PAH and soot concentrations.

In order to estimate the effect of *m*-xylene concentration on soot volume fraction, the peak volume fractions for the three flames were used to calculate the increment in soot volume above that in the baseline flame. The increment for the 5% carbon from *m*-xylene flame was divided by that for the 2.5% flame. If the *m*-xylene had a first-order effect on peak soot, the ratio would be expected to be the same as the ratio of the concentrations, i.e., 2. For pressure from 2, 3, 4, and 5 atm, the results of the calculation produced ratios from 1.5, 1.7, 1.9 and 2.0, respectively. Within the uncertainty of the measurement, these ratios are all consistent with a linear dependence of peak soot volume fraction on the *m*-xylene concentration.

### *Modeling Studies*

Calculations for the flames shown in Figure 5.102 are repeated by adding 5% *m*-xylene by mass to the fuel flow. In order to keep the total carbon mass constant while adding *m*-xylene equivalent amount of ethylene was removed from the fuel mixture. Computed temperature distributions are shown in Figure 5.116 for pressures between 1 and 5 atm. Addition of 5% Carbon from *m*-xylene did not change the temperature field of the flame at any pressure (compare Figures 5.102 and 5.113). In fact, nearly the identical OH-concentration fields are predicted (Figure 5.117) after adding *m*-xylene-suggesting that combustion process was not altered by the presence of small amounts of *m*-xylene. In support of this conclusion experiments

have also shown very little changes to the flame structure with the addition of *m*-xylene. However, a dramatic increase in soot formation ( $\sim 5$  fold increase) was also observed in the experiment. Soot distributions predicted at different pressures are shown in Figure 5.118. A comparison between soot predicted with and without *m*-xylene (Figures 5.117 and Figure 5.118) indicates that not only the flame structure but also the soot generation was not affected with the addition of *m*-xylene. This was not the case in the experiments. The discrepancy between the experiment and calculations was investigated further through changing the soot models. The two-equation soot model used in the calculations of flames in Figure 5.118 was based on acetylene concentration. A first order change to this model was proposed by replacing acetylene with benzene as soot inception species. Calculations made with this new model improved soot prediction in the *m*-xylene added flames, however, the improvement was not sufficient for increasing soot by 5 orders of magnitude. The predicted *m*-xylene concentrations are shown in Figure 5.119.



Figure 5.108 Digital photographs of the  $\text{C}_2\text{H}_4\text{-N}_2$  diffusion flame doped with 5% *m*-xylene at pressures of 1 to 5 atm.  $\text{C}_2\text{H}_4$  flow rate =  $0.95\text{mg/s}$ , *m*-xylene flow rate =  $0.047\text{mg/s}$ ,  $\text{N}_2$  flow rate =  $5.5\text{mg/s}$ .

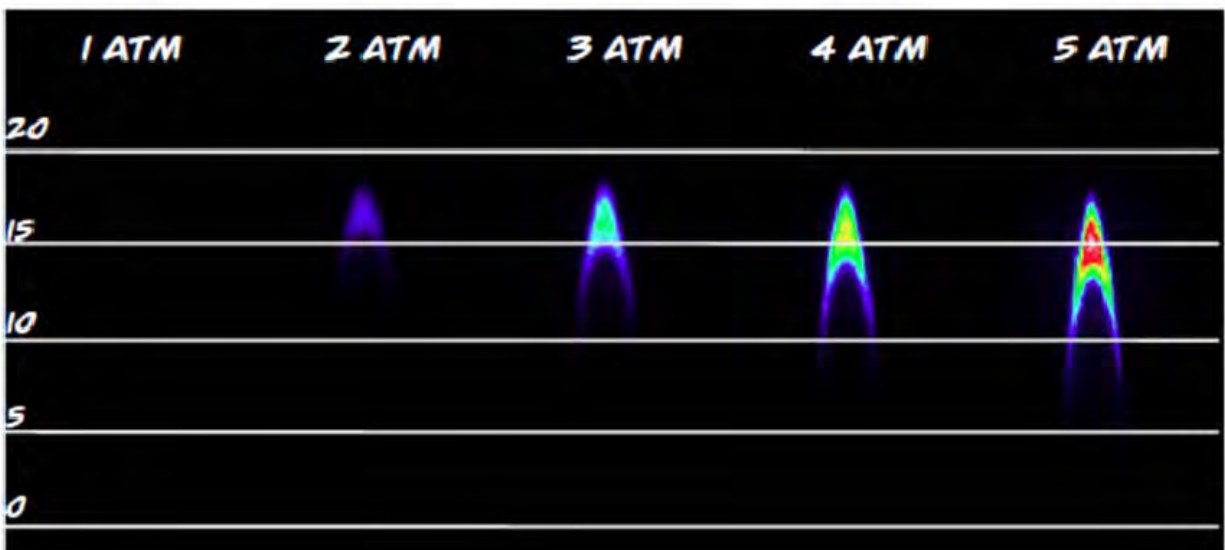


Figure 5.109 LII images of the  $\text{C}_2\text{H}_4$ - $\text{N}_2$  diffusion flame doped with 5% *m*-xylene at pressures of 1 to 5 atm.  $\text{C}_2\text{H}_4$  flow rate =  $0.95\text{mg/s}$ , *m*-xylene flow rate =  $0.047\text{mg/s}$ ,  $\text{N}_2$  flow rate =  $5.5\text{mg/s}$ .

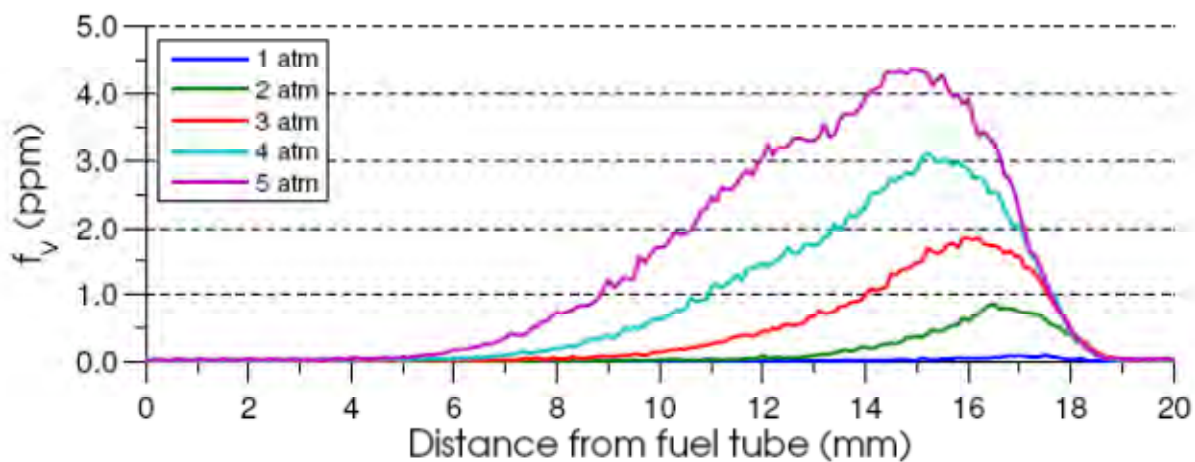
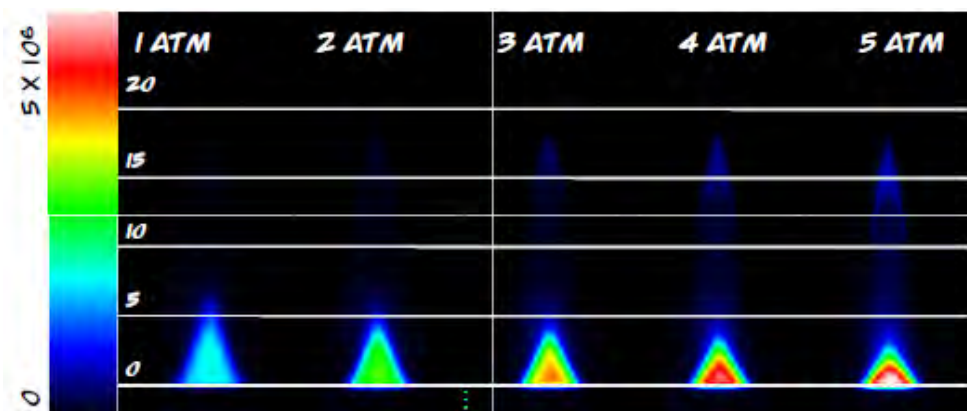
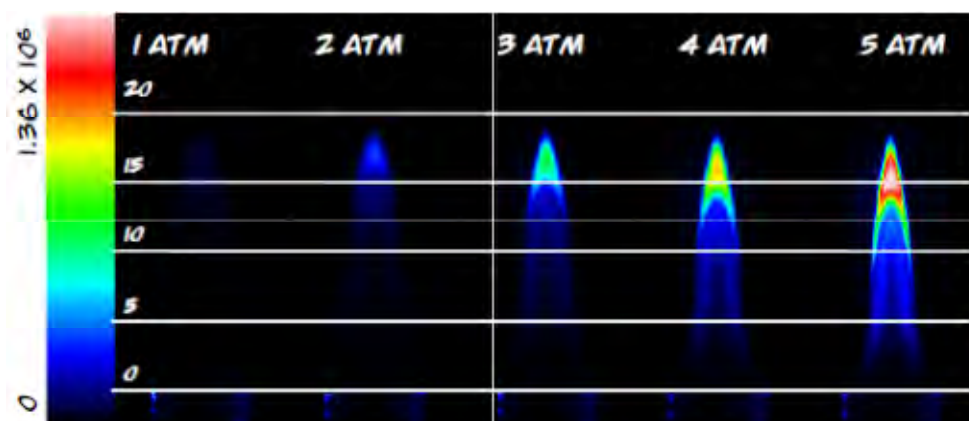


Figure 5.110 Peak Soot as function of height above burner for 5% Carbon from *m*-xylene.



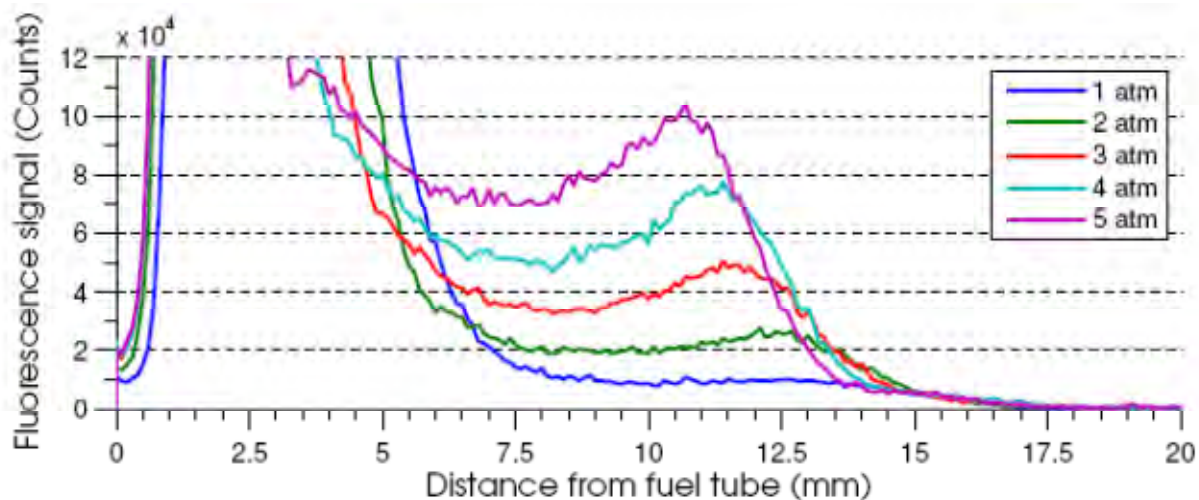
(a) Small PAH



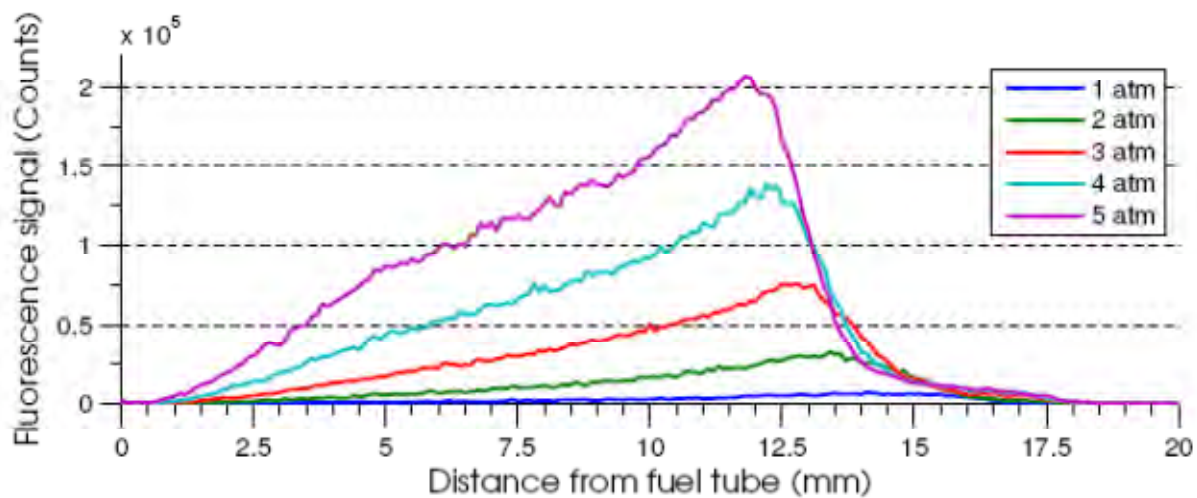
(b) Large PAH

Figure 5.111 PAH images for the ethylene diffusion flame with  $N_2$  dilution and addition of *m*-xylene at pressures of 1 to 5 atm.  $C_2H_4$  flow rate = 0.95mg/s, *m*-xylene flow rate = 0.047mg/s,  $N_2$  flow rate = 5.5mg/s. The PLIF images for the large and small PAH are on the same scale for each pressure. The LII images are normalized to the peak signal at 5 atm.



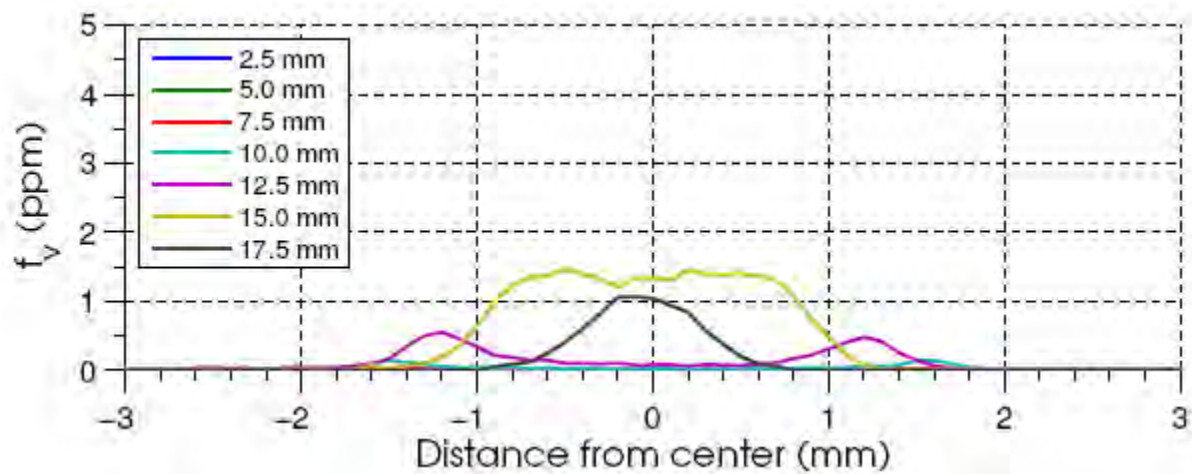


(a) Small PAH

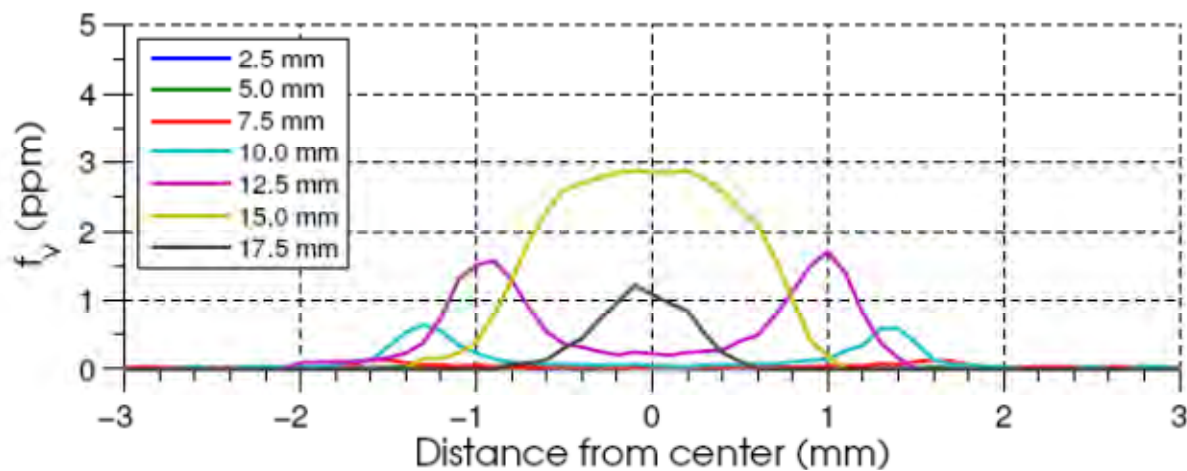


(c) Large PAH

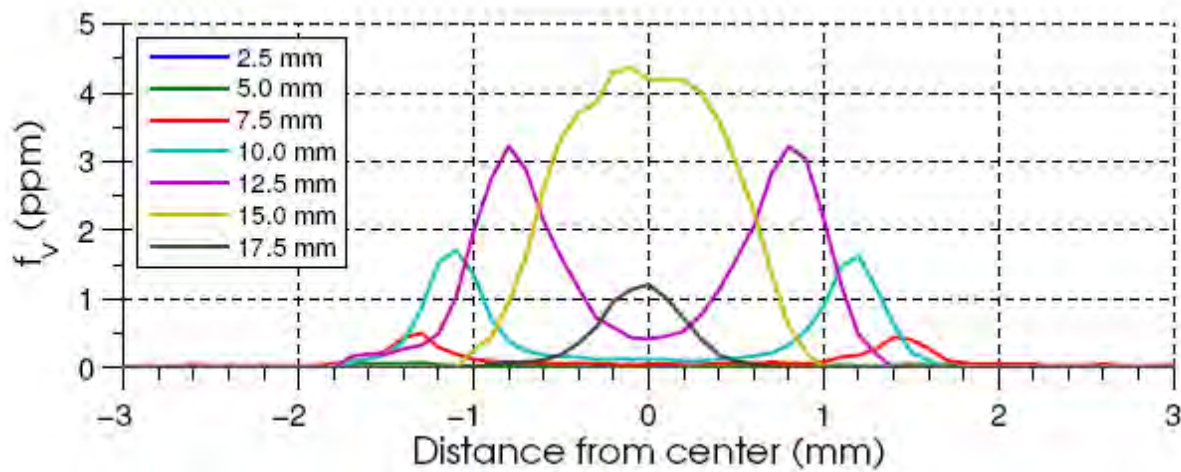
Figure 5.112 PAH fluorescence profiles for large and small PAH in 5% Carbon from m-xylene/ethylene flame as function of pressure.



(a) 3 atm



(b) 4 atm



(c) 5 atm

Figure 5.113 Radial soot profiles for 3, 4, and 5 atm with 5% Carbon from m-xylene.

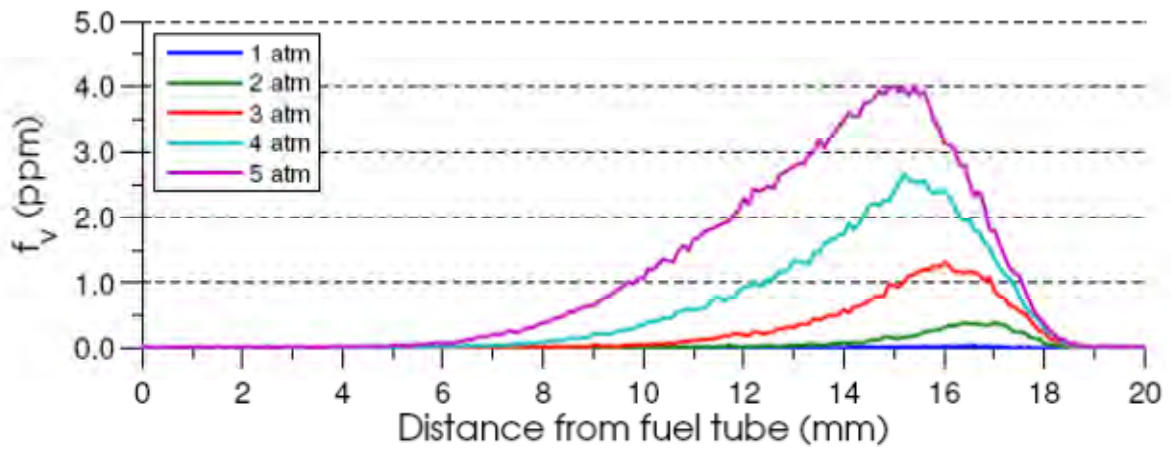
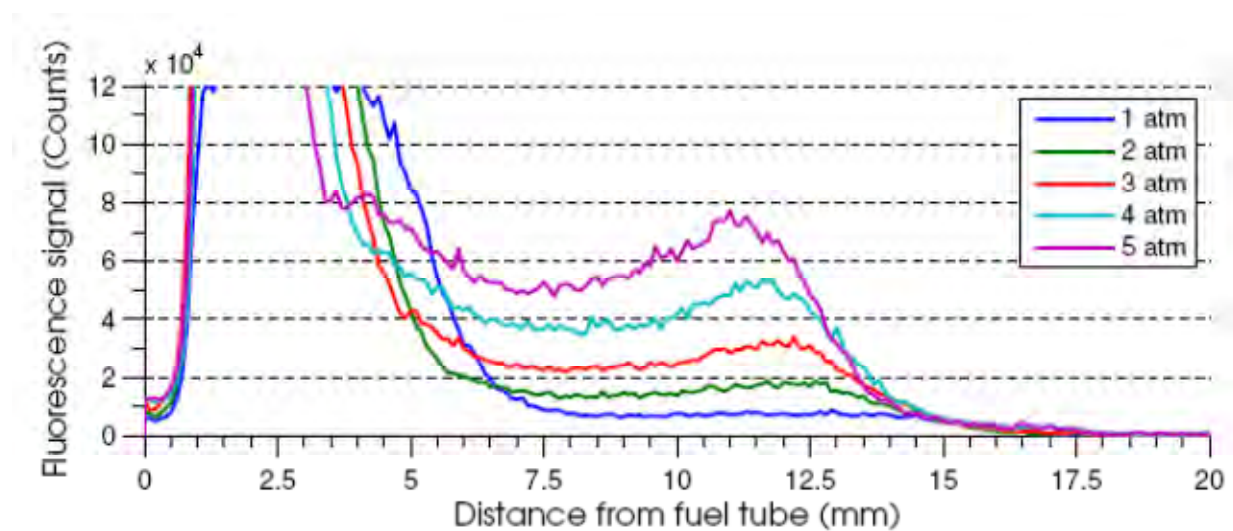
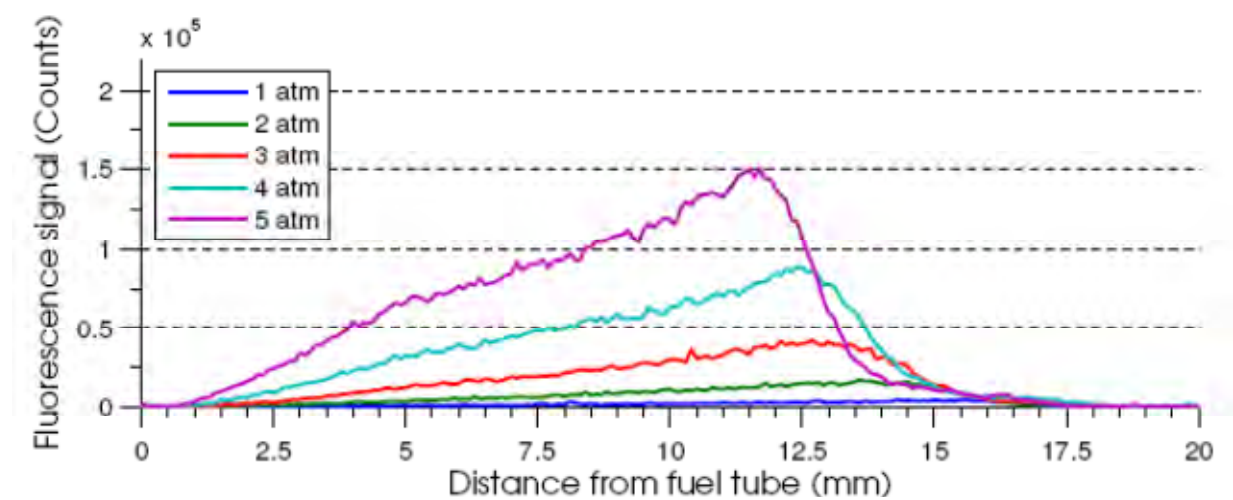


Figure 5.114 Peak Soot as function of height above burner for 2.5% Carbon from m-xylene.



(a) Small PAH



(c) Large PAH

Figure 5.115 PAH fluorescence profiles for large and small PAH in 5% Carbon from m-xylene/ethylene flame as function of pressure.

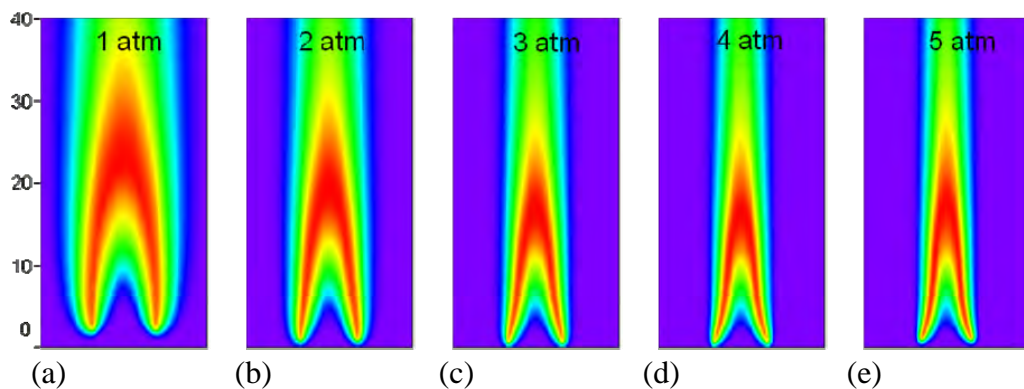


Figure 5.116 Distributions of temperature in a 5% m-xylene added, nitrogen diluted ethylene jet diffusion flame at (a) 1 atm, (b) 2 atm, (c) 3 atm, (d) 4 atm, and (e) 5 atm.

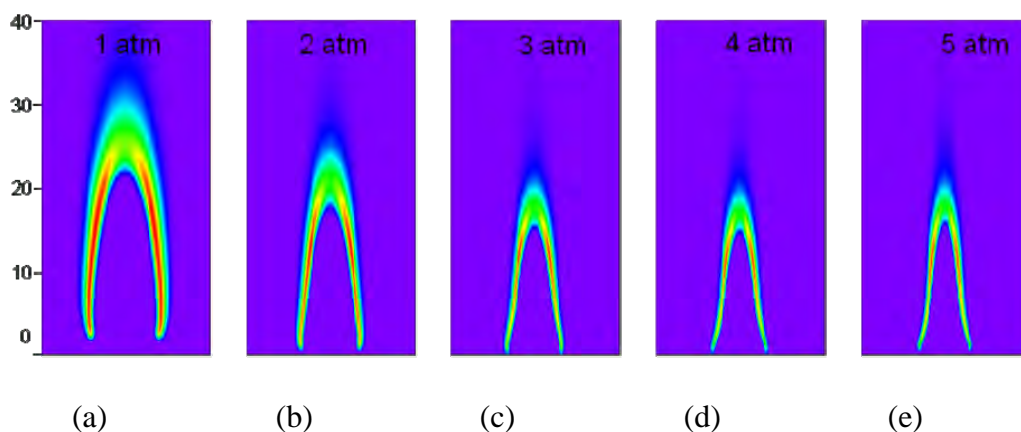


Figure 5.117 Distributions of OH concentration in a 5% m-xylene added, nitrogen diluted ethylene jet diffusion flame at (a) 1 atm, (b) 2 atm, (c) 3 atm, (d) 4 atm, and (e) 5 atm.

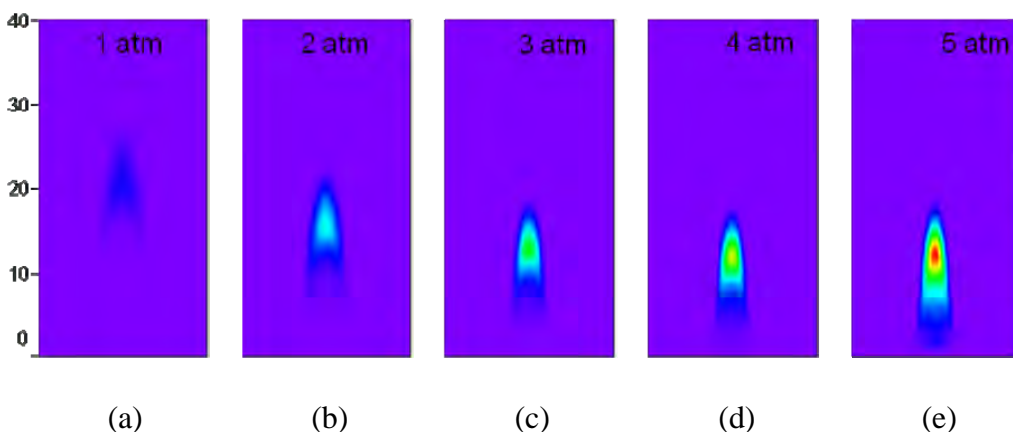


Figure 5.118 Distributions of soot in a 5% m-xylene added, nitrogen diluted ethylene jet diffusion flame at (a) 1 atm, (b) 2 atm, (c) 3 atm, (d) 4 atm, and (e) 5 atm.



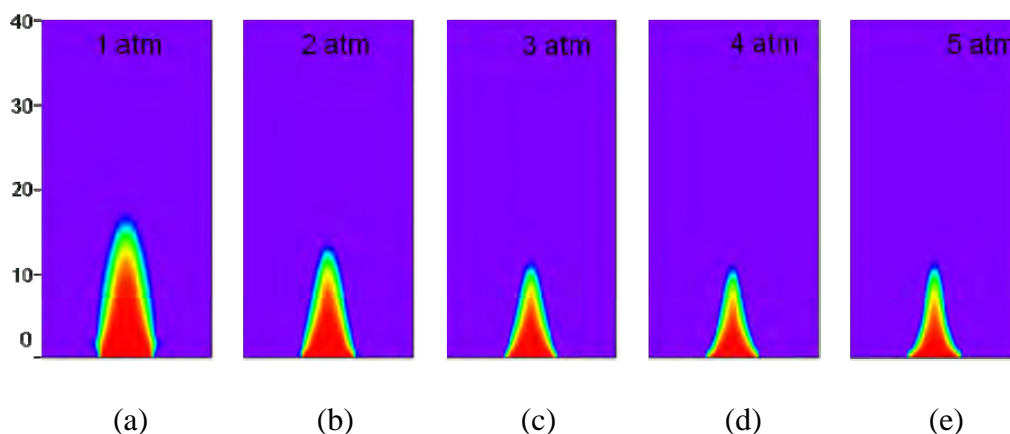


Figure 5.119 Distributions of m-xylene in a 5% m-xylene added, nitrogen diluted ethylene jet diffusion flame at (a) 1 atm, (b) 2 atm, (c) 5 atm, (d) 4 atm, and (e) 5 atm.

#### 5.2.4 Effect of Surrogate and its Components on Soot in $N_2$ -diluted Ethylene Flames

The bubbler system used in the m-xylene studies was not capable of vaporizing dodecane or JP-8 at the rates required to achieve 5% Carbon from these fuels. Therefore a new vaporizer system was developed based on the approach used by Kevin McNesby at ARL. The combustion air flows along the outside of the fuel tube inside the burner; therefore, cooling of the  $N_2$ -fuel mixture by the air flow could lead to condensation of the vaporized fuel. To avoid this problem, the air was heated to  $100^\circ\text{C}$ . In order to allow direct comparison among the fuels, including m-xylene, a new set of m-xylene soot data was collected along with data for the addition of dodecane and the surrogate, which was 23% m-xylene and 77% dodecane by volume.

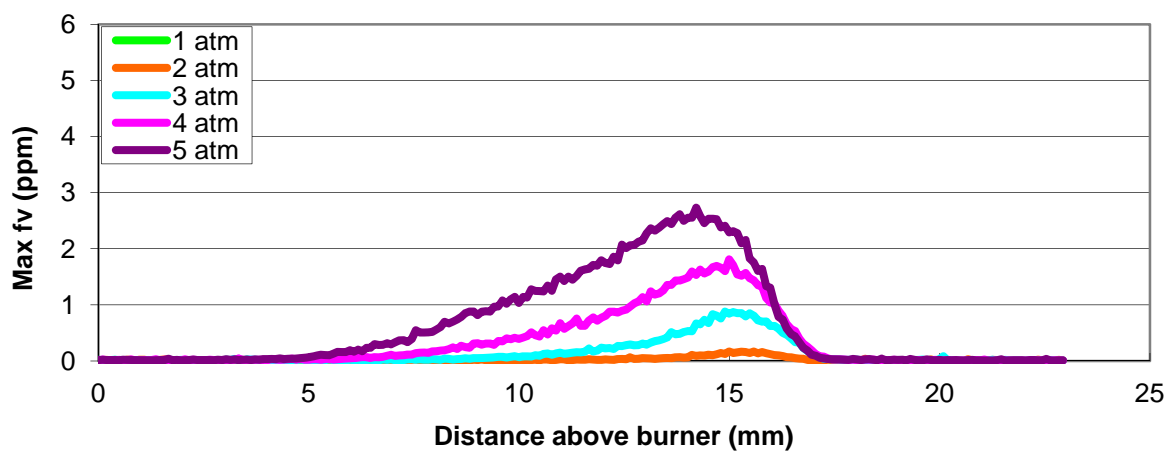
Figure 5.120 presents centerline soot profiles for the baseline  $N_2$ -diluted  $C_2H_4$  flame and the flame with m-xylene at 2.5% and 5% carbon. Comparison of these results with those in section 5.2.3 shows that increasing the air temperature led to slightly higher soot volume fractions. The radial volume fraction distributions are quite similar to those presented in section 5.2.3, so additional plots will not be presented here. (All of the 2-D image data is available in the archive for these experiments.)

Figure 5.121 and 5.122 present axial variation in peak volume fraction for the addition of dodecane and the surrogate, 23%v m-xylene/77%v dodecane. The base flame was repeated for each fuel set and was found to be very repeatable. Therefore, the base flame plots are not included in Figures 5.121 and 5.122.

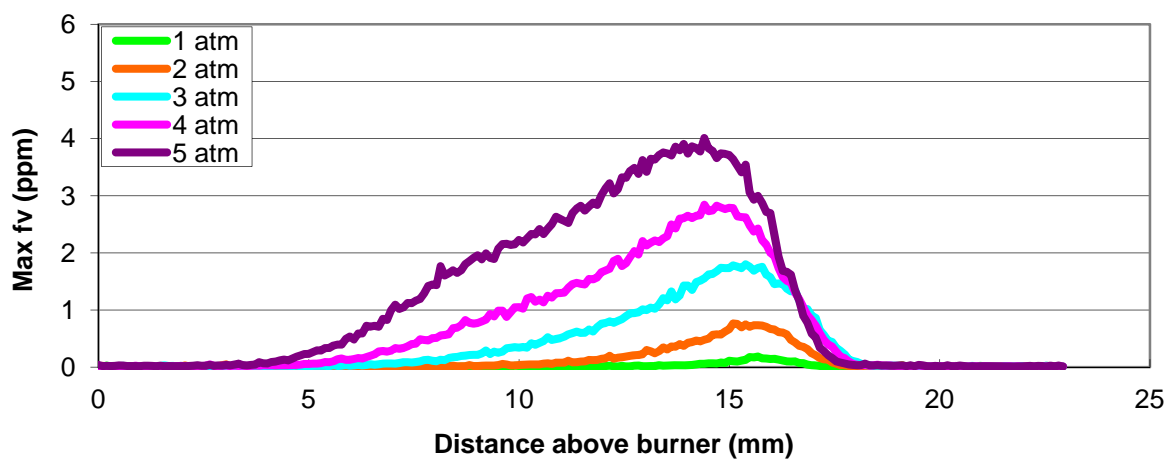
Figure 5.123 presents a plot of the peak volume fractions for these three fuels as a function of pressure for 5% carbon addition from the liquid fuel. The multiple symbols for at a given test condition represent separate experiments and provide an indication of the repeatability of the tests. As expected the m-xylene had the greatest effect on soot and the surrogate produced soot levels much closer to the dodecane values than those of the m-xylene values.

Interestingly the soot levels for the surrogate can be reasonably approximated by a linear combination of the soot increase from the two individual components weighted by their mole fractions. For the 5% carbon test condition, the soot volume fractions predicted by the weighted average are within 20% of the measured values. At all four pressures, the predicted value is always lower than the measured value.

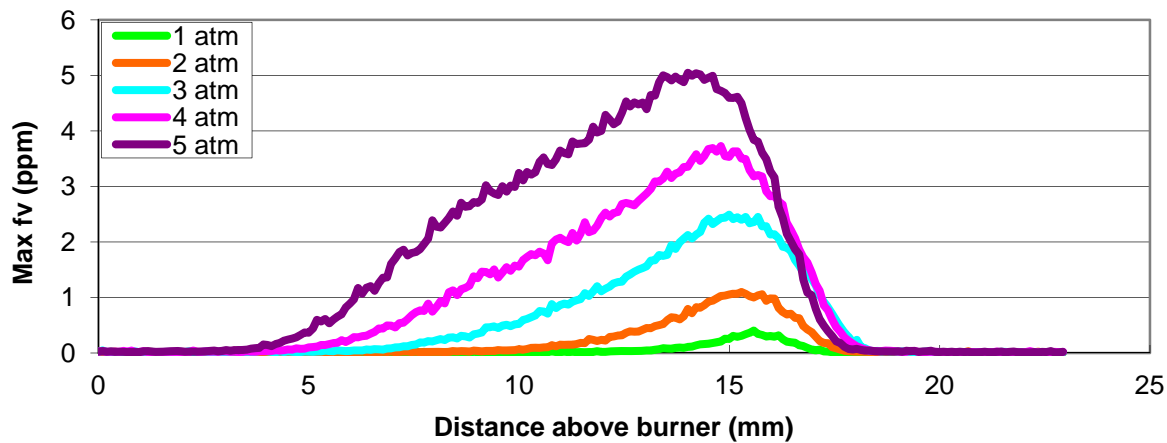
The soot volume fraction data for n-dodecane in Figure 5.124 showed an unexpected trend. The increase in peak soot volume fraction between the 2.5% and 5% carbon cases was much less than the factor of 2 observed for m-xylene. For the 3, 4, and 5 atmospheres, the ratio was an average of only 1.2. As it reacts, the n-dodecane will produce a variety of olefins, including ethylene, and alkyl radicals, including methyl. The methyl radical may combine with the abundant vinyl radicals from ethylene to enhance production of  $C_3$ - radicals that are known to be a key precursor to benzene formation. The rate of this reaction would tend to be very sensitive to addition of dodecane initially because it is 'starved' for methyl radicals. As the concentration of methyl increases, the sensitivity to further increases would decrease leading to the effect observed in the data. Modeling of the results will be undertaken prior to publishing these results in order to test this hypothesis.



(a) Baseline  $N_2$ -diluted  $C_2H_4$  flame



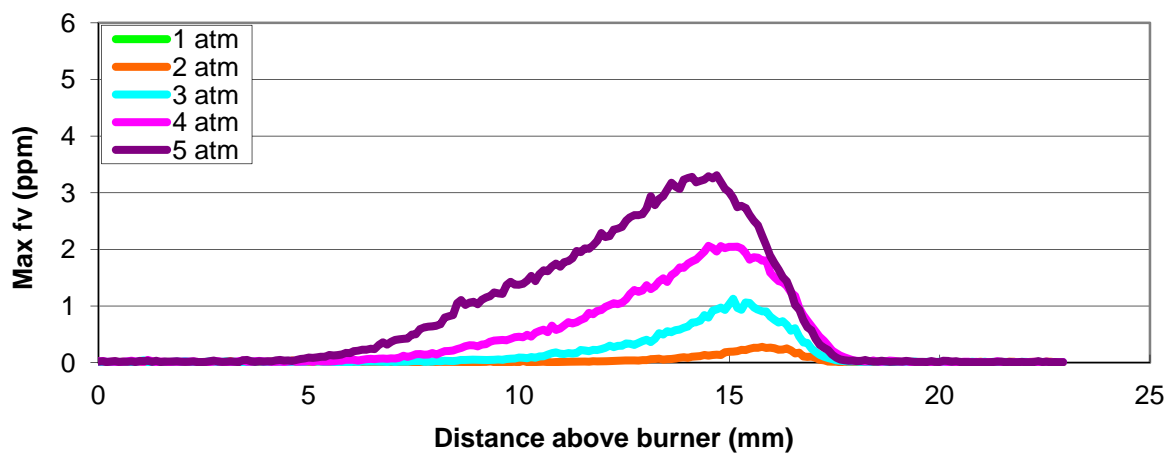
(b) 2.5% carbon from m-xylene



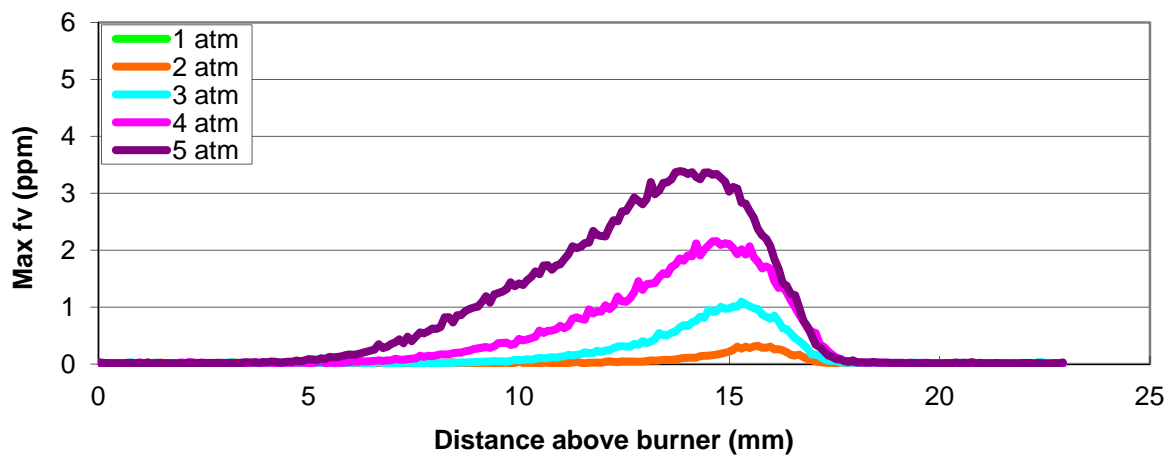
(c) 5% carbon from m-xylene

Figure 5.120 Peak soot volume fractions as a function of height above the burner for base  $N_2$ -diluted  $C_2H_4$  flame along with 2.5% and 5% carbon from m-xylene. (Air temperature is  $100^\circ C$ .)



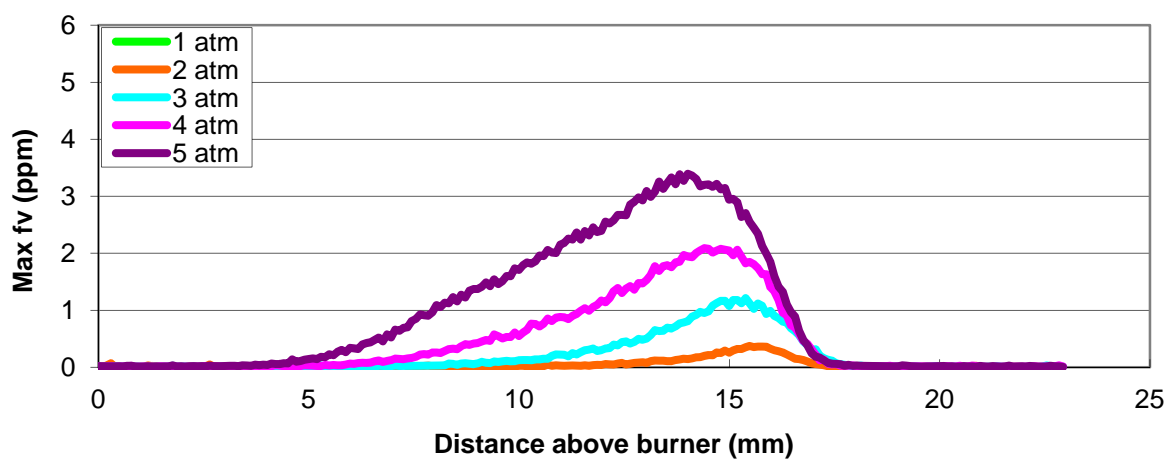


(a) 2.5% carbon from n-dodecane

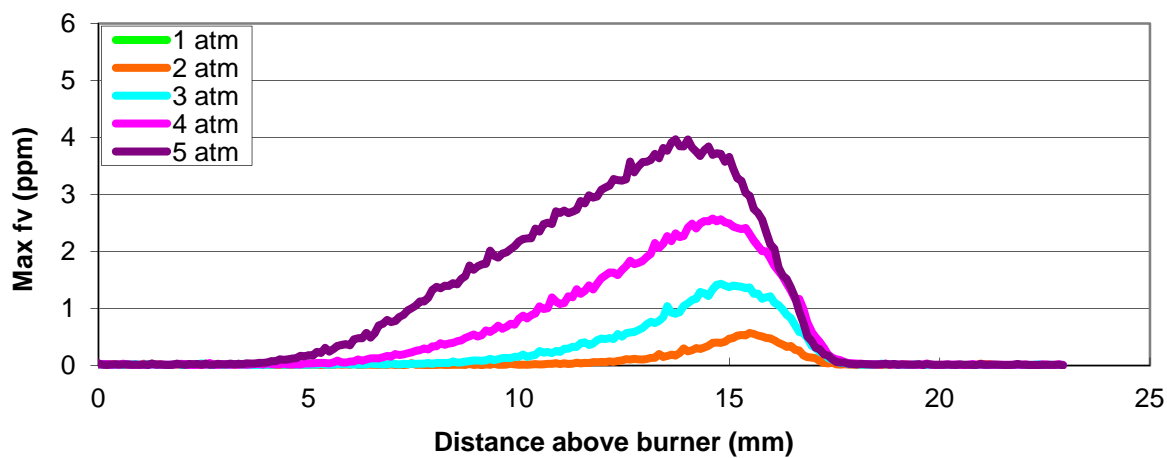


(c) 5% carbon from n-dodecane

Figure 5.121 Peak soot volume fractions as a function of height above the burner for base  $\text{N}_2$ -diluted  $\text{C}_2\text{H}_4$  flame along with 2.5% and 5% carbon from n-dodecane. (Air temperature is  $100^\circ\text{C}$ .)



(a) 2.5% carbon from surrogate



(b) 5% carbon from surrogate

Figure 5.122 Peak soot volume fractions as a function of height above the burner for base  $N_2$ -diluted  $C_2H_4$  flame along with 2.5% and 5% carbon from the surrogate fuel. (Air temperature is  $100^\circ C$ .)

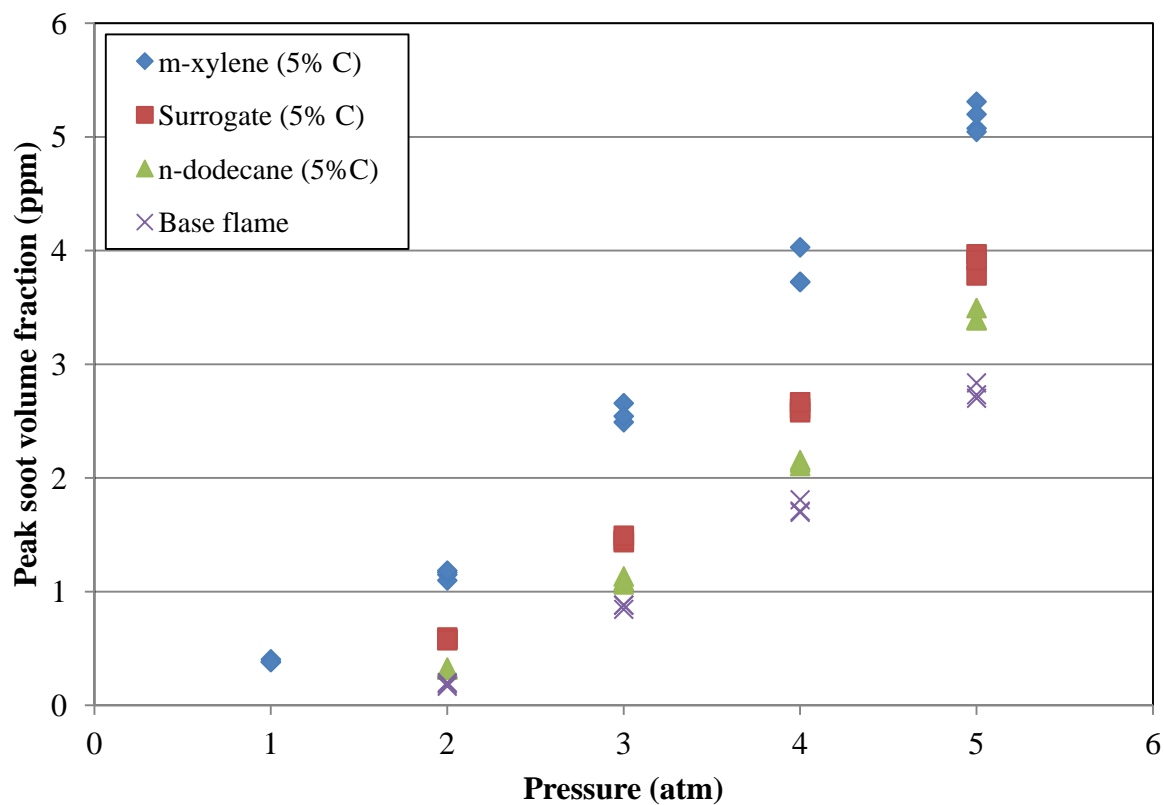


Figure 5.123 Comparison of peak soot volume fractions for the surrogate fuel and its components as a function of pressure.

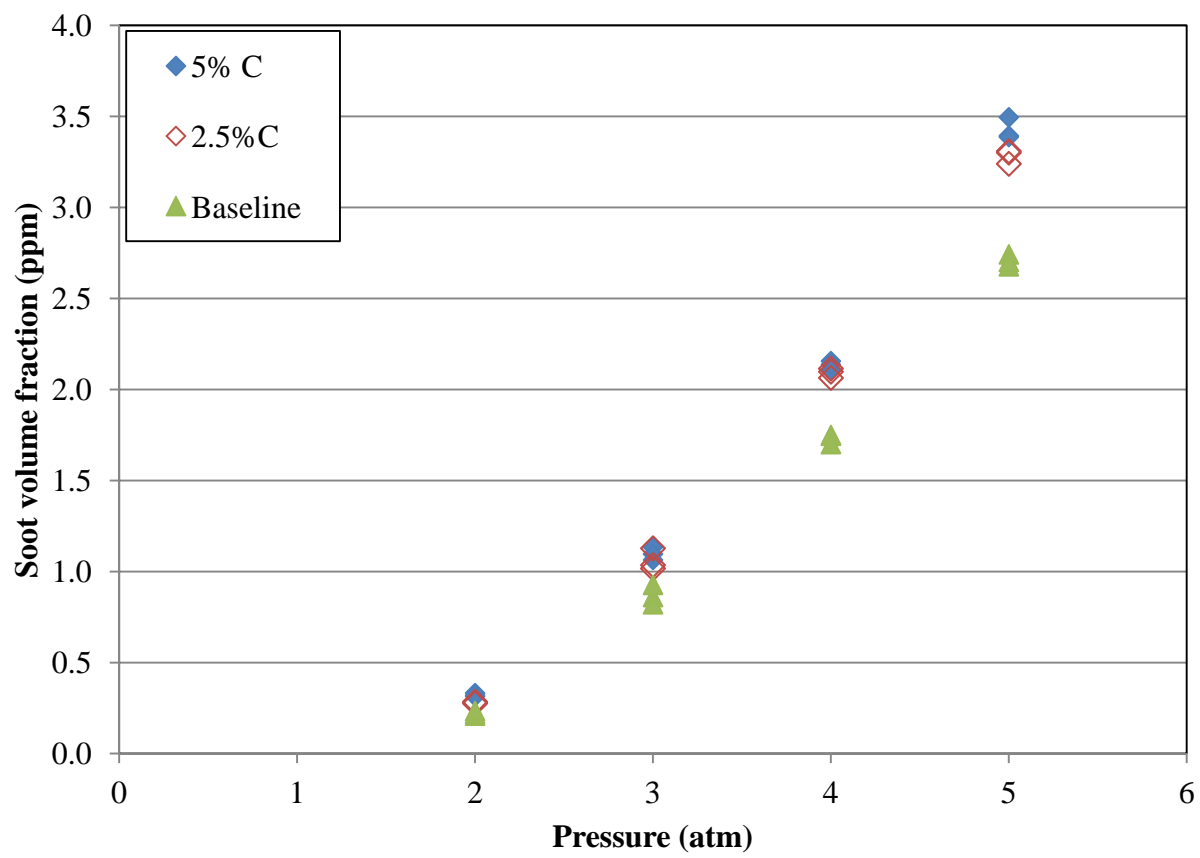


Figure 5.124 Effect of n-dodecane concentration on peak soot volume fraction.

### 5.2.5 Effect of JP-8 on Soot in N<sub>2</sub>-Diluted Ethylene Flames

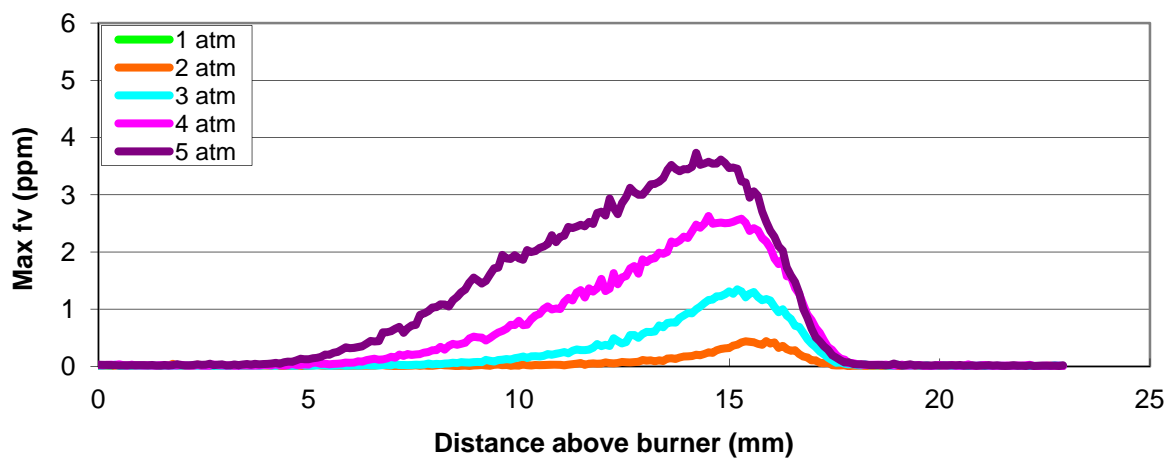
The final fuel that was run in the diluted ethylene flame was JP-8. The JP-8 was provided by Wright Patterson AFB and carried the designation, POSF-5699. It was run under the same conditions as the surrogate fuel, which was formulated to match the sooting characteristics of a typical JP-8 based on Threshold Soot Index. The JP-8 has a smoke point of 23 mm and a TSI of 22. The surrogate has a predicted TSI of 21 and a smoke height of 23 mm.

Figure 5.125 presents the peak soot volume fraction trends for 2.5% and 5% carbon contributed from the JP-8. The trends are similar to those observed with all of the other fuels. Peak soot volume fraction increases substantially with pressure. Figure 5.126 presents the peak volume fraction for JP-8 as a function of pressure for 5% carbon from the additive. The results for the surrogate and the baseline flame, run under identical conditions, are also presented.

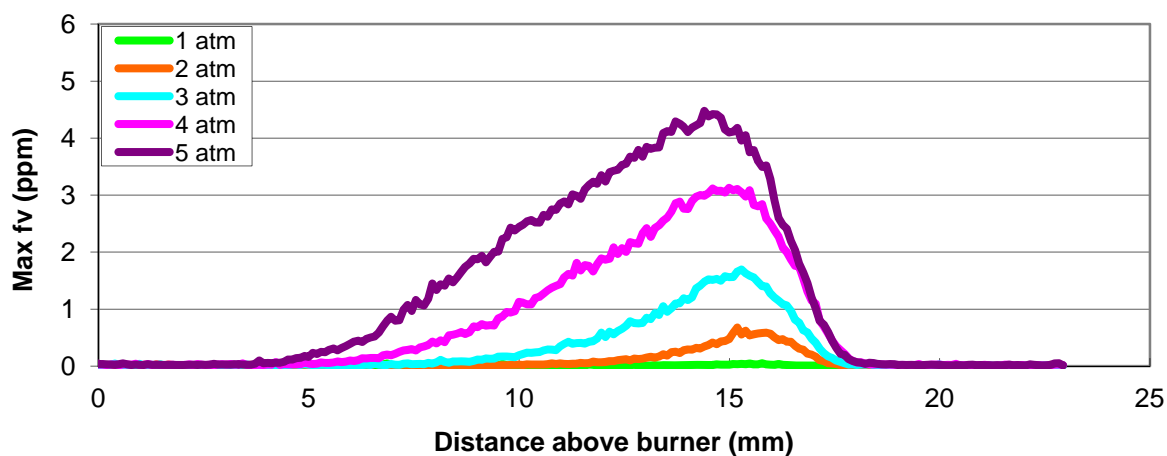
Figure 5.126 shows that the increase in peak soot levels caused by the addition of the surrogate fuel is less than that caused by the addition of JP-8. The differences are most evident at the higher pressures. At 5 atm, the increase in soot caused by JP-8 is approximately 1.6 ppm whereas that caused by the surrogate is approximately 1.2. So the surrogate is producing approximately 25% lower peak soot volume fractions. The higher volume fractions for the JP-8 are consistent with its somewhat higher TSI.

Figure 5.127 presents axial variation of peak volume fraction and centerline volume for both JP-8 and the surrogate at 5 atm with 5% of the fuel carbon from the vaporized fuel. The increase in centerline soot volume fraction occurs at a larger height above the burner than it does for the peak volume fractions. This difference reflects the fact that the peak volume fraction occurs off the centerline at lower heights. Generally, however, the maximum volume fraction in these flames occurs on the centerline or very near it.

Both charts show that the differences between the two fuels are small until the height at which the peak volume fraction occurs. The volume fractions for the flames with the vaporized fuels added begin to deviate from the base flame at approximately the same heights. Interestingly the centerline profiles for the two fuels are essentially identical until very close to the height where peak volume fraction occurs.



(a) 2.5% carbon from JP-8



(b) 5% carbon from JP-8

Figure 5.125 Peak soot volume fractions for JP-8 addition as a function of height above the burner for base  $\text{N}_2$ -diluted  $\text{C}_2\text{H}_4$  flame along with 2.5% and 5% carbon from JP-8. (Air temperature is  $100^\circ\text{C}$ .)

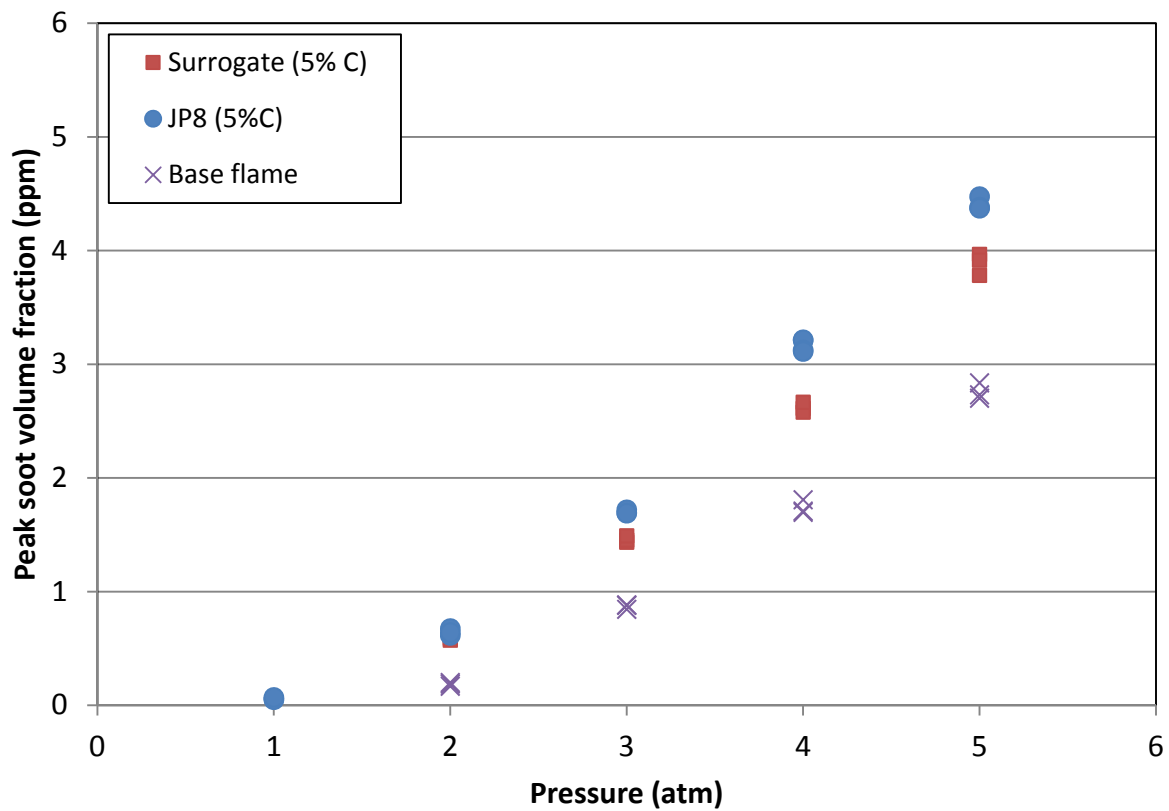
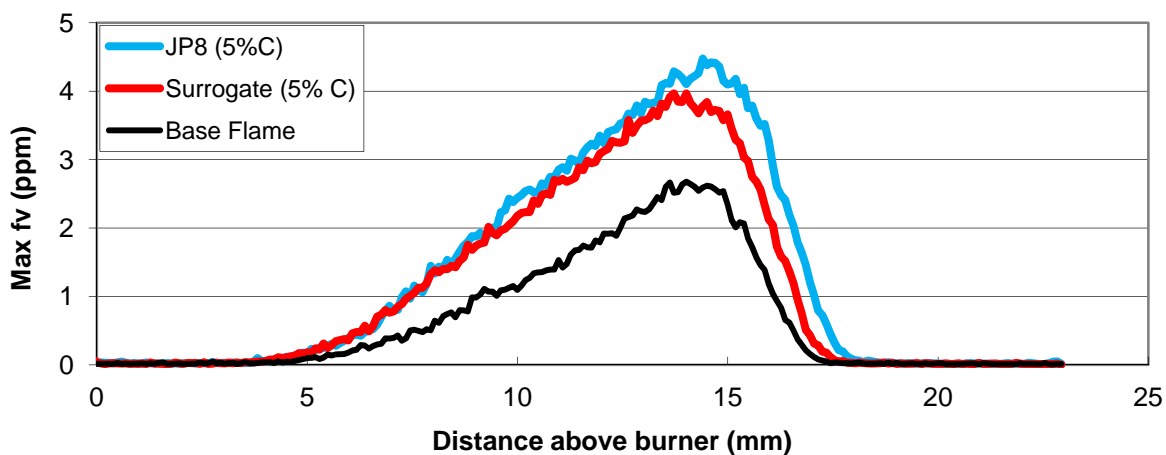
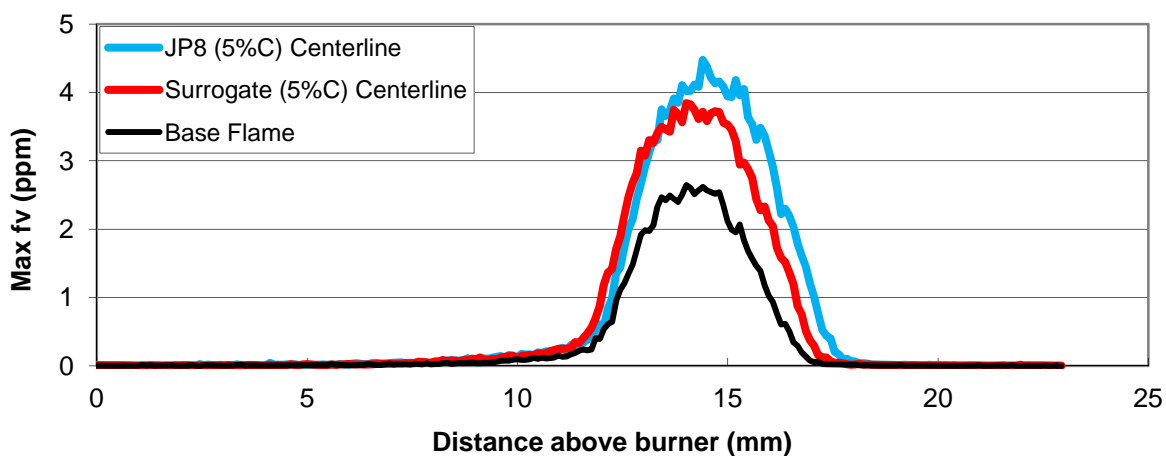


Figure 5.126 Comparison of effect of JP-8 and surrogate fuel on peak soot volume fraction for 5 atm and 5% C from the additive.



(a) Peak volume fractions



(b) Centerline volume fraction

Figure 5.127 Axial variation in peak soot volume fraction (a) and centerline volume fraction (b) for JP-8 and the JP-8 surrogate at 5% carbon from additive and 5 atm. Base flame data also presented as a reference condition. (Air temperature is 100°C.)



### 5.2.6 Simulation of Attached Co-flow Flames

The motivation of this study was to evaluate the current CFD modeling capabilities in predicting attached flames formed with JP-8 fuels. Experiments conducted for a co-flowing jet flame resulted in a stably attached flame. Time-dependent, detailed-chemistry CFD models are used for simulating this co-flowing jet nonpremixed flame. Earlier calculations using Violi chemical-kinetics model involving 161 species and 1538 reactions yielded a flame that was lifted off by about 7.7 mm from the burner exit. A new chemical kinetics model developed at Politecnico di Milano by Ranzi et al (CRECK-0810) involving 206 species and 5652 reactions is incorporated into UNICORN code for improving the liftoff predictions.

The co-flow JP-8/air flame considered in this study was previously calculated using Violi mechanism. The predicted flame was compared with the flame photograph obtained in the experiments (Katta et al. 2010) conducted at University of California at San Diego. The ratio between JP-8 to nitrogen used in the fuel jet was 0.67. Both the fuel and air streams were heated to 490 K. The velocities of the fuel and air jets were 22.8 and 43.4 cm/s, respectively. The flame photograph (Katta et al. 2010) has captured the faint blue region near the fuel nozzle exit suggesting that the flame is well anchored to the burner rim. The flame was very stable and the video taken at 30 frames/s rate did not show any oscillations. The flame was quite sooty and except near the base the entire flame was bright yellow in color. Based on the soot radiation intensity (yellow color) flame height was estimated to be ~ 60 mm.

Results obtained for the coflow JP-8/air flame with Violi mechanism are shown in Figure 5.128. JP-8 fuel in the calculation was represented with a surrogate mixture that has 23% m-xylene and 77% n-dodecane (SERDP surrogate). Computed velocity field is superimposed in Figure 5.128a on temperature distribution plotted in color. Iso contours of methane are superimposed on m-xylene concentration distribution in Figure 5.128b and OH concentration distribution is shown in Figure 5.128c. Considering the fact that flow straighteners were used in both the fuel and air ducts in the experiment, uniform velocity profiles are prescribed for the fuel and air jets in the calculations. Figure 5.128 shows that the predicted that the flame is stably anchored at about 8 mm downstream of the burner exit. Note that experiment has yielded a stably attached flame for these flow conditions. Significant mixing between m-xylene (a component in the fuel mixture) and air has taken place in the shear layer between the burner exit and flame base (Figure 5.128b), yet flame could not propagate any closer to the burner. Figure 5.128a shows that the velocity in the shear layer (dark-blue-color region established in the shear layer due to decrease in temperature) is decreasing with axial distance. This suggests that the flame propagation velocity predicted by Violi mechanism is lower than the velocity in the shear layer between the burner exit and flame base.

Flame propagation velocity in a given fuel/air mixture is couple to ignition delay time since flame ignites the mixture and propagates. Longer ignition delay time results in slower flame propagation velocity. For the correct prediction of the shape of the JP-8/air flame a more recent mechanism referred as CRECK-0810 is used. Before making calculations for the JP-8/air coflow flame using this new CRECK-0810 mechanism, ignition delay times obtained with the new mechanism are compared with those obtained using Violi mechanism. Ignition delay times computed with the two mechanisms for fuel-lean ( $\phi = 0.8$ ), stoichiometric, and fuel-rich ( $\phi =$

1.2) mixtures of various parent fuel components and surrogate mixtures are shown in Figure 5.129. Fuel-lean data are shown in blue, stoichiometric data are shown in red and fuel-rich data are shown in black. For m-xylene, Violi mechanism predicted ignition only when the temperature of the mixture was greater than 1350 K. Significant decreases in ignition delay times are obtained with the new mechanism for m-xylene (Figure 5.129a) and tetralin (Figure 5.129b). For methylcyclohexane (mch), n-dodecane, and tetradecane the ignition delay times increased slightly with the new mechanism while those of isooctane decreased. Interestingly, only marginal decreases in ignition delay times are achieved with the new mechanism for the 6-COMP and SERDP surrogate mixtures. Based on this one might expect only a marginal improvement in the predictions of coflow flame, especially in the flame base location.

Calculations for the JP-8/air coflow flame are made with CRECK-0810 mechanism using the flow conditions and grid system identical to those used in the Figure 5.128 simulation. Results obtained with the new mechanism are shown in Figure 5.130 following the format used in Figure 5.128. As expected, flame base has moved upstream from  $z = 7.7$  mm to 4 mm. However, the new mechanism also failed to yield an attached flame as suggested by the experiment.

Structures of the flame near the base obtained with Violi and CRECK-0810 mechanisms are shown in Figure 5.131. Solid lines in Figure 5.131 represent the data obtained at  $z = 6$  mm in CRECK flame and broken lines represent data obtained at  $z = 10$  mm in Violi flame. As the CRECK flame is closer to the burner its thickness near the base is smaller than that of the Violi flame. Interestingly, concentrations of the major radicals (H, O, and OH) decreased in CRECK mechanism.

Calculations in Figure 5.128 and 5.130 are made using flat velocity profiles. One could expect such velocity profiles when experiments use straight fuel tubes with flow straighteners. However, a tapered nozzle was used in the experiment performed for the JP-8/air coflow flame. Even though several levels of flow straighteners were used for obtaining uniform velocity profiles, the tapering of fuel tube near the top 2.79 cm could generate a boundary layer type velocity profile adjacent to the fuel tube on the air side. Reduction of fuel tube diameter in the open section was from 1.02 cm to 0.62 cm, which could yield a boundary layer of 2- to 3-mm thickness. Calculations for the coflow flame are repeated using velocity profiles of 2.5-mm and 5-mm boundary layers for the coflowing air. Average velocity for the air jet was still maintained at 43.4 cm/s. Velocity profiles used in these calculations are shown in Figure 5.132.

Flame obtained with 2.5-mm boundary layer is shown in Figure 5.133b and those obtained with 5.0-mm boundary layer are shown in Figure 5.133c. For comparison purpose results obtained with flat velocity profiles are shown in Figure 5.133a. A significant decrease in flame liftoff height (from 4 mm to 1 mm) resulted when a 2.5-mm thick boundary layer was introduced for the coflowing air jet. Further increase in boundary layer thickness resulted in only a marginal decrease in flame liftoff height. Assuming that the 2.5-mm boundary layer is a reasonable approximation for the tapering in the fuel tube and based on the data shown in Figure 5.133b it may be concluded that CRECK-0810 mechanism fails to simulate an attached flame under moderate velocity conditions.

Effects of boundary layer on flame liftoff height in the simulations made with Violi mechanism are shown in Figure 5.134. Temperature and velocity fields obtained with 0, 2.5-mm, and 5.0-mm thick boundary layers are shown in Figures 5.134a, 5.134b, and 5.134c, respectively. Violi mechanism also brought the flame closer to the burner exit with increase in boundary layer thickness. However, the differences between the two mechanisms (CRECK and Violi) prevail irrespective of the effects of boundary layer profile on flame liftoff. Based on these results it may be concluded that the new CRECK-0810 mechanism improves the predictions for a laminar JP-8/air jet flame (compared to Violi mechanism), however new mechanism is not sufficiently accurate for predicting the flame base attachment to the burner.

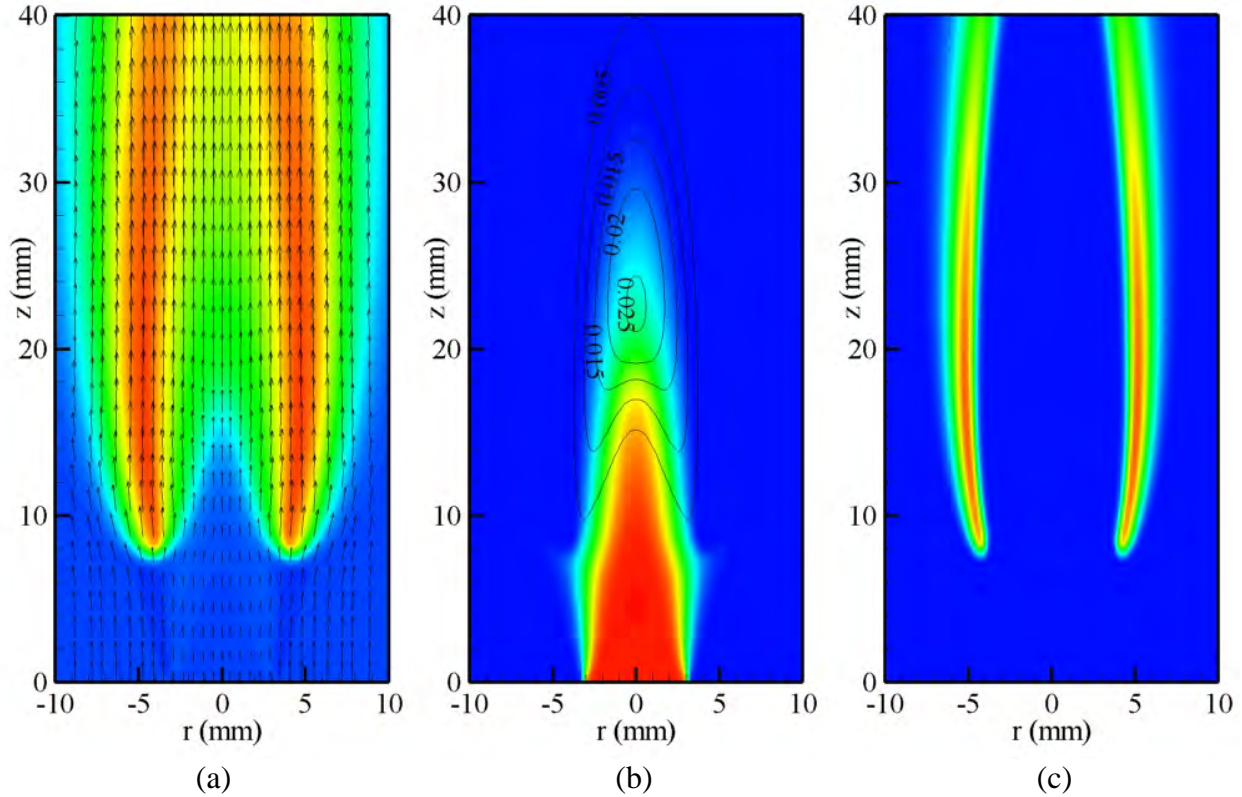


Figure 5.128 JP-8/air coaxial jet nonpremixed flame computed using Violi's mechanism. Fuel and air jet velocities are 22.8 cm/s and 43.4 cm/s, respectively. (a) Velocity field is superimposed on temperature distribution, (b) iso contours of methane are superimposed on m-xylene distribution, and (c) OH-concentration distribution. Photograph of the experiment have shown that the flame is well attached to the burner tip.

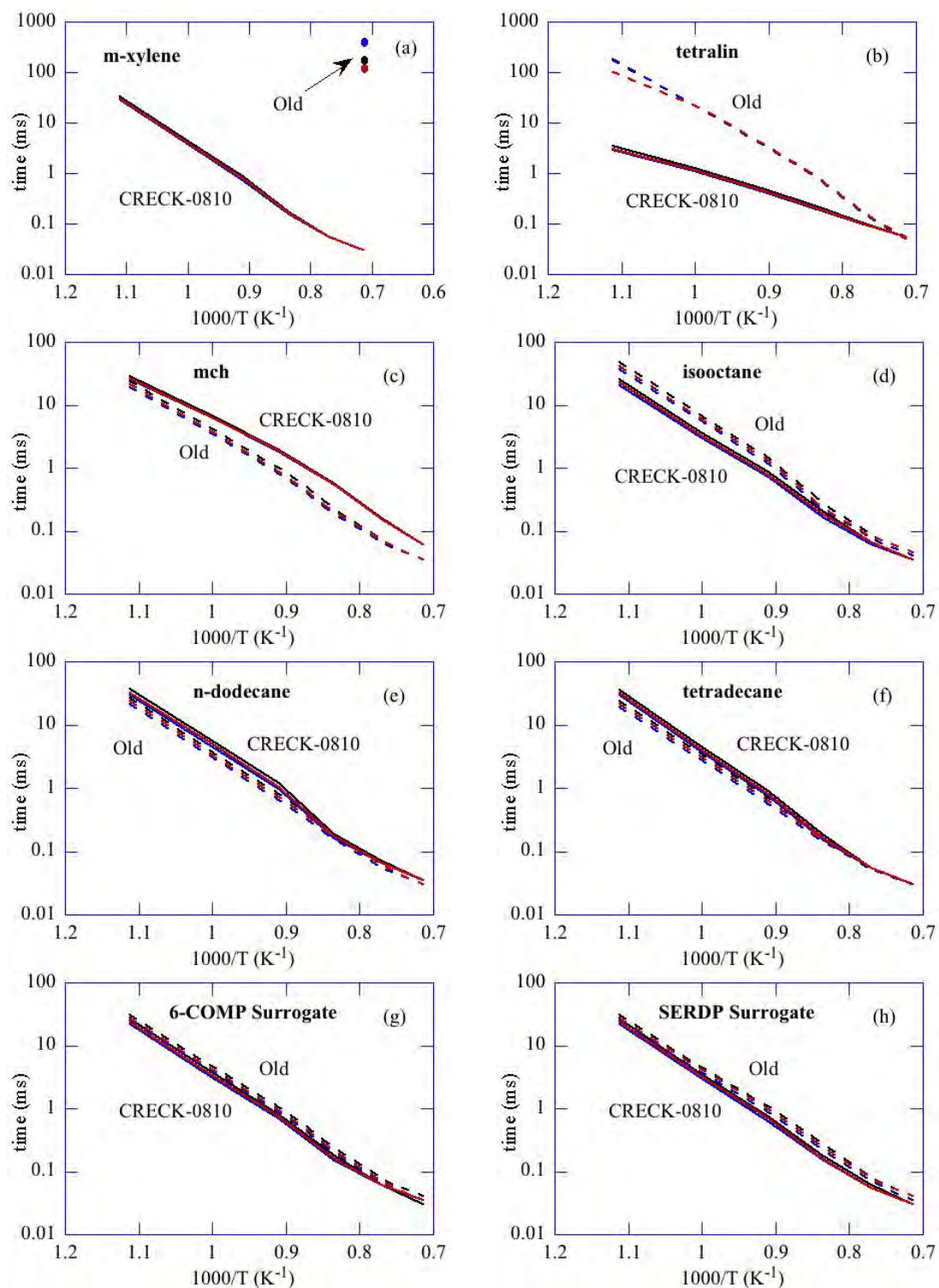


Figure 5.129 Ignition delay times computed at various temperatures with old (dashed lines) and CRECK-0810 (solid lines) mechanisms for  $f = 0.8$  (black lines),  $f = 1.0$  (red lines) and  $f = 1.2$  (blue lines). Fuels shown are (a) m-xylene, (b) tetralin, (c) mch, (d) isooctane, (e) n-dodecane, (f) tetradecane, (g) 6-COMP surrogate, and (h) SERDP surrogate.

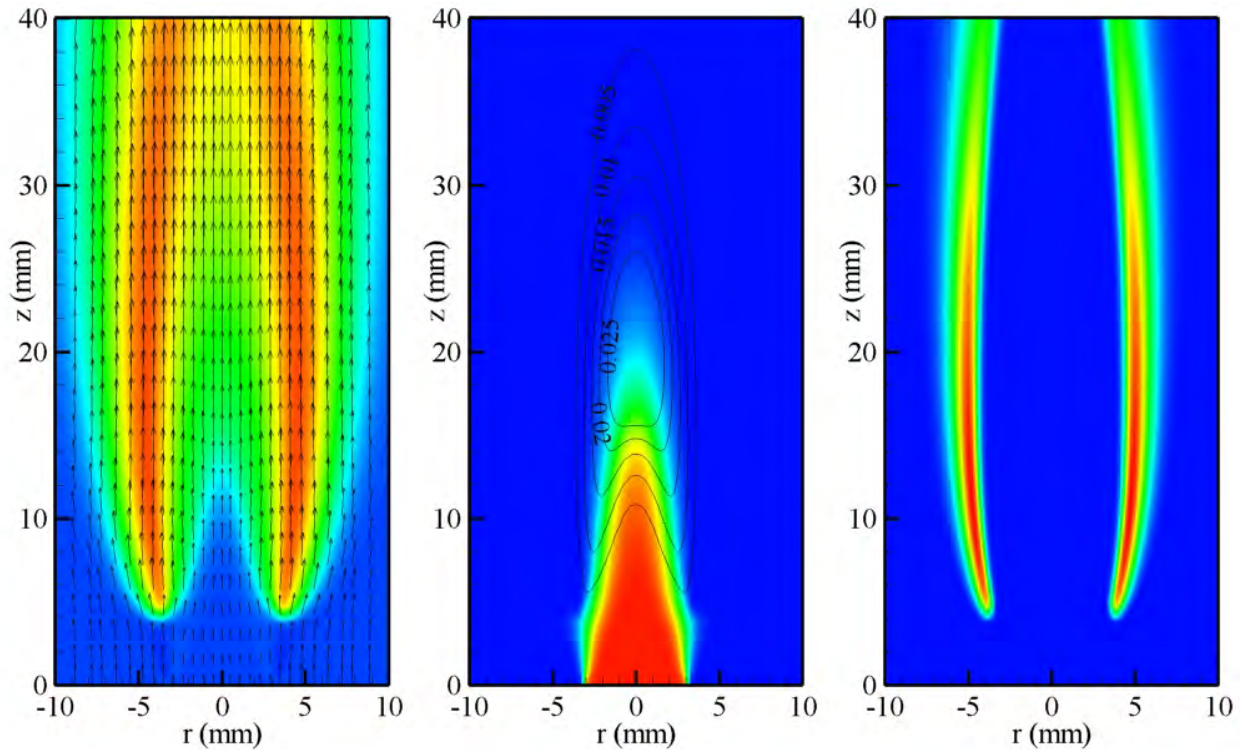


Figure 5.130 JP-8/air coaxial jet nonpremixed flame computed using CRECK-0810 mechanism. Fuel and air jet velocities are 22.8 cm/s and 43.4 cm/s, respectively. (a) Velocity field is superimposed on temperature distribution, (b) iso contours of methane are superimposed on m-xylene distribution, and (c) OH-concentration distribution.

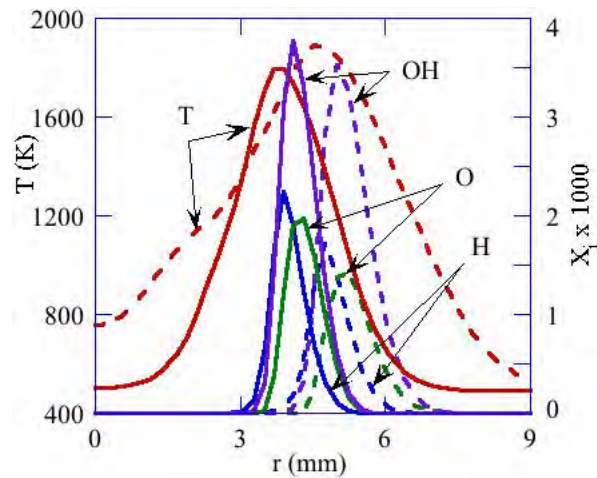


Figure 5.131 Comparison of flame-base structures obtained with Violi and CRECK-0810 mechanisms.



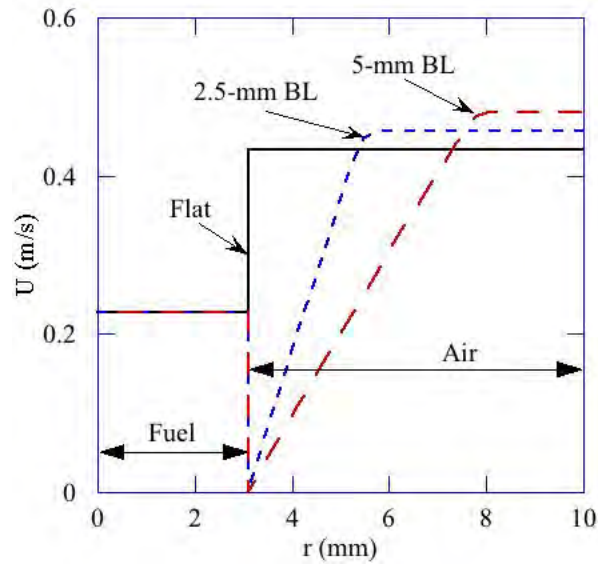


Figure 5.132 Velocity profiles used in different calculations.

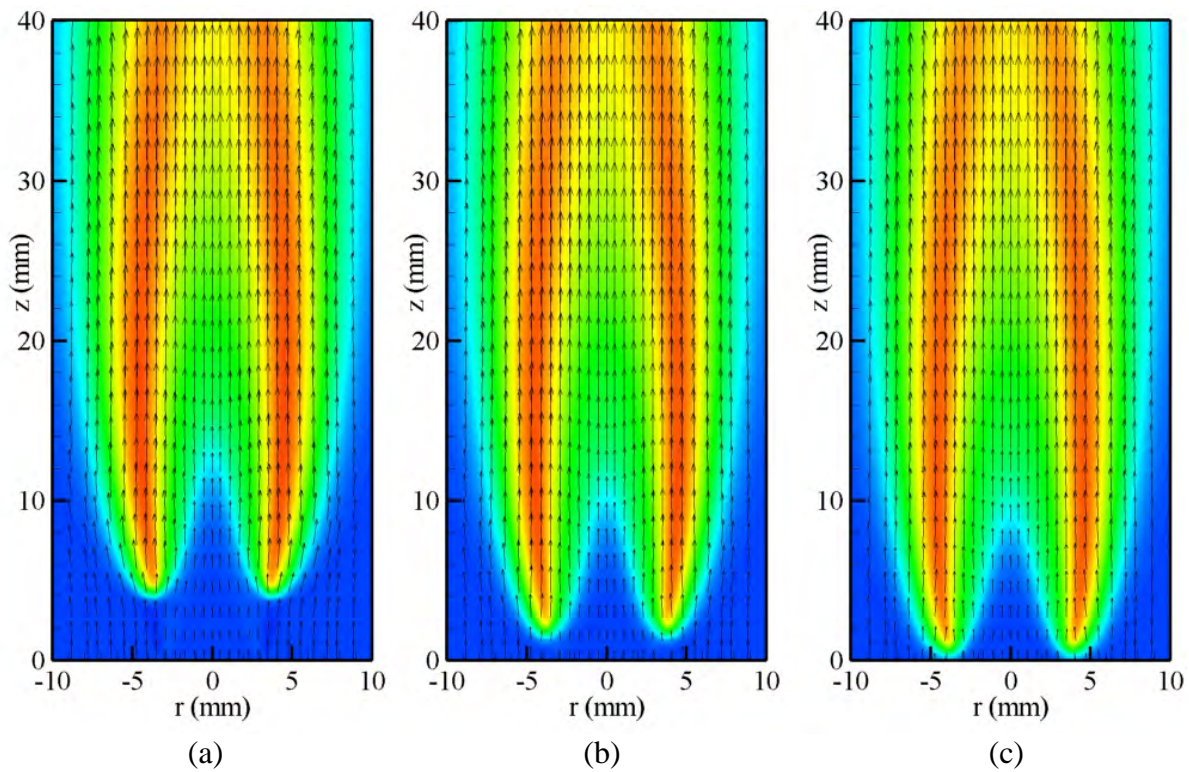


Figure 5.133 Effect of air-jet-velocity profile on the flame base location computed with CRECK-0810 mechanism. (a) Flat velocity profile, (b) 2.5-mm thick boundary layer, and (c) 5-mm thick boundary layer.

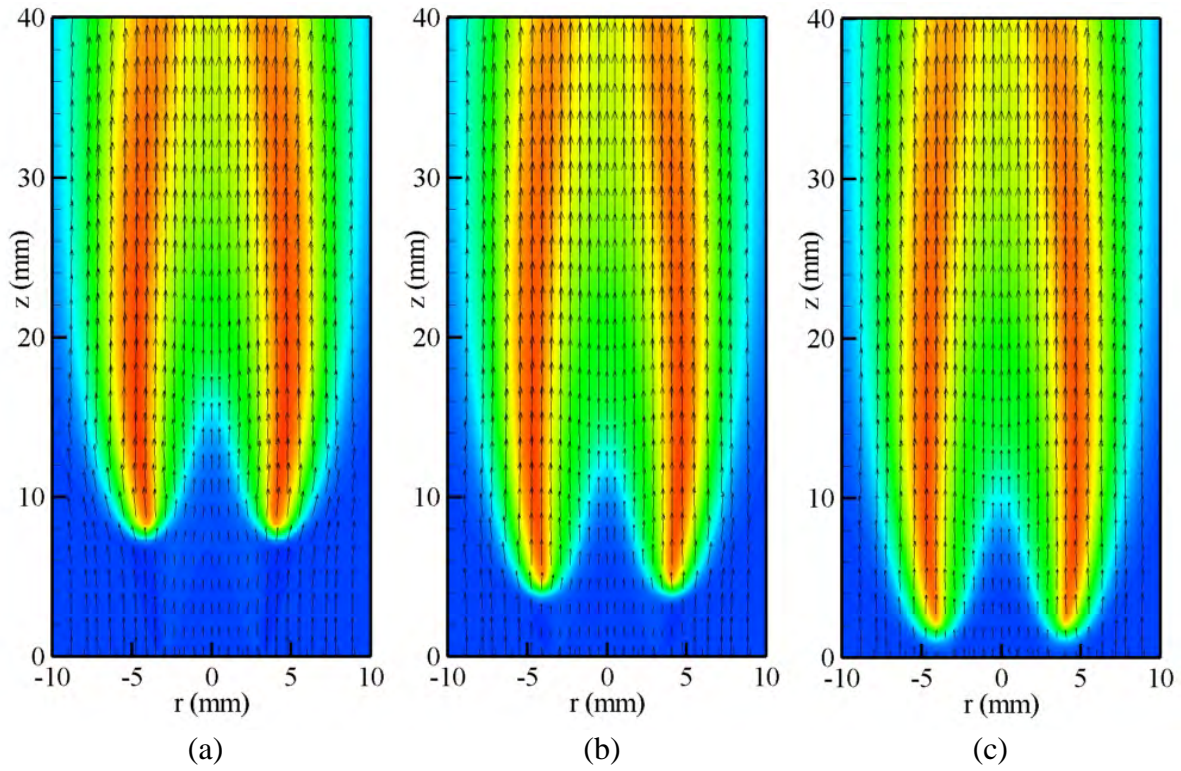


Figure 5.134 Effect of air-jet-velocity profile on the flame base location computed with Violi mechanism. (a) Flat velocity profile, (b) 2.5-mm thick boundary layer, and (c) 5-mm thick boundary layer.

### 5.3 Opposed-jet Diffusion Flame

#### *Modeling*

An effort has been made to compare modeling results using the 2-D flame simulation computer code UNICORN (Katta, 2009) with those obtained using the 1-D flame simulation software CHEMKIN Pro (Reaction Design). The opposed jet flame used for comparison was of ethylene/air, calculated using the Wang-Colket mechanism (Appel et al., 2000; Hall, 1997). Figure 5.135 shows predicted velocity and temperature profiles for the opposed jet burner using Unicorn and Chemkin Pro. The agreement between contours and peak temperatures is reasonable. Slight differences in position are most likely due to the inclusion of the shroud flow in the UNICORN calculations. CHEMKIN Pro does not allow for the inclusion of a shroud gas in the opposed jet flame program OPPDIF. Figure 5.136 shows a comparison of calculated acetylene profiles in the opposed jet ethylene/air flame (calculations are also shown using the Wang-Frenklach mechanism (Frenklach, 1991)). The predicted acetylene profiles are in reasonable agreement (peak values are within 10% of each other), with the slight difference in predicted position believed to be due to the predicted difference in velocity profiles noted above. For all species predictions using a given chemical mechanism, the agreement between UNICORN and CHEMKIN Pro was reasonable.

#### *Planar Laser Induced Fluorescence / Light Scattering*

Experiments using our liquid-fuels-capable opposed jet burner have focused on ethylene/air flames to which m-xylene ( $C_8H_{10}$ ) has been added to the fuel side at levels up to 20% by gas volume, by the methods described in section 4.4. For each flame system to which m-xylene is added, the ethylene gas flow is reduced to maintain equal carbon content in the gas flow entering the flame zone. When added in this manner, the visual effect of adding metaxylene to the fuel gas is to increase the luminosity of the sooting region of the flame (see Figure 5.137), while having limited effect on the luminous, “blue” flame region. The lower, “yellow” region of the flame may contain soot particles and aromatics. For this reason, laser induced fluorescence from this region is referred to as PAH fluorescence/light scattering.

Figure 5.138 shows two raw images of planar laser induced fluorescence/light scattering for ethylene air flames with 5% and 15% m-xylene added to the fuel gas. The fluorescence of m-xylene (excited by the 281 nm laser light) provides an additional check on the fuel additive. Figure 5.139 shows a series of pixel values of images of planar laser induced fluorescence/light scattering (measured through the burner centerline, 100 image average) for a series of ethylene/air opposed jet flames to which m-xylene has been added to the fuel side up to 20% by volume, keeping total fuel gas carbon constant. As expected and in agreement with the visual images of the flames, as m-xylene is added to the fuel gas, the scattering/fluorescence from the sooting region of the flame increases.

A surprising result is that the increase in scattering/fluorescence from the sooting region is accompanied by a decrease in OH fluorescence. Figure 5.140 shows peak values of fluorescence/light scattering versus fraction of m-xylene in fuel gas based on several series of measurements in the opposed jet burner from the initial series of tests. As this decrease was



unexpected, the addition of m-xylene to the fuel side of ethylene/air opposed jet flames was modeled using UNICORN. The results of this simulation are shown in Figure 5.141. The model predicts significant increases in soot formation with m-xylene addition (as observed) but predicts only modest decreases in OH.

Figure 5.142 and 5.143 show the results of a remeasurement of PAH fluorescence/light scattering, and OH fluorescence versus fraction of metaxylene in fuel gas (holding total C constant), focusing on the region (0-5% metaxylene) of largest decrease in OH from initial experiments. These measurements were taken after a rebuild of the atomizer. The results do not show the large drop in OH that the original measurements did. The new results are in much better agreement with predictions based upon UNICORN for the opposed flow ethylene/air flames to which metaxylene is added on the fuel side. The non-repeatability of the initial results serves to emphasize the care with which the vaporizer system must be maintained.

#### *Tunable Diode Laser Absorption Spectroscopy*

Acetylene measurements in flames has been measured using methods following the methods described in section 4.4. Work describing the application of this technique to characterization of an acetylene-air diffusion flame has been accepted for publication in Applied Optics (Quine, 2009). A reconstruction of the acetylene concentration (not temperature corrected) measured in an acetylene-air flame supported by a glass blowers torch is shown in Figure 5.144. This technique has recently been extended to measurements in the opposed flow burner. Figure 5.145 shows a measurement of acetylene absorption through the flame region, by the method described in Section 4.4, of an ethylene/air opposed flow flame to which acetylene is added on the fuel side. The feature labeled as the P23 line of acetylene demonstrates the capability of the technique to measure acetylene produced in the ethylene/air opposed jet flame. As pointed out in section 4.4, quantitative measurement of acetylene concentrations in the flame using infrared absorption techniques requires a knowledge of temperature.

#### *Imaging Pyrometry*

The imaging pyrometer described in section 4.4 was initially tested on the diffusion flame described in the previous section for acetylene measurement. A photograph of this flame (ethylene-air diffusion) is shown in Figure 5.146. Temperature maps using the imaging pyrometer technique for acetylene-air and ethylene-air diffusion flames are shown in Figure 5.147. It should be noted that the imaging pyrometer is best suited to measuring temperatures of particle laden, i.e., sooting, flames. For flames that exhibit minimal grey body emitters, or have significant discrete spectral emission, the technique may report inaccurate temperatures. As an example, Figure 5.148 shows the wavelength resolved emission from three ethylene air flames, ranging from a candle-like diffusion flame described above, to a coflowing diffusion flame, to an opposed jet flame. Each flame shows differing contributions to total emission from discrete emission. Therefore, when using this technique we believe it is mandatory that a measurement of wavelength resolved emission also be recorded. Figure 5.149 shows the imaging pyrometer technique applied to an opposed jet ethylene/air flame. The pyrometer yields reasonable temperatures in the sooting region of the flame but the blue-green emission from CH and C<sub>2</sub> cause the pyrometer to report inaccurate temperatures in the combustion region of the flame.

### *High Pressure Flame Results*

In constant molar flow mode, as the pressure is increased the densities of the fuel and oxidizer gasses change. For experiments reported here, we have run the burner in constant molar flow mode and in constant strain mode. In constant molar flow mode, the flow rate set at the flow controllers is kept constant. For the opposed flow burner configuration used here (1.4 cm diameter, 0.6 cm duct separation), the flow rate used in constant molar flow mode was 2.7 liters per minute air and 4 liters per minute ethylene. For a stagnation plane located midway between the burner ducts, this corresponds to a global oxidizer strain rate of  $97 \text{ s}^{-1}$  at a total pressure of 1 bar.

In constant molar flow mode, as pressure is increased, density decreases, so strain rate also decreases. Visually, as pressure increases, the flame changes from a mixture of blue and orange near atmospheric pressure to a bright orange at pressures greater than 2 bar. Figure 5.150 shows a series of photographs of the constant molar flow flame from atmospheric pressure to above 2 bar total pressure. These images are all taken with the red pixel matrix near 80% of saturation. Prior to each image being taken, the exposure was adjusted so that none of the color pixels corresponding to a point in the flame were at saturation. From these images, the gradual change from blue to orange is evident.

For constant strain mode, the flow rate of fuel and oxidizer gases was varied to account for changes in gas density as pressure was increased. At atmospheric pressure, the initial flame was based upon a flow rate of 2 liters per minute oxidizer and 2.9 liters per minute ethylene. At our burner configuration, this resulted in a global oxidizer strain rate of  $72 \text{ s}^{-1}$ . To maintain this strain rate up to a total pressure approaching 3 bar, oxidizer flow rate was eventually raised to 5.4 liters per minute (with a concurrent increase in fuel flow rates). Images of these flames, measured using the same methodology as for constant molar flow flames, are shown in Figure 5.151. As seen for constant molar flow rate flames, the most notable visual change with increasing pressure was an increase in luminosity as the flames changed from a mixture of blue and orange to bright orange.

Figure 5.152 shows a plot of temperatures measured using imaging pyrometry developed as part of this program. As the pressure is increased for the constant molar flow flames, the measured temperature decreases. Modeling of these flames, described in the next paragraph, showed that the flame temperature increased with pressure – at this time, the reason for this discrepancy between the data and the model is still being investigated.

Modeling was conducted using the Appel, Bockhorn, and Frenklach (ABF) mechanism, which contains 101 species, 544 reactions, and associated thermodynamic and transport files (Appel, 2000). The ABF mechanism has been validated with ethane, ethylene, and acetylene fuels and predicts the major, minor, and aromatic species up to pyrene. The ABF mechanism was executed with Cantera, which is an open-source, multi-platform, software code used to study combustion behavior, using the one-dimensional counter-flow flame configuration. Initial grid spacing between inlets was evenly set to 0.0, 0.2, 0.4, 0.6, 0.8, 1.0 cm for 1 atm calculations and then modified to 0.0, 0.1, 0.2, 0.3, 0.4, 0.5, 0.6, 0.8, 1.0 cm for simulations at elevated pressures.

Once the Newton iteration successfully converged, grid refinement was enabled and new grid points were inserted to proceed with the calculation. Final grid count included 172, 161, and 172 points for 1 atm, 2.04 atm (30 psi), and 5 atm, respectively. The computational time, using a Pentium Dual-Core T4400 processor with a 64-bit operating system, for convergence to occur was approximately 180 s. Initial conditions of the model simulations were set to the following: Ethylene as fuel, air as oxidizer, fuel/oxidizer inlet temperature of 300 K, duct separation of 1 cm, initial pressure of 1 atm, 2.04 atm (30 psi), and 5 atm for each case, and mass flux of fuel and oxidizer set to 0.47 and 0.65 kg/m<sup>2</sup>/s, respectively.

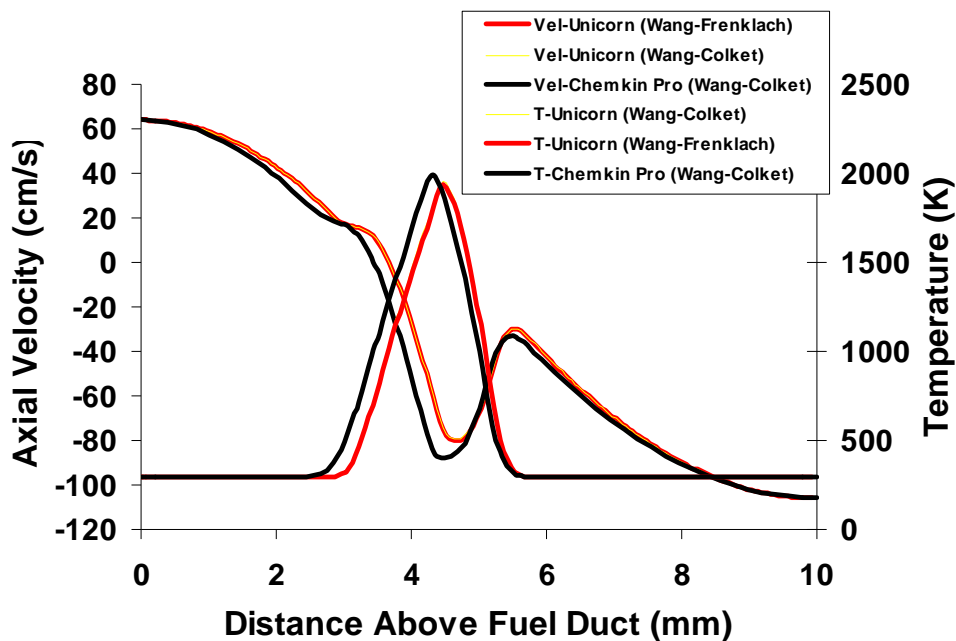


Figure 5.135 Predicted velocity and temperature profiles for the opposed jet burner using UNICORN and Chemkin Pro, ethylene/air flame, Wang-Colket mechanism.

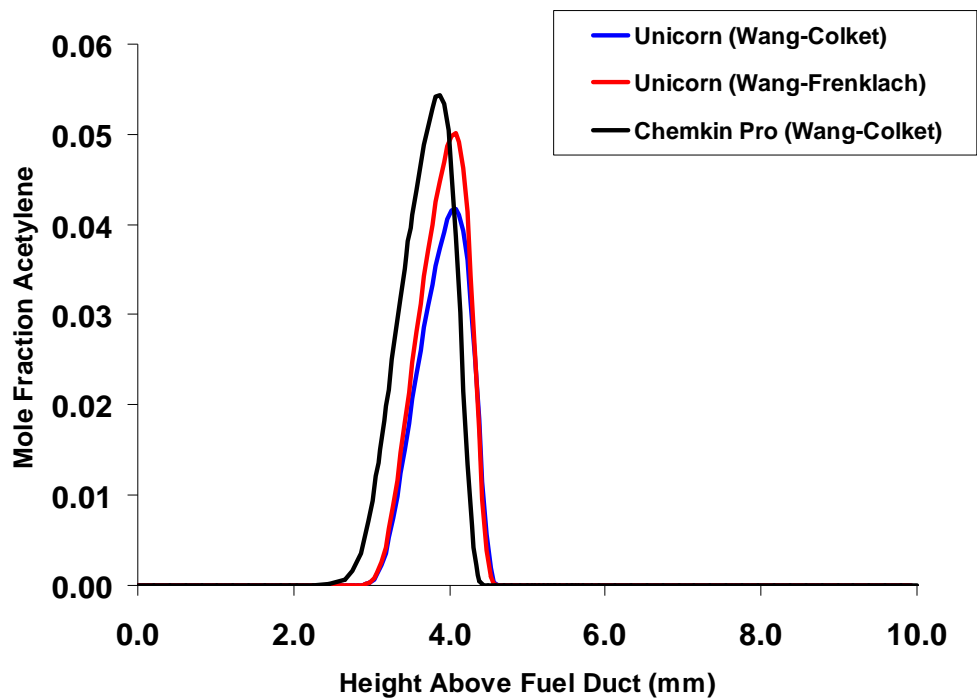


Figure 5.136 A comparison of calculated acetylene profiles in the opposed jet ethylene/air flame (calculations are also shown using the Wang-Frenklach mechanism (Frenklach, 1991)).

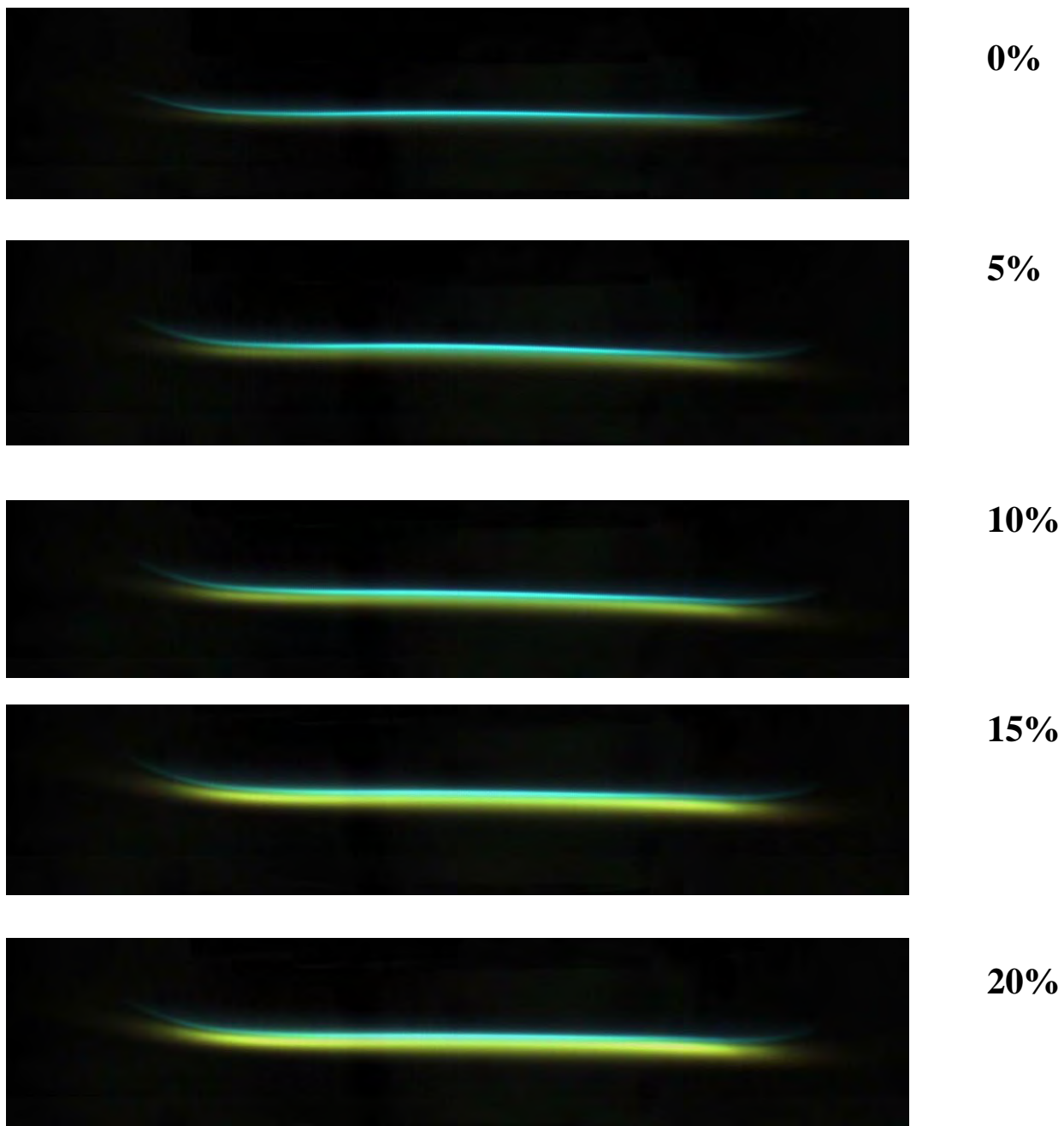


Figure 5.137 Photographs of the opposed jet ethylene/air flame with increasing amounts of m-xylene added to the fuel gas.

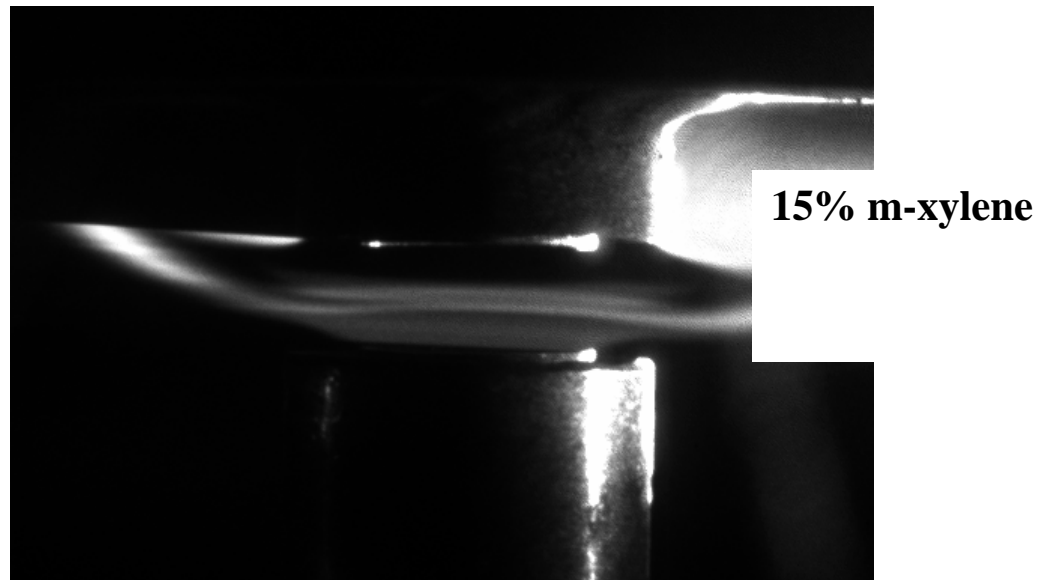
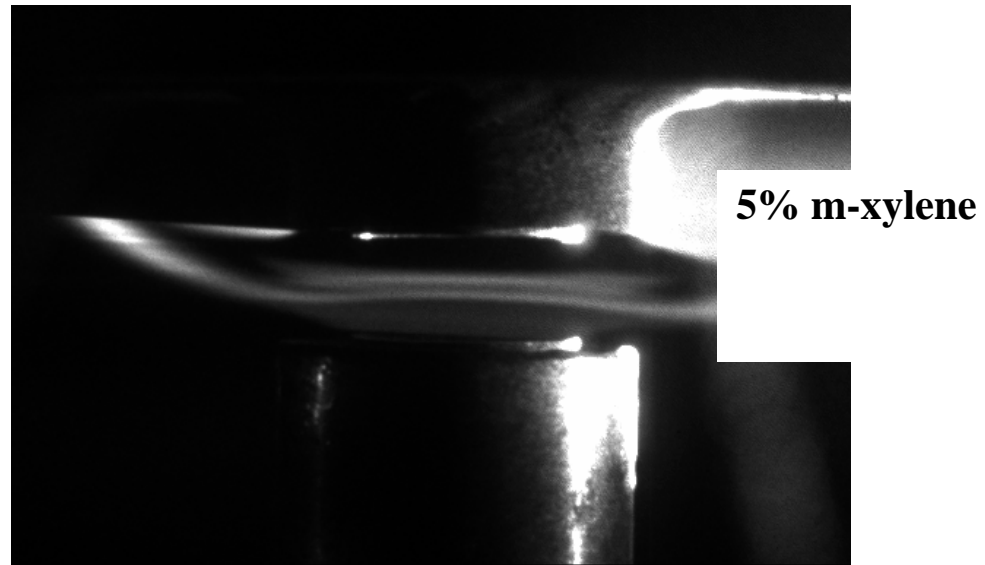


Figure 5.138 Images of planar laser induced fluorescence/light scattering for ethylene/air flames with 5% and 15% m-xylene added to the fuel gas.

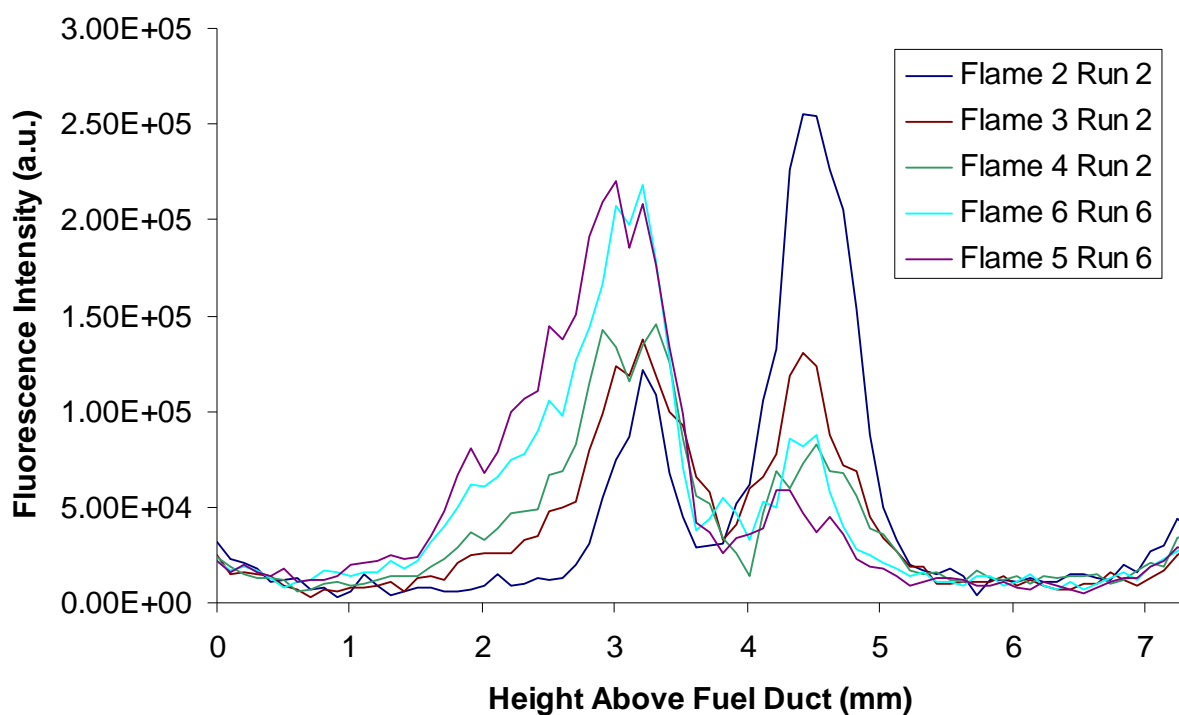


Figure 5.139 A series of pixel values from images of planar laser induced fluorescence/light scattering (measured through the burner centerline, 100 image average) for ethylene/air opposed jet flames to which m-xylene has been added to the fuel side. Flame 2: 0% m-xylene; Flame 3: 5% m-xylene; Flame 4: 10% m-xylene; Flame 5: 15% m-xylene; Flame 6: 20% m-xylene; by volume, keeping total fuel gas carbon constant.

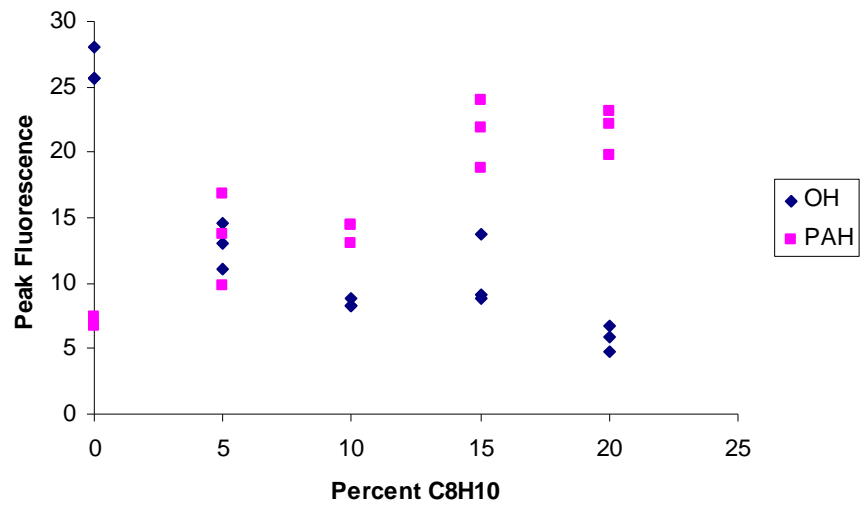


Figure 5.140 Peak values of fluorescence/light scattering versus fraction of m-xylene in fuel gas based on several series of measurements in the opposed jet burner.

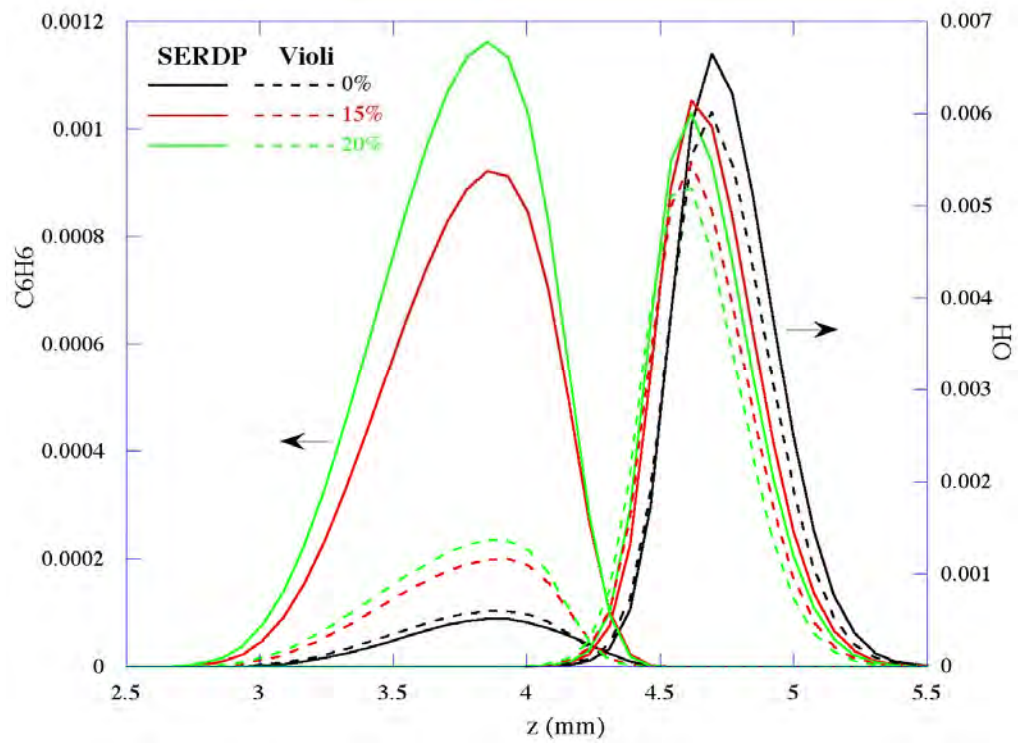


Figure 5.141 Prediction of OH and soot for addition of m-xylene to the fuel side of ethylene/air opposed jet flames, modeled using UNICORN.



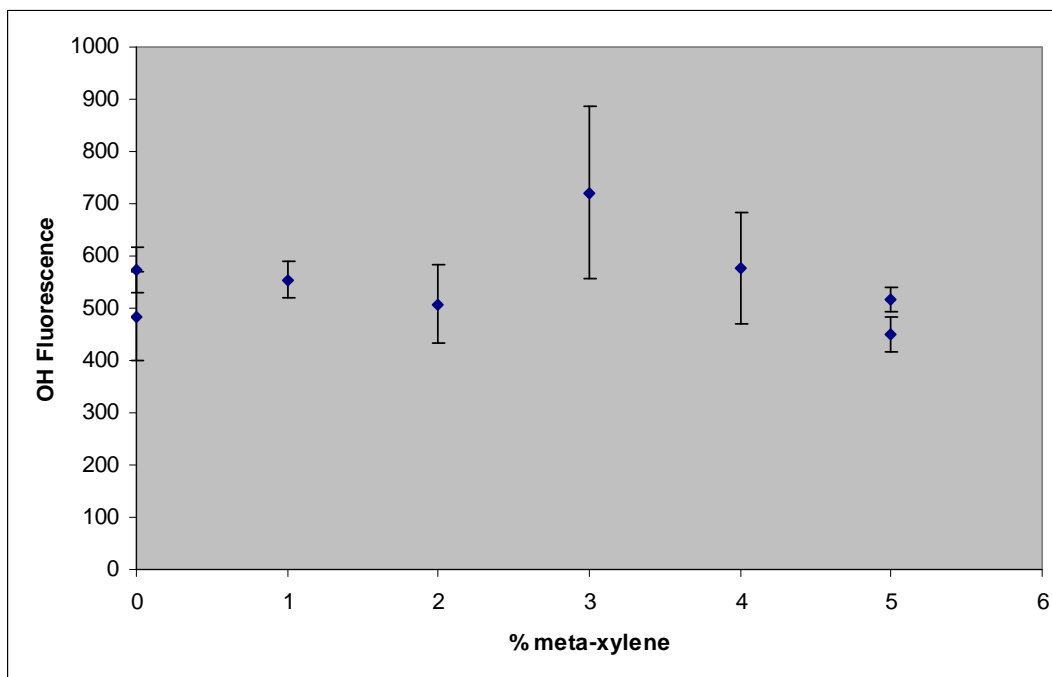


Figure 5.142 Change in OH fluorescence along the centerline of the burner, for ethylene/air opposed flow flames, with metaxylene added to the fuel side. After atomizer rebuild.

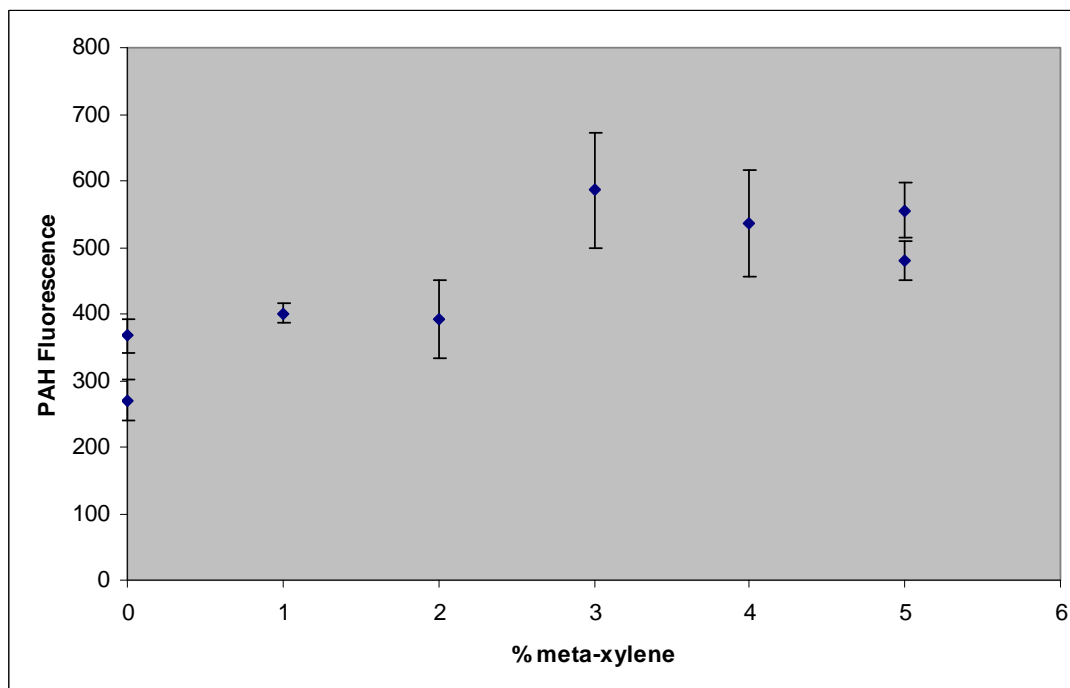


Figure 5.143 Change in PAH fluorescence along the centerline of the burner, for ethylene/air opposed flow flames, with metaxylene added to the fuel side. After atomizer rebuild.

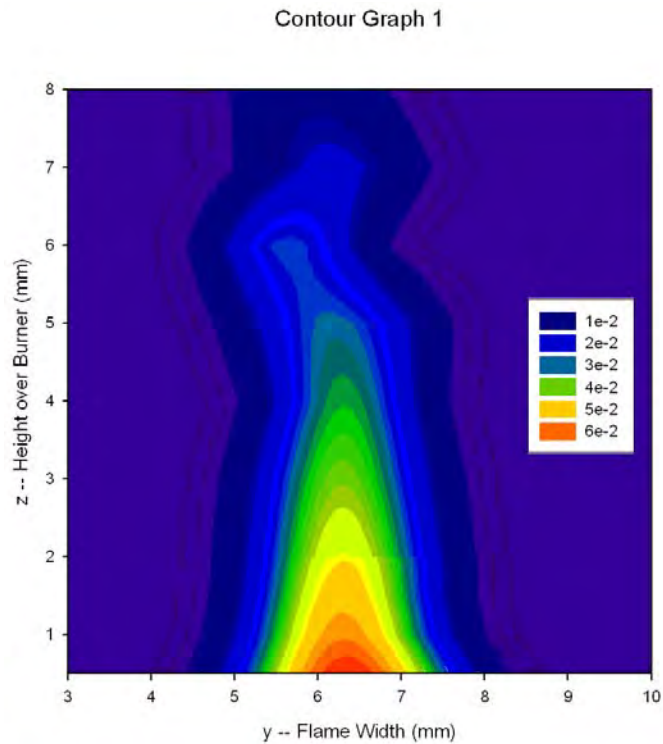


Figure 5.144 A reconstruction of the acetylene concentration (not temperature corrected) measured in absorption in an acetylene-air flame supported by a glass blowers torch. Concentration values are in arbitrary units.

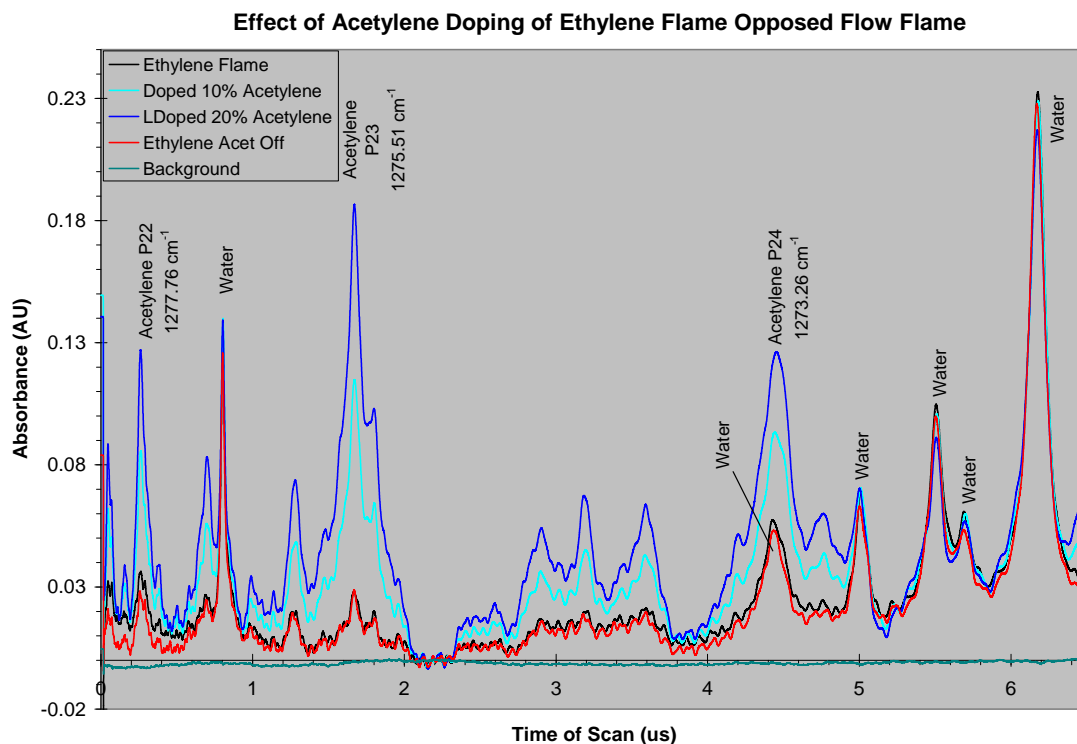
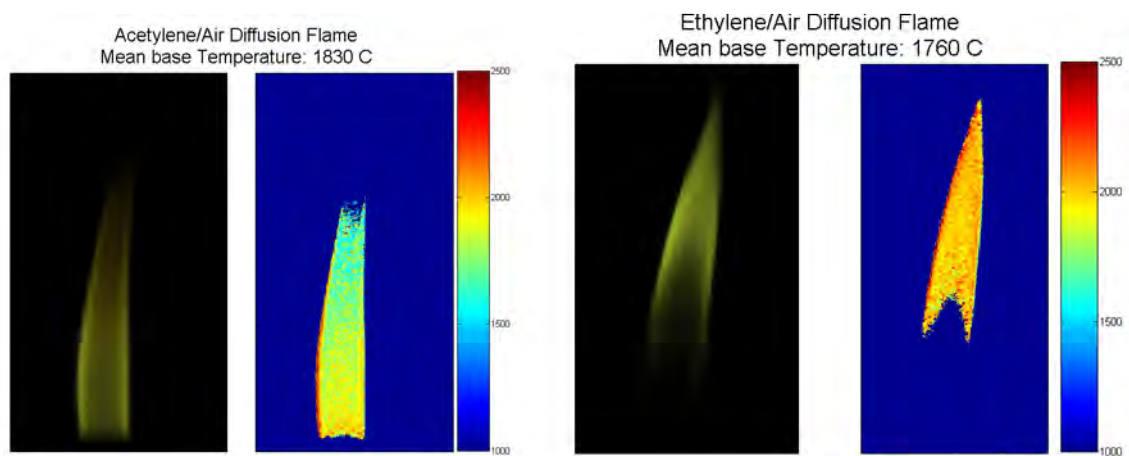


Figure 5.145 Measured acetylene absorption through the flame region, by the method described in Section 4.4, of an ethylene/air opposed flow flame to which acetylene is added on the fuel side. The feature labeled as the P23 line of acetylene demonstrates the capability of the technique to measure acetylene produced in the neat ethylene/air opposed jet flame.



Figure 5.146 A photograph of the ethylene-air candle-like diffusion flame, supported on a glass blowers torch.



- Flame Temperature of Acetylene diffusion flame ~1830 °C
- Flame Temperature of Ethylene diffusion flame ~1760 °C

Figure 5.147 Temperature maps using the imaging pyrometer technique for acetylene-air and ethylene-air diffusion flames.

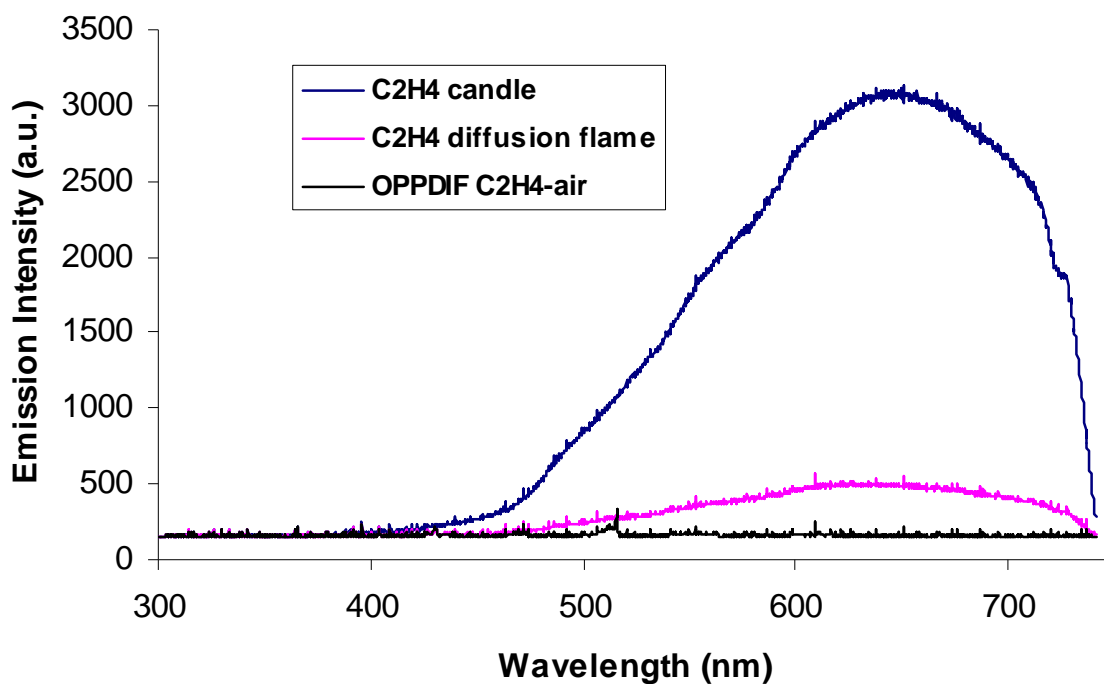


Figure 5.148 The wavelength resolved emission from three ethylene air flames, ranging from a candle-like diffusion flame, to a coflowing diffusion flame, to an opposed jet flame. Note the CH and C<sub>2</sub> emission in the opposed jet (OPPDIF C<sub>2</sub>H<sub>4</sub>-air) flame.

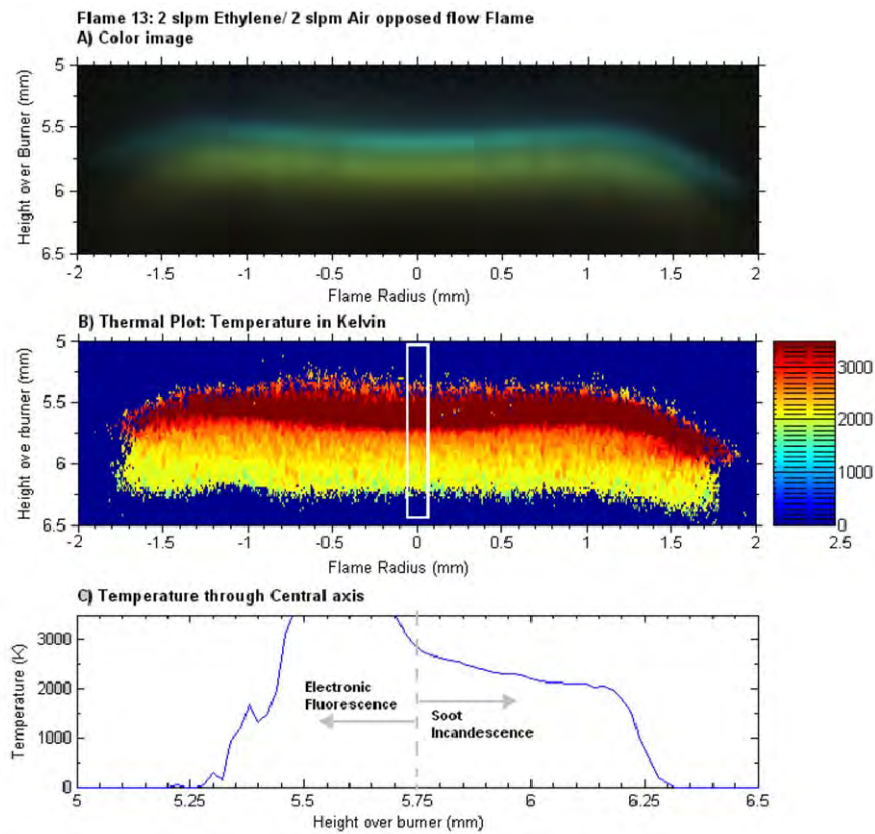


Figure 5.149 The imaging pyrometer technique applied to an opposed jet ethylene/air flame. The pyrometer yields reasonable temperatures in the sooting region of the flame but the blue-green emission from CH and C<sub>2</sub> causes the pyrometer to report inaccurate temperatures in the combustion region of the flame.

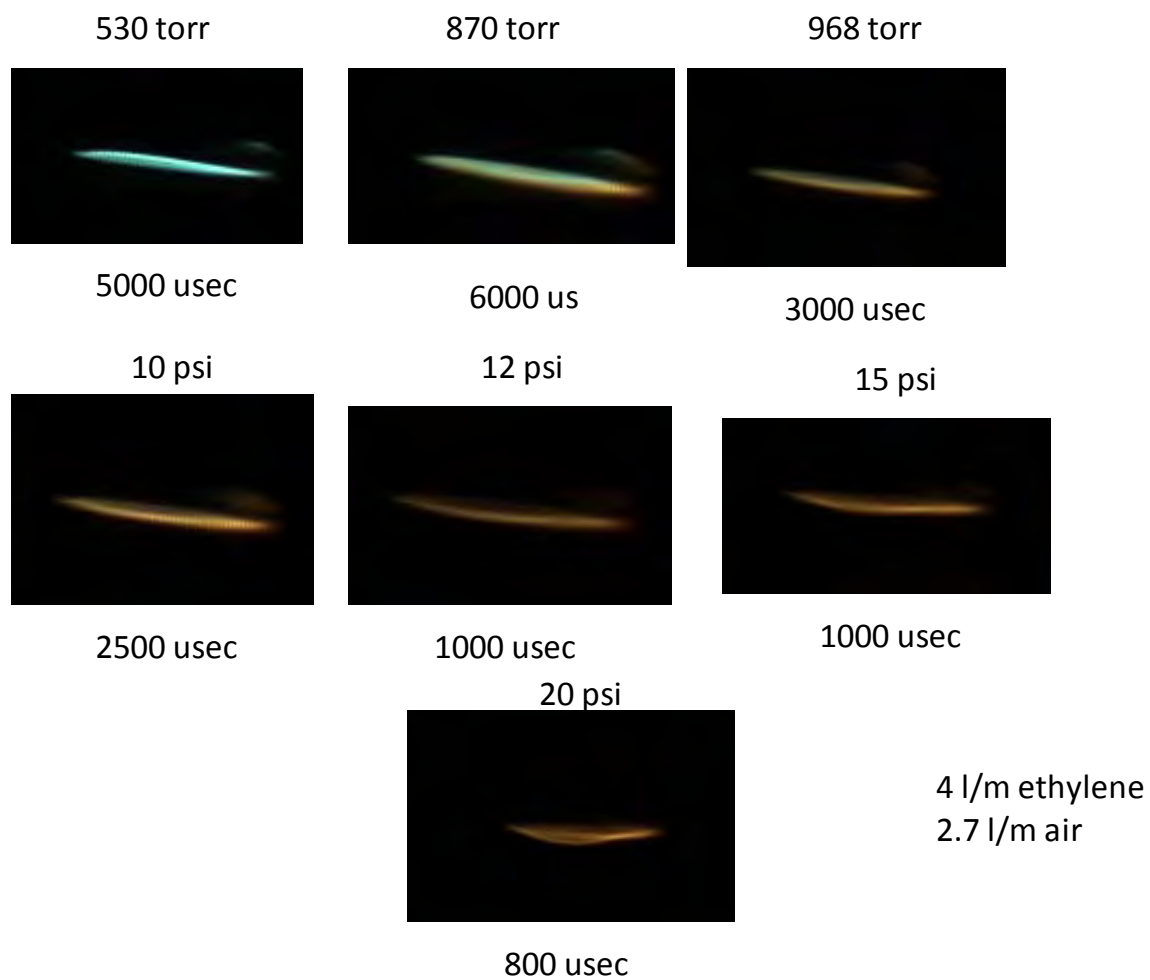


Figure 5.150 Raw images of elevated pressure opposed flow flames at constant molar flow rate taken using the high speed camera. It was necessary to adjust the camera exposure for each run to avoid saturating the camera chip. The change in flame color from blue to orange as pressure is increased is evident.

Ethylene/air opposed flow flame – constant strain - Raw

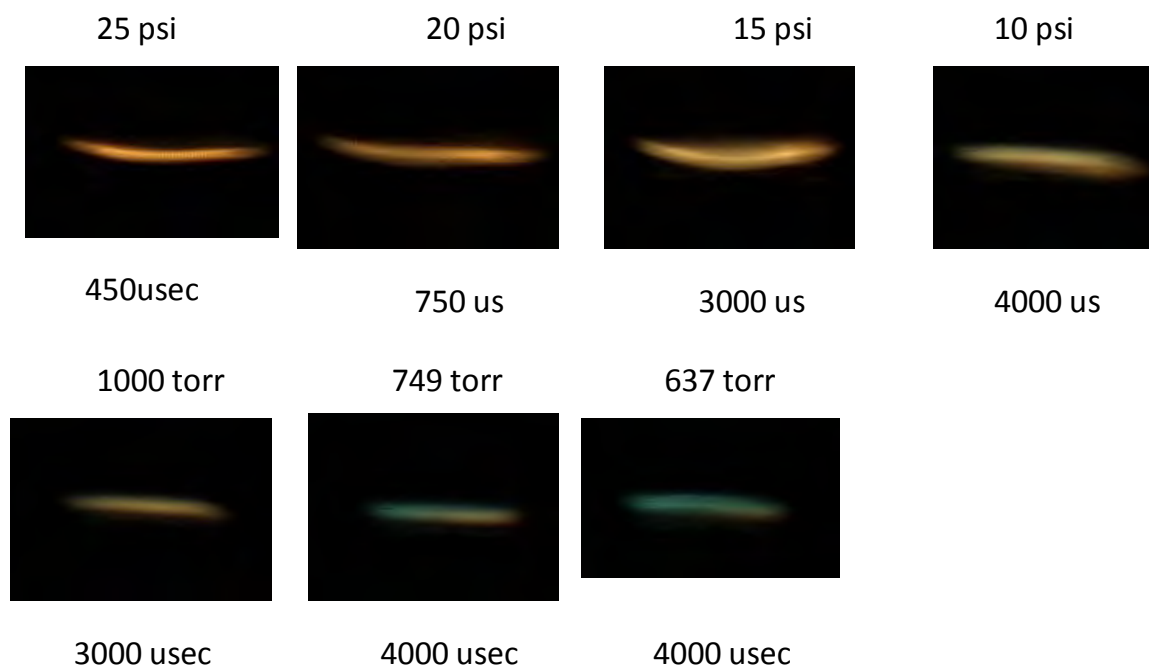


Figure 5.151 Raw images of elevated pressure opposed flow flames at constant strain rate taken using the high speed camera. It was necessary to adjust the camera exposure for each run to avoid saturating the camera chip. The change in flame color from blue to orange as pressure is increased is evident.

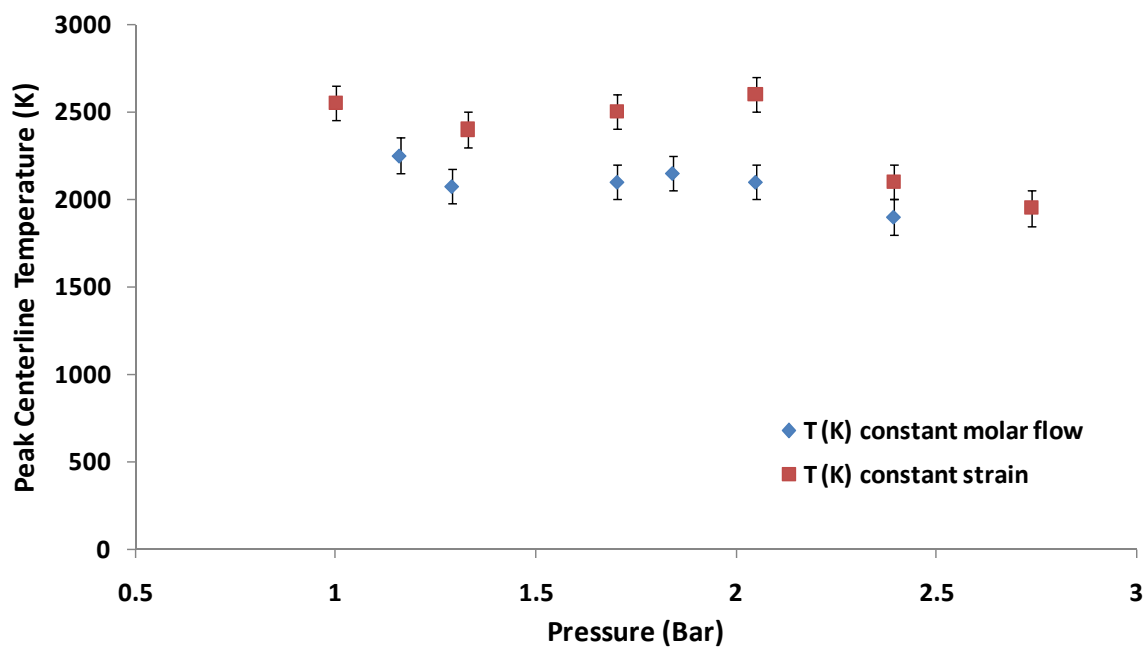


Figure 5.152 Peak centerline temperatures (K) for elevated pressure ethylene / air flames at constant molar flow and at constant strain. Elevated pressure opposed flow burner, ethylene / air flame. Temperatures are calculated using images in Figures 5.150 and 5.151.



## 5.4 Centerbody Flame

A centerbody burner (CBB), also referred to in the literature as a bluff-body burner or coannular jets with a large separation, was selected to experimentally and computationally investigate the impact of laminar recirculation zones on soot processes. CBBs have been used extensively to evaluate and develop combustion models as illustrated in the following papers (Roquemore, 1983), (Sturgess 1984), (Correa, 1992), (Fallot, 1997), (Liu, 2005), (Kempf, 2006), and (Merci, 2006). Indeed, they are well suited for model development because they have a simple geometry with clean inlet conditions for making model calculations and clear optical access for using laser diagnostics to collect data for model validation. Another important feature was that they can be operated at conditions that give radically different flow fields and flame structures as noted by (Yule 1980) for non-reacting flows and by others in reacting flows (Roquemore 1980), (Masri 1984), (Dally 1998), (Namazian 1989), (Esquiva-Dano 2001). The ability of obtaining very different flame structures was very important because it allowed a rapid, first order evaluation of models. In all of these referenced studies the CBB was operated at turbulent conditions and focused on the fluid mechanics that resulted in the different flame structures. For the SERDP soot science project, we wanted to focus on the soot processes without the complications resulting from turbulence. Since no one, to our knowledge, had investigated laminar flames established with a CBB, there was a big question about whether such flames would be suitable for soot model development studies. It turned out that a CBB was a very fortuitous choice.

The CBB has proven to be an excellent burner for investigating soot processes in laminar recirculation zones and for developing and evaluating soot models. It was found that very different sooting flame structures could be obtained by changing the CBB operating conditions. These unusual sooting flame structures could be used for first order evaluation of soot models. Also, new, interesting soot related effects have also been discovered. This was ideal for model development and evaluation because they identified new physics that needed to be integrated into the soot models in order to explain the new effects.

This section has eight subsections, each describing experiments and model prediction and evaluation results for unusual sooting flames formed with the CBB. In Section 5.4.1, the UNICORN code is used to predict the sooting behavior of CBB flames and Section 5.4.2 describes the experiments and modeling results that demonstrate the unusual sooting characteristics of three laminar CCB flames, all of which had about the same flow field. In Section 5.4.3, the stability of the very unusual lifted sooting flame is described. Section 5.4.4 describes the dynamics of a transitional sooting flame, and Section 5.4.5 describes the counter intuitive results obtained with particle premixed CBB flames that showed soot actually increased with premixing. A general description of the UNICORN model used in these studies is given in Section 4.2. Model characteristics that are specific for each of the four studies are given in the appropriate sections along with the test conditions. Each of the four studies is described in published papers that are referenced in each section.

#### 5.4.1 Predictions on Sooting Behavior of Recirculation-Zone-Supported Flames

This section presents predictions of the flow field and sooting flame shape for different air and ethylene fuel flow rates in a centerbody burner. The impact of diluting the fuel and air with nitrogen were also investigated. Effects of soot radiation on flame and soot structures are also presented. Calculations are performed using two detailed chemical-kinetics models for assessing the predictive capabilities of the state-of-the-art mechanisms for ethylene combustion. Calculations and the comparisons made with the experimental flames are presented in Section 5.4.2. A description of UNICORN is given in Katta and Roquemore (2007) and (2008).

The UNICORN code described in Section 5.4.2 is used to gain an understanding of the flame structures associated with the centerbody burner. Calculations are made for two fuel-flow cases. Pure ethylene is used as fuel for the first case and a 44-percent-diluted ethylene-nitrogen mixture is used for the second case. For both cases less sooty flames are obtained by reducing the oxygen concentration in the annular flow. The oxygen-to nitrogen ratio used in the annular flow is 0.20 (which is achieved by adding 25% nitrogen to air). The average fuel and oxidizer jet velocities are held constant at 1.25 m/s for both cases.

Results obtained for pure-fuel case are shown in Figure 5.153. Axisymmetric representation of the flame is used while displaying the data. Centerbody with fuel- and oxidizer-jet openings is displayed at the bottom of each of the figures 5.153(a) and 1(b). While velocity vectors are superimposed on the temperature field on the left half of 1(a), streamlines are superimposed on soot-volume-fraction distribution on the right half. Similarly, iso-concentration contours of ethylene (black lines) and OH (red lines) are superimposed on oxygen concentration field on the left half of 1(b) and those of benzene are superimposed on acetylene concentration field on the right half. Streamlines and velocity vectors show the two recirculation zones associated with the centerbody flames. These recirculation zones are formed due to the separation between the fuel and oxidizer jets. However, due to the differences in the momentum, the recirculation zone closer to the oxidizer jet (primary recirculation zone, PRZ) is much larger than the one closer to the fuel jet (secondary recirculation zone, SRZ). These recirculation zones play a vital role in transporting fuel toward oxidizer and in establishing a flame along the outer edge of the centerbody. The leading portion of the flame curves along the outer edge of the PRZ and then transitions into the trailing nonpremixed jet flame when PRZ is terminated at  $z \sim 30$  mm. Even though it is not that obvious, the SRZ and the PRZ terminate at the same height. Both temperature and OH profiles suggest that flame is becoming weak in this transition region.

As seen in 5.153(a), most of the soot is located within the PRZ and is not symmetrically distributed within the recirculation zone. This suggests that soot is formed in PRZ rather than formed somewhere else and transported into the recirculation zone. In fact, a significant portion of the fuel-side flame zone is within PRZ and all most all of the acetylene is produced along the outer edge of the PRZ, which is then transported toward its center. As the soot model used in the current simulations is based on acetylene, soot in Figure 5.153(a) is also being generated and grown within the PRZ. Interestingly, soot doesn't seem to accumulate in the SRZ. Velocity vectors and streamlines in Figure 5.153(a) suggest that the flow is nearly parallel to the flame surface and turns inward as it approaches the end of the recirculation zone. The flow pattern and

residence times need to be analyzed to better understand the sooting behavior of the centerbody flames.

Results obtained for the diluted-fuel case are shown in Figure 5.154. The shown variables and the display schemes used are identical to those used in Figure 5.153. As expected, the addition of nitrogen in the fuel decreases the flame temperature. Interestingly, the decrease in soot volume is more dramatic than what one would expect based on changes in temperature. A quick look at the velocity and temperature fields suggest that the flame surface has moved into the core of the vortex, especially the section where it transitioned from recirculation-supported leading flame to normal nonpremixed trailing flame. Such flame movement can be expected as the stoichiometric surface shifts closer to the fuel jet with fuel dilution. On the other hand, the sizes of the PRZ and SRZ in the diluted-fuel case are nearly the same as those in the pure-fuel case with the heights being  $\sim 30$  mm. Since the recirculation zones behind the centerbody are established due to the fuel and oxidizer jets, they are not affected by the fuel dilution (molecular weights of nitrogen and ethylene being the same). However, as the viscosity of the fluid in the upper portion of the recirculation zones decreased due to lower flame temperature, the centers of the recirculation zones moved downstream in the diluted-fuel case. Consequently, with fuel dilution, flame surface shifts toward the center of the PRZ; while, the latter moves downstream (closer to the flame surface). The changes in flame-recirculation-zone interaction Roquemore et al. (2007) led to a dramatic decrease in soot formation in diluted-fuel case.

Radial distributions of temperature and axial velocity along the centers of the PRZs for pure-fuel and diluted-fuel cases (heights of 9 and 11 mm, respectively) are shown in Figure 5.149(a). The distributions of soot volume fraction and number density are shown in Figure 5.149(b). The radial locations of the centers of the PRZs are marked on the velocity profiles with solid circles. As noted earlier, the structure of the recirculation zone did not change much with fuel dilution. The flame temperature decreased by  $\sim 120$  K and the gas temperature, at the PRZ center, increased over 200 K. A three-fold decrease in soot volume fraction due to nitrogen addition to fuel is noted in Figure 5.149(b). Soot number density, which peaks on the fuel side of the peak-temperature location, decreased by 50%. Even though the soot number density increased in the core region of PRZ with fuel dilution, the soot volume decreased dramatically.

The centerbody flames seem to produce a significant amount of soot in the leading portion of the flame and within the recirculation zones. Computations for these flames were performed assuming that radiative heat loss from soot follows that of a blackbody. Such an assumption is known to over-estimate the actual losses. To determine the effect of soot radiation on the flames shown in Figures. 5.153 and 5.154 calculations are repeated by turning it off. Flame and soot structures obtained without soot radiation are shown in Figures 5.156(a) and 5.156(b) for the pure- and diluted-fuel cases, respectively. Note the changes in the scales used for the color maps for these figures compared to those used in 5.153 and 5.154.

As expected, the flame temperature decreased by as much as 100 K when the soot radiation was considered in the model. The decrease was more in the sooty pure-fuel flame. This drop in flame temperature could be responsible for the significant decrease in soot concentration predicted with soot radiation turned on. Even though the flame structures were significantly changed due to soot radiation, the recirculation zones (PRZ and SRZ) were not significantly affected. Interestingly,

the flame weakening, in the leading-flame-to-trailing-flame transition region observed in Figures 5.153 and 5.154, disappeared when soot radiation was ignored. The soot volume distributions in Figures 5.156(a) and 5.156(b) do not indicate any increase in soot in this region. It is not clear why temperature in this transition region was more affected by soot radiation than in the leading-flame or trailing-flame regions. Moreover, even though the soot levels in diluted-fuel case are one-third of those in pure-fuel case, the flame-weakening behavior is similar in both the flames—suggesting that soot radiation itself is not responsible for such behavior.

Calculations for the pure-fuel and diluted-fuel cases are also performed using a more comprehensive chemical-kinetics model developed by NIST for ethylene fuel. Temperature, soot and species structures obtained for pure-fuel case are shown in Figure 5.157 and those for the diluted fuel case are shown in Figure 5.158. Variables shown and the display schemes used for these figures are identical to those used in Figure 5.153. Amazingly identical flame structures are obtained with Wang-Frenklach and NIST mechanisms for both the flame cases. The soot structures are also very similar. However, acetylene and benzene concentrations predicted by NIST mechanism are notable lower than those predicted by Wang-Frenklach mechanism. Such a discrepancy in the predictions of these two mechanisms was previously noted in heptane opposing-jet flame studies Katta and Roquemore (2005). Detailed measurements are required for sorting out the differences in these predictions, which will be the focus of our future work.

In summary, a time-dependent, axisymmetric, detailed-chemistry CFD model is used to simulate the ethylene air combustion in a 5.6-mm-diameter centerbody burner. Calculations show that the primary and secondary recirculation zones are not greatly affected by dilution of the fuel and air with nitrogen. However, as the fuel dilution increased, the flame formed outside the PRZ moved into the recirculation zone and altered the sooting characteristics. The flame weakening in the transition region of the leading and trailing flame sections is found to result from soot radiation. Amazingly similar flame and soot structures were obtained with the two chemical-kinetics mechanisms used in this study. The next section describes the result of an experimental investigation of soot formed in recirculation zones and an evaluation of the soot model used in UNICORN. These experiments confirm the predicted change in flame location as the fuel is diluted with nitrogen. This phenomenon will be shown to have a great impact on the unusual sooting flame shapes of the centerbody burner.

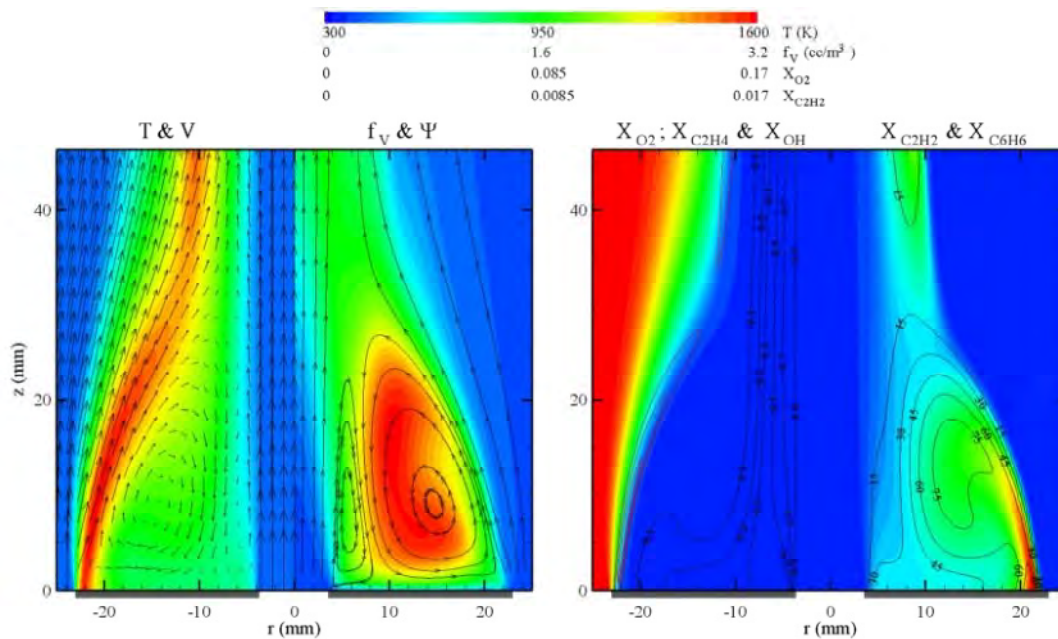


Figure 5.153 Centerbody flame with pure fuel calculated using detailed chemical kinetics. (a) Velocity vectors and streamlines are superimposed on temperature (left half) and soot-volume-fraction (right half) fields, respectively. (b) Iso contours of ethylene and benzene are superimposed on oxygen (left) and acetylene (right) fields, respectively. Red contours represent OH.

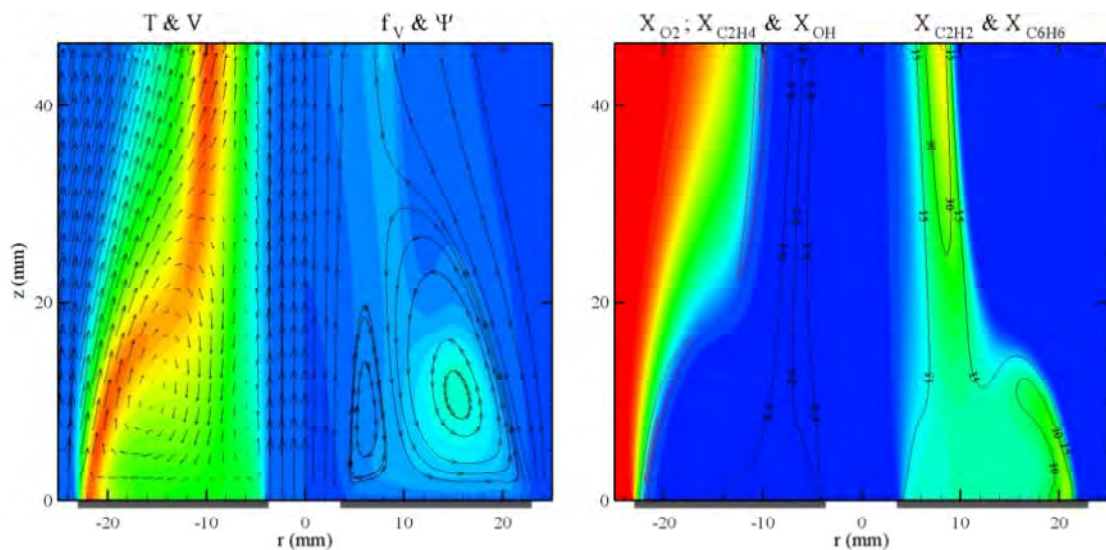


Figure 5.154 Centerbody flame with diluted fuel. Velocity, temperature, streamlines and soot volume fraction are shown in (a) and ethylene, oxygen, OH, acetylene and benzene are shown in (b). Color scales are same as the ones used in Figure 5.153.

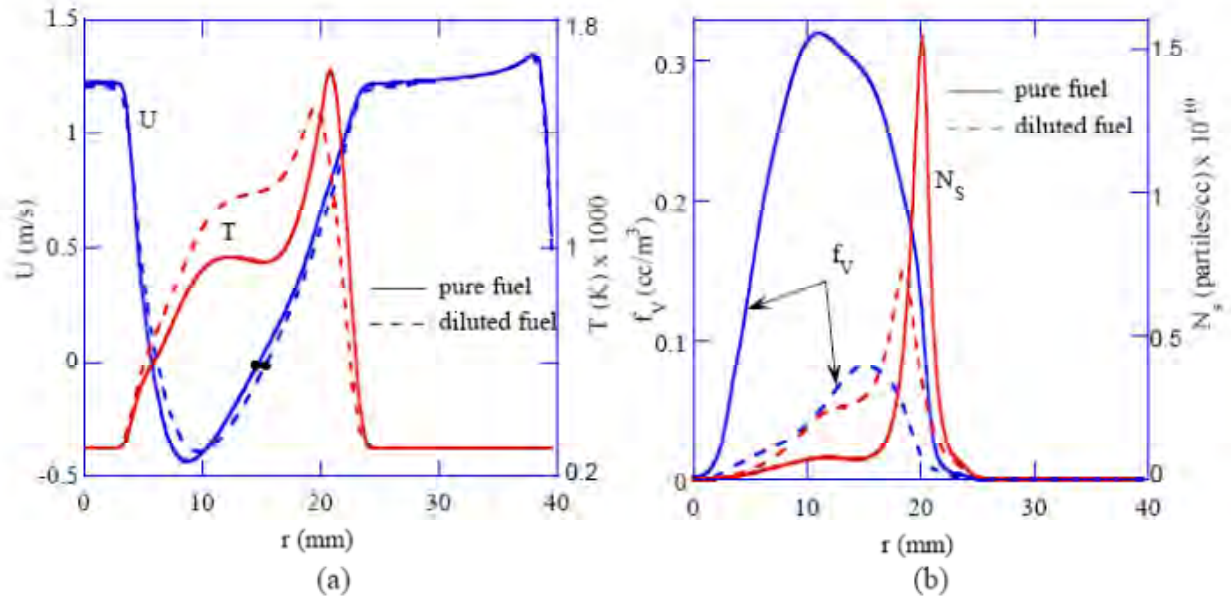


Figure 5.155 Effect of fuel dilution on (a) flame and vortex structure and (b) soot and particle distributions. Vortex centers are shown in (a) with filled circles.

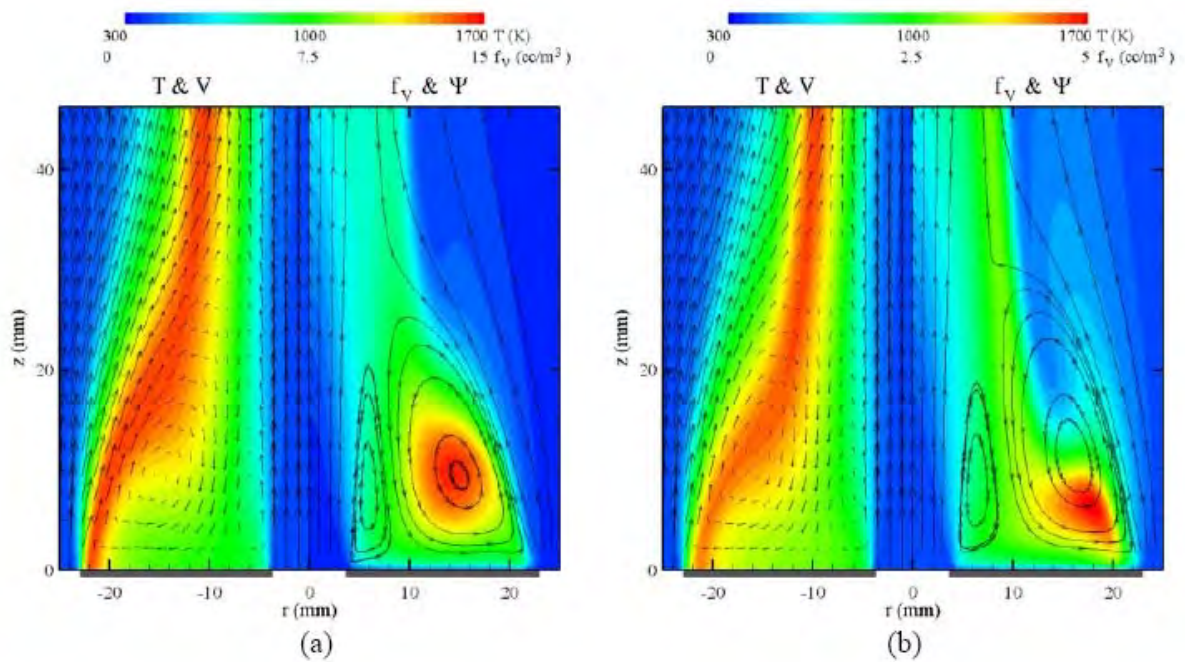


Figure 5.156 The effects of radiation on flame structure and soot formation in pure-fuel (a) and diluted fuel (b) cases. Velocity and streamlines are superimposed on temperature (left half) and soot volume-fraction (right half) fields, respectively. Note the changes in the ranges used for the variables.



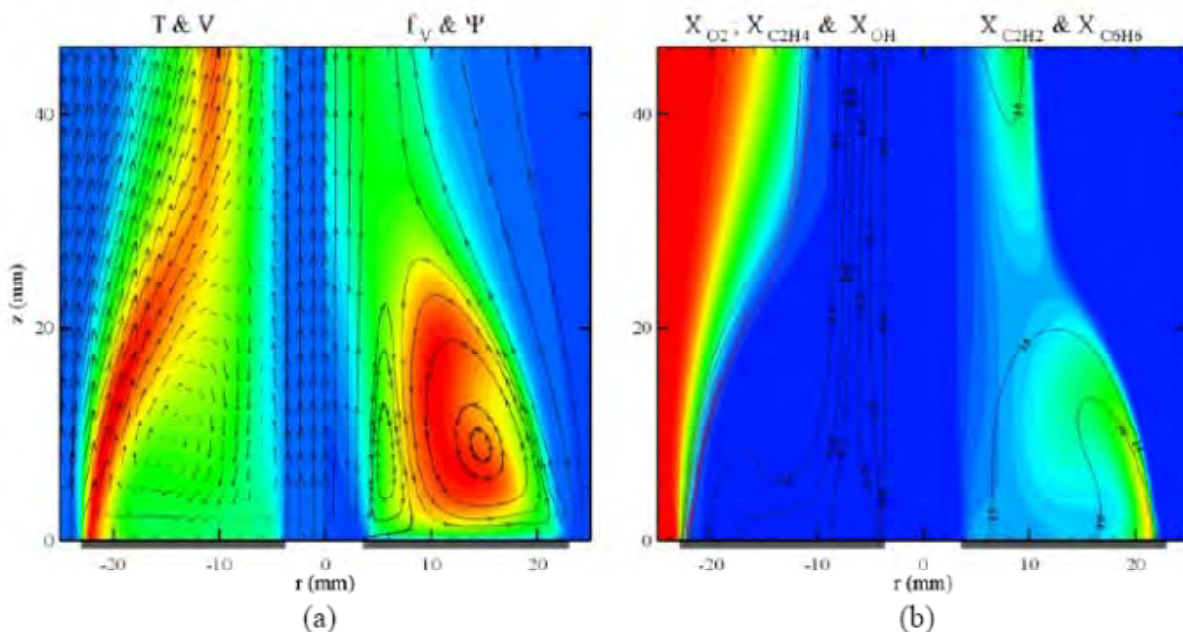


Figure 5.157 Centerbody flame with pure fuel calculated using NIST chemical-kinetics mechanism. Velocity and temperature are shown on the left side and streamlines and soot volume fraction are shown on the right side of (a). Ethylene (contours), oxygen (rainbow color), and OH (red contours) shown on the left side and acetylene (rainbow color) and benzene (contours) are shown on the right side of (b). Color scales are same as the ones used in Figure 5.153.

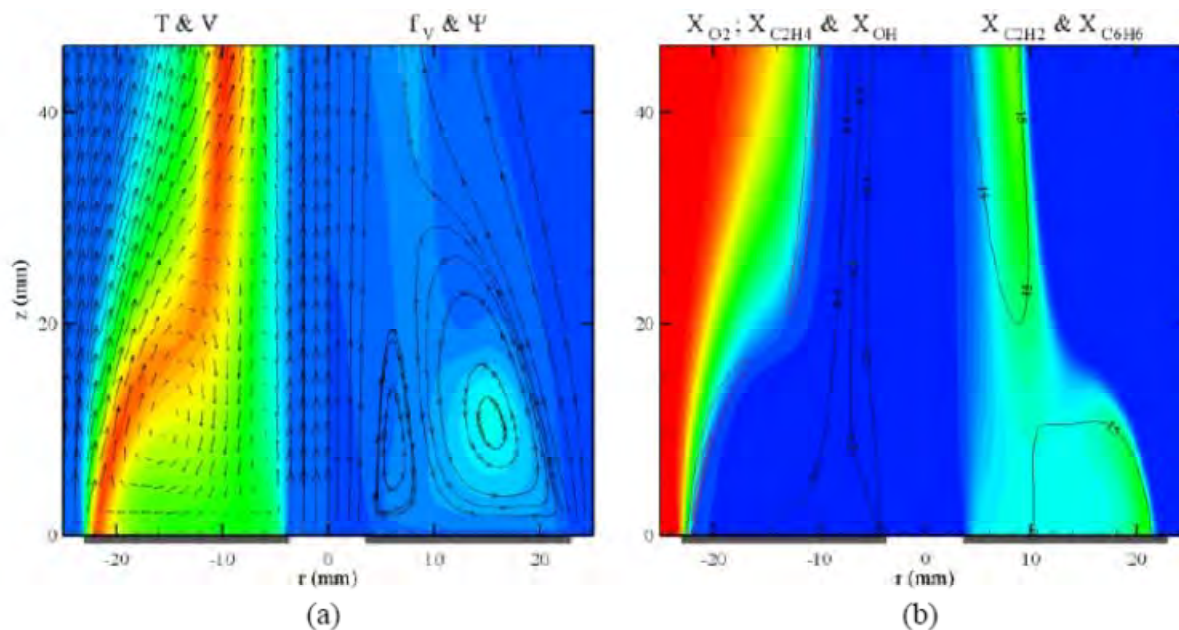


Figure 5.158 Centerbody flame with diluted fuel calculated using NIST chemical-kinetics mechanism. Velocity, temperature, streamlines and soot volume fraction are shown in (a) and ethylene, oxygen, OH, acetylene and benzene are shown in (b). Color scales are same as in Figure 5.153.

#### 5.4.2 Soot Studies of Laminar Diffusion Flames with Recirculation Zones

The purpose of the study presented in this section is to determine if a centerbody burner is suitable for long-term soot studies and evaluating soot models. In the past, we have extensively used visualization techniques to study flames and evaluate models such as UNICORN (Roquemore and Katta 2000). Simple flames were selected that had distinguishing features that could be easily visualized. A model that could not capture the distinguishing features obviously needed additional work. Although this approach is not sufficient for evaluating models, it does demonstrate a necessary requirement that the models correctly predict unusual flame features. This strategy of studying simple flames with distinguishing characteristics is adopted for this preliminary evaluation of UNICORN and a simple soot model. The predictions presented in Section 5.4.1 indicate that this may be a valid approach. Descriptions of the experimental and computational techniques are given in Sections 3.4 and 4.2, respectively. The results are presented in Roquemore et al. (2009).

Three sooting flames with very different and unusual sooting structures are selected for study. The flames are identified as: the fully sooting, donut-shaped, and ring-shaped flame. The different sooting structures are achieved by diluting the air and ethylene fuel with nitrogen ( $N_2$ ) while maintaining the air/ $N_2$  and fuel/ $N_2$  flow rates constant, which mean that the average velocities at the exit of the annular air and central fuel jets (the inlet to the burner) are also constant. The impact of this is that the flow fields of the three flames are nearly the same Roquemore et al. (1986). That is, the size, shape, velocity, and other flow characteristics of the recirculation zones established by the centerbody are nearly the same for three flames. This is confirmed by the presented flow field calculations. Maintaining constant fuel and air flow rates greatly simplifies the experiments because it removes the flow field as a variable when trying to account for the different shaped sooting structures and the unusual spiral vortices. The volumetric flow rates for the air and fuel jets are given in Table 5.7 The average inlet velocity of the air and fuel was 1.2 m/s, which corresponds to a fuel jet that just penetrates the recirculation zone Roquemore et al. (1986).

The unusual sooting structures for the fully sooting, donut-shaped, and the ring-shaped flames are shown by the color flame photographs in Figures 5.159a, 5.160.a, and 5.161a, respectively. The yellow part of the flame represents what we call the sooting structure. Although it is hard to see in the photographs, a thin blue flame, adjacent to the outer surface of the sooting flame, is “nearly attached” at the outer rim of the centerbody. The blue flame results from chemiluminescence of species such as CH and  $C_2$  and is a reasonable marker for the stoichiometric flame surface. In all three flames, soot forms on the fuel-rich side of the stoichiometric surface just as one would expect for diffusion flames.

UNICORN, with a simple soot model, has been used to calculate the characteristics of the fully sooting, donut-, and ring-shaped flames. These results are shown in (b) and (c) of Figures 5.159, 5.160, and 5.161. Caution must be used in comparing photographed and computed flames. The flame photographs are 2D images of 3D surfaces. The computed flames are 2D cross sections through the centerline of the centerbody. Only the outer edges of the observed and computed flame surfaces should be compared because this is the only location where the images overlap.



UNICORN calculations in (b) and (c) of Figures 5.159, 5.160 and 5.161 seem to capture the global features of the flames and their unusual shapes. Using enlarged transparent overlays of scaled photographs will show that the blue flames in Figures 5.159a, 5.160a, and 5.161a overlay almost perfectly with the stoichiometric surface, shown in white, and the computed high temperature colored contour images in the (b) figures. Very good agreement is obtained when the observed yellow sooting flame surface in Figure 5.159a is compared with the computed radiation-intensity surface in Figure 5.159c. When similar comparisons are made for the donut- and ring-shaped flames in Figures 5.160 and 5.161, agreement is reasonably good but there are some noticeable differences. The experimentally observed donut-shaped and especially the ring-shaped sooting surfaces are thinner and located upstream of those calculated using the soot radiation intensity. Even with these differences, UNICORN does a reasonable job capturing the global sooting flame shapes.

It is encouraging that UNICORN, with a simple soot model, does reasonably well in capturing the unusual shapes of the sooting flames. However, comparing the observed and computed sooting flame surfaces is not adequate to evaluate a soot model and can even be misleading because the radiation intensity depends exponentially on temperature. Comparing sooting flame surfaces can have more to do with a models' ability to predict temperature fields than soot fields. However, Mie scattering is a good way of evaluating soot models because it gives a direct way of visualizing the location of the soot particles. Also, the Mie scattering images provide new insights into the unusual sooting structures. These points are discussed in the next section.

Laser sheet-lit images in Figures 5.162a and 5.163a show the fully sooting and donut-shaped flames, respectively, and the soot path lines that result for the Mie scattering from the soot particles. The soot appears to form in the outer shear layer just above the edge of the centerbody face in Figure 5.162a. Some of the soot particles are entrained into the recirculation zone and follow spiral paths towards the center of the outer vortex. The soot particles tend to accumulate at the vortex center, where visual observations indicate they either oxidize or grow sufficiently large so they fall to the centerbody face. Also, the soot formed in the shear layer appears, to the eye, to be much larger than the submicron size particles one might expect. This is probably due to an enhanced soot growth process resulting from the long residence times in the recirculation zone.

The donut-shaped flame in Figure 5.163a also shows that the entrained soot particles follow path lines that spiral towards the vortex center; however, the path lines have a tighter spiral shape than that in Figure 5.162a. This is also evident when visually observing the ring-shaped flame in Figure 5.161a. The thin sooting ring is actually composed of soot particles with very tight spiral path lines swirling about the center of the vortex. Indeed, laser sheet lit images of the ring-shaped flame (not shown) and visual observations of the Mie scattered laser light show that there are very few soot particles between the centerbody face and soot ring. As will be discussed, considerable insight can be gained from this observation. Before pursuing this, it is advantageous to consider the results of UNICORN calculations.

Spiral vortices are often observed in spatial and time evolving flows such as a Kármán vortex street and Kelvin-Helmholtz vortices. However, we are only aware of one example where spiral

vortices have been observed for particles and that is for another centerbody flow Roquemore et al. (1986). As shown in the (b) Figures of 5.159, 5.160, and 5.161, the fluid follows closed path lines as expected for a stable, laminar recirculation zone. The spiral path lines represent a computational challenge and an intellectual stimulus to understand their origin.

The current version of UNICORN, with a simple soot model, does not simulate the spiral motion of the soot particles. This is evident from the soot-volume-fraction calculations shown in Figures 5.159c, 5.160c, 5.161c and results because the current model treats soot as a gas. However, UNICORN has a tracking program that can be used to follow the path of released particles with defined mass and size. It is a Lagrangian-based program with Newtonian particle dynamics that include drag, thermophoresis (Goldhirsch (1983)), gravitational forces, and flow-field characteristics calculated with UNICORN. This particle-tracking program is used to explore the path lines of particles released in the sooting zone of the flames.

Particle trajectories are obtained by tracking the particles as they are released in the shear layer at the soot-inception point near the edge of the centerbody face as noted in Figure 5.159c. Several different diameter particles were selected for UNICORN calculations with particle tracking. As will be illustrated later, the calculations show that the number of spirals is determined by the diameter of the particles. The larger particles have the fewer number of spirals. Figure 5.162b illustrates that 5- $\mu\text{m}$  diameter carbon particles are entrained into the recirculation zone and follow spiral path lines similar to those experimentally observed (Figure 5.162a). Note the size and shape of the observed and computed spiral path lines are almost identical. This suggests that the observed soot particles may have a diameter of about 5- $\mu\text{m}$ .

Figure 5.162c uses a solid-body rotation of the blackbody-radiation intensity and false coloring to illustrate how a 3D computed flame appears as a 2D image. The agreement with the flame photograph in Figure 5.162a is considered very good. Also, the observed (Figure 5.162a) and computed (Figure 5.162c) outer and inner recirculation zones are nearly the same. UNICORN, with particle-tracking calculations shown in Figure 5.163b, captures some but not all of the observed details. For example, UNICORN correctly predicts the location of the vortex center; but, the tightly spiraling path lines shown in Figure 5.163a are not predicted. That is, the computed particle path lines in Figure 5.163a have a larger diameter than those experimentally observed in Figure 5.163a. However, tight spiral path lines can be computed if additional physics is imposed on the calculation. As will be shown, this will have a significant impact on shape of the soot structures.

To gain an insight into the physics needed to compute and understand the observed tight spiral path lines, note that the donut- and ring-shaped flames result because  $\text{N}_2$  is added to the fuel and air jets (Table 1). The addition of  $\text{N}_2$  causes the stoichiometric flame surface to move towards the center of the vortex. This is evident by comparing the location of the blue flames and calculated stoichiometric surfaces (white lines) in Figures 5.159 and 5.160. Indeed, the stoichiometric blue ring flame is very near the vortex center in Figure 5.160a. This means that a considerable number of soot particles, with larger soot path line diameters, pass through the flame front. As the soot passes through the flame, oxidation takes place.

Soot oxidation is an important process missing in the soot-particle tracking model and, as we will illustrate, plays an important role in determining the shape of the sooting flame surface. A simple soot oxidation model, added to UNICORN's particle tracking program, removes all soot particles from the calculations that encounter temperatures larger than 1300K, Higgins et al., (2002). Thus, soot particles, following path lines that pass through the high-temperature flame zone, are completely oxidized. The only observable soot particles are the ones that follow path lines that do not pass through the flame zone. That is, the only soot particles that survive are the ones that follow path lines which pass between the vortex center and the temperature zone at which complete soot oxidation takes place. As N<sub>2</sub> dilution moves the flame location towards the vortex center, the surviving soot particles appear in tighter and tighter spirals around vortex center. To the eye, the soot surface appears as the donut- and ring-shaped flames in Figures 5.163a and 5.164a, respectively. UNICORN has captured this process in Figure 5.163c.

UNICORN/particle-tracking calculations show that spiral soot path lines depend on particle size. Figure 5.164a illustrates that massless particles do not spiral toward the vortex center but follow a large closed orbit similar to a streamline. Particle-tracking calculations with 1- and 5- $\mu$ m diameter carbon particles result in spiral path lines as noted in Figures 5.164b and 5.162b but the 1- $\mu$ m diameter soot particles only make 4 spirals before they are terminated at the vortex center; whereas, the 5- $\mu$ m diameter particles make more than 10 revolutions. Figure 5.164c shows that the 50- $\mu$ m diameter particles have sufficient momentum to carry them downstream without being entrained into the recirculation zone. A particle density of 1900 kg/m<sup>3</sup> is used in the calculation Lindstedt (1994).

The path line calculations in Figures 5.162b, 5.164a, and 5.164b indicate that the force, causing the spiral motion of the particles, depends on particle size and appears to have more impact on the smaller particles. The result is that they complete fewer revolutions. This suggests the thermophoretic force may be involved. When thermophoresis is removed from the 5- $\mu$ m particles calculation in Figure 5.4.2.4b, the calculation looks just like that for the massless particle in Figure 5.164a. Thus, thermophoresis is predicted to be the cause of the spiral transport of the soot particles.

In summary, the unusual sooting characteristics of three flames established by the laminar recirculation zones of a centerbody burner are investigated. The three ethylene fueled flames are identified as: fully sooting, donut-shape, and ring-shape flames. Different sooting structures are obtained by varying the N<sub>2</sub> dilution in the fuel and air jets while maintaining a constant air and fuel velocity of 1.2 m/s. All three flames have the unusual characteristic that the soot, entrained into the recirculation zone established by the bluff-body, follows path lines that spiral towards the vortex center. The questions are what cause: (1) the unusual sooting structures and (2) the spiral trajectories of the soot? Flame photographs, laser sheet visualizations, and calculations with a 2D CFD-based code (UNICORN) are used to answer these questions. Calculations indicate that the unusual shapes of the sooting flames result from: (1) the exponential dependence of the soot radiation that biases the radiation to the high-temperature surfaces, (2) changes in the location of the stoichiometric flame surface with respect to the vortex center established by the centerbody, and (3) complete oxidation of the soot following path lines that intersect the high temperature flame zone. The location of the stoichiometric flame surface moves radically towards the vortex center as N<sub>2</sub> is added to the fuel jet. The observed soot

particles are the ones that follow path lines between the flame and the vortex center. To the eye, the soot surface will appear as tighter and tighter spirals as  $N_2$  is added to the fuel, thus resulting in the donut- and ring-shaped flames. This accounts for the size variations of the spiral soot path lines in the flames with different  $N_2$  additions. The spiral soot path-lines depend on particle size with massless particles giving a closed streamline like trajectory and 50- $\mu m$  particles travel downstream without being entrained. The spiral path lines disappear when the thermophoretic force is removed from the calculation. Thus, it is predicted that the spiral soot path lines result from thermophoresis. It is concluded that the laminar centerbody burner is an excellent tool for studying fundamental soot processes and evaluating soot models.

Table 5.7  
Volumetric Flow Rates (Standard Liters/Minute, SLPM) of Studied Flames

		Fully Sooting	Donut-Shape	Ring-Shape
Annular	Air	250	200	200
Air Jet $N_2$	<u>0</u>	<u>50</u>	<u>50</u>	
<u>Annular Flow</u>	<u>Total</u>	<u>250</u>	<u>250</u>	<u>250</u>
Fuel Jet	$C_2H_4$	3.4	2.1	1.5
	$N_2$	<u>0</u>	<u>1.3</u>	<u>1.9</u>
<u>Fuel Flow</u>	<u>Total</u>	<u>3.4</u>	<u>3.4</u>	<u>3.4</u>

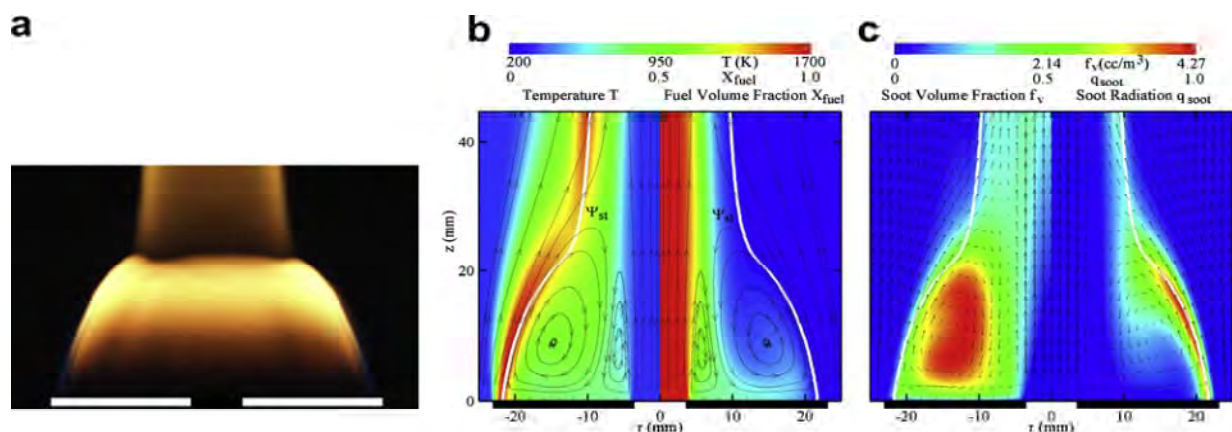


Figure 5.159 (a) Photograph of fully sooting flame, (b) computed temperature (left) and fuel volume fraction (right); and (c) relative soot volume (left) and normalized soot-radiation intensity (right). White line is calculated stoichiometric surface.

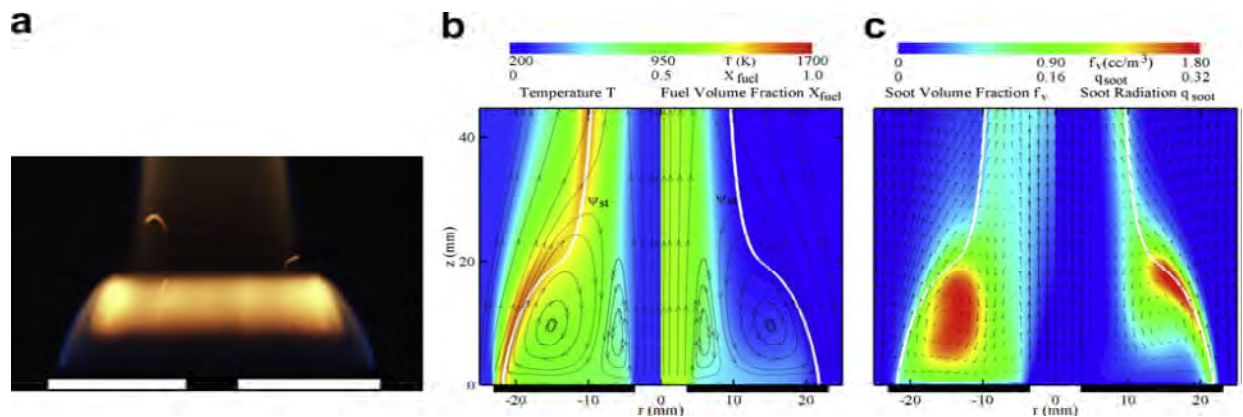


Figure 5.160 (a) Photograph of donut-shaped flame, (b) computed temperature (left) and fuel volume fraction (right), and (c) relative soot volume (left) and normalized soot-radiation intensity (right).

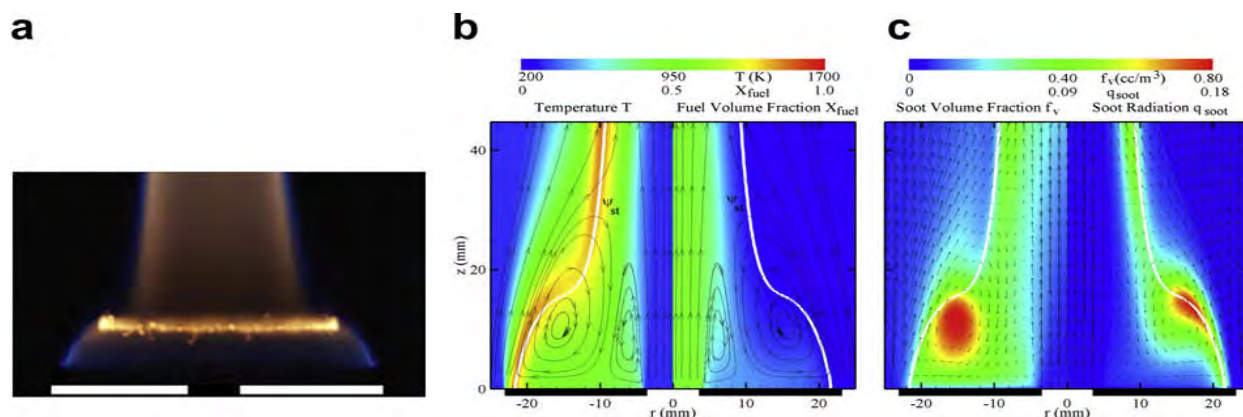


Figure 5.161 (a) Photograph of ring-shaped flame, (b) computed temperature (left) and fuel volume fraction (right), and (c) relative soot volume (left) and normalized soot-radiation intensity (right).

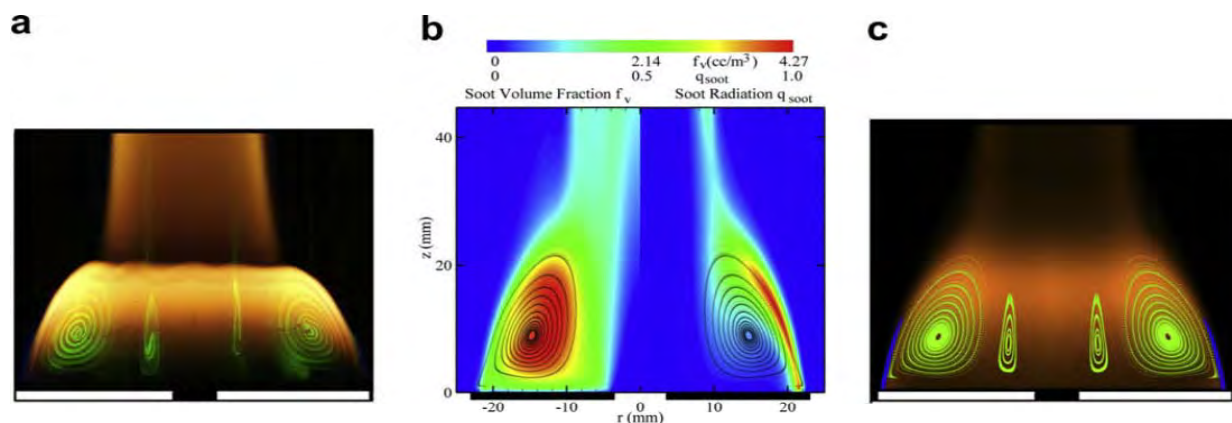


Figure 5.162 (a) Photograph of fully sooting flame, (b) computed soot volume fraction (left) and radiation intensity (right) with particle tracks, and (c) computed fully sooting flame with solid body rotation and false colors.

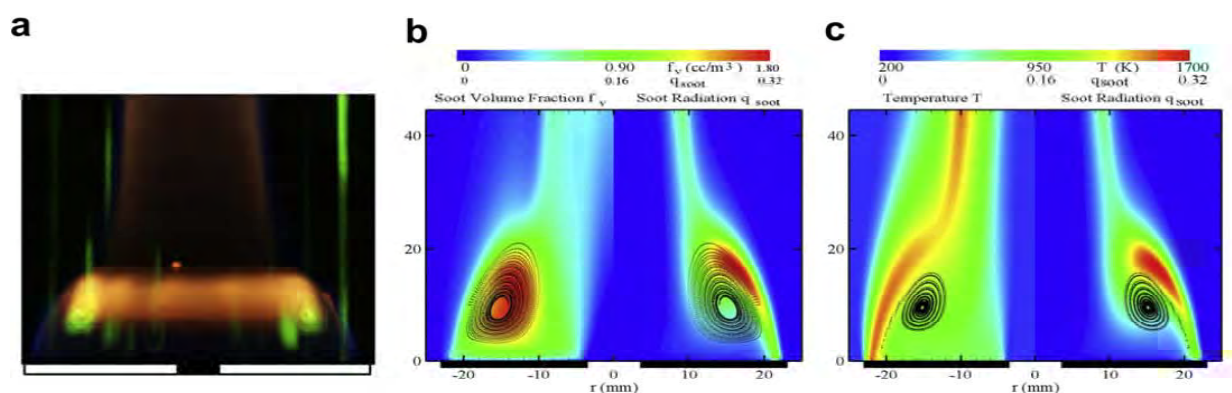


Figure 5.163 (a) Photograph of donut-shaped sooting flame, (b) computed soot volume fraction (left) and radiation intensity (right) with particle tracks, and (c) computed temperature (left) and radiation intensity (right) and oxidation of spiraling soot (right).

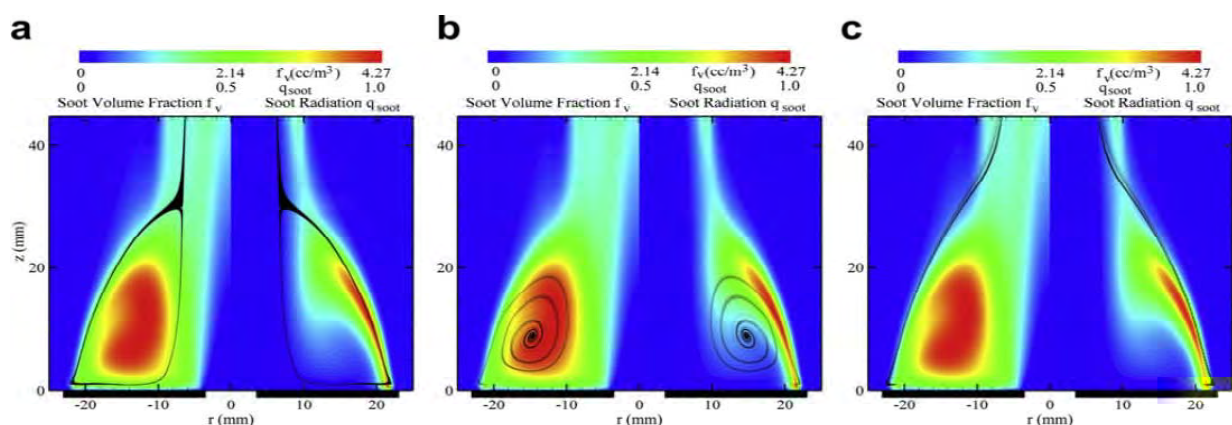


Figure 5.164 (a) Fully sooting flame with massless particles, (b) soot volume fraction (left) and radiation intensity (right) with 1- $\mu m$ -diameter particles, and (c) temperature (left) and radiation intensity (right) with 50- $\mu m$ -diameter soot particles.



### 5.4.3 Stability of Lifted Flames in Centerbody Burner

The centerbody burner was selected to investigate the coupled processes of soot formation, growth, and burn-off. As noted in Section 5.4.2, experimentally it was found that sooting characteristics of the centerbody burner could alter dramatically with the changes in operating conditions. An interesting operating regime; in which, flame lifts off and forms a column of soot, was observed when oxygen in the oxidizer stream was sufficiently reduced. The numerical studies performed for understanding the lifted/sooting flames of the centerbody burner are described in this section. The results of this section are contained in Katta and Roquemore (2008).

The geometry of the centerbody burner was described in Section 4.5. It consists of a 46-mm-diameter disc enclosed in a cylindrical chimney with an annular gap of 17 mm. A 7.6-mm-diameter hole is made at the center of the disc through which fuel (a mixture of ethylene and nitrogen) is injected at a velocity of 1.25 m/s. A mixture of air and nitrogen is flowed through the annular gap, also at a velocity of 1.25 m/s.

Concentrations of nitrogen in the fuel and oxidizer streams are varied for obtaining different types of flames. For example, as discussed in Section 5.4.2, dilution of fuel jet transforms a fully sooty flame into a donut-type sooty flame and subsequent dilution of oxidizer jet results in a ring-type sooty flame. Further experiments revealed that a lifted flame with a column of soot establishes when oxygen concentration in the oxidizer becomes sufficiently low. Direct photograph of the flame obtained with 14.7% oxygen in the oxidizer stream is shown in Figure 5.165. No nitrogen flow was used in the fuel stream. Glow from the flame has illuminated the 46-mm-diameter centerbody. Flame has lifted off from the face of the centerbody and stabilized at about 13 mm away from it. Radiation from CH and other ionized species that earmarks the reaction zone may be identified from the blue regions in Figure 5.165. A column of soot that is extended all the way to the face of the centerbody can be identified from orange color. Note that this flame is very sensitive to the flow conditions and a small variation in flow velocity or nitrogen dilution could transition it into an oscillating flame.

Calculations for the lifted flame shown in Figure 5.166 are made using a 451x251 grid system. Concentrations of ethylene in the fuel jet and oxygen in the oxidizer jet are 100 and 14.7 percents, respectively. Velocities of the jets are 1.25 m/s. Even though, time-dependent simulations are performed assuming that the resulting flowfield could be unsteady by nature, only steady state solutions are resulted in about 10,000 time steps. A description of the UNICORN code used for the calculations is given in Section 4.2.

Results obtained for the lifted flame are shown in Figure 5.166. Axisymmetric representation of the flame is used while displaying the data. While iso-concentration contours of ethylene (solid gray lines), oxygen (broken lines) and OH (solid black lines) are superimposed on temperature field in the left half, streamlines are superimposed on temperature field in the right half. Location of the stoichiometric surface is marked with a solid white line. The two recirculation-type vortices associated with the centerbody flames may be identified from the streamlines. These recirculation vortices are formed due to the separation between the fuel and oxidizer jets. However, due to the differences in the momentum, recirculation vortex closer to the oxidizer jet is much larger than the one closer to the fuel jet. These recirculation vortices play a vital role in

transporting fuel across the centerbody toward the oxidizer jet and in establishing a non-premixed flame near the oxidizer jet.

Calculations have predicted a lifted flame with the flame base shifted  $\sim 13$  mm from the centerbody. This lift-off height matches well with that observed in the experiment (5.4.3.1). Flame is stabilized on the outer edge of the oxidizer-side recirculation zone where flow (streamlines) is diverging. Stoichiometric surface (white line) in the flame region also matches well with the outer edge of the blue region in Figure 5.165. Higher concentrations of OH radicals (black contour lines) near the flame base suggest the formation of a reaction kernel Takahashi and Katta (2002 and 2005). Fuel transported by the recirculation vortices is mixing with oxygen in the inner region of the oxidizer jet and forming a partially premixed region upstream of the flame base.

Detailed structure of the flame base is shown in Figure 5.167. Here, calculated CH distribution is shown in rainbow color palette. Iso contours of temperature and acetylene are superimposed using black and gray lines, respectively. Velocity vectors are also shown in this figure. The hook-type CH-concentration distribution in two dimensions matches well with the toroidal-type flame ring captured in the three-dimensional photograph of the experiment (Figure 5.165). As depicted by acetylene distribution, ethylene fuel is decomposing into smaller fuel fragments in the flame region, which are then transported into the region between the flame base and centerbody by the recirculation vortices. Consequently, flame is established from the combustion of oxygen and fuel fragments such as methane, hydrogen and acetylene. This is evident from the deviation in the location of peak-CH-concentration region from the stoichiometric surface computed using ethylene and oxygen (white line) near the flame base. Thus, the recirculation zones are playing a vital role in transporting fuel and its lighter fragments upstream of the flame base and in stabilizing it.

Structure of the flame base is shown in Figure 5.168 through plotting radial distributions of temperature, axial velocity, and reactants and intermediate-species concentrations. Note the difference in the ranges for radial distances used in Figure 5.168(a) and 5.168(b). The small peak in temperature at  $r = 20$  mm is resulting from combustion. High temperature ( $\sim 1300$  K) in the regions  $r < 20$  mm is resulting from the products that transported by the recirculation zones. Significant mixing of fuel fragments and oxygen is taking place in the region upstream of the flame base, which forms a premixed flame at  $r = 21$  mm as evident from the sudden increase in axial velocity. Consumption of lighter fuels ( $H_2$  and  $CH_4$ ), ethylene and oxygen at this location ( $r = 21$  mm in Figure 5.168(b)) also suggest the presence of a premixed flame.

For understanding the stability of the lifted flame in Figure 5.166, calculations are repeated by increasing or decreasing the coflow air-nitrogen velocity. For each new velocity, flame base has shifted to a new location and became stabilized. Flame and flowfields at higher coflow velocity ( $V_{\text{oxidizer}} = 1.4$  m/s) are shown in Figure 5.169 and those for a lower coflow velocity ( $V_{\text{oxidizer}} = 1.0$  m/s) are shown in Figure 5.170. As expected, coflow velocity has changed the sizes of the oxidizer-side and fuel-side recirculation zones. Increasing coflow velocity destabilized the flame in Figure 5.166. However, as the flame retreats from its stable location, more fuel (original and its fragments) mixes with oxygen and leads for a stronger premixed flame, and thereby, establishes



a new stabilization location for the flame base. This can be identified from the sharper flame-base region in Figure 5.169 compared to that in Figure 5.170.

Movements of flame base and the center of the oxidizer-side recirculation-zone with coflow velocity are plotted in Figure 5.171. Overall, response of the recirculation zone center to the changes in coannular flow velocity is weaker than that of the flame base. Interestingly, flame base and recirculation zone center are located at the same radial distance for  $V_{\text{coflow}} < 1.2$  m/s. For higher velocities flame base moves closer toward the center than the center of the recirculation zone. Note lifted flame in the experiment (Figure 5.165) became unsteady for small changes in flow conditions. On the other hand, calculations have resulted in a new stable flame when the flow conditions are modified.

In summary, the sooting characteristics of a centerbody burner can change dramatically with changes in operating conditions. It was experimentally found that flame lifts off the centerbody and forms a column of soot when oxygen in the oxidizer stream was sufficiently reduced. The predicted lift-off height matched well with that of the experiment. It was found that fuel and its lighter fragments formed in the lifted flame region transported upstream toward the face of the centerbody by the recirculation zones. Mixing of oxygen and fuel and its fragments between the flame base and the face of the centerbody established a premixed flame in the flame-base region. While experiments have indicated that stability of the lifted flames is highly sensitive to the operating conditions, numerical studies conducted by increasing and decreasing the coannular flow velocity suggested that a stable flame could be established at a new location for the given velocity condition. Further experimentation and computation are needed for resolving this discrepancy.



Figure 5.165 Photograph of lifted flame obtained in centerbody burner with pure ethylene central fuel jet and coannular flow of nitrogen-diluted air.

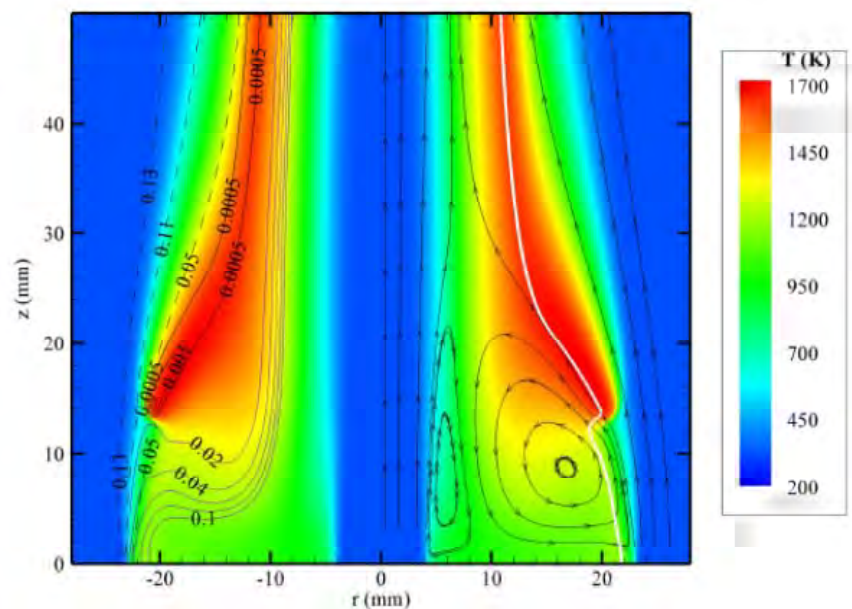


Figure 5.166 Computed lifted flame of centerbody burner. Iso contours of OH (black solid lines), ethylene (gray solid lines), and oxygen (broken lines) and streamlines are superimposed on left and right halves, respectively of color temperature map. Location of stoichiometric surface is marked with white line on right half.

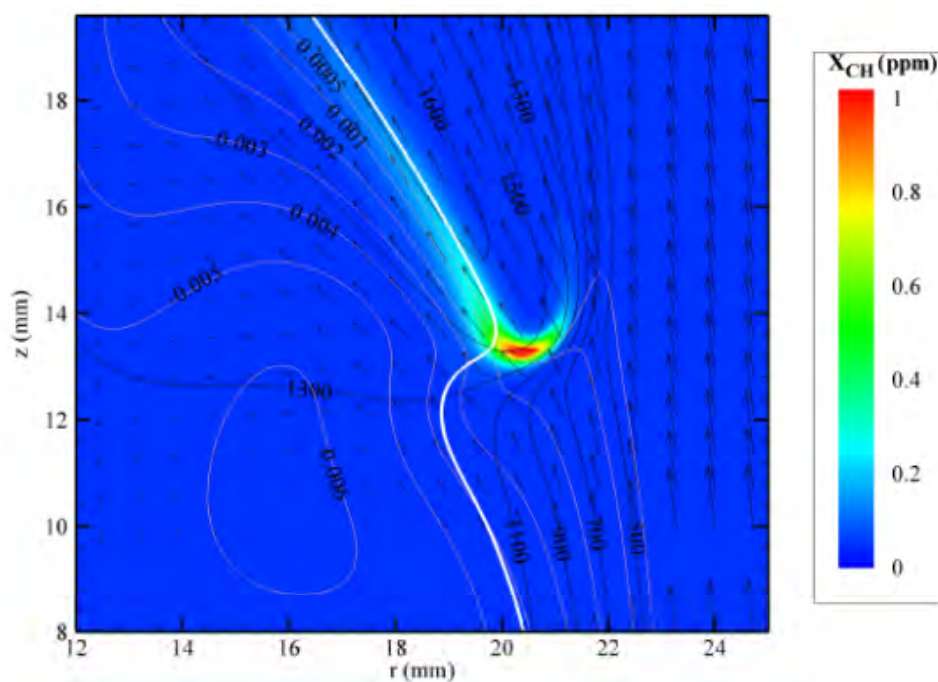


Figure 5.167 Close-up view of lifted flame base. Velocity field and iso contours of temperature (black solid lines) and acetylene (gray solid lines) are superimposed on color map of CH concentration. Location of stoichiometric surface is marked with white line.

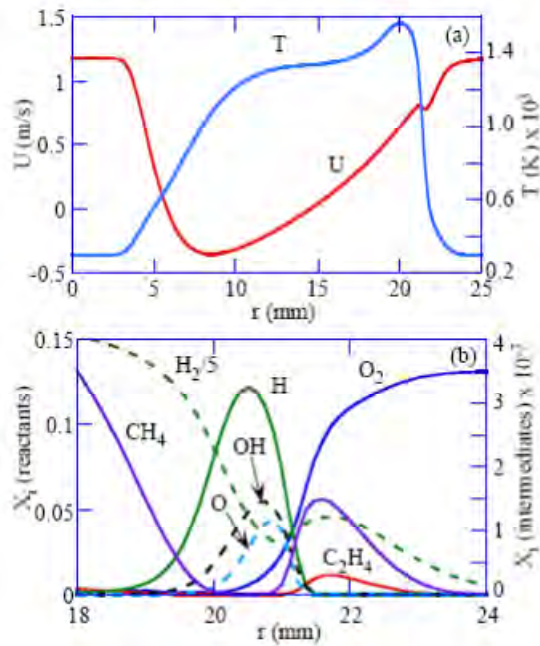


Figure 5.168 Structure of lifted flame base. Radial distributions of (a) temperature and axial velocity and (b) concentrations of reactants and intermediate species at a height of 13.8 mm above centerbody plate.

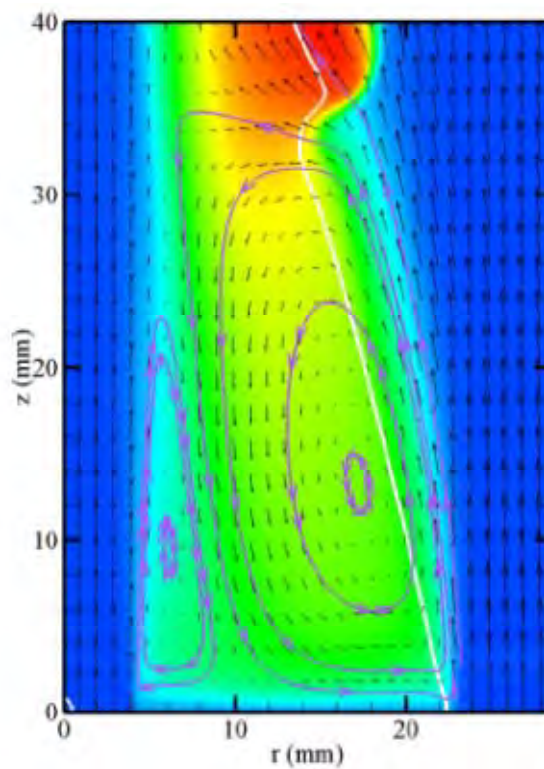


Figure 5.169 Lifted flame for higher coannular flow. Velocity field and streamlines are superimposed on color temperature map. Stoichiometry is shown with white line.

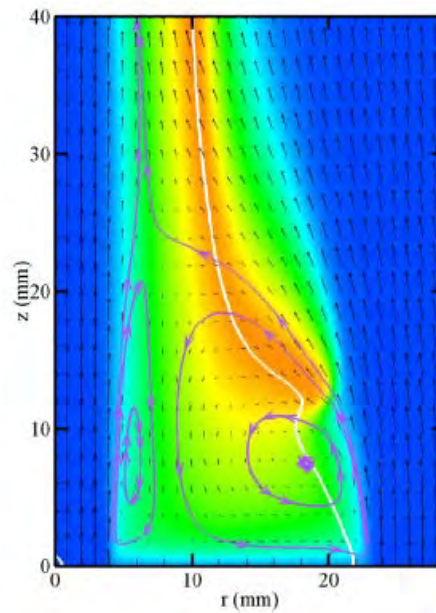


Figure 5.170 Lifted flame simulated for lower coannular nitrogen-air flow. Velocity field and streamlines (gray solid lines) are superimposed on color temperature map. Stoichiometric surface is shown with white line.

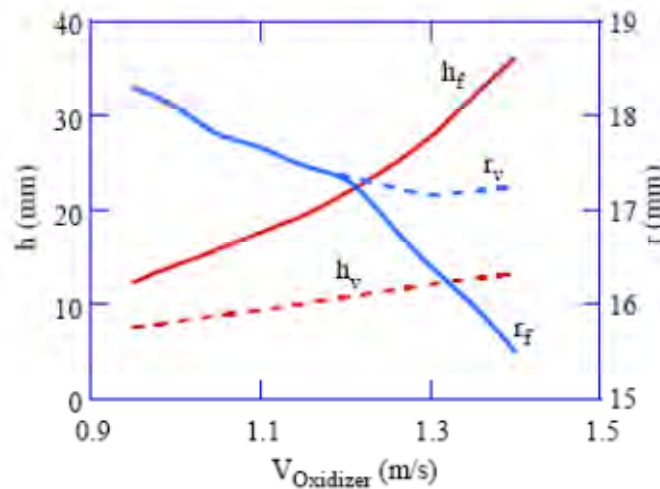


Figure 5.171 Changes in height ( $h$ ) and radius  $I$  of flame base location and recirculation zone center with respect to increase in coannular nitrogen-air velocity.

#### 5.4.4 Dynamics of the Lifted Flame Supported by a Recirculation Zone

Experimentally it was found that sooting characteristics of the centerbody burner can be altered dramatically by changing the operating conditions. In Section 5.4.3, the stability of a lifted flame with a column of soot in the middle was investigated. However, this flame is very sensitive to the flow conditions and a small variation in flow velocity, nitrogen dilution, or chimney position can

transition it into an oscillating sooting flame. The results of experimental and computational studies of this dynamic, oscillating sooting flame are presented in this section. These results are contained in Katta et al. (2009b). A description of the modeling and experimental techniques are given in Section 3.3 and 4.5, respectively.

Direct photograph of a lifted flame obtained with 13.14% oxygen in the annular flow is shown in Figure 5.172a. Fuel jet consisted of 82.4% ethylene and 16.6% nitrogen. Glow from the flame has illuminated the 46-mm-diameter centerbody. Flame has lifted from the face of the centerbody and stabilized at about 13 mm away from it. Radiation from CH and other ionized species that earmarks the reaction zone may be identified from the blue regions in Figure 5.172a. A column of soot that is extended all the way to the face of the centerbody can be identified from orange color. This flame is very sensitive to the flow conditions and a small variation in flow velocity, nitrogen dilution, or chimney position could transition it into an oscillating flame.

Calculations for the lifted flame shown in Figure 5.172a are made using a 451x251 grid system. Concentrations of ethylene in the fuel jet and oxygen in the annular jet are 82.4 and 13.14 percents, respectively. Velocities of the jets are 1.25 m/s. Simulations are performed on a Personal Computer with 2.0 GB of memory. Execution times strongly depend on the number of species considered in the chemical-kinetics model and the grid size. Typically, with 99 species and 1066 reactions (Wang-Frenklach model) on a 451X251 grid system, simulations took ~50 s/time-step on AMD-Opteron-250 computer. Even though, time-dependent simulations are performed a steady state flame is resulted in about 10,000 time steps.

Computed results obtained for the lifted flame are shown in Figure 5.172b along with the photograph of the actual flame. Streamlines (lines with arrowheads) and iso-concentration contours (thick lines) of CH radical are superimposed on flame photograph. Calculations have predicted the flame lift-off height well. The 2D, hook-type CH concentration distribution near the flame base (Takahashi, F., and Katta, V. R., (2002 and 2005)) matched well with the torroidal-type flame ring captured in the photograph. Recirculation zone consisting of air-side and fuel-side vortices can be identified from the streamlines.

Additional details of the flame structure are shown in Figure 5.173. While iso-concentration contours of ethylene (solid gray lines), oxygen (broken lines) and OH (solid black lines) are superimposed on temperature field in the left half, streamlines are superimposed on temperature field in the right half. Location of the stoichiometric surface is marked with a solid white line. The two vortices associated with the recirculation zone of the centerbody flames may be identified from the streamlines. These vortices are formed due to the separation between the fuel and annular jets. However, due to the differences in the momentums, vortex closer to the annular jet is much larger than the one closer to the fuel jet. These vortices play a vital role in transporting fuel across the centerbody toward the annular jet and in establishing a non-premixed flame near the outer edge.

It is known that a small perturbation to the flow in the experiment results in a dynamic lifted flame as shown in Figure 5.174. Sooting characteristics recognized based on this direct photograph did not change much from the steady flame shown in Figure 5.172, except that more soot seems getting accumulated in the recirculation zone when the flame is dynamic. On the

other hand, the flame base looks quite different. A hallow blue-colored torroidal ring formed at the edge of the dynamic lifted flame. First impression suggests that the flame edge rolled into a ring flame. Also, the converging core soot column starts to diverge at about one centerbody diameter. Usually this happens at the onset of turbulence (either with or without the large-scale vortices).

High-speed video and photographs are taken for the flame shown in Figure 5.174 for identifying the unsteady characteristics. Flame images obtained at two random instants are shown in Figures 5.175a and 4b. Soot column in these photographs look quite different from that in Figure 5.174. Vortical structures comparable to the jet diameter are rolling along the soot column. In fact, the base of the flame is also oscillating. Based on the convective velocity of these structures it is determined that new vortex generation is occurring at a frequency of  $\sim 50\text{Hz}$ . Blow-up of the flame base region is shown in Figure 5.175c. Due to short exposure time the blue flame is not that clear in these high-speed photographs. However, it may be noted that the ring flame seen in Figure 5.174 is not appearing in the high-speed photographs.

For understanding the processes leading to the formation of ring flame in the dynamic lifted flame, calculations are repeated for the steady-state flame by increasing or decreasing the flow rates slightly. None of such efforts led to a dynamic flame. Finer grid systems and different boundary conditions for the centerbody also did not result in an oscillating flame. Assuming that there could be some system resonance in the experiment that is leading to such 50Hz-flame oscillations, calculations are performed by sinusoidally perturbing the annular flow. The jet velocity has been changed at a frequency of 50Hz and with amplitudes up to 10% of the mean flow.

Instantaneous solutions obtained with 5% perturbation are shown in Figures 5.176a and 5b. The phase difference between these two images is 10ms. Iso contours of soot volume fraction are superimposed on color distribution of CH-radical concentration in these figures. Dancing flame edge can easily be noted from CH distributions. Wrinkling of trailing CH layers and soot column can also be noted. However, these instantaneous images did not show the formation of ring flame at the edge.

Computed instantaneous solutions of the unsteady lifted flame are time averaged over a period of 100 ms, which represents 5 perturbation cycles. Soot and CH distributions of this time-averaged data are plotted in Figure 5.176c. Surprisingly, a hallow ring showed up in the CH distribution near the flame edge. The wrinkles in trailing CH layers have disappeared. On the other hand, soot column is not affected that much due to this perturbation (instantaneous and time-averaged data look nearly the same).

Results obtained with 10% perturbation in annular flow are shown in Figure 5.177. The hollow ring in CH distribution near the flame base (Figure 5.177c) got bigger with the increased amplitude for perturbation. This CH ring looks similar to that observed in the experiment (Figure 5.174). Interestingly, the amount of soot in the recirculation zone increased with the perturbation amplitude, which follows the observation made in the experiment between the steady state (Figure 5.4.4.1) and unsteady (Figure 5.174) lifted flames.

Absence of CH ring in the instantaneous flame solutions and presence of that in the time-averaged data suggests that the blue flame ring observed in the experiment (Figure 5.174) is an illusion caused by the long time response of human eye and, similarly, the long exposure time of the photograph. Nevertheless, to the authors' knowledge, such ring flames were never observed before in either steady state or dynamic flames.

In order to understand the ring flame formed near the flame edge in the dynamic flames, instantaneous plots of temperature and concentrations of OH, H, and CH<sub>3</sub> are shown in Figure 5.178 and the corresponding time-averaged data are shown in Figure 5.179. The 10%-amplitude dynamic flame data was used in these plots. Interestingly, none of these variables show a hollow ring structure near the flame edge, even though CH<sub>3</sub> seems closer to forming one.

The effects of perturbation on trailing jet flame are shown in Figures 5.180 and 5.181. Radial distributions of several variables at a height of 40-mm above the centerbody (in the necking region of Figure 5.173) are shown for steady state and dynamic lifted flames in Figure 5.180, while those at 140-mm above the centerbody are shown in Figure 5.181. Time-averaged data were used for the dynamic flames. Interestingly, calculations have predicted that the width of the soot column decreases with the perturbation amplitude (Figure 5.181a). However, temperature field is widening with perturbation. Note that flame thickness based on either CH or OH concentration did not change much with perturbation (Figure 5.180c), whereas, it has significantly increased at  $z = 140$  mm (Figure 5.181c). As expected, both OH and CH are showing double-modal distributions in dynamic flames due to nonequilibrium chemistry.

In summary, sooting characteristics of a centerbody burner can be changed dramatically with changes in operating conditions. It was experimentally found that flame lifts off and forms a column of soot when oxygen in the annular flow was sufficiently reduced. For certain flow conditions a ring flame forms near the edge of the lifted flame. Experimentally it was observed that small perturbations in the flow can cause the lifted flame to oscillate. The oscillating flame was simulated in these studies by periodically oscillating the annular flow at different amplitudes. The base of the simulated lifted flame was found to dance around the recirculation zone while vortex structures were established on the trailing jet flame. However, none of the calculations made with varying flow conditions and perturbations yielded the experimentally observed ring-flame structure near the base of the lifted flame. Surprisingly, when time-averaged the dancing-flame data a ring flame appeared near the edge. Based on these calculations and high-speed movies of the experimental flame it was concluded that the observed ring flame was an illusion created through natural time-averaging process. Thus, the simulation was able to provide an understanding the lifted ring flame with the column of soot in the center.





Figure 5.172 (a) Photograph of lifted flame obtained in centerbody burner with central fuel jet of nitrogen-diluted ethylene and coannular flow of nitrogen-diluted air. (b) Computed flame structure overlaid on the flame photograph. Computed CH contours and streamlines are shown.

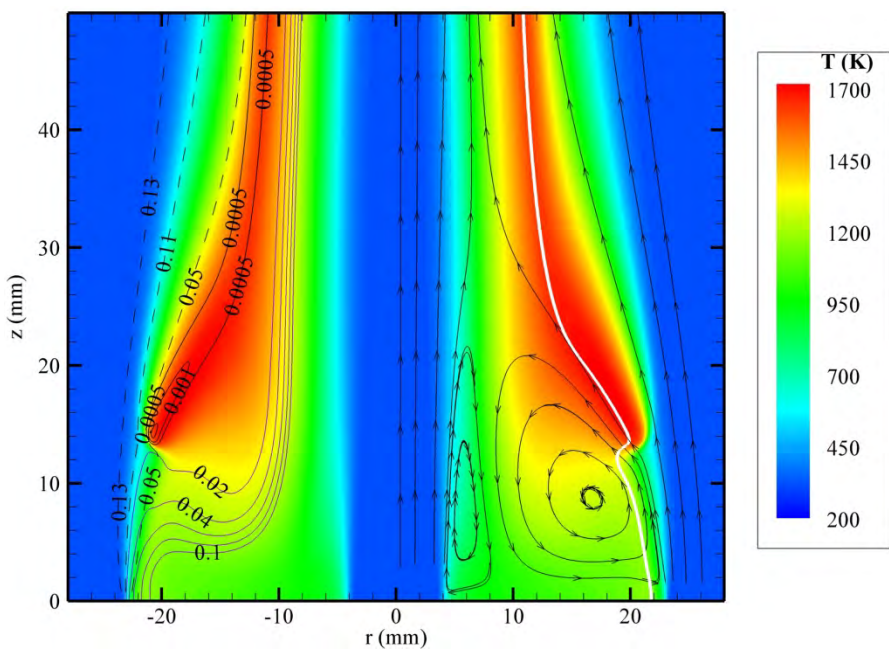


Figure 5.173 Computed lifted flame of centerbody burner. Iso contours of OH (black solid lines), ethylene (gray solid lines), and oxygen (broken lines) and streamlines are superimposed on left and right halves, respectively, of color temperature map. Location of stoichiometric surface is marked with white line on right half.





Figure 5.174 Second mode of the lifted flame obtained in centerbody burner with central and coannular flows that are slightly different from those used in Figure 5.4.4.1.

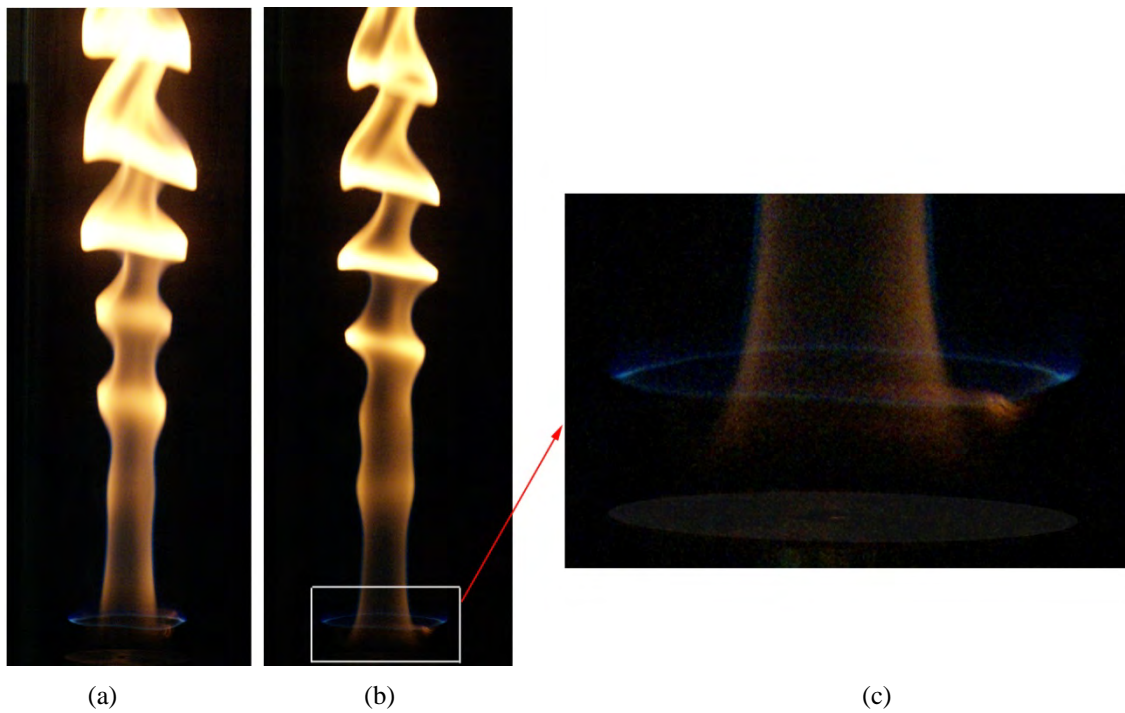


Figure 5.175 High-speed images of the flame shown in Figure 5.172 obtained with exposure time of 2 ms at two instants (a and b). Close up of the flame near the flame edge is shown in I.

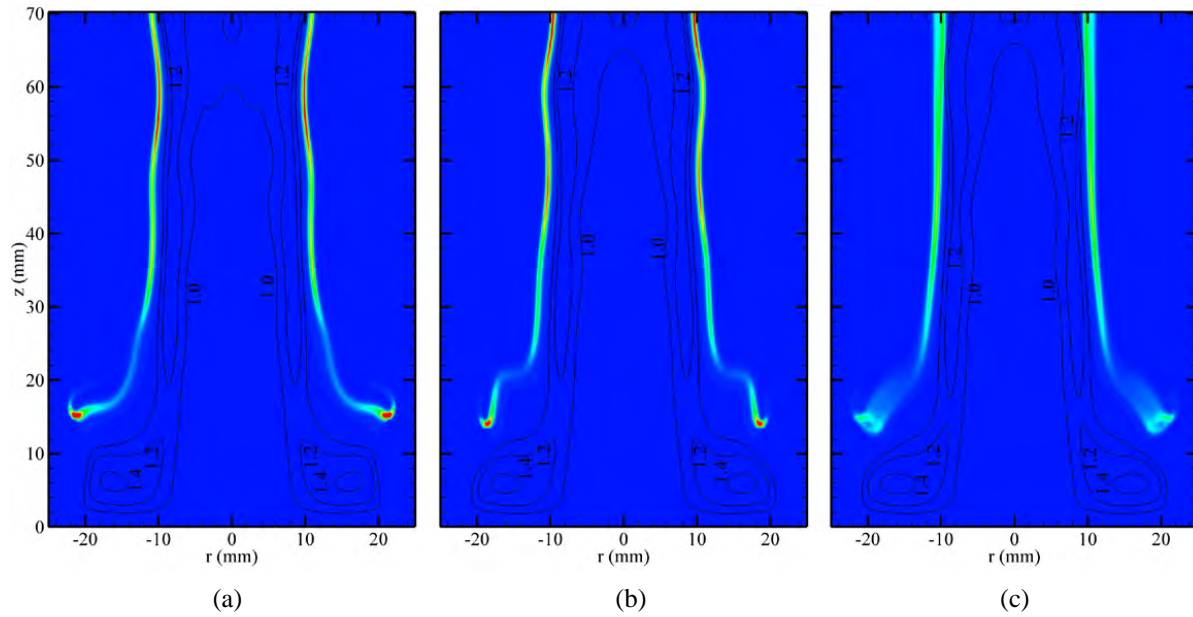


Figure 5.176 Dynamic flame computed through sinusoidally driving the coannular flow in Figure 5.173 at 50 Hz and with an amplitude of 5% of the mean flow. Iso-contours of soot volume fraction are superimposed on CH concentration distribution shown in color (blue and red represent 0 and 0.4 ppm, respectively). (a) Flame at instant  $t_0$ , (b) flame at instant  $t_0 + 10$  ms, and (c) time-averaged flame.

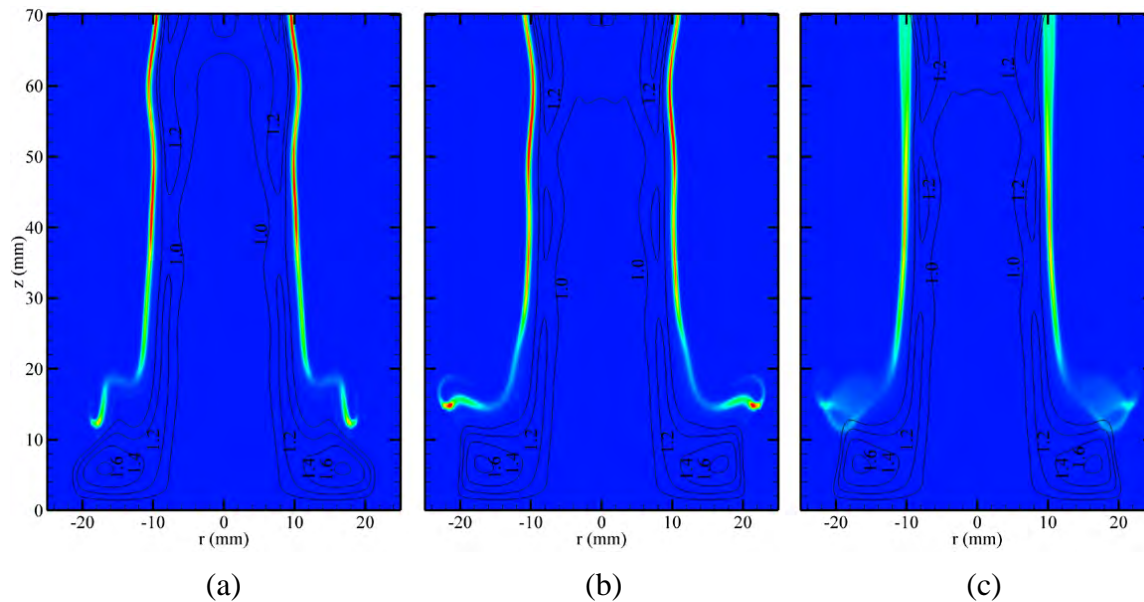


Figure 5.177 Dynamic flame computed through sinusoidally driving the coannular flow in Figure 5.173 at 50 Hz and with an amplitude of 10% of the mean flow. Iso-contours of soot volume fraction are superimposed on CH concentration distribution shown in color (blue and red represent 0 and 0.4 ppm, respectively). (a) Flame at instant  $t_0$ , (b) flame at instant  $t_0 + 10$  ms, and (c) time-averaged flame.

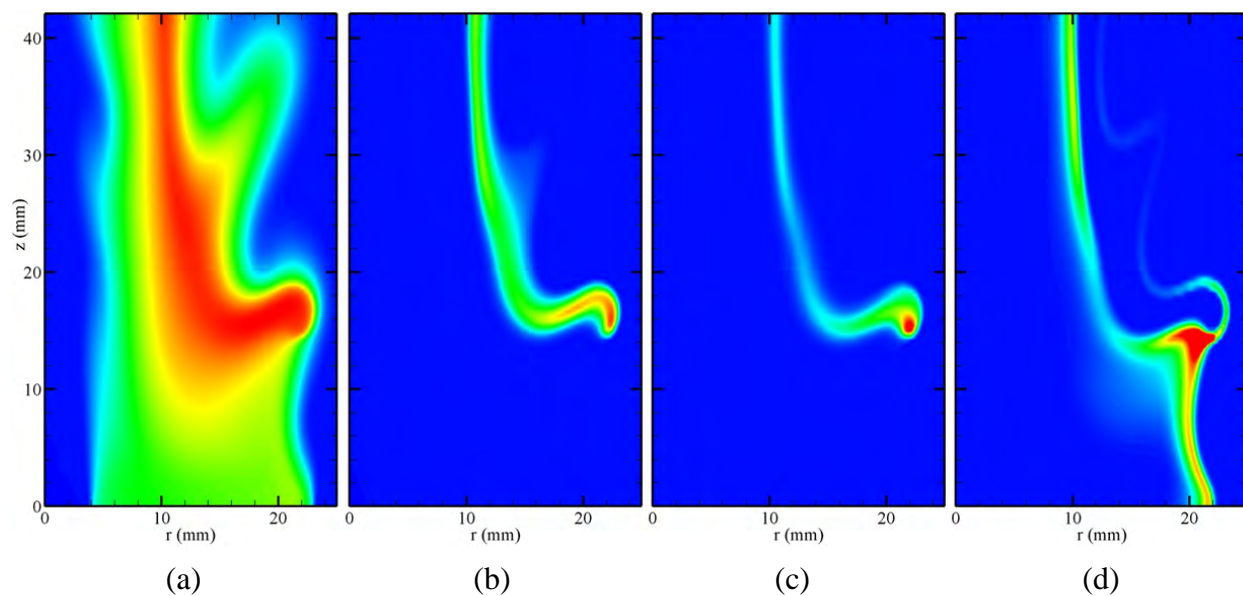


Figure 5.178 Distributions of (a) temperature and (b) OH, (c) H, and (d)  $\text{CH}_3$  concentrations of the dynamic flame shown in Figure 5.177b.

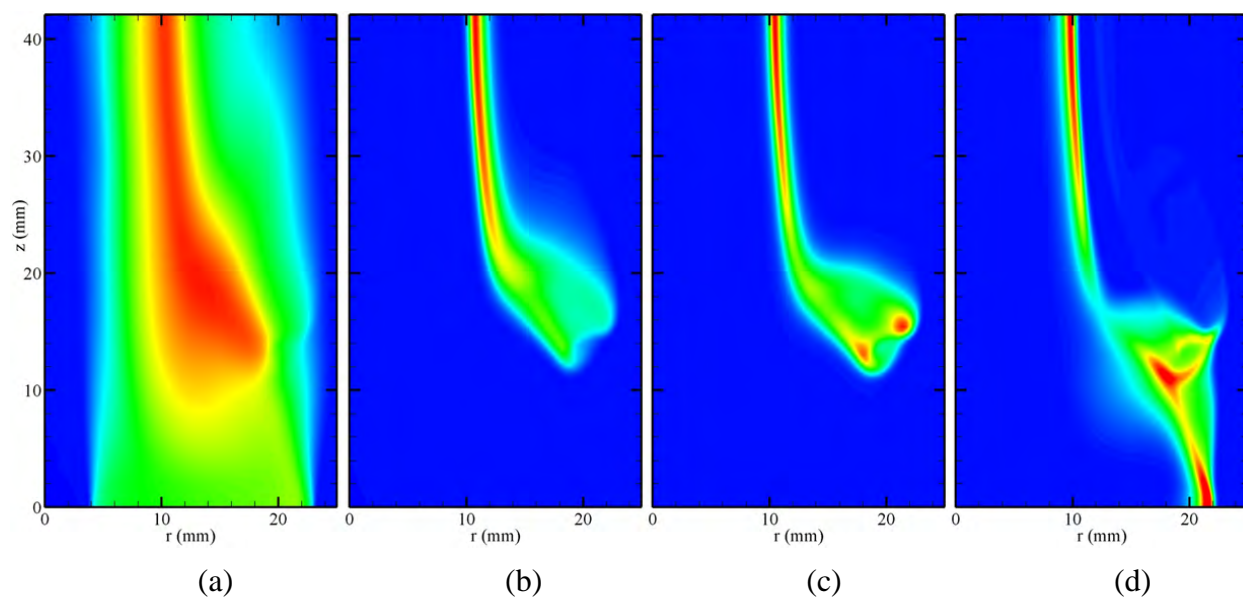
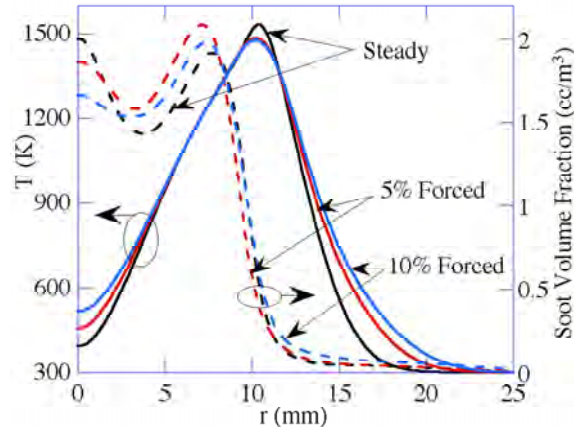
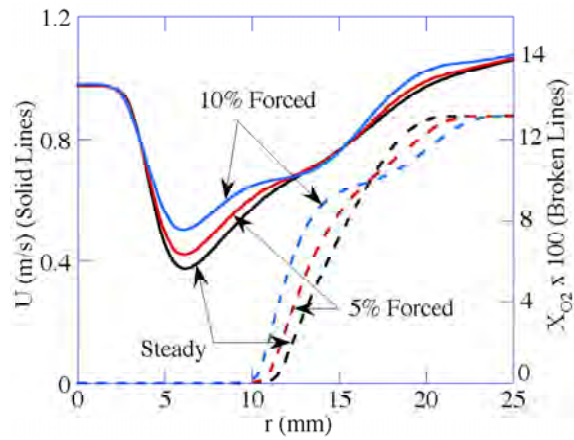


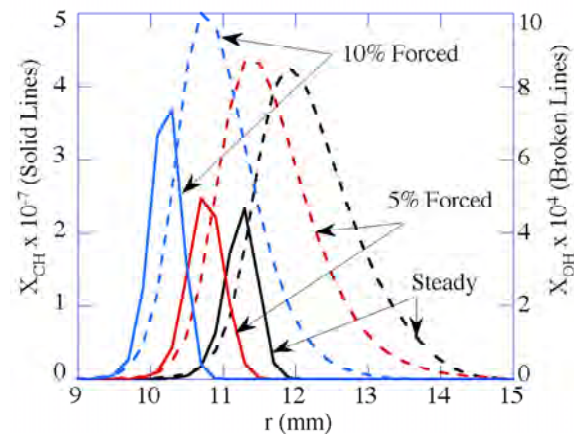
Figure 5.179 Distributions of time-averaged (a) temperature and (b) OH, (c) H, and (d)  $\text{CH}_3$  concentrations of the dynamic flame shown in Figure 5.177c.



(a)



(b)



(c)

Figure 5.180 Radial distributions of (a) temperature and soot volume fraction, (b) axial velocity and oxygen concentration, and (c) CH and OH concentrations at  $z = 40$  mm in dynamic and steady state flames. Time-averaged data is used for dynamic flames.



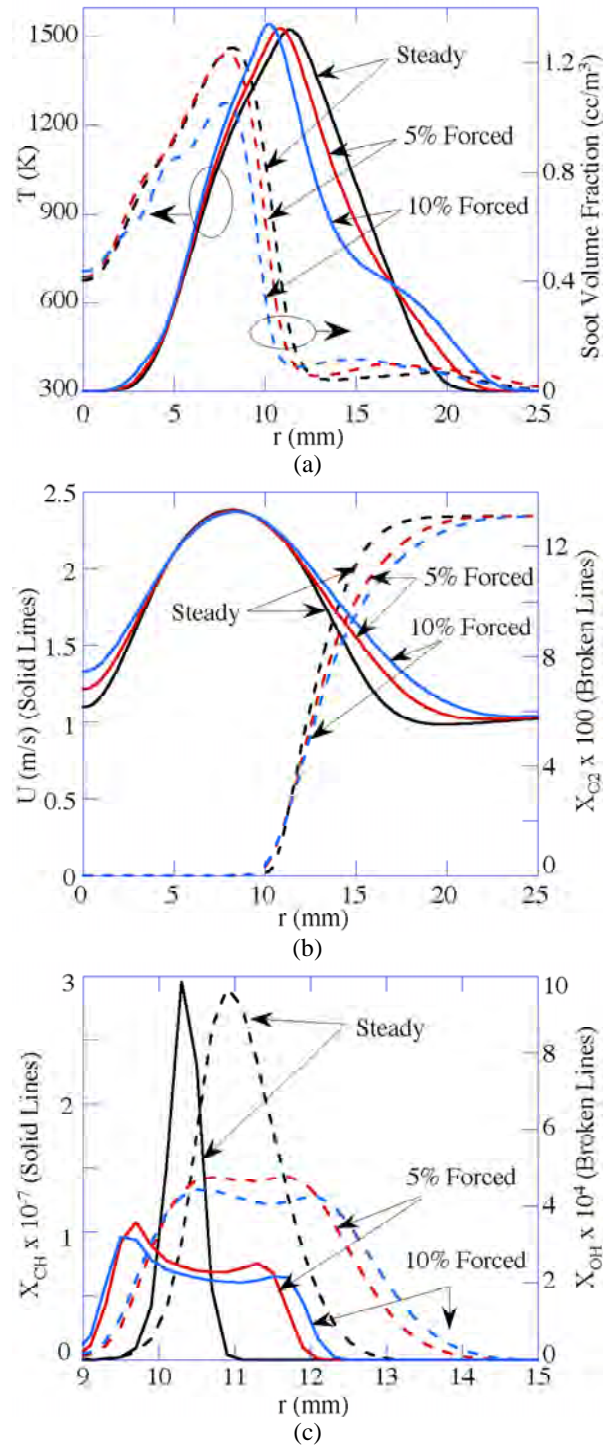


Figure 5.181 Radial distributions of (a) temperature and soot volume fraction, (b) axial velocity and oxygen concentration, and (c) CH and OH concentrations at  $z = 140$  mm in dynamic and steady state flames. Time-averaged data is used for dynamic flames.

#### 5.4.5 Sooting Characteristics of Partially Premixed Flames in Centerbody Burner

This section describes studies on sooting characteristics of partially premixed centerbody flames performed by adding air to the fuel jet. Studies of these partially premixed flames are described in Katta et al. (2009a). The centerbody configuration and experimental techniques used in these studies are described in Section 4.5. Simulations for these partially premixed flames are performed with UNICORN using a simple soot model described in Section 3.3.

Before describing the characteristics of partially premixed centerbody flames, it is useful to investigate if UNICORN can estimate the characteristics of partially premixed jet flames that have been studied in some detail by McEnally and Pfefferle (1999 and 2000). Partially premixed jet diffusion flames are obtained by adding air to the fuel stream. McEnally and Pfefferle found that the soot volume fraction decreases dramatically with the addition of air to the fuel stream. Preliminary UNICORN calculations made for partially premixed flames in the centerbody burner suggested that the soot volume fraction in the trailing diffusion flame (downstream of the recirculation zone) actually increased with air addition to the fuel stream. This observation is in contrast to the results of McEnally and Pfefferle and what one might expect from theory. This raises the question: can UNICORN correctly predict the results of McEnally and Pfefferle? To answer this question, we simulated the flames of McEnally and Pfefferle using the same code. UNICORN calculations for several of their partially premixed jet flames were made using a 301x161 grid system. Particle trajectories were used to identify the sooting behavior in these flames. Collected experimental data consist of direct photographs without and with Nd:YAG laser turned on and LII images. Computed results were obtained using contour maps, streamlines and soot-particle trajectories with and without the burnout process.

Figure 5.182 shows UNICORN simulations of the temperature fields for various equivalence ratios similar to those investigated by McEnally and Pfefferle. Note that the temperature of the flame tip increases with the amount of air added to the fuel jet. The flame transitioned from an opened-tip type to a closed-tip type. Soot fields predicted in these flames are shown in Figure 5.183. As found in the experiments, soot level decrease with the addition of air to the fuel jet. Since soot is calculated in these flames using acetylene-based model, it is hypothesized that the addition of air to the fuel jet decreases acetylene concentration and, in turn, soot concentration. Since soot radiation decreased the temperature of the flame tip in the pure diffusion flame case, reduction in soot with the addition of air to the fuel jet decreased soot radiation and, in turn, increased the temperature of the flame tip. Computed temperatures along the centerline for various equivalence ratios are shown in Figure 5.184. Corresponding soot distributions along the non-dimensional axial position are shown in Figure 5.185. For each flame, the axial distance in this figure was non-dimensionalized with the corresponding flame height. The simulated results followed the trends observed in the experiment (Figure 5.186). This study confirms that UNICORN code could correctly predict the sooting behavior of partially premixed jet flames and provided some confidence that it would also predict the behavior for partially premixed centerbody flame. However, the real test of UNICORN is to determine if the calculations would agree with experiments. The following paragraphs describe and compare the experimental and computational results for partially premixed centerbody flames.

The centerbody experiments are designed so that the laminar flow fields are about the same for the different flow conditions. However, the sooting flame structures are dramatically different depending on the fuel and air compositions. The volumetric flow rate of the mixture of air and additional nitrogen in the annular duct is 250 SLPM and the flow rate for the fuel mixture (ethylene + nitrogen + additional compounds) in the central fuel jet is 3.4 SLPM. Since the molecular weight of ethylene is about the same as air and nitrogen, maintaining the same flow rates for the different experiments is equivalent to maintaining the constant momentum in the air and fuel jets. Because of this, the recirculation zone established by the centerbody is expected to have about the same size and shape for the different flames. Nitrogen addition is used to change the soot characteristics of the flames by dilution/chemistry effects. The average velocity of the air and fuel is about 1.2 m/s for all of the experiments. According to Roquemore et al. (1986), this flow condition would correspond to a fuel jet that weakly penetrates the recirculation zone established by the annular air jet.

Computed and experimental results obtained for the partially premixed centerbody flames at different equivalence ratios (107, 46, 23, and 11) are shown in Figure 5.187. Direct photographs of the experimental flames obtained with 10-ms exposure time are shown in Figures 5.187b, 6d, 6f, and 6h while, the corresponding simulated flames are shown in Figures 5.187a, 6c, 6e, and 6g. Symmetric presentation is used while displaying the computational data. While iso-concentration contours of  $C_2H_2$  (black solid lines) and  $C_6H_6$  (white broken lines) are superimposed on temperature field on the left half, CH (solid lines) and OH (broken lines) contours are superimposed on the right half. Shapes of the computed flames matched well with the corresponding experimental flame photographs. In general, centerbody flames can be thought of as two flames: a recirculation-zone flame and a trailing jet flame downstream of the recirculation zone. As the amount of air in the fuel jet increases, that is decreasing the equivalence ratio, the recirculation-zone flame is shrinking and the trailing jet flame is getting brighter. Temperature plots in Figure 5.187 suggest that calculations have predicted the former effect very well. Since the computed temperature of the trailing jet flame remains unaffected with partial premixing, the increase in brightness of the experimental flame could be due to an increase in soot concentration. However, previous experiments of McEnally and Pfefferle (2000) suggest that soot in a partially premixed coflowing jet flame decreases with the addition of air (or oxygen) into fuel jet. Therefore, it is important to know whether the soot in the trailing jet flame of the centerbody burner is really increasing with premixing as suggested by the experimental photographs in Figure 5.187 and, if so, then why they are behaving differently compared to the normal jet flames.

The computed soot-radiation distributions are shown in Figure 5.188 along with direct photographs of the flame with the Nd:YAG laser turned on in the experiment. Streamlines are superimposed on soot-radiation distributions. Both the computed and actual flame plots clearly show the recirculation zones. The recirculation zones show the striking difference between the experiments and computations. First, the recirculation zones identified with streamlines are not changing much with premixing. There is a slight increase in the recirculation-zone size for equivalence ratio of 11. On the other hand, the recirculation zone identified from the soot particles in the experiment is shrinking with premixing similar to the observation made from changes in flame shapes.

Figure 5.188 further suggests that computed soot radiation in the trailing jet flame increases with premixing. This is similar to the observation made based on flame brightness. The increase in soot particles in trailing jet flame with premixing is also evident in experimental images in Figure 5.188 (based on the green light intensity). Soot has nearly disappeared in the recirculation zone when equivalence ratio was decreased to 11 (Figure 5.188h).

The LII images and the computed soot-volume-fraction distributions are shown in Figure 5.189. Particle trajectories are superimposed on computed soot distributions. Five-micron particles were released along the 1100-K temperature line (shown in white color). Trajectories of these particles are supposed to represent the soot lines in the experiment. It is known that soot particles burnout as they pass through high-temperature regions (typically  $\sim 1300$  K). Particle trajectories without including soot burnout process are shown on the left half and those with soot burnout process are shown on the right half. Particle trajectories in Figure 5.189 suggest that these 5-micron particles take spiral paths in the recirculation zones (note, streamlines shown in Figure 5.188 suggest closed circular paths) similar to that observed in the experiments. As demonstrated in Roquemore et al. (2009), such spiral motion for the soot particles has resulted due to thermophoretic forces developed on the particles near the flame zone. Particle trajectories with burnout match well with the experiment and provide an explanation for the experimentally observed shrinking of soot rings. The computed soot volume fraction qualitatively matches well with the LII soot images-soot decreases in the recirculation-zone flame while it increases in the trailing jet flame as premixing increases.

Radial distributions of temperature and soot volume fraction across the recirculation-zone flame ( $z = 10$  mm) are shown in Figures 5.190a and 9b, respectively for different equivalence ratios. Based on the peak temperature location it is clear that the recirculation-zone flame is moving closer to the center ( $r = 0$ ) with premixing. The flame temperature is also decreasing with premixing. On the other hand, soot volume fraction decreased up to an equivalence ratio of 23 and then starts increasing (for example, 11). This behavior matched well with that observed in LII images (near the burner surface).

Radial distributions of temperature and soot volume fraction across the trailing jet flame ( $z = 70$  mm) are shown in Figures 5.191a and 10b, respectively for different equivalence ratios. Interestingly, premixing did not affect the temperature of the trailing jet flame. However, the soot has increased by nearly 40% when the flame became partially premixed with an equivalence ratio of 11 from pure diffusion (equivalence ratio of infinity). This behavior is in contrast to that observed for normal coaxial jet diffusion flames studied by McEnally and Pfefferle (2000). Their results suggest that soot in their coflowing jet flame decreased with the addition of air (or oxygen) into fuel jet. However, they performed their experiments by keeping the ethylene flow constant while adding air. In this approach the velocity of the fuel jet increases with premixing. Note, in order not to change the fluid dynamics, studies on centerbody are done by keeping the fuel jet velocity constant. This variation in the approach of adding air to the fuel jet is not expected to change the sooting behaviors in normal jet flame and in the trailing jet flame of the centerbody. However, it is important to eliminate this variability before making conclusions on the contradicting sooting patterns observed between these two types of flames.



Calculations and experiments are repeated for the partially premixed flames shown in Figure 5.192. The specified equivalence ratio in this new set of experiments and simulations is obtained by keeping the ethylene flow rate at 3.4 l/min while adding air to the fuel jet. This increased the fuel jet velocity from 1.25 m/s (equivalence ratio of infinity) to 2.83 m/s (equivalence ratio of 11). Computed temperature distributions are compared to the flame photographs obtained in the experiment in Figure 5.192. As expected from previous constant-velocity studies recirculation-zone flame is decreasing in size with premixing while the trailing jet flame getting brighter. Calculations have correctly predicted the flame structures at all equivalence ratios. A comparison between the flames in Figure 5.187 with those in Figure 5.192 suggests that recirculation-zone flame for the given equivalence ratio shrinks further when the ethylene flow rate was held constant.

The computed soot radiation distributions and streamlines for different equivalence ratios (achieved while keeping ethylene flow rate constant) are shown in Figure 5.193 along with the corresponding photographs obtained in the experiments. Nd:YAG laser was turned on while taking these photographs. Changes in the recirculation-zone structure and increasing soot in the trailing jet flame are obvious in these figures and computations have captured these changes reasonably well.

The LII images of the flames and the soot-volume-fraction distributions for the constant-ethylene-flow-rate cases are shown in Figure 5.194. Particle trajectories obtained without imposing soot-burnout process (left side of computed flames) yielded soot spirals much larger than those observed in the experiment. On the other hand, burnout process left the soot spirals that are close to the vortex center to survive in the case of 107 equivalence ratio and completely eliminated in the other cases. Soot spirals predicted with burnout process matched well with those captured in the LII images. As expected, soot in the trailing jet flame increased with premixing.

Radial distributions of temperature and soot volume fraction across the recirculation-zone flame ( $z = 10$  mm) are shown in Figures 5.195a and 5.195b, respectively for different equivalence ratios. Comparing the temperature profiles in Figure 5.195a with those in Figure 5.190a reveals that the flame in the recirculation zone moves closer to the center for the given equivalence ratio when ethylene fuel flow was kept constant. The higher fuel jet velocity in the flames shown in Figure 5.195 enhances entrainment and, thereby, brings the flame closer to the fuel jet.

Radial distributions of temperature and soot volume fraction across the trailing jet flame ( $z = 70$  mm) are shown in Figures 5.196a and 5.196b, respectively for different equivalence ratios. Similar to that observed with constant-velocity cases (Figure 5.191) flame temperature remained nearly the same as premixing was increased and, yet, soot volume fraction increased. However, it seems, there is a maximum value for the soot generated in the trailing jet flame which occurs when the equivalence ratio reaches 23. Nevertheless, both constant-velocity and constant-ethylene-flow-rate approaches yielded higher soot in partially premixed jet flames.

For comparison purpose, calculations for the coaxial jet flame of McEnally and Pfefferle (2000) are made using UNICORN code. Radial distributions at a flame height of 40 mm are shown in Figure 5.197 for different equivalence ratios. As noted in the experiment McEnally and Pfefferle (2000), calculations have yielded increasing temperatures and decreasing soot with premixing.

As suggested by the soot model used in the present study, acetylene concentration is also decreased with premixing (Figure 5.197c). Interestingly, the acetylene concentration in the trailing jet flame of the centerbody also decreased with premixing as shown in Figure 5.198. However, soot was increasing in the trailing jet flame while it has decreased in the normal jet flame with premixing. This difference suggests that the recirculation zone established near the base of the trailing jet flame is playing a key role for the increase in soot. Acetylene distribution in the recirculation zone is shown in Figure 5.199 for different equivalence ratios.

Flame locations are also marked in this plot. For pure diffusion flame (infinity case), acetylene peaks near the flame surface. However, more and more acetylene is formed closer to the fuel jet, as air added to the fuel jet. The fuel-side recirculation zone (Figures 5.188 and 5.192) then become more effective in transporting acetylene and soot into the trailing jet flame. Such transport from recirculation zone to the trailing jet flame caused soot to increase. Due to the complex nature of the flow and chemistry in centerbody flames it is difficult to identify the exact transport mechanism for soot enhancement. However, this transport can be studied and identified through performing some numerical experiments.

In summary, calculations performed by partially premixing the fuel jet with air suggested that soot in the recirculation zone decreases and that in the trailing jet flame increases with the amount of premixing. The latter effect was surprising and contradicted the understanding gained on partially premixed coaxial jet flames; in which, soot decreased with premixing. Experimental and numerical studies were undertaken to resolve this anomaly. Calculations have reasonably predicted the structure of the partially premixed centerbody flames for various equivalence ratios. Experiments have confirmed the counterintuitive soot enhancement in the trailing jet flame with the addition of air to the fuel jet. It was found that flame movement in the recirculation zone increases soot-particle burnout and reduces the amount of soot. Such flame movement also enhances the influence of the fuel-side recirculation zone on flame structure and, thereby, increases the transport of acetylene and soot into the trailing jet flame.

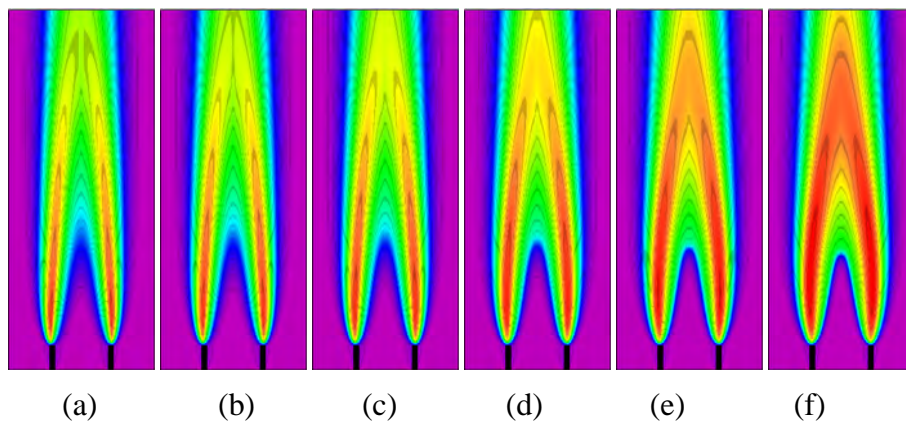


Figure 5.182 Temperature distributions computed for partially premixed jet flames for equivalence ratios (a) inf, (b) 24, (c) 12, (d) 6, (e) 4, and (f) 3.

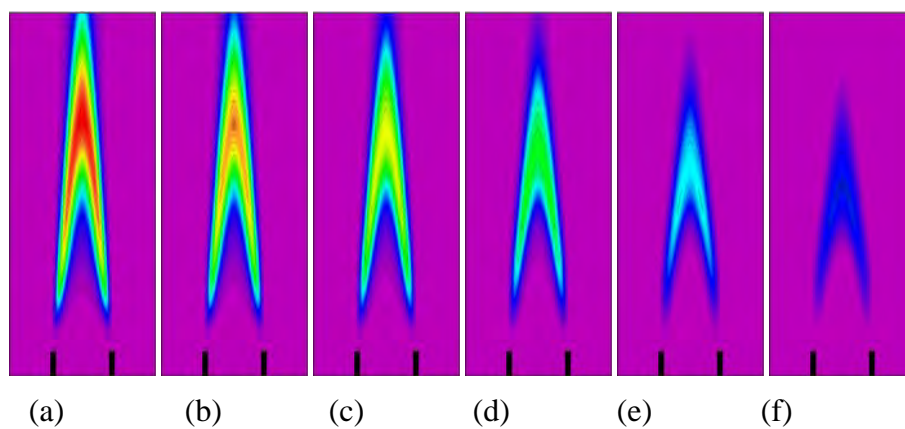


Figure 5.183 Soot distributions computed for partially premixed jet flames for equivalence ratios (a) inf, (b) 24, (c) 12, (d) 6, (e) 4, and (f) 3.

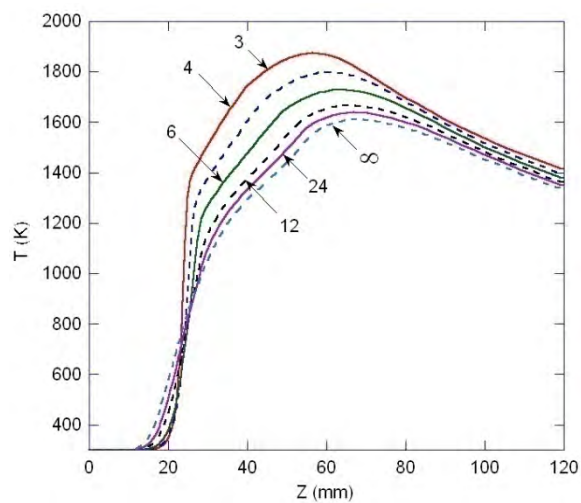


Figure 5.184 Computed temperature distributions along the centerline for various partially premixed jet flames.

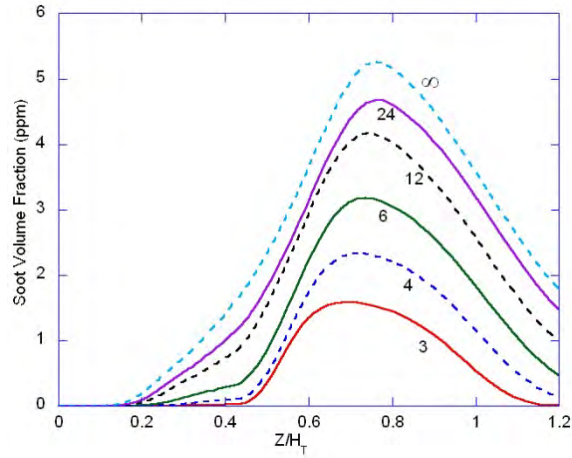


Figure 5.185 Computed soot distributions along the non-dimensional axial position for various partially premixed jet flames.

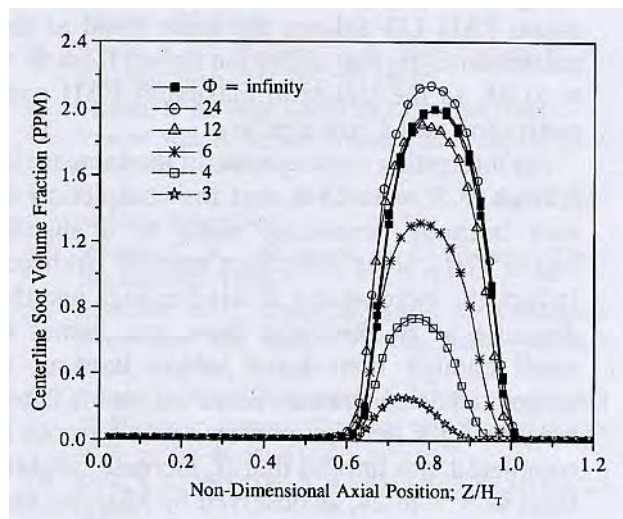


Figure 5.186 Measured soot along the non-dimensional axial position for various partially premixed jet flames.

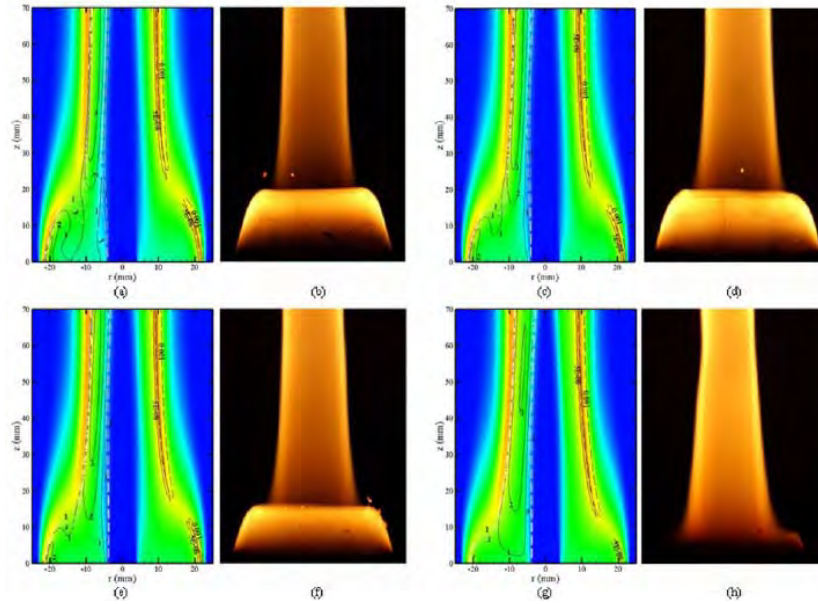


Figure 5.187 Comparisons between computed and experimental flames obtained with fixed fuel jet velocity and for equivalence ratios 107 (a and b), 46 (c and d), 23 (e and f), and 11 (g and h). Computed iso contours of  $C_2H_2$  (left side), CH (solid lines on right side), and OH (broken lines on right side) are superimposed on temperature distributions (blue and red representing 300 and 1800 K, respectively) in a, c, e, and f. Direct photographs are shown in b, d, f, and h.

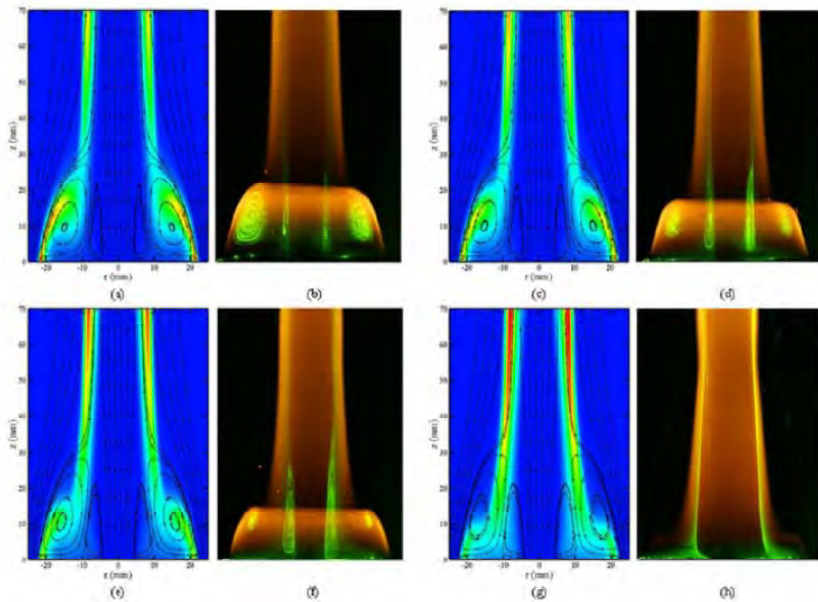


Figure 5.188 Comparisons between computed and experimental flames obtained with fixed fuel jet velocity and for equivalence ratios 107 (a and b), 46 (c and d), 23 (e and f), and 11 (g and h). Computed streamlines are superimposed on soot-radiation distributions (rainbow color with blue and red representing 0 and max, respectively) in a, c, e, and f. Direct photographs taken with Nd:YAG laser turned on are shown in b, d, f, and h.



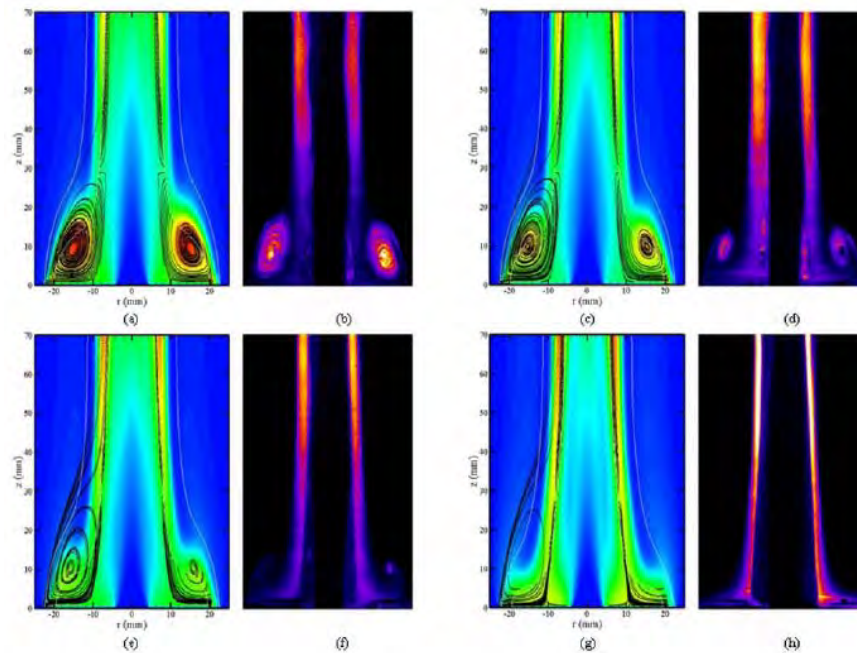


Figure 5.189 Comparisons between computed and experimental flames obtained with fixed fuel jet velocity and for equivalence ratios 107 (a and b), 46 (c and d), 23 (e and f), and 11 (g and h). Computed particle trajectories (without burn off on left half and with burn off on right half) are superimposed on soot distributions (blue and red representing 0 and 7 ppm, respectively) in a, c, e, and f. Laser induced incandescence (LII) images of soot are shown in b, d, f, and h.

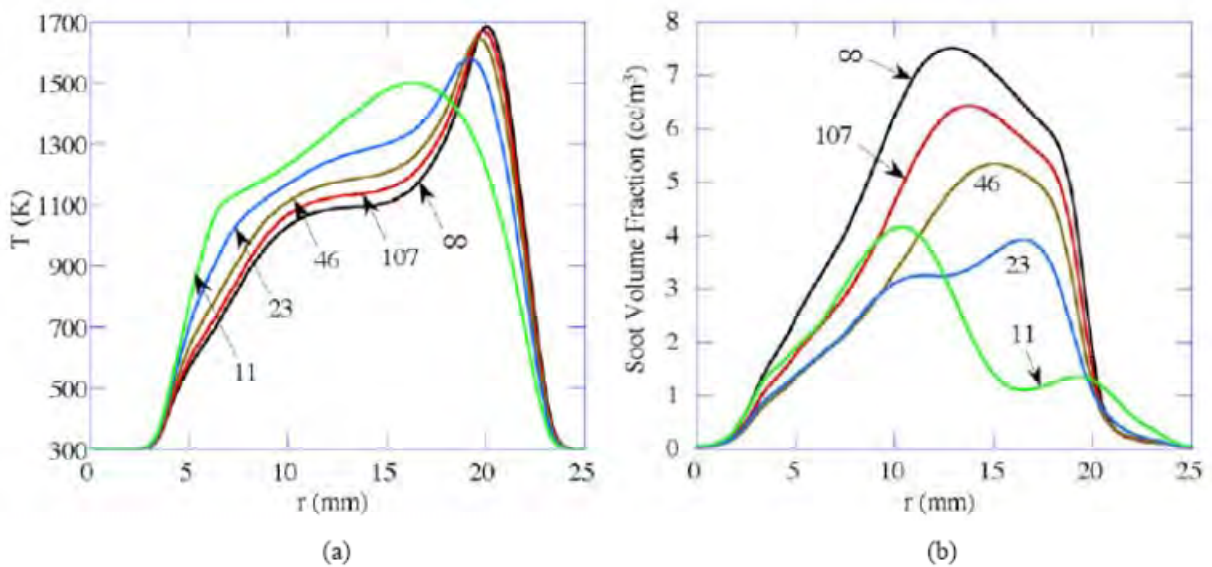


Figure 5.190 Radial distributions of temperature (a) and soot (b) in the recirculation zone 10 mm above the burner surface for different equivalence ratios achieved through keeping the fuel jet velocity constant.

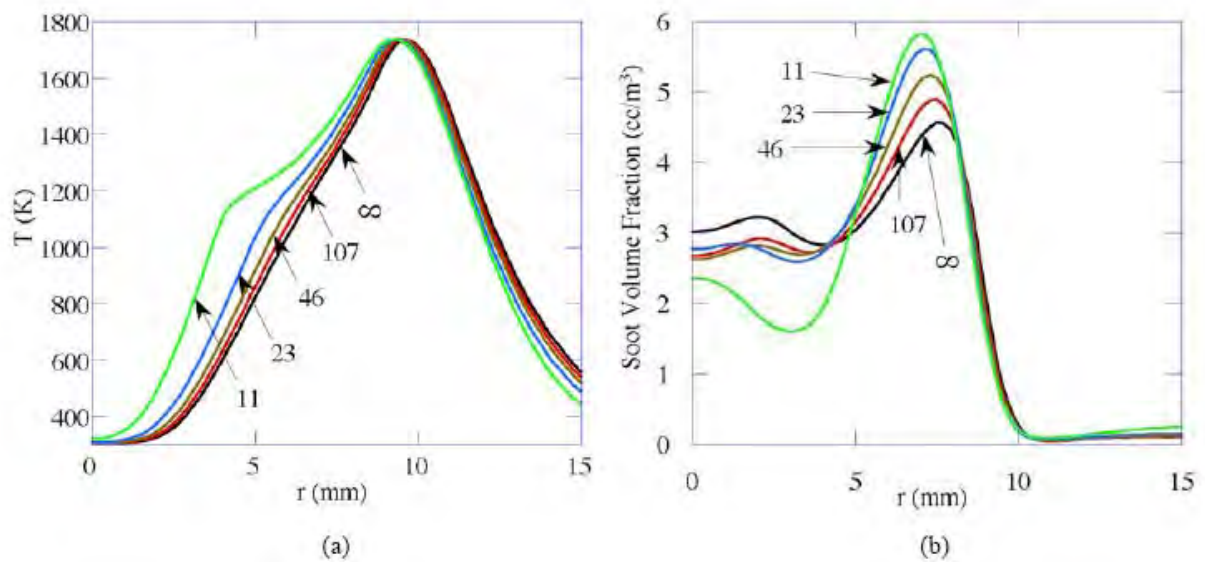


Figure 5.191 Radial distributions of temperature (a) and soot (b) in the trailing flame 70 mm above the burner surface for different equivalence ratios achieved through keeping the fuel jet velocity constant.

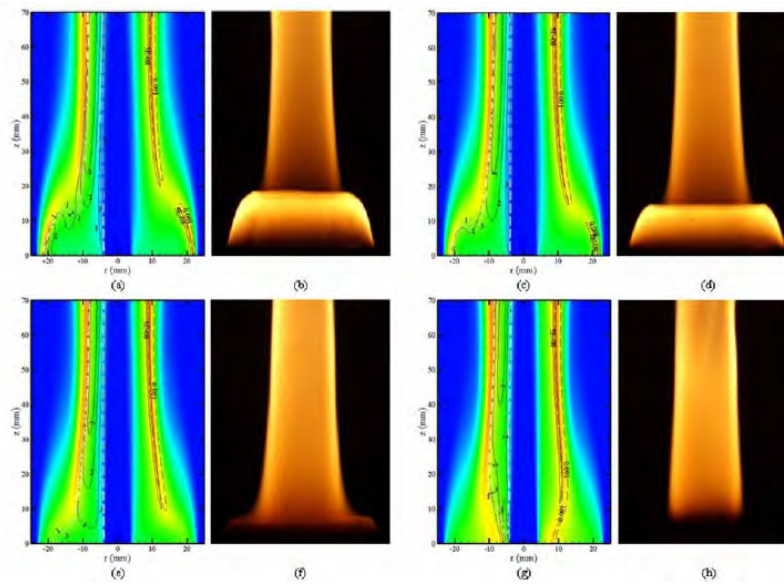


Figure 5.192 Comparisons between computed and experimental flames obtained with fixed ethylene flow rate and for equivalence ratios 107 (a and b), 46 (c and d), 23 (e and f), and 11 (g and h). Computed iso contours of  $\text{C}_2\text{H}_2$  (left side),  $\text{CH}$  (solid lines on right side), and  $\text{OH}$  (broken lines on right side) are superimposed on temperature distributions (blue and red representing 300 and 1800 K, respectively) in a, c, e, and f. Direct photographs are show in b, d, f, and h.

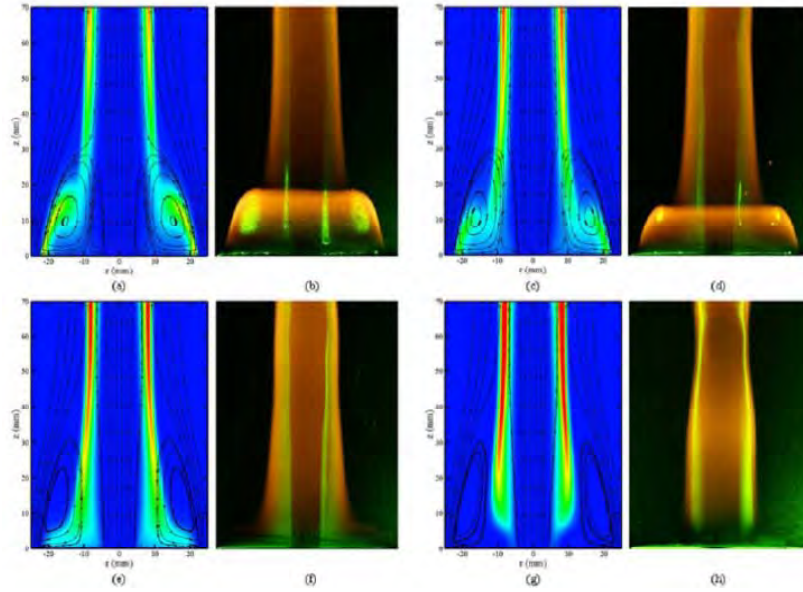


Figure 5.193 Comparisons between computed and experimental flames obtained with fixed ethylene flow rate and for equivalence ratios 107 (a and b), 46 (c and d), 23 (e and f), and 11 (g and h). Computed streamlines are superimposed on soot-radiation distributions (rainbow color with blue and red representing 0 and max, respectively) in a, c, e, and g. Direct photographs taken with Nd:YAG laser turned on are shown in b, d, f, and h.

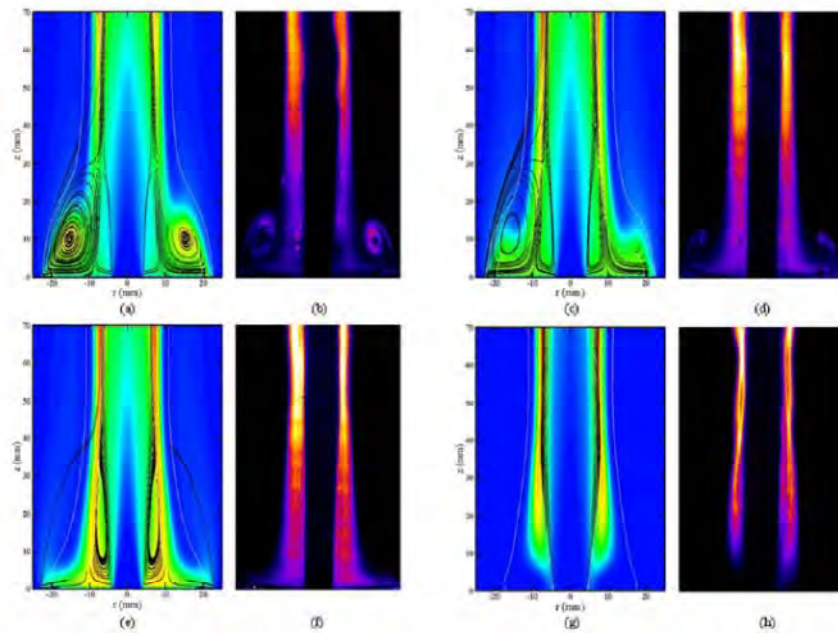


Figure 5.194 Comparisons between computed and experimental flames obtained with fixed ethylene flow rate and for equivalence ratios 107 (a and b), 46 (c and d), 23 (e and f), and 11 (g and h). Computed particle trajectories (without burn off on left half and with burn off on right half) are superimposed on soot distributions (blue and red representing 0 and 7 ppm, respectively) in a, c, e, and g. Laser induced incandescence (LII) images of soot are shown in b, d, f, and h.



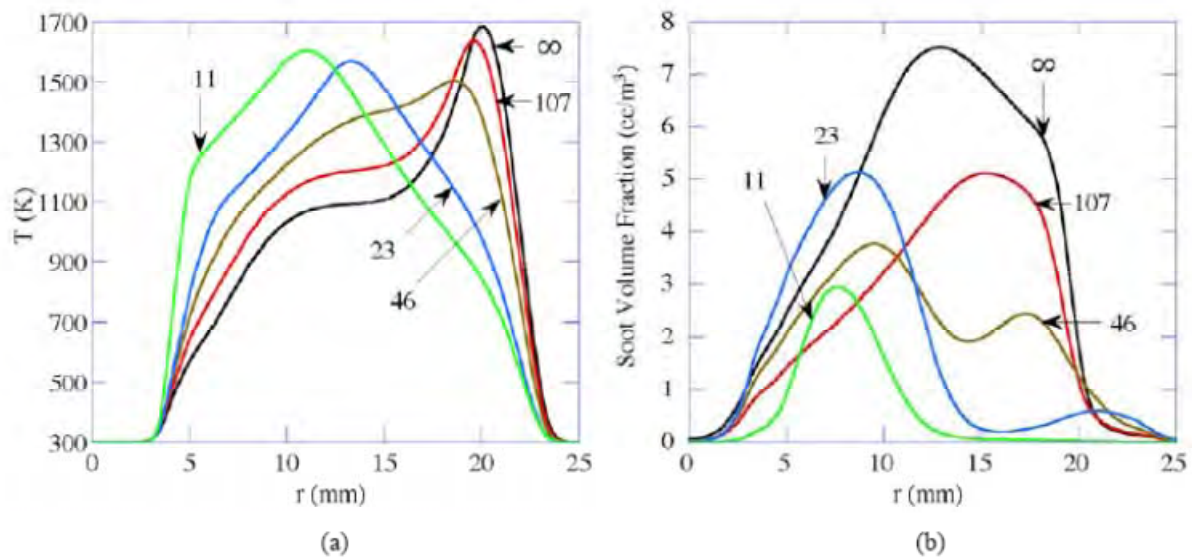


Figure 5.195 Radial distributions of temperature (a) and soot (b) in the recirculation zone 10 mm above the burner surface for different equivalence ratios achieved through keeping the ethylene flow rate constant.

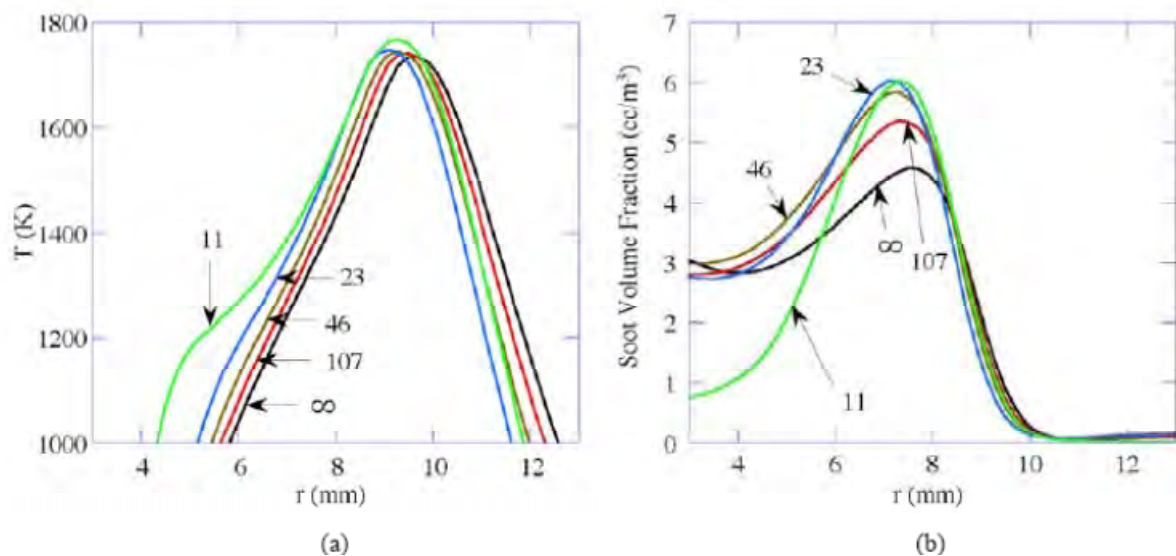


Figure 5.196 Radial distributions of temperature (a) and soot (b) in the flame 70 mm above the burner surface for different equivalence ratios achieved through keeping the ethylene flow rate constant.

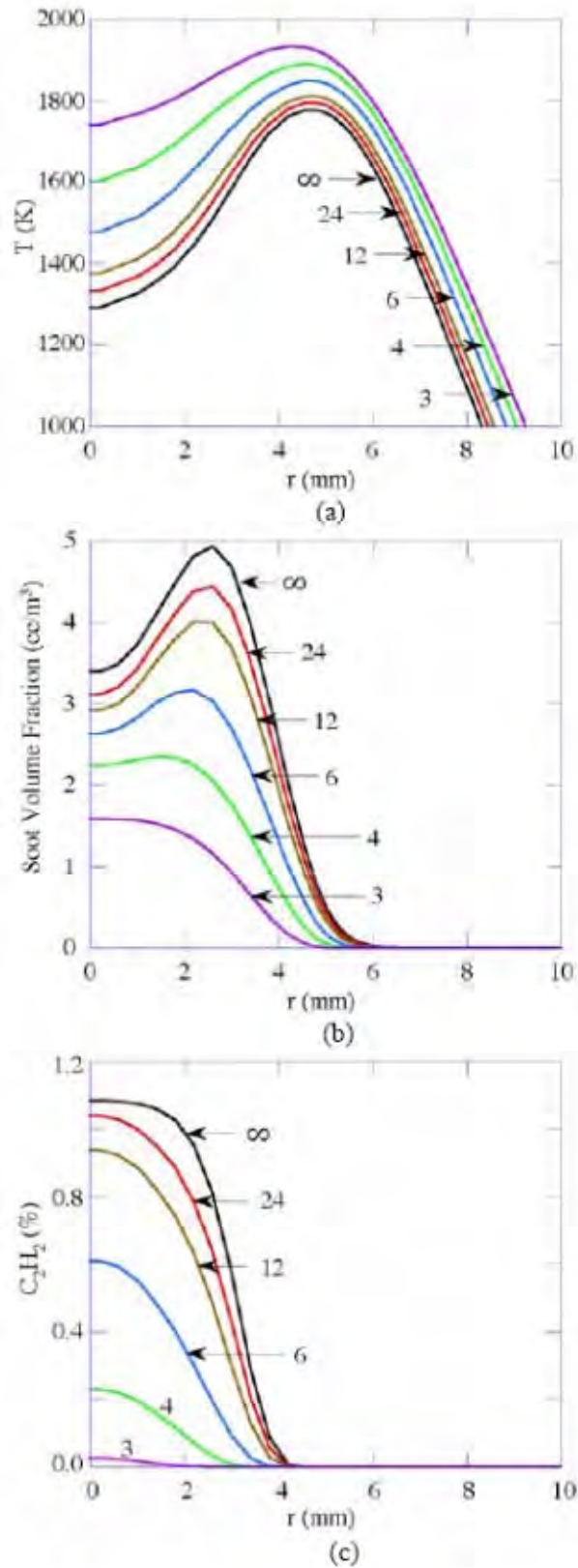


Figure 5.197 Temperature (a), soot (b), and acetylene (c) distributions for different equivalence ratios across the flames established without the recirculation zones at 40 mm above the burner.

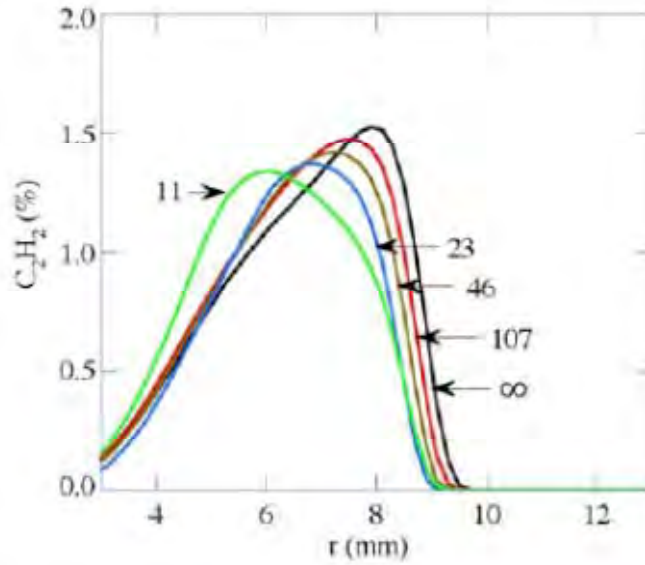


Figure 5.198 Acetylene distributions for different equivalence ratios across the trailing flames ( $z = 70$  mm) established in centerbody burner.

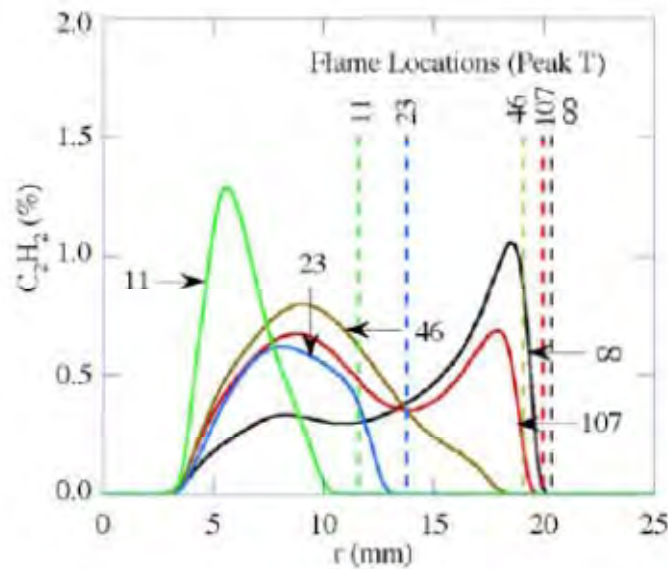


Figure 5.199 Acetylene distributions in the recirculation zones ( $z = 20$  mm) for flames established in centerbody burner with different equivalence ratios.

#### 5.4.6 Comparisons with Experiments

Quantitative soot-volume-fraction data from the LII images shown in Figure 5.189 were obtained using the analyses provided in the Diagnostic-Methods Section (4.5.3). LII data for each case are shown on both sides of the flame. Quantitative data obtained on both sides of the  $\phi = \infty$  flame at several heights are shown in Figure 5.200, along with the corresponding soot volume fractions obtained in the simulations. Radial distributions of temperature are also shown in these figures

using dashed lines. Note that the  $z = 10$  mm height corresponds to the outer recirculation zone (ORZ) center, while the  $z = 25$ -mm location falls in the region between the recirculation zone (RZ) and the trailing-jet flames. The thicknesses of the predicted soot layers at different heights, except at  $z = 25$  mm, matched well with those obtained from LII measurements. The two-equation soot model used in these simulations was developed by Lindstedt et al. (1994) for pure-ethylene jet diffusion flames and was neither modified for the centerbody-flame applications nor adjusted for the partially premixed fuels. As expected, the agreement between the predictions and the results of LII measurements is reasonable in the trailing jet flame (Figures 5.200c-5.200e) and poor in the recirculation-zone flame. The model significantly overpredicts not only the peak soot volume fraction but also the total soot (integrated) in the RZ (Figure 5.200a). The overprediction in the outer regions of the RZ ( $r > 18$  mm) could be due to insufficient soot oxidation. On the other hand, the lower concentrations of soot in the experiment near the core of the ORZ and closer to the fuel jet ( $r < 15$  mm) are due, in part, to the soot-mass losses observed in the experiment. Soot particles in the RZ grew in size and dropped off onto the face of the centerbody because of gravity. A significant amount of soot buildup occurred within a few minutes after the flame was initiated under these flow conditions. Current convection-diffusion-based soot models do not account for these losses.

Predicted soot distributions for the  $\phi = 46$  flame are compared with data from LII measurements in Figure 5.201. Soot buildup (soot loss) on the centerbody plate decreased significantly in the experiments for equivalence ratios  $< 46$ . Such decrease in soot loss correlates with the reduced amount of soot in the RZ and leads to improvement in the comparisons between measurements and predictions (Figure 5.201a). Overall, good comparisons between experiment and predictions were obtained for the  $\phi = 46$  flame case (Figure 5.201a-5.201e). Soot-layer thicknesses and magnitudes from predictions compare very well with those from measurements made in the trailing-jet flame (Figures 5.201c-5.201e) and also in the region joining the RZ and trailing-jet flames (Figure 5.201b). Predicted and measured soot volume fractions are compared for equivalence ratios of 11 and 5 in Figures 5.202 and 5.203, respectively. The following observations were made from the comparisons made in Figures 5.200-5.203:

- Soot in the trailing-jet flame increases when a very small amount of air is added to the fuel jet ( $\phi \sim 46$ ) and then decreases with further addition of air ( $\phi < 46$ ). The calculations predicted these trends. On the other hand, the model failed to predict the thinning of the soot layer with a decrease in the equivalence ratio. In fact, the calculations suggested that the soot-layer thickness of the trailing jet flame is insensitive to variations in equivalence ratio.
- The calculations predicted that soot in the RZ decreases with an increase in premixing ( $< \phi$ ). The LII measurements, in general, supported these predictions. Measurements in the  $\phi = \infty$  flame are influenced by the soot loss to the centerbody surface.
- In the calculations, soot generated and entrained into the ORZ is not completely oxidized, even when the equivalence ratio is decreased to 5. Wings in the calculated profiles resulting from the soot in the ORZ are present up to heights of 70 mm in all flames. On the other hand, in the experiments, soot generated/entrained in the ORZ was completely oxidized within the ORZ. No traces of ORZ-associated soot were found at heights  $> 25$  mm.

- In both experiments and calculations, soot generated/entrained in the IRZ was transported away from the RZ and joined with that generated in the trailing jet flame (peak in soot volume fraction developed at  $r \sim 7$  mm at 10-mm height can be traced at all other heights).
- Addition of air to the fuel jet (partially premixing) influenced the temperature profiles on the fuel side and did not affect the peak values. In comparison, its effects on soot profiles are significantly less dramatic, except in the RZs where sooting characteristics are modified significantly due to the movement of the flame surface. In other words, the observed effects of partial premixing on sooting characteristics of the centerbody burner are caused due to the changes in the physical structure (location) of the flame rather than due to the changes in the chemical structure.

Overall, the two-equation soot model performed fairly well in predicting the sooting behavior of the trailing jet flames in the centerbody burner and failed in predicting the sooting behavior of the RZ flames. It is thought that the inadequacies of the model can be corrected through the addition of a submodel that follows a Lagrangian-based particle-tracking approach.

The computed dynamic flames of centerbody burner are compared with the infrared images of the experimental flame. The direct photographs (Figure 5.175) of the dynamic centerbody flame show the necking and bulging of the soot column (yellow color) and flame surface (blue color), however they do not show the vortical structures that are actually causing such necking and bulging. The hot product gases advected away from the flame by the vortical structures can be visualized using thermal imaging. Computed flame structure is compared with an infrared image of the flame in Figure 5.204. The instantaneous image shown in Figure 5.204b was obtained using an FLIR SC4000 IR camera mounted with a 25 mm lens. The angle of divergence from the center of the flame to the camera is small; therefore the planar images provide essentially the line-of-sight (LOS) measurement through the flame. The computed flame shown in Figure 5.204a was obtained with 10% amplitude (flame in Figure 5.177) and through qualitatively matching the phase of the thermal image in Figure 5.204b. Instantaneous locations of the particles injected from the edge of the centerbody are superimposed on the left side of the color temperature plot (Figure 5.204a). Computed vortical structures matched very well with those visualized in the thermal image. The decaying of computed vortical structures in the downstream locations is due to the coarse mesh used in those regions. Particle distributions near the flame surface suggest that the vortices in upstream locations ( $z < 90$  mm) are rolling inward from top (clockwise on the left side) and are rolling outward from bottom (counterclockwise on the left side) in downstream locations ( $z > 90$  mm). The shape of the thermal image of the flame (Figure 5.204b) confirms this change in the direction of vortex roll, which was also observed by the authors in buoyant jet diffusion flames. Such change in vortex roll results from the buoyant acceleration of hot gasses along the flame surface.

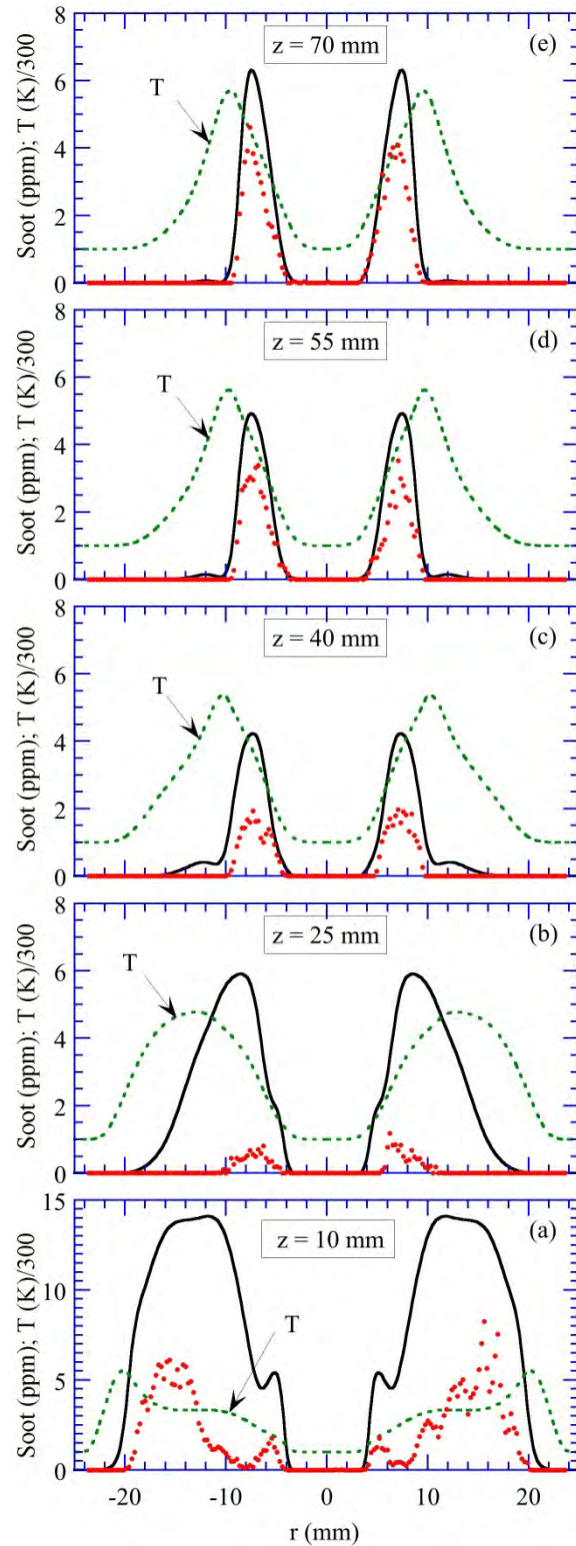


Figure 5.200 Comparison of measured and computed soot distributions in radial directions at different heights for the pure-diffusion-flame ( $f = \infty$ ) case.



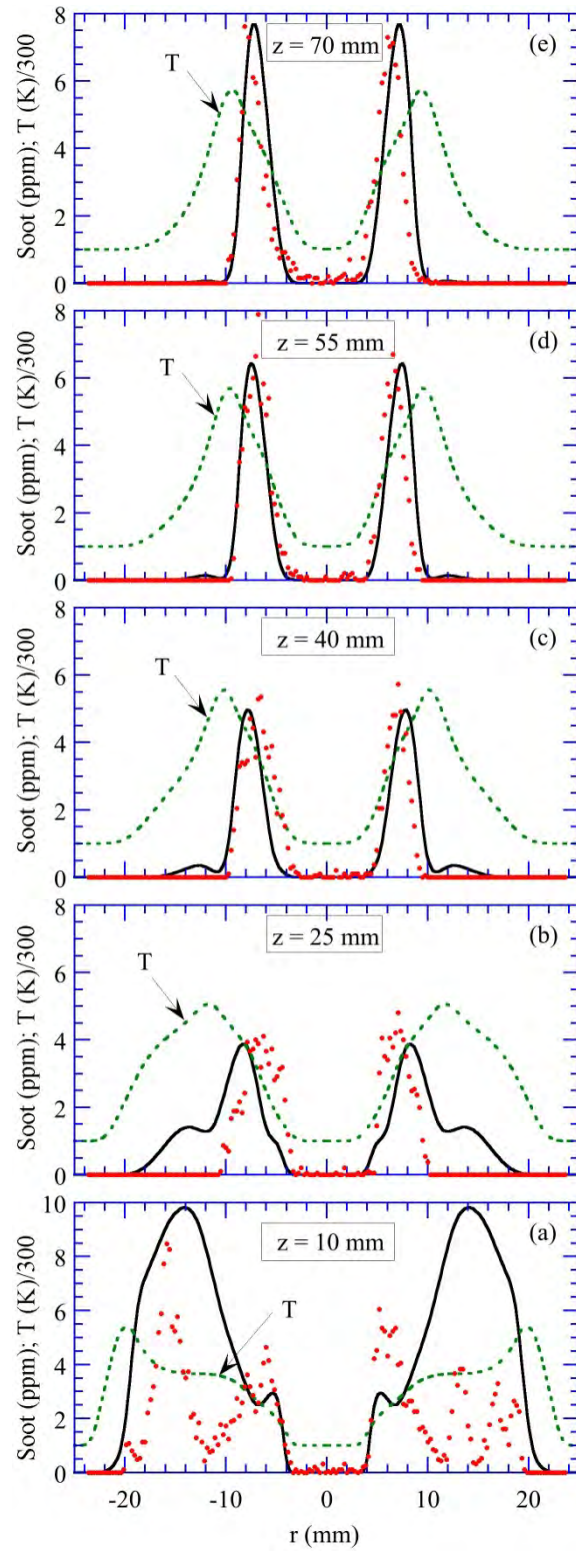


Figure 5.201 Comparison of measured and computed soot distributions in radial directions at different heights in a partially premixed flame with equivalence ratio of 46.

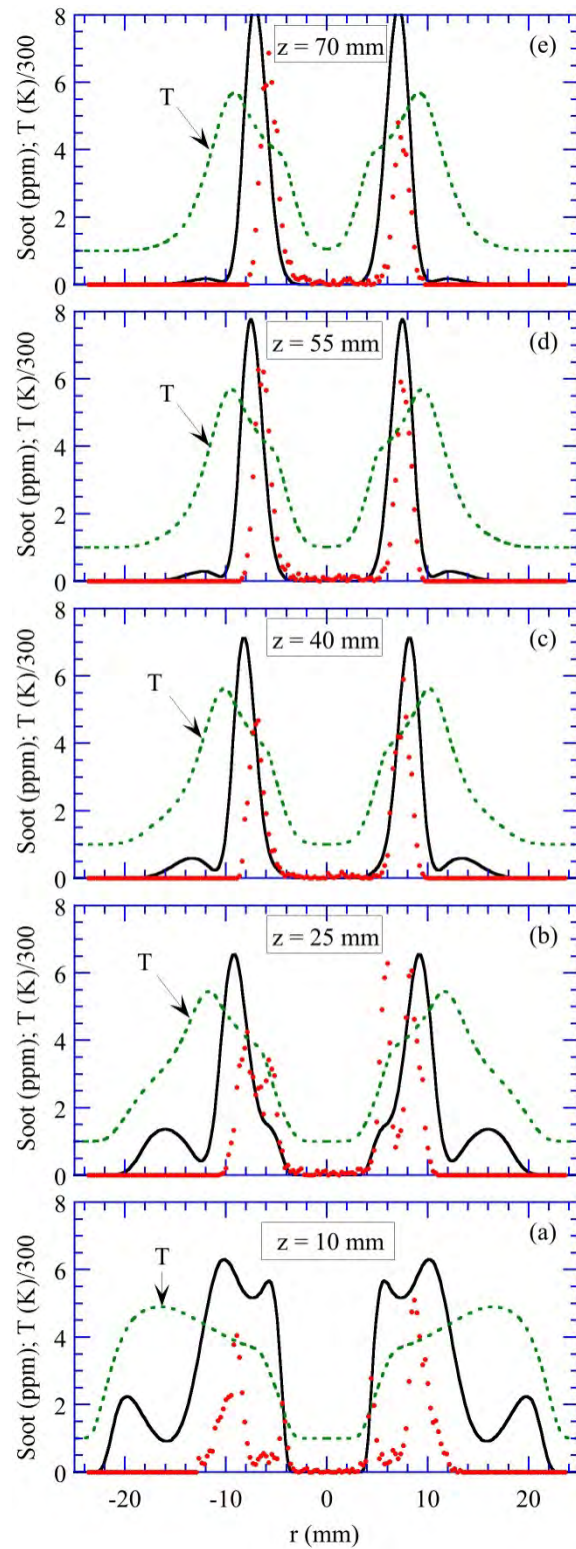


Figure 5.202 Comparison of measured and computed soot distributions in radial directions at different heights in a partially premixed flame with equivalence ratio of 11.



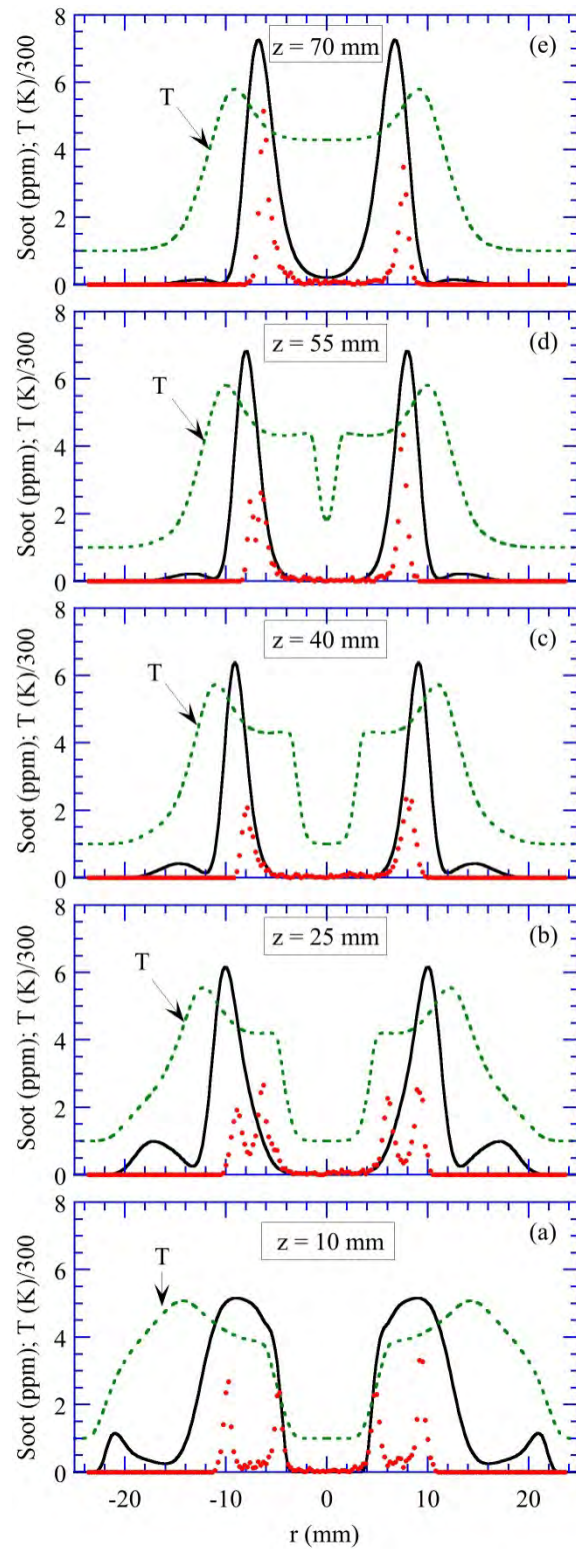


Figure 5.203 Comparison of measured and computed soot distributions in radial directions at different heights in a partially premixed flame with equivalence ratio of 5.

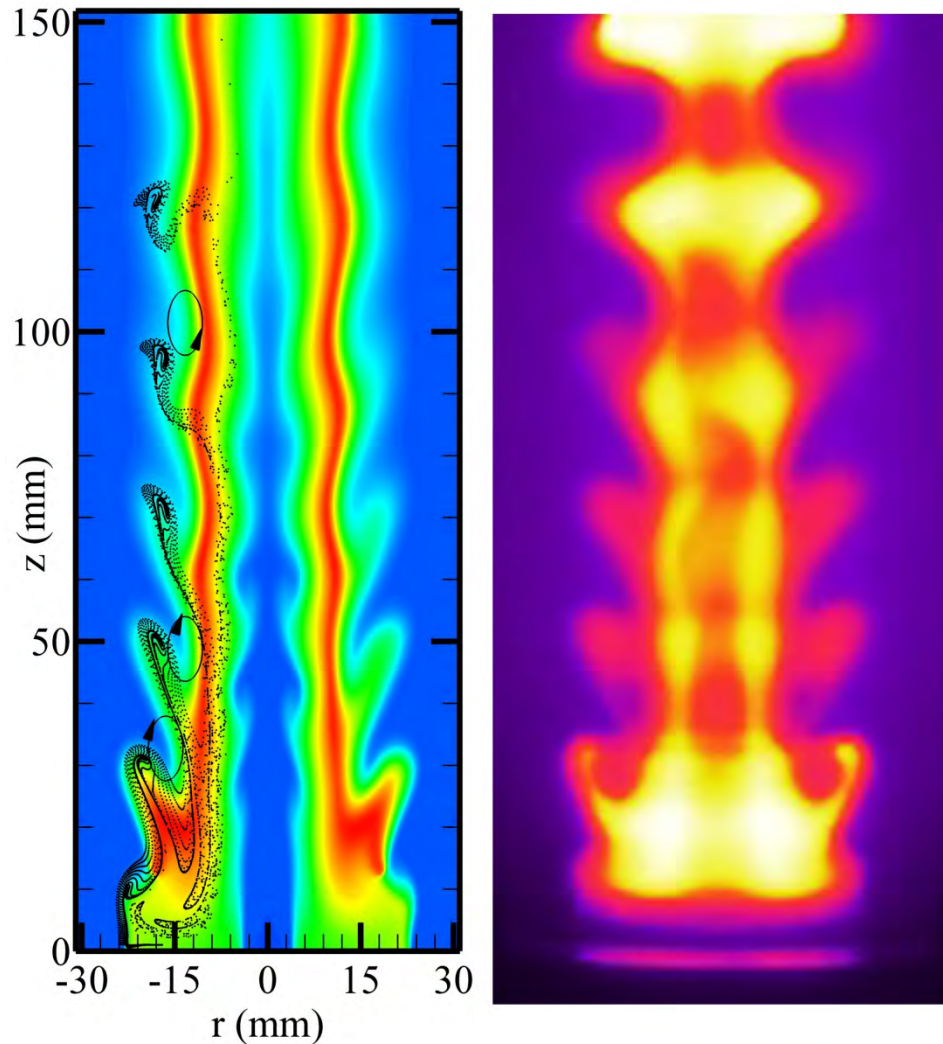


Figure 5.204 Comparison of computed instantaneous flame structure with infrared image of experimental flame in Figures 5.174 and 5.175 (a) Temperature distribution at instant  $t_0+16$  ms. Instantaneous locations of particles injected from the edge of centerbody are superimposed in left half. (b) Thermal image of flame obtained with IR camera with 1-ms exposure time.

#### 5.4.7 Autoignition Phenomenon

Numerical studies have been conducted for understanding the stabilization mechanism of the flame that is lifted and anchored by the recirculation zones of the centerbody burner. A detailed view of the base region of one such lifted flame is shown in Figure 5.205. Here, the calculated heat release rate is shown in rainbow colors. Iso-contours of temperature and CH concentration in ppm are superimposed using white and black thin lines, respectively. Iso-contours of the local equivalence ratio are shown using thick black lines, and the stoichiometry surface obtained from the global equivalence ratio is shown using a broken black line. The velocity field is also shown in this figure. As ethylene diffuses toward the flame, it begins to decompose into smaller hydrocarbon fragments and  $H_2$ . Because of this fuel decomposition, the stoichiometry surface computed based on ethylene and oxygen concentrations (black broken line) significantly deviates from the actual stoichiometry surface (black, thick solid line marked with 1) computed based on

local species concentrations. The separation between the two stoichiometric surfaces is most pronounced near the flame base.

Various branches of the flame can be identified in Figure 5.205 from the heat-release-rate distribution. All of these flame branches are separated by the local stoichiometry surface. The fuel-lean and fuel-rich branches located on the right and left sides, respectively, are conspicuous because of the significant heat release rates associated with these flames. The diffusion flame is located along the stoichiometry surface, downstream of the flame base. A triple point (TP) forms in the flame base where all three flame-branches meet. Its approximate location is shown in Figure 5.205 with a black dot. The autoignition branch located upstream of the fuel-rich flame is unique to the lifted flame that is supported by a RZ. As discussed previously, the flame base shown in Figure 5.205 is anchored at its location mainly because of the chemical reactions that are taking place along the autoignition branch in the no-flame region upstream of the flame base. Even though autoignition is occurring in the fuel-rich region because of the temperature distribution across the diffusion layer, the peak-heat-release-rate location quickly moves to the stoichiometry surface once the ignition process is completed near the flame base. Since CH production peaks on the fuel side of the flame surface, a hook-type distribution is established in its concentration field around the TP.

The structure of the autoignition branch is shown in Figure 5.206. Radial distributions of temperature, fuel species ( $C_2H_4$  and  $H_2$ ), radical species (OH and  $CH_3$ ), and axial velocity at a height of 9 mm are plotted in Figure 5.206a. The corresponding heat release rate and molar production rates of  $C_2H_4$ ,  $H_2$ ,  $CH_3$ , and OH are plotted in Figure 5.206b. The location of the stoichiometry is also indicated in these figures. The temperature is nearly constant at  $\sim 1100$  K in the recirculation region and then gradually decreases to 300 K in the diffusion layer between the ORZ and the air jet. Ethylene fuel is transported radially outward initially by the RZs and then through molecular diffusion in the diffusion layer between 21 and 24 mm. Because of the combination of temperature and ethylene and oxygen concentrations, autoignition reactions are occurring on the fuel-rich side at  $\sim 20$  mm. Small amounts of radicals are produced, and about  $6 \text{ W/cm}^3$  of heat is released from these reactions. Only a negligible rise in temperature is observed in this reaction zone. Even though the ethylene consumption rate is peaking in this reaction zone, its consumption is extended well into the RZ. Hydrogen production follows the ethylene consumption pattern. Gradual production along the autoignition branch in the no-flame region and accumulation caused the hydrogen concentration to reach  $\sim 2\%$  in the RZ.

The structure of the flame along the radial line passing through the TP ( $z = 13.5$  mm) is shown in Figure 5.207. It is assumed that the TP is located on the stoichiometry surface where the heat release rate is the highest ( $z = 13.5$  mm and  $r = 21.15$  mm). The variables shown in Figure 5.207 are identical to those depicted in Figure 5.206; however, note the differences in the scales. Ignition has taken place at this location, and exothermic reactions have started to increase the temperature. Hydrogen that has been accumulated to 2% in the RZ is now being consumed near the flame front ( $r \sim 21$  mm). The velocity at the TP has decreased slightly because of the burning of premixed mixture. Interpolation of velocity through the dip region suggests that it would have been  $\sim 0.8$  m/s had the local mixture not been ignited. This velocity is the same as that present near the stoichiometry surface in the autoignition branch (Figure 5.206)-suggesting that the flame base did not stabilize at  $z \sim 13.5$  mm due to a lower velocity. As discussed previously, the autoignition reactions that took place in the no-flame region provided the necessary ignition and

stability for the flame base. The presence of the OH peak on the fuel side of the stoichiometry surface indicates that premixed-type combustion is taking place near the TP. Oxygen diffused to the fuel side has mixed with the fuel (and its fragments) and established a premixed flame. Simultaneous progress of the fuel- and oxygen-related reactions has led to positive production rates for  $\text{CH}_3$ , OH, and  $\text{H}_2$  at the TP.

The distributions of axial and radial velocities and temperature along the stoichiometry surface (or line) are shown in Figure 5.208. Temperature has increased gradually from 552 K to 631 K in the autoignition region ( $0 < z < 13$  mm) along the stoichiometry. Axial velocity ( $U$ ) increased steeply in the boundary-layer region near the centerbody plate and then gradually in the autoignition region. As the highly viscous fluid in the flame base acts like an obstruction to the incoming fluid, axial velocity decreased upstream of the flame base and then accelerated in the flame zone due to volumetric expansion. Absence of any significant change in the radial velocity ( $V$ ) upstream of the flame base indicates that the local streamline is not curving (could happen because of ORZ) and the dip in  $U$  is due to flame obstruction only. Without the flame  $U$  would have followed the long-dashed line shown in Figure 5.208 and, clearly, would not have stabilized a diffusion or premixed flame. The temperature and velocity distributions in Figure 5.208 further support the hypothesis that the autoignition branch indeed is stabilizing the lifted flame in the centerbody burner.

The structure of the trailing flame is shown in Figure 5.209. Radial distributions of temperature, velocity, and species concentrations obtained at  $z = 40$  mm are shown in Figure 5.209a, and those of the heat release rate and species production rates are shown in Figure 5.209b. Expansion due to combustion and buoyant acceleration of hot gases usually accelerate flow near the flame surface. However, the velocity at the stoichiometry surface at  $z = 40$  mm is lower than that existing in the upstream locations (Figures 5.206b and 5.207b) because of the flow divergence taking place downstream of the RZ. The presence of  $\text{CH}_3$  and OH radicals on the two opposite sides of the stoichiometry is typical of a diffusion flame. Interestingly,  $\text{C}_2\text{H}_4$  and  $\text{H}_2$  that were diffused into the air jet in the locations upstream of the flame base were not consumed in the fuel-lean branch of the triple flame. The presence of  $\text{H}_2$  in the air stream is also evident in the concentration plots. These fuel species remained in the air jet at  $z = 40$  mm, and their consumption rates decreased to a very low value (Figure 5.209b). As a result, these fuel fractions become unburned fuels and escape along with the unused air.

It is hypothesized in this work that the recirculation-zone-supported lifted flame becomes stabilized because of the autoignition reactions that are taking place in the no-flame region upstream of the flame base. This means that events which can alter the autoignition reactions should destabilize the flame that is anchored at  $z = 13.5$  mm. Because of the low temperatures ( $< 1100$  K), soot is not produced during the autoignition process. However, calculations predicted (Figure 5.166) and experiments supported (Figure 5.165) that a significant amount of soot is present in the RZs. It is understood that in addition to combustion products, soot also becomes entrained into the RZs from the downstream flame regions. One can easily conclude that the soot in the RZ is influencing the autoignition reactions thermodynamically through radiation and chemically through the soot-oxidation (burnout) process in which soot consumes OH and O radicals in addition to  $\text{O}_2$  molecules. If the proposed hypothesis on flame stabilization is correct, then soot must be playing an important role in the stability process. This can be easily tested in the simulations by changing the sooting characteristics of the computed flame.

Calculations for the lifted flame are repeated after 1) turning off the radiation from soot, and then 2) turning off the soot production in the chemistry model. Results obtained from the first simulation are shown on the left half of Figure 5.210. Iso-contours of OH and soot concentrations are superimposed on the temperature distribution. Interestingly, the flame base moved  $\sim 5$  mm upstream when the radiation from soot was ignored. The location of the original flame base is indicated by a horizontal broken line. In the absence of radiation losses from soot, the temperature of the gasses in the RZ increased by up to 100 K, depending on the location and acceleration of the autoignition reactions, which, in turn, moved the ignition location closer to the shorter residence time. Movement of the flame base closer to the centerbody plate exposed more of the flame surface to the RZ, which, in turn, entrained more soot into the RZ. Nearly 2.7 times more soot is accumulated at the center of the ORZ in the flame shown in the left half of Figure 5.210 than that shown in Figure 5.166.

The results obtained after turning off the soot-production terms in the model are shown on the right half of Figure 5.210. The flame in Figure 5.166 was used as the initial (starting) solution. The calculations have been performed for a sufficiently long time that all of the soot in the computational domain has been transported away. As expected, the flame base moved upstream all the way to the face of the centerbody and anchored to the outer edge, yielding a flame structure similar to those obtained in the earlier studies (Figures 5.159-5.161). It is known that O and OH radicals oxidize soot and, in the process, become consumed. Absence of soot in the flame in the right half of Figure 5.210 increased the concentrations of these radical species in the RZ, which, in turn, enhanced the autoignition reactions and advanced the ignition point closer to the centerbody plate. As a sanity check, calculations were repeated using the flame shown in the right half of Figure 5.210 as the initial solution and turning on the soot-production reactions in the chemistry model, which yielded the flame in Figure 5.166 after  $\sim 5000$  time steps. The results of numerical experiments shown in Figure 5.210 confirm that the lifted flame in Figure 5.166 is stabilized by the autoignition reactions taking place in the no-flame region upstream of the flame base.

Unlike in a normal jet diffusion flame, the base of a lifted diffusion flame in a centerbody burner is established and supported by the autoignition process that takes place in the no-flame region upstream of the flame edge. The hot combustion products formed downstream of the flame base are transported toward the centerbody plate by the two RZs (ORZ and IRZ). The elevated temperature of the RZ preheats the mixing layer that is formed between the fuel fragments that are diffusing outwardly and the oxygen that is diffusing inwardly and promotes the autoignition reactions. Ignition takes place, and a flame becomes established at a location where the ignition-delay time matches the flow-residence time.

Soot transported into the RZs was found to play a key role in increasing the ignition-delay time and, thereby, the lift-off height through 1) radiation, which decreases temperature and 2) soot oxidation, which decreases O and OH radical concentrations. Ethylene and its lighter fragments that are diffused into the air jet in the no-flame region are not completely consumed by the flame and remain as unburned fuels. Concerning the three probable soot-forming species; acetylene is produced in the downstream flame locations and gets transported into the RZs, benzene and pyrene are produced in the RZ. The column-shaped soot observed in the experiments and predicted in the simulations performed with the acetylene-based soot model indicated that soot is

transported into the RZ from downstream locations, similar to that of acetylene. Centerbody flames with RZs provide a platform for studying the species that are responsible in the generation of initial soot particles.

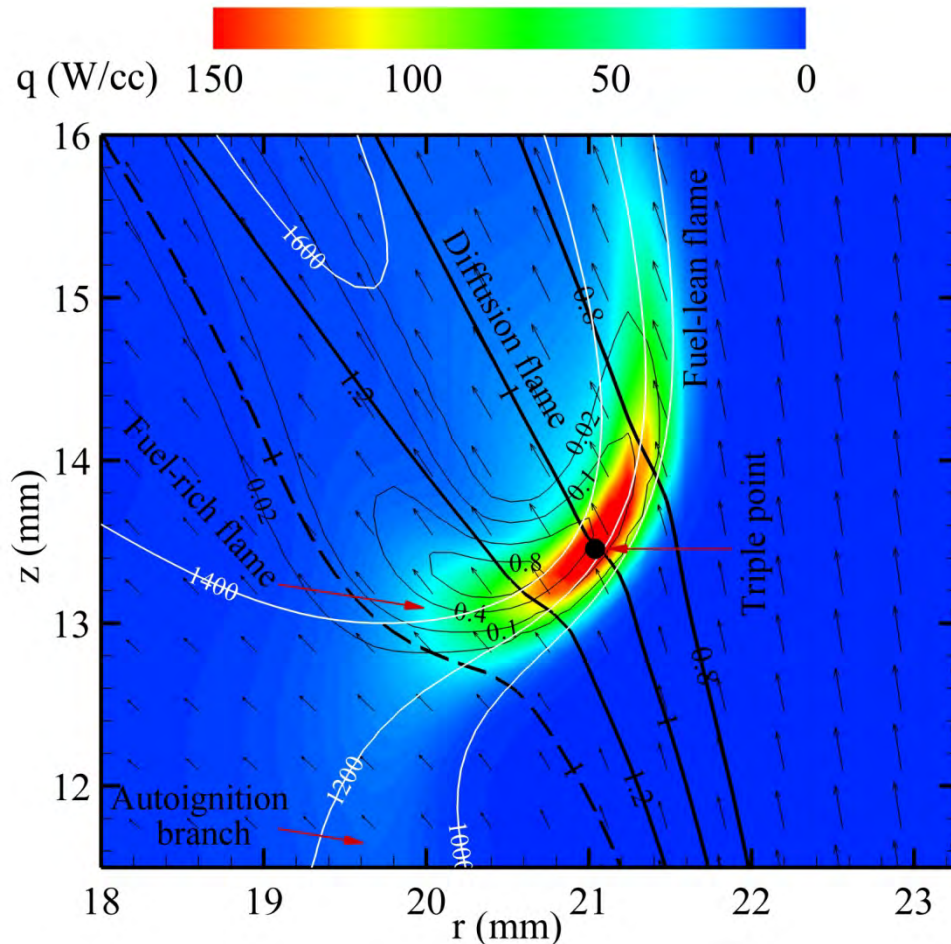


Figure 5.205 Close-up of flow structure near base of lifted flame. Velocity field and iso contours of temperature (white lines), CH concentration (thin black lines), and local equivalence ratio (thick black lines) are superimposed on color map of heat-release rate. Stoichiometry computed from original fuel ( $\text{C}_2\text{H}_4$ ) concentration is shown with broken black line.



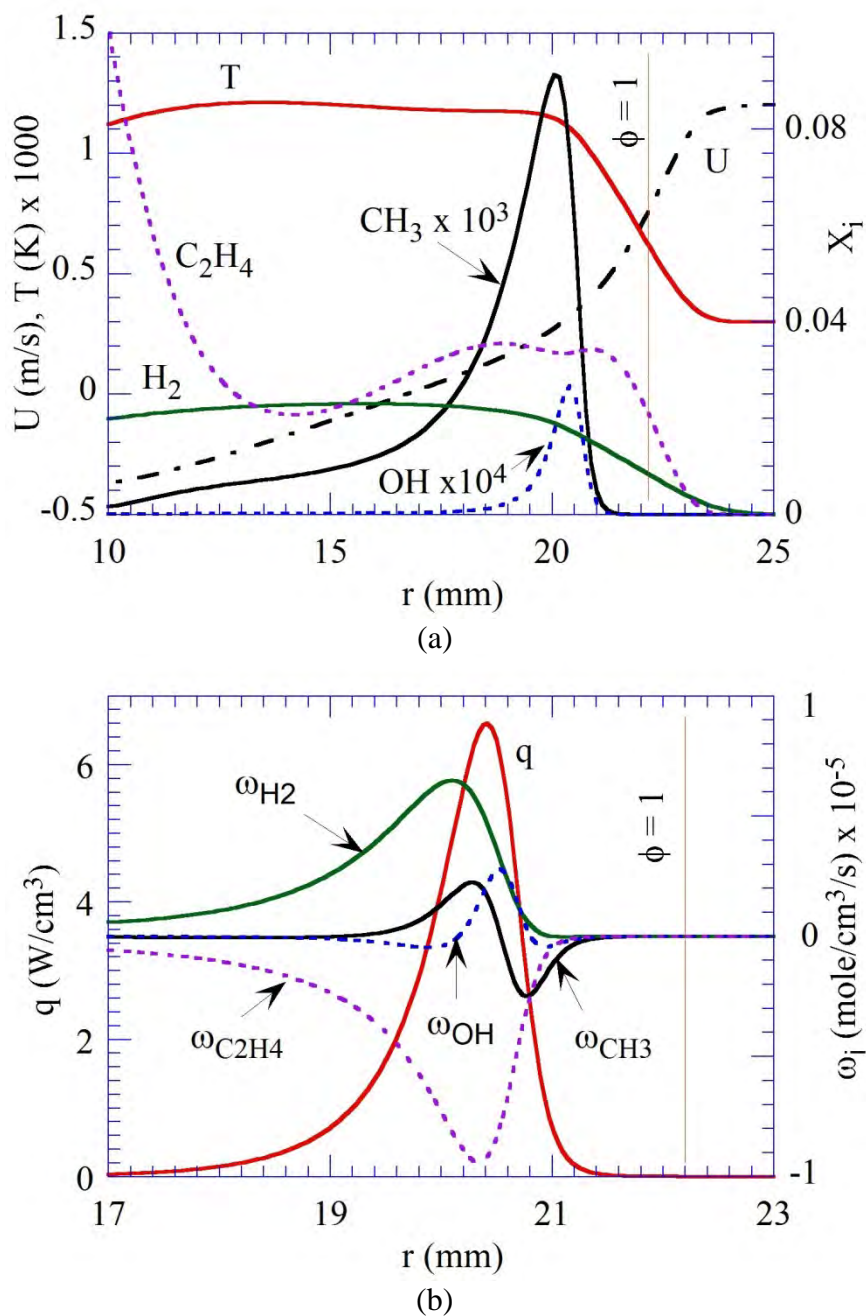


Figure 5.206 Autoignition-zone structure upstream of flame base ( $z = 9$  mm). Radial distributions of (a) velocity, temperature, and species concentrations and (b) heat-release rate and species-production rates.

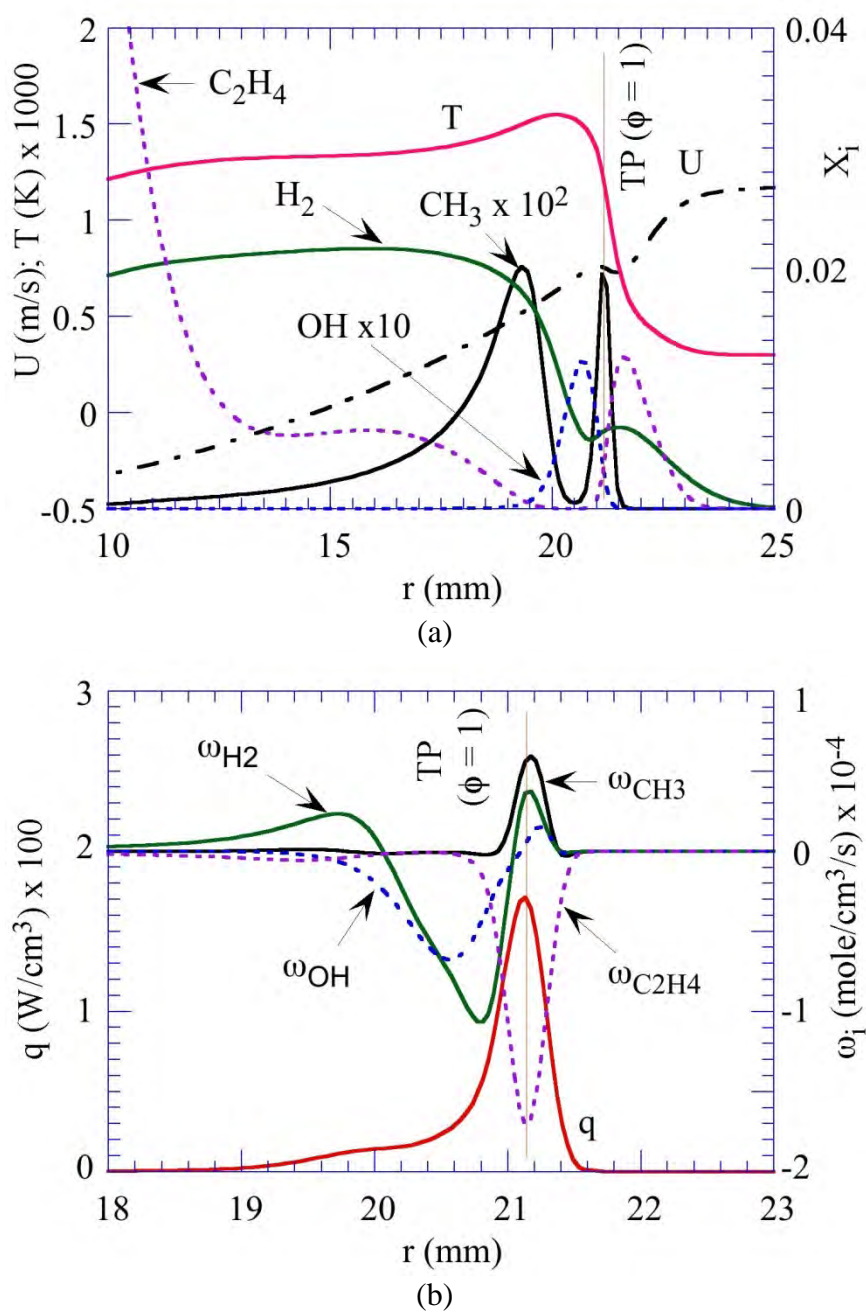


Figure 5.207 Flame structure at a location  $z = 13.5$  in base region. Radial distributions of (a) velocity, temperature, and species concentrations and (b) heat-release rate and species-production rates.



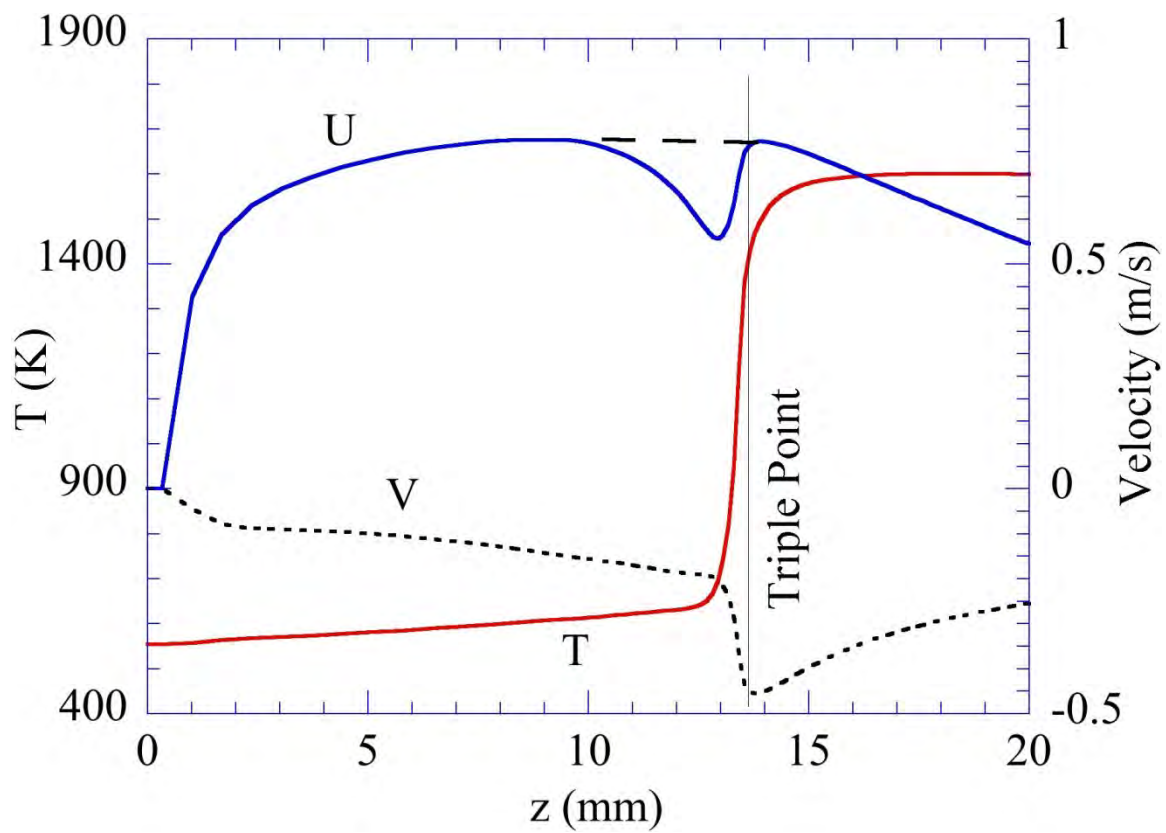


Figure 5.208 Axial velocity (U), radial velocity (V) and temperature (T) along stoichiometry.

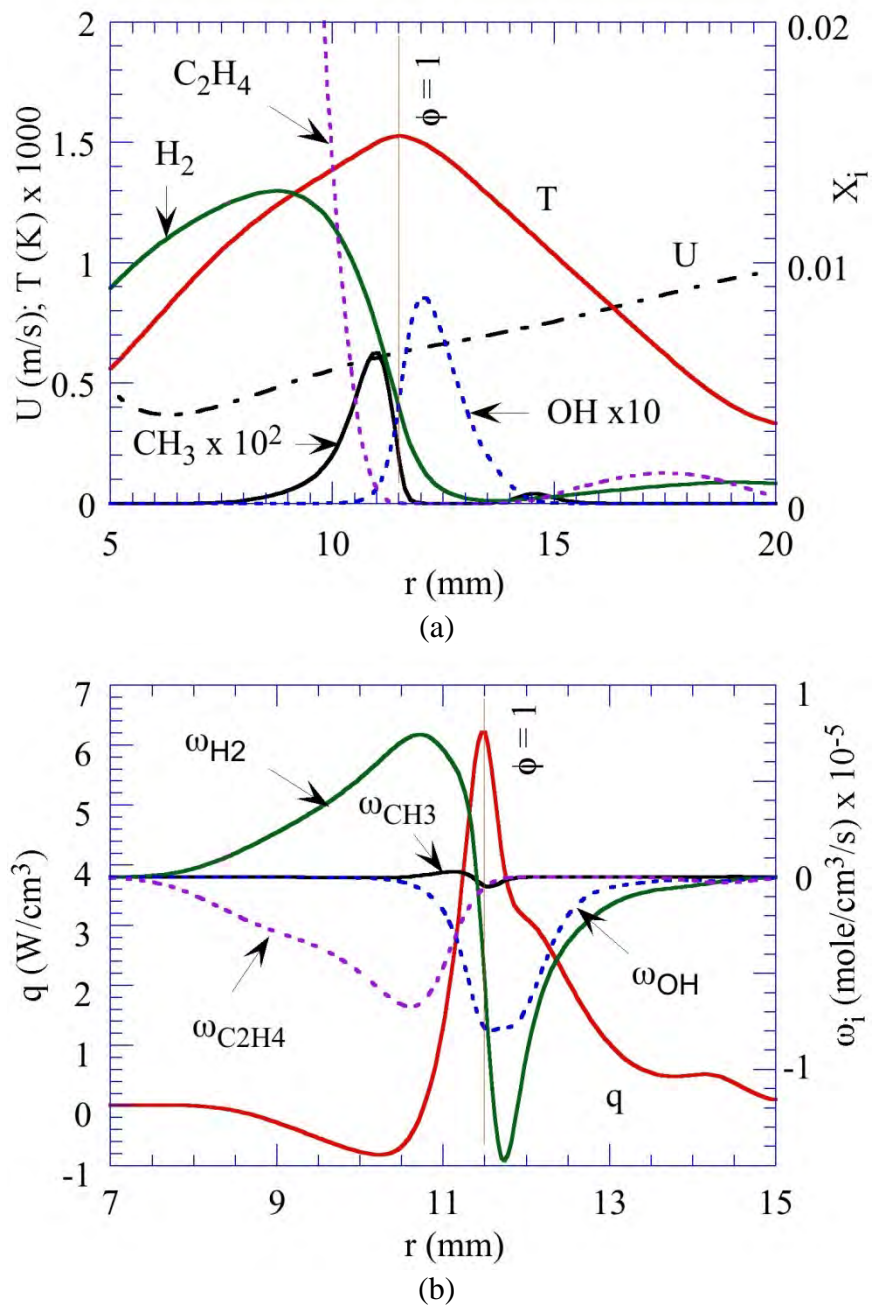


Figure 5.209 Flame structure downstream of base ( $z = 40$  mm). Radial distributions of (a) velocity, temperature, and species concentrations and (b) heat-release rate and species-production rates.

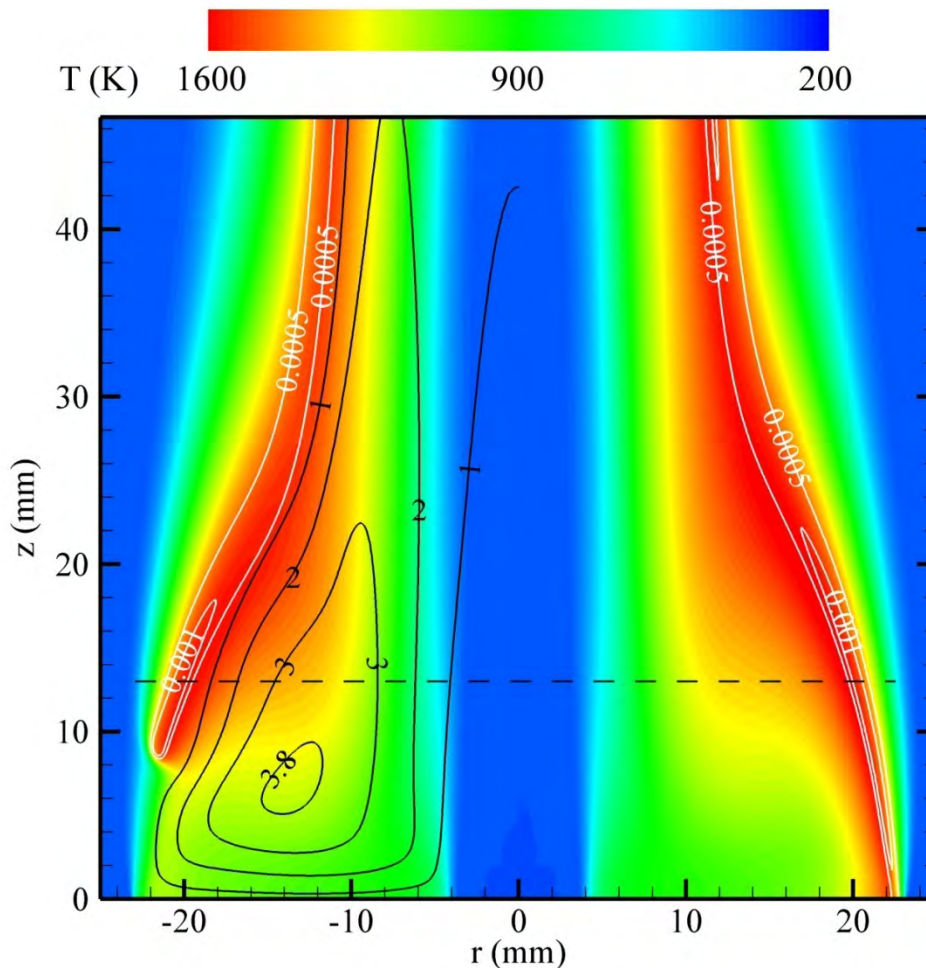


Figure 5.210 Effect of radiation and soot on flame lift-off height. Flame computed without considering radiative heat losses is shown on left half, and flame computed without considering soot and radiation is shown on right half. Iso contours of soot volume fraction in ppm (black lines) and OH (white lines) are superimposed on color maps of temperature.

#### 5.4.8 Liquid Fuels

The first experiments with liquid fuels in the centerbody burner were conducted as a proof of concept using n-heptane as the fuel because its low boiling point. A limited number of images for the heptane air flames were obtained. Figure 5.211 shows photographs of the Heptane -Air flames. The fuel flow for the flame on the left is 2 ml/min while the flow for the flame on the right is 1 ml/min. The flames are similar in shape to the other liquid fuels studied. The flame for the lower fuel flow rate had a lower visible flame height. The higher flow case was also examined using Mie scattering of from the soot as shown in Figure 5.212. It can be seen that the fuel jet stagnates before it can penetrate through the recirculation region. After hitting stagnation point the fuel was forced toward the centerbody where it joined the recirculation region.

Nitrogen dilution was added to the fuel jet for the same case and the results are shown in Figure 5.213. The flame in Figure 5.213 is at the same exposure settings as the one in 5.212 so it be seen that the soot is clearly reduced by the second dilution nitrogen. In addition, for the flame with the added  $N_2$  flow in the fuel jet, the fuel jet momentum is sufficient to penetrate through the stagnation point to the trailing flame and form a secondary recirculation zone near the fuel jet.



Figure 5.211 Heptane- Air Centerbody Flame (Air Flow = 300 g/min for both cases) (A) Fuel flow = 1.36g/min, (B) Fuel Flow = 0.68 g/min.

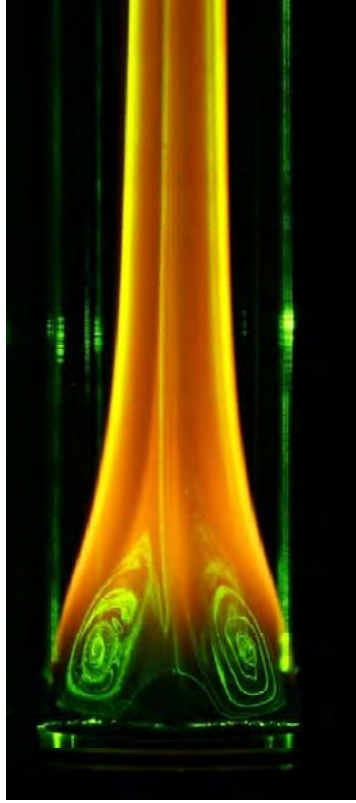


Figure 5.212 Nd-YAG Sheet Illuminated Heptane Air Flame (Air Flow = 300 g/min, fuel flow = 1.36g/min).

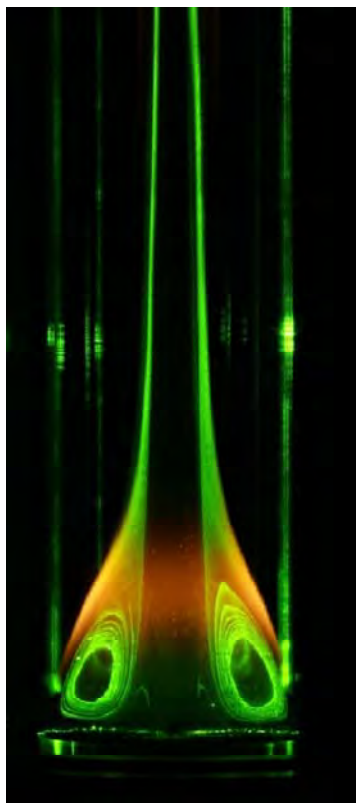


Figure 5.213 Nd-YAG Sheet Illuminated Heptane Air Flame with  $N_2$  dilution( Air = 300 g/min, Fuel = 1.38 g/min+1.16 g/min  $N_2$ ).

Direct photographs of the flames formed with JP-8 fuel are shown in Figure 5.214 for different fuel-flow rates. A constant airflow of 250 lit/min was issued through the annular gap between the centerbody and the outer chimney for all these flames. Similar to the flames formed with gaseous ethylene fuel, JP-8 flames also possessed a recirculation-zone (RZ) flame between centerbody plate and  $z = 40$  mm and a trailing jet diffusion flame at heights  $> 40$  mm. In general, RZ flame is brighter than the trailing jet flame. While the size of the RZ flame remained more or less the same when the fuel flow rate is decreased, size of the trailing flame decreased with fuel flow rate. Contrary to the observations made in gaseous flames, the RZ and trailing flame sections are connected smoothly in JP-8 flames. In fact, the trailing flame appears to be an extension of the RZ flame.

The two-component surrogate mixture for JP-8 fuel developed by Colket consists of 77% n-dodecane and 23% m-xylene. Experiments are conducted for the centerbody flames established with two-component surrogate mixture and pure n-dodecane. Volumetric fuel flow rates for these flames are set to the values used with JP-8 fuel. Note that the differences in the molecular weights among these fuels result in different quantities (by weight) of fuels used when the volumetric flow rate was kept constant. However, such variation in mass flow rates is found to be in between 3.1% and 6.8% (highest for JP-8 and lowest for n-dodecane). Direct photographs of the flames obtained with n-dodecane and surrogate mixture are shown in Figures 5.215 and 5.4.8.6, respectively, for the fuel flow rates ranging between 2 ml/min and 1 ml/min. Airflow was kept at 250 lit/min. Note that the camera settings such as exposure time, focal length and

ISO number are identical for all the pictures shown in Figures 5.214-5.216. Therefore, the flame photographs in Figures 5.214-5.216 can be compared with each other for obtaining qualitative similarities and differences among the flames formed with different fuels. It is interesting to note that the basic structure of the flame (shape and size) did not change much when JP-8 fuel was replaced with either n-dodecane or surrogate mixture. However, there are some minor differences. For example, the dark space (no-soot region) near the flame base close to the centerbody plate is more for n-dodecane flame and minimum for surrogate mixture. In general, n-dodecane flames are the brightest followed by JP-8 flames and then the ones formed with surrogate mixture.

Photographs of the flames shown in Figures 5.214-5.216 are taken again after turning on the Nd-YAG laser. They are presented in Figures 5.217, 5.218 and 5.219 for JP-8 fuel, n-dodecane fuel and surrogate mixture, respectively. A sheet of green laser light (532 nm) passing through the flame illuminated the soot particles due to Mie scattering. Note that the top one-fourth part of the flame is not illuminated with laser light. Recirculation zones associated with these flames may be identified with the soot particles trapped in them. A stagnation point along the centerline, terminating the fuel jet's penetration, develops in all these flames. The injected fuel is forced back toward the centerbody by the recirculation zones, which is then transported toward the flame surface along centerbody plate. Since fuel in these experiments is injected at very low flow rate (velocity < 15 cm/s) it doesn't have enough momentum to penetrate through the recirculation zones established with 1.25-m/s annulus airflow. As expected, the fuel penetration distance decreased significantly when the fuel flow rate was reduced from 2 ml/min to 1 ml/min.

Sooting characteristics of JP-8 and surrogate mixture are very similar as seen from Figures 5.217 and 5.219. At high flow rate (2 ml/min) soot concentration peaks along the flame edges (wing structure) in the trailing jet flame. This pattern shifted toward a more uniform distribution across the flame as the flow rate is decreased. On the other hand, n-dodecane flames maintained wing structure till the trailing flame becomes quite small at 1 ml/min. Overall, n-dodecane flames produced less soot compared to the other two fuels. Interestingly, the amount of soot present in the recirculation zone did not change significantly with either fuel flow rate or fuel type.

Calculated temperature distributions of the flames formed with n-dodecane fuel and surrogate mixture are shown in Figures 5.220 and 5.221, respectively for various flow rates. The inlet temperature for the fuel was set at 440 K, which is close to the measured wall temperature near the fuel tube. Computed flames are anchored to the outer edge of the centerbody plate. Predicted flame shapes qualitatively matched with those captured in the direct photographs of Figures 5.215 and 5.216. Similar to that seen in the experiments, fuel jet in the calculations penetrated a few millimeters into the recirculation zone. However, the change in penetration distance with flow rate is more significant in the experiment than that in the calculations. Figures 5.220 and 5.221 suggest further that 23% addition of m-xylene into pure n-dodecane fuel doesn't affect the temperature of the flame.

Soot distributions in flames formed with n-dodecane and surrogate mixture are shown in Figures 5.222 and 5.223, respectively. Streamlines are superimposed on these plots. The maximum soot volume fraction represented with red is 1.2 ppm. Calculations indicate that soot concentration in the trailing flame increases with decreasing fuel flow rate. Not much soot is generated in the recirculation zones. In fact, soot is entrained into the recirculation zones from the trailing flame.

When soot concentration along the centerline increased with a reduction in the fuel flow rate more soot got entrained into the recirculation zones. As a result, flame with 1 ml/min fuel flow rate has the most soot in the recirculation zone. Addition of m-xylene to pure n-dodecane flame also increased soot concentrations both in the trailing flame and in the recirculation zones.

An experimental and numerical study is conducted for understanding the flame structures in centerbody burner operating with liquid fuels. A conventional JP-8 fuel, its two-component surrogate mixture, and n-dodecane are considered as fuels in this study. Liquid fuels are preheated using a commercially available fluidized bed and vaporized using flashing technique. Fuel flow rates are varied while keeping the airflow constant. Direct photographs of the flames are taken with and without passing the Nd-YAG laser sheet light. These flames are simulated using a time-dependent, finite-rate-chemistry CFD model UNICORN. A semi-detailed chemical-kinetics model involving 161 species and 1538 reactions is used. Due to the low fuel flow rates used in this study, the recirculation-zone flames merged with the trailing jet flames. Decreasing fuel flow rate reduced the length of the trailing jet flame without affecting the recirculation-zone flame structure. The two-component surrogate mixture seems reproducing the overall flame and sooting structures of the JP-8 fuel very well. Simulations predicted the flame shapes reasonably well. While the calculations qualitatively predicted the soot in the trailing jet flame, they significantly under predicted the soot in the recirculation zones.

Laser induced incandescence measurements were made for JP-8, Dodecane, and 23%M-xylene-77% dodecane flames. The air flow rates were set at 250 slpm (300 g/min) and the fuel flows were adjusted between 1 and 2 ml/min. The LII images are shown in Figure 5.224-5.226 for the three fuels. The dodecane LII signals were in general lower than for the JP-8 and the m-xylene-dodecane mixture. The LII signal for the dodecane was also symmetric about the fuel jet axis. In contrast, the LII signal for the JP-8 and the M-xylene were much higher on the left side of the image. The laser sheet enters the test section from the left side. Because of the high apparent levels of soot and the fact that the highest LII signals occur on the same side of the test section through which the laser first enters, it is thought that the asymmetry is caused by a decrease in the laser power as the laser sheet passes from the left to right in the images for the M-xylene and JP-8. It should also be noted that the luminosity and Mie scattering images for these fuels did not show the same level of asymmetry.

The LII signals were converted into volume fractions, and the average soot volume fractions across the flame width as a function of height are shown in Figures 5.227 to 5.229. It can be seen that the maximum soot volume fractions were highest for the JP-8 and the Surrogate fuel. Note that because of the asymmetry the absolute soot volume fractions for the JP-8 and m-xylene are highly suspect and need further examination.



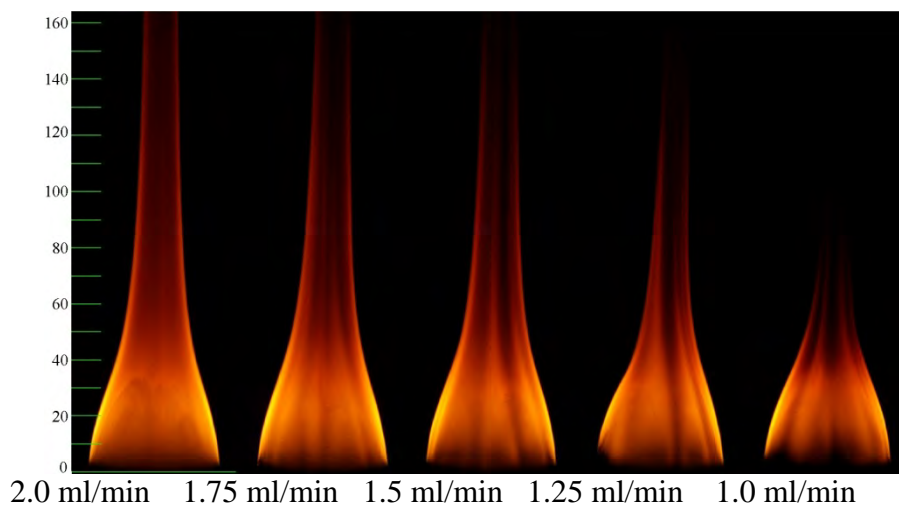


Figure 5.214 Direct photographs of the flames formed with JP-8 fuel.

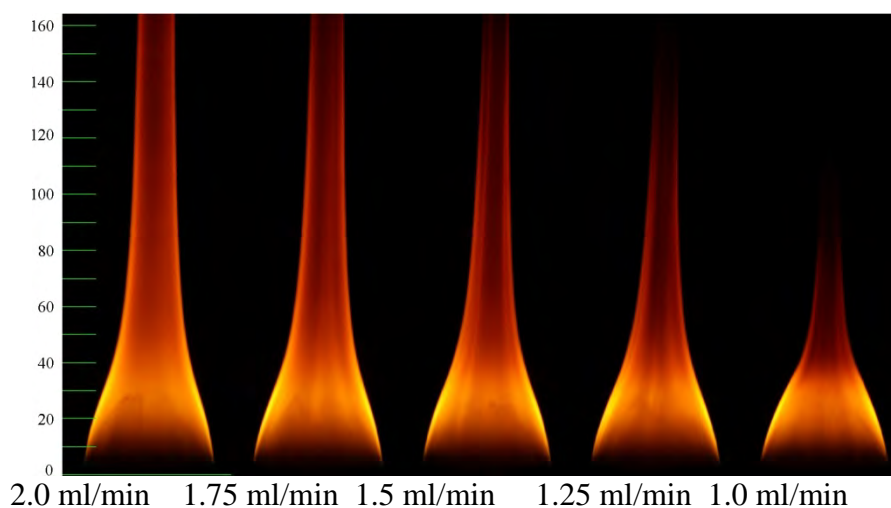


Figure 5.215 Direct photographs of the flames formed with n-dodecane fuel.

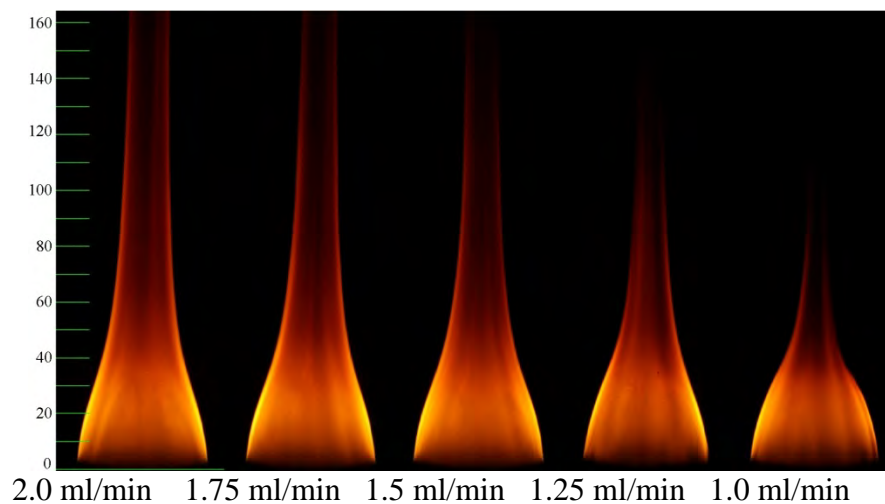
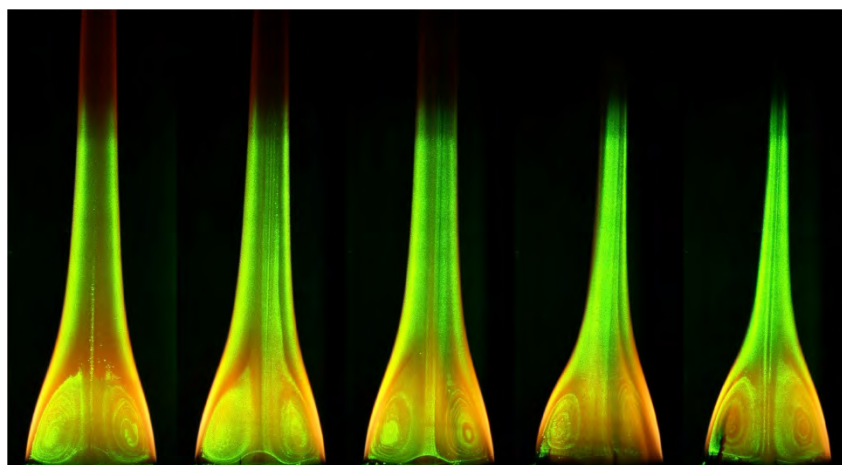
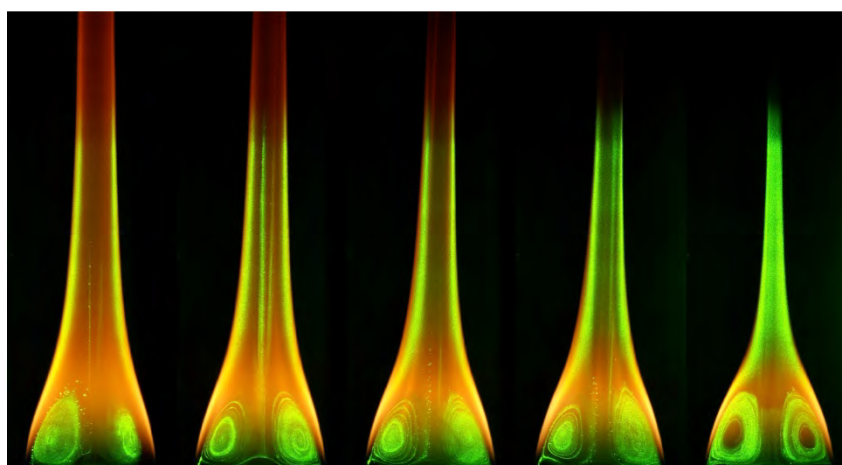


Figure 5.216 Direct photographs of the flames formed with a mixture of 77% n-dodecane and 23% m-xylene.



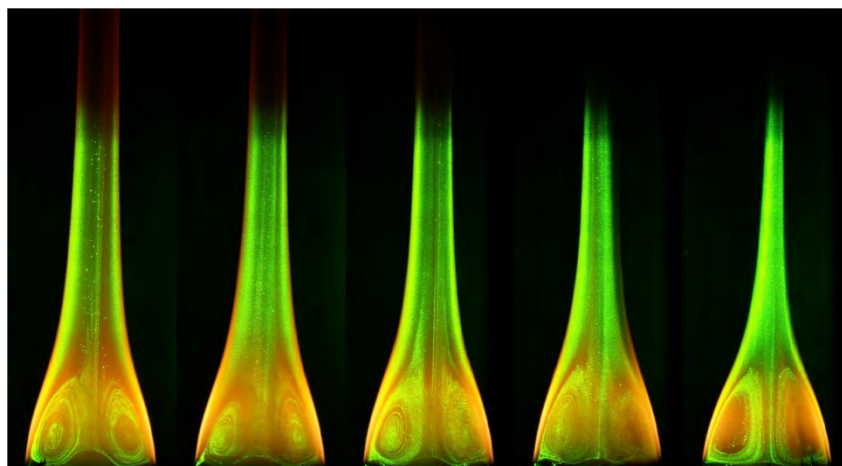
2.0 ml/min 1.75 ml/min 1.5 ml/min 1.25 ml/min 1.0 ml/min

Figure 5.217 Direct photographs of the Nd-YAG-illuminated flames formed with JP-8 fuel.



2.0 ml/min 1.75 ml/min 1.5 ml/min 1.25 ml/min 1.0 ml/min

Figure 5.218 Direct photographs of the Nd-YAG-illuminated flames formed with n-dodecane.



2.0 ml/min 1.75 ml/min 1.5 ml/min 1.25 ml/min 1.0 ml/min

Figure 5.219 Direct photographs of the Nd-YAG-illuminated flames formed with 77% n-dodecane and 23% m-xylene.

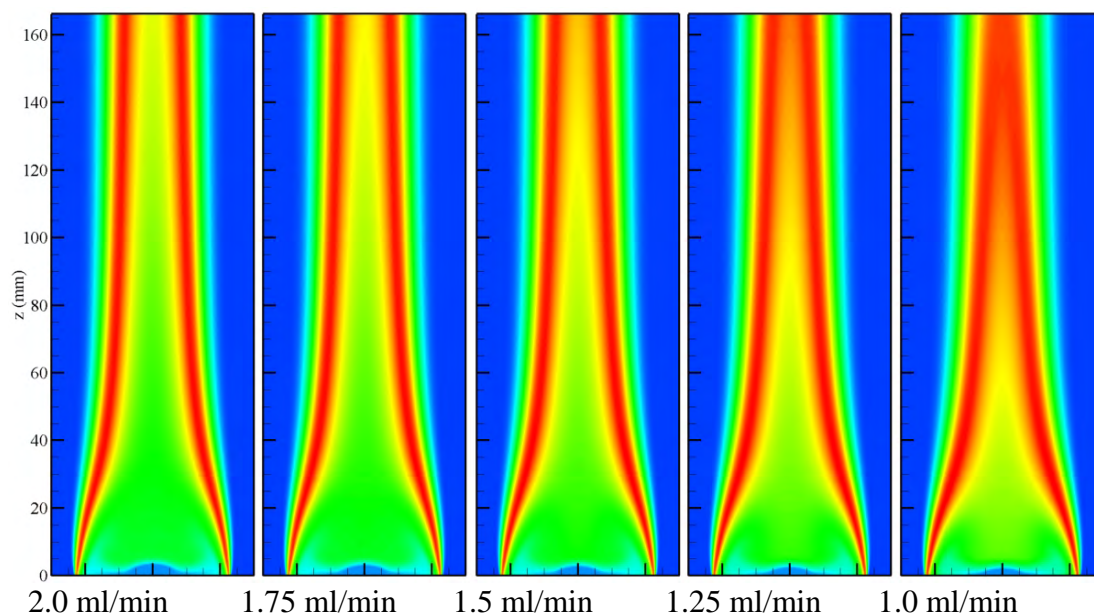


Figure 5.220 Temperature distributions of n-dodecane flames computed with a semi-detailed chemical kinetics mechanism.

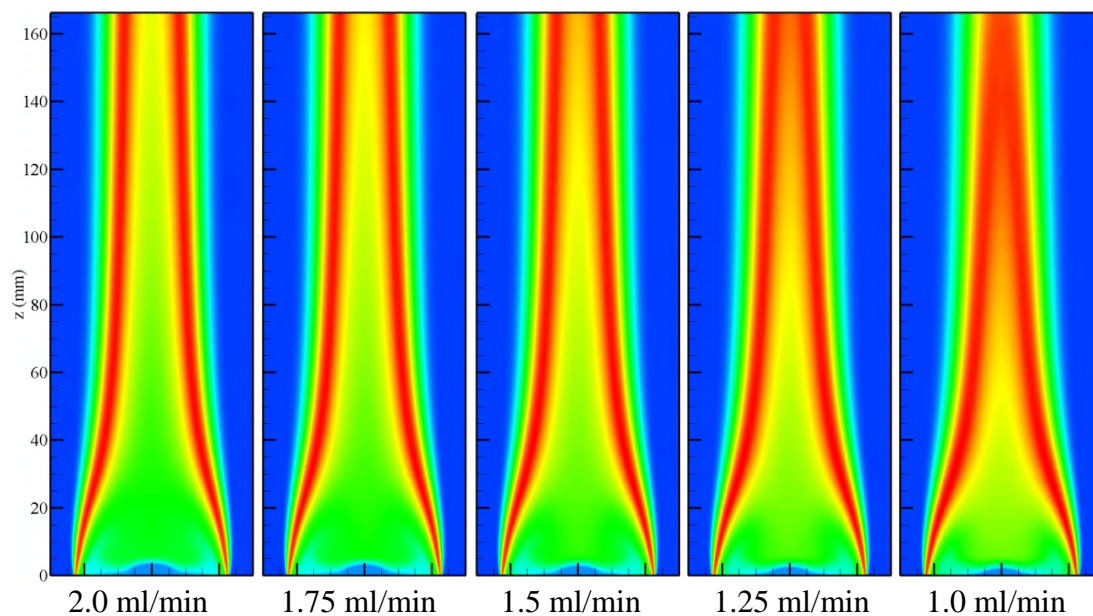


Figure 5.221 Temperature distributions of 77%-n-dodecane-23%-m-xylene flames computed with a semi-detailed chemical kinetics mechanism.

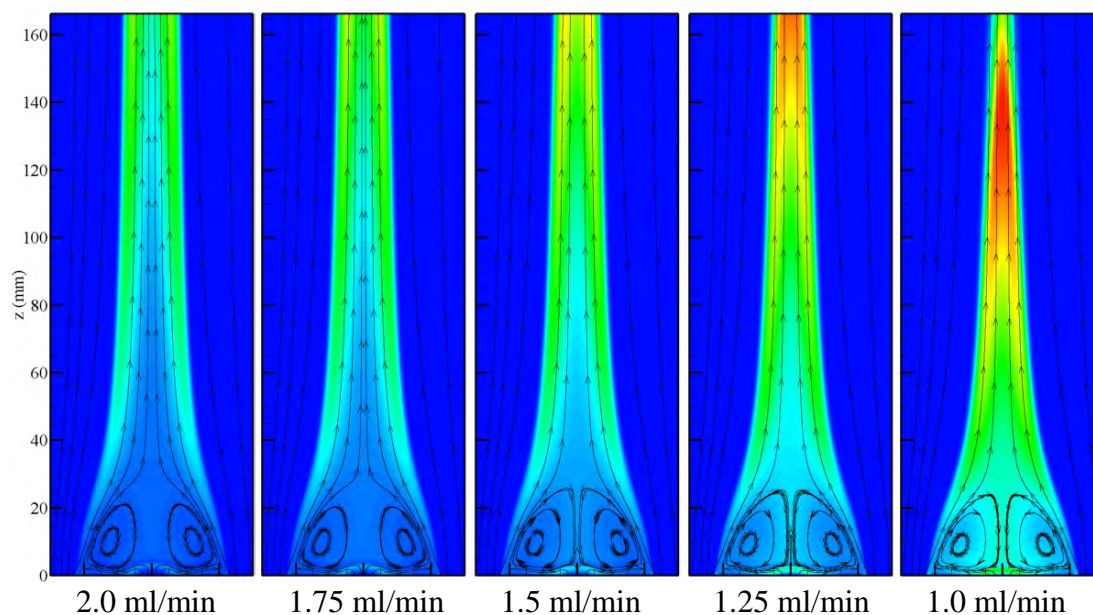


Figure 5.222 Soot distributions in n-dodecane flames computed with a semi-detailed chemical kinetics mechanism. Computed streamlines are superimposed.

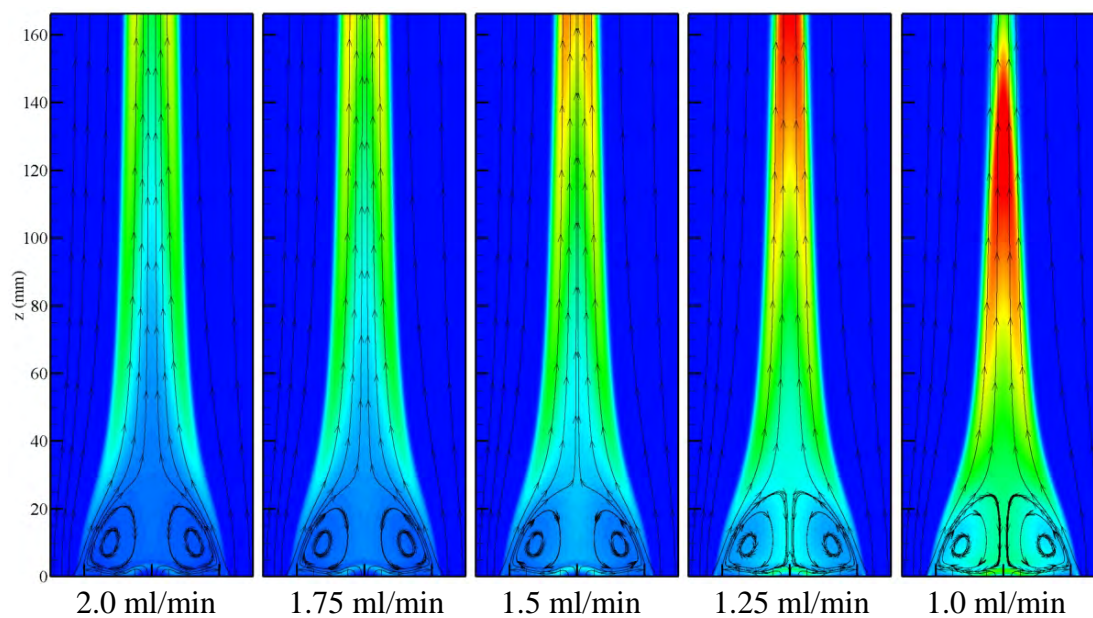


Figure 5.223 Soot distributions in 77%-n-dodecane-23%-m-xylene flames computed with a semi-detailed chemical kinetics mechanism. Computed streamlines are superimposed.



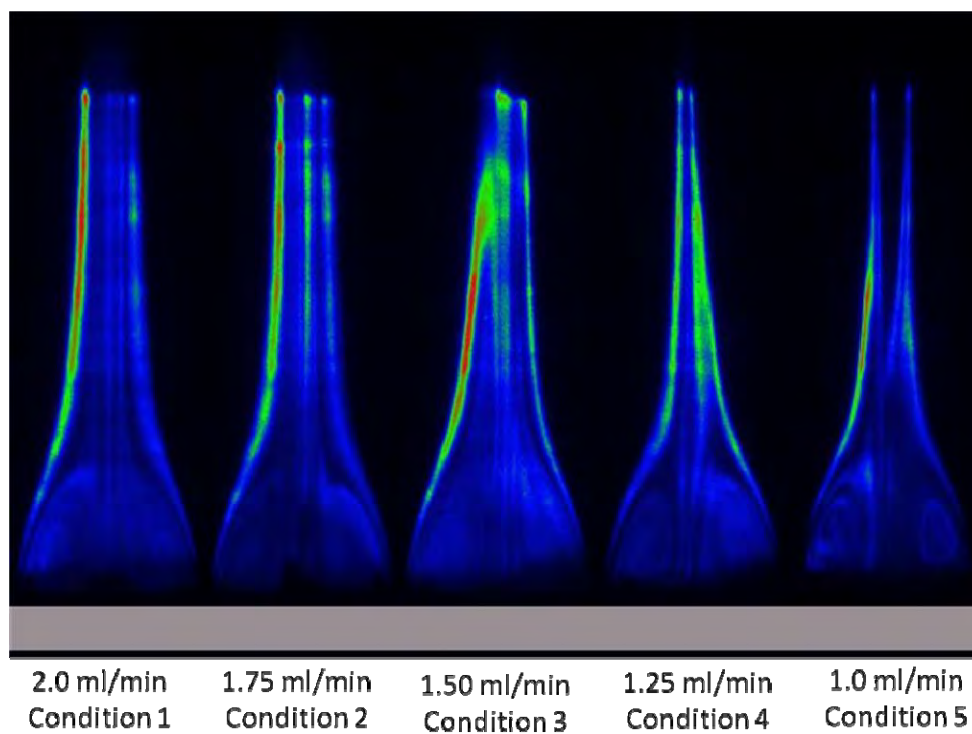


Figure 5.224 Laser Induced Incandescence (LII) Images LII images for J8.

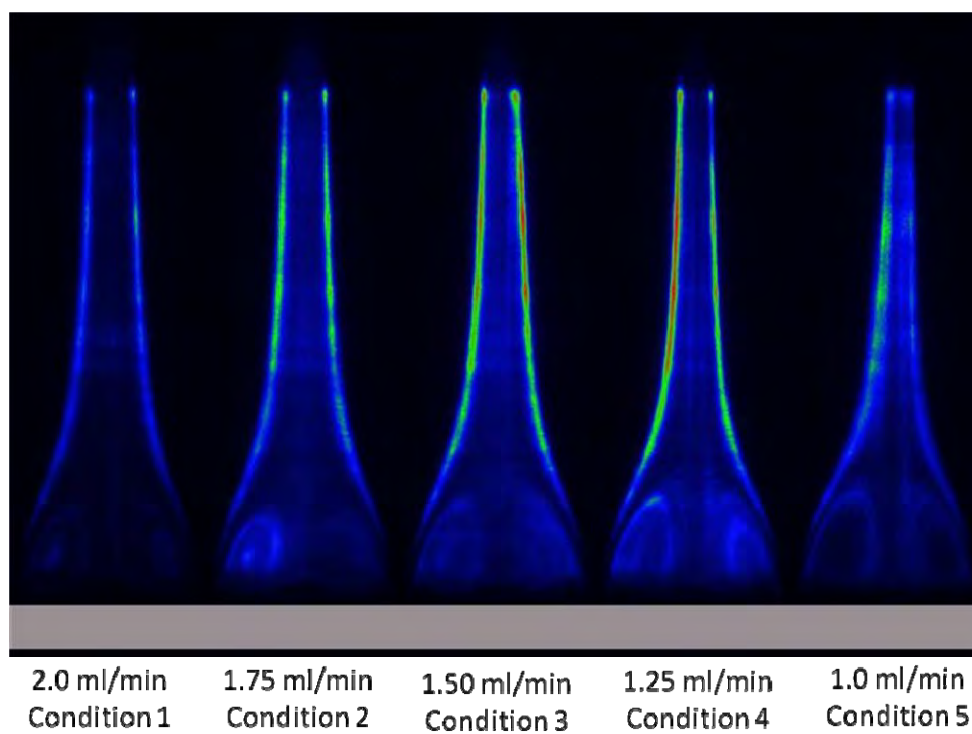


Figure 5.225 Laser Induced Incandescence (LII) Images LII images for Dodecane.

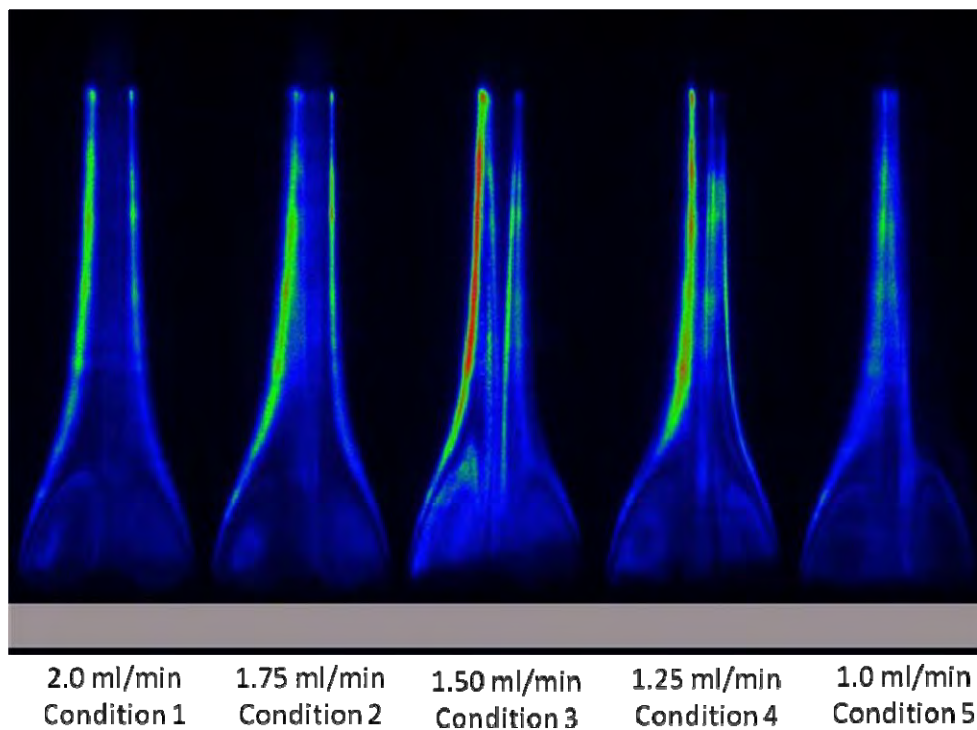


Figure 5.226 Laser Induced Incandescence (LII) Images LII images for 23% M-Xylene- 77% Dodecane.

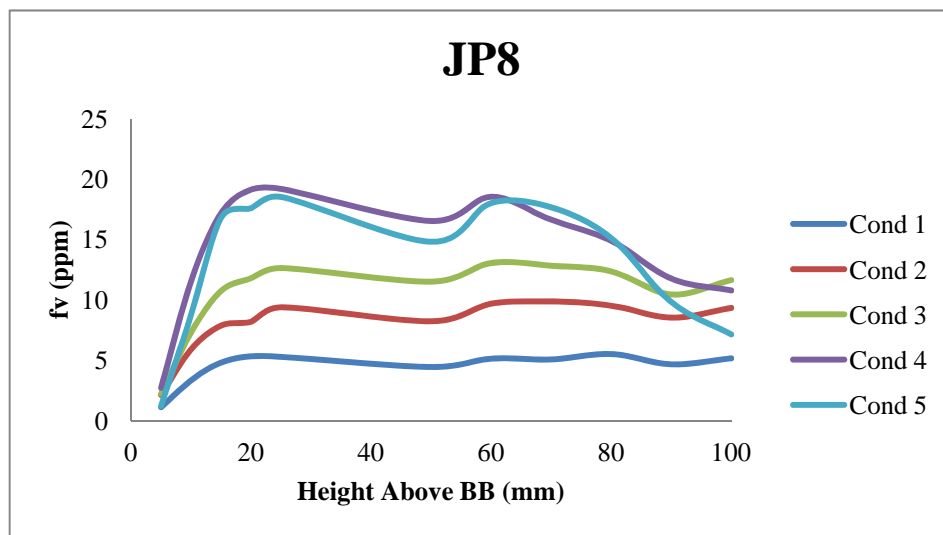


Figure 5.227 Average Soot Volume Fraction for JP-8 Flame in Centerbody.

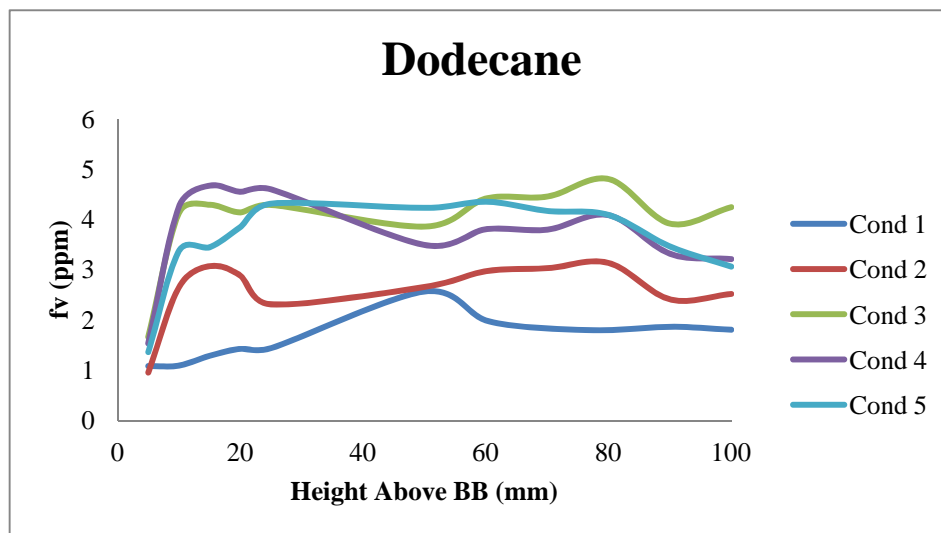


Figure 5.228 Average Soot Volume Fraction for Dodecane Fuel in Centerbody.

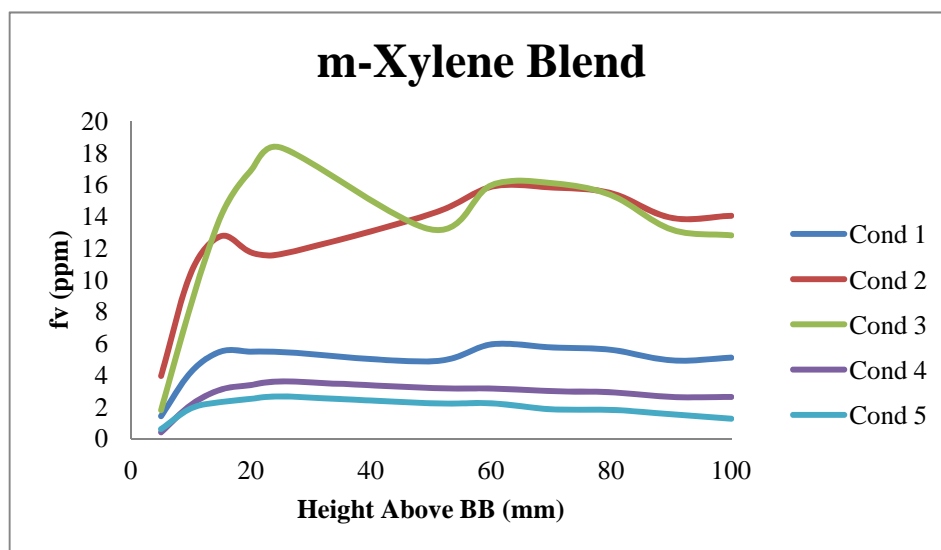


Figure 5.229 Average Soot Volume Fraction for Surrogate (77% Dodecane- 23% M-xylene).

## 5.5 Kinetic Model Evaluation Using UNICORN

Detailed chemical kinetics for describing combustion of hydrocarbon fuels involves several hundred species and several thousand elementary reactions. Traditionally, mechanisms are developed and validated through the simulations of zero- and one-dimensional flames using codes such as RUN1DL (Rogg, 1993), OPPDIF (Lutz et al., 1996), and CHEMKIN (Kee et al., 1980) and comparing the results with the available experimental data from shock tube, opposing-jet burner, premixed-flat-flame burner, etc. Extensive experimental data for the concentrations of intermediate species are required for obtaining a reasonably calibrated kinetics mechanism. However, it is not always feasible to obtain concentrations of the numerous hydrocarbon intermediates and, as a result validation of complex chemical-kinetics mechanisms is often partially performed. On the other hand, chemical-kinetics mechanisms are developed, in part, for the simulation of flames in aircraft combustors, which are multidimensional in nature. It is risky to make predictions for a practical flame using a partially validated chemical kinetics without knowing how it performs under convection-diffusion environment. Various mechanisms proposed for ethylene, heptanes and JP-8 fuels are evaluated in the following subsections using two-dimensional UNICORN code.

### 5.5.1 Ethylene Models

Five detailed chemical-kinetics models available in the literature for ethylene combustion are incorporated into UNICORN for the investigation of sooty nonpremixed flames. The first mechanism considered is Wang-Frenklach mechanism (Mechanism A). It consists of 99 species and 1066 elementary reactions. This mechanism has been extensively validated using shock-tube and flat-flame-burner data. The second one is Wang-Colket mechanism (Mechanism B). It has been developed from Wang-Frenklach mechanism by considering wider range of experimental data. It consists of 171 species and 2002 elementary reactions. Third one is San Diego (SD) mechanism (Mechanism D). It consists of 52 species and 544 elementary reactions. The fourth one is National Institute of Standards and Technology (NIST) mechanism (Mechanism C). It consists of 197 species and 2926 reactions. The fifth one is Lawrence Livermore National Laboratory (LLNL) mechanism (Mechanism E). It consists of 160 species and 1540 reactions.

This study utilized a two-equation model for soot with transport equations for particle number density,  $N_s$ , and soot mass fraction,  $Y_s$ . The two source terms in these equations are obtained using Lindstedt's model (1994), which is based on the simplifying assumption that nucleation and growth are first-order functions of acetylene concentrations.

Sooting characteristics of a vertically mounted laminar nonpremixed ethylene-air jet flame were studied experimentally by Santoro et al (1983). The atmospheric pressure, co-annular burner used in those experiments consists of 11.1-mm-inner-diameter fuel tube with a wall thickness of 0.8 mm which is enclosed in a 102-mm-inner-diameter brass cylinder. Several inserts such as ceramic honeycomb, brass screens and glass beads were used in the annular gap between the two tubes to give uniform exit velocity for the air flowing through this gap. The fuel tube, which extends 2.5 mm above the burner surface, is also partially filled with glass beads for flow conditioning. A 46-cm-long glass chimney is mounted on the outer brass cylinder for protecting



the flame from room-air disturbances. Details of the experimental procedure and the measurement techniques are given in Santoro et al. (1983).

Detailed temperature and species measurements were obtained for a nonpremixed flame in which pure ethylene was issued at a velocity of 3.91 cm/s from the fuel tube. Coannular flow consists of room-temperature air issued at a velocity of 8.8 cm/s. Calculations for this flame are performed using the five chemical-kinetics models; namely, Wang-Frenklach, Wang-Colket, San Diego, NIST and LLNL mechanisms listed previously. A computational grid of 301x101 is used for discretizing the physical domain of 46 cm x 5.1 cm. Grid clustering is used for placing most of the grid lines in the flame zone. As a result the grid spacing obtained in the flame zone is 0.2 mm in both axial and radial directions. Initial conditions (flame) for the detailed-chemistry calculations were obtained from the simulation performed using a global-chemistry UNICORN code. Calculations with all five mechanisms are carried using a time-step of 0.05 ms.

None of the five chemical-kinetics models considered in the present study were developed taking sooting characteristics into account. The two-equation soot model described earlier is added to each of these five chemical-kinetics models for predicting soot in nonpremixed flames. Since soot affects other species concentrations directly through its formation and oxidation and indirectly through heat radiation, it is important to understand the performance of a chemical-kinetics mechanism with and without having soot model added to it. Hence, calculations for the ethylene nonpremixed flame are first performed without adding the soot model and the results are compared with the measurements in Figures 5.230 and 5.231.

Predicted and measured radial distributions of temperature and CO<sub>2</sub> mole fraction are compared at 15-mm, 40-mm, and 70-mm above the fuel-tube tip in Figures 5.230a, 5.230b, and 5.230c, respectively. Amazingly, all five chemical-kinetics mechanisms resulted in similar distributions at all heights—with San Diego mechanism giving slightly higher temperatures. On the other hand, some differences in the predicted concentration distributions for species such as CO and C<sub>2</sub>H<sub>2</sub> may be noted in Figure 5.231. San Diego mechanism is giving higher CO concentrations while LLNL mechanism is predicting higher C<sub>2</sub>H<sub>2</sub> concentrations.

Figures 5.230 and 5.231 also illustrate the discrepancies that exist in both temperature and species concentrations when compared with the experimental data. Such discrepancy, in general, got worsened with height in the flame. At 70 mm, measured temperatures are lower than the predictions by as much as 500 K. However, considering the fact that the predicted temperatures are close to the measurements in the flame zone ( $r \sim 6.5$  mm) near the burner exit ( $z < 15$  mm), it may be concluded on ad hoc basis that radiation from soot is affecting the temperature distribution in the flame. Calculations are then repeated for the same flame using the five chemical-kinetics mechanisms listed previously and by adding the two-equation soot model. Results in the form of temperature and species distributions at different heights in the flame are shown in Figures 5.232 and 5.233.

A dramatic decrease in temperatures is observed when calculations considered soot in the flame. At 70 mm, predicted peak temperatures matched well with the measurements. Even though the temperatures predicted using different chemical-kinetics models with soot are in general closer to the measured values the variations among the predictions are much larger than those observed when soot was not considered (Figure 5.230). Interestingly, no improvement in the predictions of

species ( $\text{CO}_2$  and  $\text{CO}$ ) concentrations was achieved by considering soot. Drop in predicted temperatures below the measured values closer to the burner exit (at  $z = 15$  and  $40$  mm) suggest an over correction for the radiation from soot. Consistently, all five models have over predicted the amount of soot near the burner exit. Also, the two-equation soot model, independent of the chemical kinetics used, failed to predict the shape of the soot distribution. While measurements suggest a shoulder-like soot distribution models have predicted bell-shaped distributions, especially, in the downstream locations. Among the five chemical-kinetics mechanisms considered, level of soot concentration predicted by San Diego mechanism compared better with the measurements. Such an assessment on San Diego mechanism holds good even for the temperature and species predictions.

Impact of soot on temperature is shown in Figure 5.234 through plotting temperature distributions with and without considering soot in Figures 5.234a and 5.234b, respectively. Data obtained with San Diego mechanism was used. Predicted soot-volume-fraction distribution is shown in Figure 5.234c. When soot was not considered peak (or flame) temperature remained the same at different heights. Radiation from soot cooled the flame with height and transformed it into an open-tipped (flame tip burning less intensely) one.

Plots similar to those shown in Figure 5.234 were generated using the data obtained with Wang-Frenklach mechanism and are shown in Figure 5.235. The major difference in the predictions made with San Diego and Wang-Frenklach mechanisms is in the distribution and magnitude of soot volume fraction. Latter mechanism not only predicted higher amounts of soot in the flame but also provided significant delay in the generation of soot near the burner exit.

In general, initial calculations made without adding the soot model revealed that all five mechanisms result in flame structures that are close to each other. However, the predicted temperatures were found to be significantly higher, especially in the downstream locations, than the measured ones. Inclusion of soot model improved the temperature predictions but no significant improvement in the prediction of species concentrations was achieved. Among the five mechanisms, San Diego mechanism with two-equation soot model resulted in soot and temperature that were closest to the measurements. On the other hand, none of the mechanisms was able to predict the experimentally observed shoulder-like soot distribution.

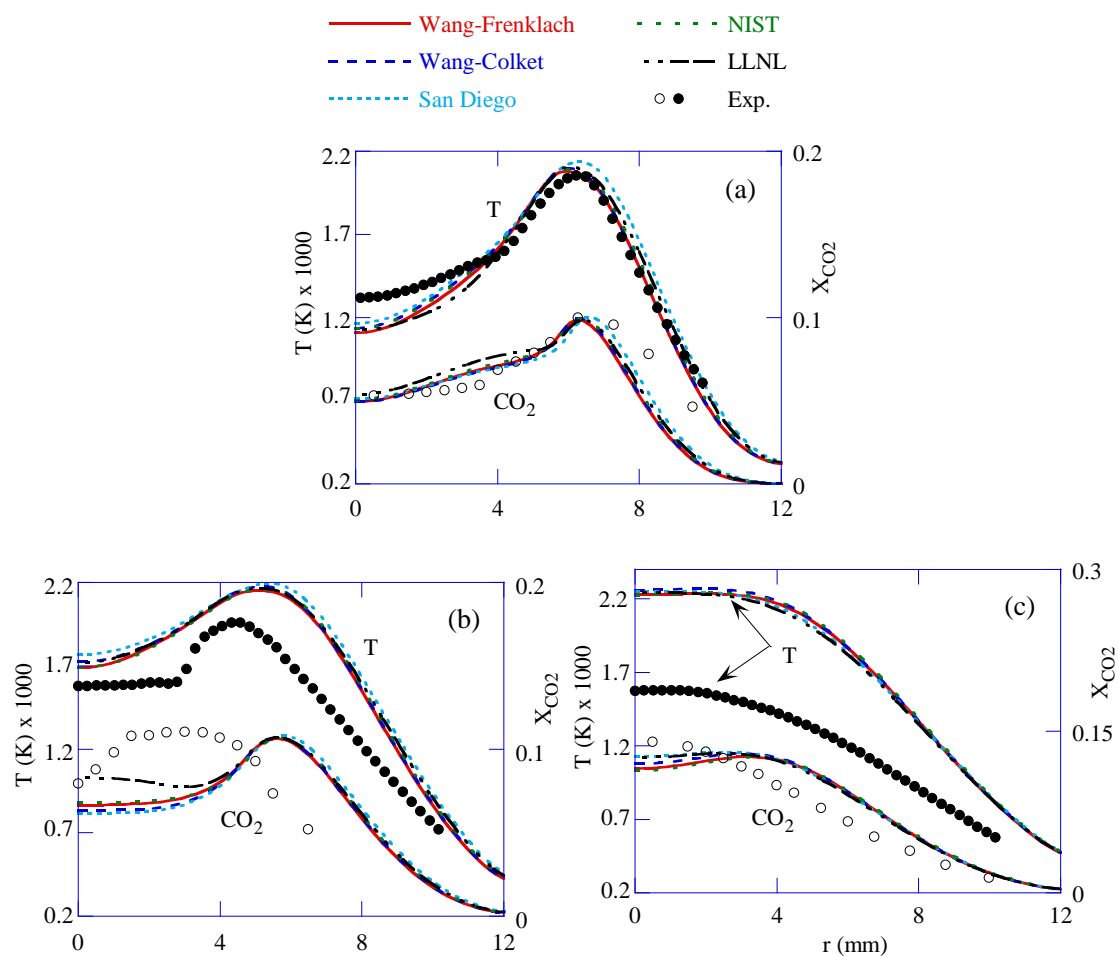


Figure 5.230 Comparison of radial distributions of temperature and CO<sub>2</sub> mole fraction obtained using several chemical-kinetics mechanisms and measurements at (a) 15-mm, (b) 40-mm, and (c) 70-mm flame heights. Simulations are made without incorporating soot sub-model.

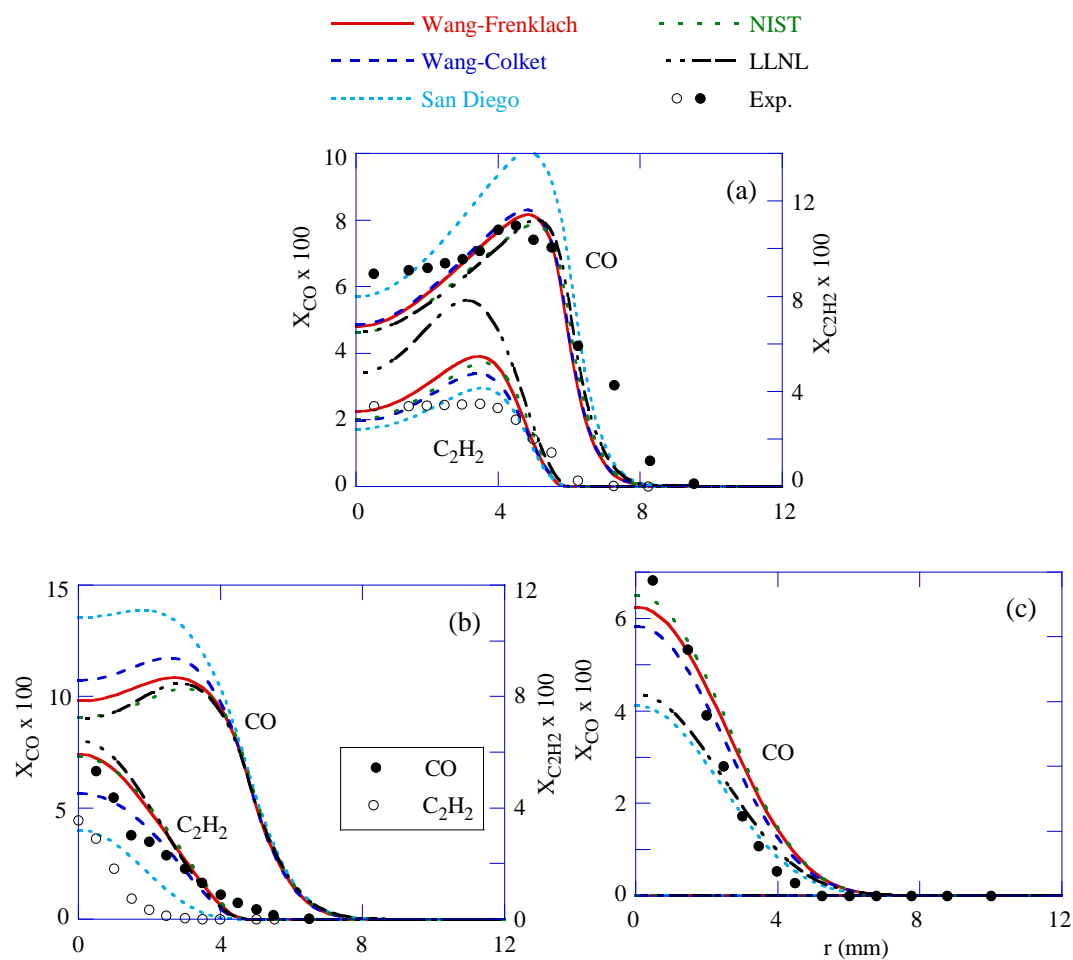


Figure 5.231 Comparison of radial distributions of CO and C<sub>2</sub>H<sub>2</sub> mole fractions obtained using several chemical-kinetics mechanisms and measurements at (a) 15-mm, (b) 40-mm, and (c) 70-mm flame heights. Simulations are made without incorporating soot sub-model.

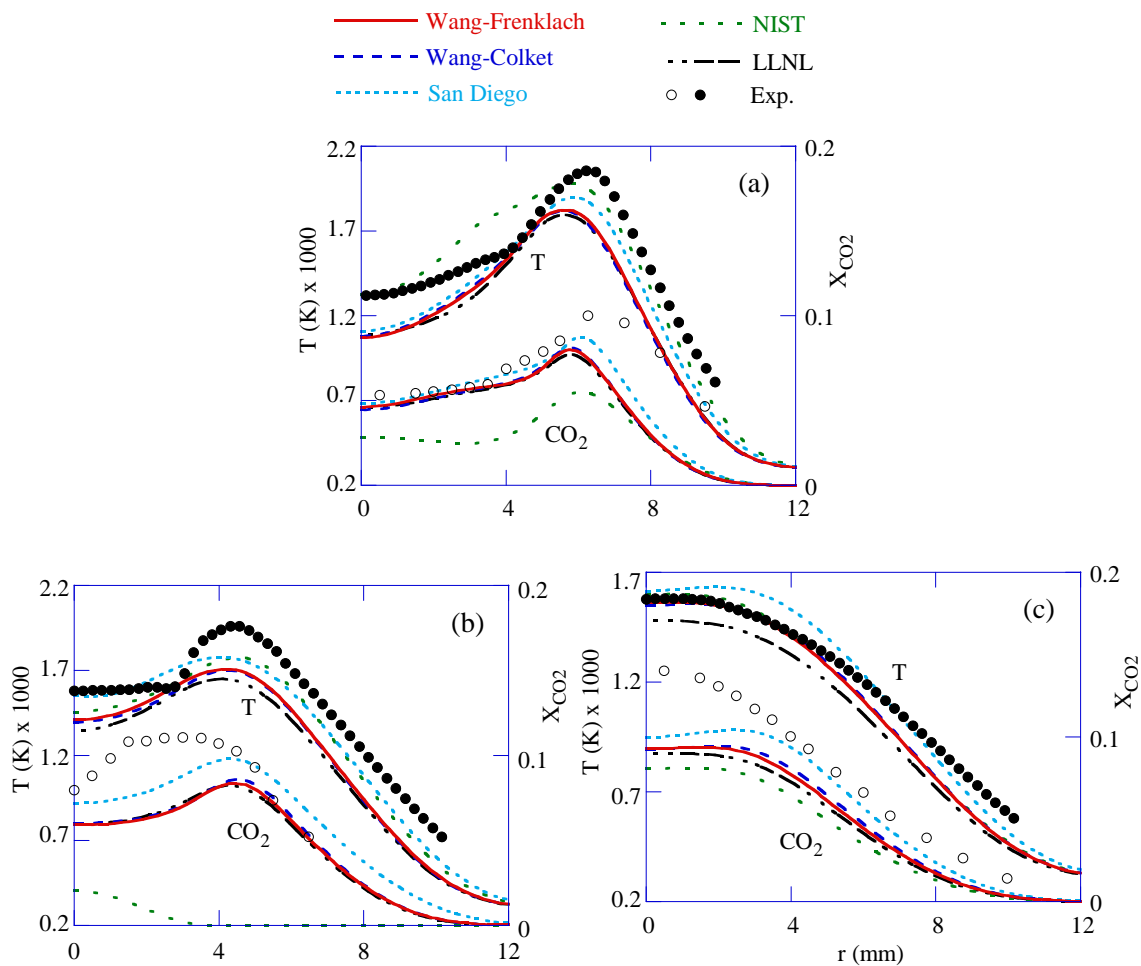


Figure 5.232 Comparison of radial distributions of temperature and CO<sub>2</sub> mole fraction obtained using several chemical-kinetics mechanisms and measurements at (a) 15-mm, (b) 40-mm, and (c) 70-mm flame heights. Simulations are made after incorporating a two-equation soot sub-model.

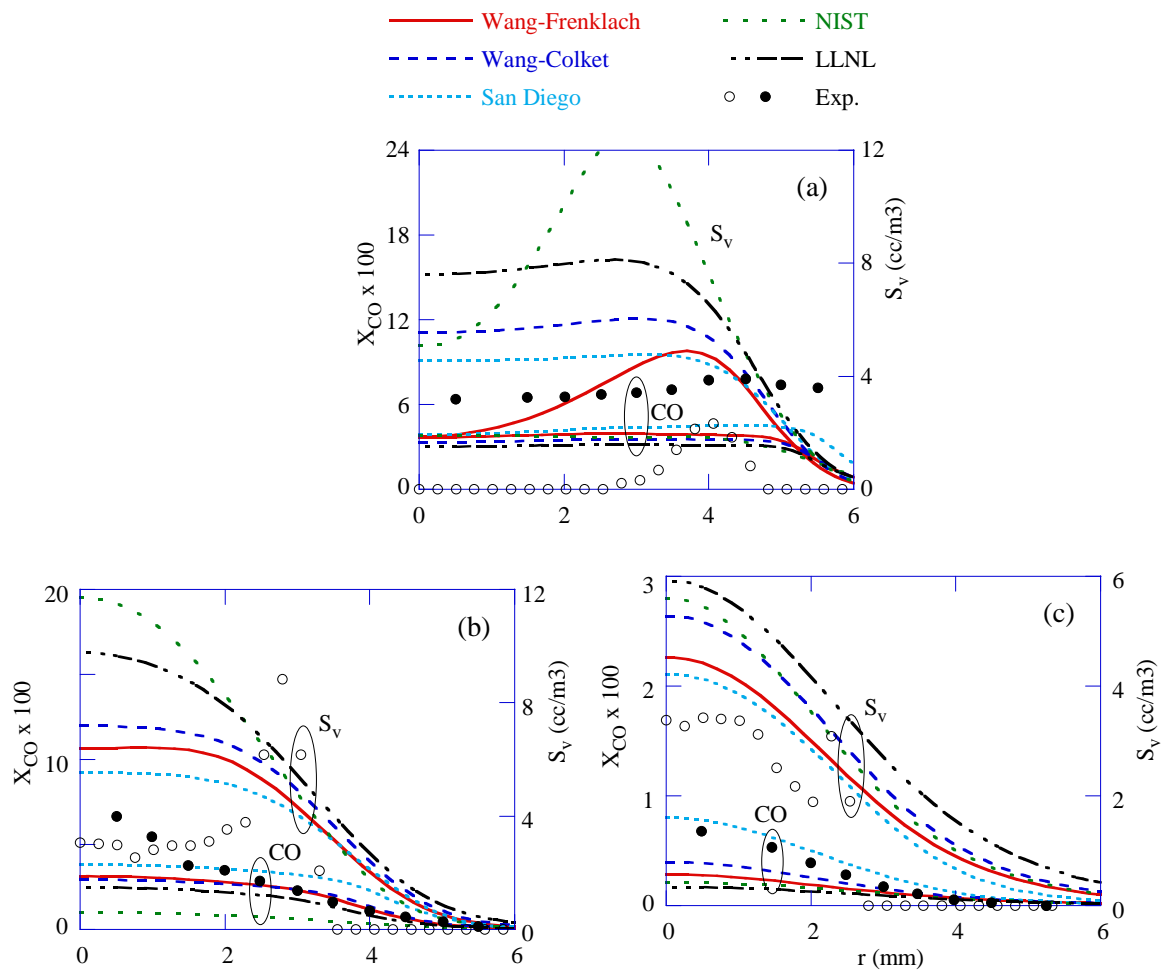


Figure 5.233 Comparison of radial distributions of CO mole fraction and soot volume fraction obtained using several chemical-kinetics mechanisms and measurements at (a) 15-mm, (b) 40-mm, and (c) 70-mm flame heights. Simulations are made after incorporating a two-equation soot sub-model.

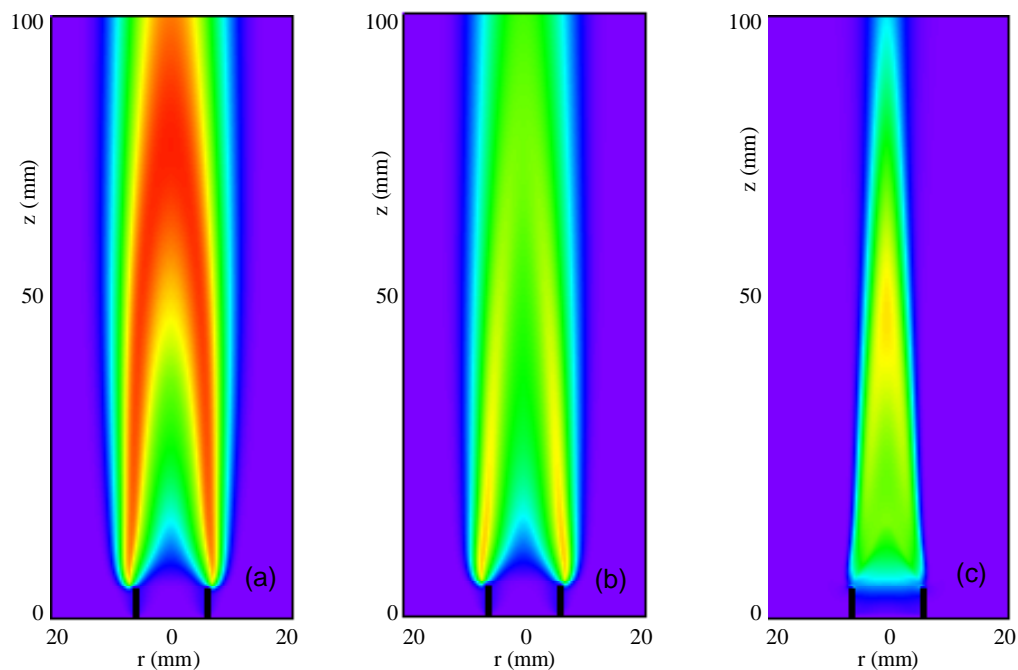


Figure 5.234 Flame structure simulated using San-Diego mechanism. (a) Temperature obtained without soot sub-model, and (b) temperature, and (c) soot volume fraction obtained with soot sub-model.

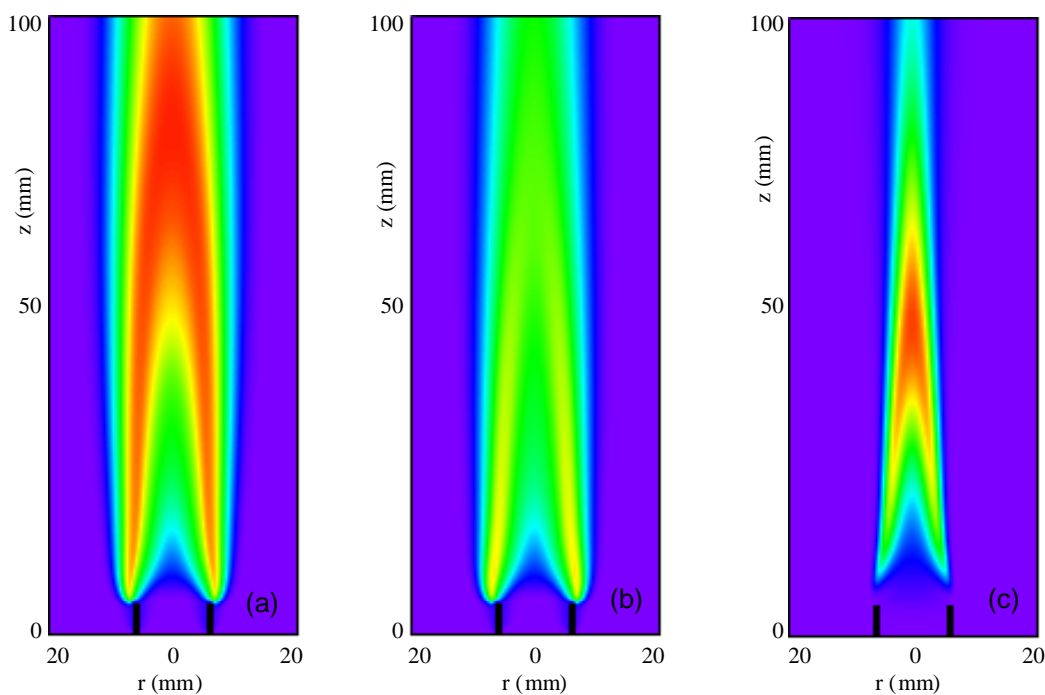


Figure 5.235 Flame structure simulated using Wang-Frenklach mechanism. (a) Temperature obtained without soot sub-model, and (b) temperature and (c) soot volume fraction obtained with soot sub-model.

### 5.5.2 Heptane Models

Three detailed chemical-kinetics models are considered for heptane combustion. First one is San Diego (SD) mechanism. It consists of 52 species and 544 elementary reactions (Mechanism D). The second one is Lawrence Livermore National Laboratory (LLNL) mechanism. It consists of 160 species and 1540 reactions (Mechanism E). And the third one is National Institute of Standards and Technology (NIST) mechanism. It consists of 197 species and 2926 reactions (Mechanism C). The simulations presented here are performed on a single cpu, AMD Opteron Personal Computer with 2.0 GB of memory. Typical execution time is ~30 s/time-step for the coaxial, non-premixed flame simulations. Steady state solutions are typically obtained in about 2,000 time steps starting from the solution obtained using the global combustion chemistry model. The calculations made for various flames with different heptane chemical kinetics models are presented below:

The opposing-jet flame considered for validating the numerical models is formed between pre-vaporized heptane and air jets. This flame represents a weakly stretched laminar flame and the experiments were carried out by Seiser et al (2000). The burner for gaseous reactants is made up of two opposing ducts with inner diameters of 22.2 mm through which reactants are introduced. The distance between the ducts is 10 mm. The mixture of n-heptane vapor and nitrogen is introduced from the bottom duct while air is introduced from the top duct. The temperatures of the fuel and air jets are 338 and 298 K, respectively. Experiments were conducted for different strain rates (velocities) and measurements for temperature and species were made along the burner centerline. For model validation purpose the data obtained at strain rate of  $150 \text{ s}^{-1}$  is considered.

$$\text{StrainRate} \quad a = \frac{2|V_2|}{L} \left( 1 + \frac{|V_1|}{|V_2|} \sqrt{\frac{|\rho_1|}{|\rho_2|}} \right)$$

Here,  $V_1$  and  $V_2$  represent the velocities of the fuel and air, respectively and  $\rho_1$  and  $\rho_2$  represent the respective densities.  $L$  is the separation between the fuel and oxidizer ducts. Fuel is composed of 15% heptane and 85% nitrogen. The fuel and air velocities used for the  $150\text{-s}^{-1}$  flame are 0.342 and 0.375 m/s, respectively. Two-dimensional simulations for the flowfield between the upper and lower ducts are performed using a  $301 \times 41$  variable grid system. This grid yielded a mesh spacing of  $33 \text{ }\mu\text{m}$  across the flame surface in the axial direction. Calculations for this flame are performed using the three chemical kinetics models. The three steady state flames obtained are shown in Figure 5.236. Temperature distributions color-coded with rainbow color scheme (red and violet representing 300 and 1700 K, respectively) are shown in Figure 5.236. The nonpremixed flame formed between the two reactant ducts is slightly curved upward toward air duct. All three mechanisms resulted in nearly identical flames in shapes and sizes.

Temperature and axial-velocity distributions along the centerline across the flame are shown in Figure 5.237. While the computed profiles are shown with lines temperature measurements obtained by Seiser et al. (2000) are plotted with solid symbols. Even though the moments of the fuel and oxidizer jets were matched, the stagnation plane (plane perpendicular to the centerline and passing through  $U = 0$  location) is located ~ 0.5 mm away from the midsection toward the fuel duct. The peak-temperature surface is located ~ 0.2 mm away from the midsection toward



the air duct, which is also the case in the experiments. All three mechanisms resulted in nearly identical temperature and velocity profiles. Calculated temperature profiles compare well with measured one. Maximum temperature predicted by NIST mechanism is  $\sim 40$  K lower than that obtained with SD or LLNL mechanism.

Distributions of fuel, oxygen,  $\text{H}_2\text{O}$ , and  $\text{CO}_2$  along the centerline are shown in Figure 5.238 along with the measured one. Once again, all three models predicted nearly the same distributions for these species. Comparisons with experiment are also reasonable. However, this is not the case for the other species such as fuel and radical species. Distributions of  $\text{H}_2$ ,  $\text{CO}$  and  $\text{C}_2\text{H}_2+\text{C}_2\text{H}_4$  are shown in Figure 5.238 and those of  $\text{CH}_4$ ,  $\text{C}_3\text{H}_6$  and  $\text{C}_2\text{H}_6$  are shown in Figure 5.240. In general, models are over predicting the concentrations for all these species. Note similar discrepancies between measurements and calculations were also obtained with a one-dimensional model CHEMKIN in conjunction with a shortened version of SD mechanism (Seiser et al. 1998). While SD and NIST mechanisms predict the same  $\text{H}_2$  concentrations LLNL mechanism is resulting in  $\sim 25\%$  more. Differences in the predictions made by the three mechanisms may be noted for all the species shown in Figures 5.239 and 5.240. However, these differences did not cause any deviations in the overall flame structures shown in Figures 5.236 and 5.237.

Using the burner described in the previous section Seiser et al. (2000) have obtained strain rates for extinguishing the flames. Selecting a particular value for the n-heptane-nitrogen ratio in the fuel jet and a matching ratio (based on flame-sheet location) for the air and nitrogen in the oxidizer jet Seiser et al. (2000) obtained critical conditions for extinction. They performed these experiments by varying the fuel and oxidizer jet velocities while allowing only a small change in the flame location by matching the momentums of these jets. Calculations with UNICORN code with SD, LLNL, and NIST mechanisms are performed for obtaining critical extinction conditions for a specific n-heptane-nitrogen ratio. The temperatures of the fuel and oxidizer streams are 345 and 298 K, respectively. Fuel is composed of 28.2% n-heptane and 71.8% nitrogen by volume. Oxidizer is composed of 20.5% oxygen and 79.5% nitrogen. Reactants ducts are separated by 10 mm. Calculations with the three mechanisms are repeated by gradually increasing the fuel and oxidizer jet velocities until the flame is extinguished. Incremental changes to the velocities were decreased as the flame approaches extinction conditions. Due to an imbalance between the heat produced in the flame and heat transported away from the flame, maximum temperature decreases with strain rate (or velocity). A typical strained flame obtained at near-extinction limit is shown in Figure 5.241. Since only the central part of the flame is strained due to the impinging reactant jets maximum temperature decreased only in this region. Flame became thin, but not infinitely thin, compared to the weakly strained one in Figure 5.236.

Results obtained in the form of changes to the maximum temperature with increase in strain rate are shown in Figure 5.242. Strain rate measured for the critical flame (just prior to extinction) is also shown in Figure 5.242 with a hatched rectangle. Significant differences are found in the flame responses predicted by the three mechanisms. LLNL mechanism is giving the most stable flame with a critical extinction strain rate of  $447\text{ s}^{-1}$ . This compares well with the measured value of  $460\text{ s}^{-1}$ . The NIST mechanism predicts lower maximum temperatures as noted in (Figure 5.237) and resulted in flame strain rate extinction of  $340\text{ s}^{-1}$ . The SD mechanism predicts higher temperatures in weakly strained flames (Figure 5.237) and resulted in a strain rate extinction of  $405\text{ s}^{-1}$ . Interestingly, one-dimensional calculations performed for this flame using LLNL

mechanism by Seiser et al. (2002) obtained an extinction strain rate of  $520 \text{ s}^{-1}$  which is  $\sim 13\%$  higher than the measured value. The two-dimensional simulations performed in this study using the same mechanism resulted extinction strain rate that is only 3% lower than the measurements. This suggests that the one-dimensional assumption for the flowfield at higher strain rates is not appropriate. Such differences in extinction conditions between the one-d and two-d simulations were also noted by Katta et al. (2007) in partially premixed flames.

Using opposing-jet flame configuration Seiser et al. (2000) have conducted autoignition experiments. They issued n-heptane-nitrogen mixture from the bottom duct and heated air from the top duct. Autoignition condition was reached by gradually increasing the air temperature. The volume fraction of n-heptane in the fuel jet was kept constant at 15% while the fuel temperature is maintained at 378 K. Experiments were performed for different strain rates. For validation purpose calculations for this configuration are performed for a strain rate of  $400 \text{ s}^{-1}$ . Two-dimensional simulations using SD, LLNL, and NIST mechanisms are performed by gradually increasing the air temperature. Since autoignition depends not only on temperature but also on induction time, calculations for this problem must be performed sufficiently long in time-beyond the time required for establishing a steady-state flowfield. Temperature distribution obtained for a 1282-K-airflow case is shown in Figure 5.243. This is computed using SD mechanism and flame has not been established, as autoignition did not take place. However, when the airflow temperature is increased by another degree to 1283 K autoignition took place.

Heated air mixes with the relatively cold fuel in the region surrounding the stagnation plane. Mixing of fuel and oxygen also simultaneously takes place. A combination of local equivalence ratio, strain rate and temperature determines the whether autoignition takes place or not. Therefore, one should not refer air temperature itself to as autoignition temperature and the ability of a chemical kinetics mechanism in predicting autoignition must be assessed by simulating the entire flowfield. Two-dimensional calculations are performed using three mechanisms. It is observed that temperature and OH concentration in the mixing region increase exponentially with air temperature. Therefore, for tracing autoignition process, computed results in the form of maximum temperature and OH concentration at different air temperatures are shown in Figure 5.244. The conditions at which autoignition took place in the calculations are marked with solid circles. The air temperature at which autoignition took place in the experiment is shown with hatched rectangle. Among the three mechanisms, NIST one is predicting autoignition process closer to the experiment. One-dimensional calculations performed with LLNL mechanism (Seiser et al., 2000) resulted autoignition when air temperature was 1237 K. Two-dimensional calculation with the same mechanism predicted (Figure 5.244) autoignition at 1264 K. In comparison experiment has suggested 1204-K air temperature for autoignition. However, there is about 50 K error margin associated with the measurements made by Seiser et al. (2000)

Flame speed is another characteristic parameter of fuel-air mixture, which needs to be represented accurately by the chemical kinetics employed. For understanding the flame-speed characteristics of the chemical-kinetics mechanisms calculations are performed for a Bunsen-type coaxial premixed flame using the three kinetics models. To allow for possible flashbacks in premixed systems a 5-mm-long fuel tube is included in the calculations. The inner and outer radii of the tube are 5.6 and 6.4 mm, respectively. Preheated stoichiometric fuel and air mixture at 400 K exits the fuel tube at an average velocity of 1.6 m/s. A parabolic, fully developed velocity

profile is assumed at the inlet of the fuel tube. A computational grid of  $201 \times 107$  is used for discretizing the physical domain of 20 cm x 5 cm in axial and radial directions, respectively. While calculations with LLNL and NIST mechanisms were carried with a time-step of 0.05 ms, calculations with SD mechanisms had to be carried with a time-step of 0.02 ms due to the difficulties with convergence. Results obtained with SD, LLNL, and NIST mechanisms are shown in Figures 5.245, 5.246, and 5.247, respectively. Temperature distributions color-coded with rainbow scheme (violet representing 300 K and red representing 2300 K) are shown in 5.245a, 5.246a, and 5.247a. Similarly,  $H_2$ -mole-fraction distributions between 0 and 0.002 are shown in b figures,  $O_2$ -mole-fraction distributions between 0 and 0.233 are shown in c figures and OH-mole-fraction distributions between 0 and 0.005 are shown in d figures.

Since the velocity profiles used in all the calculations shown in Figures 5.245 and 5.247 are the same, the surface area of the inner cone (or the height of the inner cone for equal base diameters) directly represent the flame speed. As seen from Figures 5.245a and 5.247a the SD and NIST mechanisms yielded nearly identical inner cone shapes and heights and, hence, have the same flame speeds. Both are exhibiting cellular flame structures. In fact, calculations with these two mechanisms did not reach a steady-state solution. On the other hand, calculations made with LLNL mechanism resulted in a steady flow with a smooth flame surface. Also, burning velocity estimated from inner cone height of Figure 5.246c is nearly 20% less than that obtained with the other two mechanisms. These differences and similarities in burning velocities obtained with different mechanisms are inconsistent with the extinction and autoignition properties obtained previously.

Flat flames obtained in opposing-jet configurations provide a good platform for testing the chemical-kinetics mechanisms. However, unlike most practical flames, opposing-jet flames do not have stability issues, as they do not possess leading edges. The role of chemical kinetics in the stability of jet flames is significant and, therefore, proposed chemical-kinetics mechanisms must also be tested for their ability in predicting nonpremixed jet flames as well. The advantage of codes like UNICORN is that once a chemical-kinetics mechanism is incorporated they can be used for the simulation of both opposing- and coaxial-jet flames.

Calculations for n-heptane coaxial nonpremixed jet flame are performed using the three chemical-kinetics models considered in the present work. The simulated burner has a central fuel tube of 0.6-cm radius and is surrounded by a 5-cm radius coflowing air. Preheated n-heptane at 400 K is issued at a velocity of 2.2 cm/s. Coannular flow consists of room-temperature air issued at a velocity of 9.2 cm/s. Such low-velocity conditions were chosen so that stable flames are established with all the three chemical-kinetics models. A computational grid of  $201 \times 71$  is used for discretizing the physical domain of 20 cm x 5 cm in axial and radial directions, respectively. Grid clustering is used for placing most of the grid lines in the flame zone. Initial conditions (flame) for the detailed-chemistry calculations are obtained from the simulation using a global-chemistry UNICORN code. Calculations with all three mechanisms were carried using a time-step of 0.05 ms.

Results for the coaxial nonpremixed jet flame obtained with the SD, LLNL, and NIST mechanisms are shown in Figures 5.248, 5.249, and 5.250, respectively. Temperature distributions color-coded with rainbow scheme (violet representing 300 K and red representing 2100 K) are shown in 5.248a, 5.249a, and 5.250a. Similarly,  $H_2$ -mole-fraction distributions

between 0 and 0.004 are shown in b figures,  $O_2$ -mole-fraction distributions between 0 and 0.233 are shown in c figures and OH-mole-fraction distributions between 0 and 0.003 are shown in d figures.

In general, all three models predict nearly the same flame shape with tips burning hotter than the bases. The flames are anchored to the burner rim on the outer edge. There are several differences in these predictions. LLNL mechanism predicts higher  $H_2$  concentration inside the flame than that predicted by NIST mechanism, which is higher than that predicted by SD mechanism. First part of this difference is consistent with the predictions made for the opposing-jet flame (Figure 5.239); however, the second part is not. In opposing jet flame both the SD and NIST mechanisms yielded nearly the same  $H_2$  concentrations. OH predicted by NIST mechanism is lower than those predicted by the other two mechanisms. Oxygen tends to leak from the flame base into the fuel jet for SD and NIST mechanisms while flame base is tightly anchored to the burner rim in LLNL simulation. This is consistent with the burning velocities obtained with Bunsen-type-premixed-flame calculations.

In conclusion, all three mechanisms are reasonably close to each other in predicting co-axial jet nonpremixed and premixed flames. SD mechanism is found to be slightly stiffer than the other two mechanisms, especially in solving for premixed combustion. While LLNL kinetics resulted in a steady Bunsen-type premixed flame, SD and NIST mechanisms yielded cellular-type flame structures for the same flow conditions.

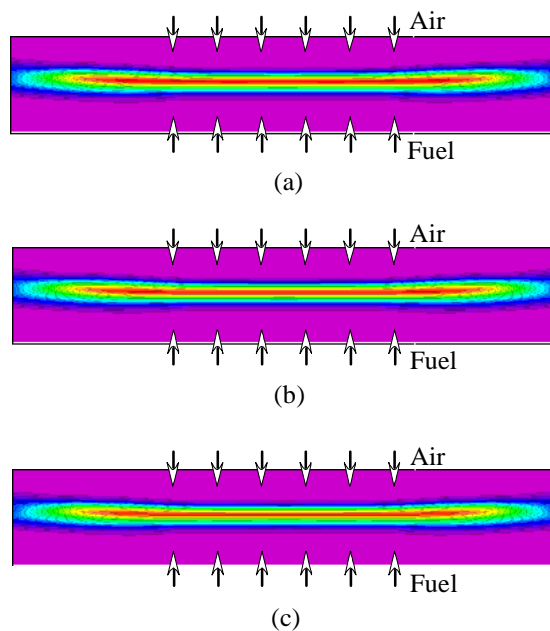


Figure 5.236 Opposing-jet non-premixed heptane flame simulated using (a) SD mechanism, (b) LLNL mechanism, (c) NIST mechanism. Global strain rate is  $150\text{ s}^{-1}$ . Temperature distributions are shown between 300 and 1700 K.

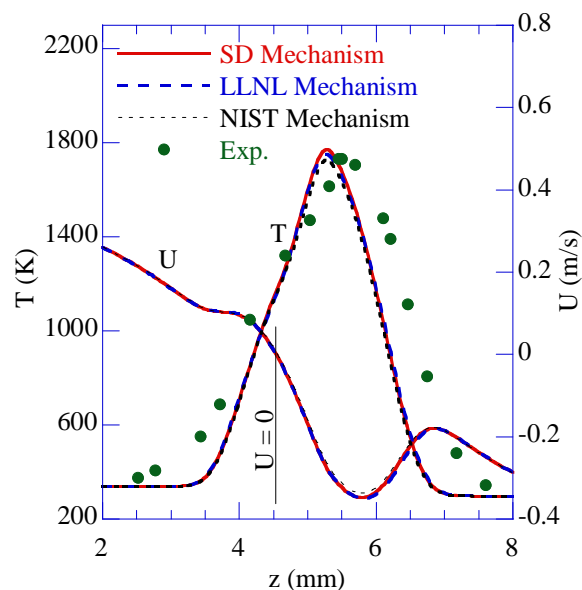


Figure 5.237 Distributions of temperature and axial velocity plotted along the centerline. Lines represent profiles computed using different chemical kinetics mechanisms and symbols represent measurements of Seiser et al. (2000) Global strain rate is  $150 \text{ s}^{-1}$ .

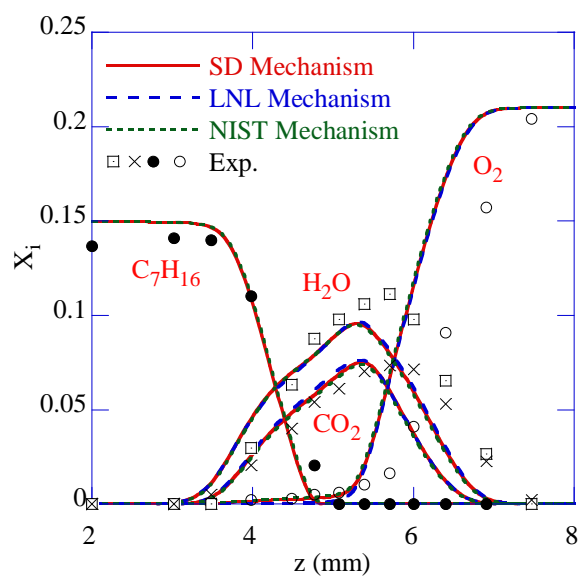


Figure 5.238 Distributions of fuel, oxygen,  $\text{H}_2\text{O}$ , and  $\text{CO}_2$  plotted along the centerline. Lines represent profiles computed using different chemical kinetics mechanisms and symbols represent measurements of Seiser et al. (2000) Global strain rate is  $150 \text{ s}^{-1}$ .

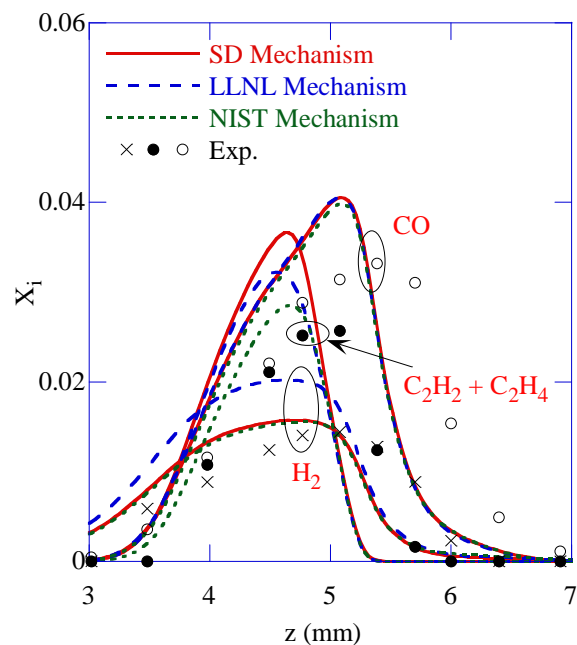


Figure 5.239 Distributions of intermediate fuel species  $H_2$ ,  $C_2H_2 + C_2H_4$ , and  $CO$  plotted along the centerline. Lines represent profiles computed using different chemical kinetics mechanisms and symbols represent measurements of Seiser et al. (2000) Global strain rate is  $150 \text{ s}^{-1}$ .

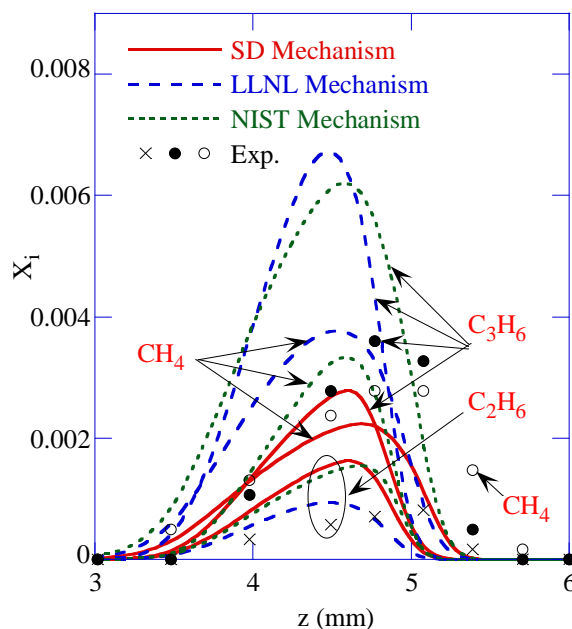


Figure 5.240 Distributions of intermediate species  $CH_4$ ,  $C_3H_6$ , and  $C_2H_6$  plotted along the centerline. Lines represent profiles computed using different chemical kinetics mechanisms and symbols represent measurements of Seiser et al. (2000) Global strain rate is  $150 \text{ s}^{-1}$ .

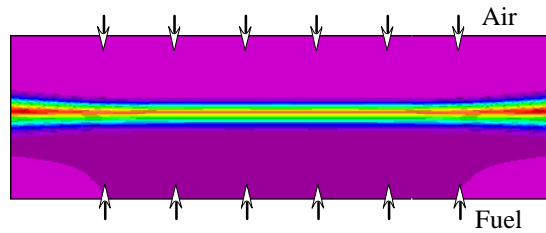


Figure 5.241 Near-extinction opposing-jet non-premixed heptane flame simulated using SD mechanism. Global strain rate is  $408 \text{ s}^{-1}$ . Temperature distribution is shown between 300 and 1800 K.

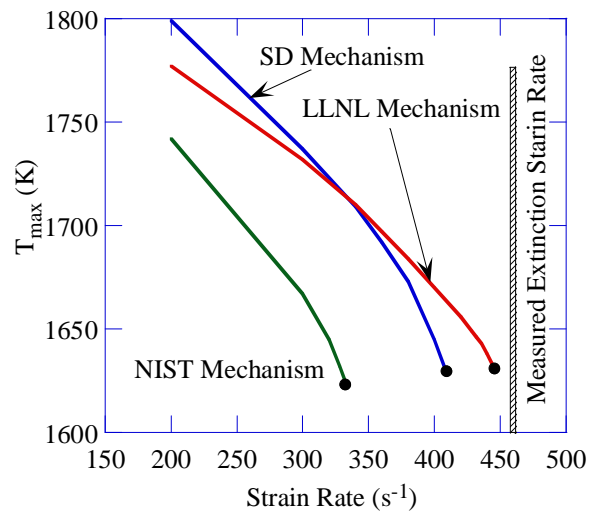


Figure 5.242 Maximum flame temperatures obtained at different strain rates. Solid circles represent extinction conditions.

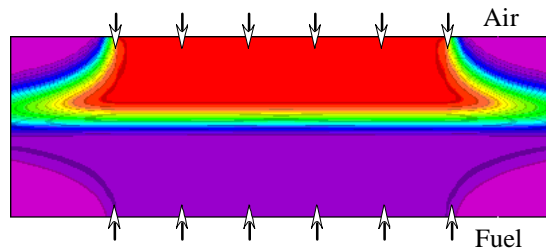


Figure 5.243 Temperature distribution between the opposing jets of premixed heptane-air fuel and 1282-K air. Global strain rate is  $400 \text{ s}^{-1}$ . Temperature distribution is shown between 300 and 1300 K.

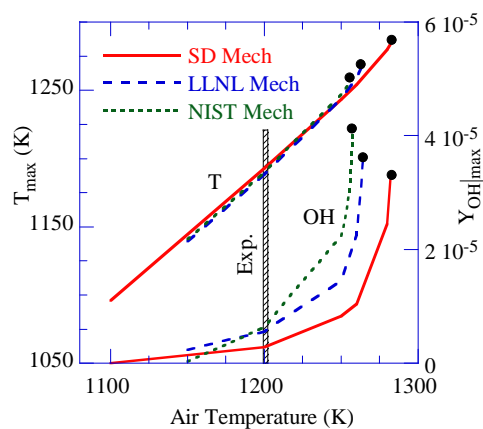


Figure 5.244 Maximum temperatures and OH concentrations obtained for different air temperatures. Solid circles represent ignition conditions.

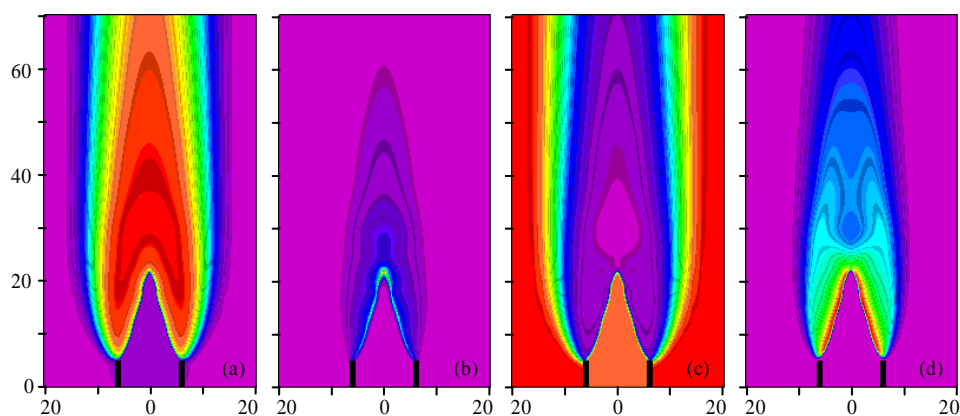


Figure 5.245 Premixed flame calculated using SD mechanism. Distributions of (a) T, (b)  $H_2$ , (c)  $O_2$ , and (d) OH.

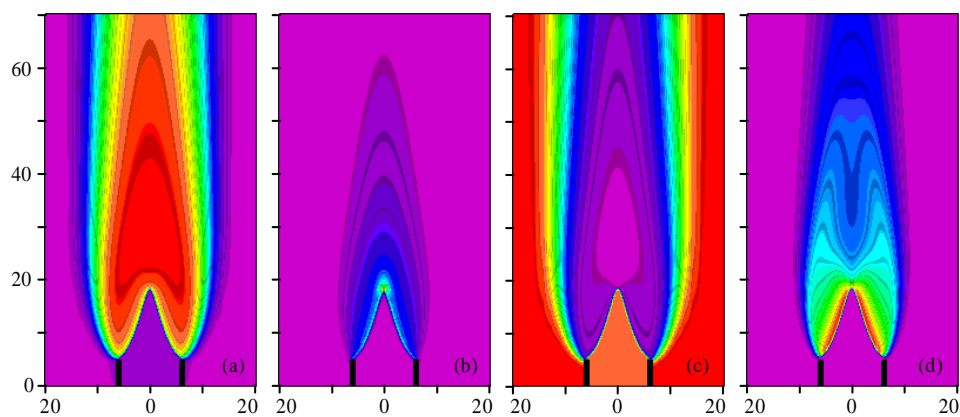


Figure 5.246 Premixed flame calculated using LLNL mechanism. Distributions of (a) T, (b)  $H_2$ , (c)  $O_2$ , and (d) OH.



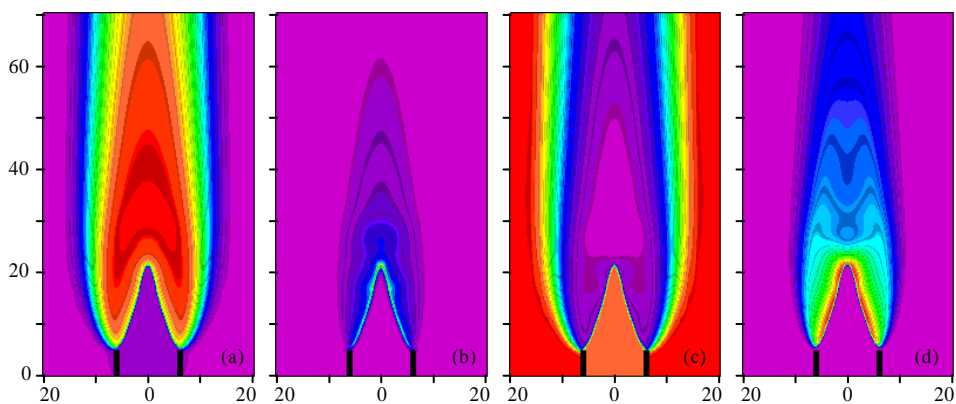


Figure 5.247 Premixed flame calculated using NIST mechanism. Distributions of (a) T, (b)  $H_2$ , (c)  $O_2$ , and (d) OH.

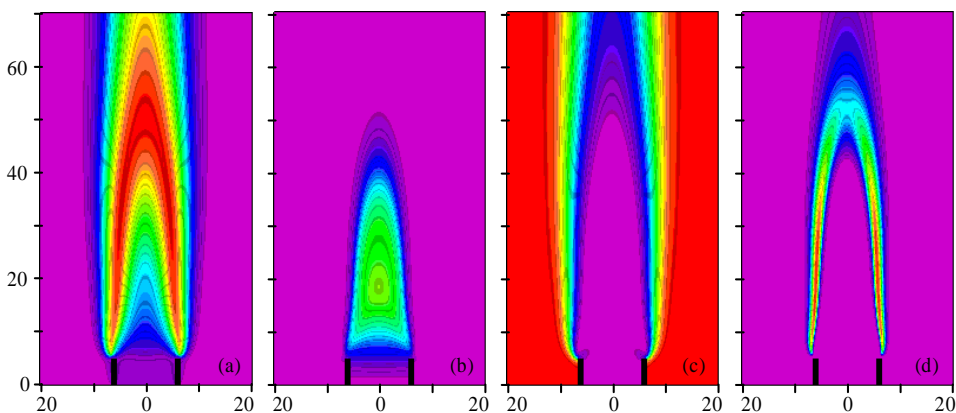


Figure 5.248 Non-premixed flame calculated using SD mechanism. Distributions of (a) T, (b)  $H_2$ , (c)  $O_2$ , and (d) OH.

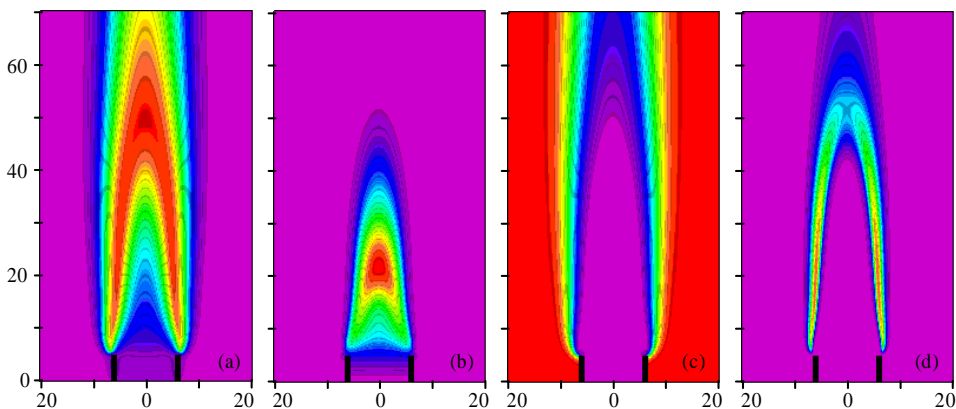


Figure 5.249 Non-premixed flame calculated using LLNL mechanism. Distributions of (a) T, (b)  $H_2$ , (c)  $O_2$ , and (d) OH.

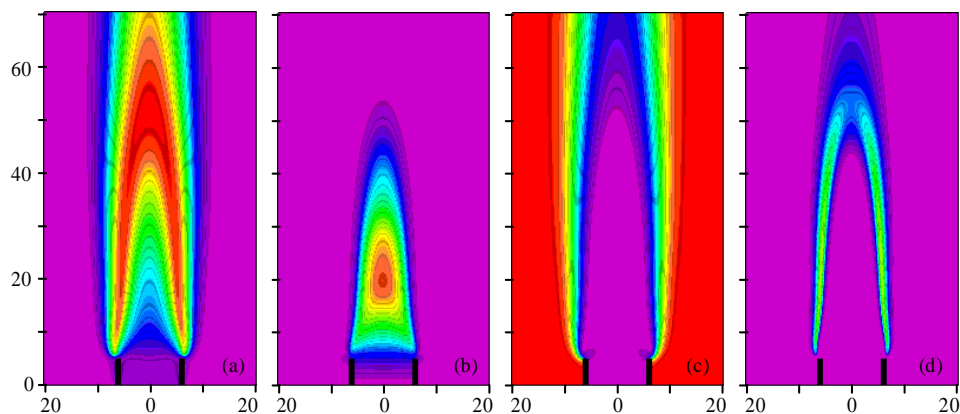


Figure 5.250 Non-premixed flame calculated using NIST mechanism. Distributions of (a) T, (b)  $H_2$ , (c)  $O_2$ , and (d) OH.

### 5.5.3 JP-8 Models

Petroleum-derived fuels are composed of a very large number of individual molecular species that can generally be grouped by their similarities in chemical structures. The major types of species found in aircraft fuels such as JP-8 are normal alkanes, iso-alkanes, cyclo-alkanes, and aromatics. The classification fractions and specific components within each classification can vary considerably. Detailed kinetic modeling of each species and their interactions is prohibitively complex given the variability, numbers, and types of individual components found in the fuels and lack of fundamental physical, thermochemical, kinetic, and transport data. A frequently applied alternative has been to use a “surrogate” fuel composed of a small number of known components to emulate the desired properties of a particular real fuel. Many surrogate mixtures are formulated based entirely on empirical test methods, and correlations to match the surrogate to the real fuel.

The number of components required in a surrogate mixture for describing a real fuel increases dramatically if both chemical and physical properties (e.g. distillation curve) are included in the properties to be replicated. The dimensional size of chemical kinetics models to accurately predict the behavior of the surrogate mixture quickly grows with the chosen number of components. Furthermore, the amount of experimental data needed to validate kinetic and transport effects for each fuel component, their interactions in the mixtures, and to compare against the real fuel behavior over the wide ranges of conditions found in practical combustion systems becomes daunting. Considering these issues research groups (Colket et al., 2007) are coming with different surrogate mixtures with minimum possible number of parent components based on their analyses and requirements. As a result one could find at least four surrogate mixtures for JP-8 (Schulz et al., 1991, Montgomery et al., 2002, Violi et al., 2002) in the literature. It is important and also necessary to understand how different (or similar) the existing JP-8 surrogates are in predicting a variety of simple laboratory combustion systems. Two JP-8 surrogates namely, 6-COMP and SERDP are evaluated in this study. The first one was developed by Violi et al. (2002) and consists of six parent components and the second one was developed by Colket (2009) which consists of two parent components. Details of these surrogate mixtures are given in Table 5.8 UNICORN is used for the simulation of opposing-jet and co-axial-jet non-

premixed flames. Detailed chemical-kinetics model (Mechanism F) developed by Violi for the combustion of JP-8 surrogates is used. It consists of 161 species and 1538 reactions. Extensive calculations are performed using different surrogate mixtures for JP-8 fuel. Numerical experiments are performed through altering the composition of the surrogate mixture and comparing the results in the form of extinction strain rates, liftoff heights, shapes, and sooting characteristics with those of the original mixture.

Calculations made for a co-axial jet non-premixed flame using 6-COMP and SERDP surrogates are shown in Figures 5.251 and 5.252. Fuel jet consists of 80 percent (by mass) vaporized surrogate mixture and the rest gaseous nitrogen. Fuel is delivered from a 6-mm diameter center tube at 8-cm/s velocity. Fuel jet is surrounded by 8.8-cm/s co-flowing air. The inlet temperatures for fuel and air jets are 400 K and 300 K, respectively. These flow conditions and tube diameter were chosen such that the established flames are reasonably long for doing probe measurements in the laboratory and not that long for making simulations with reasonable number of grid points. The computational domain of 5x15 cm is discretized using a nonuniform grid system having 71x201 points in the radial and axial directions, respectively. Computed temperature fields with 6-COMP and SERDP surrogates are shown in Figures 5.251a and 5.251b, respectively. Here, a rainbow color scheme, with red representing the peak temperature of 2000 K and purple representing the minimum temperature of 300 K, is employed. The corresponding soot distributions (between 0 and 12 ppm) are shown in rainbow color scheme in Figures 5.252a and 5.252b, respectively. As suggested by the temperature distributions, flames are lifted off of the fuel tube and stabilized at about 3 mm above the burner. Soot formed at the center of the flame is cooling the latter in the upper region and causing opened-tip-type flames. A close look at the base of the flames reveals that SERDP surrogate is predicting slightly longer liftoff height.

Calculations for an opposing-jet non-premixed flame are also performed using the two surrogate mixtures. Unlike the traditional approach of using one-dimensional analyses for obtaining flow structure along the centerline in these flames, full axisymmetric calculations using UNICORN code are performed for simulating the entire flame structure. The physical domain between the two opposing nozzles (14 mm in the axial direction and 20 mm in the radial direction) is represented using a 201x31-grid system, which resulted in a uniform grid spacing of 70  $\mu\text{m}$  across the flame. Fuel (a mixture of surrogate and  $\text{N}_2$  in the ratio of 1:11.4 by weight) is issued from the bottom nozzle while pure oxygen is issued from the top nozzle. Experiments for these flames were conducted by Holley et al (2007). The temperatures of the fuel and oxidizer streams were set to the measured values of 394 and 294 K, respectively. Initially a stable flame was established for low fuel and oxidizer velocities of 0.2 and 0.2 m/s, respectively. The corresponding global strain rate was  $28.6 \text{ s}^{-1}$ . Once a flame is established for the given strain-rate condition, the velocities of the fuel and oxidizer jets were increased gradually and a new flame solution was obtained for the higher strain-rate conditions. This process is repeated till the flame is extinguished. Solutions obtained using 6-COMP and SERDP surrogates for a strain rate of  $60 \text{ s}^{-1}$  are shown in Figure 5.253a and 5.253b, respectively. Distributions of temperature and soot volume fraction are shown in the left and right halves, respectively. The temperature and soot predicted with SERDP surrogate are slightly lower than those predicted with 6-COMP surrogate. The peak values measured along the centerline are plotted in Figure 5.254 for various strain-rate conditions. For each mixture, the strain rate was increased till the flame was extinguished. The end values on each profile in Figure 5.254 represent the extinction conditions. In general, temperature and soot predicted at all strain-rate conditions with SERDP surrogate are slightly

lower than those predicted with 6-COMP surrogate. Also, the extinction strain rate obtained with the SERDP surrogate is slightly less than that obtained with the 6-COMP surrogate.

The temperature and soot distributions shown in Figures 5.251 to 5.254 suggest that both surrogate mixtures are yielding nearly the same flame structures in different flames and for different conditions. Even though, detailed comparisons reveal some differences between the solutions predicted with the 6-COMP and SERDP surrogates, it is not possible to draw a conclusion on the accuracy of the surrogate mixtures until the relevant experiments are performed. On the other hand, just based on the computed results, it is fair to conclude that both the surrogate mixtures are generating nearly the same flames. This outcome from the calculations is rather surprising, especially, looking at the wide variations in the distributions of the parent components (Table 5.8) in the two surrogate mixtures. It raises a question whether the two surrogates that are cleverly and independently formulated to represent JP-8 are so accurate or the variations in the concentrations of the parent species in a surrogate mixture are not that important. In order to address this question a sensitivity study has been performed in the present paper using 6-COMP surrogate mixture. Variations to the flame structure when the concentration of a parent component in the 6-COMP surrogate mixture was changed by a specified amount were investigated in opposing-jet and co-flowing jet non-premixed flames.

For understanding the influence of a particular parent component in the surrogate mixture, baseline structures of the opposing-jet non-premixed flames for pure components are obtained by repeating the calculations shown in Figure 5.253 after replacing the surrogate fuel with one of its parent components. It is important to understand that these calculations are performed for establishing the role of each parent component in the surrogate mixture rather than determining the characteristics of the component itself. Violi's mechanism was developed in conjunction with the surrogate mixture and its predictive abilities for the pure components were not tested. Hence, the computed results for the pure components should only be used for understanding their role in the mixture.

The predicted responses of the opposing-jet flame to increases in strain rate for six parent components are shown in Figure 5.255 along with those obtained for the 6-COMP surrogate mixture. In general, temperatures of the m-xylene and tetralin flames are the lowest and those of the iso-octane flame are the highest at a given strain rate. Behavior of the flame formed with 6-COMP surrogate followed closely to that formed with n-dodecane up to the extinction limit. However, 6-COMP surrogate flame extinguished slightly before the n-dodecane flame on the strain-rate scale. Next closest behavior of a pure component flame to the surrogate flame may be found for tetradecane. The concentration of tetralin in the mixture is only 5% and that of m-xylene is only 15% and hence they probably did not influence the mixture behavior significantly. On the other hand, the parent species that are present in high concentrations (tetradecane, methylcyclohexane and iso-octane) also did not influence the flame behavior much. Overall, flame formed with the mixture is dominated by the characteristics of n-dodecane, the parent component that is present in the mixture in highest concentration.

Sensitivity of the flame behavior to the changes in concentrations of the parent component is studied by repeating the opposing-jet-flame calculations after increasing the concentration of a parent component in the mixture by 10%. To keep the total volumetric flow of the fuel constant percentages of the remaining parent components in the mixture were decreased proportionally.

Results obtained for all the parent components are shown in Figure 5.256 using broken lines. Behavior of the 6-COMP surrogate mixture is shown in Figure 5.256 using solid line. Interestingly, the combustion characteristics of the surrogate mixture did not change notably when the concentration of a parent component was increased by 10%. These calculations suggest that the combustion characteristics of the mixture are not sensitive to small changes in the mixture composition.

Detailed structures of the flames formed with parent component (dashed lines), 6-COMP mixture (solid lines), and a mixture with 10% additional parent component (dashed lines with symbols) are shown in Figure 5.257 for a global strain rate of  $60 \text{ s}^{-1}$ . Concentrations of  $\text{H}_2$ , OH and soot across the flame surface are plotted for each surrogate component. As expected, original mixture and the mixture with 10% more parent component gave identical profiles for all six components. In line with the observations made for flame temperature (Figure 5.255) species concentrations of the surrogate mixture followed closely those of dodecane (Figure 5.257e). While the soot produced by m-xylene and tetralin is lower than that produced by the surrogate mixture, soot produced by all the other parent components is higher. Since the sooting behavior of the parent components in relation to that of the mixture are similar to the behavior observed in combustion characteristics (T in Figure 5.255 and  $\text{H}_2$  and OH in Figure 5.257) the former behavior could be due to the changes in flame temperature.

Sensitivity studies for the co-flowing jet flame (Figure 5.251) are performed through changing the concentrations of the parent components in the mixture. The following changes to the 6-COMP surrogate mixture are considered in this sensitivity study

- removing a parent component from the mixture
- increasing the concentration of a parent component in the mixture by 10%
- increasing the concentration of a parent component in the mixture by 50%
- increasing the concentration of a parent component in the mixture by 100%
- removing all the other parent components from the mixture

All these calculations are done for the six parent components present in the 6-COMP surrogate mixture. Note that when the concentration of a particular component was changed as described above, to keep the volumetric flow rate constant, concentrations of the all other components in the mixture were adjusted accordingly. For example, when the concentration of m-xylene in the mixture was increased to 30% from its original concentration of 15% in the 6-COMP surrogate then the concentrations of the remaining components in the mixture were reduced by a factor of 0.8235. Results obtained for these modified mixtures should be viewed along with those obtained for the 6-COMP surrogate (Figure 5.251). The flames computed with 1, 4, and 5 changes made to the mixture are shown in the form of temperature distributions for all the six parent components in Figure 5.258. The striking aspect of this composite figure is that flame did not change much even though the mixture composition was widely varied. All the flames shown in Figure 5.258 are plotted with a rainbow color scheme with red and purple representing the maximum and minimum temperatures of 2000 K and 300 K, respectively. As expected, pure m-xylene flame (100% in Figure 5.258a) shifted farther downstream as this component has the lowest extinction strain rate (Figure 5.255). Surprisingly, pure tetralin flame (100% in Figure 5.258b) shifted closer to the burner even though the extinction strain rate is slightly higher than that of the surrogate mixture. Similarly, flames formed with pure iso-octane and n-dodecane did

not shift much from the location obtained with the surrogate mixture even though their extinction strain rates are significantly higher than that of the mixture. These calculations suggest that flame liftoff process (or stabilization process) is not associated with the flame extinction process. To better understand the liftoff process we also need to consider the ignition properties of the pure components and the surrogate mixture.

The flame shapes computed with various fuel mixtures and pure components (Figure 5.258) are nearly the same. This is as expected since the molecular weights of the mixtures and components are not that different from each other. The lighter components such as m-xylene and MCH are giving the shortest flames (Figures 5.258a and 5.258c). Distributions of soot volume fraction predicted in all the flames shown in Figure 5.258 are plotted in Figure 5.259 using rainbow color scheme with red representing the maximum value of 12 ppm. Soot seems more sensitive (compared to flame liftoff heights and shapes) to the variations in the fuel mixture. Tetralin produces the most soot in the flame while iso-octane produces the least. Even though, the flame shifted away from the burner when the surrogate mixture was replaced by pure m-xylene, soot inception location did not change much. Looking at Figure 5.258, based on flame shapes and liftoff heights, it could be concluded that the characteristics of 6-COMP mixture match better with those of pure n-dodecane. Similarly, looking at Figure 5.259, based on soot concentrations, it may also be concluded that the sooting characteristics of the flame formed with 6-COMP mixtures match better with those of tetradecane or dodecane.

Summary results of the various calculations made for the co-axial jet flame are shown in the sensitivity plots of Figures 5.260a and 5.260b. The liftoff height measured for each flame is plotted in Figure 5.260a and the corresponding peak soot volume fraction is plotted in Figure 5.260b. Note that since the grid spacing used in these calculations is 0.4 mm and the liftoff heights are rounded to the closest grid point, data plotted in Figure 5.260a limited by a resolution of 0.4 mm. Even though m-xylene can shift the flame significantly, its presence in the surrogate mixture did not affect the liftoff height. Note that the concentration of m-xylene in the surrogate is 15%. Even a 10% increase in its concentration did not change the liftoff height. This means that at 15% level m-xylene has no effect on the liftoff height. Similarly, tetralin by itself shifted the flame closer to the burner significantly. However, at 5% level (tetralin concentration in the surrogate) it has no impact on the flame liftoff height. Even doubling that concentration did not change the flame. Removal of MCH from the surrogate increased the flame liftoff height by 0.8 mm while MCH itself made the flame to anchor to the burner (i.e., zero liftoff height). However, even doubling its concentration in the surrogate did not change the liftoff height. Interestingly, iso-octane exhibited no sensitivity in the surrogate mixture. Flame did not change whether it is removed or its concentration is increased to 100%. Similar behavior is observed for n-dodecane also. The most unusual behavior is noted with tetradecane. Removal of tetradecane from the surrogate mixture increased the flame liftoff height while by itself it decreased the liftoff height. However, when its concentration was doubled in the surrogate mixture, flame liftoff height increased instead of decreasing. This suggests that it may not be always possible to guess a component's behavior in a mixture based on its own characteristics.

Figure 5.260b suggests that even though soot generated by the flame changes with small variations in the surrogate composition, the magnitude of the variation itself is not that much. This is because all the parent components in the surrogate are producing soot within a narrow range between 9 and 13 ppm. In general, the parent component that is producing more soot than

that in the surrogate mixture produces less soot when its concentration in the surrogate mixture is decreased and produces more when its concentration is increased. Opposite behavior is found with the parent components that are producing less soot than that in the surrogate flame. This means that qualitative sooting characteristics of a mixture can be obtained from the sooting characteristics of the individual components. In general, it is found that the parent components that are present in the surrogate in concentrations less than 15-20% do not have any influence on the combustion characteristics of the surrogate mixture.

Calculations are also performed for the centerbody flame using parent components and surrogate mixtures of JP-8 fuel. Velocities of both the central fuel jet and annulus air jet were fixed at 1.25 m/s. Fuel jet consists of 80% JP-8 surrogate or pure component and 20% nitrogen and is preheated to 400 K. Temperature distributions obtained for various centerbody flames are shown in Figure 5.261 and the corresponding soot distributions are shown in Figure 5.262.

Both SERDP and 6-COMP surrogate mixtures resulted nearly the same flames. Except for m-xylene all other parent components yielded flames similar to those obtained with the surrogate mixtures. Interestingly, only a recirculation-zone flame was established with m-xylene and the trailing jet flame was extinguished. Considering the long ignition delays found with m-xylene one could expect the latter prediction of trailing-flame extinction. However, existence of recirculation-zone flame is rather surprising. It was found in the earlier studies with ethylene fuel that under certain dilution/velocity conditions the recirculation-zone flame could get extinguished while the trailing flame is still present. The opposite behavior observed with m-xylene cannot be explained with extinction related to strain rate. It is believed that the secondary fuel components formed and carried into the recirculation zone are responsible for establishing the flame with m-xylene.

Both surrogate mixtures generated nearly the same amount of soot in the trailing flames (Figure 5.262). However, SERDP surrogate seems producing more soot in the recirculation zone. Interestingly, soot produced in the recirculation zone by the 6-COMP mixture is less than that produced by any of the six components individually. These calculations suggest that recirculation zones in flames behave very differently compared to normal jet diffusion flames.

Table 5.8 Surrogate Mixtures for JP-8 Fuel.

Parent Components	6-COMP Surrogate (%)	SERDP Surrogate (%)
m-xylene (C <sub>8</sub> H <sub>10</sub> )	15	23
tetralin (C <sub>10</sub> H <sub>12</sub> )	5	0
methylcyclohexane MCH (C <sub>7</sub> H <sub>14</sub> )	20	0
iso-octane (i-C <sub>8</sub> H <sub>18</sub> )	10	0
n-dodecane (n-C <sub>12</sub> H <sub>26</sub> )	30	77
tetradecane (n-C <sub>14</sub> H <sub>30</sub> )	20	0
<b>Molecular Weight</b>	<b>144.38</b>	<b>155.56</b>

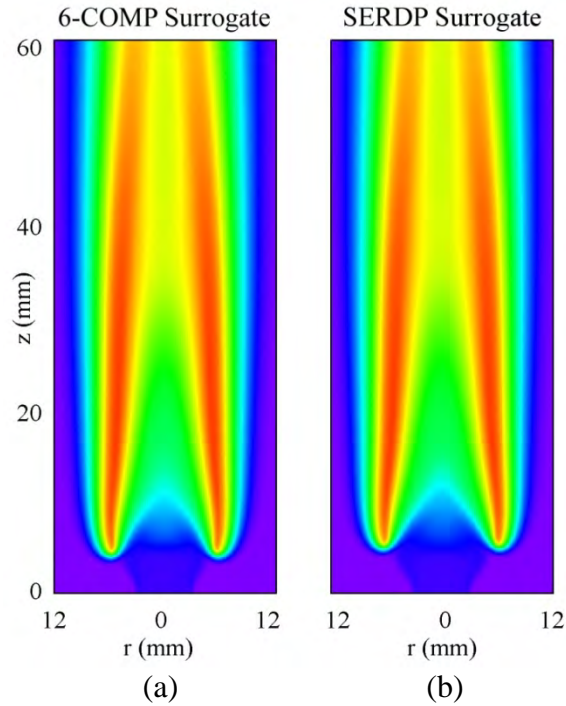


Figure 5.251 Temperature distributions of JP-8/air coaxial-jet flame simulated using (a) 6-COMP and (b) SERDP surrogate representations of JP-8 fuel.

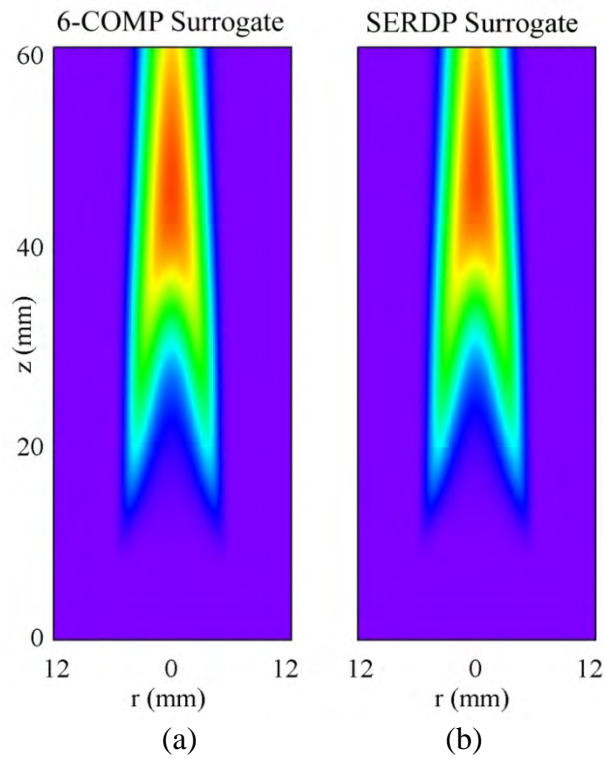


Figure 5.252 Distributions of soot in JP-8/air coaxial-jet flame simulated using (a) 6-COMP and (b) SERDP surrogate representations of JP-8 fuel.



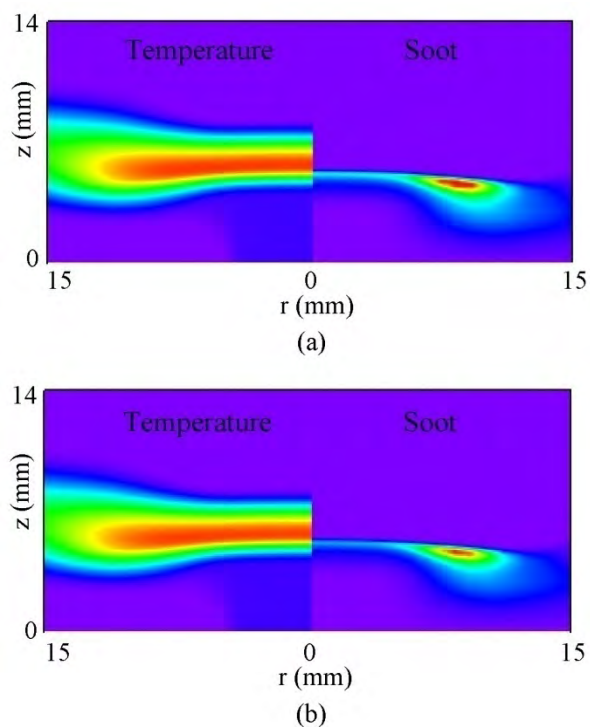


Figure 5.253 JP-8/Air opposing-jet flame simulated using (a) 6-COMP and (b) SERDP surrogate mixtures. Temperature and soot distributions are shown in the left and right halves of the images, respectively. Global strain rate is  $60 \text{ s}^{-1}$ .

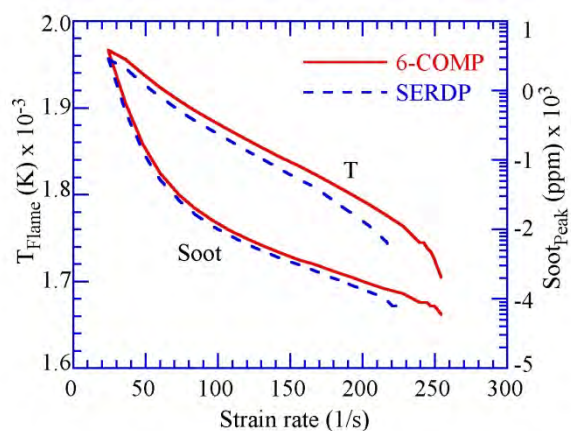


Figure 5.254 Comparison of flame characteristics (peak temperature and peak soot volume fraction) obtained with 6-COMP and SERDP surrogate mixtures at different strain rates. Right most end points of each curve represent extinction values.

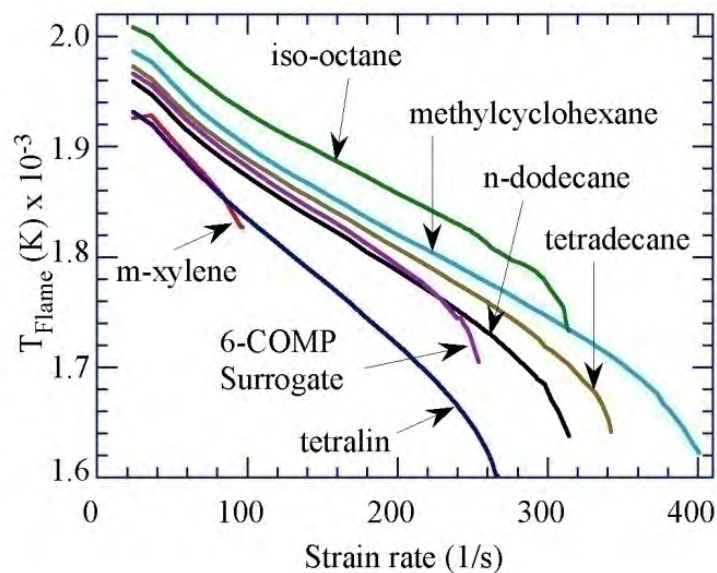


Figure 5.255 Peak temperatures of JP-8/air opposing-jet flames at different strain rates simulated assuming JP-8 fuel either as 6-COMP surrogate mixture or as individual parent components of the surrogate mixture. Right most end points of each curve represent extinction values.

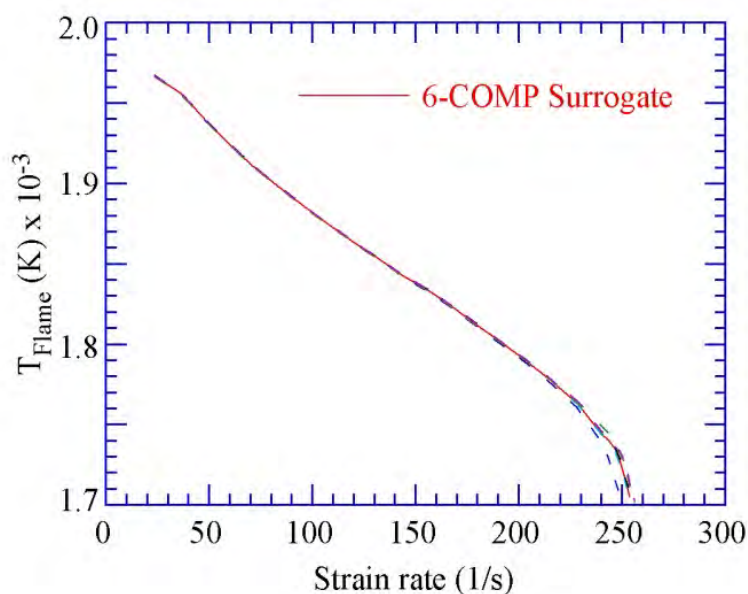


Figure 5.256 Sensitivity of flame temperature at different strain rates to the changes in the concentrations of the parent components in the 6-COMP surrogate mixture. Calculations are made after increasing the concentration of a component by 10% and reducing the concentrations of the remaining components proportionally.

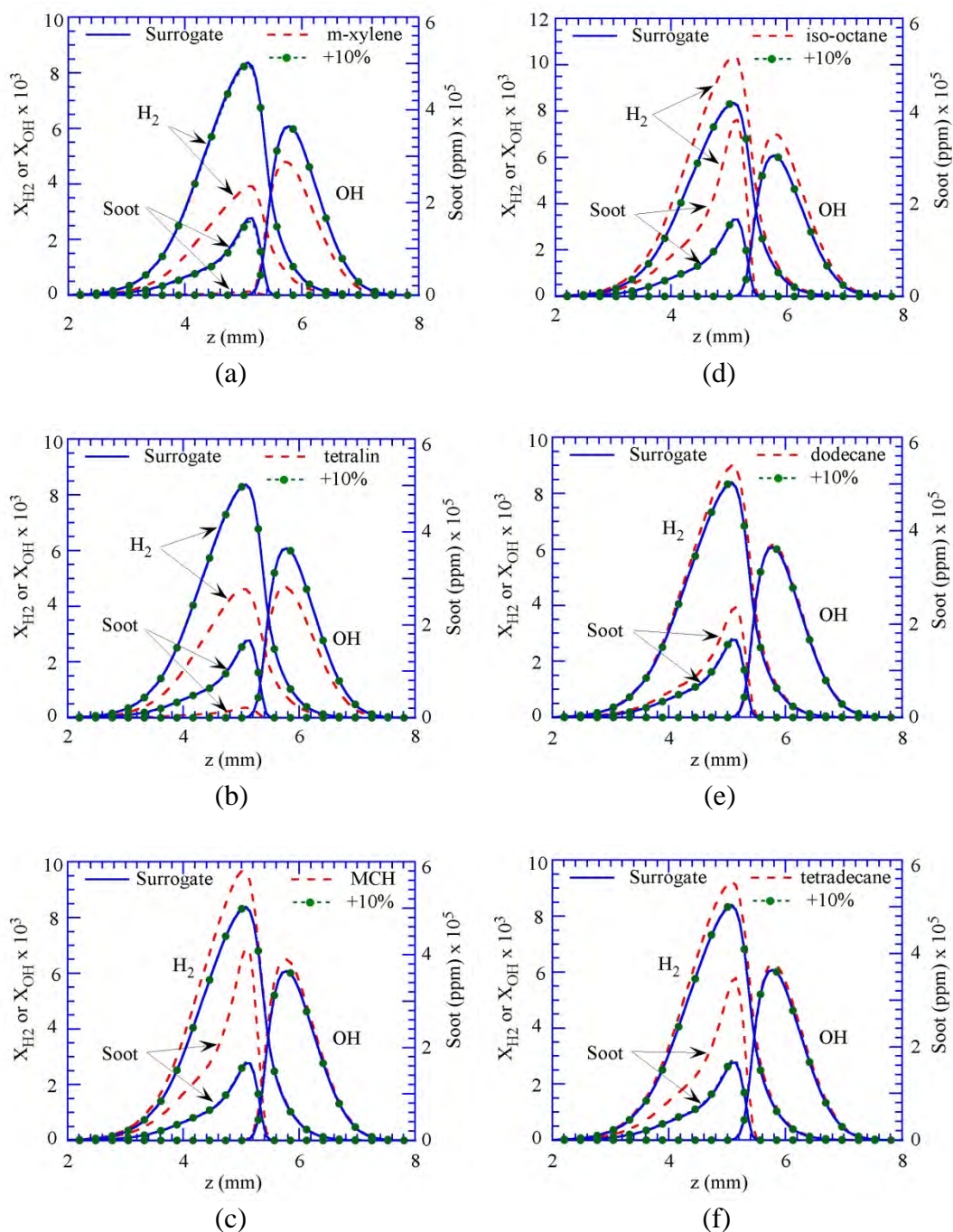


Figure 5.257 Sensitivity of opposing-jet flame to the variations in parent species concentrations. Concentrations of (a) m-xylene, (b) tetralin, (c) methylcyclohexane (MCH), (d) iso-octane, (e) n-dodecane, and (f) tetradecane in the 6-COMP-surrogate mixture are increased by 10%.

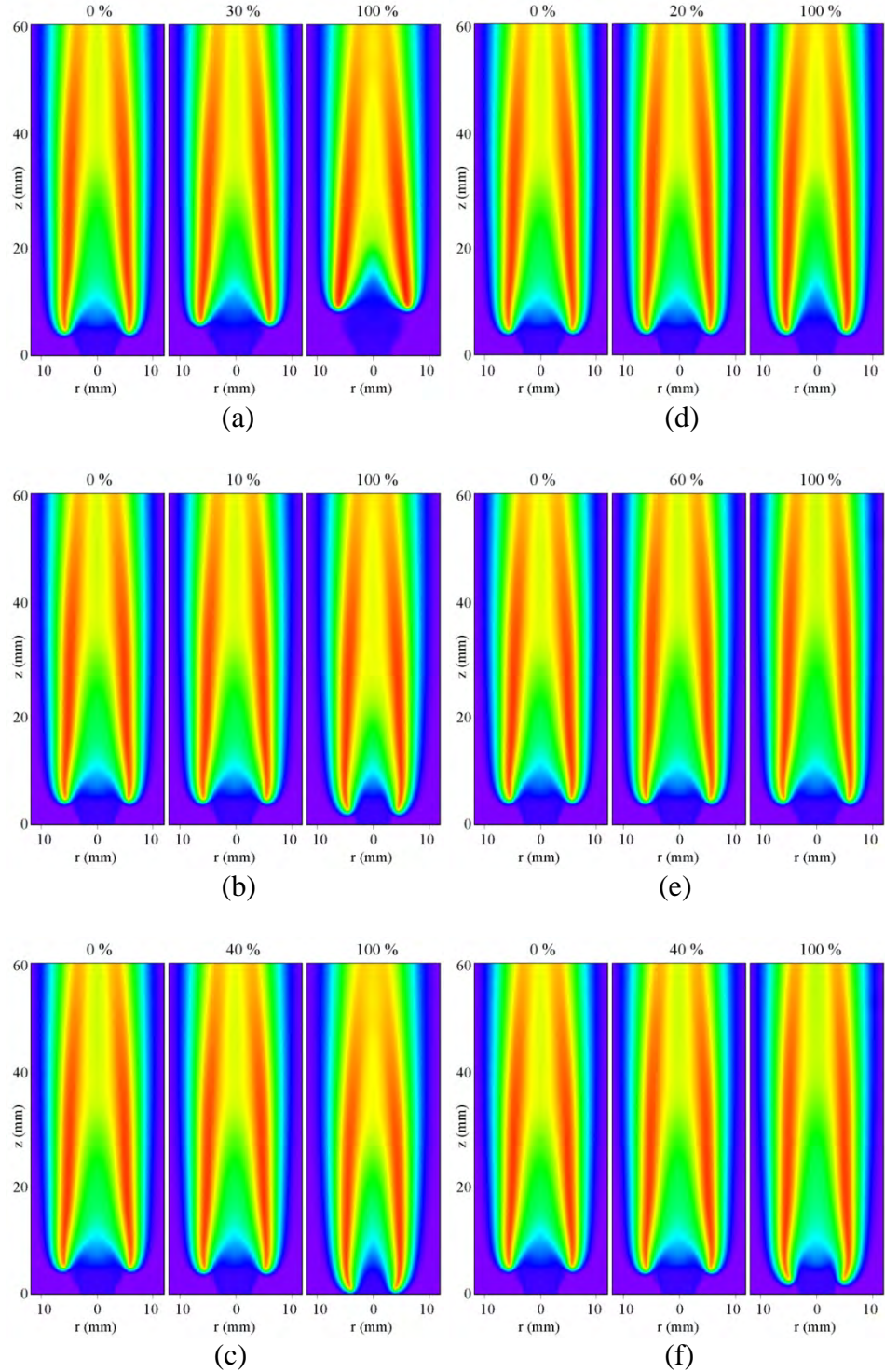


Figure 5.258 Temperature fields of coaxial-jet flame obtained after modifying the composition of surrogate mixture for JP-8 fuel. Concentrations of (a) m-xylene, (b) tetralin, (c) methylcyclohexane (MCH), (d) iso-octane, (e) n-dodecane, and (f) tetradecane in the 6-COMP-surrogate mixture are changed to 0%, double its original value, and 100%.



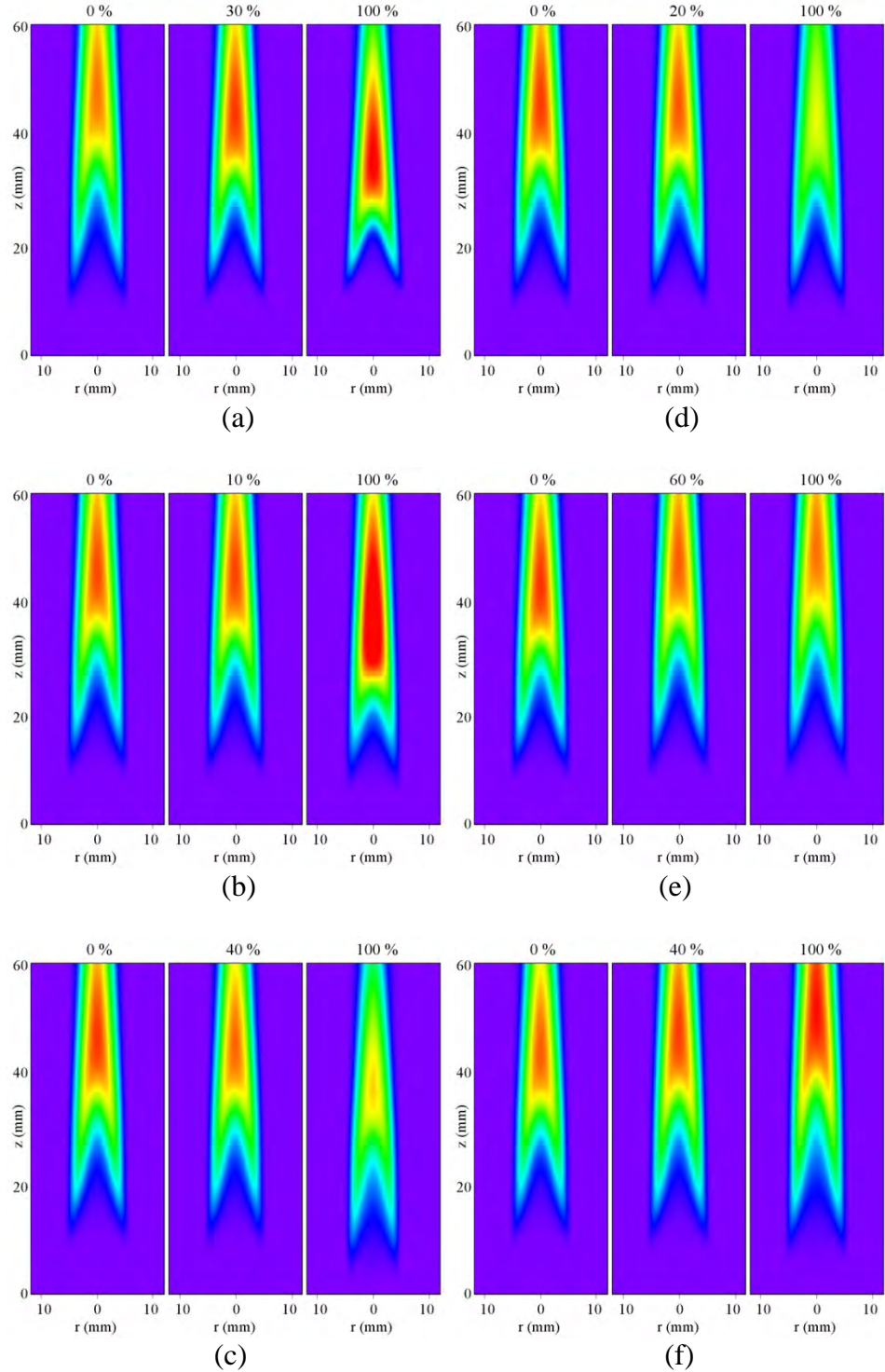


Figure 5.259 Distributions of soot in coaxial-jet flame simulated after modifying the composition of surrogate mixture for JP-8 fuel. Concentrations of (a) m-xylene, (b) tetralin, (c) MCH, (d) iso-octane, (e) n-dodecane, and (f) tetradecane in the 6-COMP-surrogate mixture are changed to 0%, double its original value, and 100%.

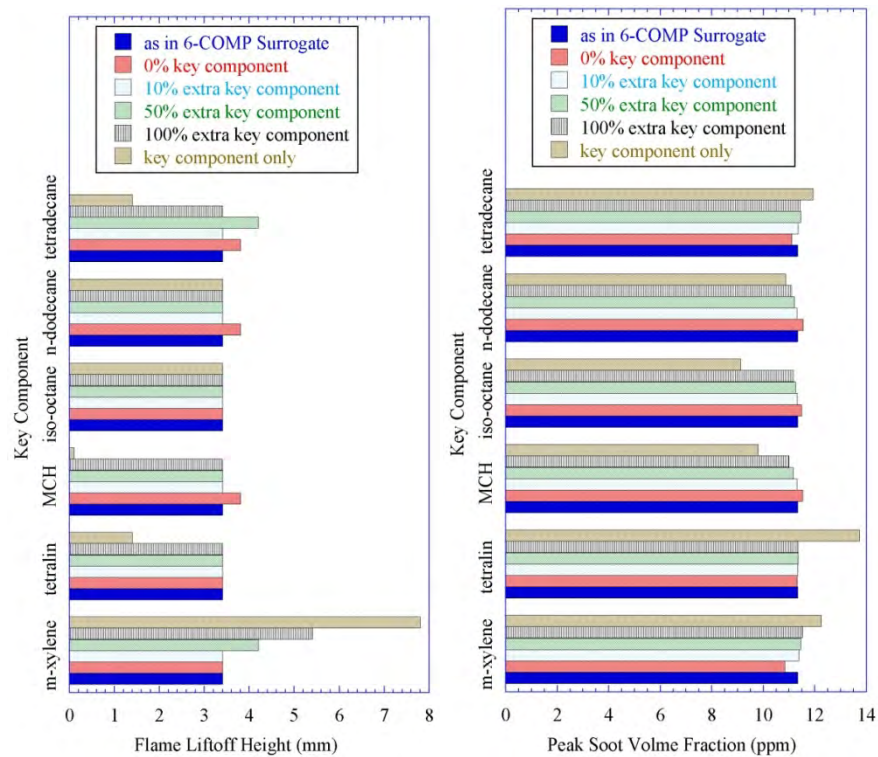


Figure 5.260 Sensitivity of various parent components of 6-COMP surrogate mixture (a) on liftoff height of co-flowing-jet flame and (b) on soot.

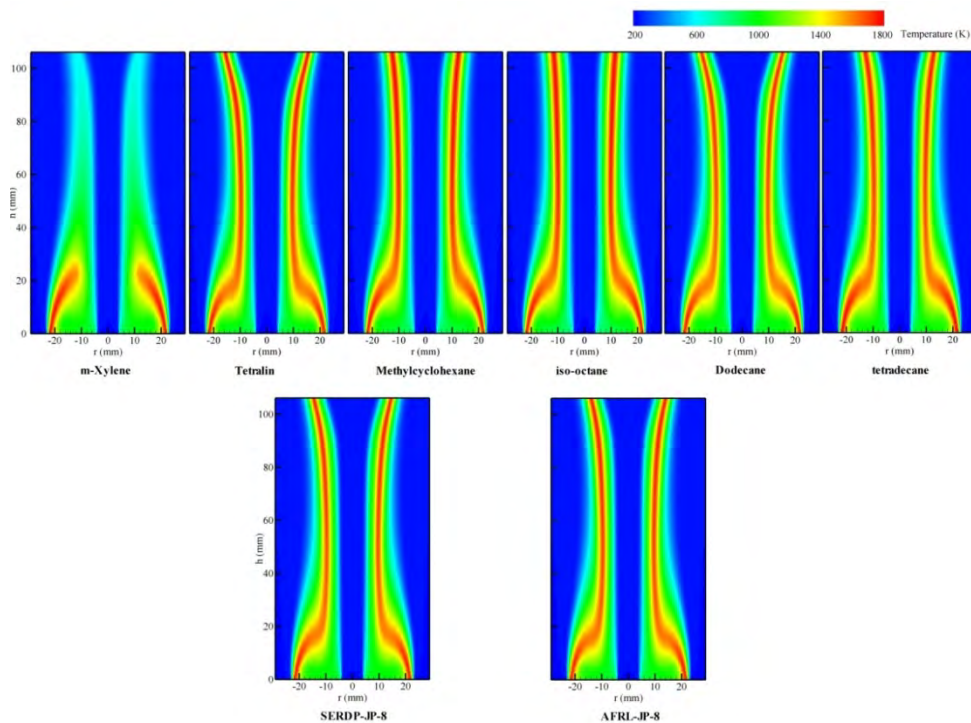


Figure 5.261 Distributions of temperature in centerbody flames simulated with pure components (top) and surrogate mixtures for JP-8 fuel (bottom).

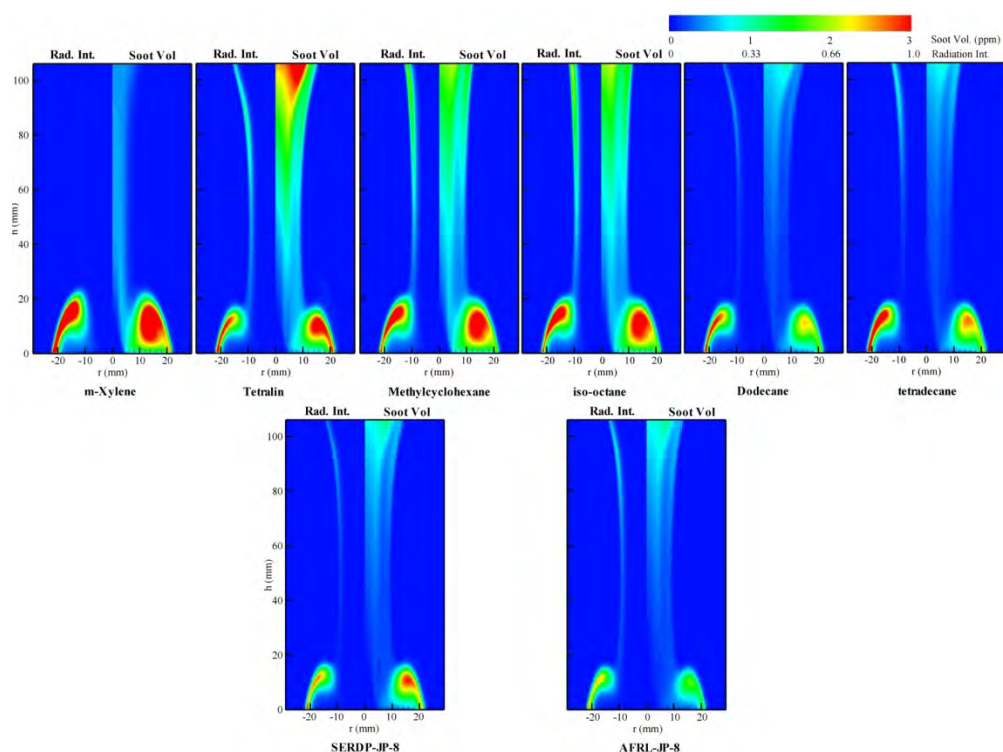


Figure 5.262 Distributions of soot radiation (left) and soot (right) in centerbody flames simulated with pure components (top) and surrogate mixtures for JP-8 fuel (bottom).

## 5.6 Simulations of Flames with Recirculation Zones using two JP-8 Surrogates

The two surrogates (6-COMP and SERDP) of JP-8 fuel predicted the structures of the counterflow and co-flow jet flames reasonably close to each other. Further studies on these surrogates in predicting the structures of the flames established with recirculation zones are performed.

### 5.6.1 Centerbody Burner

Geometry of the centerbody burner was described earlier. It consists of a 46-mm-diameter disc enclosed in a cylindrical chimney with an annular gap of 17 mm. A 7.6-mm-diameter hole is made at the center of the disc through which fuel, a mixture of fuel and nitrogen, is injected. A mixture of air and nitrogen is flowed through the annular gap. Both the fuel and air jets are set to have the same velocity of 1.25 m/s. Axisymmetry calculations for the centerbody burner are made in the physical domain of 4-cm wide in the radial direction and 30-cm long in axial direction. A nonuniform grid system of 301x161 points is used. Calculations for the JP-8 flames are performed using the two surrogate mixtures described earlier. For accommodating liquid-vaporization schemes fuel jet is assumed to contain 80% by weight of JP-8 surrogate and 20% by weight of nitrogen and is preheated to 400 K.

Distributions of the temperature in the flames obtained with 6-COMP and SERDP surrogate mixtures are shown in Figures 5.263a and 5.263b, respectively. These flames look very similar to

those obtained with ethylene fuel except for the fact that JP-8 flames tend to diverge in size at ~ 8-cm height. The gravitational force acting on the heavy JP-8 fuel retarded the fuel flow and created a recirculation bubble within the fuel jet; which, in turn, caused divergence in the flame shape. Such recirculation bubbles were also observed in propane jet diffusion flames.

A comparison between Figures 5.263a and 5.263b suggests that both 6-COMP and SERDP surrogates predict nearly the same flame structure in centerbody burner. This is rather surprising considering the wide variation in the compositions of the two surrogate mixtures (cf Table 5.8). The soot volume fraction and radiation from soot computed in these flames are shown in Figure 5.264 on the right and left hand sides, respectively. The amount of soot produced by the two surrogates in the trailing jet flame (flame downstream of the recirculation zone) is nearly the same. However, SERDP surrogate produced nearly twice the amount of soot in the recirculation zone compared to that produced by the 6-COMP surrogate.

For understanding the nearly identical flame structures produced by the 6-COMP and SERDP surrogates, the ignition characteristics of these surrogates are computed and compared in Figure 5.265. Temperature of the homogeneous mixture of fuel and air at stoichiometry is spontaneously increased to a specified value and then the new mixture temperature is calculated at different times. As shown in Figure 5.265, both 6-COMP and SERDP surrogates show identical ignition behavior for initial temperatures greater than 1500 K and nearly the same behavior for lower temperatures. Because of this the recirculation-zone supported flames in centerbody burner obtained with 6-COMP and SERDP surrogates are nearly the same (Figure 5.263).

Ignition delay times for the two surrogates obtained at different initial temperatures are compared in Figure 5.266, which shows nearly identical behavior over the range of 1300-2000 K initial temperatures. The ignition delay times computed for the six parent components are also shown in Figures 5.266a and 5.266b. Ignition characteristics of m-xylene are quite different from those of the remaining parent species. Tetralin and iso-octane have longer ignition delays at lower initial temperatures and shorter delays at higher initial temperatures compared to those of the surrogate mixtures. On the other hand, the ignition delay times of n-dodecane and tetradecane are shorter when compared to those of the surrogate mixtures. Interestingly, ignition delay times of methylcyclohexane (MCH) matched with those of the surrogates. It is surprising to note that even with a considerable variation in the ignition delay times of the individual parent species, the two surrogate mixtures formulated independently exhibit nearly the same ignition properties.

Calculations for the centerbody flames shown in Figure 5.263 are repeated after replacing surrogate fuels with individual parent components. The resulted six flames are shown in Figure 5.267. Except for m-xylene all other parent components yielded flames similar to those obtained with the surrogate mixtures. Interestingly, only a recirculation-zone flame was established with m-xylene and the trailing jet flame was extinguished. Considering the long ignition delays associated with m-xylene one could understand the latter prediction of trailing-flame extinction. However, existence of recirculation-zone flame is rather surprising. It was found in the earlier studies with ethylene fuel that under certain dilution/velocity conditions the recirculation-zone flame could get extinguished while the trailing flame is still present. The opposite behavior observed with m-xylene cannot be explained with extinction related to strain rate. It is believed that the secondary fuel components formed and carried into the recirculation zone are responsible for establishing the flame with m-xylene.



Soot produced in the flames formed with different parent species is shown in Figure 5.268. While the radiation intensity from soot is shown on the left side of each image soot volume fraction is shown on the right side. A comparison of soot formed in the recirculation zone suggests that m-xylene produces the maximum and tetralin produces the least amount. Interestingly, MCH produces significant amount of soot in the fuel-jet recirculation zone formed at 10-cm height. While SERDP surrogate has 23% m-xylene and 77% n-dodecane, the amount of soot produced in the recirculation zone by this surrogate (Figure 5.264b) is significantly lower than that produced by either m-xylene or n-dodecane. This suggests that one cannot estimate soot formed by a surrogate mixture in the recirculation zones based on its parent component's sooting behavior.

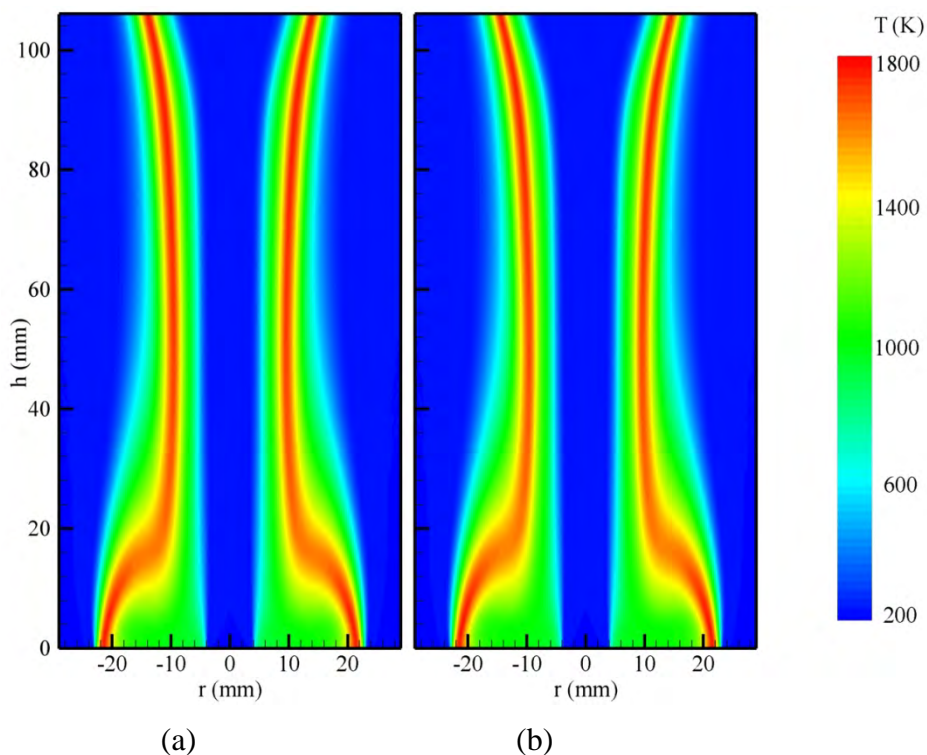


Figure 5.263 Predicted flames for centerbody burner fueled with (a) 6-COMP and (b) SERDP surrogate mixtures of JP-8.

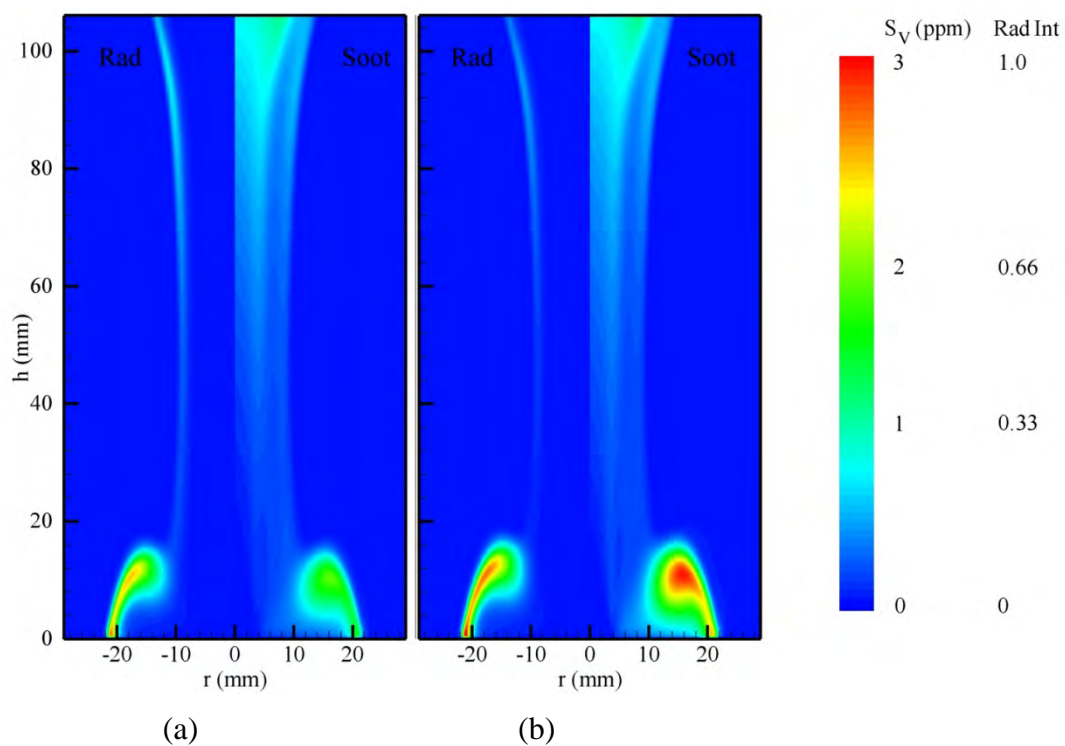


Figure 5.264 Soot radiation (left) and soot volume fraction (right) in centerbody burner fueled with (a) 6-COMP and (b) SERDP surrogate mixtures of JP-8.

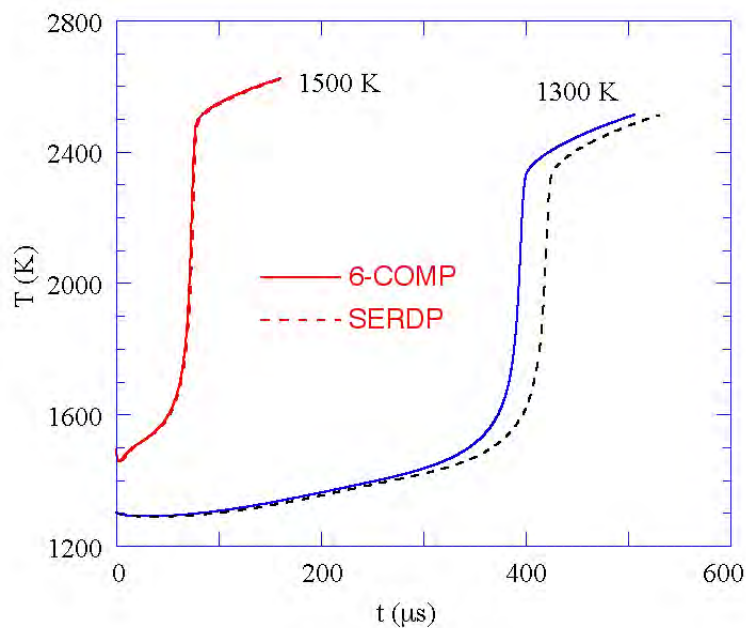


Figure 5.265 Comparison of homogeneous ignition processes of 6-COMP and SERDP surrogate mixtures of JP-8 at 1300 and 1500 K.

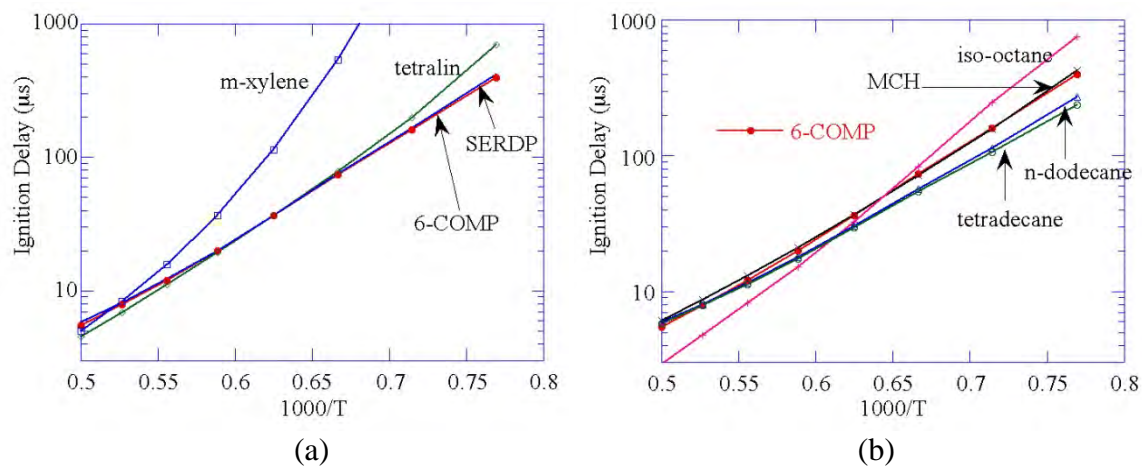


Figure 5.266 Ignition delay times of stoichiometric mixtures of air and (a) JP-8 surrogates, m-xylene and tetralin and (b) MCH, iso-octane, n-dodecane, and tetradecane for different initial temperatures.

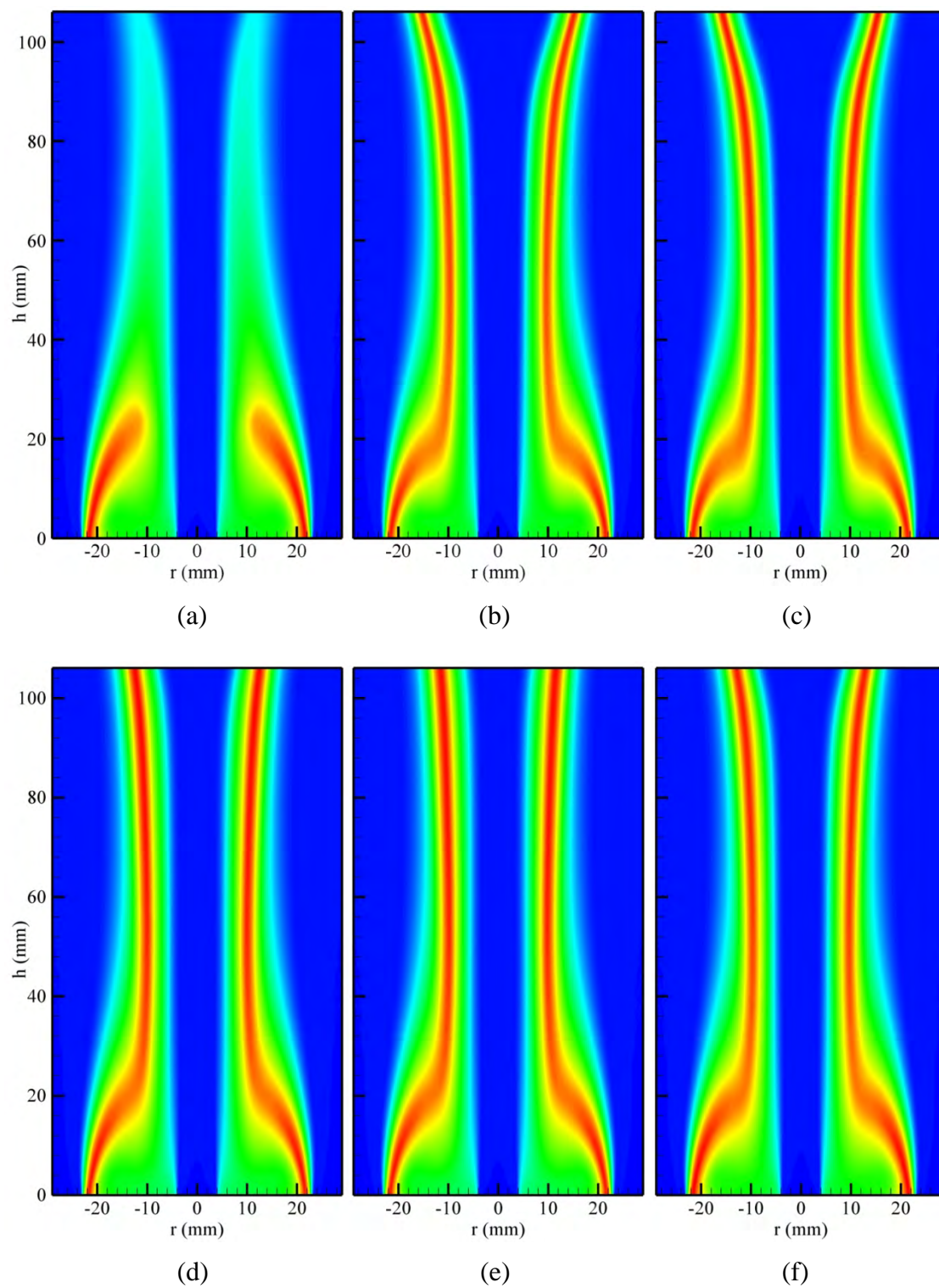


Figure 5.267 Flames obtained in centerbody burner with fuels (a) m-xylene, (b) tetralin, (c) methylcyclohexane (MCH), (d) iso-octane, (e) n-dodecane, and (f) tetradecane.

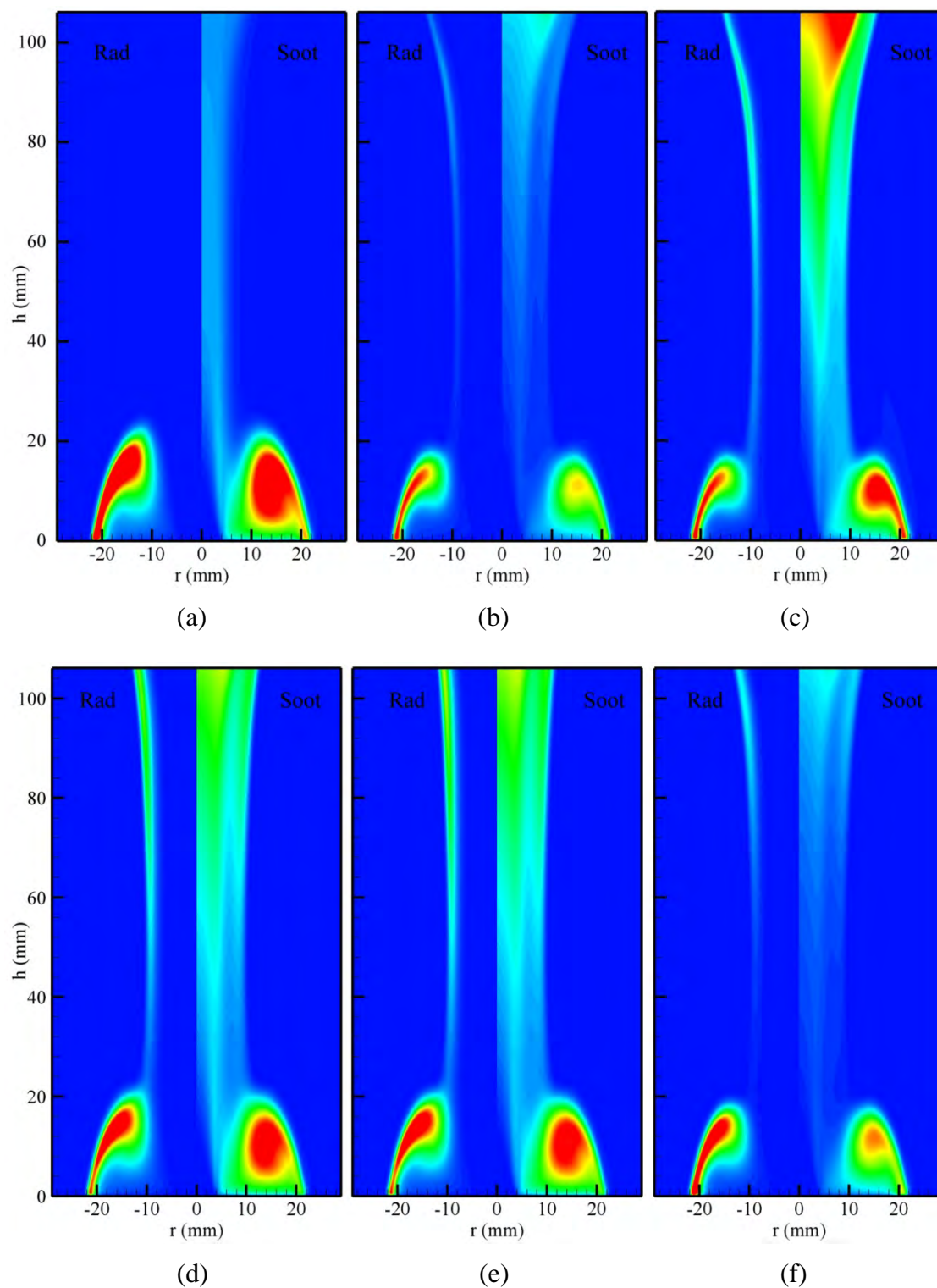


Figure 5.268 Soot radiation (left) and soot volume fraction (right) in centerbody burner obtained with fuels (a) m-xylene, (b) tetralin, (c) MCH, (d) iso-octane, (e) n-dodecane, and (f) tetradecane.

### 5.6.2 Swirl-Stabilized Turbulent Flames

The near-field structure of swirl-stabilized flames is highly dependent upon the characteristics of the fuel injector and the geometry of the surrounding flame tube. The injector configuration used in the modeled swirl-stabilized combustor is a generic swirl-cup liquid-fuel injector studied at the Atmospheric-Pressure Combustor-Research Complex of the Air Force Research Laboratory's Propulsion Directorate. It employs pressure atomization and dual-radial, counter-swirling co-flows of air to entrain the fuel, promote droplet break-up, and enhance mixing. The near-axisymmetric, conical flame obtained under overall-fuel-lean operating conditions is shown in Figure 5.269a. It composed of an outer laminar-like flame region (A) and an inner turbulent flame brush region (B) (17). The flame is stabilized by a recirculation zone (C) that brings hot combustion products upstream along the centerline. The 40-mm-exit-diameter swirl cup is installed at the entrance of a 15.25 cm  $\times$  15.25 cm square-cross-section, 48-cm long flame tube. Under fuel-rich conditions the flame tube glows with radiation from soot as shown in Figure 5.269b. After exiting the primary flame zone, the combustion products and the leftover fuel and air are allowed to go through further chemical processes in the flame tube before entering a 43-cm-long, 5.7-cm exit-diameter exhaust nozzle that is designed to create a uniform exhaust-gas temperature and concentration profiles.

Changes in overall equivalence ratio from  $\phi = 0.5$  to 1.15 were achieved in the experiments by varying the pressure drop across the fuel-spray nozzle from about 1.5 to 10 atm, which resulted in fuel mass flow rates of 1.0 to 2.2 g/s, respectively. The fuel flow rate is measured using a Max Machinery positive-displacement flow meter with  $\pm 0.5\%$  full-scale accuracy. The airflow system consists of three Sierra 5600 SLPm mass flow controllers with  $\pm 1\%$  full-scale accuracy. The inlet air is heated to 450 K with a constant flow rate of  $\sim 0.028$  kg/s. The air-pressure drop across the combustor dome was  $\sim 4.8$  to 5.2% of the main supply. Most of the airflow enters the combustor through the swirl-cup injector, but a small percentage enters through aspiration holes along the aft wall. No liner air jets are used in the secondary zone; therefore, the fuel-air ratio depends almost entirely on the flow rates through the injector cup.

The combustor is optically accessible via 75-mm-wide quartz windows along the top and sides for in-situ laser-based diagnostics. In addition, a sampling probe for measuring particulate counts is located at the exit of the combustor. Axisymmetric mathematical model for the swirl-stabilized combustor is constructed as shown in Figure 5.269c using a 17.2-cm diameter, 48-cm long chimney and with thin tubes separating the fuel and air flows at the combustor entrance. Gaseous JP-8-surrogate fuel is injected at the center while the two outer air jets are forced into the combustor with counter swirling motions. Calculations with this modeled combustor are performed using UNICORN (UNsteady Ignition and Combustion using ReactionNs) code. The computational domain was discretized using a non-uniform grid system of 251 $\times$ 126. Simulations presented here are performed on a single cpu, AMD Opteron Personal Computer with 2.0 GB of memory. Typical execution time is  $\sim 30$  s/time-step. Steady state solutions are typically obtained in about 30,000 time steps starting from the solution obtained using a global combustion chemistry model.



Calculations for the swirl-stabilized combustor shown in Figure 5.269 are made for different equivalence ratios. Flow fields obtained for a fuel-lean condition ( $\phi = 0.85$ ) with 6-COMP and SERDP surrogate mixtures are shown in Figures 5.270a and 5.270b, respectively. Iso contours in color of temperature are shown in the left half while those of OH are shown in the right half. Streamlines showing the recirculation zones are superimposed on the temperature fields. The nozzle geometry incorporated in the model is also shown in these figures. Gaseous fuel is injected from a 4-mm hole at the center with an axial velocity of 20 m/s and swirl angle of  $70^\circ$ . Such high swirl angle for the fuel jet was used in order for representing the cone angle of the liquid spray. Fuel jet is immediately surrounded with a 2-mm-thick wall and then a high-speed air jet with axial velocity of 100 m/s and a swirl angle of  $-30^\circ$ . A second air jet of 100 m/s is issued through the 5 mm annulus gap between the nozzle walls at a velocity of 100 m/s and at a swirl angle of  $45^\circ$ . The velocity of the fuel jet was changed for achieving different equivalence-ratio conditions. The two cases in Figure 5.270 are obtained with fuel velocities of 15 and 30 m/s, which correspond to equivalence ratios of 0.65 and 1.15, respectively.

Comparison of flames in Figures 5.270a and 5.270b suggests that both the 6-COMP and SERDP surrogates resulted in nearly identical flow fields. In both simulations the swirling air jets are merging together and expanding radially as they propagate downstream. Such radial expansion of high momentum air jets has created two toroidal recirculation regions, one in the corner and the other one at the center. The air jets are impinging on the combustor wall at about 10-cm height. Under this fuel-lean condition, both surrogate mixtures predicted a flame that is anchored in the region between the air jets and the center recirculation zone. However, SERDP surrogate predicted slightly higher temperatures in the combustor compared to those predicted by 6-COMP surrogate.

The instantaneous and time-averaged OH-concentration distribution obtained in the experiments using PLIF technique are shown in Figures 5.270c and 5.270d, respectively. The corresponding locations in the computational flames are marked with squares. The measured v-shaped OH distribution supports the predictions that the flame is sandwiched between the air jets and the central recirculation zone. Moreover, calculations suggest that the some fuel is carried into the corner recirculation zone after being impinged on the combustor side walls and generating another flame between the corner recirculation zone and outer air jet. The dual flames are also evident in the measured instantaneous OH data (Figure 5.270c). However, due to strong fluctuations in flame zones, time-averaged OH data shows broadening of OH layer. Following the temperature distributions, SERDP surrogate predicts OH in slightly higher concentrations.

The overall equivalence ratio has been increased to 1.0 when the velocity of the fuel jet is increased to 30 m/s. The predicted combustion fields for this stoichiometric condition along with the measured OH distributions are shown in Figure 5.271. Significant changes to flame structure could be noticed when comparing the OH distributions in Figures 5.270 and 5.271. At stoichiometry, flame did not establish between the central recirculation zone and the inner air jet even though hot combustion products are entrained into the recirculation zone. Both the instantaneous and time-averaged OH measurements confirm the existence of only one flame that is formed between the corner recirculation zone and outer air jet. Both the 6-COMP and SERDP surrogates accurately predicted this transition from double-flame to single-flame structure when equivalence ratio was increased from 0.85 to 1.0. Interestingly, for stoichiometric condition noticeably higher temperatures and OH concentrations are predicted by SERDP surrogate.

Significant amount of OH is entrained into the central recirculation zone in the calculations made with SERDP surrogate. Presence of OH in the central recirculation zone in the time-averaged measurements supports the predictions made with the SERDP surrogate.

Results obtained for equivalence ratio of 1.15 are shown in Figure 5.272. Fuel jet velocity used for this condition was 40 m/s. Flowfields and temperature and OH distributions predicted by 6-COMP surrogate are very similar to those predicted by SERDP surrogate. A thin layer of OH is formed between the corner recirculation zone and the outer air jet and very little OH is found in both the central and corner recirculation zones. Measured OH images (Figures 5.272c and 5.272d) support the predictions made with surrogate mixtures.

Temperatures at the combustor exit plane for different equivalence ratios are compared in Figure 5.273a with the thermocouple measurements made in the exhaust gases. For lean and rich conditions both the 6-COMP and SERDP surrogates yielded nearly the same exit temperatures and for the stoichiometric condition the former surrogate resulted in temperature that is about 300 K less. When compared with the measurements, both the surrogates yielded higher temperatures for fuel-lean condition and lower temperatures for fuel-rich condition. It is important to note that the measurements for temperature were made at the exit of the exhaust nozzle while the calculations were terminated at the end of the flame tube. Further mixing and radiative cooling could explain some of the differences noted between the measurements and computations.

Soot volume fraction computed with 6-COMP and SERDP surrogate mixtures are compared with the probe and LII (Laser Induced Incandescence) measurements in Figure 5.273b. Note that experimental data are plotted as the concentrations relative to those measured at equivalence ratio 1.15. Interestingly, both 6-COMP and SERDP mixtures predicted nearly the same amount of soot toward the combustor exit. As expected, for fuel-lean condition both surrogates resulted in no soot and for fuel-rich condition of  $\phi = 1.15$  both surrogates resulted in about 3.7 ppm of soot. However, for stoichiometric condition 6-COMP surrogate gave about 0.8 ppm of soot while SERDP surrogate yielded no soot. This is consistent with the observations made on OH predictions (Figure 5.271). Presence of OH in the downstream locations consumed all the soot in the SERDP simulations.

As seen in Table 5.8, the composition of 6-COMP surrogate is very different from that of SERDP surrogate. However, simulations made for swirl combustor with these surrogates resulted in only minor differences in flowfields and temperature distributions. This raises a question on the sensitivity of the individual parent species in the surrogate mixture. In other words, it is interesting to know whether the two radically different surrogate mixtures are prepared wisely to simulate the same fuel or sensitivities of certain parent species are negligibly weak in the mixture. To address this question calculations for the swirl combustor have been repeated after replacing surrogate fuel with individual parent species. Calculations are made for all the three equivalence ratios. Results in the form of temperature distributions along the centerline for 0.85, 1.0, and 1.15 equivalence ratios are shown in Figures 5.274a, 5.274b, and 5.274c, respectively. Data obtained with 6-COMP and SERDP surrogate mixtures are shown with solid lines while those of parent species are shown in dashed lines. Figure 5.274 suggests that temperature distributions spread out maximum for the fuel lean case and minimum for fuel-rich case. However, for both the fuel-lean and fuel-rich cases temperature distributions obtained



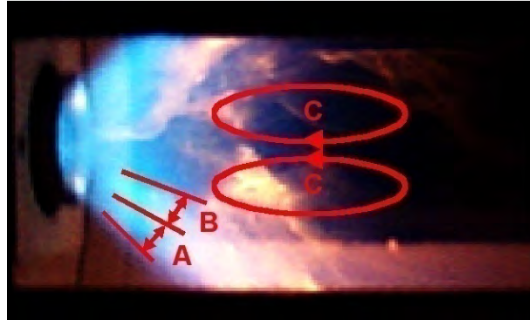
with 6-COMP and SERDP surrogates are close to each other. This suggests that the two surrogate mixtures wisely represent the same fuel even though their individual parent species characteristics are quite different.

Radial distributions of temperature at an axial distance of 50 mm are shown in Figure 5.275 for different equivalence ratios. Similar to the behavior noted in axial temperature distributions, both surrogate mixtures yielded nearly the same temperature distributions for fuel-lean and fuel-rich conditions. Individual parent species gave temperature distributions that vary significantly from the mixture values.

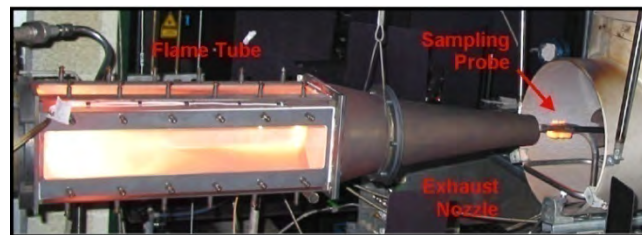
Sooting characteristics of the 6-COMP surrogate mixture are studied through plotting benzene (left) and soot volume fraction (right) distributions in Figures 5.276a, 5.276b, and 5.276c for equivalence ratios 0.85, 1.0, and 1.15, respectively. Iso contours of acetylene are superimposed on each of these figures. As expected, all the fuel in the fuel-lean case is consumed within the v-shaped flame. Benzene and acetylene are produced and consumed within this narrow flame zone, resulting in soot-free flame. Soot formed from acetylene survived in the combustor for equivalence ratio of 1.0 even though both acetylene and benzene are consumed rather quickly in the flame zone. And for fuel-rich case (Figure 5.276c) both benzene and soot survived in the combustor. Interestingly, for this case soot distribution resembled that of benzene.

Sooting characteristics of SERDP surrogate are plotted in Figure 5.277 for the three equivalence ratios considered. Plotting scheme and contour levels used in this figure are identical to those in Figure 5.276. Overall, SERDP and 6-COMP surrogates are resulting in very similar soot and benzene distributions. A close examination, however, reveals that SERDP surrogate is yielding less benzene for fuel-lean and stoichiometric cases and more for fuel-rich cases. As explained earlier, excess OH in stoichiometric case is consuming soot SERDP-surrogate simulation. As OH is confined to the flame zone in fuel-rich case its effect on soot also diminished and, as a result, soot concentration in SERDP-surrogate simulation increased in this case. However, the differences observed between 6-COMP and SERDP surrogate simulations are not that significant.

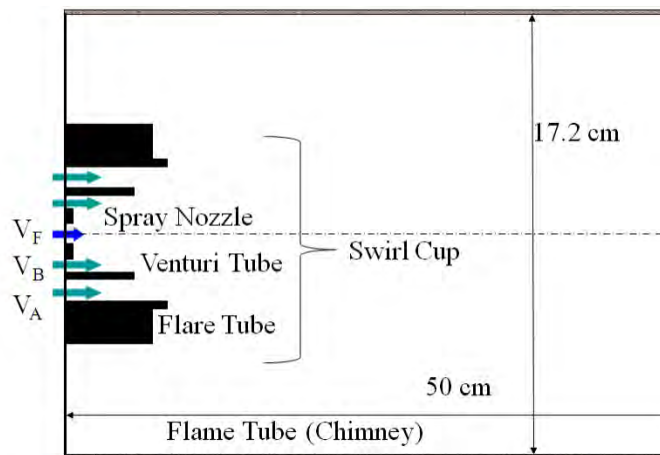
For studying the individual parent species role on surrogate behavior, axial distributions of benzene obtained with various fuels (surrogates and their parent components) are plotted in Figures 5.278a, 5.278b, and 5.278c for fuel-lean, stoichiometric, and fuel-rich cases, respectively. Note, close views of the variations in the flame zone are shown. Even though, the individual parent species are resulting in benzene over a wide range, SERDP and 6-COMP surrogates are resulting benzene close to each other--suggesting that these two surrogates are similar in predicting flames. Radial distributions of soot volume fraction at an axial location of 5 cm are shown in Figure 5.279 for the three equivalence-ratio cases. Once again, 6-COMP and SERDP surrogates are producing soot different from those generated by any of their individual parent species but similar to each other. In conclusion, detailed comparisons of flames generated with different parent species revealed significant variations in flame structures. However, the flames generated by the surrogate mixtures are nearly similar--suggesting that these mixtures are formulated for representing the same JP-8 fuel.



(a)



(b)



(c)

Figure 5.269 JP-8 fueled, swirl-stabilized, model gas-turbine combustor. (a) Photograph of the near-field flame structure operating under fuel-lean conditions, (b) photograph of the flame and test rig operating under fuel-rich conditions, and (c) axisymmetric model of the combustor used in CFD analysis.

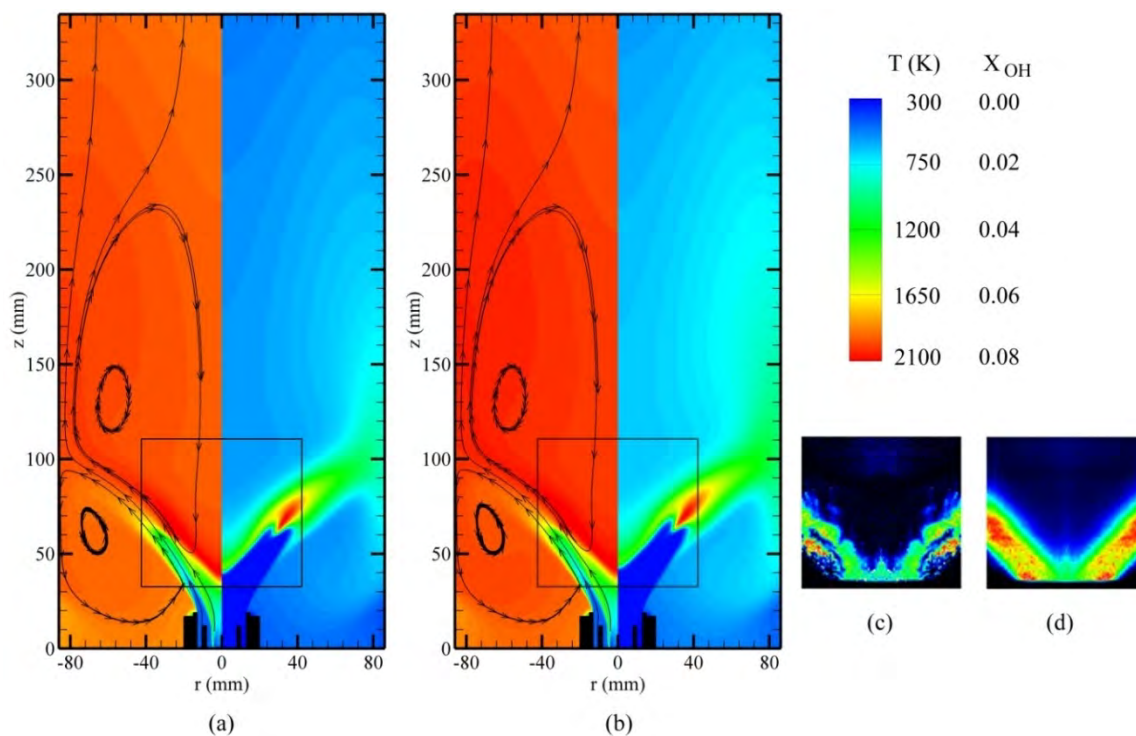


Figure 5.270 Comparison of simulated flames with experiment for  $\phi = 0.85$ . Calculations are made with (a) 6-COMP and (b) SERDP surrogate mixtures. Computed streaklines are superimposed on temperature distributions on left half while OH distributions are shown on right half. Instantaneous and time-averaged OH-PLIF signals obtained in experiment are shown in (c) and (d), respectively.

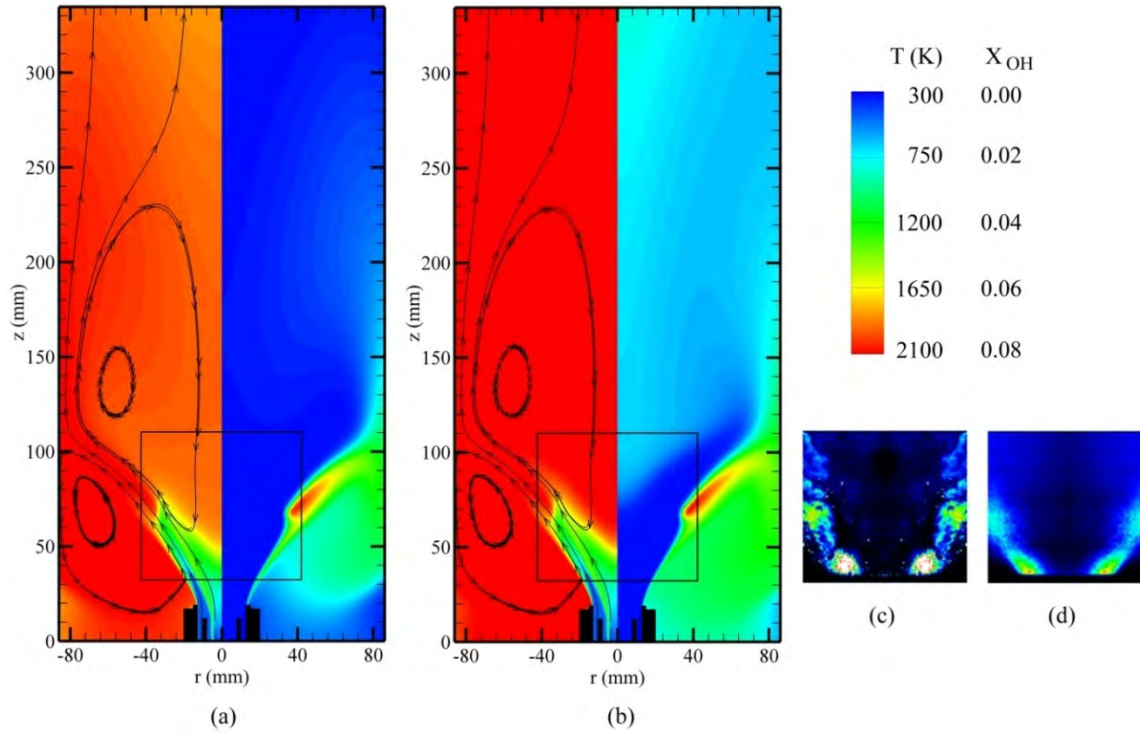


Figure 5.271 Comparison of simulations with experiment for  $\phi = 1.0$ . Flames computed with 6-COMP and SERDP surrogates are shown in (a) and (b), respectively. Instantaneous and time-averaged OH-PLIF signals of experiment are shown in (c) and (d), respectively.

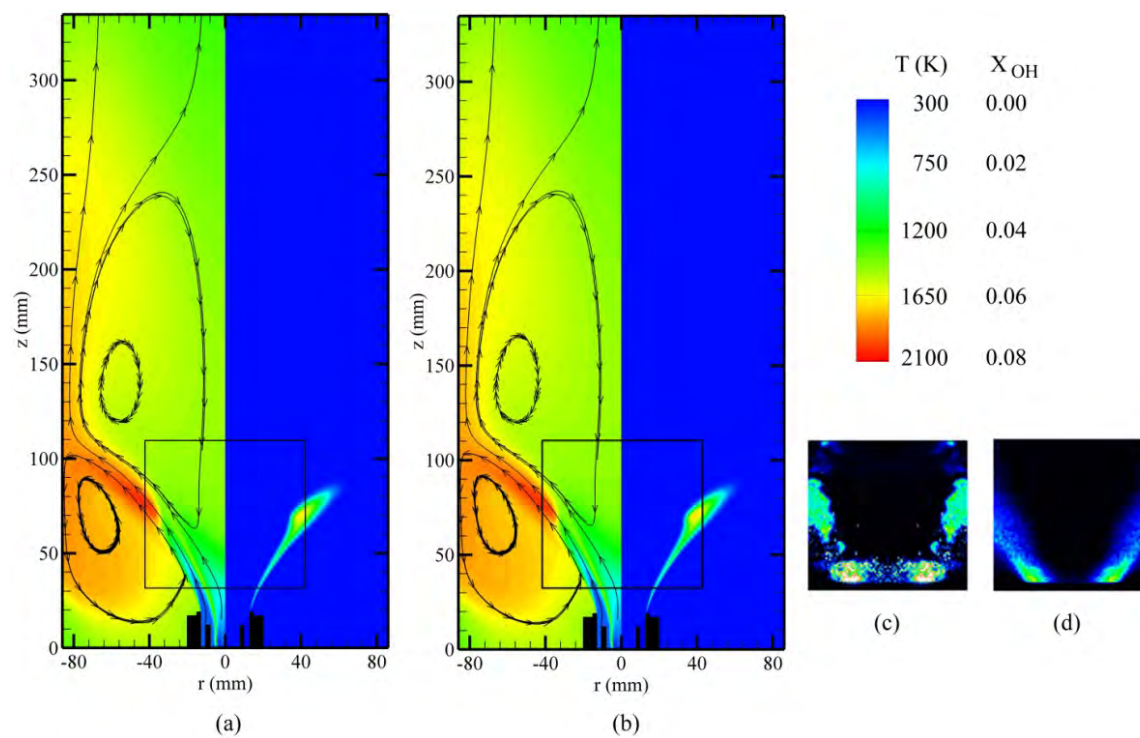
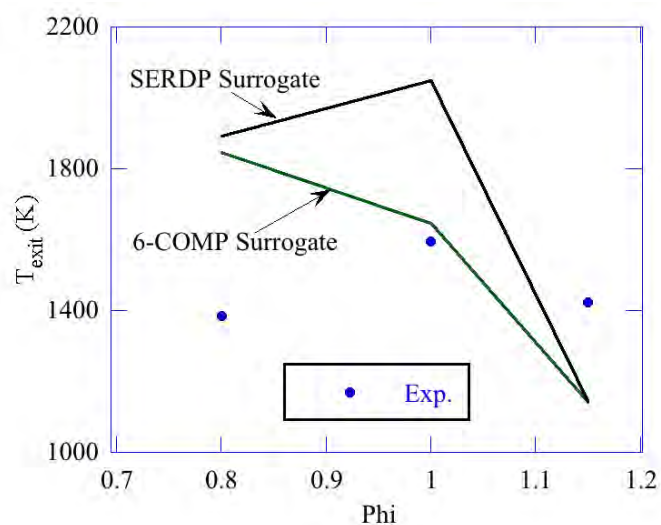
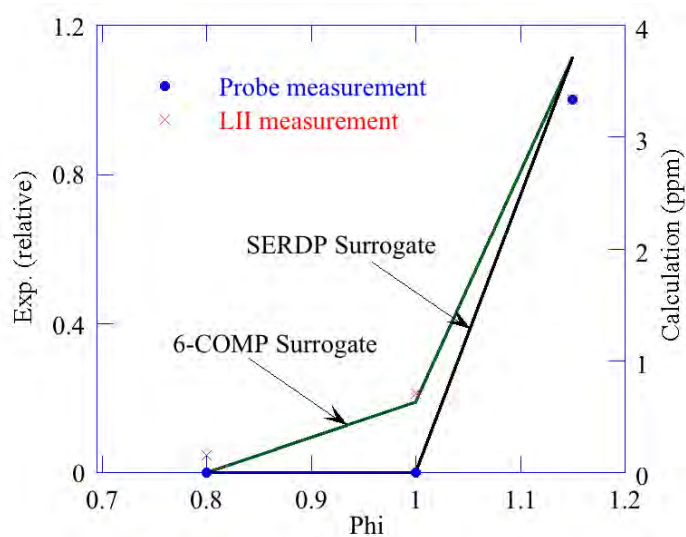


Figure 5.272 Comparison of simulated flames with experiment for fuel-rich condition of  $\phi = 1.15$ . Flames computed with 6-COMP and SERDP surrogate mixtures are shown in (a) and (b), respectively. Instantaneous and time-averaged OH-PLIF signals of experiment are shown in (c) and (d), respectively.



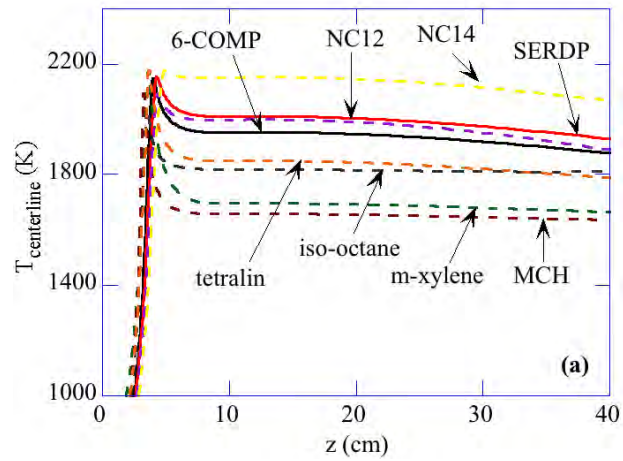
(a)



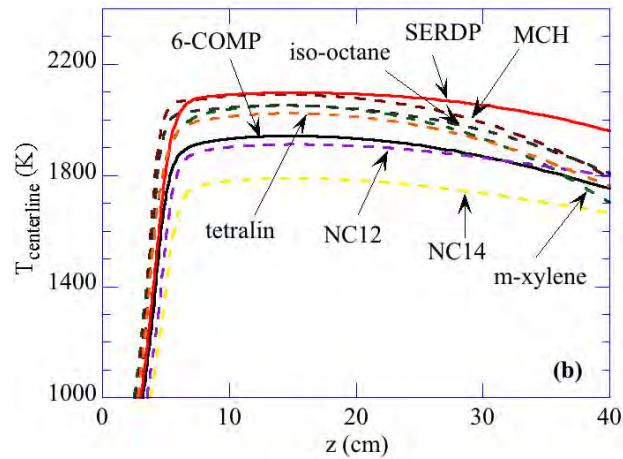
(b)

Figure 5.273 Comparison of simulated flames with experiment for different equivalence ratios. (a) Exit temperatures of the simulations performed with 6-COMP and SERDP surrogate mixtures are compared with thermocouple measurements and (b) computed soot volume fractions are compared with probe and LII measurements.

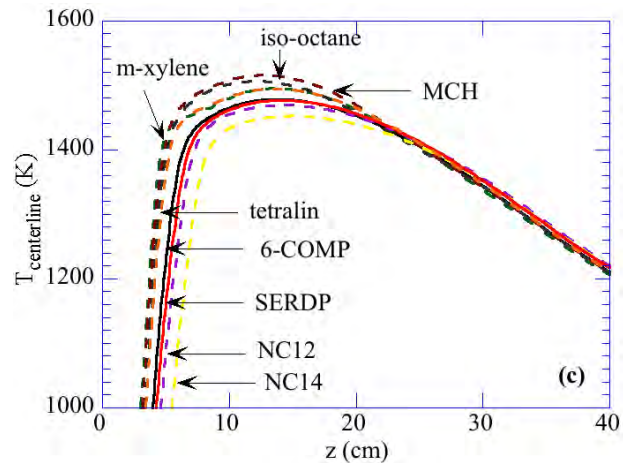




(a)

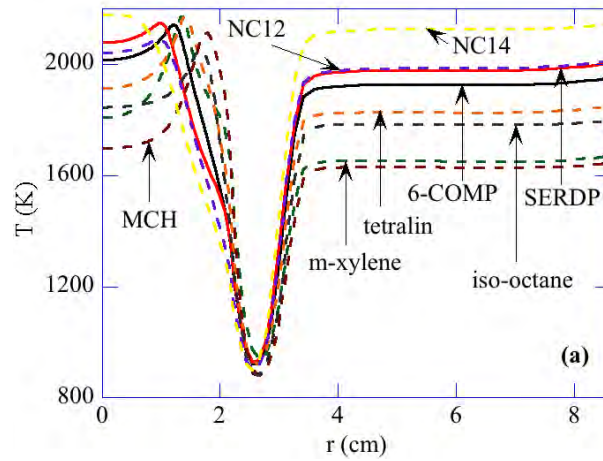


(b)

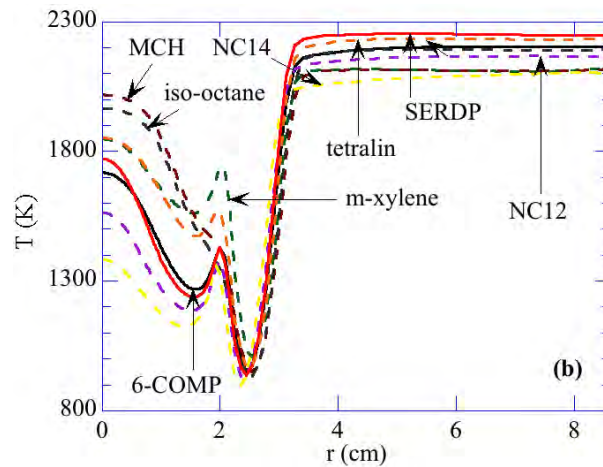


(c)

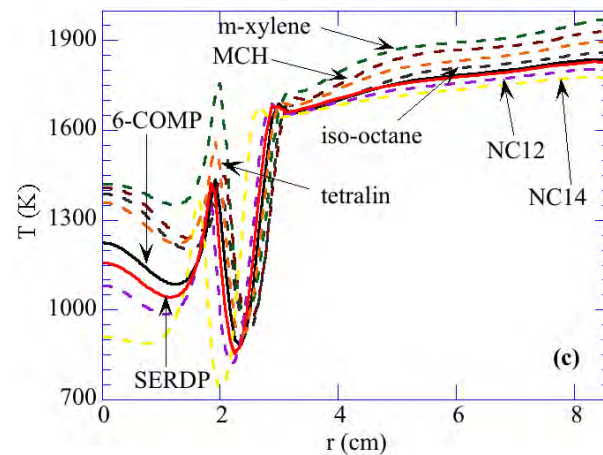
Figure 5.274 Axial distributions of centerline temperature obtained with 6-COMP and SERDP surrogates and their various parent species for equivalence ratios (a) 0.85, (b) 1.0, and (c) 1.15.



(a)



(b)



(c)

Figure 5.275 Radial distributions of temperature at an axial distance of 50 mm obtained with 6-COMP and SERDP surrogates and their various parent species for equivalence ratios (a) 0.85, (b) 1.0, and (c) 1.15.



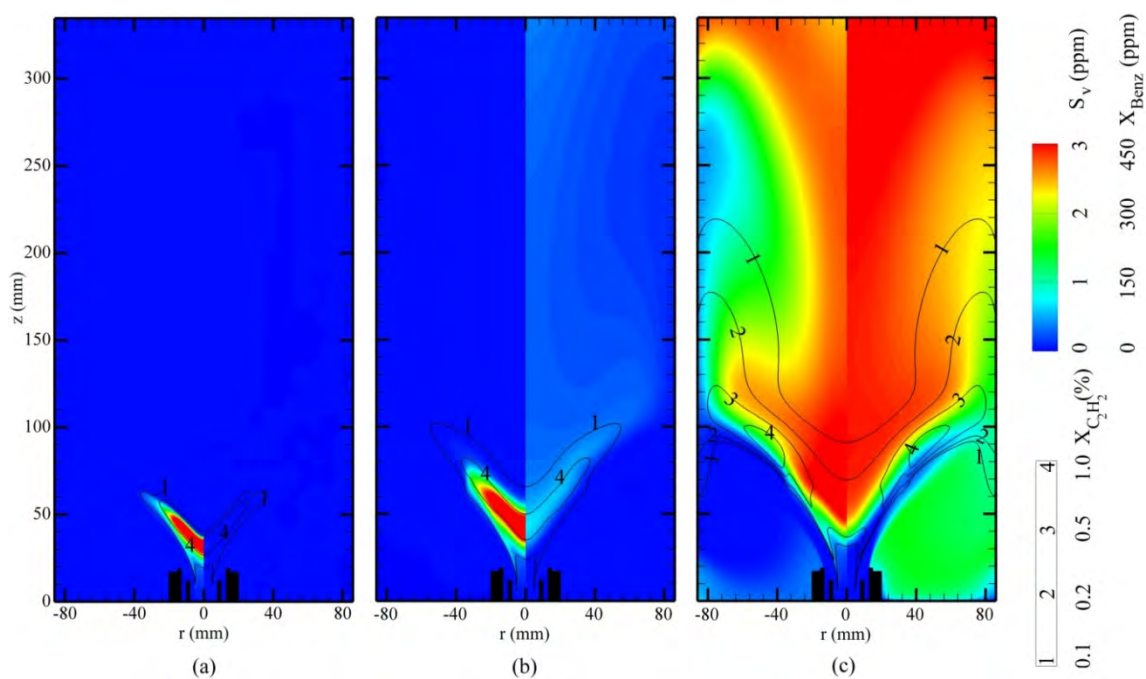


Figure 5.276 Distributions of benzene (color left), soot (color right), and acetylene (contour lines) obtained with 6-COMP surrogate mixture for equivalence ratios (a) 0.85, (b) 1.0, and (c) 1.15.

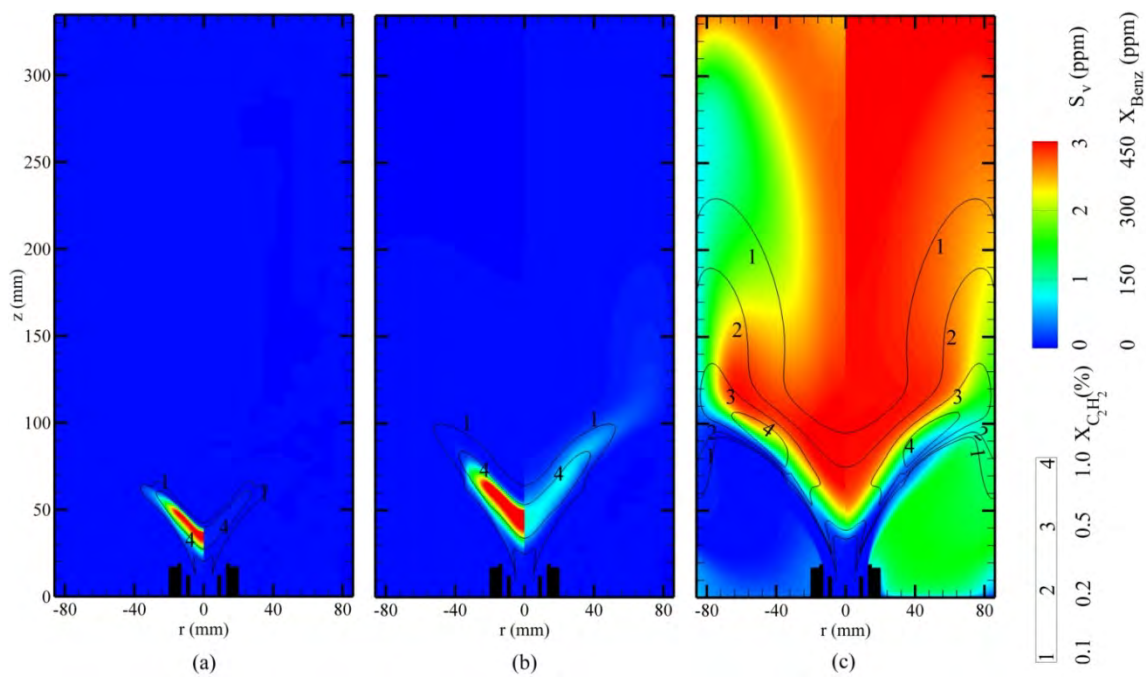
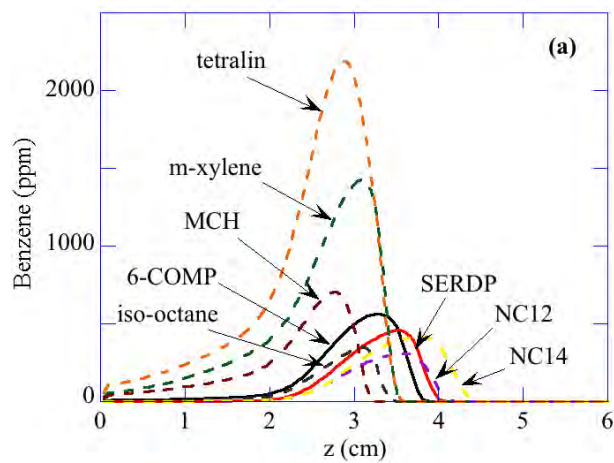
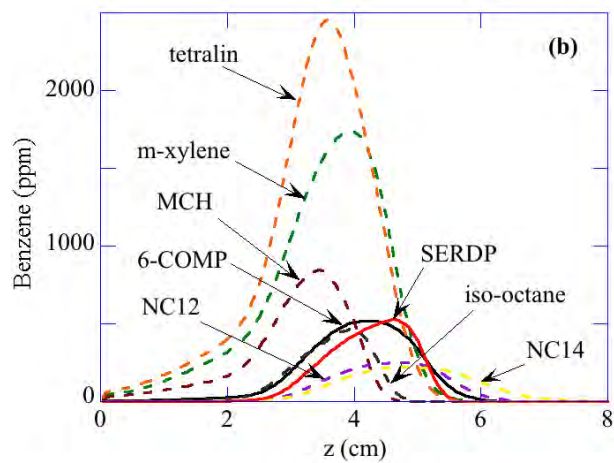


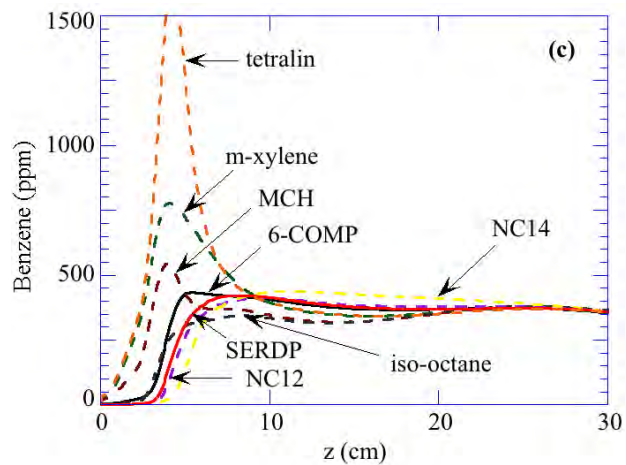
Figure 5.277 Distributions of benzene (color left), soot (color right), and acetylene (contour lines) obtained with SERDP surrogate mixture for equivalence ratios (a) 0.85, (b) 1.0, and (c) 1.15.



(a)



(b)



(c)

Figure 5.278 Axial distributions of centerline benzene concentration obtained with 6-COMP and SERDP surrogates and their various parent species for equivalence ratios (a) 0.85, (b) 1.0, and (c) 1.15.

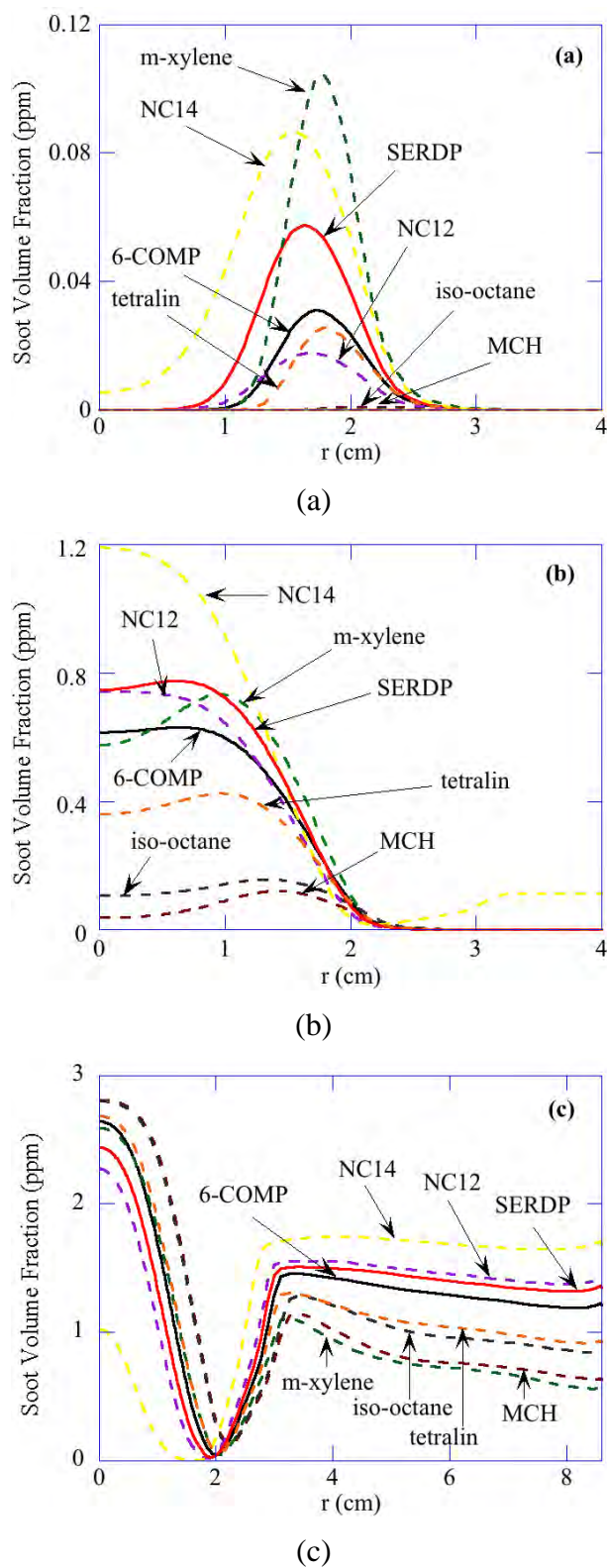


Figure 5.279 Radial distributions of soot volume fraction at an axial distance of 50 mm obtained with 6-COMP and SERDP surrogates and their various parent species for equivalence ratios (a) 0.85, (b) 1.0, and (c) 1.1.

## 5.7 Simulation of Partially Premixed Flames

UNICORN code with heptane mechanism is used for modeling partially premixed flames of Berta et al. (2006). The opposing-jet burner used by Berta et al. (2006) for obtaining detailed structures of partially premixed flames consists of upper and lower nozzles and is similar to the burners used in the studies of nonpremixed flames (Seiser et al. 1998). The diameter of each nozzle was 27.38 mm and the separation distance ( $L$ ) between them was varied between 10 and 20 mm. Fuel in the form of a mixture of pre-vaporized n-heptane, air and nitrogen was introduced from the bottom nozzle. Oxidizer was introduced from the top nozzle. A nitrogen curtain was established through an annular duct surrounding the fuel jet in order to isolate the flames from ambient disturbances. Berta et al. (2006) also built an annular duct around the top oxidizer nozzle; however, it was used for venting the gasses flowed into the burner. While the oxidizer was issued at room temperature, the fuel nozzle was heated and its temperature was controlled for maintaining the fuel-containing stream at 400 K. The fuel vaporizer and mixer are described in Berta et al. (2006).

Four partially premixed flames established in this burner are considered for the evaluation of the chemical-kinetics models. Digital images of these flames are shown in the left half of Figure 5.280. The weakly stretched weakly premixed flame in 5.280a was obtained with  $k = 50 \text{ s}^{-1}$ ,  $\phi = 15.3$ , the weakly stretched moderately premixed flame in 5.280b was obtained with  $k = 50 \text{ s}^{-1}$ ,  $\phi = 2.5$ , the moderately stretched moderately premixed flame in 5.280c was obtained with  $k = 150 \text{ s}^{-1}$ ,  $\phi = 4.1$  and, finally, the moderately stretched weakly premixed flame in 5.280d was obtained with  $k = 150 \text{ s}^{-1}$ ,  $\phi = 12.6$ . A separation of 10 mm between the fuel and oxidizer nozzles was maintained for all the flames except that in 5.280b for which the separation distance used was 20 mm. While the images in 5.280a, 5.280c, and 5.280d were taken at the same exposure time, the image in 5.7.1b was taken at double the exposure time for compensating the lower luminosity of the flame. The following visual observations were made from the flame photographs in Figure 5.280:

- An orange-red zone present below the blue layer in 5.7.1a
- Green and blue layers are well separated and flame is curved in 5.7.1b
- Green and blue layers are barely separated in 5.7.1c
- Merged green and blue layers in 5.7.1d.
- As the stretch is increased and/or the level of premixing is reduced, the premixed reaction zone (green layer) moves closer to the nonpremixed zone (blue layer), i.e., the separation between the two layers decreases.

Two-dimensional simulations for the n-heptane partially premixed flames at different strain rates and equivalence ratios ( $\phi$ ) are made using UNICORN code and with SD, LLNL, and NIST chemical-kinetics mechanisms. Boundary conditions, including the suction from the outer duct of oxidizer nozzle, were matched to those used in the experiment. Computational results corresponding to the four flames in the left half of Figure 5.280 are plotted in the right half. Temperature distributions between the upper and lower nozzles are shown in the left half of the computed flames and soot distributions are shown in the right halves. Note that the flames shown in Figure 5.280 obtained with LLNL mechanism and the other two mechanisms also yielded nearly the same flame structures. Shapes of the computed flames matched well with those seen in the experiment. The weakly stretched moderately premixed flame (Figure 5.280b) is curved all

the way from the center to the edge, while the other three flames are curved only near the edges and yielded flat-flame regions near the center. Simulations made after replacing the suction boundary condition for the oxidizer-side (top) outer duct with an inflow boundary condition similar to that used for the fuel-side (bottom) outer duct yielded flat flames for all the four cases, even though gravitational forces were included in the calculations. This suggests that the flame curvatures seen in Figure 5.280 are due to the suction employed in the experiment-but not because of the gravitational force acting on the hot products.

A comparison of calculated temperature and soot distributions of all the flames in Figure 5.280 suggest that the weakly stretched moderately premixed flame (Figure 5.280b) is the thickest and the weakly stretched weakly premixed flame (Figure 5.280a) is the sootiest. These predictions matched well with the observations made in experiments. In general, soot surfaces in all these flames are located on the fuel side (bottom) of the peak-temperature surface (red color). However, a careful examination of the computed results reveals that soot surface of the flame in Figure 5.280a is significantly away from the peak-temperature surface and this separation decreases gradually as we move through 5.280a, 5.280d, 5.280c, and 5.280b flames. This is consistent with the digital images from experiments. Soot typically forms on the fuel side of a nonpremixed flame and on the products side of a premixed flame. The soot-temperature structure of the partially premixed flame in Figure 5.280a exhibits predominantly that of a nonpremixed flame and soot surface moves closer to the peak-temperature surface as in Figures 5.280d, 5.280c, and 5.280b as the influence of premixed combustion increases. Based on the visual chemiluminescence from  $C_2$  species and radiation from CO-oxidation species Berta et al. (2006) arrived at the similar conclusions on nonpremixed and premixed reactions in these flames.

Computed structure of the weakly stretched weakly premixed flame (Figure 5.280a) along the centerline is compared with measurements in Figure 5.281. Flame structures obtained with SD, LLNL, and NIST mechanisms are shown with lines and measurements made with thermocouple and gas chromatograph are shown with symbols. Temperature and reactant species ( $nC_7H_{16}$  and  $O_2$ ) are compared in Figure 5.281a, major product species ( $H_2O$ ,  $CO_2$ ,  $CO$ , and  $H_2$ ) are compared in Figure 5.281b, fuel fragments ( $CH_4$  and  $C_2H_2$ ) are compared in Figure 5.281c, and, finally, ethylene and butene are compared in Figure 5.281d. In general, all three chemical-kinetics mechanisms resulted in nearly the same temperature and reactant and major-product-species concentrations, while significant deviations in the predicted concentrations of fuel fragments are observed. Computed temperature profile matched reasonably with that obtained in the experiment (Figure 5.81a), even though the measurements show a broader-especially, on the air side-distribution. Note that the measurements used intrusive probes, which could perturb the flame and make the distributions broader. Interestingly, LLNL mechanism predicts the premixed combustion ( $z \sim 3$  mm) more distinctly compared to the other two mechanisms and agrees better with the measurements. This is a somewhat surprising result considering the lower autoignition temperature (Figure 5.282) obtained with NIST mechanism. The structure of a partially premixed flame is characterized by synergistic interactions between the two reaction zones, with the nonpremixed zone supported by the intermediate fuels (i.e.,  $CO$  and  $H_2$ ) produced in the premixed zone, while the latter is supported by the product species generated in the nonpremixed. These interactions between the premixed and nonpremixed zones make extension of autoignition results to partially premixed flames more difficult or inappropriate. Figures 5.281c and 5.281d suggest that SD mechanism predicts  $CH_4$ ,  $C_2H_2$  and  $C_2H_4$  concentrations better than the other two mechanisms.

Flame structures obtained with the three mechanisms for the weakly stretched moderately premixed flame are shown in Figure 5.283. The strong premixed combustion that is causing the temperature to increase at  $z \sim 7.5$  mm is well captured by all the three mechanisms. However, LLNL mechanism seems to initiate this premixed combustion slightly upstream where velocity would be higher (in opposing-jet flow velocity decreases with distance from jet exit). Like in the previous case (Figure 5.81) measured temperature profile is broader than the predicted ones and is shifted toward oxidizer nozzle (Figure 5.283a). Major species concentrations except that of  $\text{H}_2\text{O}$  are well predicted. The one-dimensional calculations performed by Berta et al. (2006) using Ranzi's chemical-kinetics model (Ranzi et al. 1995) also resulted in similar discrepancy in  $\text{H}_2\text{O}$  predictions. Note that since measured  $\text{H}_2\text{O}$  values were obtained through mass balancing of all the other measured species including  $\text{N}_2$ , discrepancy between the measurements and calculations for  $\text{H}_2\text{O}$  reflects integrated discrepancy for all the species. Figures 5.283c and 5.283d indicate a good agreement between the predictions and measurements for different fuel fragments, even though SD mechanism seems to be performing better compared to the other two mechanisms.

Calculations made for the moderately stretched moderately premixed flame are compared with the measurements in Figure 5.84. The agreement among the predictions made with different chemical-kinetics models is the best for this flame. Temperature and major-product-species-concentration profiles computed with three mechanisms almost lie on top of each other. However, all three mechanisms failed to predict the temperature rise due to premixed combustion seen in the experiment (Figure 5.284a). On the other hand, computed  $n\text{C}_7\text{H}_{16}$ ,  $\text{O}_2$ ,  $\text{H}_2$ ,  $\text{CO}$ , and  $\text{CO}_2$  profiles matched well with the measurements. Contrary to the agreement obtained between the predictions and measurements for  $\text{CH}_4$  and  $\text{C}_2\text{H}_2$  in the previous two flames (Figures 5.282c and 5.283c), these fuel fragments are underpredicted in this moderately stretched moderately premixed flame (Figure 5.284c). It is believed that the higher concentrations of  $\text{CH}_4$  and  $\text{C}_2\text{H}_2$  in the experiment led to the development of the premixed-combustion branch.

Comparisons between the predictions and measurements for the moderately stretched weakly premixed flame are shown in Figure 5.285. Reasonable agreement between the measurements and predictions is obtained for this flame. Once again, the major discrepancies are found in the temperature and water comparisons. Measurements clearly show the premixed-combustion branch in the temperature profile (bulge on the fuel side), while none of the mechanisms predicted such a bulge. Instead, all the mechanisms predicted inflections in the temperature profiles on the fuel side. As shown in Figure 5.285d, concentrations of minor fuel fragments are reasonably predicted by the three chemical-kinetics mechanisms.

In summary, there are negligible differences between the predictions of the three mechanisms with respect to temperature and major species profiles ( $n\text{C}_7\text{H}_{14}$ ,  $\text{O}_2$ ,  $\text{CO}_2$ ,  $\text{CO}$ ). However, there are noticeable differences with respect to the intermediate fuel species. For instance, the NIST mechanism predicts less  $\text{C}_2\text{H}_4$ , but more  $\text{C}_4\text{H}_8$  compared to the other two mechanisms. The LLNL mechanism predicts more  $\text{H}_2$ , while the SD mechanism predicts less  $\text{C}_2\text{H}_2$  compared to the other mechanisms. LLNL mechanism also consumes  $n\text{C}_7\text{H}_{14}$  and  $\text{O}_2$  in the fuel jet faster than the other two mechanisms. All three mechanisms generally reproduced the experimental data in terms of the temperature and major species profiles, although there are some differences with



respect to these profiles. Predictions locate the peak flame temperature more toward the fuel jet, by about 0.5-1.0 mm, compared to measurements. The peak CO mole fractions are underpredicted by all three mechanisms compared to measurements. The differences between the predictions and measurements are more significant with respect to intermediate species ( $C_2H_2$ ,  $C_2H_4$ ,  $C_4H_8$ ), indicating a need for further examination of these mechanisms. The predicted rates of production of these species are slower compared to the measured rates, and their peak mole fractions are generally overpredicted by all three mechanisms compared to measurements. Also, not shown here, benzene (PAH species leading to soot production) is included only in the NIST mechanism, and its predictions exhibit reasonable agreement with the measured values, although the location of the peak predicted value is shifted slightly toward the oxidizer jet compared to the measurements.

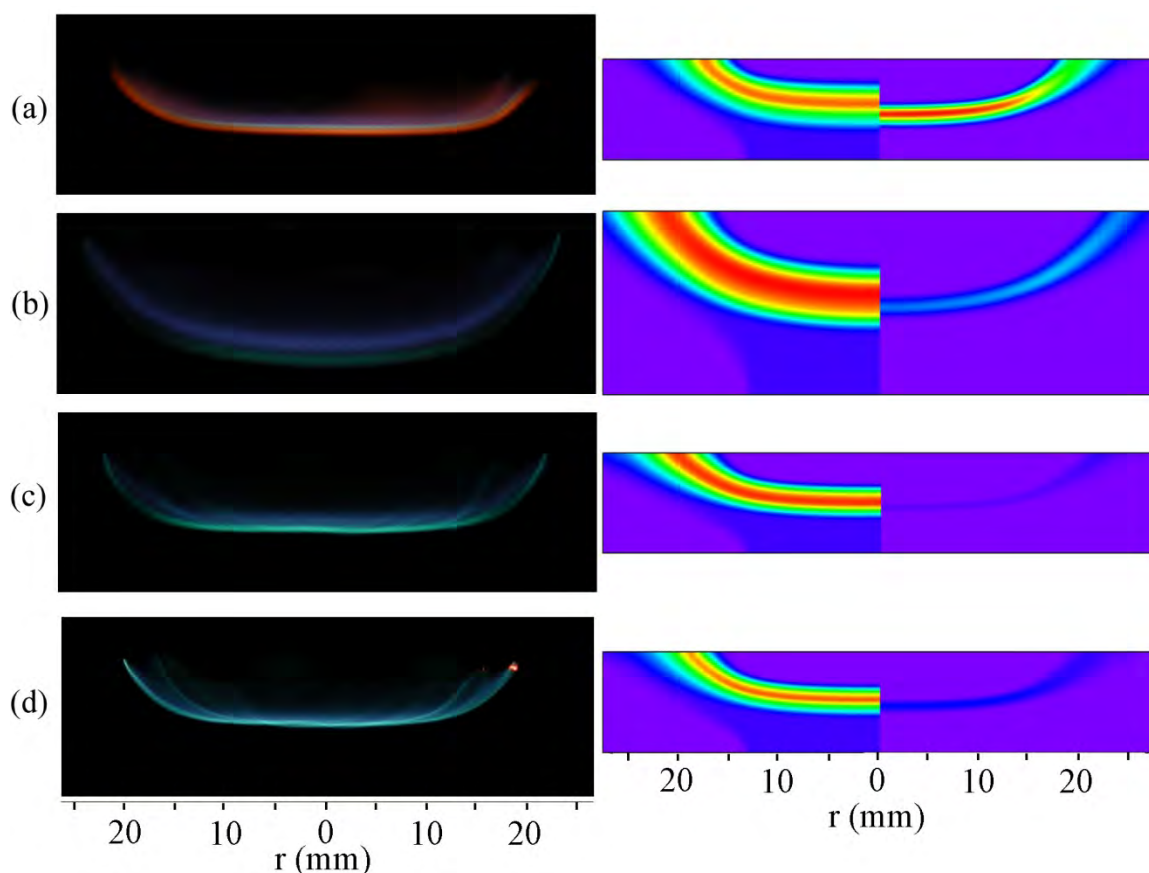


Figure 5.280 Actual and simulated opposing-jet partially premixed flames. Direct photographs and simulations made with LLNL mechanism are shown in the left and right halves, respectively for (a) weakly stretched weakly premixed flame, (b) weakly stretched moderately premixed flame, (c) moderately stretched moderately premixed flame, and (d) moderately stretched weakly premixed flame. Distributions of temperature are plotted between 300 (blue) and 2100 K (red) in the left halves and distributions of soot between 0 (blue) and 1 (red) ppm are shown in the right halves of the computational flames.

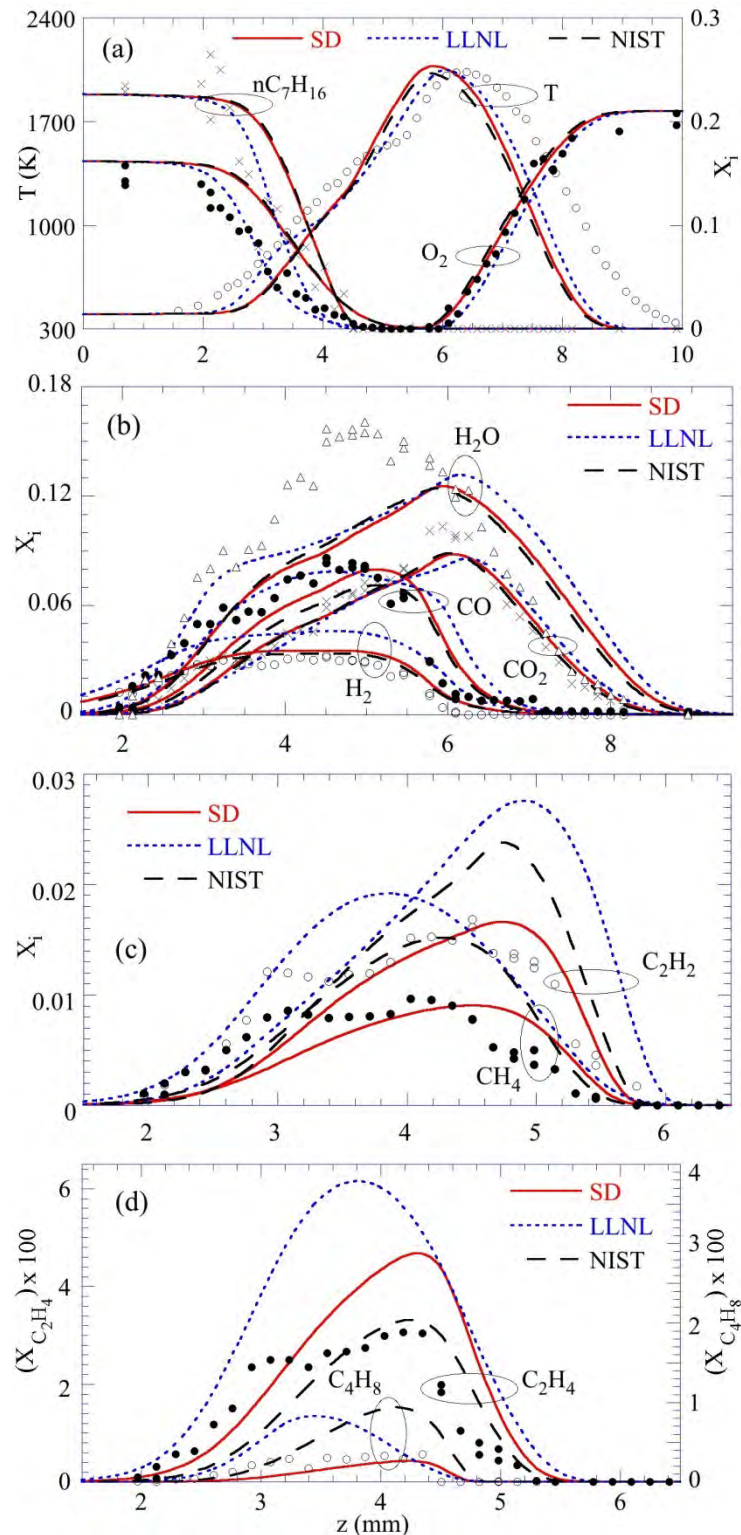


Figure 5.281 Comparisons of the structures of the weakly stretched weakly premixed flame simulated using different chemical-kinetics mechanisms (lines) with those measured (symbols). Profiles of (a) temperature and reactant species, (b) major product species, (c) methane and acetylene, and (d) ethylene and butene are compared.



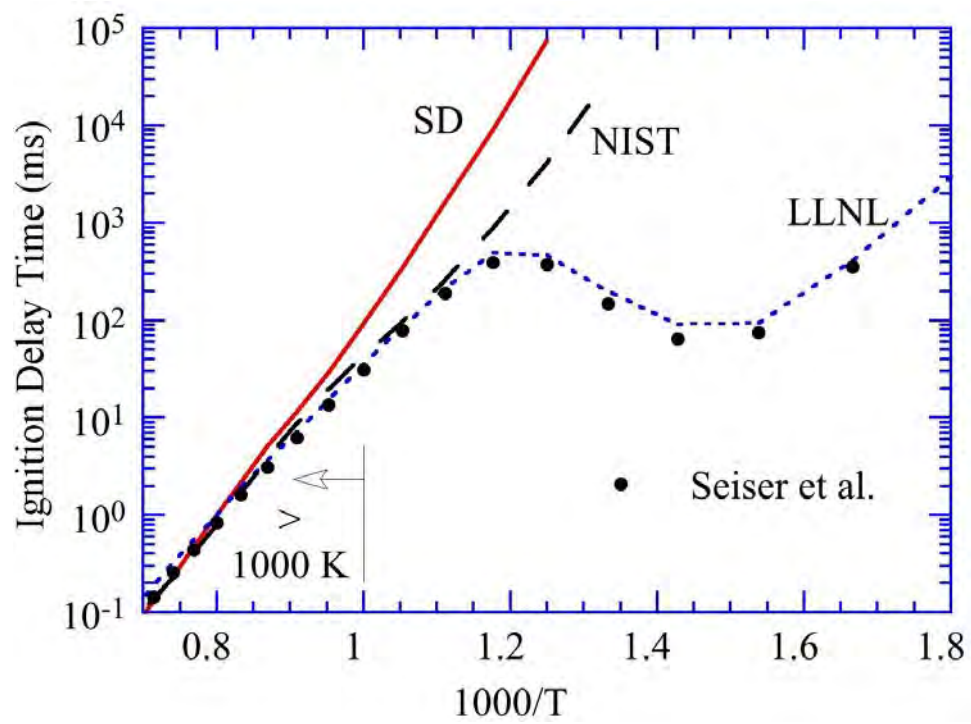


Figure 5.282 Ignition delay time in homogeneous, stoichiometric mixture of n-heptane vapor and air at different temperatures.

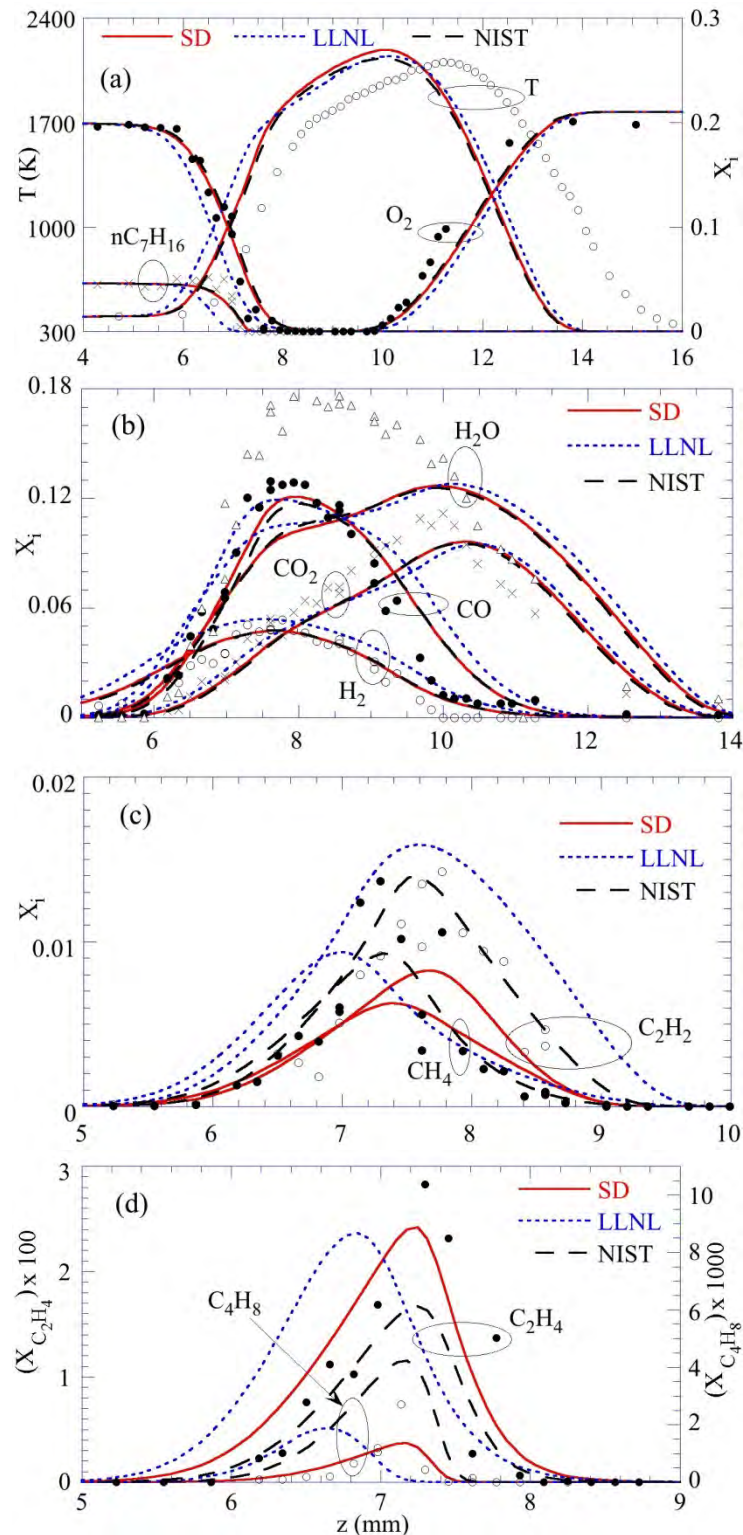


Figure 5.283 Comparisons of the structures of the weakly stretched moderately premixed flame simulated using different chemical-kinetics mechanisms (lines) with those measured (symbols). Profiles of (a) temperature and reactant species, (b) major product species, (c) methane and acetylene, and (d) ethylene and butene are compared.

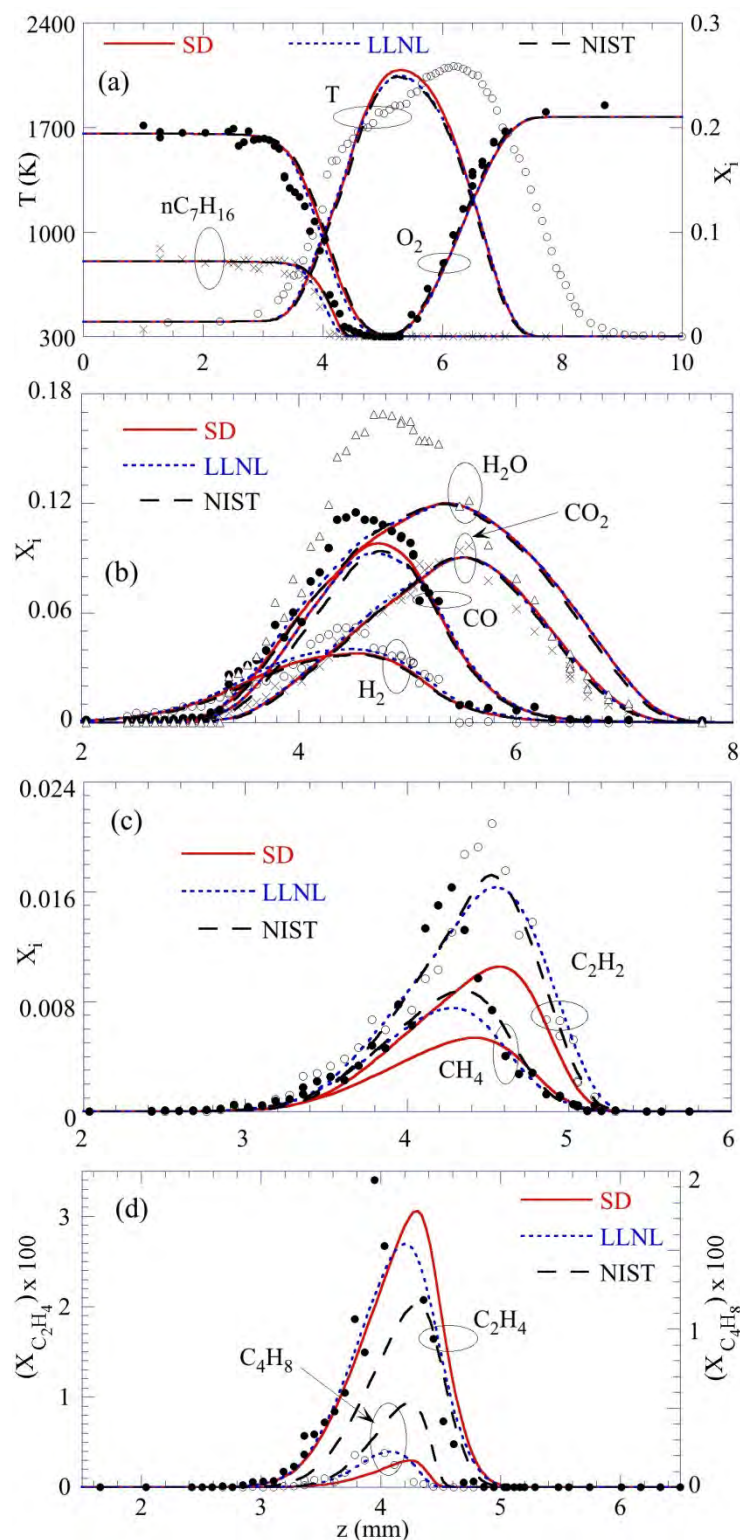


Figure 5.284 Comparisons of the structures of the moderately stretched moderately premixed flame simulated using different chemical-kinetics mechanisms (lines) with those measured (symbols). Profiles of (a) temperature and reactant species, (b) major product species, (c) methane and acetylene, and (d) ethylene and butene are compared.

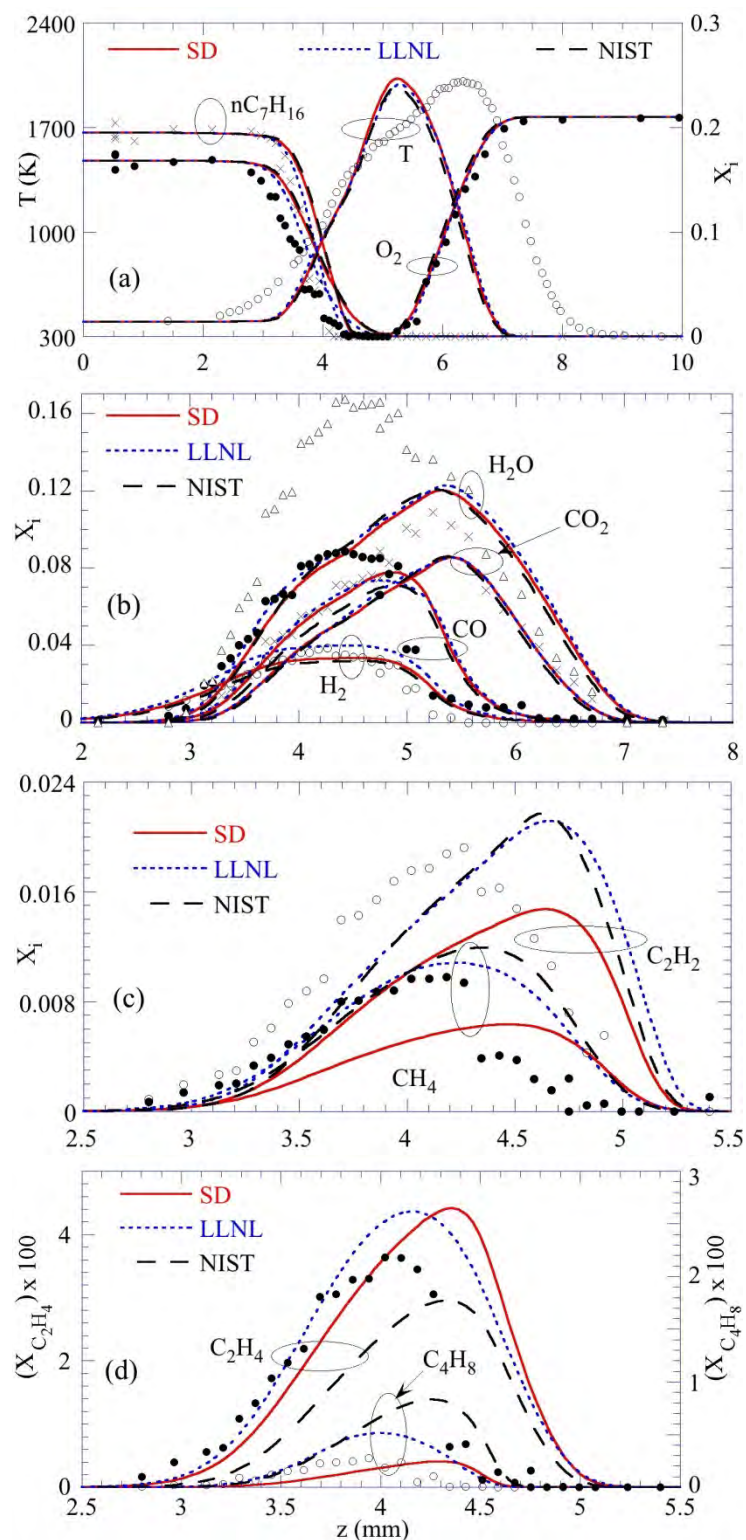


Figure 5.285 Comparisons of the structures of the moderately stretched weakly premixed flame simulated using different chemical-kinetics mechanisms (lines) with those measured (symbols). Profiles of (a) temperature and reactant species, (b) major product species, (c) methane and acetylene, and (d) ethylene and butene are compared.



## 5.8 SNETPSR Simulations of Combustor Particulate Emissions

To make predictions of soot (particulate) emissions from a combustor, we employed the Sooting Network of Perfectly Stirred Reactors (SNETPSR) code. This code is based upon a model developed to simulate emissions from a single stirred reactor (Colket, et al, 2004) and extended to treat evolution of particulates in the exhaust stream (Colket, 2009) through the use of sequential networks of reactors. The SNETPSR tool extends these capabilities by enabling any combination of series or parallel reactor networks. The reactor network used in this study was developed based on an engineer's view of the flow field within a combustor, with the mass balances, reactor volumes, and reactor interchanges identified through known airflow splits and geometries, as well as to empirical fitting of exhaust data sets of  $\text{NO}_x$  and CO emissions over a range of operating conditions (e.g.,  $P_3$ ,  $T_3$ , f/a where the subscript 3 refers to the combustor conditions). A schematic representation of the fluid dynamics occurring within a combustor is shown in Figure 5.286.

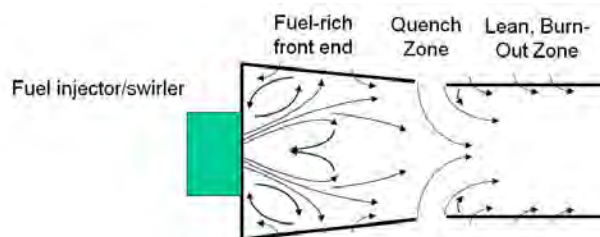


Figure 5.286 Averaged Fluid Dynamics in Combustor.

A pictorial representation of a reactor network for such a combustor is provided in Figure 5.287, with various reactors colored based on the character of the reactor.

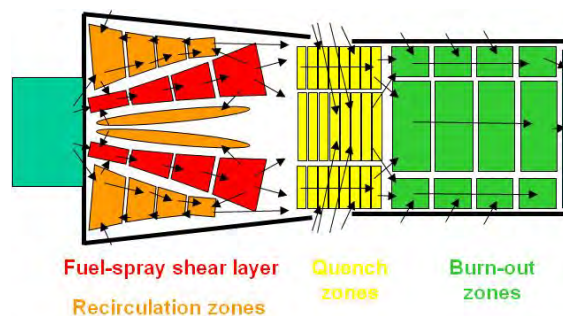


Figure 5.287 Reactor Network for Combustor Simulations.

Originally, this model was used to predict the character of soot formation in the burner. The heptane mechanism (Babushok and Tsang, 2004), together with the PAH reaction sequence developed in a prior SERDP funded effort, were utilized. With the SNETPSR code, the evolution of soot particulates through this computer could be computed. Such computations were performed for simulated take-off conditions at 811K and 16.3 atmospheres. Before describing the results on soot predictions, it is worthwhile to describe a global observation from these simulations. In particular, the surface growth rates and the oxidation rates could be computed

from each reactor volume. For each volume, a local equivalence ratio was known and hence the growth and oxidation rates could be plotted vs. the local equivalence ratio. Such data is provided in Figure 5.288, where the specific oxidation rates ( $\text{g}/\text{cm}^2/\text{sec}$ ) by OH and by  $\text{O}_2$  are separately provided. From these results, it is clear that for these (near full power conditions, the oxidation rates are dominated by OH. This result is similar to the result for more conventional laboratory flames for which oxidation rates are dominated by OH in super-equilibrium levels. There is scatter in this plot both in the oxidation and growth rates due to the large variation in reactivity conditions across the domain of this reactor network.

Of interest is that surface growth rates do not begin to dominate over oxidation rates until the equivalence ratio extends beyond an equivalence ratio of 1.5. At conditions leaner than 1.5, acetylene concentrations are negligible and OH concentrations are large. At equivalence ratios beyond 2.5, reaction temperatures decay below temperatures at which surface growth rates are significant.

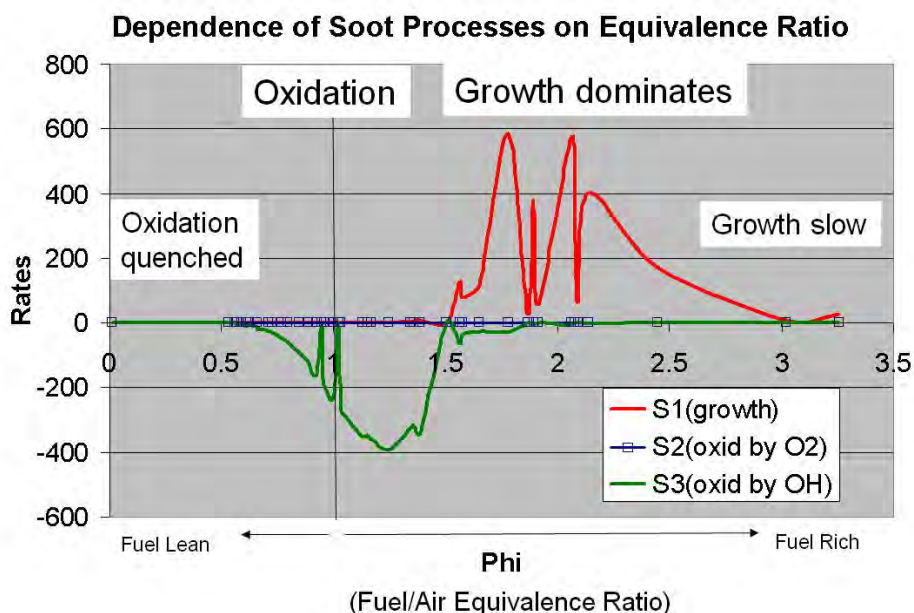


Figure 5.288 Specific growth and oxidation rates (per particle surface area) in SNETPSR for run at 811 K and 16 atm.

Predicted particle size distributions (PSD) in the sequential fuel-spray shear layer zones (red reactors in Figure 5.287) are shown in Figure 5.289. For this reactor sequence (#1-5), a dramatic increase in soot concentrations (by over two orders of magnitude) is observed as the gas-phase equivalence ratio increases from about one to over two. The residence times in each of these volumes are about 0.3 milliseconds. The unusual shape in these predicted profiles at high particle diameter is due to an empirical cut-off of surface growth rates for particles with diameters above 80 nanometers. Particle size may continue to grow due to coagulation. The existence of particles in Reactor number one is due to back mixing within the fuel spray shear region and from the recirculation zones (orange reactors in Figure 5.287).

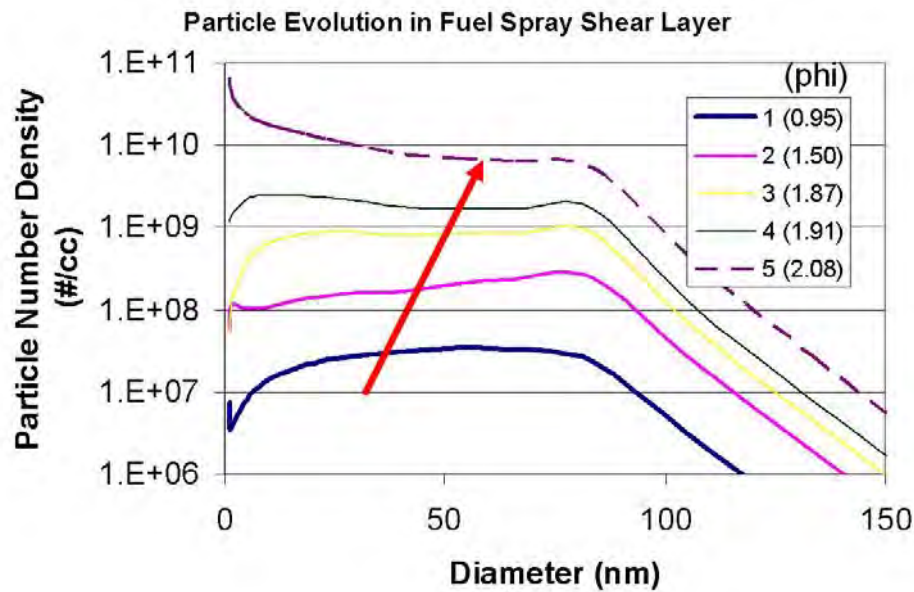


Figure 5.289 Predicted PSD in Fuel Spray Shear Layer.

Figure 5.290 depicts the particle size distribution (PSD) as it changes going through the quench zone (yellow reactors). Upon entrance into this region (Reactor 10a) the local equivalence ratio is still very rich (~2.5) and soot can still grow, although only small changes are observed as the local residence time per reactor is about 20-50 microseconds. The growth is primarily observed (see red arrow) only in the nucleation mode (diameters less than 10 nanometers). It is not until the local equivalence ratio drops below 1.5 that oxidation predominates (green arrow) and the small particles are consumed very rapidly, dropping by 2-4 orders of magnitude. Decreases in the concentrations of the larger particles also occur but only on the order of one order of magnitude.

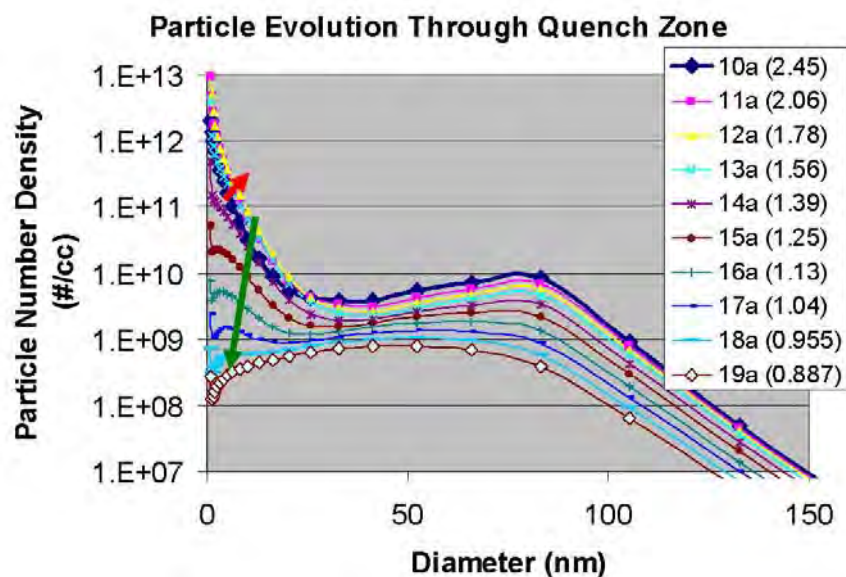


Figure 5.290 Predicted PSD Evolution through Quench Zone.

Figure 5.291 provides the evolution of particles in the burn-out zone (green reactors in Figure 5.287). Through this region, there is no more formation, and particles reduce in size and number. Average residence times per volume are on the order of 0.3 milliseconds. Number densities reduce (see green arrow) by about an order of magnitude and average particle diameters reduce by 20-30%. As particle mass is proportional to (diameter)<sup>3</sup>, these changes, plus those occurring in the quench zone, represent a significant reduction (factor of 100-1000) in total soot mass emissions relative to that present at the end of the fuel-rich zone.

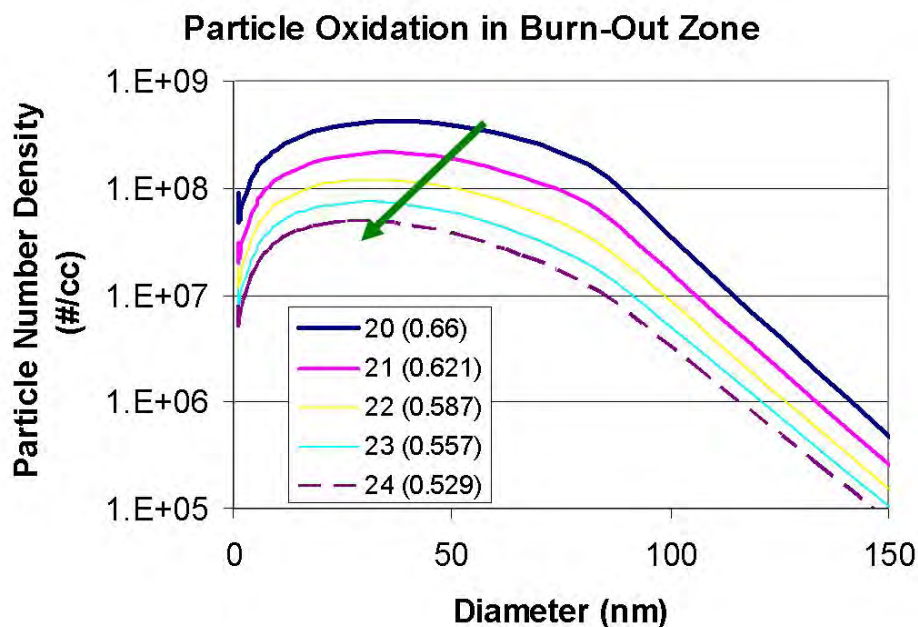


Figure 5.291 Evolution of PSD through Burn-Out Zone.

Using this model construction, the detailed chemical kinetics model (SERDP\_SURR v2) was then used in the Sooting Network Perfectly Stirred Reactor code (SNETPSR) to make predictions of soot emissions (mass, number, and particle size distributions) from a model combustor. Simulations were performed using the SERDP surrogate (23% m-xylene/77% n-dodecane) for JP-8 and a surrogate for a F-T derived JP-8 (100% n-dodecane). The intention for computing performance with these two fuels was to compare to relative experimental data from engines when burning JP-8 and with an F-T fuel. Predicted soot emissions using the surrogate fuel were similar to the experimental data (with a factor of two in mass, and similar size distributions), but initial computations with the F-T surrogate resulted in only 20-30% decrease in soot emissions. Meanwhile, the data indicated a 60-80% decrease in soot emissions when changing from JP-8 to F-T fuel.

Similar modeling results, e.g., the inability to reproduce the magnitude of soot reductions with high H/C fuels, has been obtained in collaborative work with Professor Mitch Smooke and Robert Hall for coflowing methane flames with added hydrogen (unpublished) and by Vish Katta when attempting to model soot emissions from flames fueled by n-dodecane and by the n-dodecane/m-xylene mixture. In the latter case, the model yielded virtually no difference in the soot field, yet several experienced researchers expect substantial differences. Consequently, we explored alternate soot growth models.



Specifically, we examined the soot inception and soot surface growth models. Our inception model is based upon the pyrene dimerization model that Appel, et al (2000) described, e.g.,

$$\frac{d[S_{\text{inception}}]}{dt} = k_{\text{inception}}[C_{16}H_{10}]^2 \times 2 \times 192$$

where  $S_{\text{inception}}$  is the mass production rate in the first, or smallest, soot bin in grams/cc/sec,  $k_{\text{inception}}$  is the bimolecular rate coefficient (cc/moles/sec) for the dimerization reaction,  $(C_{16}H_{10})$  is the molar concentration of pyrene (moles/cc), and the factor  $2 \times 192$  is the mass of carbon in the dimer (g/mole).

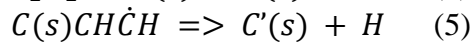
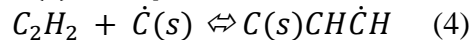
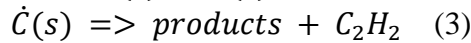
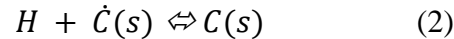
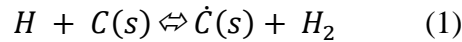
Of the various inception models proposed, this approach is believed to provide the greatest dependency on fuel type without adding much greater complexities to the simulation of gas-phase poly cyclic aromatic hydrocarbon species.

The surface growth rate can be determined via

$$d[S_{\text{surface\_growth}}]/dt = k_{\text{growth}} SA[C_2H_2]$$

where SA represents the total surface area of the soot particulates available for surface growth. SA is, of course, dependent on local values of particle number density and primary particle diameter. The proportionality to acetylene is consistent with the Harris and Weiner 1983 argument (HW) that acetylene is the principal surface growth species. An activation energy (32 kcal/mole) consistent with that determined by Hura and Glassman (1988) is utilized.

Alternatively, the surface growth can be computed by the HACA mechanisms (hydrogen abstraction, carbon addition) suggested by Appel, et al (2000). We prefer the slightly modified approach (CH) suggested by Colket and Hall (1994) as it avoids the use of an ageing parameter ( $\alpha$ ).



A corrected (CH) expression for soot mass production rate due to surface growth is given in Colket and Hall (1994). The main path for soot production via this route can be seen from reaction sequence 1, 4 and 5. The overall step can be written  $C(s) + C_2H_2 \rightleftharpoons C'(s) + H_2$ , and is nominally consistent with the Harris and Weiner surface growth steps.

Both the HW reaction rate and the CH expression result in similar results, since both were empirically fit to the soot growth data from premixed flames.

In examining the inception process and the two growth models, we conclude that the growth model, as presently defined, cannot account for the trends of substantially decreasing soot emissions with increasing fuel H/C ratio since the acetylene concentration is only weakly dependent on the fuel H/C ratio. (Note that reaction (2) and the reverse of (1) can suppress the acetylene addition process, with increased presence of H<sub>2</sub> and H-atoms, but we believe this is a secondary effect.) Hence, unless the system is dominated by soot inception processes – or an alternative soot growth process, we conclude in retrospect that our model should not exhibit a substantial fuel H/C ratio effect as implied by the results described above.

We reviewed the relative computed values of inception and surface growth rates, inception in fact does play a substantial role in two of the largest soot producing volumes and hence could be contributing to the observed differences. But as these differences (between the predictions from dodecane as the fuel to a dodecane/m-xylene blend) are small, we looked for alternative explanation.

In particular, we considered the role of condensation of polycyclic aromatic hydrocarbons (PAH) onto to small soot particles. In such case, the surface growth expression is modified to be

$$d[S'_{\text{surface\_growth}}]/dt = k_{1,\text{growth}} SA[C_2H_2] + k_{2,\text{growth}} SA[PAH],$$

where the 2<sup>nd</sup> rate constant is determined from collision frequency and an assumed (sticking) efficiency factor. Values from the model assuming a sticking coefficient of 5% resulted in a small increase in predicted soot, but predicted values with a 50% sticking efficiency resulted in soot levels for the n-dodecane /m-xylene mixture 50% enhanced over the predicted soot for dodecane.

In addition, a brute force sensitivity analysis on predictions of soot formation from a network reactor code identified uncertainties in ring formation and growth mechanisms as contributing factors that limit better simulation of trends in predicted soot formation with different fuel types. By slightly altering (decreasing) rates of ring growth reaction steps from n-alkane hydrocarbons, slightly better simulations were obtained. These simulations (made in conjunction with the modified surface growth expression described above) are shown in Figure 5.292 for the JP-8 fuel (dodecane/xylene) and for the FT fuel (dodecane). Here the differences in predicted values from the two fuels are as much as 50%, Still, since the soot observed when burning the FT fuel has been found to be 10-30% of that produced when burning JP-8, research in this area remains. Reactor design has been identified as a possible additional contributor to the inability to predict fuel-type effects. and while not the same change as indicated from the experimental data, these results are encouraging. Nevertheless, additional work remains to be completed.

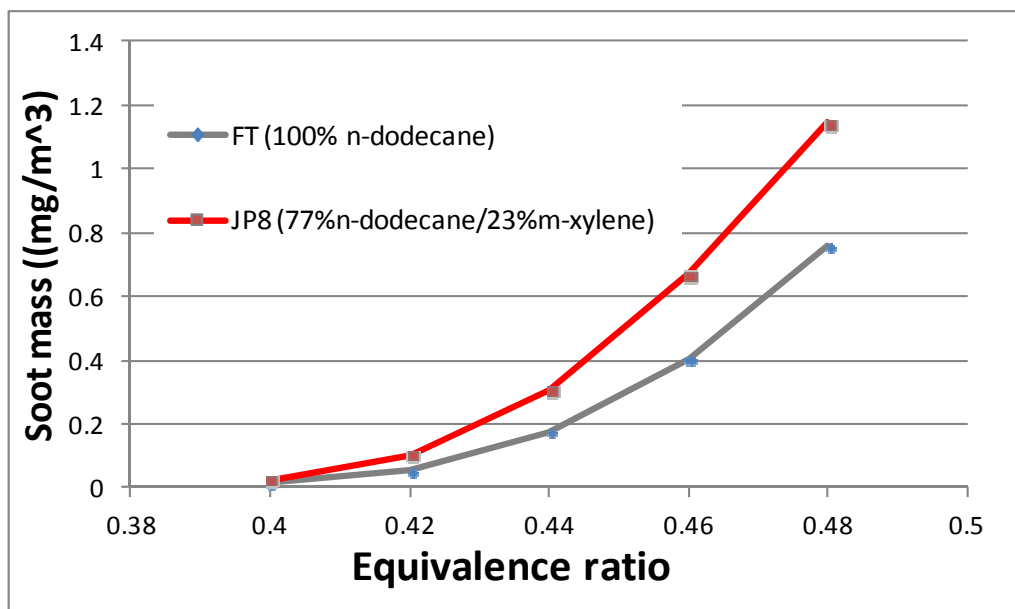


Figure 5.292 Predicted trends in particulate emissions with f/a ratio for two surrogate fuels.

## 6.0 Conclusions and Recommendations

An outline of the research results and accomplishments obtained on this program are given in the Executive Summary. As noted, we believe the program has significantly advanced the ability to develop and evaluate models for predicting soot emissions from gas turbine combustors through the creation of a validation database for a surrogate JP-8 and alternative fuels, and through the creation and validation of chemical kinetic models for the surrogate fuels. The validation database and the surrogate fuel model will be made broadly available to the combustion community. The database will serve as a robust test for chemical kinetic models as well as for the development and evaluation of soot models and combustion simulation codes. Indeed, it is believed that the presented kinetic model for the surrogate fuel will serve as the foundation for future work to improve the prediction of PAH and soot formation.

Even though considerable progress has been made in advancing the understanding of soot processes for a wide range of combustor flows, there remain many issues that need to be addressed. The findings of the program indicate the need to continue the development of both the kinetic models and the simulation tools. Simulations of flames with recirculation zones, such as the centerbody flame, point to the need to improve the diffusive and convective transport in the models. The current program included initial simulation of a single-cup swirl burner; those results point to the need to investigate more fully, both numerically and experimentally, the role of turbulence in soot formation. The kinetic models created in the program were focused on simulation of PAH and soot, but they include reactions that form hazardous air pollutants (HAPs) such as formaldehyde, butadiene, benzene and naphthalene. Current regulations address total hydrocarbon emissions. However, this is expected to change as the ability to measure HAPs and other hydrocarbon species improve. Also, models that can predict HAPs and other species are in the early stage of development. Thus, there is a need to advance the database as well as improve the modeling capabilities for hydrocarbons and other emissions from gas turbine engines.

It is recommended that future work continue to expand the database to develop and validate kinetic models for simulating the production of soot as well as HAPs, and other species emitted from gas turbine engines burning JP-8 and a wide range of alternative fuels.

## 7.0 References

- Adams, Jr., J. E., (1995) "Interactions between color plane interpolation and other image processing functions in electronic photography. SPIE, 2416 (144), pp.144-151.
- Adam, Jr., J. E., (1997) "Design of practical color filter array interpolation algorithms for digital cameras," SPIE, 3028 (117), pp. 117-125.
- Amadio, A. R., Petersen, E. L., Crofton, M. W., (2006) "Test-time extension behind reflected shock waves using CO<sub>2</sub>-He and C<sub>3</sub>H<sub>8</sub>-He driver mixtures," Shock Waves, 16, pp. 157-165.
- Appel, J., Bockhorn, H., Frenklach, M., (2000) "Kinetic model of soot formation with detailed chemistry and physics: Laminar premixed flames of c2 hydrocarbons," Combustion and Flame, 121 (1-2), pp. 122-136.
- ASTM, (2003) "Standard Tables for Reference Solar Spectral Irradiances: Direct Normal and Hemispherical on a 37° Tilted Surface," ASTM G143-03.
- Babushok, V. I., and Tsang, W., (2004) "Kinetic Modelling of Heptane Combustion and PAH Formation," Journal of Propulsion and Power, 20 (3) pp.403-414.
- Baker, J. A., Skinner, G. B., (1972) "Shock tube studies of ignition of ethylene-oxygen mixtures," Combustion and Flame, 19 (3), pp. 347-350.
- Balagurunatham, J., Flora, G., Saxena, S., Kahandawala, M., Sidhu, S., DeWitt, M., Corporan, E., (2011) "Ignition Delay times of a Range of Alternate Jet-Fuels and Surrogate Fuel Candidate Hydrocarbons under Fuel-Lean Conditions: a Shock Tube Study," 49th AIAA Aerospace Sciences Meeting including the New Horizons Forum and Aerospace Exposition., Orlando FL.
- Bardin, F., McBride, R., Moore, A., Morgan, S., Williams, S., Jones, J., Hand, D., (2004) "Real time temperature measurement for process monitoring of laser conduction welding," Proceedings of the 23<sup>rd</sup> International Congress on Applications of lasers and electro-optics.
- Battin-Leclerc, F., Bounaceur, R., Belmekki, N., Glaude, P. A., (2006) "Experimental and modeling study of the oxidation of xylenes," International Journal of Chemical Kinetics, 38, pp. 284-302.
- Bayer, B. E., (1976) "Color Imaging Array" U.S. Patent No. 3 971 065.
- Bento, D. S., Thomson, K. A., Gülder, Omer L., (2006) "Soot formation and temperature field structure in laminar propane-air diffusion flames at elevated pressures," Combustion and Flame, 145 (4), pp.765-778.
- Beretta, F., D'Alessio, A., D'Orsi, A., Minutolo, P., (1992) "U. V. and Visible Laser Excited Fluorescence from Rich Premixed and Diffusion Flames," Combustion Science and Technology, 85 (1), pp. 455-470.

- Berta, P., Aggarwal, S. K., and Puri, I. K., "An experimental and numerical investigation of n-heptane/air counterflow partially premixed flames and emission of NO<sub>x</sub> and PAH species," *Combustion and Flame* 145:640-764 (2006)
- Bilyeu, D., Yu, S. T., Davis, D., (2009) "Simulation of Shock-Tube Flows with Detailed Finite-Rate Chemistry by the CESE Method," American Institute of Aeronautics and Astronautics, AIAA 47th ASM, Orlando, Florida.
- Bounaceur, R., Da Costa, I., Fournet, R., Billaud, F., Battin-Leclerc F. (2005), "Experimental and Modeling Study of the Oxidation of Toluene," *International Journal of Chemical Kinetics*, 37, pp. 25-49.
- Brocklehurst, H. T., Priddin, C. H., Moss, J. B., (1997) "Soot predictions within an aero gas turbine combustion chamber", American Society of Mechanical Engineers, 97-GT-148.
- Brown, C. J., Thomas, G. O., (1999) "Experimental studies of shock induced ignition and transition to detonation in ethylene and propane mixtures," *Combustion and Flame*, 117 (4), pp. 861-870.
- Cadman, P., Bambrey, R. J., Box, S. K., Thomas, G. O., (2002) "Ethylene combustion in high-temperature shock waves," *Combustion Science and Technology*, 174 (11-12), pp. 111-127.
- Chaos, M., Dryer, F. L., (2010) "Chemical-kinetic modeling of ignition delay: Considerations in interpreting shock tube data," *International Journal of Chemical Kinetics*, 42 (3), pp. 143-150.
- Chen, L. D., Seaba, J. P., Roquemore, W. M., Goss, L. P., (1988) "Buoyant Diffusion Flames," *Proceedings of the Combustion Institute*, 22, pp. 677-684.
- CIE, (2010) International Commission on Illumination (accessed September 20, 2010) <http://cie.co.at/>.
- Colket, M. B., (1987) unpublished data.
- Colket, M. B., Hall, R. J., Stouffer, S. D., (2004) "Modeling Soot Formation in a Stirred Reactor," *Proceedings of ASME Turbo Expo*, Paper No. GT2004-54001, Vienna Austria, June 14-17, 2004.
- Colket, M., (2009) "Modeling Particle Formation and Growth in a Stirred Reactor and its Exhaust," in *Combustion Generated Fine Carbonaceous Particles*, ed. By H. Bockhorn, A. D'Anna, A.F. Sarofim, and H. Wang, KIT Scientific Publishing, pp. 483.
- Colket, M. B., (2009) Interim Report submitted to Strategic Environmental Research and Development Program (SERDP).
- Colket, M., Edwards, T., Williams, S., Cernansky, N., Miller, D., Egolfopoulos, F., Dryer, F., Bellan, J., Lindstedt, P., Seshadri, K., Pitch, H., Sarofim, A., Smooke, M., Tsang, W., (2008)

“Identification of Target Validation Data for Development of Surrogate Jet Fuels,” AIAA 972, 46<sup>th</sup> AIAA Aerospace Sciences Meeting and Exhibit, Reno NV, January 7-10.

Colket, M. B., Edwards, T., Williams, S., Cernansky, N. P., Miller, D., Egolfopoulos, F., Lindstedt, P., Seshadri, K., Dryer, F. L., Law, C. K., Friend, D., Pitsch, H., Sarofim, A., Smooke, M., Tsang, W., (2007) “Development of an Experimental Database and Chemical Kinetic Models for Surrogate Jet Fuels,” AIAA Paper 770.

Colket, M. B., Hall, R. J., (1994) “in Soot Formation in Combustion, Mechanisms and Models,” (H. Bockhorn, ed.) Springer Series in Chemical Physics, 59, Springer-Verlag, New York, pp. 442-470.

Colket, M. B., Seery, D. J., (1993) “Reaction Mechanisms for Toluene Pyrolysis,” Proceedings of the Combustion Institute, 25, pp. 883-891.

Colket, M. B., Spadaccini, L. J., (2001) “Scramjet Fuels Auto-ignition Study,” Journal of Propulsion and Power, 17 (2), pp. 315-323.

Cooper, P., (1996) “Explosives Engineering,” Wiley-VCH, New York.

Correa, S. M., Gulati, A., (1992) “Measurements and Modeling of a bluff body stabilized flame,” Combustion and Flame, 89 (2), pp. 195-213.

Curran, H. J., Gaffuri, P., Pitz, W., and Westbrook, C. K., (2002) “A Comprehensive Modeling Study of Iso-Octane Oxidation,” Combustion and Flame, 129, pp. 253-280.

D’Anna, A., Kent, J. H., Santoro, R. J., (2007) “Investigation of Species Concentration and Soot Formation in a Co-Flowing Diffusion Flame of Ethylene,” Combustion Science and Technology, 179 (1), pp. 355-369.

Dagaut, P., Cathonnet, M., (2006) “The Ignition, Oxidation, and Combustion of Kerosene: A Review of Experimental and Kinetic Modeling,” Progress in Energy and Combustion Science, 32 (1), pp. 48-92.

Dally, B. B., Masri, A. R., (1998) “Instantaneous and Mean Compositional Structure of Bluff-Body,” Combustion and Flame, 114 (1-2), pp. 119-148.

Dasch, C. J., (1992) “One-dimensional tomography: a comparison of Abel, onion-peeling, and filtering back projection methods,” Applied Optics 31, (8), pp. 1146-1152.

Davidson, D. F., Hanson, R. K., (2004) “Interpreting Shock Tube Ignition Data,” International Journal of Chemical Kinetics, 36 (9), pp. 510-523.

Davis, R. W., Moore, E. F., Santoro, R. J., Ness, J. R., (1990) “Isolation of Buoyancy Effects in Jet Diffusion Flame Experiments,” Combustion Science and Technology, 73, pp. 625-635.

Davis, R. W., Moore, E. F., Chen, L. D., Roquemore, W. M., Villimpos, V., Goss, L. P., (1991) "Preliminary Results of a Numerical-Experimental Study of the Dynamic Structure of a Buoyant Jet Diffusion Flame," *Combustion and Flame*, 83 (3-4), pp. 263-270.

Davis, S. G., Wang, H., Brezinsky, K. and Law, C. K., (1996) "Laminar burning speeds and oxidation kinetics of benzene/air and toluene/air flames." *Proceedings of the Combustion Institute*, **26**, pp. 1025-1033.

De Iuliis, S., Barbini, M., Benecchi, S., Cignoli, F., Zizak, G., (1998) "Determination of the soot volume fraction in an ethylene diffusion flame by multiwavelength and analysis of soot radiation," *Combustion and Flame*, 115 (1-2), pp. 253-261.

de Vries, J., Petersen, E. L., (2007) "Auto-ignition of methane based fuel blends under gas turbine conditions," *Proceeding of Combustion Institute*, 31, pp. 3163-3171.

De Witt, D. P., Nutter, G. D., (1988) "Theory and Practice of Radiation Thermometry," John Wiley and Sons.

Densmore, J., Biss, M., McNesby, K., Homan, B., (2011) "High Speed Digital Color Imaging Pyrometry," accepted by *Applied Optics*.

Dobbins, R. A., (1996) *Comb. Science and Tech.*, 121 (103) 1996.

Dobbins, R. A., (1997) "The Early Soot Particle Formation in Hydrocarbon Flames," Gordon and Breach Science Publishers, The Netherlands, *Physical and Chemical Aspects of Combustion*, Ch. 5, pp. 107-133.

Drummond, L. J., (1968) *Aust. J. Chem.*, 21, pp. 2641.

Dryer, F. D., see <http://www.princeton.edu/~combust/MRUI/>.

Dunlap, J. C., Bodegom, E., Widenhorn, R., (2010) "Correction of dark current in consumer cameras," *Journal of Electronic Imaging*, 19, (1) pp. 013010.

Duxbury, G., Langford, M., McCulloch, M., (2007) "Rapid Passage induced population transfer and coherences in the 8 micron spectrum of Nitrous Oxide," *Molecular Physics*, 105 (5-7), pp. 741-754.

Dworkin, S. B., Cooke, J. A., Bennett, B. A. V., Smooke, M. D., Hall, R. J., Colket, M.B., (2009) "Distributed-Memory Parallel Computation of a Forced, Time-Dependent, Sooting, Ethylene/Air Co-flow Diffusion Flame," accepted for publication by *Combustion Theory and Modeling*.

Ellzey, J. L., Laskey, K. J., Oran, E. S., (1990) *Proceedings of the Combustion Institute*, 23, pp. 1635-1640.



Ellzey, J. L., K. J. Laskey, and E. S. Oran (1991) "A Study of Confined Diffusion Flames," *Combustion and Flame*, 84, pp. 249-264.

Emdee, J., Brezinsky, K., Glassman, I., (1991) "High-Temperature Oxidation Mechanisms of m- and p-xylene," *Journal Physical Chemistry*, 95 (4), pp. 1626-1635.

Esquiva-Dano, H. T., et al., (2001) "Influence of a bluff-body shape on the stabilization regime of non-premixed flames," *Combustion and Flame*, 127 (4), pp. 2167-2180.

Fallot, L., Gonzalez, M., Elamraoui, R., Obounou, M., (1997) "Modelling Finite-Rate Chemistry Effects in Nonpremixed Turbulent Combustion: Test on the Bluff-Body Stabilized Flame," *Combustion and Flame*, 110 (21), pp. 298-318.

Fairweather, M. Jones, W. P., Lindstedt, R. P., (1992) "Predictions of radiative transfer from a turbulent reacting jet in a cross-wind," *Combustion and Flame*, 89 (1), pp. 45-63.

Fieweger, K., Blumenthal, R., Adomeit, G., (1994) "Shock tube investigation of the self-ignition of hydrocarbon-air mixtures at high pressures," *Combustion and Flame*, 25 (1), pp. 1579-1585.

Fieweger, K., Blumenthal, R., Adomeit, G., (1997) "Self-ignition of S.I. engine model fuels: A shock tube investigation at high pressure," *Combustion and Flame*, 109 (4), pp. 599-619.

Finlayson, G. D., Hordley, S., Hubel, P. M., (1995) "Recovering device sensitivities with quadratic programming," In the Sixth Color Imaging Conference: Color Science, Systems and Applications, pp. 90.

Flora, G., Saxena, S., Kahandawala, M. S. P., and Sidhu, S. S., (2011) "Investigation of Ignition Delay Time for n-Dodecane and n-Dodecane/m-Xylene Mixtures," appearing 7th U.S. National Combustion Meeting, March 20-23, Georgia Institute of Technology Atlanta GA.

Flora, G., Nagulappali, A., Saxena, S., Kahandawala, M. S. P., and Sidhu, S. S., (2011) "Simulation of Reflected Shock Combustion Experiments Using Multiple Computational Approaches," appearing 7th U.S. National Combustion Meeting, March 20-23, Georgia Institute of Technology Atlanta GA.

Frazier, C., Petersen, E. L., Kassab, A., (2007) "Wall heat transfer in shock tubes at long test times," *Shock Waves*, 26, pp. 195-200.

Frenklach, M., (2009) "PrIME – Process Informatics Model, <http://prime.citris-uc.org/>, also: <http://primekinetics.org/>

Frenklach, M., Harris, S. J., (1987) "Aerosol dynamics modeling using the method of moments," *Journal of Colloid and Interface Science*, 118 (1), pp. 252-261.

Frenklach, M., Wang, H., (1990) *Proc. Comb. Inst.*, 23, pp. 1559-1566.

Frenklach, M., Wang, H., (1991) "Twenty-third Symposium (International) on Combustion," The Combustion Institute, Pittsburgh, pp. 1559-1566.

Frenklach, M., Wang, H., (1994) "In Soot Formation in Combustion: Mechanisms and Models," (H. Bockhorn, Ed.), Springer-Verlag, Heidelberg, pp. 165-189.

Frenklach, M., Wang, H., (1997) "A detailed kinetic and modeling study of aromatics formation in laminar premixed acetylene and ethylene flames," *Combustion and Flame*, 110 (1-2), pp. 173-221.

Frenklach, M., Wang, H., and Rabinowitz, M. J., (1992) "Optimization and analysis of large chemical kinetic mechanisms using the solution mapping method - combustion of methane," *Progress in Energy and Combustion Science*, 18 (1) 47-73.

Fried, L., Souers, P. (1994) "CHEETAH: A Next Generation Thermochemical Code," UCRL-ID-117240, Lawrence Livermore National Laboratory, November 1994.

Fu, T., Cheng, X., Shi, C., Zhong, M., Liu, T., Zheng, X., (2006a) "The set-up of a vision pyrometer," *Measurement Science and Technology*, 17, pp. 659-665.

Fu, T., Cheng, X., Yang, Z., (2008) "Theoretical evaluation of measurement uncertainties of two-color pyrometry applied to optical diagnostics," *Applied Optics*, 47 (32), pp. 6112-6123.

Fu, T., Cheng, X., Fan, X., Ding, J., (2004) "The analysis of optimization criteria for multiband pyrometry," *Metrologia*, 41 (4), pp. 305-313.

Fu, T., Cheng, X., Zhong, M., Liu, T. (2006b) "The theoretical prediction analysis of the measurement range for multi-band pyrometry," *Measurement Science and Technology*, 17 (10), pp. 2751-2756.

Fu, T., Wang, Z., Cheng, X., (2010) "Temperature measurements of diesel fuel combustion with multicolor pyrometry," *Journal of Heat Transfer*, 132 (5), pp. 051602.

Gail, S. and Dagaut, P. (2007) "Oxidation of m-xylene in a JSR: Experimental study and detailed chemical kinetic modeling," *Combustion Science and Technology*, 179 (5-6), pp. 813-844.

Gaydon, A. G., (1941) "Applications of spectroscopy to combustion," *Rep. Prog. Phys.*, 8, pp. 50-70.

Gaydon, A. G., (1974) "The spectroscopy of Flames," Chapman and Hall, London.

Gelbard, F., Seinfeld, J. H., (1980) "Simulation of Multicomponent Aerosol Dynamics," *J. Coll. Int. Sci.* 78, pp. 485-501. Also see Gelbard, F., Tambour, Y., Seinfeld, J. H. (1980) "Sectional Representation for Simulating Aerosol Dynamics," *J. Coll. Int. Sci.*, 76 (2), pp. 541-556.

Gibson, F., Bower, M., Summers, C., Scott, F., Mason, C., (1958) "Use of electro-optical methods to determine detonation temperatures in high explosives," J. Appl. Phys., 29 (4), pp. 628.

Gill, R. J., Olson, D. B., (1984) "Estimation of soot thresholds for fuel mixtures," Combustion Science and Technology, 40 (5-6), pp. 307-315.

Goldhirsch, I., Ronis, D., (1983) "Theory of Thermophoresis I: General considerations and mode coupling analysis," Phys. Rev. A., 27, pp. 1616-1634.

Gomez, A., Rosner, D., (1993) "Thermophoretic Effects on Particles in Counter-flow Laminar Diffusion Flames," Combustion Science and Technology, 89 (5-6), pp. 335-362.

Goroshin, S., Frost, D. L., Levine, J., Yoshinaka, A., Zhang, F., (2006) "Optical pyrometry of fireballs of metalized explosives," Propellants, Explosives, Pyrotechnics, 31 (3), pp. 169.

Goroshin, S., Frost, D. L., Levine, J., Zhang, F., (2004) "Optical pyrometry of fireballs of metalized explosives," 18<sup>th</sup> International Symposium on the Military Aspects of Blast and Shock (MABS 18), Bad Reichenhall, Germany, September 27 – October 1, 2004.

Grum, R., Becherer, R. J., (1979) "Optical Radiation Measurements," Academic Press.

Gudiyella, S., Malewicki, T., Comandini, A., Brezinsky, K., (2011) "High pressure study of m-xylene oxidation," Combustion and Flame, 158 (4), Special Issue on Kinetics, pp. 687-704.

Gunturk, B. K., Glotzbach, J., Altunbasak, Y., Schafer, R. W., Mersereau, R. M., (2005) "Demosaicking: color filter array interpolation" IEEE Signal Processing Magazine, Jan (44).

Hall, R. J., (1994) "Radiative Dissipation in Planar Gas-Soot Mixtures," Journal of Quantitative Spectroscopy and Radiative Transfer, 51 (4), pp. 653-644.

Hall, J. M., Rickard M. J. A., and Petersen E. L., (2005) "Comparison of Characteristic Time Diagnostics for Ignition and Oxidation of Fuel/Oxidizer Mixtures Behind Reflected Shock Waves," Combustion Science and Technology, 177 (3), pp. 455-483.

Hall, R. J., Smooke, M. D., Colket, M. B., (1997) "Predictions of Soot Dynamics in Opposed Jet Diffusion Flames," in Physical and Chemical Aspects of Combustion: A Tribute to Irvin Glassman, Sawyer, R. F., Dryer, F. L., eds., Combustion Science and Technology Book Series, Gordon and Breach, Langhorne, PA. pp. 189-230.

Hall, J. M., Petersen, E. L., (2006) "An optimized Kinetics Model for OH Chemiluminescence at High Temperatures and Atmospheric Pressures," International Journal of Chemical Kinetics, 38, pp. 714-724.

Hall, J. M., Petersen, E. L., de Vries, J., Amadio, A. R., (2005) "Towards a Kinetics Model of CH Chemiluminescence," AIAA Paper 1318, 43<sup>rd</sup> AIAA Aerospace Sciences Meeting & Exhibit, Jan. 10-13, 2005, Reno, NV.

Harris, S. J., Weiner, A. M., (1983) "Determination of the Rate Constant for Soot Surface Growth," *Combustion Science & Technology*, 32 (5-6), pp. 267-275.

Harris, S. J., Weiner, A. M., (1984) "Soot Particle Growth in Premixed Toluene/Ethylene Flames," *Combustion Science and Technology*, 38 (1-2), pp. 75-84.

Herbinet, O., Marquaire, P.-M., Battin-Leclerc, F., Fournet, R., (2007) "Thermal decomposition of n-dodecane: Experiments and kinetic modeling," *Journal of Analytical and Applied Pyrolysis*, 78 (2), pp. 419-429.

Herzler, J., Jerig, L., Roth, P., (2004) "Shock tube study of the ignition of propane at intermediate temperatures and high pressures," *Combustion Science and Technology*, 176, pp. 1627-1637.

Hidaka, Y., Kataoka, T., Suga, M., (1974) "A shock tube investigation of the ignition in ethylene-oxygen-argon mixtures," *Bulletin of the Chemical Society of Japan*, 47 (9), pp. 2166-2170.

Hidaka, Y., Gardiner, W. C., Eubank, C. S., (1982) "Shock tube and modeling study of ethylene pyrolysis and oxidation," *Communications in Journal of Molecular Science*, 2 (4), pp. 141-153.

Hidaka, Y., Nishimori, T., Sato, K., Henmi, Y., Okuda, R., Inami, K., Higashihara, T., (1999) *Combust. Flame*, 117, pp. 755-776.

Higgins, K. J., Jung, H., Kittelson, D. B., Roberts, J. T., Zachariah, M. R., (2002) "Size-selected nanoparticle chemistry: kinetics of soot oxidation," *J. Phys. Chem. A.*, 106, pp. 96-103.

Hoffmann, M., W. G. Bessler, C. Schulz, and H. Jander (2003) "Laser-Induced Incandescence for Soot Diagnostics at High Pressures," *Applied Optics*, 42(12), pp. 2052–2062.

Holley, A. T., Dong, Y., Andac, M. G., Egolfopoulos, F. N., Edwards, T., (2007) "Ignition and extinction of non-premixed flames of single-component liquid hydrocarbons, jet fuels, and surrogates," *Proceedings of the Combustion Institute*, 31 (1), pp. 1205-1213.

Horning, D. C., (2001) Ph.D. Thesis, Department of Mechanical Engineering, Stanford University, Stanford, CA.

Hsieh, W. H., Char, J. M., Zanutti, C., Kuo, K. K., (1990) "Erosive and Strand Burning of Stick Propellants, Part I: Measurements of Burning Rates and Thermal-Wave Structures," *Journal of Propulsion and Power*, 6 (4), pp. 392-399.

Hubel, P. M., Sherman, D., Farrell, J. E., (1994) "A comparison of methods for sensor spectral sensitivity estimation," in *IS&T and SID's 2<sup>nd</sup> Color Imaging Conference: Color Science, Systems and Applications*, pp. 45.

Hunter, S., Frassoldati, A., Granata, S., Faravelli, T., Ranzi, E., Seiser, R., Seshadri, K., "Experimental and kinetic modeling study of combustion of JP-8, its surrogates and reference components in laminar nonpremixed flows," Proceedings of the Combustion Institute 31 (2007) 393-400.

Hura, H. S., Glassman, I., (1988) "Soot Formation in Diffusion Flames of Fuel/Oxygen Mixtures," Proceedings of the Combustion Institute, 22 (1), pp. 371-378.

Hwang, J. Y., Chung, S. H., (2001) "Growth of soot particles in counterflow diffusion flames of ethylene," Combustion and Flame, 125, pp. 752-762.

Hyun, I. J., Gulder, O. L., (2008) "Pressure dependence of soot formation in diffusion flames," Proceedings of ASME Turbo Expo, Paper GT2008-50437, June 9-13.

IEC., (1999) "International Electrotechnical Commission," IEC 61966-2-1: Multimedia systems and equipment, Color measurements and management, part 2-1: Color management, default RGB color space: sRGB.

Jacquemart, D., Mandin, J.-Y., Dana, V., Claveau, C., Vander Auwera, J., Herman, M., Rothman, L. S., Régalia-Jarlot, L., Barbe, A., (2003) "The IR acetylene spectrum in HITRAN: update and new results," Journal of Quantitative Spectroscopy & Radiative Transfer, 82 (1-4), pp. 363-382.

Jahne, B., (2004) "Practical Handbook on Image Processing for Scientific and Technical Applications," CRC Press.

Ji, C., Moheet, A., Wang, Y. L., Colket, M., Wang, H., Egolfopoulos, F. N., (2009) "An Experimental Study of Premixed m-Xylene/Air Flames," presentation at the 6<sup>th</sup> U.S. National Combustion Meeting, Ann Arbor, Michigan, May 18-20.

Jochowitz, et al., (2005) "Propargyl Radical: Ab Initio Anharmonic Modes and the Polarized Infrared Absorption Spectra of Matrix-Isolated HCCCH<sub>2</sub>," Journal of Physical Chemistry A, 109 (17), pp. 3812-3821.

Johnston, R. J. and Farrell, J. T., (2005) "Laminar burning velocities and Markstein lengths of aromatics at elevated temperature and pressure," Proceedings of the Combustion Institute, 30 (1), pp. 217-224.

Joo, H. I., Gülder, M. L., (2009) "Soot formation and temperature field structure in co-flow laminar methane-air diffusion flames at pressures from 10 to 60 atm," Proceedings of the Combustion Institute, 32 (1), pp. 769-775.

Kahandawala, M. S. P., PhD. Dissertation (2004), Energy and Environmental Engineering, University of Dayton, Dayton, OH.

Kahandawala, M. S. P., DeWitt, M. J., Corporan, E. and Sidhu, S. S., (2008) "Ignition and Emission Characteristics of Surrogate and Practical Jet Fuels," *Energy & Fuels*, 22 (6), pp. 3673-3679.

Kahandawala, M., Corera, S. A. P., Williams, S., Carter, C. D., Sidhu, S. S., (2006) "Investigation of kinetics of iso-octane ignition under scramjet conditions," *International Journal of Chemical Kinetics*, 38 (3), pp. 194-201.

Kalitan, D. M., Petersen, E. L., Hall, J. M., (2005), "Ignition and Oxidation of Ethylene – Oxygen-Diluent Mixtures with and without Silane," *Journal of Propulsion and Power*, 21 (6), pp. 1045-1056.

Katta, V. R., Roquemore, W. M., (1993) "Role of Inner and Outer Structures in Transitional Jet Diffusion Flame," *Combustion and Flame*, 92 (3), pp. 274-282, IN3-IN4, 279-282.

Katta, V. R., and Roquemore, W. M., "Effect of Nitromethane on Soot Formation in Heptane Jet Diffusion Flame", *Proceedings of 4<sup>th</sup> Joint Meeting of the U. S. Sections of the Combustion Institute*, 2005.

Katta, V. R., Hu, S., Wang, P., Ritz, R., Roquemore, W. M., Gord, J. R., (2007) "Investigation on double-state behavior of the counter-flow premixed flame system," *Proceedings of the Combustion Institute*, 31, pp. 1055-1066.

Katta, V. R., Roquemore, W. M., (2008) "Stability of lifted flames in centerbody burner," *Proceedings of the 2008 Technical Meeting of the Central States Section of the Combustion Institute*.

Katta, V. R., Roquemore, W. M., (2008) "Calculation of Multidimensional Flames Using Large Chemical Kinetics," *AIAA Journal*, V. 46, No. 7, pp. 1640-1650.

Katta, V. R., Roquemore, W. M., Santoro, R. J. (2008) "Comparison of chemical kinetics mechanisms through predicting a nonpremixed ethylene jet flame," *Proceedings of the 2008 Technical Meeting of the Central States Section of the Combustion Institute*, Tuscaloosa, AL, April 20-22, 2008.

Katta, V. R., (2009) ref to most recent version of UNICORN.

Katta, V. R., Stouffer, S. D., Forlines, R., Anderson, W., Zelina, Z., (2009b) "Sooting characteristics of partially premixed flames in centerbody burner," 6<sup>th</sup> U.S. National Combustion Meeting, Ann Arbor, Michigan, May 18-20, 2009.

Katta, V. R., Roquemore, W. M., Stouffer, S. D., (2009a) "Dynamics of lifted flame supported by a recirculation zone," 6<sup>th</sup> U.S. National Combustion Meeting, Ann Arbor, Michigan, May 18-20, 2009.

Katta, V. R., Newman-Lehman, T., Seshadri, K., Zelina, J., Roquemore, W. M., (2010) "Performance of JP-8 surrogate models in predicting laboratory flame," AIAA-2010-950, Aerospace Sciences Meeting, Orlando Florida, January 4-8, 2010.

Katta, V. R., Aggarwal, S. K., Roquemore, W. M., (2011) "Evaluation of chemical-kinetics models for n-heptane combustion using a multidimensional CFD code," Fuel, doi 10.1016/j.fuel.2011.10.035.

Kee, R. J., Miller, J. A., Jefferson, T. H., (1980) "CHEMKIN: A General-Purpose, Problem-Independent, Transportable, Fortran, Chemical Kinetic Code Package," Technical Report SAND80-8003, Sandia National Laboratories.

Kee, R. J., Rupley, F. M., Miller, J. A., Coltrin, M. E., Grcar, J. F., Meeks, E., Moffat, H. K., Lutz, A. E., Dixon-Lewis, G., Smooke, M. D., Warnatz, J., Evans, G. H., Larson, R. S., Mitchell, R. E., Petzold, L. R., Reynolds, W. C., Caracotsios, M., Stewart, W. E., Glarborg, P., Wang, C., Adigun, O., Houf, W. G., Chou, C. P., Miller, S. F., (2002) "Chemkin Collection," Release 3.7, Reaction Design, Inc., San Diego, CA.

Kempf, A., Lindstedt, R. P., Janicka, J., (2006) "Large-Eddy simulation of a bluff-body stabilized nonpremixed flame," Combustion and Flame, 144 (1-2), pp. 170-189.

Kennedy, I. M., Yam, C., Rapp, D. C., Santoro, R. J., (1996) "Modeling and measurements of soot and species in a laminar diffusion flame," Combustion and Flame, 107, pp. 368-382.

Kijima, T., Nakamura, H., Compton, J., Hamilton, J., (2007) "Image sensor with improved light sensitivity," U.S. Patent No. 0 177 236.

Kinney, G., Graham, K., (1985) "Explosive Shocks in Air, 2<sup>nd</sup> Ed," Springer-Verlag, New York.

Kosterev, A., Tittel, F., (2002) "Chemical sensors based on quantum cascade lasers," IEEE Journal of Quantum Electronics, 38 (6), pp. 582-591.

Lange, S., Luther, K., Rech, T., Schmoltner, A. M., and Troe, J., (1994) "C-C and C-H Bond Splits of Laser-Excited Aromatic Molecules. 4. Specific Rate Constants and Branching Ratios for the Dissociation of the Xylenes," Journal of Physical Chemistry, 98 (26), pp. 6509-6513.

Lentati, A. M., Chelliah, H. K., (1998) "Dynamics of Water Droplets in a Counterflow Field and their Effect on Flame Extinction," Combustion and Flame, 115 (1), pp. 157-179.

Leung, K. M., Lindstedt, P., Jones, W. P., (1991) "A Simplified Reaction Mechanism for Soot Formation in Nonpremixed Flames," Combustion and Flame, 87, pp. 289-305.

Levendis, Y., Estrada, K., Hottel, H., (1992) "Development of multicolor pyrometers to monitor the transient response of burning carbonaceous particles," Rev. Sci. Instrum., 63 (7), pp. 3608-3622.

Li, H., Owens, Z. C., Davidson, D. F., and Hanson, R. K., (2008) "A Simple Reactive Gasdynamic Model for the Computation of Gas Temperature and Species Concentrations behind Reflected Shock Waves," *International Journal of Chemical Kinetics*, 40 (4), pp. 189-198.

Li, J., Zhao, Z., Kazakov, A., Dryer, F. L. (2004) "An Updated Comprehensive Kinetic Model of Hydrogen Combustion," *International Journal of Chemical Kinetics*, 36 (10), pp. 566-575.

Lindstedt, R. P., (1994) "In Soot formation in Combustion: Mechanisms and Models (H. Buckhorn, Ed.)" Springer-Verlag, Heidelberg, pp. 417-439.

Liu, K., Pope, S. B., Caughey, D. A., (2005) "Calculations of bluff-body stabilized flames using a joint probability density function model with detailed chemistry," *Combustion and Flame*, 141 (1-2), pp. 89-117.  
Livermore

Lottero, R. E., (2005) ARL Tech Report ARL-TR-3411, January.

Lu, H., Ip, L., Mackrory, A., Werrett, L., Scott, J., Tree, D., Baxter, L., (2009) "Particle surface temperature measurements with multicolor band pyrometry," *AICHE*, 55, pp. 243.

Lukac, R., Plantiotis, K. N., (2005) "Color filter arrays, design and performance analysis," *IEEE Transactions on Consumer Electronics*, 51 (4), pp. 1260-1267.

Lukac, R., Plataniotos, K., (2006) "Color Image Processing: Methods and Applications," CRC Press.

Lukac, R., (2009) "Single-Sensor Imaging: Methods and Applications for Digital Cameras," CRC Press.

Lutz, A. E., Kee, R. J., Grcar, J. F., Rupley, F. M., (1996) "OPPDIF: A Fortran Program for Computing Opposed flow Diffusion Flames," SAND96-8243, Sandia National Laboratories, CA.

Mader, C. L., (2008) "Numerical Modeling of Explosives and Propellants," 3<sup>rd</sup> Ed. CRC Press, Boca Raton Florida 2008

Maun, J. D., Sunderland, P. B., Urban, D. L., (2007) "Thin-filament pyrometry with a digital still camera," *Applied Optics*, 46 (4), pp. 483-488, 2007.

Masri, A. R., Bilger, R. W., (1984) "Twentieth Symposium (International) on Combustion," The Combustion Institute, Pittsburgh, pp. 319-320.

Matsui, Y., Kamimoto, T., Matsuoka, S., (1979) "A study on the time and space resolved measurement of flame temperature and soot concentration in a d.i. diesel engine by the two-color method," Technical Report 790491, SAE Tech. Paper.

Mehra, J., Rechenberg, H., (1982). "1". *The Historical Development of Quantum Theory*, New York, Springer-Verlag.



Mensch, A., Santoro, R.J., Litzinger, T.A., Lee, S.-Y. (2010) "Sooting Characteristics of Surrogates for Jet Fuels," *Combustion and Flame*, 157 (6), pp. 1097-1105.

Merci, B., Roekaerts, D., Naud, B., Pope, S. B., (2006) "Comparative Study of Micromixing Models in Transported Scalar PDF Simulations of Turbulent Nonpremixed Bluff-Body Flames," *Combustion and Flame*, 146 (1-2), pp. 109-130.

Miller, J., Mallarad, W., Smyth, K. C., (1982) "The observation of laser induced visible fluorescence in sooting diffusion flames," *Combustion and Flame*, 47, pp. 205-214.

Minsek, D. W., Chen, P. J., (1990) "Photoelectron Spectrum of the Propargyl Radical in a Supersonic Beam," *Phys. Chem.*, 94 (22), pp. 8399-8401.

Montgomery, C. J., Cannon, S. M., Mawid, M. A., Sekar, B., (2002) "Reduced chemical kinetic mechanisms for JP-8 combustion," AIAA Paper 2002-0336.

Moss, J. B., Aksit, I., M. (2007) "Modeling Soot Formation in a Laminar Diffusion Flame Burning a Surrogate Kerosene Fuel," *Proceedings of the Combustion Institute*, 31 (2), pp. 3139-3146.

Müller, A., Beck, M., Faist, J., (1999) "Electrically tunable room-temperature quantum-cascade lasers," *Applied Physics Letters*, 75 (11), pp.1509-1511.

Murphy, J. J., Shaddix, C. R., (2004) "Soot properties and species measurements in a two-meter diameter JP-8 pool fire," SANDIA Report SAND2004-8085.

McEnally, C. S., Pfefferle, L. D., (1999) "Experimental study of nonfuel hydrocarbon concentrations in co-flowing partially premixed methane/air flames," *Combustion and Flame* 118, pp. 619-632.

McEnally, C. S., Pfefferle, L. D., (2000) "Experimental study of nonfuel hydrocarbons and soot in co-flowing partially premixed ethylene/air flames," *Combustion and Flame*, 121, pp. 575-592.

McEnally, C. S., Schaffer, A. M., Long, M. B., Pfefferle, L. D., Smooke, M. D., Colket, M. B., Hall, R. J., (1998) "Computational and Experimental Study of Soot Formation in a Co-flow, Laminar Ethylene Diffusion Flame," *Proceedings of the Combustion Institute*, 27, pp. 1497-1505.

McNesby, K., Miziolek, A. W., Nguyen, T., Delucia, F. C., Skaggs, R. R., Litzinger, T. A., (2005) "Experimental and computational studies of oxidizer and fuel side addition of ethanol to opposed flow air/ethylene flames," *Combustion and Flame*, 142, pp. 412-427.

McNesby, K., Homan, B., Piehler, T., Lottero, R., (2006) "Spectroscopic Measurements of Fireballs Produced by Enhanced Blast Explosives," ARL-TR-3318; U.S. Army Research Laboratory: Aberdeen Proving Ground, MD.

McNesby, K., Homan, B. E., Piehler, T. N., Lottero, R. E., (2005) "Real-Time Optical Measurements for Improved Understanding of Enhanced Blast Materials," ARL-TR-3483, May 2005.

McNesby, K. L., Homan, B. E., Ehlers, R. Z., McAndrew, B. A., (2008) "Energy Release Mechanisms in Enhanced Blast Explosives: Comparison to TNT," ARL-TR-05, July 2008.

McNesby, K. L., Homan, B. E., Ritter, J. J., Quine, Z., Ehlers, R. Z., McAndrew, A., (2010) "Afterburn Ignition Delay and Shock Augmentation in Fuel Rich Solid Explosives," *Propellants, Explosives, Pyrotechnics*, 35 (1), pp. 57-65.

Nagle, J., and Strickland-Constable, R. F., (1962) "Oxidation of Carbon between 1000-2000 C," in *Proceedings of the Fifth Carbon Conference*, 1, (Pergamon Press, Oxford).

Nakamuri, J., (2006) "Image Sensors and Signal Processing for Digital Still Cameras," CRC Press.

Namazian, M., Kelly, J., Schefer, R. W., Johnston, S. C., Long, M. B., (1989) "Nonpremixed bluff-body burner flow and flame imaging study," *Exp. Fluids* 8 (3-4), pp. 216-228.

Neoh, K. G., Howard, J. B., Sarofim, A. F., (1981) "Soot Oxidation in Flames," in *Particulate Carbon: Formation During Combustion*, Siegl, D. C., Smith, G. W., eds., Plenum, New York.

Normand, E., Duxbury, G., Langford, N., (2001) "Characterization of the spectral behavior of pulsed quantum cascade lasers using a high resolution Fourier transform infrared spectrometer," *Optics Communications*, 197 (1-3), pp. 115-120.

Oehlscaeger, M. A., Davisdon, D. F., Hanson, R. K., (2004) "Shock tube measurements of branched alkane ignition times and OH concentration time histories," *International Journal of Chemical Kinetics*, 36, pp. 67-68.

Oehlsclaeger, M. A., Shen, H. S., Vanderover, J., (2008) "A shock tube study of iso-octane ignition at elevated pressures; The influence of diluents gases," *Combustion and Flame*, 155, pp. 739-755.

Oppenheim, A. K., (1985) "Dynamic features of combustion." *Phil. Trans. R. Soc. Lond.* 315, pp. 471-508.

Oppenheim, A. K., Vermeer, D. J., Meyer, J. W., (1972) "Auto-ignition of hydrocarbons behind reflected shock waves," *Combustion and Flame* 18, pp. 327-336.

Pagni, P. J., Bard, S., (1978) "Particulate volume fractions in diffusion flames," In *Proceedings of the 17<sup>th</sup> Symposium (International) on Combustion*, pp. 1017.

Panagiotou, T., Levendis, Y., Delichatsios, M., (1996) "Measurements of particle flame temperatures using three-color optical pyrometry," *Combustion and Flame*, 104 (3), pp.272-287.

Petersen, E. L., (1998) Ph.D. Thesis, Department of Mechanical Engineering, Stanford University, Stanford, CA.

Planck, M., (1901) "Ueber das gesetz der energieverteilung im normalspectrum," *Annalen der Physik*.

Planck, M., (1914) "The theory of heat radiation," second edition, translated by M. Masius, Blackiston's Son & Co, Philadelphia.

Prado, G. A., Garo, A. Ko, Sarofim, A., (1985) "Polycyclic aromatic hydrocarbons formation and destruction in a laminar diffusion flame," *Symposium (International) on Combustion* 20 (1), pp. 989-996.

Quine, Z. R., McNesby, K. L., (2009) "Acetylene measurement in flames by chirp-based quantum cascade laser spectrometry," *Appl. Opt.*, 38, pp. 3075-3083.

Quoc, H. X., Vignon, J.-M., Brun, M., (1991) "A new approach of the two-color method for determining local instantaneous soot concentration and temperature in a diesel combustion chamber," *Technical Report* 910736.

Ramaath, R., Synder, W. E., Yoo, Y., Drew, M. S., (2005) "Color image processing pipeline," *IEEE Signal Processing Magazine*, January (34).

Ramaath, R., Synder, W. E., Bilbro, G. L., Sander, W. A., (2002) "Demosaicking methods for Bayer color arrays," *Journal of Electronic Imaging*, 11 (3), pp. 306-315.

Ranzi, E., Gaffuri, P., Faravelli, T., Dagaut, P., "A wide range modeling study of n-heptane oxidation," *Combustion and Flame* 103:91-106 (1995).

Richards, A. A., (2005) "Applications for highspeed infrared imaging," 26<sup>th</sup> International Congress on High-Speed Photography and Photonics, 5580 (1), pp. 137-145.

Rogg, B., (1993) "RUN1DL-The Cambridge Universal Laminar Flamelet Computer Code," in *Reduced Kinetic Mechanisms for Applications in Combustion Systems*, N. Peters and B. Rogg (Eds), *Lecture Notes in Physics* m15, Springer-Verlag, Heidelberg, Germany, pp. 350-351.

Roquemore, W. M., Bradley, R. P., Stutrud, J. S., Reeves, C. M., Krishnamurthy, L., (1980) "Preliminary Evaluation of a Combustor for Use in Modeling and Diagnostics Development," *ASME Publication* 80-GT-93.

Roquemore, W. M., Bradley, R. P., Stutrud, J. S., Reeves, C. M., Obringer, C. A., Britton, R. L., (1983) "Utilization of laser diagnostics to evaluate combustor models," *AGARD CP* 353 (19), pp. 36-1 - 36-21.

Roquemore, W. M., Tankin, R. S., Chiu, H. H., Lottes, S. A., (1986) "A study of a bluff-body combustor using laser sheet lighting," *Exp. Fluids*, 4, pp. 205-213.

Roquemore, W. M., Katta, V. R., (2000) "Role of flow visualization in the development of UNICORN," Journal of Visualization, 2 pp. 257-272.

Roquemore, W. M., Katta, V. R., Belovich, V., Pawlik, R., Lynch, A., Stouffer, S. D., Arstingstall, M., Justinger, G., Zelina, J., Roy, S., and Gord, J. R., Experimental and Numerical Studies of Centerbody Flames, Paper No. D36, Proceedings of the 5<sup>th</sup> US National Combustion Meeting of the Combustion Institute, San Diego, CA, March 25-28, 2007.

Roquemore, W. M., Katta, V. R., Stouffer, S. D., Belovich, V., Pawlik, R., Arstingstall, M., Justinger, Gord, J. R., Lynch, A., Zelina, J. and Roy, S., Soot studies of laminar diffusion flames with recirculation zones, Proceedings of the Combustion Institute, 32: 729-736 (2009)

Russ, J. C., (2002) "The Imaging Processing Handbook," Fourth Edition, CRC Press.

Santoro, R. J., Semerjian, H. G., (1984) Proceedings of the Combustion Institute, 20, pp. 997-1006.

Santoro, R. J., Semerjian, H. G., Dobbins, R. A., (1983) "Soot particle measurements in diffusion flames," Combustion and Flame, 51, pp. 203-218.

Santoro, R. J., Shaddix, C. R., (2002) "Laser-Induced Incandescence," Applied Combustion Diagnostics, Taylor & Francis, New York.

Saxena, S., Kahandawala, M. S. P., and Sidhu, S. S., (2010) "A shock tube study of ignition delay in the combustion of ethylene" Combustion and Flame, web-published, Nov' 2010.

Saxena, S., Flora, G., Kahandawala, M., and Sidhu, S., (2011) "A Shock Tube Experimental Study and Modeling of M-xylene Ignition Delay," 49th AIAA Aerospace Sciences Meeting including the New Horizons Forum and Aerospace Exposition, Orlando FL.

Saylam A., Ribaucour M., Pitz, W. J., Minetti R., (2007) "Reduction of Large detailed Chemical Kinetic Mechanisms for Autoignition using joint Analyses of Reaction Rates and Sensitivities", International Journal of Chemical Kinetics, 39 (4), pp. 181-196.

Schulz, C., Kock, B. F., Hofmann, M., Michelsen, H., Will, S., Bougie, B., Suntz, R., Smallwood, G., (2006) "Laser-Induced incandescence: recent trends and current questions," Applied Physics B, 83, pp. 333-354.

Schulz, W., (1991) "Oxidation products of a surrogate JP-8 fuel," ACS Petroleum Chemistry Division Preprints, 37 (2), pp. 383-392.

Seiser, R., Pitsch, H., Seshadri, K., Pitz, W. J., Curran, H. J., (2000) "Extinction and Autoignition of n-Heptane in Counter-flow Configuration," Proceedings of the Combustion Institute, 28, pp. 2029-2037.

Seiser, R., Truett, L., Trees, D., Seshadri, K., (1998) "Structure and extinction of non-premixed n-heptane flames," Proceedings of the Combustion Institute, 27, pp. 649-657.

Shaddix, Chris, (2008) private communication.

Sheen, D., Wang, H., You, X., Lovas, T., (2009) "Spectral uncertainty quantification, propagation and optimization of a detailed kinetic model for ethylene combustion," Proceedings of the Combustion Institute, 32, pp. 535-542.

Shen, H. S., Steinberg, J., Vanderover, J., and M. A. Oehlschlaeger, (2009) "A shock tube study of the ignition of n-heptane, n-decane, n-dodecane, and n-tetradecane at elevated pressures," Energy and Fuels, 23 (5), pp. 2482-2489.

Shi, Y., Ge, H.-W., Brakora, J., and Reitz, R. D., (2010) "Automatic chemistry mechanism reduction of hydrocarbon fuels for HCCI engines based on DRGEP and PCA methods with error control," Energy & Fuels, 24 (3), pp. 1646-1654.

Shultz, W. D., ACS Petroleum Chemistry Division Preprints, 37 (1991) 383-392.

Siddall, R. G., McGrath, I. A., (1962) "The emissivity of luminous flames," Proceedings of the 9<sup>th</sup> Symposium (International) on Combustion, pp. 102.

Simmie, J. M., "Detailed Chemical Kinetic Models for the Combustion of Hydrocarbon Fuels," (2003) Progress in Energy and Combustion Science, 29 (6), pp. 599- 634.

Simonini, S., Elston, S., Stone, C., (2001) "Soot temperature and concentration measurements from color charge coupled device camera images using a three color method," Proc Instn Mech Engr, 215, pp. 1041.

Sirjean, B., Dames, E., Sheen, D. A., You, X., Sung, C., Holley, A. T., Egolfopoulos, F. N., Wang, H., Vasu, S. S., Davidson, D. F., Hanson, R. K., Pitsch, H., Bowman, C. T., Kelley, A., Law, C. K., Tsang, W., Cernansky, N. P., Miller, D. L., Violi, A., Lindstedt, R. P., (2009) "A High-Temperature Chemical Kinetic Model of *n*-alkane Oxidation", JetSurF version 1.0, September 15, 2009. ([http://melchior.usc.edu/JetSurF/Version1\\_0/Index.html](http://melchior.usc.edu/JetSurF/Version1_0/Index.html)).

Sitarski, M. and Seinfeld, J. H., (1977) "Brownian coagulation in the transition regime," J. Coll. Int. Sci., 61 (2), pp. 261.

Sivaramakrishnan, R., Tranter, Robert S., Brezinsky, K., (2006) "High pressure pyrolysis of toluene. Experiments and modeling of toluene decomposition," Journal of Physical Chemistry A, 110 (30), pp. 9388-9399.

Sivaramakrishnan, R., Tranter, Robert S., Brezinsky, K., (2005) "A high pressure model for the oxidation of toluene," Proceedings of Combustion Institute, 30, 1165-1173.

Smooke, M. D., McEnally, C. S., Pfefferle, L. D., Hall, R. J., Colket, M. B., (1999) "Computational and Experimental Study of Soot Formation in a Co-flow, Laminar Diffusion Flame," *Combustion and Flame*, 117, pp. 117-139.

Smooke, M. D., Hall, R. J., Colket, M. B., Fielding, J., Long, M. B., McEnally, C. S., Pfefferle, L. D., (2004) "Investigation of the Transition from Lightly Sooting Towards Heavily Sooting Co-flow Ethylene Diffusion Flames," *Combustion Theory and Modeling* 8 (3), pp. 593-606.

Smooke, M. D., Long, M. B., Connelly, B. C., Colket, M. B., Hall, R. J., (2005) "Soot Formation in Laminar Diffusion Flames," *Combustion and Flame*, 143, pp. 613-628.

Sturgess, G. J., McManus, K. R., (1984) "Calculations of Turbulent Mass Transport in a Bluff-body Diffusion- Flame Combustor," *American Institute of Aeronautics and Astronautics, Aerospace Sciences Meeting*, 22<sup>nd</sup>, Reno, NV, Jan. 9-12.

Suzuki, M., Moriwaki, T., Okazaki, S., Okuda, T., Tanzawa, T., (1973) *Astronaut. Acta.*, 18 (5), pp. 359-365.

Takahashi, T., and Katta, V. R., "Reaction kernel structure and stabilizing mechanisms of jet diffusion flames in microgravity," *Proceedings of the Combustion Institute*, 29:2509-2518 (2002).

Takahashi, T., and Katta V. R., "Further Studies of the Reaction Kernel structure and stabilization of jet diffusion flames," *Proceedings of the Combustion Institute*, 30:383-390 (2005).

Thomson, K. A., Gülder, O. L., Weckman, E. J., Fraser, R. A., Smallwood, G. J., Snelling, D. R., (2005) "Soot concentration and temperature measurements in co-annular, non-premixed CH<sub>4</sub>/air laminar flames at pressures up to 4 Mpa," *Combustion and Flame*, 140, pp. 222-232.

Tolpadi, A. K., Danis, A. M., Mongia, H. C., Lindstedt, R. P., (1997) "Soot Modeling in Gas Turbine Combustors," 97-GT-149 IGTI Conference.

Trussell, H. J., Saber, E., Vrhel, M., (2005) "Color image processing," *IEEE Signal Processing Magazine*, January 2005, pp. 14.

Tsang, W., (2004) "Progress in the development of combustion kinetics databases for liquid fuels," *Data Science Journal*, 3 (1-9).

Vasu, S.S., Davidson, D. F., Hong, Z., Vasudevan, V., and Hanson, R. K. *Proceedings of the Combustion Institute*, 32 (2009) 173-180.

Violi, A., Yan, S., Eddings, E. G., Sarofim, A. F., Granta, S., Faravelli, T., Ranzi, E., (2002) "Experimental Formulation and Kinetic Model for JP-8 Surrogate Mixtures," *Combustion Science and Technology*, 174 (11-12), pp. 399-417.

Vision Research (2010) “High speed cameras,” August 30, 2010, <http://www.visionresearch.com>.

Vision Research (2011) Private Communications.

Vora, P. L., Farrell, J. E., Tietz, J. D., Brainard, D. H., (1997) “Digital color cameras – 1 response models,” Technical Report Hewlett-Packard Co. HPL-97-53.

Wang, H. Frenklach, M., (1997) “A detailed kinetic modeling study of aromatics formation in laminar premixed acetylene and ethylene flames,” *Combustion and Flame*, 110, pp. 173-221.

Wang, H., You, X., Joshi, A. V., Davis, S. G., Laskin, A., Egolfopoulos, F., Law, C. K., (2007) “USC Mech Version II. High-Temperature Combustion Reaction Model of H<sub>2</sub>/CO/CI-C<sub>4</sub> Compounds. [http://ignis.usc.edu/USC\\_Mech\\_II.htm](http://ignis.usc.edu/USC_Mech_II.htm).

Wang, H., Colket, M., (2008) Interim report submitted to Strategic Environmental Research and Development Program (SERDP).

Wang, H., Sirjean, B., Dames, E., Sheen, D., You, X., Sung, C., Holley, A. T., Egolfopoulos, F., Vasu, S. S., Davidson, D. F., Hanson, R. K., Pitch, H., Bowman, C. T., Kelley, A., Law, C. K., Tsang, W., Cernansky, N. P., Miller, D. L., Violi, A., Lindstedt, R. P., (2008) “A high-temperature chemical kinetic model of n-alkane oxidation, *JetSurF*, 0.2, September 8, 2008 [http://melchior.usc.edu/JetSurF/Version0\\_2/Index.html](http://melchior.usc.edu/JetSurF/Version0_2/Index.html).

Warnatz, J., “Hydrocarbon Oxidation High Temperature Chemistry,” (2000) *Pure and Applied Chemistry*, 72 (11), pp. 2101-2110.

Yamanaka, S. (1977) “Solid State Color Cameras,” U.S. Patent No. 4 054 906

Yoshinaka, A., Zhang, F., Anderson, J., Legare, L., (2004) “Near-field reflected temperatures in fireballs of heterogeneous explosives,” 18<sup>th</sup> International Symposium on the Military Aspects of Blast and Shock (MABS 18), Bad Reichenhall, Germany, September 27 – October 1, 2004.

Yoshizawa, Y., Kawada, H., (1973) *Bull. Jpn. Soc. Mech.*, 16 (93), pp. 576-587.

You, X., Egolopoulos, F. N., Wang, H., (2009) “Detailed and simplified kinetic models of n-dodecane oxidation: The role of fuel cracking in aliphatic hydrocarbon combustion,” *Proceedings of the Combustion Institute*, 32 (1), pp. 403-410.

Yule, A. J., Chigier, N. A., Ralph, S., Boulderstone, R., Ventura, J., (1980) “Combustion-transition interaction in a jet flame,” *AIAA Journal*, 19, pp. 752-760.

Zhang, H., (2005) “Numerical Combustion of Commercial Fuels,” Ph.D. Thesis, University of Utah.

Zhao , J. Li, Z., Kazakov, A. and Dryer, F. L., Fall Technical Meeting of the Eastern States Section of the Combustion Institute, Penn State University, University Park, PA, October 26-29, 2003.



## Appendix

### List of Papers and Publications

#### *Archival Publications*

Evaluation of Chemical-kinetics models for n-heptane combustion using a multidimensional CFD code, V. R. Katta, S. K. Aggarwal, W. M. Roquemore, *Fuel* (2011); online <http://doi:10.1016/j.fuel.2011.10.035>.

Infrared imaging, computations, and tomography of bluffbody stabilized laminar diffusion flames, B. A. Rankin, D. L. Bluck, V. R. Katta, S. D. Stouffer, and J. P. Gore, *Combustion and Flame* (under review).

A shock tube study of ignition delay in the combustion of ethylene, Saxena, S., Kahandawala, M. S. P., and Sidhu, S. S., (2011) to be published in *Combustion and Flame*

Fuel Additive Effects on Soot across a Suite of Laboratory Devices, Part 2: Nitro-alkanes, Litzinger, T., Colket, M., Kahandawala, M., Lee, S.-Y., Liscinsky, D., McNesby, K., Pawlik, R., Roquemore, M., Santoro, R., Sidhu, S., and Stouffer, S., (2011) to appear in *Combustion Science and Technology*

Experimental and computational study on partially premixed flames in a centerbody burner, V. R. Katta, R. A. Forlines, W. M. Roquemore, W. S. Anderson, J. Zelina, J. R. Gord, S. D. Stouffer, S. Roy, *Combustion and Flame*, 158 (2011) 511-524.

Stability of lifted flames in centerbody burner,” V. R. Katta, S. D. Stouffer, W. M. Roquemore, *Combustion and Flame* 158 (2011) 1149-1159.

Dynamic lifted flame in centerbody burner, V. R. Katta, W. M. Roquemore, S. D. Stouffer, D. Blunck, *Proceedings of the Combustion Institute*, Vol. 33, (2011) 1187-1194.

Distributed-Memory Parallel Computation of a Forced, Time-Dependent, Sooting, Ethylene/Air Coflow Diffusion Flame, Dworkin, S.B., Cooke, J.A, Bennett, B.A.V., Smooke, M.D., Hall, R.J., and Colket, M.B., (2009), to be published in *Combustion Theory and Modeling*.

Spatially resolved measurements of acetylene in a diffusion mixed flame by chirp-based quantum cascade laser spectrometry, Quine Zachary, McNesby Kevin, accepted for *Applied Optics*.

Computational and experimental study of the effects of adding dimethyl ether and ethanol to nonpremixed ethylene/air flames, Bennett, B.V. McEnally, C.S., Pfefferle, L.D., Smooke, M.D., Colket, M.B., *Combustion and Flame* 156, pp.1289-1302.

A study on the effect of experimental setup configuration on soot formation in a laminar premixed ethylene-air flame, (2009) G. Gothaniya, Lee, S.-Y., Menon, A.V., Iyer, S., Linevsky,

M.J., Santoro, R.J., Litzinger, T.A., Combustion Generated Fine Carbonaceous Particles, Karlsruhe University Press, pp.697-711.

Modeling Particle Formation and Growth in a Stirred Reactor and its Exhaust, (2009) Colket, M., Combustion Generated Fine Carbon Particles, Karlsruhe University Press.

Soot studies of laminar diffusion flames with recirculation zones. William Roquemore, Vish Katta, Scott Stouffer, Vince Belovich, Robert Pawlik, Mike Arstingstall, Garth Justinger, James Gord, Amy Lynch, Joe Zelina, Sukesh Roy, Proceedings of the Combustion Institute, 32: 729-736 (2009).

Impact of soot on flame flicker. Viswanath Katta, William M. Roquemore, Arvind Menon, Seong-Young Lee, Robert J. Santoro, Thomas A. Litzinger, Proceedings of the Combustion Institute, 32: 1343-1350 (2009).

Computational and experimental Investigation of the interaction of soot and NO in coflow diffusion flames, Connelly, B.C., Long, M.B., Smooke, M.D., Hall, R.J., and Colket, M.B., Proceedings of Combustion Institute, 32:777-784 (2009).

Fuel additive effects on soot across a suite of laboratory devices, part 1: Ethanol  
Litzinger, T.; Colket, M.; Kahandawala, M.; Katta, V.; Lee, S.-Y.; Liscinsky, D.; McNesby, K.; Pawlik, R.; Roquemore, M.; Santoro, R.; Sidhu, S.; Stouffer, S.; Wu, J. Source: Combustion Science and Technology, v 181, n 2, p 310-328, February 2009.

Calculation of multidimensional flames using large chemical kinetics, Katta, Viswanath R.; Roquemore, William M. Source: AIAA Journal, v 46, n 7, p 1640-1650, July 2008.

Fuel Additive Effects on Soot Across a Suite of Laboratory Devices, Part 2: Nitroalkanes, T. Litzinger; M. Colket; M. Kahandawala; S.-Y. Lee; D. Liscinsky; K. McNesby; R. Pawlik; M. Roquemore; R. Santoro; S. Sidhu; S. Stouffer: Combustion Science and Technology, 183:8, pp 739-754 (2011).

Experimental and Computational studies of oxidizer and fuel side addition of ethanol to opposed flow air/ethylene flames, Kevin L. McNesby; Andrzej W. Miziolek; Thuvan Nguyen; Frank C. Delucia; R. Reed Skaggs; Thomas A. Litzinger: Combustion and Flame, 142, pp 413-427 (2005).

High-speed two-camera imaging pyrometer for mapping fireball temperatures, John M. Densmore; Barrie E. Homan; Matthew M. Biss; Kevin L. McNesby: Applied Optics, v. 50 No. 33, pp 6267 (2011).

Effects of m-xylene addition on aromatics and soot in laminar, N<sub>2</sub>-diluted ethylene co-flow diffusion flames from 1 to 5 atm; Geraldine Mouis, et. al. Combustion and Flame, paper in review (2011).

### *Conference Papers*

Lean blowout limits for JP-8 surrogates and their parent components, V. R. Katta, T. Newman-Lehman, K. Seshadri, W. M. Roquemore, "AIAA-2011-0413, Aerospace Sciences Meeting, Orlando, FL, Jan. 4-7, 2011.

Infrared Imaging, Computations, and Tomography of Bluff Body Stabilized Laminar Diffusion Flames, Brent A. Rankin, David L. Blunck, Viswanath R. Katta, Scott D. Stouffer, Jay P. Gore, AIAA Paper 2011-0690, 49<sup>th</sup> Aerospace Sciences Meeting, Orlando, FL, Jan. 4-7, 2011.

A Shock Tube Experimental Study and Modeling of m-xylene Ignition Delay, Saxena, S., Flora, G., Kahandawala, M., and Sidhu, S., (2011) 49th AIAA Aerospace Sciences Meeting including the New Horizons Forum and Aerospace Exposition, Orlando FL, Jan 2011.

Ignition Delay times of a Range of Alternate Jet-Fuels and Surrogate Fuel Candidate Hydrocarbons under Fuel-Lean Conditions: a Shock Tube Study, Balagurunatham, J., Flora, G., Saxena, S., Kahandawala, M., Sidhu, S., DeWitt, M. and Corporan, E., (2011) 49th AIAA Aerospace Sciences Meeting including the New Horizons Forum and Aerospace Exposition., Orlando FL, Jan 2011.

Experimental and numerical studies on JP-8 flames in centerbody burner, V. R. Katta, A. O'Neil, S. Stouffer, W. M. Roquemore, Paper No. 2D17, Proceedings of the 7th US National Meeting of the Combustion Institute, March 20-23, 2011, Atlanta, GA.

Role of autoignition in stabilizing flames with recirculation zones, V. R. Katta and W. M. Roquemore, 13<sup>th</sup> International Conference on Numerical Combustion, Corfu, Greece, April 27-29, 2011.

Characterization of m-xylene combustion products: A shock tube study, Flora, G., Nagulappali, A., Saxena, S., Kahandawala, M. S. P., and Sidhu, S. S., (2011) poster appearing in 7th International Conference on Chemical Kinetics, July 10-14, 2011, MIT, Cambridge, MA.

Characterization of n-dodecane and n-dodecane/ m-xylene combustion products: A shock tube study, Flora, G., Nagulappali, A., Saxena, S., Kahandawala, M. S. P., and Sidhu, S. S., (2011) poster appearing in 7th International Conference on Chemical Kinetics, July 10-14, 2011, MIT, Cambridge, MA.

Investigation of Ignition Delay Time for n-Dodecane and n-Dodecane/m-Xylene Mixtures, Flora, G., Saxena, S., Kahandawala, M. S. P., and Sidhu, S. S., (2011) " 7th U.S. National Combustion Meeting, March 20-23, 2011 Georgia Institute of Technology Atlanta GA.

Simulation of Reflected Shock Combustion Experiments Using Multiple Computational Approaches, Flora, G., Nagulappali, A., Saxena, S., Kahandawala, M. S. P., and Sidhu, S. S., (2011) 7th U.S. National Combustion Meeting, March 20-23, 2011 Georgia Institute of Technology Atlanta GA.

Calculation of JP-8 jet diffusion flame using a semi-detailed chemical mechanism, V. R. Katta, W. M. Roquemore, Paper No. C10-33, Proceedings of the 2010 Technical Meeting of the Central States Section of the Combustion Institute, Urbana, IL, March 21-23, 2010.

Performance of JP-8 surrogate models in predicting laboratory flames, V. R. Katta, T. Newman-Lehman, K. Seshadri, J. Zelina, W. M. Roquemore, "AIAA-2010-950, Aerospace Sciences Meeting, Orlando, FL, Jan. 4-8, 2010.

Liftoff and blowout of heptane jet diffusion flame, V. R. Katta, T. Newman-Lehman, K. Seshadri, W. M. Roquemore, Paper No. C10-32, Proceedings of the 2010 Technical Meeting of the Central States Section of the Combustion Institute, Urbana, IL, March 21-23, 2010.

A Shock Tube Experimental and Kinetic Modeling of M-Xylene using a Modified Chemkin Program and 1-D CFD, Saxena, S., Flora, G., Kahandawala, M., and Sidhu, S. (2010) Poster presentation at 33<sup>rd</sup> Symposium (International) on Combustion, 2010, Beijing, China.

Experimental Study and Modeling of Shock Tube Ignition Delay Times for M-Xylene–Oxygen–Argon Mixtures, Saxena, S., Kahandawala, M., and Sidhu, S., (2010) " Proceedings of the 2010 Technical Meeting of the Central States Section of The Combustion Institute, University of Illinois at Urbana Champaign, Mar 2010.

Performance of JP-8 surrogates and parent species in a swirl combustor, V. R. Katta, W. M. Roquemore, GT2010-22301, ASME Turbo Expo 2010: Power for Land, Sea and Air, Glasgow, UK, June 14-18, 2010.

An Experimental Study of Premixed m-Xylene/Air and n-Dodecane/m-Xylene/Air Flames, Ji, C., Moheet, A., Wang, Y.L., Colket, M., Wang, H., Egolfopoulos, F.N., 6th U.S. National Combustion Meeting, Ann Arbor, Michigan, May 18-20, 2009.

Dynamics of lifted flame supported by a recirculation zone, Viswanath Katta, William Roquemore, Scott Stouffer, 6th U.S. National Combustion Meeting, Ann Arbor, Michigan, May 18-20, 2009.

Sooting characteristics of partially premixed flames in centerbody burner. Viswanath Katta, Scott Stouffer, Robert Forlines, Wesley Anderson, Zoseph Zelina, 6th U.S. National Combustion Meeting, Ann Arbor, Michigan, May 18-20, 2009.

Sooting Characteristics of Partially Premixed Flames in Centerbody Burner, V. R. Katta, R. A. Forlines, W. M. Roquemore, W. S. Anderson, J. Zelina, J. R. Gord, S. D. Stouffer, S. Roy , " Paper No. 31E4, Presented at the 6th US National Meeting of the Combustion Institute, May 18-20, 2009, Ann Arbor, MI.

Ignition of Methane-Hydrogen and Heptane-Hydrogen Mixtures at High Pressure, B. D. Adhikary, S. K. Aggarwal, V. R. Katta, " Paper No. 13F4, Presented at the 6th US National Meeting of the Combustion Institute, May 18-20, 2009, Ann Arbor, MI.

Cumulative Effect of Parent Species in a Surrogate Mixture on Flame Extinction, V. R. Katta, W. M. Roquemore, AIAA Paper 2009-4969, Presented at the 45th Joint Propulsion Conference, August 3-5, 2009, Denver, CO.

Evaluation of Chemical Kinetics Models in Predicting Heptane-Air Partially Premixed Flames, S. K. Aggarwal, V. R. Katta, AIAA Paper 2009-5521, Presented at the 45th Joint Propulsion Conference, August 3-5, 2009, Denver, CO.

Combustion of JP-8 surrogate and parent components in centerbody burner, V. R. Katta, W. M. Roquemore, " Proceedings of the 2009 Fall Technical Meeting of the Eastern States Section of the Combustion Institute, College Park, MD, October 18-21, 2009.

Flame flicker in high pressure diffusion flames. A. Menon, S.-Y. Lee, S. Iyer, T. Litzinger, R. Santoro, Poster presentation at 32<sup>nd</sup> Symposium (International) on Combustion, 2008.

Ignition Delay in Combustion of Ethylene: A Shock Tube Study, Saxena, S., Kahandawala, M., and Sidhu, S., (2009) Proceedings of Fall Technical Meeting of the Eastern States Section of the Combustion Institute, University of Maryland College Park, October 2009.

Impact of Pressure on Hydrocarbon Emissions and Soot Formation in the Combustion of Ethylene: A Shock Tube Study, Saxena, S., Kahandawala, M., and Sidhu, S., (2009) Proceedings of Fall Technical Meeting of the Eastern States Section of the Combustion Institute, University of Maryland College Park, October 2009.

Pressure effects on ignition delay, soot and hydrocarbon emissions from ethylene combustion. S. Saxena, M.P.S. Kahandawala, S.S. Sidhu, Poster presentation at 32<sup>nd</sup> Symposium (International) on Combustion, 2008.

Calculation of multidimensional flames using large chemical kinetics, Katta, Viswanath R.; Roquemore, William M. Source: Collection of Technical Papers - 37th AIAA Fluid Dynamics Conference, v 3, p 2065-2079, 2007, Collection of Technical Papers - 37th AIAA Fluid Dynamics Conference.

Development of an experimental database and kinetic models for surrogate jet fuels Colket, Meredith; Edwards, Tim; Williams, Skip; Cernansky, Nicholas P.; Miller, David L.; Egolfopoulos, Fokion; Lindstedt, Peter; Seshadri, Kalyanasundaram; Dryer, Frederick L.; Law, Chung K.; Friend, Daniel; Lenhert, David B.; Pitsch, Heinz; Sarofim, Adel; Smooke, Mitchell; Tsang, Wing Source: Collection of Technical Papers - 45th AIAA Aerospace Sciences Meeting, v 14, p 9446-9466, 2007, Collection of Technical Papers - 45th AIAA Aerospace Sciences Meeting.

Experimental and Numerical Studies of Centerbody Flames, William Roquemore, Vish Katta, Vince Belovich, Robert Pawlik, Amy Lynch, Scott Stouffer, Mike Arstingstall, Garth Justinger, Joe Zelina, Sukesh Roy, and James Gord, Proceedings of 5<sup>th</sup> US Combustion Meeting, March 2007.

Evolution of Particle Size Distributions in a Gas Turbine Combustor, M. Colket and S. Zeppieri, SAE 2007 AeroTech Congress & Exhibition, September 17 – 20, 2007, Los Angeles, California, USA

The Effects of Oxygenated Compounds on PAH and Soot across a Suite of Laboratory Devices, Litzinger, T.; Colket, M.; Kahandawala, M.; Katta, V.; Lee, S.-Y.; Liscinsky, D.; McNesby, K.; Pawlik, R.; Roquemore, M.; Santoro, R.; Sidhu, S.; Stouffer, S.; Wu, J., Proceedings of 5<sup>th</sup> US Combustion Meeting, March 2007.

The Effects of Nitrogen-containing Compounds on PAH and Soot across a Suite of Laboratory Devices, Colket, Litzinger, T.; M.; Kahandawala, M.; Katta, V.; Lee, S.-Y.; Liscinsky, D.; McNesby, K.; Pawlik, R.; Roquemore, M.; Santoro, R.; Sidhu, S.; Stouffer, S.; Proceedings of 5<sup>th</sup> US Combustion Meeting, March 2007.

The Effects of Phosphorus Compounds on PAH and Soot across a Suite of Laboratory Devices, Sidhu, S., Colket, M.; Katta, V.; Liscinsky, D.; Litzinger, T.; McNesby, K.; Roquemore, M.; Santoro, R.; Stouffer, S.; Proceedings of 5<sup>th</sup> US Combustion Meeting, March 2007.